NATIONAL TECHNICAL UNIVERSITY of ATHENS

SCHOOL OF MECHANICAL ENGINEERING

THERMAL ENGINEERING DEPARTMENT

INTERNAL COMBUSTION ENGINES LABORATORY

Development and Evaluation of a Semi–empirical Multi–zone Thermodynamic Model for the Estimation of Nitric Oxide Emissions and Formation History in Diesel Engines Using the Measured Cylinder Pressure Trace.

DOCTORAL DISSERTATION:

Savva S. Nicholas

Dipl. Mechanical Engineer NTUA

SUPERVISOR:

Dr. D. T. Hountalas

NTUA Professor

Athens, June 2015

NATIONAL TECHNICAL UNIVERSITY of ATHENS

SCHOOL OF MECHANICAL ENGINEERING

THERMAL ENGINEERING DEPARTMENT

INTERNAL COMBUSTION ENGINES LABORATORY

Development and Evaluation of a Semi–empirical Multi–zone Thermodynamic Model for the Estimation of Nitric Oxide Emissions and Formation History in Diesel Engines Using the Measured Cylinder Pressure Trace.

DOCTORAL DISSERTATION:

Savva S. Nicholas

Dipl. Mechanical Engineer NTUA

DOCTORAL SUPERVISORY COMMITTEE:

1. D.T. Hountalas, Prof. NTUA (Supervisor)
2. C.D. Rakopoulos, Prof. NTUA
3. M.A. Founti, Prof. NTUA

DOCTORAL EXAMINATION COMMITTEE:

1. D.T. Hountalas, Prof. NTUA (Supervisor)
2. C.D. Rakopoulos, Prof. NTUA
3. M.A. Founti, Prof. NTUA
4. K.A. Antonopoulos, Prof. NTUA
5. E.G. Giakoumis, A. Prof. NTUA
6. S. Karellas, A. Prof. NTUA
7. R.G. Papagiannakis, A. Prof. HAFA

Athens, June 2015

The presented research study was supported from **Alexander S. Onassis Public Benefit Foundation** (56, Amalia str., 10558 Athens) by providing to the author a four year full scholarship (1st Oct. 2010 – 30th Sept. 2014) and from Cyprus Scholarship Foundation (7, Florinis str., 1687 Nicosia) for providing to the author a three year complementary scholarship.

Η παρούσα διδακτορική διατριβή υποστηρίχθηκε οικονομικά από το κοινωφελές ίδρυμα **Αλέξανδρος Σ. Ωνάσης** (Αμαλίας 56, 10558 Αθήνα) παρέχοντας στον συγγραφέα τετραετή πλήρες υποτροφία (1η Οκτ. 2010 – 30η Σεπτ. 2014) και από το ίδρυμα κρατικών υποτροφιών Κύπρου παρέχοντας στον συγγραφέα τριετή συμπληρωματική υποτροφία.

ACKNOWLEDGMENTS

In the present research study, a simplified, semi–empirical, multi–zone thermodynamic model for the estimation of Nitric Oxide emissions and formation history in Diesel engines utilizing the actual in–cylinder pressure was developed, evolved and implemented on various types of Diesel engines. This research was attained in a time period between January 2010 and May 2015 at the Internal Combustion Engines Lab of Mechanical Engineering School of National Technical University of Athens.

At this point, I would like to express my gratitude to **Alexander Onassis Public Benefit Foundation** for providing me a four year full scholarship (1st Oct. 2010 – 30th Sept. 2014). Thanks are also attributed to the Cyprus Scholarship Foundation for providing me a three year complementary scholarship. Without this funding, I would not been able to conduct my Ph.D. research.

Furthermore, I would like to express my appreciation and thankfulness to my supervisor Professor Dimitrios Hountalas who guide me throughout this research providing me useful information, valuable advices and guidelines stemming from his many years of experience and deep knowledge in the field of internal combustion engines. He also provided me with the experimental data derived from his cooperation with research organizations, engine manufactures and on–board measurements on ships and power plants.

Many thanks are also attributed to the members of my Doctoral Supervisory Committee, Professor Constantine Rakopoulos and Professor Maria Founti for their precious help.

Finally, I would like to thank my colleagues and friends: Sakellaridis Nikolaos, Raptotasios Spyros, Zovanos George, Antonopoulos Antonis and Dimaratos Athanasios for their help on this research by providing me with their scientific opinion and for the constructive conversations we had on the field of our research.

Savva Nicholas

Athens, April, 2015

TABLE OF CONTENTS

ACKNOWLEDGMENTS ..... **I**

TABLE OF CONTENTS ..... **III**

ABSTRACT **1**

THESIS STRUCTURE **3**

NOMENCLATURE **5**

Acronyms 5

Abbreviations 6

Subscripts 7

Superscripts 8

Greek Symbols 9

CHAPTER 1 INTRODUCTION **11**

1.1 Diesel Engines 11

1.2 Combustion and NO_x Formation in DI Diesel Engines 11

1.2.1 Brief Description of the Diesel Thermodynamic Cycle and Combustion in DI Diesel Engines 12

1.2.2 The Theory for NO_x Formation in DI Diesel Engines 18

1.3 Pollution from NO_x Emissions and Future Legislation NO_x Limits for Diesel Engines 20

1.3.1 Adverse Effects of NO_x on Human Health and Environment 20

1.3.2 NO_x Legislation for Diesel Engines 21

1.4 Methodologies for NO_x Emissions Abatement 24

1.4.1 Introduction 24

1.4.2 Primary/In–Cylinder Measures for NO_x Control 25

1.4.2.1 General Description of the In–Cylinder Methods for NO_x Control 25

1.4.2.2 Fuel Injection Strategy for NO_x Control 25

1.4.2.3 Valve Timing Strategy–Compression Control–Miller Cycle Concept for NO_x Control 26

1.4.2.4 Temperature Control by using Water Injection for NO_x Control 27

1.4.2.5 Exhaust Gas Recirculation for NO_x Control 29

1.4.3 Secondary/After–Treatment Methods for NO_x Control 32

1.4.3.1 Selective Catalytic Reduction 32

1.4.3.2 Lean NO_x Trap 34

1.5 Motivation and Objective of the Present Dissertation 34

CHAPTER 2 LITERATURE REVIEW – EXISTING MODELS FOR NO_x PREDICTION **39**

2.1 Introduction 39

2.2 Multi–zone, Three–dimensional, Phenomenological Models 40

2.2.1.1 Introduction 40

2.2.1.2 Hiroyasu 3D Multi–Zone Phenomenological Model 41

2.2.1.3 NTUA Multi–Zone three Dimensional Phenomenological Model 42

2.3 Single–zone, Empirical and Semi–Empirical Models 44
2.3.1.1 Introduction 44
2.3.1.2 Callahan Empirical NO_x Model 45
2.3.1.3 P–Φ Empirical Models for NO_x at Flame Front 45
2.3.1.4 Gartner Semi–Empirical NO_x Model 45
2.3.1.5 Wu and Peterson Semi–Empirical NO_x Model 46
2.3.1.6 Miller Empirical NO_x Model 47
2.3.1.7 Park Semi–Empirical, Real–Time NO_x Model 47
2.3.1.8 D'Ambrosio Control–Oriented, Semi–Empirical NO_x Model 48
2.3.1.9 Asprion Empirical–Phenomenological NO_x Model 50
2.3.1.10 Timoney Semi–Empirical NO_x Model 52
2.3.1.11 Guardiola Engine Control Oriented NO_x Model 54
2.4 Zero–dimensional, Semi–Empirical/Phenomenological, Multi–zone, Thermodynamic Models 55
2.4.1.1 Introduction 55
2.4.1.2 Egnell Zero–Dimensional Multi–Zone NO Model 56
2.4.1.3 Horrocks Quasi–Dimensional Phenomenological Diesel Engine Exhaust Model 58
2.4.1.4 Weisser Multi–Zone Quasi–Dimensional Combustion and Emissions Model . 59
2.4.1.5 Diotallevi Multi–Zone NO_x Model 61
2.4.1.6 Seykens Physically–Based Multi–Zone Phenomenological Model 63
2.4.1.7 Andersson Multi–Zone Physically–Based Real–Time NO_x Model 65
2.4.1.8 Hernandez Phenomenological Multi–Zone Combustion Model 68
2.4.1.9 Maiboom Phenomenological, Six–Zone Combustion Model 68
2.4.1.10 Ericson Zero–Dimensional Two–zone Quasi–Steady Combustion and Gas Exchange Model 70
2.4.1.11 Wilhelmsson Two–Zone Physically Based NO_x Model 72
2.4.1.12 Scappin NO_x and Engine Performance Model for Marine Engines 74
2.4.1.13 Goldsworthy Thermodynamic NO_x Model for Marine Engines 75
2.4.1.14 Borkowski Semi–Empirical, Multi–Zone, Phenomenological NO_x Model for Marine Engines 77
2.5 The Outcome of the Literature Review 78

CHAPTER 3 DEVELOPMENT OF THE PROPOSED MODEL 81

3.1 Introduction 81
3.2 Pressure Trace Processing 82
3.2.1 The Motivation to Use the Measured Pressure Trace 82
3.2.2 In–Cylinder Pressure Measurement 82
3.2.3 Smoothing the Measured Pressure Trace 84
3.3 Prerequisite Calculations for the Heat Release Rate and NO models 86
3.3.1 Required Inputs for the Model and Initial Conditions 86
3.3.2 Fuel Mass Distribution to each Engine Cylinder per Cycle 87
3.3.3 Intake Air Mass Flow Rate 88
3.3.4 Calculation of Cylinder Volume, Wall Area and Piston Speed as Functions of Piston Position 89

3.3.5 Calculation of Initial Conditions for Large–Scale, 2–Stroke Engines – Scavenging Model Description 90
3.3.6 Calculation of Initial Conditions for Large–Scale 4–Stroke Engines 93
3.3.7 Calculation of Initial Conditions for Automotive 4–Stroke Engines 94
3.4 Heat Release Rate and Fuel Burnt Rate Calculation 95
3.4.1 Importance of the Heat Release Rate Analysis 95
3.4.2 Analytical Description of the Heat Release Rate Model 97
3.4.3 Heat Release Rate Model Flow Chart 101
3.4.4 Initial Calculation of Start of Combustion (SOC) 102
3.4.5 Single–Zone Combustion Concept 105
3.4.6 End of Combustion Estimation 106
3.4.7 Heat Exchange through the Cylinder Wall – Annand Model Description 107
3.5 Description of the Proposed Nitric Oxide Model 110
3.5.1 Presentation of the Model's Concept 110
3.5.2 Unburnt Zone Evolution inside the Combustion Chamber 114
3.5.3 Combustion Zone Generation 116
3.5.4 Combustion Zone Evolution inside the Combustion Chamber 118
3.5.5 Calculation of Zone Composition before and after Combustion 119
3.5.6 Chemical Dissociation Scheme 122
3.5.7 Nitric Oxide Formation Mechanism 128
3.5.8 Calculation of the Zone Equivalence Ratio Φ 134
3.5.9 The Flow–Chart of the Proposed NO_x Model 144
3.5.10 Calibration of the NO_x Model 145

CHAPTER 4 APPLICATION OF THE PROPOSED MODEL 147

4.1 Model Application on Large–Scale Diesel Engines 147
4.1.1 Description of the Test Engines 147
4.1.2 Test Cases Examined 148
4.1.3 NO_x Variation with Engine Power 149
4.1.3.1 Stationary Power Plant Engines 149
4.1.3.2 Marine 2–Stroke Main Engines 151
4.1.3.3 Marine 4–Stroke Auxiliary Engines 154
4.1.4 Evaluation of Model Capability to Predict NO_x with the Start Of fuel Injection (SOI) Variation 155
4.1.4.1 Stationary 2–stroke, power plant engines 155
4.1.4.2 Marine 2–stroke main engines 156
4.1.5 NO_x Variation with Change of Fuel Type from HFO to DFO 157
4.1.6 Overall Results and Statistical Analysis 164
4.2 Model Application on Automotive Engines 166
4.2.1 Description of the Test Engines 166
4.2.2 Test Cases Examined 166
4.2.3 Heavy–Duty Truck Diesel Engine (Engine D1) 167
4.2.3.1 Prediction of NO Emissions for the Extended European Stationary Cycle (EESC) 167
4.2.3.2 NO Variation with Engine Settings 171
4.2.3.3 Overall Results and Statistical Analysis 173

4.2.4 Light–Duty Automotive Diesel Engine (Engine D2) 174
4.2.4.1 NO Variation with EGR 174
4.2.4.2 NO Variation with Fuel Injection Pressure 176
4.2.4.3 NO Variation with SOI Setting 179
4.2.4.4 NO Variation with Intake Manifold Pressure 181
4.2.4.5 Overall Results and Statistical Analysis 182
4.3 NO_x Formation History inside the Combustion Chamber 184
4.3.1 Introduction 184
4.3.2 NO_x Formation History with Load Variation 185
4.3.2.1 Large–Scale DI Diesel Engines 185
4.3.2.2 Heavy–Duty Automotive DI Diesel Engine 189
4.3.2.3 Light–Duty Automotive DI Diesel Engine 190
4.3.3 NO_x Formation History with SOI Variation 191
4.3.3.1 Large–Scale DI Diesel Engines 191
4.3.3.2 Heavy–Duty Automotive DI Diesel Engine 193
4.3.3.3 Light–Duty Automotive DI Diesel Engine 194
4.3.4 NO_x Formation History with EGR Rate Variation 195
4.3.4.1 Heavy–Duty Automotive DI Diesel Engine 195
4.3.4.2 Light–duty automotive DI Diesel engine 196
4.3.5 NO_x Formation History with Fuel Injection Pressure Variation 197
4.3.5.1 Heavy–Duty Automotive DI Diesel Engine 197
4.3.5.2 Light–Duty Automotive DI Diesel Engine 199
4.3.6 NO_x Formation History with Intake Manifold Pressure Variation 200
4.3.6.1 Heavy–Duty Automotive DI Diesel Engine 200
4.3.6.2 Light–Duty Automotive DI Diesel Engine 201
4.3.7 General Outcomes Regarding NO Formation History inside the Combustion Chamber 202
4.4 Evaluation of Model Computational Time 203
4.4.1 Parameters Affecting Model Computational Time 203
4.4.2 Zone Equivalence Ratio (Φ_z) Effect 204
4.4.3 Crank Angle Calculation Step Effect 204
4.4.4 NO_x Integration Calculation Step Effect 205
4.4.5 Cylinder Number Effect 206
4.4.6 Trapped Mass Amount Effect 207
4.4.7 Computer System Power Effect 209

CHAPTER 5 SUMMARY AND CONCLUSIONS 211
5.1 Summary 211
5.2 Justification of the Dissertation 213
5.3 Conclusions of the Dissertation 215
5.4 Novelty Features of the Present Dissertation 218
5.5 Future Work 219
5.6 Publications 222

REFERENCES 225

APPENDIX **241**

a. Calculation of Exhaust Mass Flow with Carbon Balance Method 241

b. Conversion of NO_x from [ppmv] Dry to [g/h] Wet / IMO Concept 242

c. Conversion of NO_x [g/h] Wet to [g/kWh] and [g/kg fuel] 243

d. NASA Polynomials for Constant Pressure Specific Heat Capacity, Enthalpy and Entropy 243

e. Calculation of Gas Properties (k, μ) using NASA Polynomials 247

f. Finite Differences for the Calculation of Pressure Derivatives 248

g. Modified False Position Method for Root Finding 248

CURRICULUM VITAE **251**

ΕΥΧΑΡΙΣΤΊΕΣ **259**

ΠΕΡΊΛΗΨΗ **261**

ΕΚΤΕΤΑΜΈΝΗ ΠΕΡΊΛΗΨΗ **263**

ΚΕΦΆΛΑΙΟ 1 ΕΙΣΑΓΩΓΉ **263**

Κινητήρες Diesel 263

Θερμοδυναμικές Διαδικασίες, Καύση και Σχηματισμός NOx στους Κινητήρες Diesel 263

Δυσμενείς Συνέπειες από τις Εκπομπές NO_x 266

Όρια για τις εκπομπές NO_x 267

Τεχνικές Λύσεις για την μείωση των NO_x 269

Ο Ρόλος των Μοντέλων Προσομοίωσης στην Προσπάθεια περιορισμού των Εκπομπών NO_x 270

Κίνητρο και Στόχος της Διατριβής 272

ΚΕΦΆΛΑΙΟ 2 ΕΠΙΣΚΌΠΗΣΗ ΒΙΒΛΙΟΓΡΑΦΊΑΣ – ΔΙΑΘΈΣΙΜΑ ΜΟΝΤΈΛΑ ΠΡΌΒΛΕΨΗΣ NO_x . 273

Πολυζωνικά, Τρισδιάστατα (*3D*) Φαινομενολογικά Μοντέλα 273

Μονοζωνικά, Εμπειρικά και Ημιεμπειρικά Μοντέλα 274

Μηδενδιάστατα, Ημιεμπειρικά/Φαινομενολογικά, Πολυζωνικά, Θερμοδυναμικά 274

ΚΕΦΆΛΑΙΟ 3 ΑΝΆΠΤΥΞΗ ΤΟΥ ΠΡΟΤΕΙΝΌΜΕΝΟΥ ΜΟΝΤΈΛΟΥ **275**

Πλεονεκτήματα από τη Χρήση του Δυναμοδεικτικού Διαγράμματος 275

Δεδομένα Εισόδου 277

Μοντέλο Ρυθμού Έκλυσης Θερμότητας (HRR) 282

Εντοπισμός της Έναυσης 284

Στοιχειομετρία της Καύσης 285

Εντοπισμός του Τέλους της Καύσης 286

Μοντέλα Συναλλαγής Θερμότητας 287

Μοντέλο υπολογισμού των NO 288

Υπολογισμός του Λόγου Ισοδυναμίας στις Ζώνες 293

Μοντέλο Χημικής Διάστασης 294

Μηχανισμός Σχηματισμού των NOx Zeldovich 295

Βαθμονόμηση του Μοντέλου 296

ΚΕΦΆΛΑΙΟ 4 ΕΦΑΡΜΟΓΉ ΤΟΥ ΠΡΟΤΕΙΝΌΜΕΝΟΥ ΜΟΝΤΈΛΟΥ **297**

Εφαρμογή του Μοντέλου σε Κινητήρες Μεγάλης Κλίμακας 297

Εφαρμογή του Μοντέλου σε Οδικούς Κινητήρες 305

Ιστορικό Σχηματισμού των NO 314

Υπολογιστικός Χρόνος..... 317

ΚΕΦΆΛΑΙΟ 5 ΣΥΜΠΕΡΆΣΜΑΤΑ 321

ABSTRACT

The objective of the present dissertation, is the development and evaluation of a simplified, semi–empirical, multi–zone, thermodynamic model for the prediction of tail–pipe NO_x emissions and history inside the combustion chamber, during the closed cycle of *DI* Diesel engines. The model is implementable on different engine configurations by using the measured cylinder pressure trace.

The motivation for this work, emerges from the requirement of the internal combustion engines industry to control pollutant emissions. This requirement is attributed to the strict legislation limits that the governments worldwide have adopted. One of the most affected engine type from this legislation is the *DI* Diesel engine because it is widely used in the transportation sector (maritime and automotive), in non–road application (heavy–duty industry), in power generation in distant/isolated areas and in the passenger car sector. Specifically, in the last sector, Diesel engines have gained important share against gasoline engines the last years. Moreover, one of the most important controlled pollutant, in these sectors, is NO_x. For these reasons, in the present work, the author focuses on the field of NO_x control in *DI* Diesel engines, targeting on the development and validation of a simplified model that can contribute to the deployment and application of NO_x control strategies.

A variety of simulation models exist which can predict performance and emissions of Diesel engines. These models are divided into three major categories:

1. Three dimensional models (i.e. *CDF*, spray phenomenological models).
2. Zero dimensional models (i.e. physical–thermodynamic models).
3. Statistical/empirical models.

The models of the first category, provide a detailed and strong physical (fundamental) description of the processes taking place inside the combustion chamber, but suffer from high complexity and computational cost. Because of these, this kind of models is inadequate for practical and real–time applications. The models of the second category make use of the basic thermodynamic laws and chemistry following a theoretical approach rather than a detailed spatial description of the combustion chamber processes. Their philosophy is to divide the in–cylinder charge into zones. Thus there exist models that make use one to multiple zones. Single zone models are not appropriate for NO_x emission prediction because they provide only the mean in–cylinder temperature which is too low to cause NO_x formation. The use of zero dimensional multi–zone models is a solution to this drawback. Nevertheless, the existing models of this kind, make use of semi–empirical or phenomenological correlations for the prediction of fuel distribution inside the zones, air entrainment, etc. which increase model's complexity, calibration effort and computational cost. The third category comprises models that make use of totally empirical correlations derived from experimental data processing. These models are usually applicable only on the engine type for which they have been developed and validated. Their implementation range, regarding engine operating points, is limited due to the lack of physical base. However, these modes are very simple and

provide directness (since they use actual engine operating data, e.g. from *ECU* and sensors) and very low computational cost.

Considering the advantages and disadvantages of the models of the aforementioned categories, it was decided to develop a model that combines the merits of the zero–dimensional multi–zone and empirical models in conjunction with the use of the measured pressure trace on which the most important phenomena taking place inside the combustion chamber are reflected on.

Thus, a new model for NO_x prediction for *DI* Diesel engines was developed and evaluated. The proposed model makes use of the engine's geometry data, measured in–cylinder pressure trace and basic engine operating parameters. Initially, it utilizes the measured pressure trace to estimate the fuel combustion rate via heat release rate analysis. From this, a temporal distribution of the burnt fuel is created in the engine cycle. Then, the resulting elementary fuel amounts burnt consecutively at each time instance and attributed to individual combustion zones, following a multi–zone approach. The amount of the requisite unburnt in–cylinder charge in each zone, is determined from the zone fuel–air equivalence ratio. This parameter is calculated from an empirical correlation developed in the present work and is assumed constant for all zones. This correlation involves engine operating parameters and data derived from the pressure trace processing and heat release rate analysis. The aforementioned parameter is considered constant during the engine cycle but varies with operating conditions, engine settings and engine type. Each zone, after its generation, behaves as a closed thermodynamic system and evolves inside the combustion chamber having its own history of chemical composition, temperature and volume, while maintaining the in–cylinder measured pressure prevailing at each crank angle step. The amount of NO_x formed inside each zone is calculated using the extended Zeldovich mechanism. The total amount of NO_x emissions at the engine exhaust is calculated from the sum of zone NO_x at exhaust valve opening. According to this concept, the model provides the time history (zonal and total) of NO_x formation inside the combustion chamber.

The proposed model has been validated and evaluated on various types of supercharged *DI* Diesel engines such as large–scale, *2*–stroke engines used for ship propulsion and stationary engines used for power generation, large–scale *4*–stroke engines used as auxiliary engines on ships or at power plants and a heavy and a light–duty *4*–stroke automotive engine, utilizing a total of *221* test cases. These cases correspond to various engine operating points and engine adjustments/settings. Thus, the ability of the model to predict the absolute NO_x values for each test case and capture the effect of the variation of these parameters on NO_x formation, has been examined. The parameters considered are the following:

- Engine load
- Engine speed.
- Fuel type.
- Injection timing.
- Exhaust gas recirculation (*EGR*) rate.
- Fuel injection pressure.
- Intake manifold pressure.

As revealed from the implementation of the model on the aforementioned extensive range of engine types and operating points, it is capable to predict NO_x emissions with

adequate accuracy for the majority of the test cases examined. The most important is its ability to capture the NO_x variation (i.e. trend) as engine parameters vary. The last is accomplished for various engine configurations without significant calibration effort, since only a single multiplier for each engine is used to correct the model's results. Another significant advantage of the proposed model is the low computational cost. These encourage its use for engine research, development and optimization in the scope of NO_x reduction, real–time/model–based and close–loop NO_x control, NO_x monitoring and verification.

THESIS STRUCTURE

In the first chapter of the present dissertation, a brief description of the Diesel engine and its advantages, is provided. At next the theory of combustion and NO_x formation inside the combustion chamber is presented and analyzed. To indicate the necessity for NO_x control enhancement, the adverse effects of NO_x pollution on human's health and environment are described. Due to these effects, the NO_x legislation limits for the maritime and automotive sector are steeply descending. These limits and the grade of their descent the last years are also presented. It follows a brief description of the current and future primary and after–treatment technologies for the NO_x control.

In the second chapter a comprehensive literature review is presented, for the simulation models that are commonly used for NO_x prediction. These models are categorized in three major categories according to their complexity, reliability and computational cost:

1) Multi–zone, three–dimensional phenomenological.
2) Single–zone, purely empirical and semi–empirical.
3) Zero–dimensional, semi–empirical/phenomenological, multi–zone, thermodynamic. Emphasis is given in the last category, in which the proposed model falls into.

The model is presented analytically in the third chapter. Initially a description of the cylinder pressure trace acquisition and processing is demonstrated. The calculation for the initial conditions, which are used in both, heat release and NO_x model, follows. Then, the methodology adopted for the calculation of: heat release rate, heat exchange with the cylinder wall, start and end of combustion and finally combustion rate, is comprehensively described. The NO_x model is analyzed at next, by presenting its main gist and concept and by describing the rationale followed for the combustion zones and the unburnt zone. The sub–models that are used for the NO_x calculation, namely the chemical dissociation scheme (for the calculation of equilibrium composition) and the extended Zeldovich mechanism (thermal NO_x calculation, i.e. NO), are also presented. The calibration of the model is described at last.

The results of the application of the proposed model are presented in the fourth chapter. At first, the NO_x predictions from the application on large–scale Diesel engines, where the capability of the model to capture the NO_x against engine load/speed variation, start of injection and fuel type variation, is examined. Then, the model is implemented on a heavy–duty truck engine and a light–duty passenger car engine, where the model's capability

to capture the *NO* against the variation of engine load, engine speed, injection timing, *EGR* rate, injection pressure and intake manifold (boost) pressure, is examined. From the results analysis, the ability of the model to capture the NO_x trends with the variation of the aforementioned parameters is proven. Furthermore, the statistical analysis of the results is presented, revealing adequate agreement between calculated and measured NO_x values. At last, an investigation for the *NO* formation history is conducted using the proposed model.

Eventually, in the last chapter (fifth), the summary and conclusions of this dissertation are presented. Also the development and novelty features of the proposed model, the proposed future work are presented and the scientific publications resulted from this work are listed.

NOMENCLATURE

Acronyms

ABDC After Bottom Dead Center
ACT Apparent Combustion Time
AFR Air to Fuel Ratio
AFT Adiabatic Flame Temperature
ASIC Application Specific Integrated Circuit
ATDC After Top Dead Center
BDC Bottom Dead Center
bsfc brake specific fuel consumption [g/kWh]
CA Crank Angle [° ABDC]
CASS Combustion Air Saturation System
CCAI Calculated Carbon Aromaticity Index
CFD Computational Fluid Dynamics
CGHR Cumulative Gross Heat Release [J]
CHR Cumulative Heat Release [J]
CN Cetane Number
CNHR Cumulative Net Heat Release [J]
COC Center Of Combustion [° ABDC]
CPU Central Processing Unit
CR Compression Ratio
CRL Connecting rod length [m]
DFO Diesel Fuel Oil
DI Direct Injection
DWI Direct Water Injection
ECAs Emission Control Areas
ECU Engine Control Unit
EESC Extended European Stationary Cycle
EGR Exhaust Gas Recirculation
EIAPP Engine International Air Pollution Prevention
EOBD End of Blow Down period [° ABDC]
EOC End Of Combustion [° ABDC]
EPA Environmental Protection Agency
EU European Union
EVC Exhaust Valve Closure [° ABDC]
EVO Exhaust Valve Opening [° ABDC]
FA Fresh Air
FPGA Field Programmable Gate Arrays
GPU Graphics Processing Unit
HAM Humid Air Motor
HCCI Homogenous Charge Compression Ignition
HFO Heavy Fuel Oil
HR Heat Release [J]

HRR Heat Release Rate [J/°]
ICE Internal Combustion Engines
IMO International Maritime Organization
IVC Intake Valve Closure [° ABDC]
IVO Intake Valve Opening [° ABDC]
LHV Lower Heating Value [J/kg]
LNT Lean NO_x Trap
LTC Low Temperature Combustion
MARPOL MARitime POLlution
MW Molecular Weight [kg/kmol]
NHRR Net Het Release Rate [J]
ODE Ordinary Differential Equation
PC Personal Computer
PCCI Premixed Charge Compression Ignition
PM Particulate Matter
RAM Random Access Memory
RG Residual Gas
RMSE Root Mean Square Error [%]
SAM Scavenging Air Moistening
SCR Selective Catalytic Reduction
SF Scaling Factor
SFWI Stratified Fuel Water Injection
SMD Sauter Mean Diameter
SOC Start Of Combustion [° ABDC]
SPC Scavenging Port Closure
SPO Scavenging Port Opening
STDV STandard DeViation
TC Turbo Charger
TDC Top Dead Center [180° ABDC]
US United States
VEC Variable Exhaust valve Closure
VGT Variable Geometry Turbine
VIT Variable Injection Timing
VVA Variable Valve Actuation
VVL Variable Valve Lift
VVT Variable Valve Timing
WaCoReG Water Cooled Residual Gas
WFE Water Fuel Emulsion

Abbreviations

A Area [m^2]
a, b, c Annand formula coefficients
c polynomial coefficients
C Sensor calibration constant [bar/V]
c_n Savitzky–Golay coefficients
comb. max maximum combustion pressure [Pa], [° ABDC]
compr. start start of compression [° ABDC]

cp	specific heat capacity at constant pressure [J/kmol/K] or [J/kg/K]
D	cylinder bore [m]
f	function
f_s	sampling rate frequency [Hz]
G	Gibbs free energy [J]
g	partial molar Gibbs function [J/kmol]
H	enthalpy [J]
h	specific enthalpy [J/kmol] or [J/kg]
hp	products enthalpy [J/kg] or [J/kmol]
hr	reactants enthalpy [J/kg] or [J/kmol]
i	current step, operating point sequence number
k	thermal conductivity [W/m/K], reaction rate constant [m^3/kmol/s]
Kp	equilibrium constants
M	chemical substance, third body element, total number of test cases
m	mass [kg], carbon (C) mass fraction in the fuel [kmol/kg fuel]
$\dot{m}$	*mass flow [kg/h]*
N	engine speed [rpm]
n	number (amount), molar amount [kmol], hydrogen (H) mass fraction in the fuel [kmol/kg fuel]
n_{cyl}	cylinder number
P	normalized pressure, Power [kW]
p	pressure [bar] or [Pa]
p	sulfur (S) mass fraction in the fuel [kmol/kg fuel]
Q	heat [J]
q	oxygen (O) mass fraction in the fuel [kmol/kg fuel]
R	crank radius [m], reaction rate
$\bar{R}$	universal constant for ideal gas 8314.47 [J/kmol/K]
R^2	coefficient of determination
r	nitrogen (N) mass fraction in the fuel [kmol/kg fuel]
Re	Reynolds number
S	Cylinder stroke [m], total entropy [J/K]
s	specific/molar entropy [J/kmol]
Sp	mean piston speed [m/°]
str.	number of strokes per engine cycle, equals *2* or *4* for *2* and *4*–stroke respectively
t	time [s]
T	Temperature [K]
Tp	products enthalpy [K]
V	Volume [m^3], Voltage [V]
v	specific volume [m^3/kg]
W	Window of values
x	piston displacement [m], mole fraction
y	mass fraction

Subscripts

$_0$	initial or reference value
$_{ABS}$	absolute
$_{air}$	air

amb	ambient
aver	average
b	burnt
beg	pegging point
c	clearance, conductivity
ch	charge
cyl	cylinder
dv	dynamic viscosity
diss	dissociation
eng	engine
eq	equilibrium
exh	exhaust
f	fuel
form	formation
G	gross
g	Gibbs
h	enthalpy
IA	Intake Air
IM	Intake Manifold
j	j^{th} chemical element/species
L	Left
m	cylinder sequence number
max	maximum
min	minimum
N	Net, Nominal
peg	pegging
r	reaction
R	Rig11ht
ref	reference
REL	relative
s	smoothed, entropy
sc	scavenging
sens	sensible
st	stoichiometric
t	sequence number of the test cases
tr	trapped
ub	unburnt
w	wall
z	zone, zone sequence number

Superscripts

-	reverse
+	forward
0	standard–state
eq	equilibrium
k	current iteration sequence number

Greek Symbols

γ	isentropic exponent, ratio of heat capacities (cp/cv)
$\Delta\theta$	crank angle interval, crank angle resolution [°]
$\delta\xi$	differential of the extent of reaction
η	efficiency
θ	crank angle [°]
μ	dynamic viscosity [Pa s], chemical potential [J/kmol]
ν	stoichiometric coefficient
ρ	density [kg/m^3]
σ	Stefan Boltzmann constant (σ=5.6704*10^{-8} [W/m^2 K^4])
Φ	fuel/air equivalence ratio

Chapter 1 INTRODUCTION

1.1 Diesel Engines

The Diesel engines are reciprocating internal combustion engines (*ICE*) converting the chemical energy of the fuel into useful work. These engines are commonly used in vehicles, non–road applications, marine and stationary applications (e.g. power generation). The Diesel engine was invented from the engineer Rudolf Diesel (*1858 – 1913*) in *1890*, who received a number of patents for his work [1,2,3,4]. His objective was to increase the efficiency of the existing type of engines (i.e. steam–engines) and to use low quality–distillation liquid fuel such as petroleum–fuel oil. He suggested to directly inject the fuel inside the combustion chamber at the appropriate instance during the compression phase, where the temperature of the trapped air is adequately high to cause auto–ignition of the injected fuel, avoiding the use of a spark–plug. This is the reason that Diesel engines are also called compression–ignition engines. Rudolf Diesel's patents were bought from MAN (Maschinenfabrik Augsburg Nürnberg) company and from Sulzer Brothers (*1893*) where his invention was further developed [5]. From these years until today, Diesel engines have significantly evolved and technologically improved in the section of power output, efficiency, emissions, manufacturing materials, control systems, etc.

Currently, the Diesel engine finds widespread application in both stationary and transportation powertrain systems. Due to its superior fuel efficiency (up to *55%*), durability, reliability, flexibility, long lifetime, high torque output and the ability to use a variety of low–cost fuels, the Diesel engine has a prevailing role in transportation (i.e. cars, trucks, locomotives, ships, etc.), heavy–industry (factories, quarries, mines, construction, etc.) and power generation applications. Indicatively, it is mentioned that more that *95%* of maritime applications make use of Diesel engines [6,7].

However, the Diesel engine still remains a significant pollution source, especially concerning nitrogen oxides (NO_x) and particulate emissions (*PM*). To overcome this, researchers and engineers are intensively working on the optimization of the combustion processes to increase engine efficiency, improve performance and reduce pollutant emissions to comply with increasingly stringent environmental regulations (i.e. EURO V/VI (*EU*), Stage III/IV (*EU*), TIER II/III (*IMO*), etc.)

1.2 Combustion and NO_x Formation in DI Diesel Engines

In the present section, the combustion and NO_x formation processes taking place inside the combustion chamber of direct injection (*DI*) Diesel engines are briefly described.

1.2.1 Brief Description of the Diesel Thermodynamic Cycle and Combustion in DI Diesel Engines

DI Diesel engines are divided into two major categories: the *2*–stroke and the *4*–stroke engines. The engines of the first category are mostly used in large–scale applications (i.e. vessel propulsion and power plants) while the *4*–stroke Diesels are used in automotive sector, heavy–industry, locomotive and smaller power generation applications. Currently, both *2*–and *4*–stroke Diesel engines are usually supercharged [8,9,10]. The essential difference of the thermodynamic cycle of the aforementioned Diesel types is the intake and exhaust phases, namely the scavenging procedure which determines the amount and the composition of the trapped charge. In *4*–stroke engines, intake air is forced into the cylinder through the intake valves forced from the compressor or due to the vacuum resulted from the downward piston move. After combustion, the exhaust gasses are forced outside the cylinder through the exhaust valves mostly due to the upward piston move. In *2*–stroke engines, the compressed air enters the cylinder through intake ports when the piston is in its lower position. The compressed intake air displaces the exhaust gasses from the previous cycle throughout the cylinder from the exhaust valve or exhaust ports, utilizing the pressure difference between intake and exhaust manifolds/receivers. However, the processes taking place during the closed cycle is quite similar for both engine categories.

After intake valve/s or ports closure, the trapped charge is compressed and its temperature rises. At the appropriate time instant, usually when the piston arrives slightly before top dead center (*TDC*) (or slightly after *TDC*), fuel is injected inside the combustion chamber at high–pressure through the extremely small orifices of the injector to form the fuel spray (fuel atomization). Then, the fuel evaporates and is mixed with air and then is auto–ignited due to the high prevailing temperature. This causes a rapid increase of the in–cylinder pressure which then forces the piston downwards and hence useful work is produced. The production of work (positive work) initiates from the top dead center (*TDC*) until the time where the piston reaches the lowest point of its stroke, namely bottom dead center (*BDC*). The exhaust procedure begins when the exhaust valves/ports open. At next, a schematic description of both Diesel thermodynamic cycles, *2* and *4*–stroke, is provided, where the aforementioned processes are depicted.

In Fig. 1.1 and 1.2, are depicted the indicative thermodynamic cycles, in the form of pressure–volume (*p*–*V*) diagram for two engines, a *4*–stroke and a *2*–stroke. These diagrams are derived from measured in–cylinder pressure traces. These pressure traces correspond to a *4*–stroke passenger car *DI* Diesel engine (Fig. 1.1) and a *2*–stroke vessel propulsion *DI* Diesel engine (Fig. 1.2). The experimental data from the specific engines were utilized in the present work. Both engines are supercharged. The two cycles are quite similar

with the exception of intake and exhaust procedures where their differences are clear. Moreover, the gradient of the *log(p)–log(V)* diagram at compression and expansion phase provides an indication for the corresponding polytropic index *n* ($pV^n=const.$) of the charge.

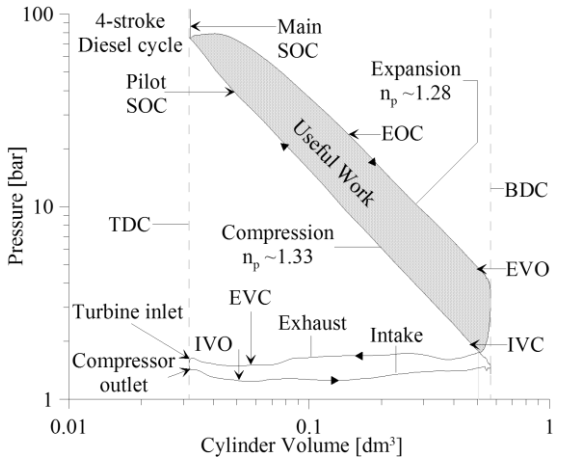

Figure 1.1: p–V diagram (on log. axis) of a light–duty, supercharged, common rail, DI, 4–stroke Diesel engine using pilot injection of a passenger car running on 2500 rpm and mid–load (31.3 kW).[1]

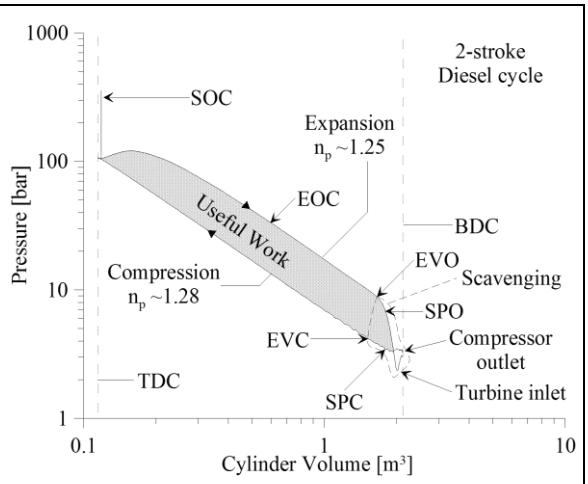

Figure 1.2: p–V diagram (on log. axis) of a large–scale, uniflow scavenging, DI Diesel engine used for vessel propulsion operating on 80% of its maximum continuous rating (MCR) brake power which is 68.3 MW. Scavenging port opening and closing is denoted with SPO and SPC respectively.

For Diesel engines, the fuel injection is a determinant procedure because it drives the combustion evolution inside the combustion chamber affecting pollutant formation and engine performance. Moreover, the amount of the injected fuel per engine cycle, determines the engine load.

The highly compressed liquid fuel is injected into the cylinder through the injector with a spray form as shown in Fig. 1.3. The injected fuel is atomized into small droplets and penetrates inside the combustion chamber. During jet penetration, the fuel droplets vaporize, due to the high prevailing temperatures, and mix with the unburnt entrained charge (ambient air, exhaust gas recirculation (*EGR*) and residual gas (*RG*)) forced from the spray momentum and charge flow (swirl, quench and squish, see Fig. 1.4). Then, when the conditions (local

[1] The exhaust valve closure (EVC) occurs before intake valve opening (IVO) which does not happens in general. The last causes negative valve overlap (both valves are closed) which is one of the reasons for the pumping work losses. The EVC occurs some degrees before TDC and the IVO occurs some degrees after TDC to avoid possible collision of the valves and piston [252] since this engine has a very high compression ratio (18:1). In this figure are also depicted the intake valve closure (IVC), start of combustion (SOC), end of combustion (EOC) and exhaust valve opening (EVO).

equivalence ratio, temperature and pressure) become suitable, the fuel reacts with the oxidizer (i.e. O_2) according to highly complex, degenerated chain branching mechanisms [11] driving it to auto–ignite.

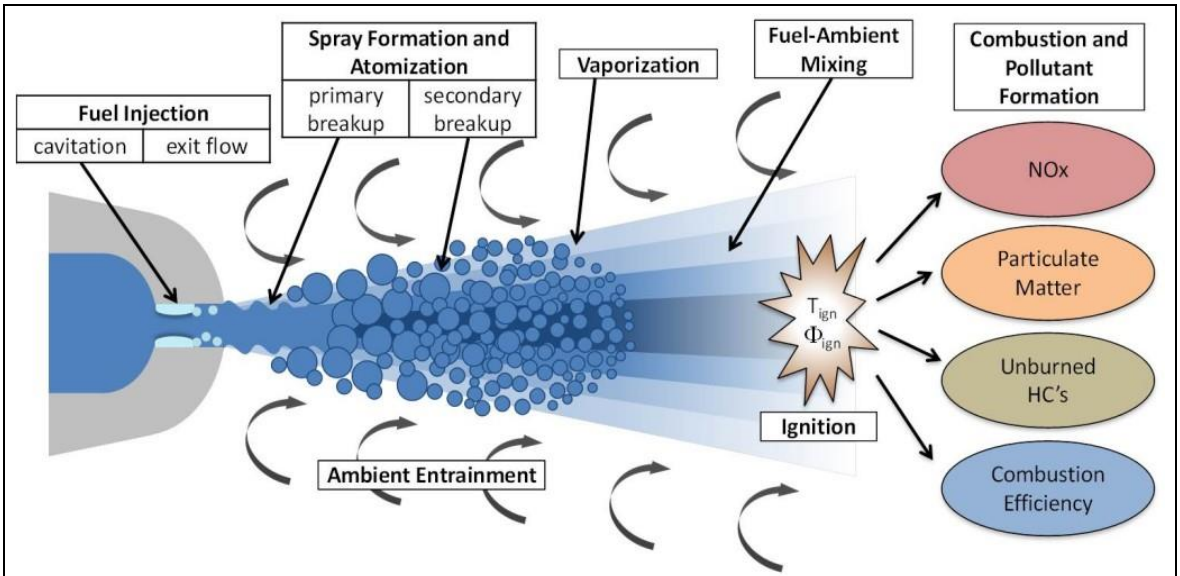

Figure 1.3: Schematic description of Diesel spray physical processes leading to ignition under high–temperature and pressure conditions [12].

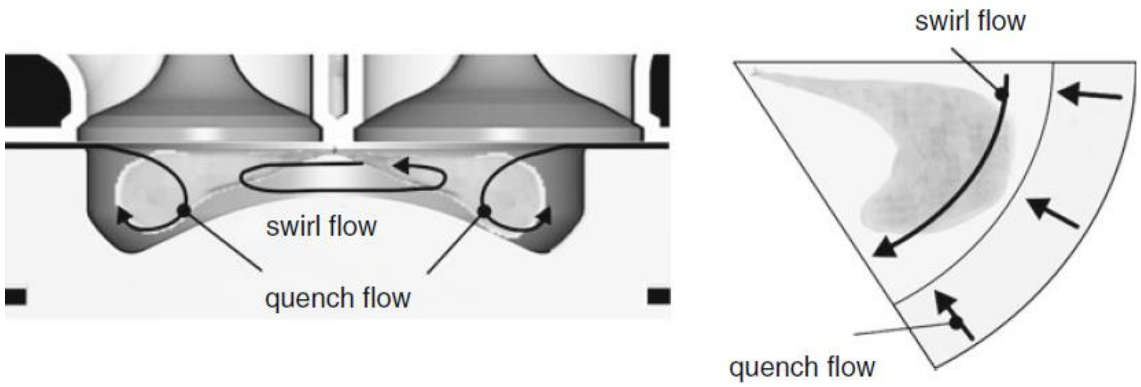

Figure 1.4: Combustion chamber flow [13].

The stages that the combustion process of *DI* Diesel engines can be divided into [8,13,14], are presented at next:

- Ignition–delay (prior combustion).
- Premixed phase (rapid combustion).
- Mixing–controlled phase (diffusion combustion).
- Reaction–controlled phase (late combustion).

The time period between the start of injection (*SOI*) and ignition (i.e. the start of combustion (*SOC*)) is called ignition–delay. Ignition–delay period depends mostly on fuel type/quality which is defined from the injected fuel ignitability (ignition index, cetane number (*CN*) for Diesel fuel, Calculated Carbon Aromaticity Index (*CCAI*) for heavy fuel oil – higher *CN* indicates lower auto–ignition temperature). Other parameters that affect (directly or indirectly) the physical (fuel atomization, vaporization and mixing) and chemical (pre–combustion reactions) preparation of the mixture and hence ignition delay are the flowing:

The injection pressure, injector design (injector type and orifice number and diameter, shape and angular position in reference with cylinder axis) (the lasts affect atomization and droplets speed, penetration, dispersion, mixing, etc.), injection timing (i.e. charge temperature and pressure during injection), fuel viscosity at injection time, fuel volatility, compression ratio, combustion chamber design (charge perturbation), exhaust gas recirculation (*EGR*) rate and residual gas (*RG*) fraction (i.e. charge chemical composition) and cylinder temperature have a significant impact on ignition delay [8,13].

During the ignition delay period, a nearly homogeneous mixture of fuel and oxidizer is formed. This mixture combusts almost instantaneously resulting in a sharp pressure rise (depends on the time, regarding *TDC*, where ignition occurs and on the length of ignition delay period). It is auto–ignited and burns rapidly causing, in some cases, a first heat release rate (*HRR*) peak. In this combustion phase, *HRR* is controlled by chemical reactions speed (reaction rate), the amount of combustible mixture formed during ignition delay and the grade of homogenization. To minimize the effect of this phase, which is the major reason of combustion noise and possible "Diesel knock" but also of increased temperatures and thus NO_x formation, the duration of ignition–delay period and the prepared amount of the premixed mixture should be both reduced. This is achieved by applying retarded *SOI* and/or pilot injection or, if the possibility exists, use of fuel with higher *CN*, etc.

After premixed combustion, the combustion process evolves simultaneously with spray penetration and mixture formation. Combustion is then controlled by mixture formation (mixing–controlled – diffusion combustion) [13]. Due to the gradual combustible mixture preparation in parallel with combustion, occurring in Diesel engines, this process is characterized by heterogeneous mixture formation and combustion. Diesel engines operate on a fuel lean global equivalence ratio, however due to the direct injection, the mixture presents various equivalence ratios locally, ranging from very reach to very lean. An indicative illustration of mixture stratification in the fuel spray is depicted in Fig. 1.5. This figure was derived from the combination of laser–based planar imaging diagnostics, empirical measurements and piecewise analyses with chemical kinetic codes as presented in the investigations of Dec [15] and Flynn et al. [16] for the understanding of the processes occurring in Diesel combustion. Such mixture stratification leads inevitably to the formation of pollutants,

especially soot particles and NO_x [13] as also shown in Fig. 1.5. An indicative photographic illustration of the combustion process in a Diesel engine is depicted in Fig. 1.6 [17]:

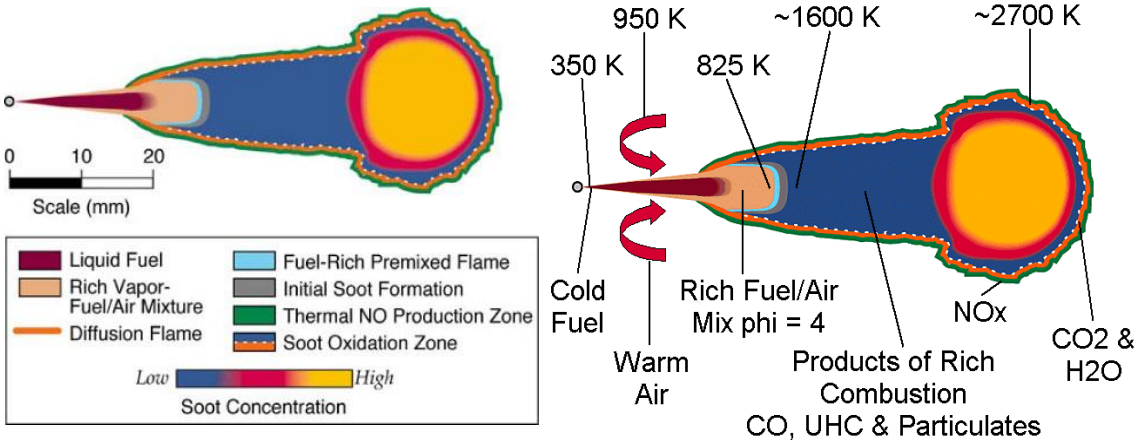

Figure 1.5: Model for Diesel combustion according to Dec [15] and Flynn et al [16].

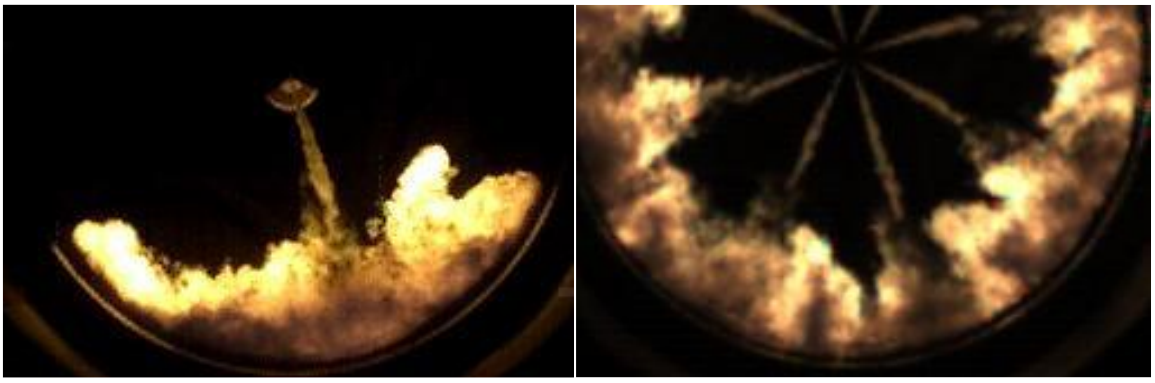

Figure 1.6: One combustion flame compared to eight combustion flames at 1500 bar injection pressure. This image is derived from the licentiate thesis of Dembinski H. W. R. [17].

The mixing–controlled phase represents the most important part of combustion where more than *80%* of the total injected fuel is burnt [8]. During this stage, the *HRR* is controlled by the turbulent mixing procedure between the fuel vapor and unburnt charge, which determines the amount of combustible mixture at each time instance. This mixture burns essentially as a turbulent diffusion flame with yellow–white or/and orange luminosity due to the presence of carbon particles [8]. In this phase, several processes are evolved inside the combustion–chamber simultaneously, such as:

- injection of liquid fuel,
- spray breakup,
- atomization,
- droplet evaporation,
- mixing of vaporized fuel with unburnt charge (air and residuals),
- pre–flame chemical reactions,
- combustion reactions,
- flame propagation and
- pollutant formation.

Mixing–controlled combustion continues after fuel injection completion if the other processes (penetration, vaporization, mixing, etc.) are still evolving. Due to the high inhomogeneity caused from these processes, each formed pocket of fuel–unburnt charge burns with a different combustion rate. A snapshot of combustion during this phase is depicted in Fig. 1.5 and 1.6 [17]. Particularly, in Fig. 1.5 [15,16] some of the characteristics of the spray and combustion flame are indicatively shown. Among the partially oxidized products of the premixed combustion, precursor species are also found, which lead to particle formation further downstream, in the middle of the flame. The diffusion flame is formed around the injection spray on a surface with a close to stoichiometric equivalence ratio. The partially oxidized products of the rich premixed combustion and the particles formed, move further downstream and are transported into the diffusion flame, where they are completely (usually) oxidized into carbon dioxide and water. Due to the high temperatures of the diffusion flame front and post–flame gases in conjunction with the high oxygen concentrations, NO_x formation is favored.

At the last part of combustion, namely the late combustion phase which persists throughout the expansion stroke, the combustion rate is significantly decreased. This is due to the decay of momentum introduced from the injection resulting in decrease of air–entrainment rate and due to the consumption of the greatest amount of the injected fuel. However, the total *HR* during this phase is distinguishable since is represents the energy of about *20%* of the total injected fuel [8]. At this phase, *HR* originates from the complete oxidation of fuel rich combustion products and soot derived from the previous combustion phase and did not be oxidized during the turbulent diffusion combustion and also from the small fraction of vaporized fuel which has remained from the previous phase. As cylinder volume increases during expansion, the charge temperature decreases and hence reaction rates decrease. Namely, the chemical kinetics become slower which promotes complete combustion and less dissociation of the combustion products [8,13]. Indicatively, in Fig. 1.7, the *HR* rate (*HRR*) diagram and the various combustion phases along with the in–cylinder pressure and mean temperature diagrams of a light–duty, *DI* Diesel engine of a passenger car are depicted:

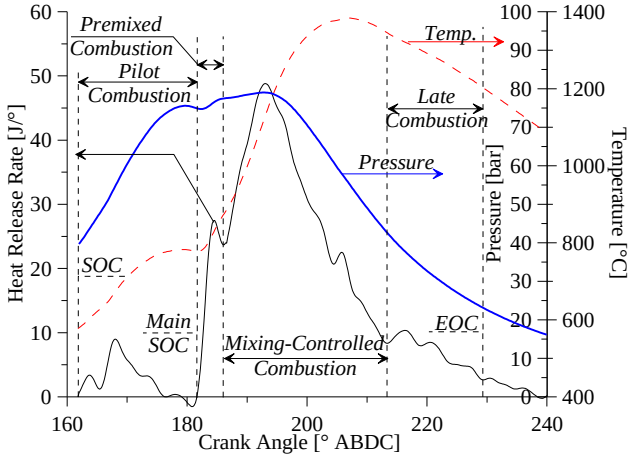

Figure 1.7: HRR diagram and the combustion phases along with the in–cylinder pressure and mean temperature diagrams of a light–duty, supercharged, common rail, DI, 4–stroke Diesel engine using pilot injection of a passenger car running on 2500 rpm and mid–load (31.3 kW).

1.2.2 The Theory for NO_x Formation in DI Diesel Engines

The most important pollutants formed in Diesel engines are the NO_x, SO_x (for marine and power station engines fuels) and soot (particulate matter: *PM*) [8,14,18]. All of these harmful emissions can be efficiently controlled using a combination of appropriate technologies. In this study only the NO_x emissions are examined.

NO_x are chemical compounds of nitrogen (*N*) and oxygen (*O*). There exist a total of eight NO_x structures denoted as N_yO_x where *x=1, 2...6* and *y=1* or *2*. However, the major NO_x types that formed inside the combustion chamber of Diesel engines are the nitric oxide (*NO*), nitrous oxide (N_2O) and nitrogen dioxide (NO_2) of which the structure is depicted in Fig. 1.8:

 NO	 N_2O	 NO_2
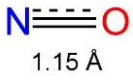	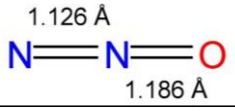	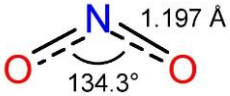
nitric oxide (NO)	*nitrous oxide (N_2O)*	*nitrogen dioxide (NO_2)*

Figure 1.8: The chemical structure of the NO_x occurring in Diesel engines [19]. ($Å=10^{-10}$ m)

Nitric oxide (*NO*) consists the majority of NO_x amount, usually more than *90%*. However, at low load operation, where high air excess exists, greater amount of NO_2 is formed, up to *10–30%*, which is decreasing at higher engine speeds [8]. NO_2 is formed when *NO* molecules, coming from high–temperature regions, are transported through the mixing process towards low temperature regions where they find significant concentrations of HO_2, which together with radical *OH* are used as the main oxidant agents in the conversion from *NO* to NO_2 [20,21]. It is emphasized that NO_2 has higher toxicity than *NO* as well as higher potential than *NO* to form photochemical smog [20,22]. At mid and high loads and also during transient operation, N_2O, NO_2 and other NO_x except *NO*, are negligible [8,23,24,25].

NO, which is a colorless and odorless gas, can be produced in the lab from oxygen (O_2) and nitrogen (N_2) under high pressure and temperature conditions according to the following endothermic chemical reaction which is described in Eq. (1.1) [26]:

$$N_2 + O_2 \rightarrow 2 \cdot NO - 182.4\ kJ/mol \tag{1.1}$$

Obviously, NO_x formation in Diesel combustion chamber is much more complicated. Nonetheless, various simple mechanisms have been proposed for its modeling. The most recognized mechanisms describing the NO_x formation are the following:

1. Thermal NO_x formation.
2. NO_x formation from intermediate N_2O.
3. Prompt NO_x formation.
4. Fuel NO_x formation.

The predominant NO_x formation mechanism is the thermal NO_x formation, while the other mechanisms have a rather small contribution. Thermal NO_x is formed in both flame front and high temperature post–flame gases [8,27]. The formation of thermal NO_x is determined from the highly temperature–dependent chemical reactions proposed by Zeldovich [28,29] and thus also called Zeldovich mechanism. These chemical reactions are described in Eq. (1.2) and (1.3):

$$O + N_2 \leftrightarrow NO + N \tag{1.2}$$

$$N + O_2 \leftrightarrow NO + O \tag{1.3}$$

Later, Lavoie et al [30] introduced an additional reaction which has been shown to contribute to the formation of thermal NO_x, particularly at near–stoichiometric conditions and in fuel–rich mixture, which is described in Eq. (1.4):

$$N + OH \leftrightarrow NO + H \tag{1.4}$$

The mechanism that contains Eqs (1.2) – (1.4), is called extended–Zeldovich mechanism, is kinetically–controlled and is strongly dependent on the local availability of N_2 and especially O_2, local temperature (exponential dependency) and residence time at high temperatures, namely higher than *1800 K* where NO_x formation is more intensive. The high temperatures are required to brake the strong triple bound of N_2 which has high dissociation energy (*941 kJ/gmol*). However, late during expansion, where the in–cylinder temperatures decreases significantly, NO_x formation reaction rates are reduced, thus NO_x concentration freezes. Furthermore, NO_2 formation initiates from the oxidation of *NO* at low temperature regions [8,25,30,31,32].

NO_x formation from intermediate N_2O mechanism is favored at elevated pressures, high O_2 concentrations (since *O* is mostly derived from O_2 dissociation) but not very high temperatures. Thus, when Diesel engines are operated at low temperatures (i.e. low temperature combustion (*LTC* engines [33], i.e. homogenous or premixed charge compression ignition engines (*HCCI* and *PCCI*)), high exhaust gas recirculation (*EGR*) rates, etc.) in order to prevent thermal NO_x formation, the intermediate N_2O mechanism may contribute up to *30%* in total NO_x [32,34,35,36]. The aforementioned mechanism can be described from the Eq. (1.5) – (1.7) [30] where *M* is a third body element:

$$\mathrm{H} + N_2O \leftrightarrow N_2 + OH, (M + N_2O \leftrightarrow N_2 + O + M) \tag{1.5}$$

$$\mathrm{O} + N_2O \leftrightarrow N_2 + O_2 \tag{1.6}$$

$$\mathrm{O} + N_2O \leftrightarrow 2NO \tag{1.7}$$

Prompt NO_x is formed at the flame front, in the lower temperature regions (about *1000 K*) [13] from chemical compounds derived from the reaction of nitrogen (N_2) comprised in the trapped air with the fuel hydrocarbon radicals (*HC*) and carbon atoms (*C*) produced during the combustion pre–reactions in very fuel–rich regions. From this reactions *CN* or/and *HCN* compounds are formed, which subsequently react with *O* atoms to form *NO*

[27]. The prompt mechanism was first identified from Fenimore [37] and is described from the following reaction routes (Eq. (1.8) – (1.11)):

$$CH + N_2 \leftrightarrow CHN + N \tag{1.8}$$

$$N + O_2 \leftrightarrow NO + O \tag{1.9}$$

$$CHN + OH \leftrightarrow CN + H_2O \tag{1.10}$$

$$CN + O_2 \leftrightarrow NO + CO \tag{1.11}$$

The major contributors (see Eq. (1.8)) in this mechanism are the *CH* and CH_2 but also *C*, C_2H, etc. may participate. Prompt NO_x formation is proportional to the carbon atoms concentration and is independent of the parent hydrocarbon identity. The quantity of *HCN* formed increases with the concentration of hydrocarbon radicals which in turn increases with equivalence ratio. As equivalence ratio increases, prompt NO_x production increases at first, then passes a peak, and finally decreases due to the deficiency in oxygen [32]. Nevertheless, the contribution of prompt NO_x to total NO_x is rather small in Diesel engines [27].

Finally, the fuel NO_x mechanism causes NO_x formation from fuel–bound nitrogen compounds comprised in the fuel, such as ammonia (NH_3), pyridine (C_5H_5N), quinoline (C_9H_7N), pyrroles (C_4H_5N) and many other amines which can be designated as RNH_2, where *R* is an organic radical or *H* atom [27]. This mechanism is important when heavy fuel oils (low distillation fuels) are used, which comprise noticeable amounts of *N*. The extent of conversion of fuel nitrogen to NO_x depends on the local combustion characteristics and the initial concentration of nitrogen–bound compounds. Fuel–bound compounds that contain *N* are released into the gas phase when the fuel droplets or particles are heated during the vaporization stage [32].

It should be noted that the NO_x formation process is much more complicated than the one described from the aforementioned mechanisms, which however provide a realistic picture of the formation mechanism and decent predictions when utilized in modeling. Nevertheless, numerous models can be found in literature, which adopt more detailed description of NO_x formation by making use of a greater number of chemical reactions and use less assumptions, however introducing high computational cost and sensitively [38,39,40,41].

Regardless the NO_x formation mechanism, due to the hazardous consequences that NO_x induce on human health and environment, governments worldwide have adopted strict regulations to limit NO_x emissions. At next, the basic legislation limits that have been set in many countries are presented.

1.3 Pollution from NO_x Emissions and Future Legislation NO_x Limits for Diesel Engines

1.3.1 Adverse Effects of NO_x on Human Health and Environment

Environmental air quality and human health deterioration due to exhaust gas emissions [42,43] has become a severe problem that governments are enforced to deal with

worldwide. NO_x, which is mainly anthropogenic, causes acid rain, smog and ground level ozone. The adverse effects of these phenomena on human health and environment are summarized below [43,44,45]:

1. Decrease in–lung function, resulting in breathing difficulty, shortness of breath, and other symptoms.
2. Respiratory symptoms, including bronchitis, aggravated coughing, and chest pain.
3. Increased incidence/severity of respiratory problems (e.g. aggravation of asthma, susceptibility to respiratory infection) resulting in more hospital admissions and emergency room visits.
4. Chronic inflammation and irreversible structural changes in the lungs that, with repeated exposure, can lead to premature aging of the lungs and other respiratory illness such as edema of lungs and pulmonary emphysema.
5. Respiratory irritation, headaches, eye irritations, loss of appetite, corrosion of teeth, nausea, skin irritation, serious developmental delays in children and even cancer.
6. Acidification of surface water, reducing biodiversity and killing fish.
7. Forests damage through direct impacts on leaves and needles and by soil acidification and depletion of soil nutrients.
8. Damage of forest ecosystems, trees, ornamental plants, and crops through ground–ozone formation.
9. Contribution to coastal eutrophication, killing fish and shellfish.
10. Contribution to decreased visibility (regional haze) and especially in crowded cities with high traffic where the atmosphere becomes suffocating.
11. Speeding up of weathering of monuments, buildings, and other stone and metal structures.

In order to restrict NO_x pollutant in the atmosphere and thus improve the standard of living of citizens and limit the deterioration of environmental impact, regional, national and international organizations/unions have adopted strict limits for NO_x emissions from internal combustion engines (*ICE*) and other combustion sources. In the present study, where the NO_x emissions from Diesel engines are examined, the current and future limits, which correspond to the specific engines, are presented.

1.3.2 NO_x Legislation for Diesel Engines

For the Diesel engines installed on vessels, (for propulsion and power generation) with output power over *130 kW*, the International Maritime Organization (*IMO*) has set strict limits for NO_x emissions (*regulation 13, Annex VI* [46]). These limits are described by the requirements of the Engine International Air Pollution Prevention (*EIAPP*) certificate and the subsequent demonstration of the in service compliance in accordance with the requirements of the mandatory, regulations *13.8* and *5.3.2* respectively, NO_x Technical Code *2008*

(resolution MEPC.177(58)) [47]. These regulations indicate three different limits determined from engine speed and engine construction date. These limits and the percentage reduction of the last two are listed in Table 1.1 [46,47]:

Tier	Ship construction date on or after	Total weighted cycle emission limit *[g/kWh]* n: engine's rated speed *[rpm]*		
		$n < 130$	$130 \leq n \leq 1999$	$n \geq 2000$
I	1 January 2000	17.0	$45 \cdot n^{-0.2}$	9.8
II	1 January 2011	14.4	$44 \cdot n^{-0.23}$	7.7
III	1 January 2016*	3.4	$9 \cdot n^{-0.2}$	2.2
Reduction from Tier II to III [%]		76	~80	71

* Subject to a technical review, this date could be delayed, regulation 13.10.

Table 1.1: Tier I, II and III NO_x limits for ship engines with engine power over 130 kW.

The European Union (*EU*) NO_x emissions standards for various types of Diesel engines, corresponding to the most recent directives (*EURO IV–VI*, *Stage II–IV* (2002/80/EC, 715/2007, 2005/55/EC, 595/2009, 2002/88/EC, 2010/26/EU, 2010/22/EU), etc.) [48], are

presented in Table 1.2 [49]. From this table, the steep decrease of NO_x emissions limits is obvious.

Engine Type	EURO IV	EURO V	EURO VI	Limit descent from EURO IV to VI
	2005	2009	2014	
	NO_x [g/km]	NO_x [g/km]	NO_x [g/km]	[%]
Diesel Passenger Cars	0.25	0.18	0.08	68
Diesel Light Commercial Vehicles (<1305 kg)	0.25	0.18	0.08	68
Diesel Light Commercial Vehicles (1305–1760 kg)	0.33	0.235	0.105	68
Diesel Light Commercial Vehicles (1760–3500 kg)	0.39	0.28	0.125	68
Diesel Light Commercial Vehicles (3.5–12 tonnes)	-	0.28	0.125	-
	2005	2008	2013	
	NO_x [g/kWh]	NO_x [g/kWh]	NO_x [g/kWh]	[%]
Heavy–Duty Diesel Engines	3.5	2.0	0.4	89
	Stage II	Stage III B	Stage IV	Limit descent from Stage II to IV
	2001/2/3/4	2011/12/13	2014	
	NOx [g/kWh]	NOx [g/kWh]	NOx [g/kWh]	[%]
Non–road Diesel engines ($130 \leq P \leq 560$)	6	2.0	0.4	93
Non–road Diesel engines ($75 \leq P < 130$)	6	3.3	0.4	93
Non–road Diesel engines ($37 \leq P < 75$)	7	3.3	0.4	94
Non–road Diesel engines ($18 \leq P < 37$)	8	4.7(incl. HC)-		-

Table 1.2: NO_x emissions standards for Diesel engines applied in EU.

At next, the current–future and previous NO_x emissions limits which have been set from United States (*US*) Environmental Protection Agency (*EPA*) are presented in Table 1.3 [50]. From Table 1.3 is also distinguishable the significant tightening of these limits.

Engine Type	Previous	Current and Future		Limit descent [%]
	NO_x [g/kWh]	Year	NO_x [g/kWh]	
Heavy–Duty Highway Compression-Ignition Engines And Urban Buses	2.98	2007+	0.15	95
Non–road Compression-Ignition Engines P≥560kW	9.20	2015+	3.50	62
Non–road Compression-Ignition Engines P<560kW	9.20	2015+	0.40	96
Non–road Compression-Ignition Engines P≥560kW (for generator sets)	9.20	2011+	0.67	93
Locomotives (Line haul)	4.10	2015+	0.97	76
Locomotives (Switch)	3.73	2015+	0.97	74

Table 1.3: Previous and current–future NO_x emissions limits for Diesel engines applied in US.

Most of the developed countries have embedded the *EU* or *US* NO_x emissions standards to their corresponding legislation or adopted quite similar regulations. Detailed description of these regulations can be found in Ref. [51] and at the corresponding agencies of each country. In the next section, a number of methods for the control of NO_x emissions from Diesel engines are described.

1.4 Methodologies for NO_x Emissions Abatement

1.4.1 Introduction

As already mentioned in section 1.3, in order to limit the adverse effects of NO_x emissions on human health and environment, the legislation for the corresponding limits is becoming very strict. Since the internal combustion engine (*ICE*) is a major source of pollution, *ICE* industry has been compelled to take measures to control NO_x emissions. For this reason, the *ICE* manufacturers and end–users are seeking for efficient methods to control NO_x formation in order to comply with regulations and guarantee their presence in the market. Moreover, the control of NO_x emissions for the in–service engines is imperative, especially in power generation and maritime industries, in order to avoid the very high fines and the substantial sanctions. The available methods to achieve the NO_x control are divided into two main categories: in–cylinder emission control (primary methods – internal measures) and exhaust after–treatment (secondary methods).

1.4.2 Primary/In–Cylinder Measures for NO_x Control

1.4.2.1 General Description of the In–Cylinder Methods for NO_x Control

The primary methods for NO_x control promote NO_x reduction inside the combustion chamber via its formation mechanism. Their objective is to reduce flame temperature and oxygen availability which drive NO_x formation, by controlling fuel–unburnt charge mixing, unburnt charge composition, heat capacity and initial temperature, pressure and heat release evolution inside the combustion chamber. The most important of these methods are the following:

- optimization of combustion chamber design [52],
- exhaust gas recirculation (*EGR*),
- direct water injection (*DWI*) in the combustion chamber,
- water emulsification of the fuel,
- humidification of scavenging air,
- reduction of the air temperature at the start of compression via the Miller concept,
- modification of fuel injection strategy (injection: timing, pressure, profile, pilot and post injection, low–temperature and premixed/homogeneous combustion concepts, etc.),
- optimization of injector design,
- optimization of valve design, timing and lift (i.e. internal *EGR*, variable valve timing (*VVT*) [53] and lift (*VVL*) – or actuation (*VVA*), camless valve trains [54], etc.) and
- combination of the previous.

These methods intent to achieve optimum NO_x, soot (*PM*) and brake specific fuel consumption (*bsfc*) trade–off.

1.4.2.2 Fuel Injection Strategy for NO_x Control

The most common method used currently in large–scale Diesel engines, is the control of NO_x by retarding the start of injection (*SOI*) using a variable injection timing system (*VIT*) [55,56]. When fuel is injected late in the cycle, the combustion process is shifted later during expansion and hence lower in–cylinder pressure and thus temperature are developed during combustion and expansion. Hence less NO_x amount is formed. On the other hand, *bsfc* and soot formation tend to increase. This problem is treated using common–rail fuel injection systems in combination with electronically controlled injectors (commonly in automotive engines but also in the new large–scale ones (*RT–Flex* [57,58])). These systems provide direct control of injection timing and injection rate profile and also the possibility for different injection pressures in the cycle (i.e. by using two rails in combination with two injectors in each cylinder). Thus the injection profile can be modified to reduce *bsfc* and control soot formation using e.g. post injection to enhance soot oxidation. Moreover, sophisticated injection strategies using pilot, pulse or sequential injection [59,60,61] (see Fig. 1.9)

through single or multiple, advanced design, injectors can also contribute to NO_x control accompanied with low *bsfc* penalty.

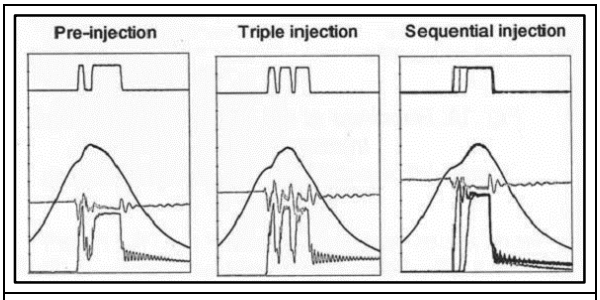

Figure 1.9: Different fuel injection patterns for emission control optimization [61].

1.4.2.3 Valve Timing Strategy–Compression Control–Miller Cycle Concept for NO_x Control

Another concept to reduce *bsfc* while injection timing is retarded (to control NO_x formation), is the use of increased effective compression ratio (i.e. decrease of cylinder clearance volume, advance of exhaust valve closure (*EVC*) for uniflow *2*–stroke, i.e. by using variable *EVC* [58]), intake valve closure (*IVC*) advance, namely as close as possible to the bottom dead center (*BDC*) (for *4*–stroke) or/and increase of scavenging (boost) pressure, etc.). This preserves the highest possible useful work per cycle (*p*–*V* diagram enclosed area) but at the same time, the pressure rise introduced from combustion is lower and in combination with the lower residence time in the high temperature regimes, NO_x formation decreases [62]. The last is schematically described in Fig. 1.10. In some modern engines, valve actuation (timing or/and lift) can be electronically controlled (i.e. *VVA*), which provides the ability to vary the effective compression ratio and internal *EGR* rate according to the engine operating conditions, targeting to limit NO_x emissions but preserve or improve the *bsfc* [54,62].

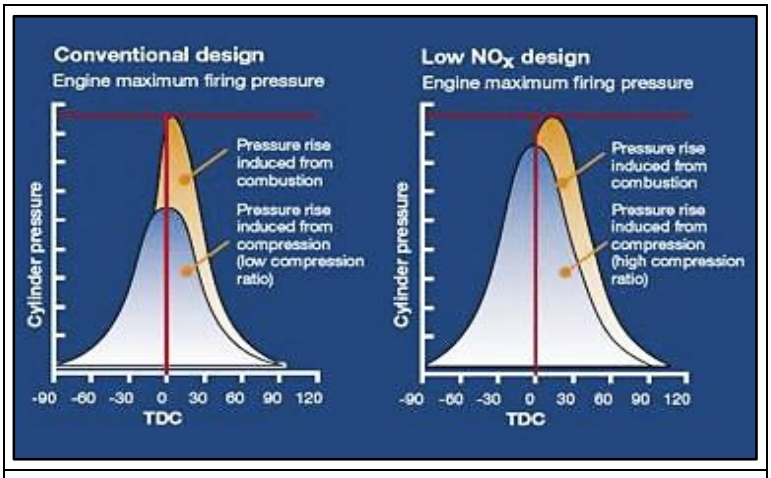

Figure 1.10: Increased effective compression ratio concept for reducing NO_x formation [62].

A similar concept that aims to control NO_x emissions, regarding *4*–stroke Diesel engines, is the operation according to the Miller cycle, where, in general, the effective com-

pression stoke is shorter compared to the power–stroke. According to a version of this concept, the intake valve closes much earlier before the piston reaches bottom dead center (*BDC*). This causes an in–cylinder pressure drop as the piston continues downwards and hence the temperature of the trapped charge is reduced (Boyles and Charles' Law). This, also allows the use of a higher than normal pressure turbocharger and hence higher compression pressure that provides the potential for a retarded injection timing without deteriorating *bsfc* (see the previous scenario – Fig. 1.10) or/and even engine performance improvement. Although the engine is still doing work as the piston is descending during the inlet stroke, there is a saving in work during the compression stroke and the maximum air temperature and pressure is reduced on compression. Therefore lower combustion pressure and temperature will occur and hence NO_x formation is reduced while *bsfc* is not increased significantly [62,61]. It is noted that, a late intake valve closure version of the Miller concept also exists which can also achieve lower NO_x and improved performance [63].

Likewise the Miller cycle, reduced scavenging air temperature leads to lower combustion temperature and thus lower NO_x emissions, lower heat losses, better volumetric efficiency and increased performance. This can be achieved by making use of intercoolers, namely cooling of the supercharged intake air or with even more sophisticated supercharging using intermediate intercooling (i.e. *2*–stage turbocharging [64,65]), etc. In Fig. 1.11 is depicted an application example of a *2*–stage turbocharging concept:

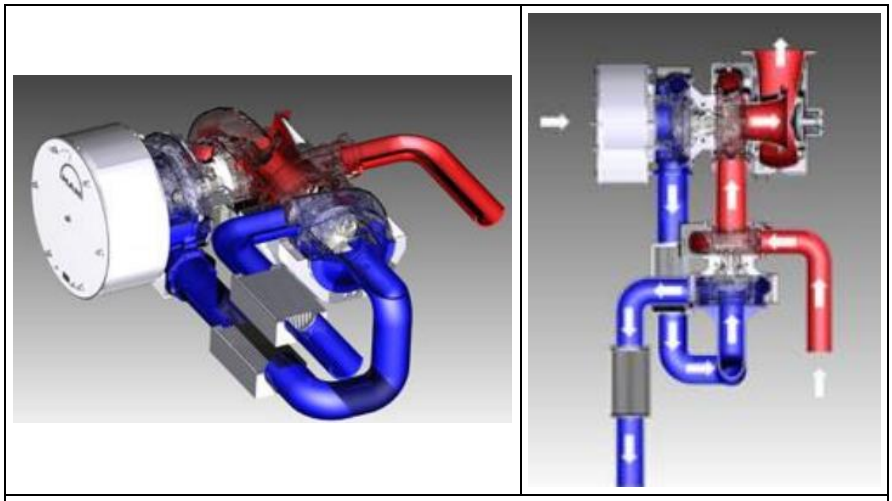

Figure 1.11: 2–stage turbocharging applied on a large–scale engine [65].

1.4.2.4 Temperature Control by using Water Injection for NO_x Control

Especially for large–scale *DI* Diesel engines, but also in the automotive sector, water is used to induce in–cylinder temperature reduction since it absorbs significant amounts of latent heat and increases the heat capacity of the in–cylinder charge. Water can be introduced in the cylinder through intake air by the use of humidification methods such as direct water injection in the intake duct (combustion air saturation system (*CASS*) [66],

scavenging air moistening (*SAM*) [67] and humid air motor (*HAM*) [68]). The aforementioned methods are depicted in Fig. 1.12:

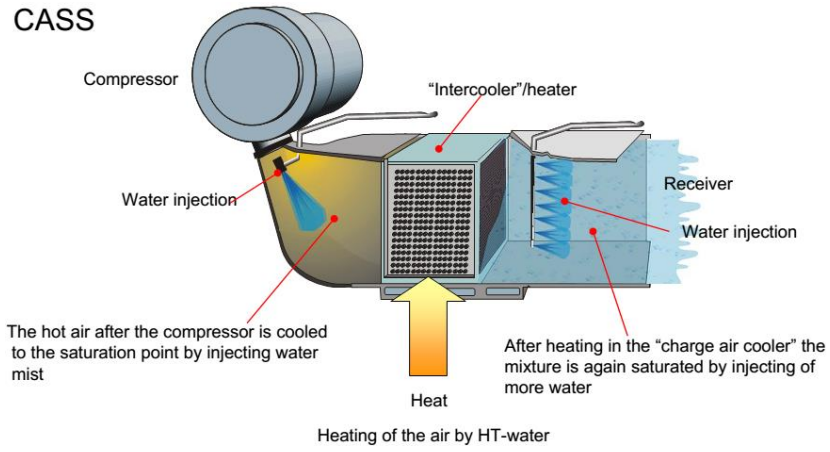

CASS [66]

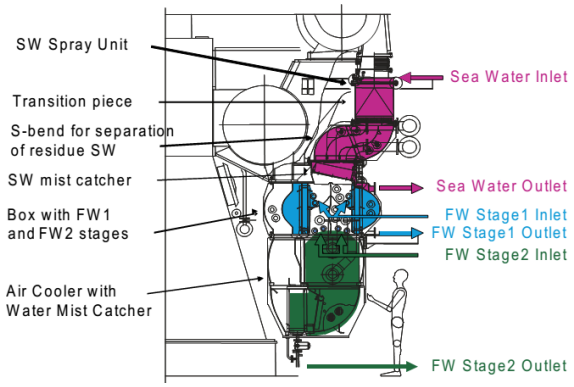

SAM [67]

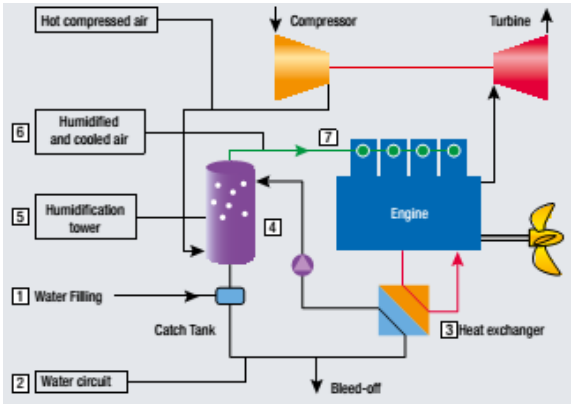

HAM [66]

Figure 1.12: Humidification of intake air concepts.

Other efficient methods are the direct water injection (*DWI*) [66,69] into the cylinder, the use of water/fuel emulsion (*WFE*) [67,70,71] or a combination of these, namely stratified fuel water injection (*SFWI*) [72,73,74,75]. *WFE* and *DWI* place the water more directly in the combustion region, where it has maximum effect on NO_x production. *WFE*

can reduce smoke, while humidification can increase smoke [59,61,76]. Some of the aforementioned methods are depicted in Fig. 1.13:

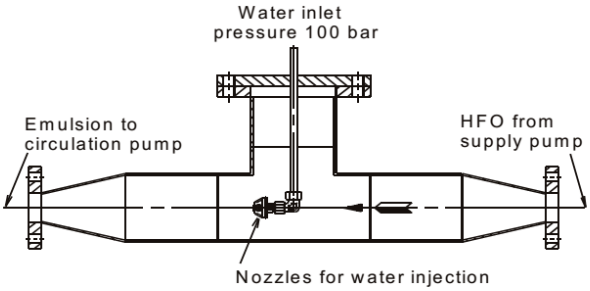

WFE [67]

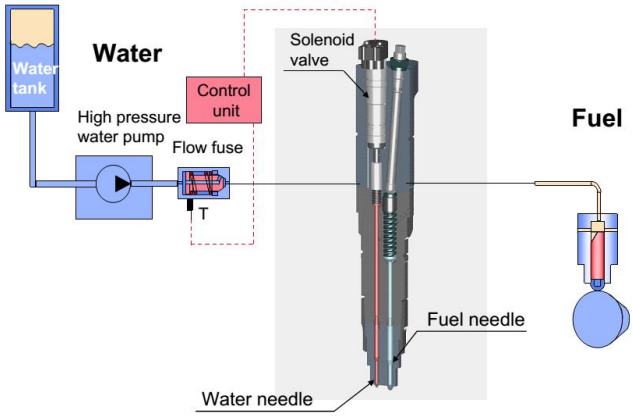

DWI [66]

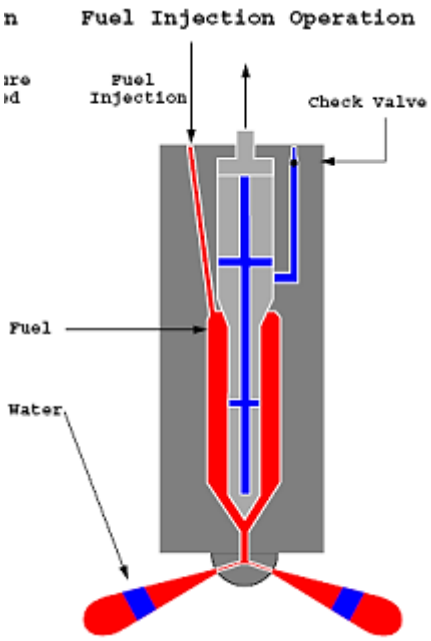

SFWI [75]

Figure 1.13: Methods for direct entrance of water in the combustion chamber.

1.4.2.5 Exhaust Gas Recirculation for NO_x Control

EGR is the most effective and common primary method for NO_x reduction in automotive engines [77], however in the near future, large–scale engine manufacturers [76] intent to adopt this method in order to comply with *IMO Tier III* standards [46]. The *EGR* system is described in general as a flow passage devised between the exhaust and the intake manifolds regulated with a throttling valve.

In general, *EGR* provides to the combustion chamber additional CO_2 and H_2O vapor thus restricting the O_2 and N_2 fractions of the trapped charge. This, results in an increase of charge heat capacity and thus the in–cylinder temperature drops (thermal effect). Moreover, the decrease of O_2 availability causes deceleration of the mixing between O_2 and fuel resulting in an extension of the flame region (i.e. expanding combustion). Due to this, the gas quantity that absorbs released heat increases, resulting in a lower flame temperature.

In addition, the lower O_2 availability causes reduction of the oxygen partial pressure which has a restricting effect on the kinetics of the elementary NO_x formation reactions (dilution effect). Furthermore, the recirculated CO_2 and H_2O vapor are dissociated during combustion by absorbing heat, since their dissociation reactions are endothermic, resulting in lower flame temperature (chemical effect) [78,79].

Three major types of *EGR* techniques exist [80], which are schematically depicted in Fig. 1.14:

1. Low pressure *EGR* loop between the turbine outlet and the compressor inlet.
2. High pressure *EGR* loop between the turbine inlet and compressor (or intercooler) outlet.
3. Intermediate *EGR* loop between the turbine outlet and compressor (or intercooler) outlet where the pressure difference ($p_{turb.}$-$p_{compr.}>0$) is controlled from an additional blower (or *EGR* pump).

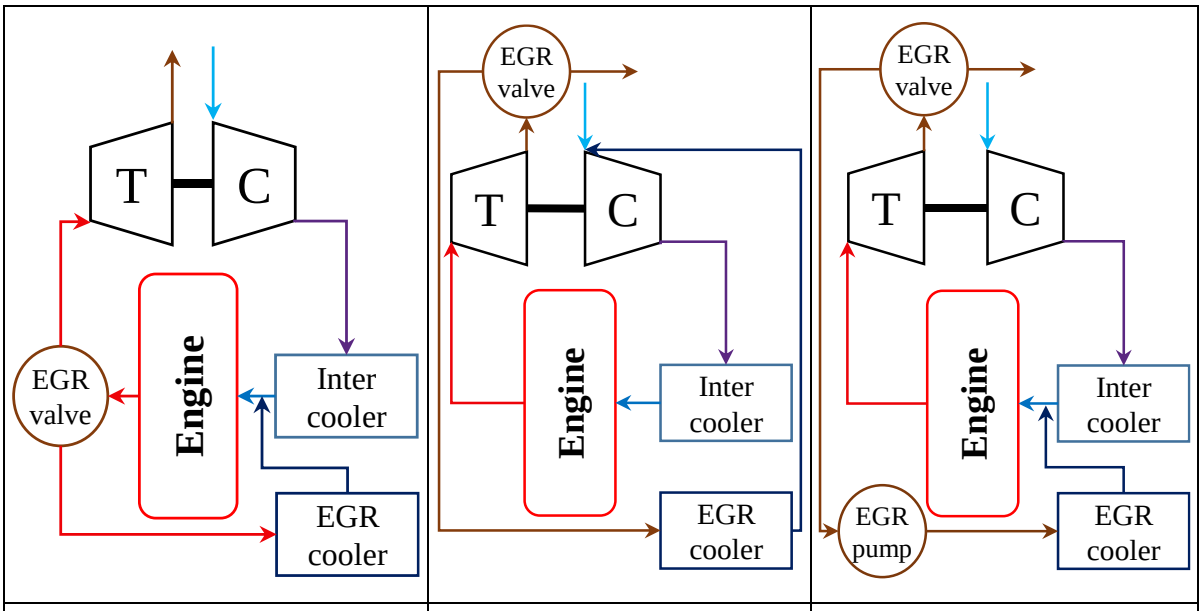

High pressure EGR loop | *Low pressure EGR loop* | *Intermediate EGR loop*

Figure 1.14: Schematic description of the ERG establishments.

The high pressure *EGR* is the most commonly used. In modern engines, the control of this system is closely tied to the variable geometry turbine (*VGT*) control [81].

Low pressure *EGR* requires special compressors and coolers because the respective common ones are not designed to endure high temperature operation and exhaust fouling. In order to reduce the initial temperature of the intake charge (air + *EGR* gas), which affects significantly the engine's volumetric efficiency (decreases with temperature rise) and compression temperature, hence combustion temperature and therefore NO_x formation (increases with temperature), the *EGR* gas is cooled via a heat–exchanger (cooler) [82].

Nevertheless, in future/modern large–scale, *2*–stroke Diesel engines, a high pressure *EGR* loop will be used to limit NO_x formation in conjunction with a SO_x treatment using a scrubber system. The *EGR* system can be activated only in emission control areas (*ECAs*) where the limitations for NO_x emissions will be stricter (as currently for SO_x) as imposed

from *Tier III*. When *EGR* is on, an amount of the exhaust gas contained in the exhaust receiver, bypasses the turbine and passes sequentially through a pre–scrubber (cooling the exhaust gas), *EGR* cooler, main scrubber and water mist catcher (*WMC*). At last, the *EGR* gas is compressed and transferred into the scavenge air receiver where it meets the intercooled intake air derived from the compressor. Due to the nature of the scavenging process in *2*–stroke engines, the pressure in the exhaust receiver, namely before turbine inlet, is lower than the one of intake receiver, namely after compressor, and additionally, due to the pressure drop resulted from the passing of the gas from the aforementioned devices, the pressure of *EGR* gas should be risen. This is accomplished by using an *EGR* blower. Turbocharger (*TC*) cut–out/bypass concepts are also used in order to fit the turbocharger map when the engine operates in *EGR* mode [67,83]. A schematic preview of the *EGR* scenario in large–scale, *2*–stroke Diesel engines, derived from Ref. [83], is depicted in Fig. 1.15:

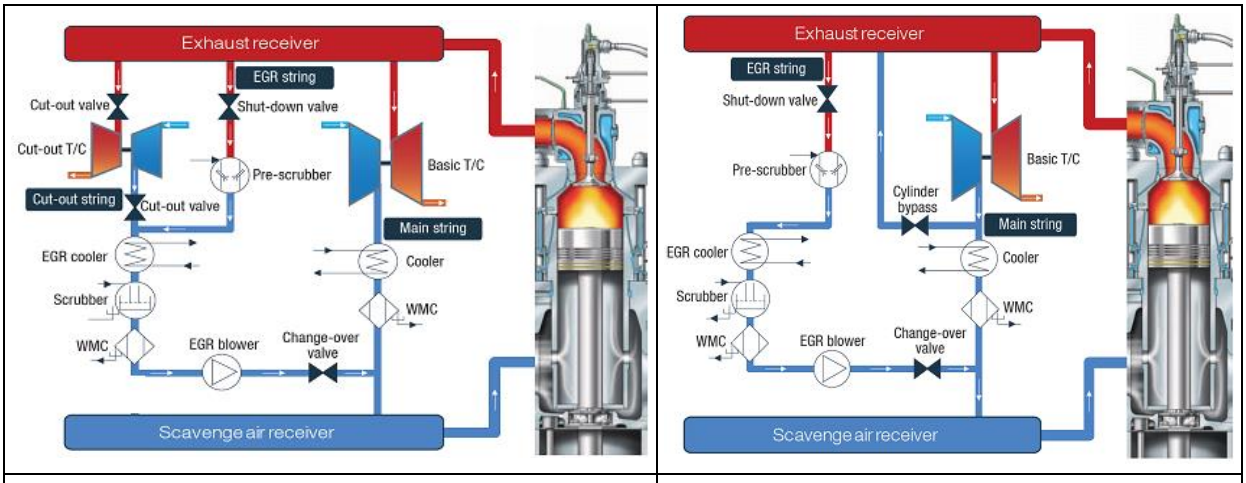

EGR system with T/C cut–out. | *EGR system with T/C bypass.*

Figure 1.15: Schematic description of the ERG concept in 2–stroke, large–scale .Diesel engines [83].

Another method, which combines *DWI* and internal *EGR*, is the water cooled residual gas (*WaCoReG*), used in slow–speed engines. Internal *EGR* is achieved by reducing the scavenging ports' area, by using smaller turbocharges or/and by controlling the timing and lift of the exhaust valve (i.e. electronically controlled) in order to reduce the scavenging flow [60]. As already mentioned, *EGR* reduces NO_x formation at source by reducing the in–cylinder O_2 availability and increasing the heat capacity of the charge. However, internal *EGR* results in an increase of engine's thermal load. For this reason, water injection is applied to reduce the temperature levels, thereby keeping thermal loads much the same as when running without internal *EGR* [59].

These methods, if applicable, are advantageous because they do not present the drawbacks of the after–treatment methods described in the next section 1.4.3.

1.4.3 Secondary/After–Treatment Methods for NO_x Control

Secondary methods reduce NO_x in the exhaust gas by downstream treatment (after–treatment methods). The most widely recognized after–treatment methods for tail–pipe NO_x control are the following:

1. Selective Catalytic Reduction (*SCR*).
2. Lean NO_x trap (*LNT*).

1.4.3.1 Selective Catalytic Reduction

The most applicable and successive method of after–treatment technology for Diesel engines NO_x control is the Selective Catalytic Reduction (*SCR*), especially for large–scale engines established on vessels and power plants (see Fig. 1.16) but also for heavy–duty engines on trucks, locomotives and non–road applications. Using this method, a NO_x reduction of more than *90%* can be achieved. In a high temperature *SCR* system, the exhaust gas, at a temperature between *~300* and *600°C* [84], is mixed with a chemical reducing agent, commonly ammonia (NH_3) in the form of a solution of urea ($CO(NH_2)_2$) in water. This introduces single nitrogen (*N*) atom, creating a reducing atmosphere before passing through a special catalyst. The NO_x is reduced to nitrogen (N_2) and water (H_2O). The main chemical reactions taking place inside the catalyst for the dissipation of NO_x are shown in Eq. (1.12):

$$\begin{aligned} 4 \cdot NH_3 + 4 \cdot NO + O_2 &\rightarrow 4 \cdot N_2 + 6 \cdot H_2O \\ 2 \cdot NH_3 + NO + NO_2 &\rightarrow 2 \cdot N_2 + 3 \cdot H_2O \\ 8 \cdot NH_3 + 6 \cdot NO_2 &\rightarrow 7 \cdot N_2 + 12 \cdot H_2O \end{aligned} \tag{1.12}$$

The catalyst core is often composed of a heat resistant ceramic honeycomb with a catalytically active material, such as metal oxide mixtures based on vanadium supported with titanium in anatase form and promoted with tungsten or molybdenum [84], dispersed on the catalyst's surface. The contact surface of the catalyst and exhaust gas needs to be

extremely large in order for all the molecules of NO_x and N to touch a catalytically active site [85].

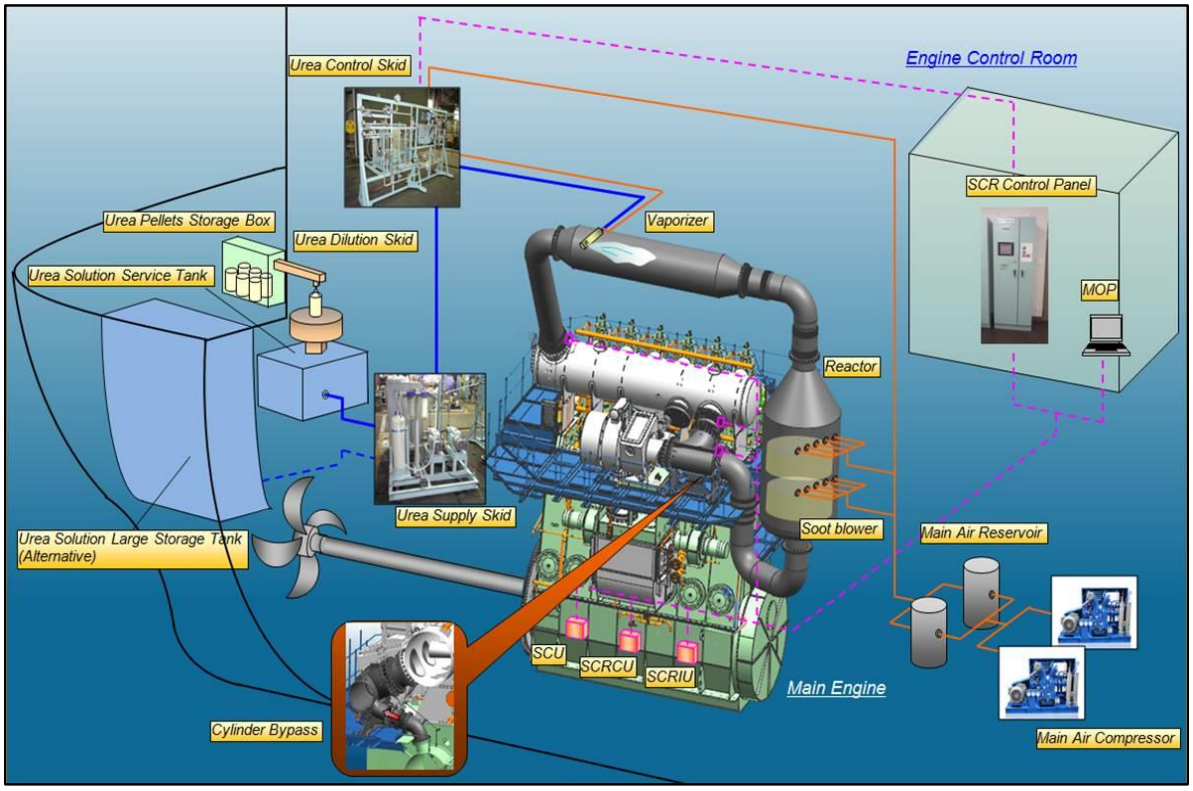

Figure 1.16: Schematic description a SCR system established on a vessel [86].

The use of this *SCR* system is a common practice for NO_x reduction in heavy–duty truck *DI* Diesel engines and its implementation on light–duty engines has been initiated recently. In Fig. 1.17, is depicted a typical layout of an *SCR* system used in the automotive sector.

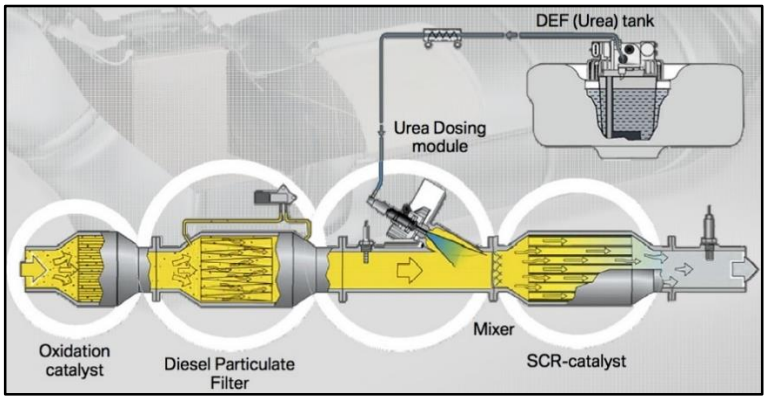

Figure 1.17: Schematic description of the SCR system used in the automotive sector.

For passenger cars and light–duty Diesels engines, recently, sophisticated *SCR* systems are employed which are compact and can operate in low temperatures (i.e. below *300 °C*) utilizing zeolite catalyst etc. [87,88,89].

1.4.3.2 Lean NO_x Trap

The alternative of *SCR* for Diesel engines, is the use of lean NO_x trap (*LNT*) which can achieve *de–*NO_x efficiencies up to *70 – 80%* [89].

The *LNT* uses a catalyst (i.e. platinum (*Pt*), barium (*Ba*) or rhodium (*Rh*)) that absorbs the NO_x from exhaust gas storing it as solid state on its surface, operating as storage device during lean engine operation where O_2 is in abundance. As the storage sites are occupied, the trap efficiency is progressively reduced, therefore requiring regeneration. Regeneration is typically accomplished by injecting additional fuel, producing a stream of reducing exhaust gases (i.e. deprived of oxygen and comprising high concentration of *CO* and unburned hydrocarbons), flowing through the converter. Under rich conditions, the stored NO_x is released from the catalyst sites and catalytically reduced to N_2. The accompanied products of these reactions are the CO_2 and H_2O [90]. In Fig. 1.18 is depicted a schematic description of *LNT* operation principle and a typical *LNT* system layout used in automotive engines.

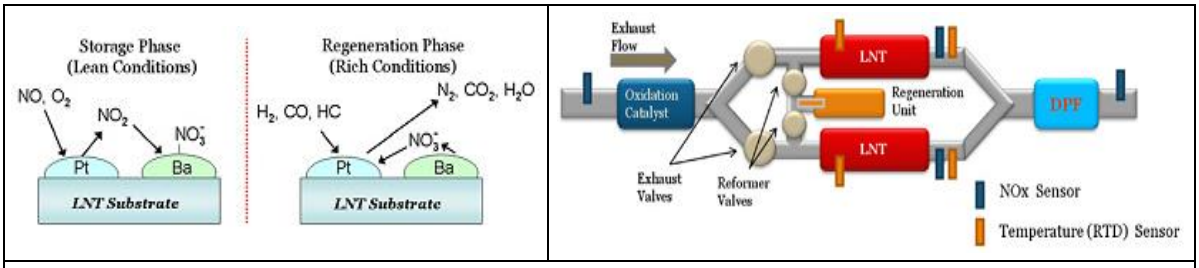

Figure 1.18: Schematic description of LNT operation principle (left) and a typical LNT system layout (right). Both images are derived from Ref. [87].

Nonetheless, the use of after–treatment techniques introduces two major disadvantages:

1. High installation and operating cost.
2. Significant space and weight penalty.

Some other cons are the high pressure drop of exhaust gas introduced from the placement of the catalyst in the exhaust duct, the time requirement for the system heat–up, safety aspects such as the handling of ammonia (for *SCR*), recycling of used catalysts, etc. [85].

Thus, the industry of *ICE* manufacturers and end–users are focusing on the primary (in–cylinder) measures, which alone or combined, can provide adequate NO_x decrease. However, when the NO_x standards are extremely strict, the use of the secondary measures is inevitable.

1.5 Motivation and Objective of the Present Dissertation

Environment and human health and life quality are severely deteriorated due to emission of pollutants which are mainly caused from human activity. The major contributors to the atmosphere pollution are the power generation and transport sectors. Thus the governments of the developed countries have adopted strict regulations to mitigate pollution from these sources. One of the most affected industry from these regulations is the internal combustion engine (*ICE*) industry. Hence, the *ICE* manufactures and end–users worldwide are

seeking for efficient methods to control pollutant emissions to comply with regulations in order to maintain their presence in the markets, avoid the substantial fines and sanctions and also to increase their competitiveness.

The reciprocating engines and particularly the *DI* Diesel engines, occupy a great share of the *ICE* sector, since they are used widespread in passenger cars, automotive transportation, locomotives, non–road applications, sea transportation (maritime) and for power generation as backup or emergency units and as major power generation units in distant areas (i.e. islands) which are not connected to the central grid. Thus, the Diesel engine sector presents great interest, especially regarding performance and emissions. Emissions legislation regulations for NO_x emissions make the Diesel engine development and improvement even more challenging.

There exist various solutions to achieve satisfactory performance and emissions trade–off, keeping exhaust emissions under the legislation limits. These solutions may include primary or secondary measures or a combination of both, as has already described in section 1.4. However, their development, evolution and application require extensive research involving the use of both, computational and experimental techniques. The last, in many cases and especially for large–scale engines (due to their size), are very costly in money, time and labor.

Simulation models can assist this effort by providing low cost, fast and reliable predictions. They can be utilized during engine development in design of experiment (*DOE*) methodologies, physical interpretation and direct oversight of the in–cylinder processes, optimization of the engine's components design and operation characteristics. Moreover, they can be employed in real–time and closed–loop control and operation/optimization of the emission control techniques (primary and secondary (see section 1.4)). Also they can be used for on–board performance and emission monitoring, verification, completion of emission legislation transcripts/reports, etc.

A variety of simulation models exists which can predict the performance and emissions of Diesel engines. These models are distinguished into three major categories:

1. Three dimensional models (i.e. *CDF*, spray phenomenological models).
2. Zero dimensional (i.e. physical–thermodynamic models).
3. Statistical/empirical models.

The most accurate and fundamental of the aforementioned models are the ones of the first category, namely, the multi–zone, *3D*, phenomenological spray models and the *CFD* ones combined with detailed chemical kinetics schemes. Multi–zone, *3D*, phenomenological models [91,92,93,94,95] simulate the fuel spray in the three dimensions by dividing the spray elements into zones of which their spatial location and evolution inside the combustion chamber are determined according to the injection and spray evolution and the considered spray pattern. On the other hand, *CFD* models [96,97,98,99,100] are characterized from their robust physical background and detailed space discretization (mesh). These models attempt to simulate the actual procedures taking place inside the cylinder providing detailed information for the in–cylinder conditions spatially and temporally. Despite the reliable results that they can provide, both model types and especially the *CFD* ones, have significantly increased computational cost which is still a drawback for research and practical applications.

Additionally, they have relatively high complexity and sensitivity to the initial or boundary conditions and require significant effort for their calibration, which limits the possibility for their implementation on real–time (i.e. model–based control) or field applications. Moreover, both model types require an accurate injection profile to achieve meaningful results [95]. The last, for practical and filed applications is usually not available.

The models of the second category make use of the basic thermodynamic lows and chemistry following a theoretical approach rather than a detailed spatial description of the combustion chamber events. These models do not present such high computational cost and complexity as the ones of the first category. Their philosophy is to divide the in–cylinder charge into zones. Thus, these models are divided into single–zone (homogeneous charge) [101,102,103,104], two–zone (bunt and unburnt zone) [105,106,107] and multi–zone (further discretization of the charge) [108,109,110,111,112,113,114,115,116,117]. Single zone models are not appropriate for NO_x emission prediction because they provide only the mean in–cylinder conditions. Hence, the inhomogeneity of the charge and distinguish in high temperature regions, which determine the NO_x formation locally, cannot be accounted for. The last can be compensated for by introducing empirical or semi–empirical/phenomenological concepts or by incorporating zero dimensional multi–zone models or both to simulate the charge temperature distribution inside the combustion chamber.

Finally, the third category comprises models that make use of totally empirical correlations derived from experimental data processing [118,119,120]. Nevertheless, these statistical models require an extended experimental database for the reliable determination of their coefficients (i.e. calibration), but even in this case, they cannot reliably predict emissions outside their calibration range due to the lack of physical base. On the other hand, these modes are very simple and provide directness (since they use actual engine operating data, e.g. from *ECU* and sensors) and very low computational cost and complexity.

Considering the advantages and disadvantages of the models of the aforementioned categories and having in mind the low computational cost demand for real–time and practical applications, a new subcategory is emerged. This subcategory consists the semi–empirical models [121,122,123,124,125,126]. These models combine the merits of the zero–dimensional and empirical models.

In Fig. 1.19, a brief depiction of the categorization of the models used for the performance and emissions analysis is presented:

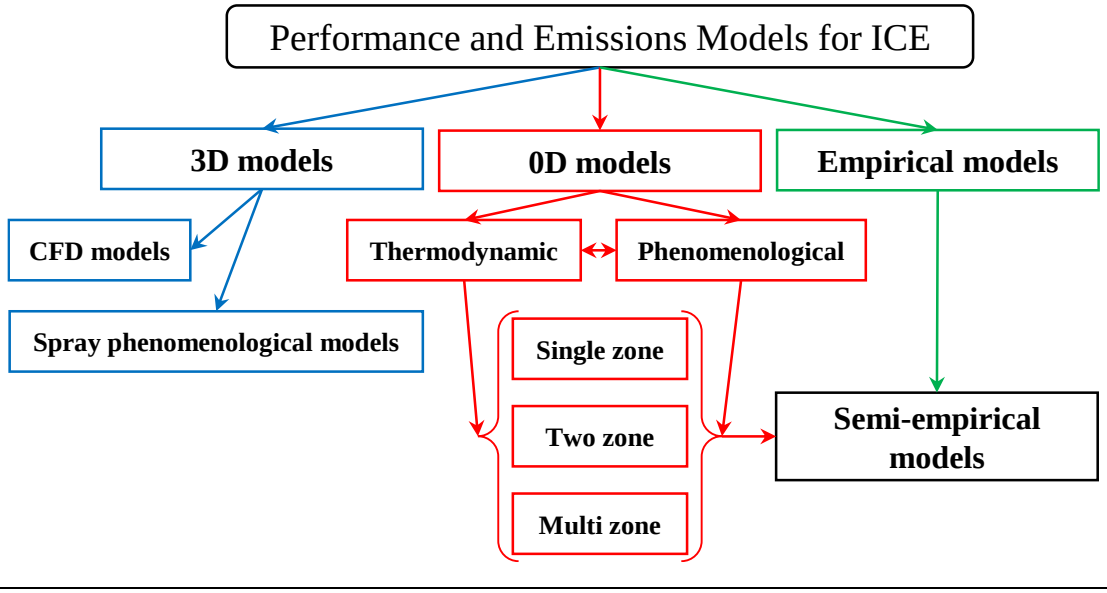

Figure 1.19: Categorization of the models used for the performance and emissions analysis of Diesel engines.

In order to enhance the predictive ability of the semi–empirical NO_x predictive models, is required to include, as input data, actual characteristics of the in–cylinder processes in model calculations. Towards this direction, many researchers have adopted the use of the measured in–cylinder pressure trace, on which the in–cylinder processes are directly or indirectly reflected. The following parameters contribute to the "shaping" of the pressure trace:

- cylinder–combustion chamber geometry/design,
- initial conditions of the charge (temperature, pressure, composition),
- valve timing,
- injection characteristics,
- injection rate and strategy,
- fuel quality and characteristics, etc.

The contribution of the aforementioned parameters can be considered for implicitly via the measured cylinder pressure trace and *HRR* analysis, providing useful information for engine performance and pollutants formation at each instance during an engines cycle. Hence, the use of pressure trace for experimental and real–time applications adds to these models the potential to physically capture the in–cylinder processes. Additionally, on–board/real–time measurement of in–cylinder pressure is now standard practice for large–scale engines since it is used for fault detection and diagnosis. Currently on–line cylinder pressure measurement is possible and being applied (especially in large–scale engines). Also, as the cost of the pressure sensors is dropping, the in–cylinder pressure measurement will also be implemented in automotive sector as well, for real–time applications (i.e. closed–loop control, cylinder pressure–based control and model–based control) [127,128,129,130,131,132,133]. However, even if direct measurement of the pressure trace

is not feasible, a calculated pressure trace may be used derived from a well validated, fast, single–zone model.

Considering the following:

- the requirement of the *ICE* industry for development and evolution of technologies/methodologies for NO_x emissions control,
- the continually stringent legislation for NO_x emissions abatement,
- the hazardous effects on the environment and human health,
- the available technologies for emissions control,
- the existing literature and projects for the control and improvement of these technologies using simulation models,
- the potential of direct in–cylinder pressure acquisition and
- the fact that NO_x is one of the most important controlled pollutant of Diesel engines,

we were motivated to develop a simplified, semi–empirical, multi–zone, thermodynamic model for the estimation of NO_x emissions and formation history in *DI* Diesel engines using the measured in–cylinder pressure trace and an empirical scenario for the determination of the zone equivalence ratio Φ. The proposed model also aims to have a wide range of implementation regarding engine types (e.g. large–scale, automotive, etc.) and engine operating conditions/settings.

Thus, the objective of the present dissertation is the development and evaluation of a fast and simplified NO_x prediction model for *DI* Diesel engines targeting to the following:

1. Reduction of research, design and experimental cost (time, money, labor).
2. Contribution to the understanding/oversight of *NO* formation during the engine cycle and thus its effective control.
3. Prediction of NO_x emissions, for various engine types and operating parameters/configuration.
4. Real–time NO_x monitoring and verification.

The basic characteristics of the proposed simulation model are:

1. Simple structure and simplified concept.
2. Low computational cost.
3. Strong physical background (thermodynamics, thermochemistry).
4. Utilization of the measured pressure trace.
5. Combination of the model with empirical/statistical additions for optimum results.
6. Wide range of implementation with low calibration effort.
7. Versatility of implementation (*2* and *4*–stroke, low and high speed engines, *EGR*, *VIT*, etc.).
8. Low complexity and easy handling.

In the next chapter (Chapter 2), a literature review of the existing models used for NO_x emission prediction for Diesel engines is presented. The characteristics and rationale of some of these models were taken into account during the development of the proposed model, which is comprehensively described in Chapter 3.

Chapter 2 LITERATURE REVIEW – EXISTING MODELS FOR NO_X PREDICTION

2.1 Introduction

In the present chapter, a literature review of NO_x emissions models is presented. At first, some multi–zone, three–dimensional (*3D*), phenomenological models are described in section 2.2, intending to reveal their basic difference from the other types of models presented at next. The basic difference is the geometrical/spatial (i.e. *3D*) consideration of the fuel spray and flame. These models are able to approach realistically the spray and flame evolution inside the combustion chamber and after calibration (e.g. matching of the calculated and measured compression and maximum combustion pressure), they can provide useful information for the in–cylinder processes. The extracted information can be utilized for performance and emissions optimization. However, these models have a relatively high computational cost and increased complexity but are considerably faster than *CFD* (computational fluid dynamics) ones. They are also more versatile than *CFD* when used in conjunction with other models e.g. turbocharging models etc., for instance in optimization investigations involving design of experiments (*DOE*) by using simulation models.

To overcome the high computational cost and complexity issues, some researchers have developed simplest models than the aforementioned *3D*, phenomenological ones, such as purely empirical/statistical, single–zone empirical and semi–empirical. Some indicative models of this category are presented in section 2.3. These models are extremely fast and adequate for real–time/on–board and closed–loop control, however, due to lack of physical base, they are only valid inside their calibration range and for the specific application, namely for the engine type that they are designed for.

In order to face the drawbacks of the aforementioned types of models and adopt their advantages, attempts have been made for the deployment of zero–dimensional, multi–zone, semi–empirical/phenomenological, thermodynamic models, which are faster and less complicated than *CFD* and *3D* phenomenological ones but more physically robust and with wider implementation range than empirical models. Some indicative models of this category are presented in section 2.4.

Zero–dimensional, multi–zone, semi–empirical/phenomenological, thermodynamic models are making use of at least two zones to simulate the in–cylinder processes. However, the discretization does not correspond to the geometrical, *3D* modeling of the spray or of the space inside the combustion chamber, although it accounts for the imposed constrains from the engine cylinder geometry. Instead, the content of the cylinder is separated into zones. The zones evolve inside the combustion chamber as the time elapses, according to physical laws (e.g. thermodynamics, etc.) or phenomenological correlations. In addition, to improve their predictions, they utilize the measured or predicted in–cylinder pressure trace, heat release rate (*HRR*) analysis and empirical/statistical or semi–empirical correlations.

The use of the measured pressure trace or predicted pressure trace from a well validated model, accompanied with heat release rate (*HRR*) analysis, provide direct or indirect information about the mechanisms and processes taking place inside the cylinder. This adds an immediacy and reliability to the model. Furthermore, the addition of empirical or semi–empirical concepts enables significant simplifications in the model without deteriorating its predictive abilities. Moreover, it allows the direct insertion of engine characteristics or/and engine operation parameters that cannot accounted for otherwise. Furthermore, it provides the potentials for model adjustment/regulation for a specific application.

The aforementioned features provide to the zero–dimensional, multi–zone, semi–empirical/phenomenological, thermodynamic models the ability to predict NO_x emissions in a wide range of engine types, operating conditions and engine settings/adjustments. Additionally, due to their simple structure and physical base, they are very fast and reliable, making them capable to be utilized in the research and applied/practical (e.g. model–based control, real–time monitoring/verification/diagnosis, etc.) field.

Considering the potentials and the advantages of the lastly mentioned model category, it was decided to develop a new, semi–empirical, multi–zone, thermodynamic model, which uses the measured in–cylinder pressure trace and is oriented for real–time applications. Among the new concept and characteristics of the proposed model, many features and innovating ideas of the existing models, presented at the following sections (2.2–2.4), were adopted, evolved and combined to compose a new, reliable and fast NO_x emissions model.

The new model aims to overcome the introduced complexity from the use of phenomenological concepts and thus minimize the calibration effort. But at the same time, aims to avoid the low versatility of the totally simplified/empirical models, targeting to a wide range of implementation regarding engine type and engine operating conditions.

2.2 Multi–zone, Three–dimensional, Phenomenological Models

2.2.1.1 Introduction

The term detailed, multi–zone, *3D*, phenomenological model, is attributed to the models that discretize, spatially and temporally the fuel spray (i.e. vaporization, air entrainment, mixing, etc.) and combustion flame into zones. The zone evolution as crank angle (*CA*) time elapses during an engine cycle, is described from physical laws and phenomenological correlations.

To calculate the *HRR* and local conditions (pressure, temperature chemical composition), the injected fuel is divided into packages (discreet volumes), called zones. During an engine cycle, the zones are evolving inside the cylinder, accounting for the geometry constrains, according to a geometrical spray pattern (spray cone *3D* discretization). The development of the spray and the evolution of the zones (thermochemical characteristics and interaction between them) as time elapses are determined by using:

1. physical laws/principles, i.e.:
   - conservation of mass,

- conservation of energy
- conservation of momentum,
- ideal gas consideration,
- chemical reactions,
- etc. and

2. semi–empirical/phenomenological correlations for:
   - spray characteristics such as spray brake–up length, angle and penetration, droplet size, vaporization rate, wall impingement, air entrainment rate,
   - intake flow from the valves or ports,
   - combustion mixture preparation,
   - ignition delay,
   - diffusion flame propagation and quenching,
   - swirl and squish flows of the charge,
   - reaction rates,
   - heat transfer,
   - mass transfer between the zones,
   - etc.

From this approach, the performance characteristics (i.e. fuel consumption, power, etc.) and emissions (i.e. NO_x, SO_x, CO_x, *HC*, *PM*, etc.) can be estimated. At next, indicatively, two of these models are presented.

2.2.1.2 Hiroyasu 3D Multi–Zone Phenomenological Model

One of the most successful *3D*, multi–zone, phenomenological model is the one developed from Hiroyasu et al [91,134]. This model concept is the base for the models of this category, some of which are currently used in commercial Diesel engine simulation tools like *GT–Power* [95]. Hiroyasu et al developed a model which consists a Heat Release Rate (*HRR*) sub–model and an emission formation sub–model. In the *HR* model, the fuel, which is injected through a nozzle, forms a spray with a conical *3D* structure (see the right side of Fig. 2.1). The spray cone is divided into *250* packages (*10* packages in the radial direction and 25 in the axial direction) [134] with the same fuel mass amount. It was assumed that there is no mixing between the packages. Spray impinging on walls and swirl are considered for. The air entrainment into the spray is given by the conservation of momentum and the spray behavior is determined by the experimental equation of spray penetration observed without combustion. Droplet evaporation, which is assumed to start immediately after injection, is also considered for. The *HRR* is calculated in each package and by summing up the *HR* from each package, the *HR* in the combustion chamber is obtained, from which is possible to calculate the average cylinder temperature and pressure. Heat transfer to the walls is also accounted for. A heterogeneous temperature field is assumed. The adiabatic flame temperature $T_B(\theta_a)$ is calculated assuming ideal combustion. After combustion, the temperature changes in each package following the isentropic compression/expansion process. The species concentrations are calculated from the *HR* model. *NO* is formed via the extended Zeldovich mechanism [28,29,30]. The *NO* concentration equation is integrated for each package from the start of combustion to a crank angle (*CA*) where reaction rates are so low that *NO* concentration (Y_{NO}) no longer changes. Finally, Y_{NO} is summed up over all the packages to

calculate the total *NO* formation. Soot formation is also modeled. The evolution of a mass package is depicted in left part of Fig. 2.1:

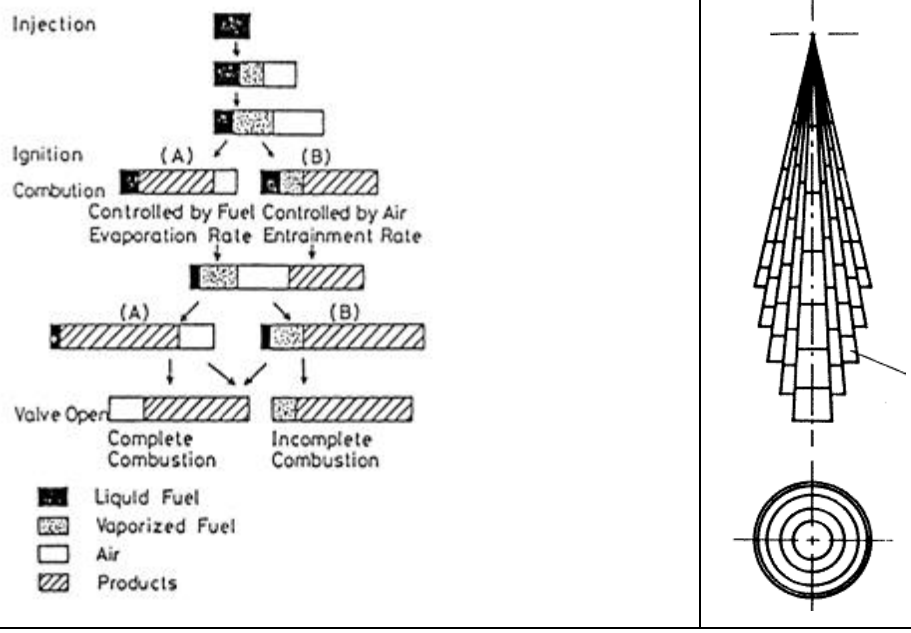

Figure 2.1: A mass system package evolution at the left and the schematic diagram of the divided packages at the right [91].

Hiroyasu applied this model to optimize a *DI* Diesel engine regarding performance and emissions [91,134]. The parameters optimized were the number of nozzle holes, the diameter of nozzle hole, diameter of toroidal, swirl ratio, clearance volume, intake valve closing timing, injection timing, injection duration and the exhaust valve opening timing.

2.2.1.3 NTUA Multi–Zone three Dimensional Phenomenological Model

Kouremenos, Rakopoulos and Hountalas, [135] developed a *3D*, phenomenological, multi–zone, spray model for the prediction of both performance and emissions regarding Diesel engines. This model is a *3D*, multi–zone one, where each zone has its own history of temperature, composition, etc.

Hountalas et al [136] further developed and validated this model on various types of Diesel engines also including large–scale ones [94,137,138].

The conditions inside each zone are calculated by using the first thermodynamic law and the conservation equations for mass and momentum. The resulting fuel jet is divided into zones using a concentric consideration as shown in Fig. 2.2. The division of the fuel jet into zones is provided by such a model in the initial direction of the jet axis "*x*" and in the two dimensions normal to it, "*r*" and "*z*". The number of axial zones is determined from the duration of the fuel injection period and the calculation time step used. The number of zones

in the radial and circumferential direction are chosen arbitrary intending to the optimum predictions quality–computational cost trade–off.

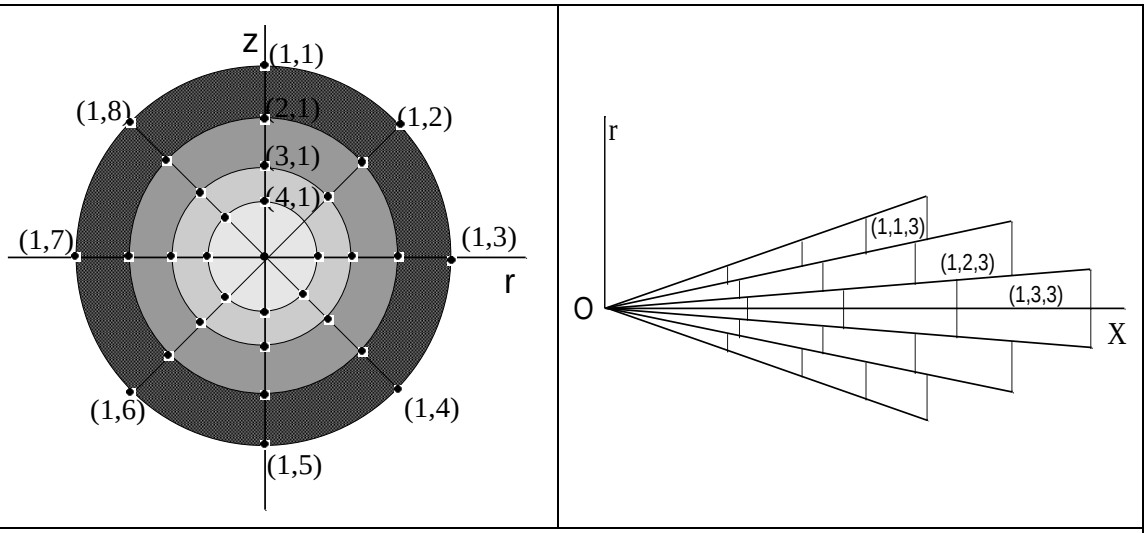

Figure 2.2: Zone formation on the "r–z" plane normal to injection direction at left side and zone formation on the "x–r" plane at the right. Presently a number of five zones are used in the radial direction and eight in the circumferential direction [137].

The aforementioned model makes use of a number of sub–models to estimate performance and NO_x emissions. For heat–transfer the Annand formula was used [139,140], where the characteristic velocity for the heat transfer calculations is obtained from the turbulent kinetic energy viscous dissipation rate $k\sim\varepsilon_t$ model. The heat exchange rate is then distributed to the zones according to their mass, temperature and specific heat capacity.

The spry model is based on model proposed by Amsden et al [141] and Nishida and Hiroyasu [142]. The fuel jet angle and the penetration of each zone inside the combustion chamber are estimated using empirical correlations that provide the velocity along the spray axis and its radial component [141,143,144]. The effect of air swirl on zone velocity is also considered for using the approach described in Ref. [141]. From the previous considerations in conjunction with the use of momentum and mass conservation, the position of each zone inside the combustion chamber is estimated. After wall impingement the wall jet theory of Glauert [144] is used to determine the jet history on the cylinder walls.

The air entrainment rate into each zone is estimated from momentum conservation. The air–entrainment rate adjustment coefficient is used to adjust the overall air entrainment rate and is determined by matching the calculated peak firing pressure value to the measured one. Inside each zone, the fuel is divided into packages (groups) where the droplets have the same Sauter Mean Diameter (*SMD*) which is calculated via a semi–empirical correlation. The distribution of droplet diameter in the packages is given by a chi–squared distribution function [8]. For the evaporation process, the model of Borman and Johnson [145] is used.

Ignition delay of each spray element (i.e. zone) after its injection is also determined from a semi–empirical correlation [141]. The local combustion rate $(\dot{m}_{fb})$ is derived using an Arrhenius type expression as described in Eq. (2.1):

$$\dot{m}_{fb} = K_b \cdot C_f^{af} \cdot C_o^{ao} \cdot e^{\frac{-E_c}{T}} \cdot \frac{1}{6 \cdot N} \tag{2.1}$$

where K_b is a constant, E_c the reduced activation energy and C_f, C_o the mass concentrations of fuel and oxygen respectively.

The fuel injection mechanism is modeled as proposed in [8,146] but by adapting modifications when applied on marine *2*–stroke engines. In the last case the following control volumes were considered:

- high pressure pump chamber,
- delivery valve chamber,
- delivery pipe from pump to injector
- and injector.

The exhaust gas exchange between inlet and exhaust manifold and the cylinder, which determines the in–cylinder trapped mass, is model by the means of filling and emptying technique. For the case of *2*–stroke engines a scavenging model is used [146] accounting for short–circuiting [9] during scavenging.

The *NO* formation is calculated in each zone via the extended Zeldovich mechanism [29,30] and chemical kinetics, after the calculation of the chemical composition of each zone. The last is attained by using the combustion chemical reactions, fuel and charge composition, temperature, pressure and volume of the zone and also using a chemical dissociation scheme [147] to calculate the equilibrium concentrations [137].

2.3 Single–zone, Empirical and Semi–Empirical Models

2.3.1.1 Introduction

In this section, some of the existing simplified models for NO_x prediction, which are reported in the literature, are presented indicatively for the sake of completeness. These models are very fast, however they require extended calibration to provide adequate predictions, mostly in the range of their calibration range and for the engine type on which they were developed.

Empirical and semi–empirical models make use of engine operating data such as in–cylinder pressure, temperature, intake air flow, fuel flow rate, engine speed, O_2 in exhaust gas, etc. which can be derived directly from real–time measurement or from maps stored in engine's electronic control unit (*ECU*). These parameters are correlated directly with tail pipe NO_x emissions via empirical or semi–empirical correlations.

The simplest way to formulate a model, is to postulate an equation dependent on chosen parameters and then select the values of constants in the equation to fit experimental results. This kind of models are characterized as purely empirical.

2.3.1.2 Callahan Empirical NO_x Model

Callahan et al [148] developed an empirical emission model which accounts for the effects of transient operation. By using regression techniques they obtained the Eq. (2.2):

$$Emission = \prod_{i=0}^{14} exp(c_i \cdot x_i) \tag{2.2}$$

where c_i are the regression constants and x_i are system parameters. The constants c_i depend on the engine type and engine characteristics [149].

2.3.1.3 P–Φ Empirical Models for NO_x at Flame Front

Some researchers [150,151] used models of high pressure practical combustors for the calculation of *NO* at the flame front, relying on empirical correlations (*f*) which involve equivalence ratio (*Φ*) and pressure (*p*) dependencies of flame–front *NO*. These models have the form described in Eq. (2.3) [39]:

$$(NO)_{flme-front} = f(\Phi) \cdot p^{\frac{1}{2}} \cdot (NO)_{equil.} \tag{2.3}$$

2.3.1.4 Gartner Semi–Empirical NO_x Model

Gartner et al [152], after an extensive investigation, concluded that the center of combustion (*COC*) (the crank angle where the 50% of the fuel has burnt) is a marker for the end of the thermal *NO* formation for an internal combustion engine (*ICE*). They also stated that the NO_x mass that is formed until the *COC* correlates well with the engine tail–pipe NO_x emissions level and that its quantitative level depends primarily on the position of the *COC* to top dead center (*TDC*). The proposed methodology also introduces the effect of the in–cylinder charge mass and the mass of O_2. NO_x emissions are estimated through a linear empirical correlation described in Eq. (2.4):

$$log(NO_x) = c_0 + c_1 \cdot COC + c_2 \cdot m_{cyl} + c_3 \cdot m_{O_2} \tag{2.4}$$

where NO_x is calculated as the ratio of its mass and fuel mass *[g/Kg]*, *COC* is in *[°CA]* after *TDC*, m_{cyl} and m_{O2} are the in–cylinder air and oxygen mass respectively per cycle and displaced volume and c_0, c_1, c_2, c_3 are model coefficients. The *COC* was derived from *HR* analysis using the measured pressure trace. The above correlation (Eq. (2.4)) was validated on *920* experimental points on various heavy–duty Diesel engines.

2.3.1.5 Wu and Peterson Semi–Empirical NO_x Model

Wu and Peterson [153] developed a model which requires the following inputs to evaluate the *NO* emission index, *EINO* (*EINO* is defined as *g NO/kg fuel*):

- in–cylinder temperature,
- fuel burning rate,
- engine speed,
- start of combustion (*SOC*) and
- end of combustion (*EOC*).

In the specific model, is assumed that the mass of *NO* formed can be evaluated from the following correlation:

$$dm_{NO} = MW_{NO} \cdot \int_0^{\tau_m} \frac{d[NO]}{dt} \cdot dt \cdot dV_b$$

$$\frac{d[NO]}{dt} = 2 \cdot k_f \cdot [N_2] \cdot [O] \tag{2.5}$$

$$N + O_2 \overset{k_f}{\leftrightarrow} NO + O$$

where $d[NO]/dt$ is the rate of *NO* formation, τ_m is the mixing time scale, t is the time, V_b is the volume of the burned gases and k_f is the forward reaction rate constant assuming the reverse reactions to be negligible and *[N]* to be at steady state. During the mixing time τ_m, turbulent mixing causes the temperature of the burnt gases to decrease and the radicals involved in *NO* formation to recombine. They assumed that $2 \cdot k_{1f} \cdot [O] \cdot dV_b \sim e^{\frac{-E}{R \cdot T}} \cdot dm_f$ (dm_f is the mass of fuel), uniform temperature (T) in dV_b and τ_m inversely proportional with engine speed (N) [154], thus they obtained the following:

$$EINO \sim \int_{\vartheta_{SOC}}^{\vartheta_{EOC}} \int_0^{\tau_m} exp\left(\frac{-E}{R \cdot T}\right) \cdot dt \cdot \frac{dF_f}{d\vartheta} \cdot d\vartheta$$

$$\tau_m = \left(\frac{N_{ref}}{N}\right)^{\frac{2}{3} or\ 1} \tag{2.6}$$

where E is the overall activation energy which is a model's parameter, $dF_f/d\theta$ is the specific fuel burning rate, N_{ref} is a reference engine speed and θ is the crank angle. The inner integral accounts for the turbulent mixing process and the outer for the coupling between the temperature history and the fuel burning rate.

The plausibility of assuming uniform temperature in dV_b was validated by calculating flame temperatures in ideal mixing models [155]. The calculations differed by roughly *+100 K* which was the same as the uncertainty in the experiments that they performed. If the

temperature is assumed to be constant during combustion (i.e. characteristic temperature (T^*)) then the Eq. (2.6) is reduced to the following simplified correlation [149,153]:

$$EINO \sim \left(\frac{N_{ref}}{N}\right)^{\frac{2}{3}\,or\,1} \cdot exp\left(\frac{-E}{R \cdot T^*}\right) \tag{2.7}$$

2.3.1.6 Miller Empirical NO_x Model

Some researchers, use empirical interventions to achieve better *NO* predictions. For instance, Miller et al [41], to deal with the *NO* levels overestimation from their model, which was more than *20%*, incorporated an empirical parametric variation of the reaction $N + O_2 \overset{k_1}{\leftrightarrow} NO + O$ by modifying the reaction rate constant k_1 with a pressure coefficient as follows:

$$k_1 = C_p(p) \cdot 1.8 \times 10^{14} \cdot exp(-38370/T) \tag{2.8}$$

where C_p is a function of the instantaneous in–cylinder pressure (p) in atmospheres. They found that this modification, decreases the reaction rate by factor of five, producing accurate *NO* predictions as a function of load [41,156].

2.3.1.7 Park Semi–Empirical, Real–Time NO_x Model

Park et al [126] developed a semi–empirical, real–time *NO* prediction model which makes use of the measured in–cylinder pressure and data from engine *ECU*. They used a *CFD* model (*Star–CD* [157]) to validate their model. To avoid the calculation of the total amount of *NO* by integration of the instantaneous *NO* formation rate $\frac{d[NO]}{dt}$, which requires the calculation of temperature and O_2 and N_2 concentrations at every step, they used the average *NO* formation rate multiplied by the *NO* formation duration inside an engine cycle as described in Eq. (2.9):

$$[NO] = \int \frac{d[NO]}{dt} \cdot dt \approx \left(\frac{d[NO]}{dt}\right)_{aver} \cdot (duration) \tag{2.9}$$

Their investigation revealed that the maximum *NO* formation rate is directly proportional to the average *NO* formation rate. Therefore, the maximum *NO* formation rate is used as a representative value of the averaged *NO* formation rate, which is given in a simplified Zeldovich form [8] from Eq. (2.10):

$$\left(\frac{d[NO]}{dt}\right)_{aver} \sim \left(\frac{d[NO]}{dt}\right)_{max} = \frac{A}{T_{max}^{1/2}} \cdot e^{-\frac{69090}{T_{max}}} \cdot [O_2]_{max}^{1/2} \cdot [N_2]_{max} \tag{2.10}$$

For the determination of *NO* formation duration (see Eq. (2.9)), the authors' investigation revealed that the *CA* time step where the *20%* and *90%* of total *NO* is formed, should be chosen as the start and end points of the *NO* formation process during an engine cycle, because they can be determined easier than the corresponding *0%* and *100%*. The

difference between the total amount of *NO* formed (0–*100%*) and the *NO* amount formed in the *CA* interval which is defined from the *CAs* where the *20%* and *90%* of total formed *NO* occurs, is compensated using the empirical constant *A* in Eq. (2.10).

In order to determine this *CA* interval, the authors connected the *NO* formation initiation (i.e. *20%* of total *NO*) and completion (i.e. *90%* of total *NO*) *CAs* with the fuel mass fraction burned (*MFB*) at these *CAs*. The *MFB* is obtained from the integration of the *HRR*, which is calculated using the in–cylinder pressure. The matching between *NO* formation and *MFB* indicated that the *CA* where the *40%* of the fuel is burnt matches with the *CA* where the *20%* of the total formed *NO* and the *CA* where the *80%* of the fuel is burnt matches with the *CA* where the *90%* of the total formed *NO*. Thus the *NO* duration term of Eq. (2.9) is calculated directly from the *HRR*.

Maximum temperature (T_{max}), O_2 and N_2 concentrations, and constant *A* are required to predict the maximum *NO* formation rate according to Eq. (2.10). These inputs are calculated using the available *ECU* data and in–cylinder pressure. To calculate the T_{max}, the adiabatic flame temperature (T_{ad}) was calculated at first, from a second–order formula described in Eq. (2.11), which was derived from the available database (*130* simulation results under various *AF*, *EGR* and initial temperature conditions) by using the *Chemkin–III* software [158].

$$T_{ad} = (5.7401 \cdot [O_2]^2 - 4.6043 \cdot [O_2] + 1.2616) \cdot T_{SOC} + (-22072 \cdot [O_2]^2 + 16718 \cdot [O_2] - 30276) \quad (2.11)$$

In the previous relation, T_{SOC} is the temperature at the start of combustion (*SOC*) calculated from ideal gas state equation, data from *ECU* and measured in–cylinder pressure. Then the T_{max} is calculated assuming isentropic compression ($\gamma = const = 1.3$) and using the measured pressure at *SOC* (p_{SOC}), maximum in–cylinder pressure (p_{max}) and the calculated T_{ad}. This calculation is given from Eq. (2.12):

$$T_{max} = T_{ad} \cdot \left(\frac{p_{max}}{p_{SOC}}\right)^{\frac{\gamma-1}{\gamma}} \quad (2.12)$$

The model validation indicated that is able to adequately predict *NO* for various *EGR* rates and injection timings. It also provided satisfactory results when applied on the new European driving cycle (*NEDC*).

2.3.1.8 D'Ambrosio Control–Oriented, Semi–Empirical NO_x Model

D'Ambrosio et al [159] developed a fast, control–oriented, semi–empirical model that is capable of predicting NO_x emissions in Diesel engines under steady state and transient conditions. The model takes into account the maximum in–cylinder burned gas temperature

of the main combustion (i.e. the one resulted from the main injection), ambient gas to fuel ratio, mass of injected fuel, engine speed and injection pressure.

The authors considered the following effects on *NO* formation:

- the exponential temperature (*T*) dependence proposed from the extended Zeldovich mechanism,
- the effect of O_2 and N_2 availability which are functions of the mass of the unburned gas that participates in diffusive combustion, which is in turn proportional to the mass of injected fuel (m_{fuel}) and to unburnt ambient gas to fuel ratio (α_{st}^{u}),
- the effect of diffusive combustion dilution with the surrounding charge and the re–entrainment of the hot gases into the jet, which are functions of in–cylinder turbulence and injected fuel velocity which are in turn a function of injection pressure (p_f) and engine speed (*N*) and
- the effect of atomization and fuel/air mixing which are also largely depended on p_f.

Accounting for the aforementioned effects, the authors proposed the semi–empirical correlation described in Eq. (2.13), which provides the mass of *NO* formed during an engine cycle. They also observed that the gas temperature of the burned gas, used for the NO_x correlation, should be the maximum one during the burning of the main injection ($T_{bmax,main}$).

$$\dot{m}_{NO_x} = K \cdot e^{\frac{K_1}{T_{bmax,main}}} \cdot (a_{st}^{u})^{K_2} \cdot \left(\dot{m}_{fuel}\right)^{K3} \cdot (N)^{K4} \cdot \left(p_f\right)^{K5}$$

$$a_{st}^{u} = 132.08 \cdot \left(\frac{X_{r,tot}}{\lambda}\right)^{4} - 78.471 \cdot \left(\frac{X_{r,tot}}{\lambda}\right)^{3} + 38.115 \cdot \left(\frac{X_{r,tot}}{\lambda}\right)^{2} + \tag{2.13}$$

$$13.695 \cdot \frac{X_{r,tot}}{\lambda} + 14.379$$

In the previous correlations, *K*, K_1–K_5 are tuning factors, $X_{r,tot}$ the total *EGR* and residual gas fraction and λ the global relative air to fuel ratio. The parameters: $X_{r,tot}$, λ, m_{fuel}, p_f and *N* are obtained from engine's *ECU*. The $T_{bmax,main}$ was evaluated using a three–zone thermodynamic model which makes use of the measured in–cylinder pressure, developed previously from the authors [116]. However, when cylinder pressure measurement is not available and hence the use of the three–zone thermodynamic model is not feasible, the authors used the following two simplified correlations for $T_{bmax,main}$ (see Eq. (2.14)). These correlations were

derived from a statistical analysis investigation conducted on various experimental test cases by implementing the three–zone thermodynamic model.

$$T_{bmax,main} = 1832.8 \cdot \left(\dot{m}_{fuel}\right)^{0.0165} \cdot (N)^{-0.0080} \cdot (T_{SOImain})^{0.2688} \cdot (a_{st}^{u})^{-0.4950}$$

$$T_{SOImain} = T_{int}\left(\frac{V_{BDC}}{V_{SOImain}}\right)^{m-1} \qquad (2.14)$$

or

$$T_{bmax,main} = 7031.2 \cdot (p_{int})^{0.1160} \cdot (T_{int})^{-0.3069} \cdot (a_{st}^{u})^{0.2133}$$

In the previous expressions *m* represent the polytropic index, *V* is the cylinder volume and the subscripts *BDC*, SOI_{main} and *int* denotes the bottom dead center, start of main injection and intake manifold respectively. The calculation of the temperature *[K]* at SOI_{main}, which is according to polytropic compression, takes into account the effect of the engine compression ratio on the charge temperature. The use of a_{st}^{u} is related to the in–cylinder oxygen concentration. The fuel mass flow ($\dot{m}_{fuel}$ *[g/cyc/cyl]*) and engine speed (*N [rpm]*) are used because they can be related to the heat transfer effects, which are dependent from engine load and speed.

The model was validated and evaluated on a *DI* Diesel engine using both, indirect and direct acting piezoelectric injection systems [160], on the urban and extra–urban phases of the new European driving cycle (*NEDC*). A good agreement was found between the predicted and experimental values of the instantaneous and cumulated mass *NO* emissions. The model's calculation time is of the order of some tens of a microsecond when the elaboration is performed on a Pentium D *PC*.

2.3.1.9 Asprion Empirical–Phenomenological NO_x Model

An interesting prospective is the combination of empirical and phenomenological models for NO_x prediction to comply with typical requirements of computationally demanding fields such as engine dynamic optimization and model–based control applications, able to provide adequate NO_x predictions during transients.

Asprion et al [122,123] developed such a model and validated it using data from three different engines. For the development and validation, the required intermediate quantities (i.e. *SOC*, p_{SOC}, T_{SOC} [122]) were obtained from the measured in–cylinder pressure. Their model is characterized by a physical base, empirical correlations derived from experimental data and the use of a set–point relative formulation. This formulation, which comprises one map and *10* scalar parameters, is used to simplify the model's structure and improve the extracted results qualitatively. Moreover, this model makes use of a single representative package, instead of adopting a multi–package scenario, which attempts to capture the spatial and temporal distribution of temperature inside the combustion chamber. This is justified from the authors who postulate that the temperature and composition profiles of the multiple packages are similar [120].

This model requires as inputs the following parameters:

- engine speed,
- injected fuel mass,
- cylinder trapped mass and its composition and
- *SOC* event and the corresponding pressure and temperature.

The latest can either be obtained from measured in–cylinder pressure trace or may be calculated from quantities provided by a sub–model for the air path of the engine.

As mentioned, their model was used for engine dynamic control optimization [123]. The control parameters used for this procedure are the following:

- boost level (controlled by a variable–geometry turbine),
- combustion timing and
- common–rail pressure.

The specific model aims to predict the effect of these parameters on NO_x emissions. Additionally, the effect of the external *EGR* is inherently accounted for, since the model is sensitive to the gas composition.

For NO_x formation the single global reaction described in Eq. (2.15) was used

$$\frac{1}{2}\cdot N_2+\frac{x}{2}\cdot O_2 \leftrightarrow (2-x)\cdot NO+(x-1)\cdot NO_2 \equiv NO_x$$

$$r_{fw}=k_{fw}(T)\cdot [N_2]^{\frac{1}{2}}\cdot [O_2]^{\frac{x}{2}} \qquad (2.15)$$

$$r_{bw}=k_{bw}(T)\cdot [NO_x]$$

NO_x formation rate, i.e. the net reaction rate multiplied with the volume participating in the reaction, is integrated over one combustion cycle, yielding the amount of NO_x produced, as described in Eq. (2.16):

$$\frac{n_{NO_x}}{6\cdot N_{eng}}=\int_{\theta_{SOC}}^{\theta_{EVO}} V_{reac}(\theta)\cdot\Big(r_{fw}(\theta)-r_{bw}(\theta)\Big)\cdot d\theta \qquad (2.16)$$

where n_{NO_x} is the number of moles of NO_x, r_{fw} and r_{bw} are the forward and backward reaction rates respectively, T is the temperature, θ is the crank angle, V_{reac} is the reacting volume and N_{eng} is the engine speed which is finally omitted since it eventually cancels in the set–point relative formulation. After some mathematical processing and by introducing some assumptions and in conjunction with the set–point map, they ended up to the following correlation:

$$\tilde{n}_{NO_x,fw}=\tilde{V}_{reac}\cdot\int_{\theta_{SOC}}^{\theta_{SOC}+30^{\circ}} k_{fw}(T)\cdot d\theta \qquad (2.17)$$

The temperature used in the previous correlation (Eq. (2.17)) is the temperature of the single representative package. Its initial value is chosen to be the adiabatic flame temperature. The evolution of this temperature is defined throughout the cycle from the following effects:

- compression and expansion of the cylinder charge and
- heat losses from the formation zone to the cooler surrounding gas.

The polytropic compression and expansion assumption was adopted, whereas the latter is expressed by a temperature reduction due to heat–losses. The reacting volume ($\tilde{V}_{reac}$) is defined from a semi–empirical correlation based on spray theory:

$$\tilde{V}_{reac} = \left[p_{rail} - \left(p_{cyl}(\theta_{SOC}) + k_p \cdot m_f\right)\right]^{k_v}$$
$$k_v = k_{v,0} + N_{eng} \cdot m_f^{0.25} \tag{2.18}$$

where p_{rail} is the rail pressure during injection, p_{cyl} is the in–cylinder pressure, m_f is the fuel mass injected and k_p, $k_{v,0}$ and $k_{v,1}$ are model parameters.

Execution speed is roughly 500 times faster than real–time and throughout the entire engine operating range, also during transient operation, relative errors are below *10%* even for the largest allowable, simultaneous variation of all inputs.

2.3.1.10 Timoney Semi–Empirical NO_x Model

Timoney et al [160] developed a semi–empirical model for NO_x emissions, based on the instantaneous in–cylinder pressure by combining fundamental thermodynamic principles and key empirical constants which have been derived using statistical techniques. The validation of the model was relied on the availability of an extensive bank of experimental data from three different designs *DI* Diesel engine, each utilizing common rail fuel injection systems and in some cases, with the use of multiple injections per cycle.

This model employs the rate of fuel mass burned, adiabatic temperature and chemistry of NO_x formation. Simplified calculations, based on these three factors, derived from the in–cylinder pressure trace, result in reduced computational time for the final NO_x model. For the rate of NO_x formation a simplified Zeldovich mechanism scheme is used:

$$N_2 + O_2 \leftrightarrow 2 \cdot NO$$
$$O_2 \leftrightarrow 2 \cdot O$$
$$\frac{dN}{dt} \cong 0 \tag{2.19}$$
$$\frac{d[NO]}{dt} = \frac{const.}{T^{1/2}} \cdot exp\left(\frac{-E_a}{T}\right) \cdot [N_2]_e \cdot [O_2]_e^{0.5}$$

where $d[NO]/dt$ is the molar rate of NO_x formation, T is the local temperature, E_a is the activation energy and $[N_2]_e$ and $[O_2]_e$ are equilibrium concentrations of nitrogen and oxygen respectively in a mixture of gases dissociated at high temperatures. The authors accounted

for the most important NO_x formation processes occurring at the flame front during diffusion combustion. Thus only this aspect was modeled avoiding the approximation of unknown local data for the post–flame zone.

The adiabatic flame temperature was incorporated as the characteristic temperature in Eq. (2.19). The concentrations of N_2 and O_2 were taken assuming stoichiometric conditions at the flame front. The equilibrium concentration of O_2 and N_2 were therefore defined as admission values and it was assumed that there was no internal *EGR* in the combustion chamber. This is consistent with the assumptions made in the calculation of the adiabatic flame temperature.

The angular resolution (*NSTEP*) was *0.5* crank angle degrees (ΔCAD). The volume associated with the current increase of NO_x formation in the model is the incremental volume ΔV_b associated with the current flame front. This was related to the increase of mass burned (ΔFMB) during the angular interval, comprised of burned fuel, which is derived from the experimental *HRR* and stoichiometric air, using the ideal gas law. The estimated total NO_x formed during the entire diffusion combustion process is then computed by the following integral:

$$e_{NO_x}(kmol) = const. \cdot \sum_{CAD=SOC}^{EOC} exp\left(\frac{-E_a}{T}\right) \cdot [N_2]_e \cdot [O_2]_e^{0.5} \cdot \frac{R_u \cdot T_{ad}^{\frac{1}{2}}}{P \cdot MW_b} \cdot \left(1 + \frac{1}{SFAR}\right) \cdot \Delta FMB \cdot \frac{\Delta CAD}{6 \cdot N \cdot NSTEP} \tag{2.20}$$

$$I_{e_{NO_x}}\left(\frac{g\ NO_x}{Kg\ fuel}\right) = \frac{MW_{NO_x} \cdot e_{NO_x} \times 1000}{M_f}$$

where *N* is the engine speed *[rpm]* and *P* the measured in–cylinder pressure.

Afterwards, the authors used the estimations $\left(I_{e_{NO_x}}\right)$ from Eq. (2.20) and correlate them with the measured NO_x $\left(I_{NO_x}\right)$ values via statistical analysis, from which the following semi–empirical correlation was emerged:

$$ln\left(I_{NO_x}\right) = c_0 + c_1 \cdot ln(FAER) + c_2 \cdot ln(N) + \\ + c_3 \cdot ln\left(I_{e_{NO_x}}\right) + c_4 \cdot [ln(N)]^2 + c_5 \cdot \left[ln\left(I_{e_{NO_x}}\right)\right]^2 \tag{2.21}$$

where $c_0 - c_5$ are model constants derived from statistical software to fit the experimental data. These constants change with the engine type.

This model was tested and validated on a light–duty and a heavy–duty Diesel engine, operating over a wide variety of engine conditions. The results of both analyses are seen to fall on a common linear trend when the semi–empirical correlation is applied. Also, adequate agreement between observed $ln(I_{NOx})$ data and predicted values in all cases have been attained.

2.3.1.11 Guardiola Engine Control Oriented NO_x Model

Guardiola et al [125] developed a fast NO_x predictive model oriented for engine control in Diesel engines, which uses the in–cylinder pressure trace as the only instantaneous input signal required, along with several mean variables that are available from the *ECU* (air mass flow, injected fuel mass, etc.) during normal engine operation. This model is based on the instantaneous evolution of the heat release rate (*HRR*) and the adiabatic flame temperature. The NO_x reduction due to the re–burning mechanism, which is schematically described in Fig. 2.3, is also accounted for.

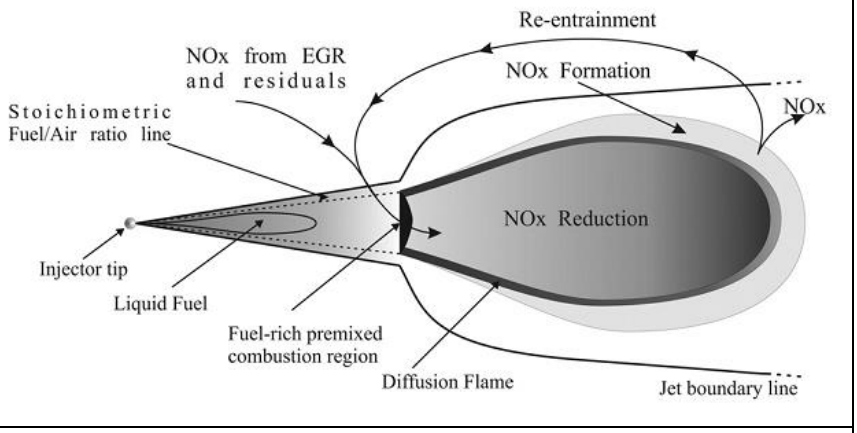

Figure 2.3: Theoretical re-burning scheme [125].

The basic model is based on the one presented by Arrègle et al [121] which, in order to increase its reliability and accuracy, has been modified with an improved heat release calculation. This model is based on the Zeldovich thermal NO_x mechanism. NO_x are initially calculated from a base model [121] as described in Eq. (2.22):

$$m_{NO_x,base} = \int dQ_b(\theta) \cdot K_1 \cdot \left(\frac{n}{2000}\right)^{K2} \cdot e^{\left(\frac{K3}{T_{ad}(\theta)}\right)} \cdot d\theta \tag{2.22}$$

where $m_{NOx,base}$ is the total predicted NO_x per cycle, n is the engine speed and *K1*, *K2* and *K3* are constants that have to be experimentally fitted, dQ_b is the *HRR* determined from the measured in–cylinder pressure and mean variables, T_{ad} is the adiabatic flame temperature during diffusion flame and θ is the crank angle. The adiabatic flame temperature diffusion flame is determined from the following set of equations:

$$T_{ad} = T_{ub} + \Delta T_{nd}(a) + \Delta T_{diss}(a)$$

$$\Delta T_{nd}(a) = 37630.5 \cdot \left(\frac{y_{O_2}(a)}{3.48 \cdot Fr}\right)$$

$$if\ T_{ub} + \Delta T_{nd}(a) < 2600K\ then\ \Delta T_{diss}(a) = 1.554 \times 10^{-7} \cdot \left(T_{ub} + \Delta T_{nd}(a)\right)^{2.677} \tag{2.23}$$

$$if\ T_{ub} + \Delta T_{nd}(a) > 2600K\ then\ \Delta T_{diss}(a) = 7.136 \times 10^{-10} \cdot \left(T_{ub} + \Delta T_{nd}(a)\right)^{3.36}$$

In the previous expressions, y_{O2} and T_{ub} are the O_2 mass fraction at intake valve closure (*IVC*) and unburned gas temperature evolution along the cycle (calculated) respectively, ΔT_{nd} (non–dissociated species) is the shift in the temperature due to the heat release during the combustion and ΔT_{diss} is the correction due to dissociation of species. This model also takes into account the NO_x reduction mechanism as proposed by Dec [15] (see Fig. 2.3). The percentage of NO_x disappearance depends on the local temperature and composition as well as on the residence time at high temperature regions and is strongly linked to the mixing rate of the combustion products [161]. Finally the reduced $NO_{x,re}$ due to the re–burning mechanism is calculated from Eq. (2.24):

$$m_{NO_x,re} = \frac{m_{NO_x,comb} \cdot (1 - K_{re} \cdot Fr \cdot \epsilon)}{m_a + m_f + m_{EGR} \cdot Fr \cdot \epsilon} \cdot (m_a + m_f) \tag{2.24}$$

where $m_{NOx,comb} = m_{NOx,base}$ is the NO_x mass produced at the current combustion time instance, m_a, m_f and m_{EGR} are the fresh air, fuel and *EGR* mass respectively, Fr is the fuel–air equivalence ratio, K_{re} is the fraction of gas re–entrained (*0.5* was used), and ϵ is the efficiency of NO_x reduction due to re–burning mechanism. After some statistical processing, intending to add generality to the model, the authors developed the following semi–empirical correlation for the prediction of NO_x:

$$m_{NO_x} = m_{NO_x,0} \cdot \frac{(A \cdot B_0)}{A_0 \cdot B}$$

$$A = \left(\int dQ_b(a) \cdot e^{\left(\frac{K3}{T_{ad}(a)}\right)} \cdot da \right) \cdot \left(1 - K_{re} \cdot \left(\frac{m_a}{m_f}\right) \cdot \epsilon\right) \cdot (m_a + m_f) \tag{2.25}$$

$$B = m_a + m_f + m_{EGR} \cdot \left(\frac{m_a}{m_f}\right) \cdot \epsilon$$

where subscript *0* denotes the reference conditions which were taken as the conditions at nominal engine operation.

The model exhibits a good behavior when varying the *EGR* rate, boost pressure, intake temperature, engine speed and injection settings. Concerning calculation time, the model can be used in real–time applications, since it provides results in less time than the time required for an engine cycle completion (rpm^{-1}). Specifically, using a MATLAB code in a *3 GHz PC*, the total calculation time is about *4.5 ms* which is smaller than an engine cycle. Regarding the accuracy, this model has a global mean error of about *15%*.

2.4 Zero–dimensional, Semi–Empirical/Phenomenological, Multi–zone, Thermodynamic Models

2.4.1.1 Introduction

The zero–dimensional, multi–zone models which are based on physical laws (i.e. thermodynamic laws) combined with empirical, semi–empirical and/or phenomenological concepts in conjunction with the use of in–cylinder pressure trace (measured or predicted)

can be used in order to provide fast and reliable predictions for NO_x emissions for a wide range of engine configurations and operating conditions. They combine the merits of *3D*, detailed, multi–zone phenomenological and empirical or semi–empirical models. These models do not discretize the spray cone geometrically in the combustion chamber. Instead, the cylinder content is divided into multiple zones having no specific spatial meaning. The classification into zones, each one determined from a corresponding portion of in–cylinder content and its physical and chemical properties, introduces the concept of the in–cylinder inhomogeneity. The zones are evolving during engine cycle according to physical laws in combination with empirical, semi–empirical and/or phenomenological correlations. These models can be used in real–time applications as well as in basic/fundamental research because they are very fast, reliable, simplified, easy to handle, require low calibration effort, are versatile and have a wide implementation range and can be easily embedded to control/monitoring systems.

As already mentioned, the model developed herein falls into this category. In the present section, a number of these models that can be found in the relevant literature, is presented. These models have thoroughly been studied and evaluated in an effort to develop a new NO_x predictive model of this category by adopting their positive features, combining them with new concepts in order to face their drawbacks.

2.4.1.2 Egnell Zero–Dimensional Multi–Zone NO Model

Egnell [108] developed a zero-dimensional, multi–zone model using the measured pressure trace for the calculation of *HRR*, local temperatures and concentrations of *NO* and other species. He used an arbitrary lambda value in each zone for the calculations. The proposed model was implemented on a premixed *DI* stratified charge natural gas *SI* engine and a *DI* Diesel engine. The data from these engines were used to study the effect of fuel injection duration on the average local lambda and *NO* formation history during the engine cycle.

The input data for the specific model's application are the measured emissions of CO_2, *CO*, O_2, *HC* (to calculate mass flow, global lambda and combustion efficiency), NO_x (used as a target value at the calculations for the determination of the average local lambda) and the measured pressure trace. Also, the temperature and pressure at the inlet and exhaust systems, *EGR* fraction if used and the cylinder geometry, are required.

The number of zones, their corresponding air/fuel ratio and mass fraction are chosen arbitrarily and tailored to give the average NO_x concentration that matches the measured respective one. At first, the *HRR* is calculated via the first thermodynamic law by using the engine geometry, inlet conditions and measure pressure trace. The heat transfer model used was the one suggested by Woschni [162]. The *HRR* is used to calculate the mass of the fuel burnt during each time step. Subsequently, the fuel mass is splitted into different lambda zones and the corresponding unburnt charge (i.e. air, residual (*RG*) and *EGR* gases) is calculated. Then, the volume and temperature of each zone are determined. The calculation of the composition and temperature of the combustion products follows. Using these, the number of *NO* moles formed in each zone, can be calculated.

Every preset lambda value corresponds to a generated zone at *SOC*. At each new *CA* step, during combustion, new lambda zones are created which are the evolution of the corresponding previous ones. At each time step, the temperature and content of the previous zones is updated and the number of *NO* moles is recalculated. Apparently, the previous zones correspond to the post–combustion zones (see Fig. 2.4). This means that the number of zones handled at the end of combustion is given by the number of lambdas and the number of time steps during combustion. Therefore, the number of zones (*N*) is given from Eq. (2.26):

$$N = \sum_{i=1}^{n_{step}} n_{lambda} \cdot \left(n_{step} + 1 - i\right) \tag{2.26}$$

where n_{lambda} is the number of lambdas, n_{step} is the number of time steps during combustion and i denoted the current time step. The multi–zone concept is depicted in Fig. 2.4:

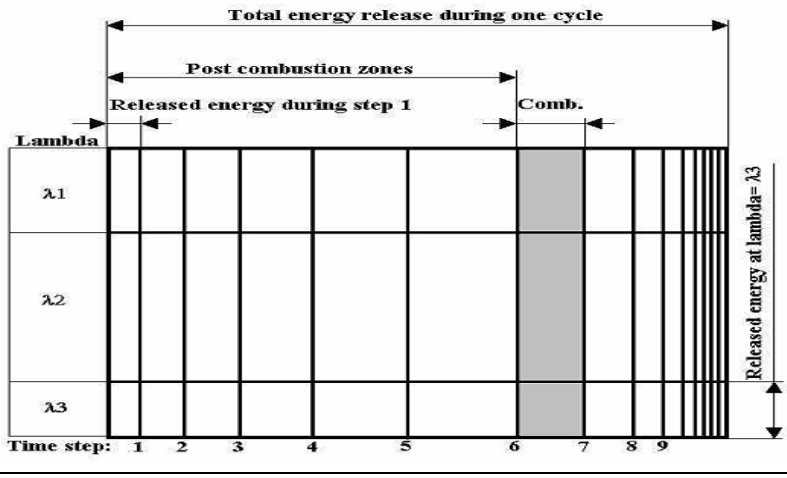

Figure 2.4: Definition of time and lambda zones [108].

The fuel burnt at each time step (provided from *HRR*) is distributed to the chosen lambda zones according to the arbitrary chosen proportions. Using the fuel mass and the corresponding preset lambda, the requisite unburnt charge (air+*EGR*+*RG*) is calculated. The temperature of the unburnt charge (i.e. prior combustion) is calculated considering isentropic variation. The lambda zone temperature, namely after combustion initiation, is calculated using an iterative procedure evolving adiabatic flame temperature (via the first thermodynamic law) and chemical dissociation of the combustion products assumed to be *CO*, CO_2, H_2, H_2O, O_2 and N_2. The heat of vaporization of the fuel is also accounted for in the temperature calculation of the combustion zones. The equilibrium constants are calculated by the minimization of Gibbs free energy. The internal energy is obtained from JANAF tables as a function of temperature.

As mentioned, at each time step the contents of lambda zones are updated and their temperature varies due to changes in the pressure and volume in the cylinder. The temperature of the charge affects the equilibrium constants and thus the composition of the products. The calculations in the post–combustion zones are performed in the same manner as in the combustion zones (i.e. based on the first thermodynamic law and chemical dissociation).

The derived zone temperature and equilibrium composition of the species are used to calculate *NO* via the Zeldovich mechanism [28]. Finally, the calculation of the *NO* formed in each zone, is added to give the total amount of *NO* which is assumed to be representative of the total NO_x.

Egnell observed that although the *NO* concentrations in early burning zones are very high, these zones may not be the main contributors in total emissions of *NO*. He also found that the temperature at intake valve closure (*IVC*) has a decisive effect on *NO* formation. From the investigation on how air entrainment affects the predicted NO_x, he found that under the given conditions, increased mixing of fuel and air would give higher NO_x.

2.4.1.3 Horrocks Quasi–Dimensional Phenomenological Diesel Engine Exhaust Model

Horrocks [156] used a quasi–dimensional, phenomenological Diesel engine exhaust model ("Merlin Combustion–Emissions Model" – Lloyd's Register *DEEPC* – developed by the Performance Technology Department at Lloyd's Register) which is based on a multi–zone combustion modeling concept. It takes into consideration, on a zonal basis, details of the fuel spray formation, droplet evaporation, air–fuel mixing, spray–wall interaction, swirl, heat transfer, auto–ignition and reaction rate. The model uses chemical equilibrium considerations as well as kinetics of fuel, *NO*, *CO* and soot reactions to calculate the pollutants concentrations within each zone and the whole cylinder.

The injection spray has the form of intermittent pockets of fuel being emitted from the nozzle hole during each calculation time step, thereby making segments of fuel as injection proceeds. All the droplets in the spray segment are assumed to have the same Sauter mean diameter (*SMD*). At the start of atomization, each spray segment is divided into a definite number of combustion zones. Air entrainment rate depends on the physical position of each zone, with centerline zones receiving the least air and edge zones receiving the most air. Swirl affects the shape of the spray and the rate of entrainment and is accounted for by modifying spray angle and penetration. Spray–wall impingement is assumed to take place when the moving zone reaches the nearest wall.

Ignition is assumed to start at the vapor phase in each zone. The ignition delay is measured from the point of atomization and is related to zone temperature and air–fuel ratio through phenomenological correlations. Heat transfer is modeled on a zonal basis and both convective and radiation heat transfers are modeled. Zone temperature, volume and mass for a fixed cylinder pressure are calculated from the energy equation in conjunction with mass conservation and then equation of state is solved iteratively for each zone [163]. Chemical equilibrium within each zone is calculated by the method outlined by Olikara and Borman [164].

Moreover, this model considers the thermal *NO* formation which is modeled according to the extended Zeldovich mechanism [29,30], taking into account the kinetics of *NO* formation. The fuel–bound nitrogen is assumed to be converted to *NO* directly during the course of combustion development. The prompt *NO* mechanism is not taken into account.

The model is used to examine the effect of *EGR* on NO_x formation in light–duty *DI* Diesel engines. Moreover, the significance of the Zeldovich mechanism rate constants

was proved. Horrocks proposed modified Zeldovich mechanism rate constants to improve the model's results.

2.4.1.4 Weisser Multi–Zone Quasi–Dimensional Combustion and Emissions Model

Weisser [109] developed a multi–zone, quasi–dimensional (phenomenological) model for the combustion and exhaust emissions. Combustion is considered to be governed by the chemical time scales during the premixed combustion phase and by the turbulent time scales during the mixing–controlled combustion phase where the turbulent time scales are determined from variants or derivatives of a turbulence model. The transition between the two combustion phases is modeled on the basis of phenomenological considerations. For the simulation of NO_x formation, detailed model of the post–flame chemistry are employed.

This model employs dimensional considerations for the determination of the spray propagation, which influences the downstream processes such as turbulence evolution, mixing and combustion. However, the multi–zone approach does not involve any spatial discretization with respect to the location of the individual zones. Weisser used this multi–zone concept to capture the charge inhomogeneity inside the combustion chamber during the relevant phases (injection and combustion).

A single fresh gas zone is considered during the compression stroke until start of injection (*SOI*), when an additional mixture zone is introduced. After combustion has started, various exhaust gas zones are formed subsequently, which are then subject to mixing with the residual unburnt charge until the exhaust valve opening (*EVO*). The individual zones are considered internally homogeneous. It is assumed perfect mixing of the intake air with exhaust gas recirculated gas either internally or externally. The open part of the engine cycle was simulated with the simulation tool *CIRCE* [165] in order to properly define the initial conditions at intake valve closure (*IVC*).

For each zone, the conservation equations of mass, species mass fractions and energy are solved simultaneously. In the energy equation, the energy required to heat up and evaporate the fuel droplets is considered as an additional heat exchange term. This is done in order to assure full coupling with the liquid phase. The individual zones have the same constant pressure (the in–cylinder pressure) at each time step. Therefore, the distribution of

the total volume change among the zones is performed appropriately in order to comply with the constant pressure condition at the end of each time step and with the volume constraint.

The aforementioned model comprises the following sub–models which use phenomenological/semi–empirical correlations:

1. Spray model:
   - spray propagation,
   - droplet evaporation and
   - mixture formation.
2. Turbulence model:
   - charge air motion without injection and
   - injection–generated turbulence).
3. Combustion model:
   - ignition, premixed combustion,
   - mixing–controlled combustion and
   - distribution of the fuel among the two combustion phases assuming $\Phi=1$.
4. Heat exchange model.
5. Mass transfer model.
6. NO_x formation model.

For the heat–exchange $\dot{Q}_{j\to W}$ between an individual zone j and the cylinder wall (w), the Annand approach [139,140] is used as described in Eq. (2.27):

$$\dot{Q}_{j\to W} = -\frac{V_j}{V_{cyl}} \cdot G_{cyl} \cdot \left(C_{conv} \cdot \frac{\lambda}{2 \cdot R_{cyl}} \cdot Re^{0.7} \cdot \left(T_j - T_W\right) + C_{rad} \cdot \left(T_j^4 - T_W^4\right) \right) \quad (2.27)$$

where V_{cyl} and G_{cyl} are the volume and wall surface area of the cylinder at the examined instant respectively, T represents temperatures and C_{conv} and C_{rad} are the convection and radiation constants which are obtained from calibration.

Regarding mass transfer, the fresh gas is mixed with the evaporated injected fuel, forming the stoichiometric mixture zone. This latter zone is depleted in the course of combustion. The combustion products are feeding the latest–built exhaust gas zone. All the exhaust gas zones are subject to mixing with the residual fresh gas. For consistency with the combustion modelling approach, only mixing of the residual fresh gas with the individual

exhaust gas zones is considered for and any interaction between exhaust gas zones is neglected. The mixing procedure is schematically described in Fig. 2.5:

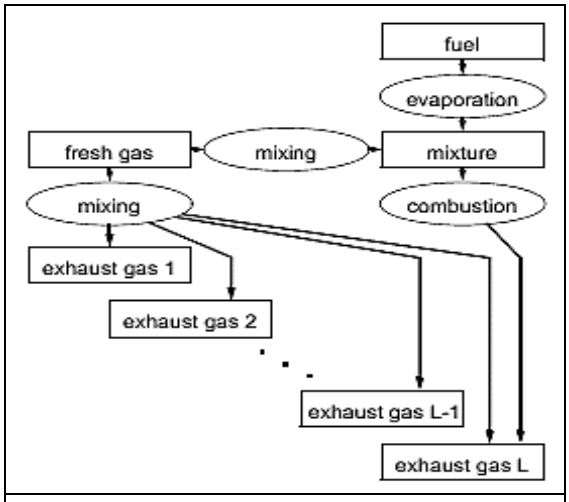

Figure 2.5: Schematic description of the mass transfer pathways between the individual zones as proposed by Weisser [109].

The NO_x model takes into account both, *NO* and NO_2 formation. It uses a detailed kinetic scheme for thermal NO_x formation [38], using the flame temperature of each zone, which consists of *77* reactions involving *23* species including the oxidation of *CO*. For each individual zone, the concentration changes due to the individual reactions which are determined from their reaction rates via the *CHEMKIN* code [158] and *ODE* solver [166]. Moreover, the recirculated NO_x are modeled as inert species in this context during the computation of the adiabatic flame temperature and the equilibrium composition of the combustion products.

2.4.1.5 Diotallevi Multi–Zone NO_x Model

Diotallevi [113] developed of a multi–zone model for NO_x formation in Diesel engines based on the one proposed by Egnell [108]. The model has been validated using test sessions on a single cylinder engine based on a heavy–duty, six–cylinder Diesel engine. Diotallevi used the in–cylinder pressure trace to calculate the *HRR* and from this the fuel burnt at each crank angle (*CA*) interval, using Eq. (2.28):

$$dQ_{hr} = \frac{\gamma}{\gamma - 1} \cdot p \cdot dV + \frac{V}{\gamma - 1} dp + dQ_w \tag{2.28}$$

where p is the measured in–cylinder pressure, dQ_{hr} is the energy released from the combustion of a fuel element, dQ_w is the heat exchange with the cylinder wall calculated using Annand formula for convective and radiative heat transfer [139,140], V is the cylinder volume and γ is the ratio of specific heats which is calculated accounting for the temperature and the composition of the in–cylinder charge via a *MATLAB* function using gas properties from the *JANAF* tables [167].

The model requires the following inputs:

- mass of intake air per cycle,
- injected fuel (m_f) per cycle,
- global lambda (λ_{gl}),
- *EGR* rate,
- *CA* of intake valve closure (*IVC*),
- *CA* of exhaust valve opening (*EVO*),
- conditions at *IVC* and
- engine geometry.

The residual gas is calculated from state equation for ideal gas using the clearance volume and exhaust pressure and temperature. The unburnt charge comprises ambient air, *EGR* and residual gases. The *CA* where the start of combustion (*SOC*) occurs is calculated from the in–cylinder pressure derivative. The temperature of the unburnt zone is calculated assuming polytropic ($\gamma=f(T)$) compression.

The first combustion zone is generated at the *SOC* determined from the respective fuel burnt at the specific time step calculated from *HRR* analysis and the accompanied unburnt charge mass assuming stoichiometric combustion. Afterwards, a new zone is created at every time step. There is no interaction between the combustion zones. Only mixing with the unburnt charge is permitted (dilution). This consideration is justified from the fact that the effect of the mixing between combustion zones and unburned zone is much more significant than the mixing between the zones themselves. This is because the unburned zone has a completely different composition (basically air) and temperature compared to the zones which contain high temperature combustion products. Namely, it was considered that the higher difference in temperature and composition causes higher heat and mass transfer.

Furthermore, it is noted that the zones do not have any specific physical meaning and spatial consistency but they provide a discretization of the in cylinder content during combustion process at every time step, in order to approach the temperature and composition inhomogeneity of *DI* Diesel combustion.

The combustion zone temperature corresponds to the adiabatic flame temperature, which is calculated assuming stoichiometric combustion in conjunction with an equilibrium scheme. This scheme accounts for the following chemical species: CO_2, H_2O, N_2, O_2, *CO*, *O*, *H*, *OH* and *NO*. The temperature decrease (ΔT) due to fuel vaporization and the required heat to increase the fuel vapor temperature to the mixture temperature according to Eq. (2.29), is also accounted for:

$$\Delta T = \frac{m_f \cdot Q_v + m_f \cdot cp_v \cdot \Delta T_v}{m_{tot} \cdot cp_{tot}} \tag{2.29}$$

where Q_v is the heat of vaporization of the fuel (*250 kJ/kg*), cp_v is the fuel vapor specific heat capacity at constant pressure and subscript *tot* denoted the total mixture in the zone.

Each zone, after its generation, evolves inside the combustion chamber according to isentropic compression/expansion, thus a new temperature and volume is calculated at

each time step for every existing zone. The zonal concept that Diotallevi adopted is depicted in Fig. 2.6:

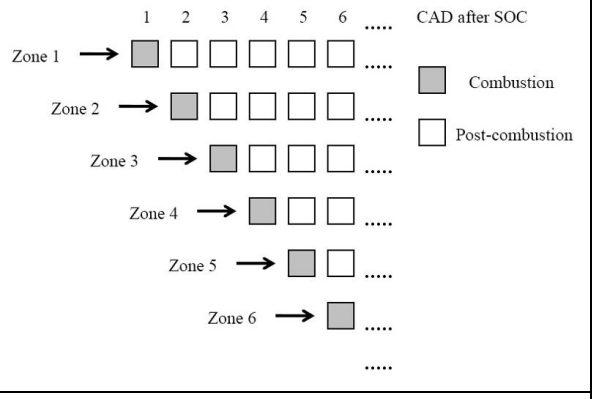

Figure 2.6: Zones creation at every time step (i.e. 1 °CA) [113].

During compression/expansion of each zone, a portion of the in–cylinder unburnt charge, enters inside the zone and is diluted with the combustion products. This portion, called dilution mass ($m_{ub,dil}$) is calculated from Eq. (2.30) [168]:

$$m_{ub,dil} = m_{ub,exc} \cdot \left\{1 - exp\left[-6.908 \cdot \left(\frac{\theta - \theta_{SOC}}{\theta_{SOC} - \theta_{EVO}}\right)^{M_x}\right]\right\}$$
$$m_{ub,exc} = m_{ub,tot} \cdot \left(1 - \frac{\lambda_c}{\lambda_{gl}}\right) \quad (2.30)$$

where $m_{ub,exc}$ is the excess unburnt charge mass, $m_{ub,tot}$ represents the total trapped, λ_c and λ_{gl} are the combustion (local) and global air–fuel equivalence ratio respectively, θ is the current *CA* and M_x is a shape factor. This factor was set equal to *2* to obtain optimum results.

During combustion and compression/expansion of each zone, the extended Zeldovich mechanism [28,29,30] is used to calculate *NO* using the calculated temperature and equilibrium composition. *NO* formation rate, which is kinetically controlled, is represented from the differential equation extracted from the Zeldovich mechanism [8]. This equation is integrated in time (i.e. as zone evolves) using as initial value the result (*NO* amount) from the previous step.

Diotallevi validated his model using *17* test cases by varying engine speed, load and intake pressure. The results have shown a good correlation with the experimental data in most cases.

2.4.1.6 Seykens Physically–Based Multi–Zone Phenomenological Model

Seykens [115] developed a physically–based, multi–zone, phenomenological model which predicts the interaction between the fuel injection rate and *HRR* and between the fuel injection process and emissions of *NO* and soot for both conventional and advanced, high–*EGR*, compression ignition combustion. Although the model has been developed to be

generally applicable, the validation process has been limited to heavy– duty *DI* Diesel engines. The concept of the Seykens model is schematically described in Fig 2.7:

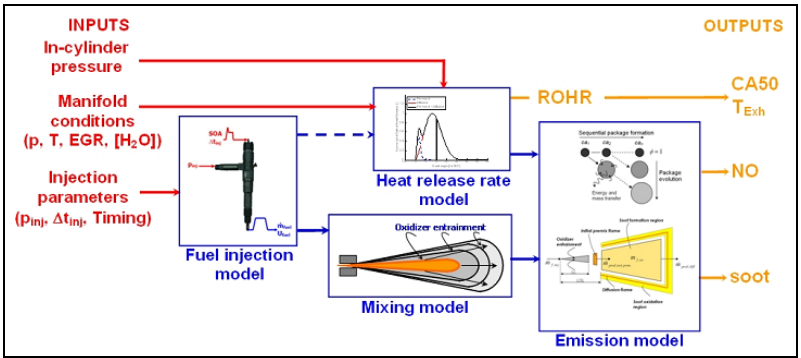

Figure 2.7: Overview of the Seykens model using in–cylinder pressure as input [115].

The *NO* model comprises three main sub–models as indicated in Fig. 2.8:

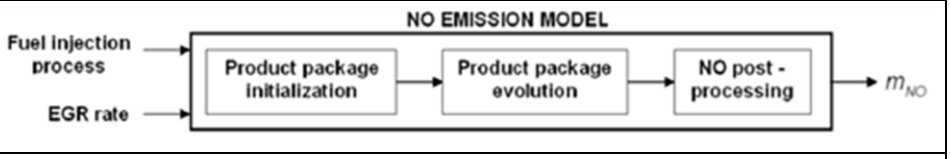

Figure 2.8: The sub–models comprised in the main NO model [115].

This model, which follows the method of Murayama [169], describes the in–cylinder *NO* formation in multiple evolving packages of combustion products, which are subsequently diluted with fresh oxidizer. A package is a volume of combustion products in which *NO* formation occurs. The combustion products packages are sequentially formed. The formation rate follows the *HRR* profile (measured or predicted). The main assumptions of this *NO* model are the following:

- *NO* formation from premixed combustion is neglected,
- only post–flame *NO* formation is accounted for,
- the mixing is considered spray dominated,
- no mixing of combustion products (zones) is occurs and
- *NO* formation has no influence on the combustion process.

The initial combustion products (package formation) temperature and composition are determined from the oxidizer temperature and composition and from the initial liquid fuel temperature and chemical composition. Temperature calculations include the following:

- fuel evaporative cooling,
- adiabatic combustion including dissociation,
- hot soot particle radiative cooling and
- flame straining by turbulence.

After package formation and during combustion period, the packages interact with the surroundings following a radiation heat loss mechanism and accounting for the entrainment of fresh oxidizer (air + residuals + *ERG* gases). The temporal evolution is de-

scribed by conservation of mass and energy. The package composition is calculated assuming that combustion product packages do not exchange mass. At every time instant, a package can be taken to consist of stoichiometric combustion products and an additional amount of fresh oxidizer as a result of entrainment.

Because both, the composition and temperature of the added fresh oxidizer is known, the zone temperature is calculated directly from the energy balance. The mixing process is thus quantified by the evolution of the equivalence ratio of a specific zone. This evolution is predicted on the basis of a one–dimensional model of the fuel spray.

The spray model used is based on the fuel mass and momentum balances over the control surface, as proposed by Naber and Siebers [170]. *NO* formation is calculated using the output variables of the product zone evolution model. The output variables are the following:

- zone mass,
- zone temperature,
- zone species mass fractions,
- zone specific volume and
- pressure as a function of *CA* per zone.

In line with the aforementioned phenomenological modeling approach, *NO* formation is approached on the basis of a description of the chemical reaction kinetics. Limitations have to be imposed with respect to the *NO* reaction pathways accounted for and the evolution of species concentrations on the basis of the corresponding chemical time scales. Only the thermal *NO* and N_2O – intermediate pathway are accounted for. To encounter *NO* formation at low–temperature combustion ($T < 1800\ K$), e.g. high–*EGR* combustion, where thermal *NO* formation pathway is no longer dominant [34,171,172], the N_2O–intermediate pathway was used as the primary *NO* formation pathway at elevated pressures [35]. The total *NO* formation rate equation is given by the sum of the two above *NO* formation mechanisms. However these mechanisms require the instantaneous concentrations of species O_2, N_2, *O*, *OH*, *N* and N_2O. To avoid the time consuming solving of the kinetics differential equations, which calculate the amount of each species inside each zone, Seykens adopted the global or final equilibrium assumption for all species except *NO*. This assumption is widely accepted and is based on the fact that chemical time scales associated with the *NO* formation process are much longer than those associated with the combustion process.

Finally, the physically based model for *NO* emissions developed by Seykens, contains five calibration parameters which have to be tuned by hand to fit the combustion system.

2.4.1.7 Andersson Multi–Zone Physically–Based Real–Time NO_x Model

Andersson et al [111] have developed a simplified, zero–dimensional, multi–zone, physically–based, real–time model for the conventional and partially premixed Diesel combustion, fuel injection, ignition delay, premixed and diffusion combustion *HRR*. The model can be used for both, traditional high temperature combustion and for high–*EGR*, low temperature combustion.

This model consists of the NO_x model and a *HRR* model that feeds the NO_x model with input data. Initially the *HRR* model predicts combustion rate with a *CA* resolution of *0.2°*. This model is consisted from phenomenological correlations for the calculation of the following [109]:

- heat transfer,
- injection velocity,
- injection flow rate,
- ignition delay,
- premixed combustion,
- diffusion combustion,
- turbulent kinetic energy due to spray and
- turbulent kinetic energy due to in–cylinder swirl.

The model calibration constants are tuned to match the experimental data (e.g. ignition delay, fuel mass flow, experimental *HRR*, etc.).

From the predicted *HRR*, the formation of combustion products at each time step is calculated, assuming that all fuel is combusted at equivalence ratio of one. Then, the derived data are used as inputs in the NO_x model.

Cylinder pressure *p*, which is also required as an input to the NO_x model, is calculated according to the first thermodynamic law as described from Eq. (2.31), by using the predicted net *HRR* ($dQn/d\theta$), which has been calculated from the corresponding model.

$$\frac{dp}{d\theta} = \left(\frac{dQ_n}{d\theta} - \frac{\gamma}{\gamma - 1} \cdot p \cdot \frac{dV}{d\theta}\right) \cdot \left(\frac{\gamma - 1}{V}\right) \tag{2.31}$$

In the previous equation, γ is ratio of specific heats, which is dynamically calculated depending on current in–cylinder temperature and composition, V is the current cylinder volume and θ is the crank angle.

The NO_x model uses the fuel burning rate acquired from the predicted *HRR* and divides it into fuel elements as combustion proceeds to generate multiple zones. After combustion of each fuel element, the burned gas element is mixed with cooler cylinder gas (composed of intake air, *EGR* and residual gases). The speed of mixing is governed by a characteristic mixing time given from the following semi–empirical correlation:

$$t_{char} = C_{mix} \cdot 6 \cdot N(rpm) \cdot \frac{l}{\sqrt{k}} \tag{2.32}$$

where t_{char} is the characteristic mixing time in crank angle degrees *[°CA]*, C_{mix} is a constant *[°CA]*, l is a characteristic length *[m]* and k is the density of turbulent kinetic energy $[m^2/s^2]$. A new value of t_{char} is calculated for each new fuel element that burns.

NO_x formation is modeled according to the extended Zeldovich mechanism. At low temperature combustion (which occurs e.g. at very high *EGR* rates), where the Zeldo-

vich mechanism cannot give accurate predictions because other mechanisms are predominant, a simple empirical compensation algorithm is used for the burned zones with a NO_x formation of less than *60 ppm* as described in Eq. (2.33):

$$ppmNO_{corr} = 11.8 \cdot (ppmNO_{uncorr})^{0.43} \tag{2.33}$$

For the NO_x calculations, the equilibrium temperature and species concentrations are required. To avoid the use of the slow iterative procedure of Gibbs free energy minimization methodology for every zone, the model uses tabulated results of Gibbs free energy which are functions of pressure, equivalence ratio and temperature. There is also a lookup table to calculate the equilibrium temperature. The temperature input to the aforementioned lookup table is the one which corresponds to complete combustion (i.e. without dissociation). Furthermore, there are additional lookup tables for each species participating in NO_x formation. The temperature input to these tables is the equilibrium temperature. For the calculation of this temperature, initially adiabatic flame temperature is calculated, which is then reduced due to heat radiation to the cylinder wall. No further heat losses from the burned zones were taken into account. The radiative heat transfer is calculated from Eq. (2.34):

$$\dot{Q}_{rad} = \dot{n}_{burned} \cdot C_{rad} \cdot T_{ad}^4 \tag{2.34}$$

where $\dot{n}_{burned}$ is the burned gas production rate, C_{rad} is the heat radiation constant and T_{ad} is the adiabatic combustion temperature. Afterwards, the temperature trace of the zone (not considering dissociation) is calculated over a range of *CA* degrees relevant to NO_x formation. This temperature trace is achieved by assuming isentropic compression between each time step. Also, at each time step, cool unburned cylinder gas is mixed into the burned zone and the total enthalpy of added gas and burned gas is conserved. Subsequently, using the temperature lookup table, the same temperature trace is re–calculated considering dissociation. Thus, the local temperature (i.e. zone temperature) is now calculated by accounting for the chemical dissociation effect. Also, the species equilibrium concentrations are obtained using the corresponding lookup tables. The species equilibrium concentrations are required in the NO_x formation calculations of the extended Zeldovich mechanism used in the NO_x model.

The main calibration parameters of the NO_x model are the characteristic mixing time constant C_{mix} (which governs the mixing of cooler unburned cylinder gas with hot burned gas) and the heat radiation constant (which determines the temperature drop due to wall heat loses).

Both models (in conjunction) were applied on a single cylinder research engine based on a heavy–duty *DI* truck Diesel engine where multiple geometrical and operating parameters varied. The investigation revealed that the model is able to maintain high calculation accuracy and speed for NO_x emissions. The root mean square of the relative error (*RMSE*) was *16 %* and the calculation speed was around one second on a *PC*. Combustion characteristics such as ignition delay, center of combustion (*COC*) and the general shape of the heat release rate were well predicted by the combustion model. The authors assert that it would be possible to identify time–consuming calculation processes in the model and allocate them to an Application Specific Integrated Circuit (*ASIC*) and thus drastically decrease the required calculation time [173].

2.4.1.8 Hernandez Phenomenological Multi–Zone Combustion Model

Hernandez et al [20] developed a phenomenological multi–zone combustion model, which considers the space and time evolutions of a reacting Diesel fuel jet aiming to estimate the instantaneous NO_x concentration in a Diesel engine cylinder from the start of injection (*SOI*) until exhaust valve opening (*EVO*). The total injected fuel mass has been divided into different fuel packages, using the fuel injection rate, to take into account the heterogeneous nature of the Diesel combustion process.

A method based on the theory of turbulent gas jets [174], developed from Arrègle et al, has been used to calculate the instantaneous air entrainment in each package from the experimental *HRR*, which is obtained through a thermodynamic diagnostic model. The authors used the empirical model of Arrègle et al [175], which calculates an "apparent combustion time" (*ACT*) defined as the time interval ($t_{mix}(t,z)$) between the injection of the fuel package and its complete stoichiometric combustion, and use it to calculate the instantaneous amount of air which mixes with each fuel package. Thus, they ended up to the semi–empirical correlation, described in Eq. (2.35), that provides the instantaneous $(F/A)_r$ ratio *[kg/kg]* for each package.

$$\left(\frac{F}{A}\right)_r (t,z) = \frac{K^2(z)}{\left(\frac{F}{A}\right)_{st} \cdot t_{mix}^2(t,z) \cdot Y_{O_2}(t) \cdot \rho_\alpha(t)} \tag{2.35}$$

In the previous expression, K is a calibration constant, Y_{O2} is the oxygen mass fraction in the combustion chamber, ρ_α is the density of the entrained air, z correspond to the examined package and t to elapsing time.

Owing to the importance of the kinetics on the formation and dissipation mechanisms of the main pollutant species (e.g. NO_x) and radicals, the instantaneous composition of each fuel package has been calculated using a chemical reaction mechanism which considers 27 species and 59 reactions. The main model input data, is the *HRR* and mean gas temperature which are derived from the implementation of the combustion diagnostic procedure on the instantaneous in–cylinder pressure trace obtained during the engine tests.

A single cylinder Diesel engine was tested to validate the model and to analyze the influence of the injection parameters (injection pressure, injection timing and injected fuel mass flow) on NO_x emissions. A good agreement between the theoretical results and the experimental ones was accomplished when the aforementioned injection parameters were modified. The proposed model also provides a better knowledge of the local mixing fuel/air processes, which represents one of the most important uncertainties when modelling Diesel combustion.

2.4.1.9 Maiboom Phenomenological, Six–Zone Combustion Model

Maiboom et al [114] developed a zero dimensional, phenomenological, six–zone combustion model for *DI* Diesel engines, which provides local information, such as mean equivalence ratio and temperature in the various zones. The model is based on the well–

known Dec's "conceptual" model [15] for *DI* Diesel combustion. This model uses the following sub–models:

- injection rate model based on instantaneous injection rate measurements,
- spray model from Siebers et al [176,177] (maximum liquid–phase fuel penetration, vapor–phase fuel penetration, spray spreading angle, lift–off length and air–fuel equivalence ratio),
- entrainment model of the ambient gas,
- premixed and diffusion combustion model partially based on Barba's simplified turbulent kinetic calculation [178],
- and energy balance in each zone providing the corresponding mean temperatures.

The combustion chamber is divided into six zones as demonstrated in Fig. 2.9:

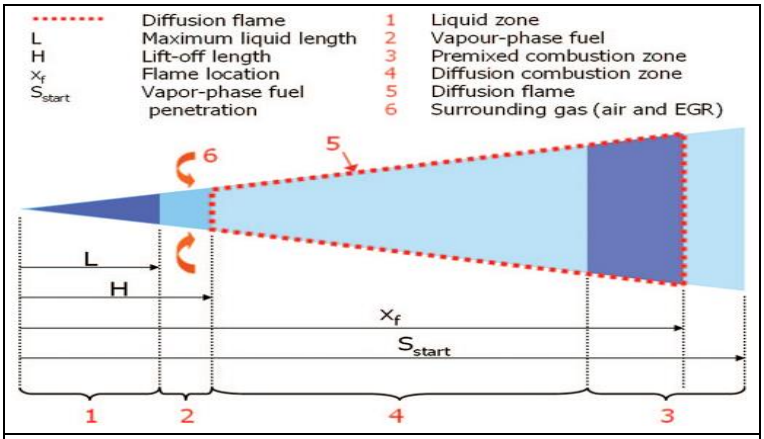

Figure 2.9: Zone description [114].

Zone *1* is the "liquid" zone and is defined from the nozzle hole to the maximum liquid fuel penetration. Zone *2* is the air–fuel mixture between the maximum liquid penetration *L* and the lift–off length *H*. If *H* is greater than *L*, zone *2* contains the fuel that is completely evaporated downstream of the liquid penetration. If *H* is smaller than *L*, zone *2* contains the liquid fuel downstream of the lift–off length. Zone *3* is the premixed combustion zone that consists the combustion of air–fuel vapor phase which has been prepared during ignition delay. Zone *4* is the diffusion combustion zone from the lift–off length to the vapor phase fuel penetration. Zone *5* is the diffusion flame surrounding zones *3* and *4*. And finally zone *6* is the surrounding gas (air and *EGR*). These zones are allowed to exchange mass and energy as evolving in the combustion chamber during the engine cycle following a concept proposed by the authors [114]. The empirical constants comprised in the aforementioned sub–models are determined using experimental data such as experimental *HRR* etc. and values from the literature.

Model validation revealed that it is able to capture principal trends when varying engine load and speed, inlet air temperature, boost pressure, injection pressure and *EGR* rate. It also calculates *HRR* with adequate accuracy. The authors state that their model can be used to interpret experimental emission trends (NO_x and *PM*).

2.4.1.10 Ericson Zero–Dimensional Two–zone Quasi–Steady Combustion and Gas Exchange Model

Ericson et al [179] developed a zero–dimensional, two–zone combustion model in combination with a quasi–steady gas exchange model (including models for *EGR* and variable geometry turbocharger (*VGT*)), focusing on the calculation of tail–pipe NO_x and engine parameters such as in–cylinder pressure, temperature and gas flows. The combustion model uses fuel flow parameters to generate *HRR* data and from these to calculate the corresponding pressure trace.

The temperature and equilibrium concentrations in the zones are calculated by a simplified combustion model. The corresponding NO_x concentration is given by the original Zeldovich mechanism. Authors assert that their model is capable of predicting the tail–pipe NO_x flow and exhaust temperature. They validated their model on an inline six–cylinder experimental engine using cooled *EGR*. The engine is equipped with a *VGT* and common rail fuel injection system.

For the combustion model two zones were used, one unburned and one burned zone. At first, the fuel flow is calculated using the measured rail pressure. Using the fuel flow and calculating the heat losses, the net *HRR* and the corresponding pressure differential are determined. Then the *HRR* is used to calculate the elementary fuel mass burnt at each time instance. During combustion process, the adiabatic flame temperature of the burning fuel mass element, at the current time instance, is calculated. Thereafter, the derived freshly burned charge is added to the burned zone, which has been updated by expanding/compressing isentropically its previous contents. The burned zone temperature is compensated for dissociation of the combustion products and finally the amount of NO_x formed in the current time step is calculated. This sequence of calculations is performed with a fixed *CA* interval. Typically the burned zone temperature and NO_x concentration calculations are performed more sparsely than the *HRR* part in order to save time.

The combustion of the fuel mass elements is assumed locally stoichiometric ($\lambda_{local}=1$). The requisite air mass element for the combustion of each fuel element is derived from the unburnt zone. No additional air entrainment from the unburnt to burned zone occurs. The initial combustion products composition is derived from the stoichiometric combustion equation. Adiabatic flame temperature ($T_{flame,ad}$) is then calculated trough enthalpy balance between an unburned mass element and a perfectly burned mass element. These enthalpies are calculated from thermodynamic polynomials [180]. Then the cooling effect of dissociation is taken into account using tabulated data of species (*CO*, CO_2, H_2, *H*, *OH*, *O*, O_2, *NO*, H_2O, N_2 and *N*) and a function (f_{eq}) of pressure (p), temperature and local air–fuel equivalence ratio (λ_{local}). Thus the $T_{flame,ad}$ and the final temperature $T_{flame,ht}$, where the temperature reduction due to radiative heat transfer $dQ_{ht,rad}$ is accounted for, are calculated as follows:

$$\begin{aligned} T_{flame} &= T_{flame,ad} - f_{eq}\left(p, T_{flame,ad}, \lambda_{local}\right) \\ dQ_{ht,rad} &= C_{rad}\left(n_{eng}, \delta\right) \cdot T_{flame}^4 \\ T_{flame,ht} &= T_{flame,ad} - \frac{dQ_{ht,rad}}{C_p} \end{aligned} \tag{2.36}$$

In the previous equations, C_p *[J/kg/K]* is the constant pressure specific heat of the combustion mixture and C_{rad} is calculated using a black box expression (a linear regression model) depending on speed (n_{eng}) and injected fuel mass (δ). C_{rad} is not a strictly physical parameter but is used in the final step of the combustion model as a tuning parameter to fit simulated to measured NO_x.

The burned zone temperature evolution (T_{exp}) is calculated from the temperature of the previous step (before taking dissociation into account ($T_{burn,perf}$)) and its isentropic expansion/compression using a fixed γ value. From energy balance and the fact that the specific heat value has a weak temperature dependence in the examined temperature range (thus specific heats of the freshly burned element (*flame*) and of the expanding burning zone can be assumed equal), the temperature of the burning zone (T_{burn}) is calculated from Eq. (2.37):

$$T_{burn,perf}(\theta) = \frac{T_{exp} \cdot m_{burn}(\theta - 1) + T_{flame,ht} \cdot \left(m_{burn}(\theta) - m_{burn}(\theta - 1)\right)}{m_{burn}(\theta)}$$
$$T_{burn} = T_{burn,perf} - f_{eq}\left(p, T_{burn,perf}, \lambda_{local}\right) \quad (2.37)$$

where θ is the current *CA* step, m_{burn} denotes the mass in the burned zone and $m_{flame}=m_{burn(\theta)}-m_{burn(\theta-1)}$ is the mass of the freshly burned element (*flame*). The T_{burn} is used to calculate the equilibrium and rate constants for the Zeldovich *NO* mechanism, which is used to model the *NO* formation. The equilibrium O_2 and N_2 concentrations in the burned zone, which are required in the *NO* formation mechanism, are given from tables derived from minimization of Gibbs free energy. It is also mentioned that the gas exchange model provides the simulated inlet manifold pressure and *EGR* rate to the combustion model, which in turn, calculates the exhaust temperature required by the gas exchange model.

The external inputs are the following:

- inlet manifold temperature,
- engine speed,
- *EGR* valve and *VGT* actuator signals,
- injected fuel mass,
- injection timing and
- rail pressure (of the common rail injection system).

The typical outputs are the following:

- inlet and exhaust manifold pressure,
- *EGR* rate,
- *NO* concentration,
- peak cylinder pressure and
- exhaust temperature.

The model was validated in two stages by using:

1. steady state data to validate the combustion model, with mean relative error of *10.4%* and
2. transient data to validate the complete model on the European Transient test Cycle (*ETC*) with a mean relative error of *7.14%*.

Moreover, the computational time was *0.05* seconds per time step using un–compiled *MATLAB* code on a *1.6 GHz PC*.

2.4.1.11 Wilhelmsson Two–Zone Physically Based NO_x Model

Wilhelmsson et al [107] developed a two–zone, physically based NO_x model to predict NO_x formation during the engine cycle as well as NO_x formation trends, suitable for vehicle on–board, on–line implementation, feasible for an embedded system, i.e. embedded processor or embedded electronic hardware (field programmable gate arrays (*FPGA*)).

The proposed model divides the combustion chamber content into two zones, the burnt (where the NO_x are formed) and the unburnt one. The temperature of the burned zone is calculated using the number of moles of the two zones, the global temperature and the temperature of the unburned zone (which is calculated assuming isentropic compression), rather than using the iterative energy balance approach. Using this method the physical interpretation can be maintained while the algorithm is significantly simplified. The authors used the ideal gas law for the total combustion chamber and for each zone separately assuming uniform pressure and accounting for the cylinder volume constrain, they calculated the temperature of the burnt zone. The concept is described from the following equations:

$$
\begin{aligned}
n_{uz} \cdot T_{uz} + n_{bz} \cdot T_{bz} &= \frac{p \cdot V_{uz}}{\tilde{R}} + \frac{p \cdot V_{bz}}{\tilde{R}} = \frac{p}{\tilde{R}} \cdot V_g = n_g \cdot T_g \\
n_{uz} &= n_g - n_{bz} = n_0 - n_{bz} \\
n_{bz} &= \frac{Q}{Q_{LHV} \cdot n_f} \cdot \left(1 + \frac{n_f \cdot \lambda \cdot (AFR)_{st}}{n_a}\right) \\
T_g &= \frac{p \cdot V}{n_0 \cdot \tilde{R}} \\
T_{uz} &= T_{g0} \cdot \left(\frac{p}{p_{g0}}\right)^{\frac{\gamma-1}{\gamma}} \\
T_{bz} &= \frac{n_g \cdot T_g - (n_0 - n_{bz}) \cdot T_{uz}}{n_{bz}}
\end{aligned}
\tag{2.38}
$$

In the previous equations, is assumed that the number of moles is not significantly changed due to combustion (small augmentation of charge mass due to fuel addition at each time step and also the values of air and exhaust gas molecular weight are close). Thus, the global number of moles (n_g) remains constant (n_0) throughout the complete cycle. Furthermore, T_g is the global temperature, T_{g0} and P_{g0} are the known temperature and pressure respectively at combustion initiation, used to calculate the temperature of the unburned zone. γ is the ratio of specific heats which was assumed constant. Q is the total heat released from the start of combustion to the current *CA*. λ is the local air/fuel ratio introduced as a tuning parameter and assumed constant. $(AFR)_{st}$ is the stoichiometric air/fuel ratio. n_f and n_a are the total moles of fuel and air respectively. p is the given in–cylinder pressure (experimental or calculated). Subscripts *uz* and *bz* correspond to unburned and burned zone respectively.

This model uses the Zeldovich mechanism to estimate *NO* formation in the burnt zone. The equilibrium concentrations of free oxygen (*O*), nitrogen (N_2) and nitric oxide (*NO*), which are used as inputs in the Zeldovich mechanism, are calculated as functions of temperature, pressure and local λ by taking dissociation reactions into account. The dissociation reactions in combination with the corresponding Gibbs free energy and carbon, hydrogen, oxygen and nitrogen balances are put together to form a system of nonlinear equations. The solution of this system provides the equilibrium concentrations. Once the equilibrium concentrations are known, it is possible to compute the NO_x formation rate using the Zeldovich mechanism as described in Eq. (2.39):

$$\frac{\partial c_{NO}}{\partial t} = \frac{15.2 \times 10^{13} \cdot e^{\frac{-38000}{T}} \cdot c_O^e \cdot c_{N_2}^e \cdot \left(1 - \left(\frac{c_{NO}}{c_{NO}^e}\right)^2\right)}{1 + \frac{7.6 \times 10^{13} \cdot e^{\frac{-38000}{T}} \cdot c_O^e \cdot c_{N_2}^e}{1.5 \times 10^9 \cdot e^{\frac{-19500}{T}} \cdot c_{NO}^e \cdot c_O^e} \cdot \frac{c_{NO}}{c_{NO}^e}} \tag{2.39}$$

where *c* denotes the concentration *[mol/cm^3]* and subscript *e* the equilibrium.

The authors modified the Zeldovich mechanism taking into account the variation of the burned zone volume during combustion:

$$\frac{dc_{NO}}{dt} = \frac{\partial c_{NO}}{\partial t} + \frac{\partial c_{NO}}{\partial V} \cdot \frac{dV}{dt} = \frac{\partial c_{NO}}{\partial t} + \frac{\partial \left(\frac{n_{NO}}{V}\right)}{\partial V} \cdot \frac{dV}{dt} = \frac{\partial c_{NO}}{\partial t} - \frac{c_{NO}}{V} \cdot \frac{dV}{dt} \tag{2.40}$$

where $\frac{\partial c_{NO}}{\partial t}$ is derived from the original Zeldovich mechanism, $\frac{dV}{dt}$ and *V* represent the volume derivative and volume respectively of the burned zone calculated using the ideal gas law and the previously calculated temperatures and mole numbers of the burned zone. However, the authors attest that in existing multi–zone models, each zone does not vary significantly in volume, because the number of zones increases. Thus the implementation of the original Zeldovich mechanism is valid in these cases.

Authors validate their model using experimental data from a single–cylinder version of a passenger car Diesel engine. The tuning parameter of the model, namely the burned zone λ, was chosen equal to *1.088* giving the best match of predicted and measured *NO* values. The maximum error was about *30%* and the absolute average error of roughly *20%*. The authors recognize that the model is very sensitive to this parameter (λ).

To accomplish application on embedded systems, the authors were pre–calculate and tabulate some parameters and then express the solution as a function of its input variables as shown in Eq. (2.41):

$$\frac{\partial c_{NO}}{\partial t} = f(T_{bz}, p, c_{NO}) \tag{2.41}$$

2.4.1.12 Scappin NO_x and Engine Performance Model for Marine Engines

Scappin et al [106] developed a zero–dimensional model for the prediction of NO_x and engine performance for marine low–speed Diesel engines. The proposed zero–dimensional model evaluates engine performance by means of an energy balance and a two–zone combustion model using ideal gas law equations over a complete engine cycle and a scavenging model for the calculation of the scavenging efficiency. The combustion process is divided into intervals and the composition products and flame temperature are calculated in each interval. NO_x emissions are predicted using the extended Zeldovich mechanism.

Model's ability to adequately predict brake specific fuel oil consumption (*bsfc*) and NO_x emissions was validated using experimental data from two large–scale electronically controlled marine Diesel engines. The engine variation parameters were the start of injection (*SOI*), which affects the maximum combustion pressure, exhaust valve opening (*EVO*) timing and scavenging pressure. The last two affect the scavenging efficiency and compression pressure.

The authors used the double Wiebe function following the Miyamoto model [181] to calculate *HRR* and Woschni correlation [162] to estimate the gas to wall heat transfer. The *HRR* model was calibrated to match measured data, by selecting the correct timing of fuel injection and adjusting combustion shape parameters. The combustion and NO_x formation models are integrated in a loop which divides the combustion duration into equal steps.

Before the initiation of the procedure, combustion parameters are calculated such as total heat release, global air to fuel ratio, ignition delay, Wiebe parameters and an initial guess of adiabatic flame temperature (*AFT*). During the iterative procedure, two zones are considered, a zone with combustion and a zone containing the remaining cylinder gas.

The iterative procedure initiates by solving a system of ordinary differential equations by integration. This system includes equations for heat losses by Woschni, energy and mass balances, ideal gas law and Wiebe function *HRR* consideration. The solution of the system provides values of temperature, pressure, volume, mass and *HRR* over the time interval of the examined *CA* step. The mass of burnt fuel is provided from *HRR* and the mass of oxygen involved is found by multiplying the local lambda value with the mass of burnt fuel divided by the concentration (at the examined step) of oxygen in the cylinder charge. By this way, the mass of the charge in the combustion zone is scaled to keep the oxygen concentration constant. The local lambda is constant for the *360*° engine cycle and is correlated with load. The combustion products composition, which is needed for the *AFT* calculation, is obtained from an eleven species chemical equilibrium scheme described in Rakopoulos et al [147]. Then, NO_x formation is modeled and lastly the gasses from the two zones are mixed, at the end of each interval to form the new composition of the cylinder charge. This is done by adding the components (by mass weighted) of the two zones together and dividing by the total mass of the charge.

NO_x is calculated using the extended Zeldovich mechanism [182]. The temperature used in this mechanism is the *AFT* of the burning zone. For the aforementioned calculations, the trapped mass in the cylinder at the i_{th} cycle is required. It is calculated using the ideal gas law and taking into account the estimated residual gas fraction X_r, exhaust gas

temperature T_{exh}, intake temperature T_i and cylinder pressure and volume at exhaust valve closure (*EVC*) as described in Eq. (2.42):

$$\begin{gathered} m_c(i) = \frac{P_{EVC} \cdot V_{EVC}}{R \cdot T_{mix}(i)} \\ T_{mix}(i) = (1 - X_r) \cdot T_i(i) + X_r \cdot T_{exh}(i-1) \\ X_r = 1 - SE_V \\ SE_V = 1 - exp(k_0 + k_1 \cdot SR_V + k_2 \cdot SR_V^2) \end{gathered} \tag{2.42}$$

The residual gas fraction (X_r) for the two–stroke, uniflow–scavenging engines calculation method, is obtained from Ref. [183] where SE_V is the volumetric scavenge efficiency, SR_V is the scavenge ratio, or the ratio between the delivered fresh air and the swept volume of the combustion chamber. The correlation factors k_0, k_1 and k_2 are the scavenging coefficients [183].

The results revealed that the model can capture the trends of *bsfc* and NO_x emissions with injection timing and *EVC* timing, within the *95%* confidence interval of the measurements. The authors state that their model is very fast and provides good accuracy, with respect to essential engine performance characteristics. Furthermore, their model has demonstrated capability of responding well to tuning engine parameters regarding *bsfc* and NO_x emissions. Thus, they propose their model to explore different scenarios, i.e. *bsfc* minimization within the *IMO* NO_x emission limits [47] and for energy system analysis.

2.4.1.13 Goldsworthy Thermodynamic NO_x Model for Marine Engines

Goldsworthy [110] developed a thermodynamic model for predicting NO_x emissions from slow–speed marine Diesel engines. His model is a zero–dimensional one, makes use of chemical kinetics for NO_x formation in multiple burnt gas zones, and runs in real–time on a standard *PC*. The mean fuel/air mixture, where NO_x forms, and the rate of dilution of the burnt gas by unburnt air, are adjustable. Two large–scale, low–speed Diesel engines were used for the model validation. Effects such as variations in fuel spray interaction with load are accounted for in the calibration of the model. This model aims to investigate the effect of dilution rate and equivalence ratio on NO_x formation.

The investigation revealed that, under certain conditions, there is a critical burnt gas dilution rate which maximizes NO_x. The model responds adequately to changes in engine load and to NO_x control measures such as water injection, injection timing retard, exhaust gas recirculation and humidification. Measurements were used from *E3* test cycle (propeller law) [46] for this study.

This model employs multiple burnt gas zones [109], adiabatic flame temperature, chemical kinetics, *NO* formation on the lean side of the flame, mixing of the burnt gas with unburnt air and extra cooling by metal surfaces. The model does not use detailed spray and turbulence calculations, since it is oriented for real–time applications. Turbulent mixing rates are derived empirically from the combustion rate (derived from *HRR*), which is inferred from measured peak cylinder pressure and engine power at a number of representative engine

operating conditions. The power output, in–cylinder pressure, *HRR*, exhaust temperature and thermal efficiency are calculated from an in–house model (AMC's marine Diesel simulator) which uses a simple combustion model [184] based on the Whitehouse–Way method for the *HRR* estimation. *HRR*, from which the fuel burnt rate is calculated, and in–cylinder pressure are required as inputs in the NO_x model.

The multi–zone model for NO_x emissions has been coupled onto this simple combustion model. To create a realistic temperature history for the *NO* formation regions, a number of zones of known mass are created as combustion proceeds and the evolution of *NO* in each of these zones is followed kinetically. The number of zones is much less than the total number of calculation steps for the combustion period. To reduce computation time, the number of zones was set at *10*. At the end of combustion, the total amount of *NO* is found by averaging the *NO* from subsequent zones and summing the average values, weighted according to the mass of fuel burnt between the starting angles of the subsequent zones.

The temperature history of each *NO* zone is followed by a simplified energy analysis which accounts for the compression/expansion, heat transfer and mixing of the gas with unburnt air (controlled by a dilution rate). The initial temperature of each *NO* zone is the constant pressure adiabatic flame temperature at that time. The equivalence ratio for the flame temperature calculations is set at a single value less than one (fuel–lean) for all zones. This value is an input to the model. The chosen equivalence ratio determines the *NO* zone temperature and composition. The heat transfer rate is taken as a proportion of the total cylinder heat transfer rate, weighted by the mass of the *NO* zone. The zones are distributed through time by setting one zone at the start of combustion, one at maximum cylinder pressure and two zones in between. An additional number of six zones are distributed between maximum pressure and end of combustion.

For the calculation of *NO*, the reduced kinetics scheme developed by Zabetta and Kilpinen [185,186] was used because it was derived in the context of large marine propulsion Diesel engines. It involves the extended Zeldovich mechanism, a two–step N_2O–intermediate path and five additional reactions, called the "N_2O extension" path, which involves oxidation of N_2O to *NO* via *NH* and *HNO* intermediates. This scheme is likely to provide significant *NO* production in fuel lean areas.

Model predictions revealed that NO_x trend with load is adequately captured. The model parameter used for tuning was the dilution factor which was adjusted with load. The initial equivalence ratio for combustion was assumed constant and close to stoichiometry ($\Phi=0.96$). The author states that this model can be fitted to the parent engine test data, which are available from the technical file of any engine certified in accordance with the NO_x Technical Code [46]. Then it could be used to predict the deviation from the certified values of the emissions of an in–service engine, under the influence of varying operating conditions. The author also asserts that his model is able to provide adequate predictions of the impact of the major primary NO_x control measures on NO_x emissions and *bsfc*.

2.4.1.14 Borkowski Semi–Empirical, Multi–Zone, Phenomenological NO_x Model for Marine Engines

Borkowski [112] also dealt with large–scale engines. He developed a semi–empirical, multi–zone, phenomenological model which uses in–cylinder measured pressure trace to calculate NO_x emissions for marine slow–speed Diesel engines for transient operation. He defined combustion rate in functional form to match experimentally observed *HRR* profiles derived from the measured pressure trace.

Borkowski model makes use of the basic phenomenological concepts for Diesel combustion by describing the three primary phases:

- ignition delay,
- premixed–combustion and
- slower mixing–controlled fuel burning phase.

The fraction of injected fuel that burns in each of these phases is empirically linked to the duration of the ignition delay. One algebraic function (f_1) is used to describe the premixed *HRR* phase and a second one (f_2) to describe the mixing–controlled phase. These two functions are weighted with the phase proportionality factor β, which is mostly a function of the ignition delay. Thus the burning rate is obtained from the Eq. (2.43):

$$\frac{m_{f,b}(t')}{m_{f,0}} = \beta \cdot f_1 + (1-\beta) \cdot f_2$$

$$t' = \frac{t - t_{ign}}{\Delta t_{comb}}$$

$$f_1 = 1 - (1 - t'^{K1})^{K2} \qquad (2.43)$$

$$f_2 = 1 - exp(-K3 \cdot t'^{K4})$$

$$\beta = 1 - \frac{a \cdot \Phi^2}{\tau_{id}^c}$$

where $m_{f,b}$ is the mass of the burnt fuel, $m_{f,o}$ is the total fuel mass injected per cycle, *t'* is the time from ignition, *K1*, *K2*, *K3* and *K4* are empirical coefficients, Φ is the overall equivalence ratio and *a*, τ_{id}, and c are empirical constants.

The concept of the model assumes that the liquid fuel injected into the combustion chamber via several jets, is divided into many small zones. All combustion events in each zone, namely droplet break–up, evaporation, air–fuel mixing, ignition, premixed *HRR*, mixing–controlled *HRR*, heat transfer and formation of exhaust emissions, are accounted for in zonal temperature and composition calculation.

The model is consisted from the following sub–models:

- spray development model,
- air entrainment and mixing model,
- droplet evaporation model,
- heat transfer model,

- combustion model and
- NO_x formation model.

The engine combustion model is based on undisturbed turbulent gas jets, also referenced as the "*Cummins model*", where Diesel spray is treated as quasi–steady gas jet penetrating into gaseous environment of combustion air. The result is a continuous profile of fuel vapor concentration ranging from very rich at the core to very lean mixture at the periphery of the spray. The amount of fresh air, which is continuously entrained into the spray, is a determinant factor for the combustion and pollutant formation rates. For the calculation of these rates, a set of evolving discrete combustion zones is superimposed on the continuous calculated fuel–air distribution. This distribution is determined from semi–empirical/phenomenological correlations derived from experimental spray investigations.

The contribution of each zone to the total wall heat transfer is based on the product of zone mass and temperature. The change of composition and internal energy of each zone caused by the mixing between the zones can be determined similarly to energy and mass balance equations for various zones [187]. After the calculation of the temperature and composition of each zone, the model uses the extended Zeldovich mechanist to calculate NO_x formation.

The model has been validated on a seven–cylinder large–scale (*10MW*) test bed engine. It was revealed that the model is able to predict satisfactorily the exhaust NO_x emissions. It can also provide the NO_x formation history during an engine cycle. The author notes that the sub–models of spray development and air entrainment have to be carefully calibrated to increase model predictive ability.

2.5 The Outcome of the Literature Review

The outcome of the presented literature review is that a significant number of models exists for the combustion simulation and exhaust emissions prediction for *DI* Diesel engines. These models are categorized into detailed *3D* (phenomenological and *CFD* models), totally empirical and zero–dimensional, physically–based, semi–empirical/phenomenological models. For the reasons explained in the introduction section of this chapter (section 2.1) and also in section 1.5 it was decided to developed a model with the characteristics of the third category.

Some indicative models of this category were presented briefly in section 2.4. These models have been studied thoroughly from the author in order to get familiarized with the philosophy and rationale of this model category and spot the advantageous features and drawbacks of each one of these models. This investigation provided the potential to develop a new model that combines, selectively, some of the merits of the existing models and adopts new concepts, in an effort to overcome their shortcomings.

Specifically, the presented models in the literature review can be placed between the following bounds:

- model concepts: from very simplified to very complicated ones,
- nature: from physics–base to fully statistical/empirical,
- computational cost: from extremely low to very high,
- calibration effort: from small or zeroth to significant,
- three or zero dimensional
- designed for a specific application or for a wide range of implementation,
- using calculated pressure trace and *HRR* or measured/experimental ones,
- etc.

Considering the previous we focused on the development of a model with the following characteristics:

- prediction of the tail–pipe NO_x, as well as the NO_x history inside the combustion chamber, of *DI* diesel engines,
- low computational cost, thus able to be used in real–time applications,
- simple structure, thus easy to handle and with low calibration effort demands,
- robust physical base, thus able to capture the effects of unexpected variations,
- use of the measured pressure trace and the derived experimental *HRR*, thus able to account for the actual in–cylinder conditions and processes (adds to the model directness and hence reliability and versatility) and
- addition of empirical concepts in order to optimize the extracted results and enhance its versatility.

In the present work an effort has been made to adopt the aforementioned characteristics and develop a simplified, fast, versatile and reliable, zero–dimensional, multi–zone model with a wide range of implementation regarding engine types (i.e. marine, automotive, *2*–stroke, *4*–stroke, etc.) and engine operating conditions (i.e. account for the effect of engine load and speed, intake conditions, injection strategy, *EGR* rate and of other primary measures for emissions control, etc.). In the following chapter (Chapter 3), the development of the proposed model is comprehensively described.

Chapter 3 DEVELOPMENT OF THE PROPOSED MODEL

3.1 Introduction

Considering the demand of the Diesel engine field, for reliable and accurate NO_x prediction with low computational cost and low complexity, in the present work, a simplified, semi–empirical, multi–zone, thermodynamic model has been developed and validated. Model development and validation involved through many evolution stages [188,189,56,190] up to its last form, presented herein.

The proposed model utilizes the actual in–cylinder pressure trace, which can be easily and accurately measured and also makes use of the major engine geometry and operating parameters to estimate NO_x emissions.

From the measured pressure trace, the model calculates the heat release (*HR*) and combustion rate accounting for the chemical composition of the fuel, ideal combustion reactions, initial charge condition, engine operating conditions and engine geometry. From this analysis the elementary fuel amount burnt at each time instance can be calculated. Additionally, the analysis of the pressure trace and *HR* rate (*HRR*) provides useful data such as the start, center and end of combustion (*SOC, COC, EOC*), maximum cylinder pressure, etc. which are also utilized in model calculations.

After the calculation of the elementary fuel amount burnt at each time instant, the NO_x sub–model is implemented. It is assumed that each one of these elementary fuel amounts forms an independent combustion zone, also comprising the requisite amount of unburnt charge which carries the oxidizer (i.e. O_2). The zone continues to evolve in the cylinder until the end of closed engine cycle without exchanging mass or energy with the neighbor zones. NO_x is calculated using the extended Zeldovich mechanism [29] which uses the zone temperature, volume and composition and in–cylinder pressure. The first thermodynamic law is used to calculate the zone temperature and volume at each time instant. During zone generation, is assumed that the fuel burns instantaneously. Then the zone is being expanded or compressed (depends on in–cylinder pressure derivative) continuing to contribute to NO_x formation until exhaust valve opening (*EVO*). Zone composition is calculated from combustion chemistry accounting for the chemical dissociation. Pressure is assumed constant at each time instant and equal to the measured one. NO_x is calculated for all existing zones at the examined time instant, hence the NO_x history of each zone is obtained. From the sum of the zone NO_x formed at each time instant, the history of the in–cylinder NO_x is derived and thus, at the end of engine closed cycle, namely when *EVO*, the tail–pipe NO_x is derived.

In the following paragraphs an analytical description of the model is presented. Initially, the main concept of the model is described comprehensively. Then a brief description of pressure trace processing is provided. Thereafter, the sub–models for the determination of the initial conditions are described. A detailed *HRR* analysis follows and finally the NO_x sub–model is presented.

3.2 Pressure Trace Processing

3.2.1 The Motivation to Use the Measured Pressure Trace

The most essential characteristic of the proposed model is the employment of in–cylinder measured pressure trace. The actual in–cylinder pressure trace is a powerful tool for the engineer because it provides significant information for the mechanisms taking place inside the combustion chamber. The pressure, temperature and chemical composition of the cylinder charge, which drive NO_x formation, are determined from these mechanisms which comprise compression, fuel–air mixing, combustion, expansion, etc. [8,14]. The aforementioned mechanisms are directly affected from the following:

- charge initial conditions,
- engine geometry,
- fuel type/properties
- heat exchange with the cylinder wall,
- blow–by leakages,
- charge turbulence,
- fuel injection profile and timing,
- etc.

Hence, the use of the actual in–cylinder pressure trace, which can be accurately and reliably measured, adds to the model the ability to account for the most important factors affecting combustion and thus NO_x formation. This is important because the variation of these factors has an impact on the actual in–cylinder pressure. By using the proposed methodology, the effect of this variation on NO_x formation is captured by the model.

Moreover, significant information can directly obtained from the pressure trace such as:

- compression pressure,
- maximum combustion pressure,
- start of combustion (*SOC*) crank angle (*CA*),
- *CA* of the exhaust valve opening (*EVO*),
- etc.

Furthermore, after mathematical processing, the measured pressure trace can be used to calculate engine indicative power, mean indicative pressure and also heat release rate (*HRR*).

3.2.2 In–Cylinder Pressure Measurement

The pressure trace is measured using pressure sensors (piezoelectric sensors) [191] which are mounted either directly on the cylinder's head (flush mounted) or indirectly on the cylinder's ventilator/pressure–duct (i.e. in large–scale engines). These sensors generate voltage potential strictly proportional (for a specific frequency zone) to the applied pressure.

The obtained analog signal is then amplified and converted to digital through an analog to digital converter in order to be processed [191]. The pressure range of the common

pressure sensors used for combustion engines is *0* to *250–300 bar* [192]. It should be noted that these sensors present a thermal drift during operation, which can be easily compensated. Moreover, electrical noise and noise from other sources such as digitization errors and errors due to dynamic phenomena close to the sensor location (i.e. due to pressure waves in the measuring duct [193]) may exist in the primary measurements, which can be removed using digital filters [194,195].

To utilize the measured pressure trace, it must be coupled and synchronized with the crank angle (*CA*) timing. To accomplish this, the position of the point of the pressure trace which corresponds to the top dead center (*TDC*), must be determined with maximum accuracy. The last can be managed either with the use of experimental/applied, either simulation methods. A common method to measure the *TDC* is to use the pulse obtained from an inductive sensor when an indicator, located on the flywheel at a specific *CA*, cross the magnetic field of the sensor [25]. Alternatively, the determination of *TDC* can be achieved by using thermodynamic methods [196,197].

In addition, the *CA* timing (piston position) must be coupled with pressure sampling timing. This can be achieved ideally by using a *CA* encoder, which is coupled on the engine axle. In this case, the encoder triggers the analog to digital converter to acquire a pressure measurement with a fixed *CA* step. According to this method, the pressure signal measurement is attained in the *CA* domain, namely the pressure signal is obtained at a specific *CA* sampling rate. This method is the most reliable and accurate one because it accounts for the variation of the instantaneous engine speed during the engine cycle. Although this is a common method used in laboratories during experiments, it is not convenient for practical and real–time applications because of the difficulties of the encoder coupling on the engine and calibration of the *TDC*.

The common sampling methods are conducted in time domain and must be converted in *CA* domain. This conversion is managed assuming constant speed during the engine cycle or by using correcting correlations to approach the actual speed [198]. However the assumption of constant speed in a specific cycle is not far from reality especially for large scale or/and multi–cylinder engines. Considering the previous, the sampling rate (frequency – f_s *[Hz]* or *[s^{-1}]*) is determined from the engine speed (*N [rpm]*) and the desirable angle resolution ($\Delta\theta$ *[°]*) as described in Eq. (3.1):

$$f_s = \frac{360°}{\Delta\theta} \cdot \frac{N}{60\frac{s}{min}} = \frac{6 \cdot N}{\Delta\theta} \tag{3.1}$$

Finally, many methods exist for the pegging of measured pressure trace, namely for the calculation of the absolute pressure (e.g. making use of the measured scavenging pressure) which can be found in literature [199]. The actual absolute pressure is calculated from Eq. (3.2):

$$p_i = C \cdot \left(V_i - V_{peg.}\right) + p_{peg.} \tag{3.2}$$

In the previous expression, p_i is the pressure *[bar]* in a specific time step *i*, V_i *[V]* is the digitalized voltage of the respective point, V_{peg} is the voltage at the pegging point, $p_{peg.}$ is the

known pegging pressure and *C [bar/V]* is the sensor calibration constant provided from the manufacturer.

In the present work only steady–state engine operation was examined. Thus, for the examined operating points, the pressure trace of the examined cylinder is derived from the average of approximately *20–100* consecutive engine cycles depending on the application (higher number for higher speed engines) [191,194,200,201] aiming to attenuate the errors due to cyclical variation, signal noise and sampling procedure errors. The final pressure traces of all cylinders can be used for more detailed analysis, however the pressure trace of a representative cylinder can be used as the "average cylinder" assuming that the other cylinders have similar behavior. The last, is a common technic for automotive engines.

In the present study, the aforementioned pressure trace pre–processing was attained from an in–house, well validated diagnostic tool, for a part of the test cases examined. These measurements where accomplished on–board in ships and in real–time at power stations during actual engine operation. The remaining part of measurements were provided from *AVL* and *ETH* during cooperation under an *EU* funded project. These measurements were obtained under controlled – laboratory conditions and the pre–processing was done from the provider.

3.2.3 Smoothing the Measured Pressure Trace

After the measurement of in–cylinder pressure and its pre–processing described in section 3.2.2, the pressure trace may not yet be appropriate for utilization due to the remaining signal noise, which is intensified in pressure derivatives. This is because the pressure diagram spikes (discontinuities) result in high differences between consecutive (regarding *CA*) pressure values which in turn result in high pressure derivatives, since they are calculated using finite differences schemes. The pressure derivatives have a major role in the calculation of *SOC* and *HRR*. For this reason the pressure trace has to be filtered.

In the present study three smoothing methods, namely low–pass filters, were tested:

- Moving average: this method makes use of the pressure points comprised in a predefined sampling window (filter width) around the examined point and calculates the average value without using weighting factors. This action is repeated consequently for each point in order to construct the smoothed trace.
- Median: according to this method the pressure values of the points comprised in a predefined sampling window around the examined point are rearranged in ascending order. The chosen value for the smoothed trace is the one in the center of this order.
- Savitzky–Golay [202]: this method is similar with the moving average method however, it uses weighting factors for the points comprised in the filter window to calculate the smoothed value of the examined point. The use of these factors (convolution coefficients) is exactly equivalent to fitting the data to a polynomial.

Each one of the aforementioned smoothing methods present pros and cons. Moving average is the fastest method comparing with the others but trends to underestimate local

maximums and minimums. Savitzky–Golay method is not as aggressive as the moving average method and provides much better results because it does not address to all values comprised in the sampling window the same significance. Also, the smoothed pressure derivative can be directly provided from the raw pressure data. The gist of the Savitzky–Golay filter is that it regress a polynomial through the raw values comprised in the filter window using least squares method and hence the smoothed value is the one provided from this polynomial. In addition, an extended investigation described in Ref. [203] comparing Savitzky–Golay filter with zero–phase and butterworth filters, has indicated that the Savitzky–Golay filter is the most appropriate for smoothing the pressure trace. On the contrary, the Median filter is appropriate for pressure traces that present noise with high amplitude – spikes. However, this filter cause problems at the points of *SOC* and maximum pressure where significant variations of pressure occur. It should be only used during the late expansion and exhaust phases.

The quality of the smoothed pressure diagram is strongly dependent on the width of the filter window and the quality of the raw diagram. Small windows result in poor smoothing. However, wider windows cause exorbitant smoothing and important characteristics of the pressure trace may be lost or miscalculated, such as *SOC* and maximum combustion pressure, and also significantly deform the entire pressure trace and hence distort the *HRR* diagram. For these reasons the sample window should be chosen with care.

In this work, the Savitzky–Golay filter was used because it provided adequate smoothing for both, pressure and pressure derivative traces. The filtering window was chosen in order to attain adequate quality for pressure derivative and *HRR* diagrams for the examined cases.

At next the Savitzky–Golay smoothing method is described in brief. A comprehensive presentation of the method can be found in Refs [202,204,205,206,207]. The algorithm used in the present work is based on the guidelines of Ref. [207].

In order to use a digital filter, the raw pressure data $p_i = p(CA_i)$ must be equally spaced. The filter width is defined from a left and right window comprising n_L and n_R raw measurement points respectively around the center point which is the one to be smoothed. The smoothed value p_SM_i at CA_i results from the implementation of the filter as described in Eq. (3.3):

$$p\_SM_i = \sum_{n=-n_L}^{n_R} c_n \cdot p_{i+n} \tag{3.3}$$

where c_n are the Savitzky–Golay coefficients. These coefficients represent the weighting factors and are obtained from the convolution of the polynomial used to regress the raw measured values, as mentioned before. Savitzky A. and Golay M. J. E. have proven that these convolution coefficients are unique and independent of the input data. The set of convolution coefficients depends only on the order of the regression polynomial used and on the length of left and right sample windows. Namely, the smoothed value which would had been derived from the polynomial resulted from the regression of the raw measured values in the filter window, is now equivalently calculated from Eq. (3.3) using the convolution coefficients c_n which are constant for the entire spectrum of the measured raw values. Another

important advantage of Savitzky–Golay smoothing method is the direct calculation of the smoothed pressure derivative from the raw measured pressure trace using the corresponding convolution coefficients. The detailed mathematical analysis of this method can be found in the relevant literature [202,207].

3.3 Prerequisite Calculations for the Heat Release Rate and NO models

3.3.1 Required Inputs for the Model and Initial Conditions

The major inputs for the proposed *NO* model is the combustion rate (i.e. the fuel amount burnt in each instance) calculated using the measured pressure trace via a heat release rate (*HRR*) analysis, basic engine geometry i.e.:

- number of cylinders,
- cylinder bore,
- cylinder stroke,
- connecting rod length,
- crank radius,
- compression ratio,
- engine type: *2* or *4*–stroke,
- *CA* at start of compression – beginning of closed engine cycle and
- *CA* at the end of expansion phase, namely at *EVO* – end of closed cycle

and engine operating characteristics such as:

- engine speed,
- fuel mass flow,
- intake air or exhaust gas mass flow,
- exhaust gas recirculation rate (*EGR*),
- scavenging (at inlet manifold) temperature and
- scavenging pressure.

Nevertheless, to achieve a robust physical approach and attain more reliable and representative results, the initial conditions parameters should be determined with the maximum possible accuracy. These parameters are:

- the trapped mass in the cylinder and
- the chemical composition of the trapped mass before *SOC*.

The aforementioned calculations require, among others, the following data for ambient conditions:

- temperature,
- pressure,
- relative humidity and
- chemical composition (the typical air composition is assumed).

The fuel type, lower heating value (*LHV*) and chemical composition (carbon *C*, hydrogen *H*, sulfur *S*, oxygen *O* and nitrogen *N* mass content) are used indirectly for the

calculation of the initial conditions (e.g. intake mass flow rate calculation, composition of *RG*, *EGR* fractions) and later in the main algorithm, in both models, *HRR* and *NO*.

At this point, it is noted that both models use iteration procedures and hence in order to reduce calculation time, the arrays which are only a function of *CA* are calculated only once. These arrays are the following:

- cylinder pressure (derived from smoothing model – section 3.2.3),
- pressure derivative (derived from smoothing model – section 3.2.3),
- cylinder volume and
- cylinder wall area.

Engine geometry and engine speed are used for the calculation of the last three arrays, as described in section 3.3.4.

3.3.2 Fuel Mass Distribution to each Engine Cylinder per Cycle

As mentioned in the previous section (3.3.1), the fuel and air mass flow rates *[kg/h]* are obtained from the input data. The fuel mass flow rate can be obtained from:

- Direct measurement in *[m^3/h]* using a volumetric flow–meter and the temperature of the fuel at the point of the measurement. The last, is used for the calculation of fuel density *[kg/m^3]* via an empirical correlation. The coefficients of this correlation depend on fuel type. Thereafter, the fuel volume flow and its calculated density are used to calculate the fuel mass flow rate in *[kg/h]* unit.
- Direct measurement in *[kg/h]* using a mass flow–meter. The operating principle of these flow–meters is based on Coriolis Effect.
- Validated simulation model, which uses the measured in–cylinder pressure trace via *HRR* analysis to calculate the burnt fuel throughout an engine cycle.
- Mapped fuel mass flow rate (i.e. stored in engine's *ECU*) which is a function of engine operating conditions (i.e. power, speed, etc.).

In the present work, for the large–scale engines examined, the estimated values of the fuel mass flow rate were used, provided from a validated [208] in–house diagnostic system [209,210,138,132], since the direct fuel flow rate measurement is difficult for these engines, especially when the measurements are performed on–board. For the examined automotive engines (passenger car and truck engines), the available laboratory measurements were used, which were accomplished using a volumetric flow meter.

Specifically for the large–scale engines where the pressure traces of all engine cylinders have been measured, the engine fuel flow rate should be distributed to each cylinder. This is imperative, since each cylinder may has different fuel consumption. This can be attributed to a number of reasons i.e. wear of cylinder, injection beck and/or fuel pump, inappropriate adjustments, etc. It is emphasized that, regarding the examined large–scale engines, each cylinder is fueled with its own individual fuel pump which is mechanically controlled. Considering the previous, a simple concept for the distribution of the total fuel mass flow to the cylinders is adopted: The net *HRR* (*NHRR*) of each cylinder is calculated, using the corresponding pressure trace, via Eq. (3.29), as described in section 3.4.2 and from this, the cumulative net *HR* (*CNHR*) is derived. Then, the *CNHR* values of each cylinder at

the end of combustion (*EOC*), which is determined from the tail of net *HRR* diagram as described in section 3.4.6, are summed up in order to calculate the total theoretical energy released resulted from the combustion of total injected fuel (neglecting heat losses through cylinder wall). Thereafter, the ratio between each cylinder's *CNHR* at *EOC* and the respective total one is calculated. Then the fuel mass flow of each cylinder is calculated from the product of the corresponding ratio and the known total engine fuel flow rate. The procedure is described in Eq. (3.4).

$$\dot{m}_{f\,m} = \dot{m}_{f\,eng} \cdot \frac{CNHR_{EOC\,m}}{\sum_{m=1}^{m=n\_cyl} CNHR_{EOC,m}} \tag{3.4}$$

In the previous expression, $\dot{m}_f$ *[kg/h]* denotes the fuel mass flow, subscripts *m* and *eng* indicate the sequence number of the examined cylinder and the engine respectively and n_{cyl} the number of cylinders.

It is noted that the aforementioned calculation omits the cylinder wall heat exchange since its calculation would require measured injected fuel amount per cylinder for the calibration of the wall heat exchange model used, which is described in section 3.4.7. However, this concept provides an adequate indication for the fuel distribution to the cylinders, since the percentage of heat losses is small compared to the total fuel energy released and also heat losses fluctuation from cylinder to cylinder is not significant, thus the error is negligible.

3.3.3 Intake Air Mass Flow Rate

The intake air mass flow rate *[kg/h]* can be obtained from:

- Direct measurement of the intake air flow *[m^3/h]* using a flow–meter in combination with ambient temperature, pressure and humidity measurement to calculate the air mass flow via equation of state for ideal gas. If exhaust gas recirculation (*EGR*) is used, the *EGR* composition and *EGR* rate, which is determined from the *EGR* valve position, are also accounted for.
- The intake air mass flow, *EGR* rate and the estimated residual gas (*RG*) fraction can directly obtained from engine *ECU* where are mapped as functions of engine speed and load (rack position – fuel mass flow).
- Direct estimation of intake air mass flow using the measured pressure and temperature at intake manifold and the in–cylinder pressure via a simplified zero–dimensional model [211,212].
- Indirect estimation using the measured exhaust oxygen content (e.g. by using oxygen/lambda sensor).
- Calculation of intake air mass flow using the measured fuel mass flow and exhaust gas flow. The last is calculated using the stack diameter (area), exhaust gas density and velocity. The gas velocity can be directly measured using a pitot tube [213].
- Indirect estimation of intake air mass flow using exhaust emissions measurement derived from an emissions analyzer. From this measurement combined with the use of fuel mass flow and ambient conditions, the exhaust mass flow can be cal-

culated via the carbon balance method as described in Appendix a [46], or carbon/oxygen balance method [8,214,215]. Apparently, the air mass flow rate is derived from the subtraction of fuel mass flow rate from the exhaust mass flow rate.

In the present study, for the large–scale engines, the last mentioned method was used. On the contrary, the first method was used for the automotive engines where laboratory measurements were available. Furthermore, the mass flow rates are converted from *[kg/h]* to *[kg/cycle]* units, since the model calculations correspond to a single engine cycle. This is achieved using Eq. (3.5):

$$\dot{m}(kg/cycle) = \dot{m}(kg/h) \cdot \frac{str.}{120 \cdot N} \tag{3.5}$$

where *str.* is the number of strokes in the engine cycle, *4* for the *4*–stroke engines and *2* for the *2*–stroke engines and *N [rpm]* is the engine speed.

3.3.4 Calculation of Cylinder Volume, Wall Area and Piston Speed as Functions of Piston Position

The cylinder volume ($V\ [m^3]$), exposed area to the in–cylinder charge ($A_{cyl}\ [m^2]$) and piston speed ($Sp\ [m/°]$), as functions of piston position (*CA*), are utilized in both, *HRR* and *NO* models. Moreover, these data are only a function of *CA* thus they are calculated only once for each operating point to save computational time. Once they have been calculated, they are stored next to pressure and pressure derivative arrays in a data file to be used from these models.

For the calculation of the cylinder volume and area as a function of *CA*, the piston displacement as a function of *CA* should be calculated at first. In the present work, the maximum piston displacement, which appears at the bottom dead center (*BDC*) and which is equal with the cylinder stroke, corresponds to *0°* i.e. *0° ABDC*. The piston displacement is described from Eq. (3.6):

$$x_i = R \cdot \left(1 + cos\left(\frac{\pi \cdot \theta_i}{180}\right)\right) + CRL \cdot \left(1 - \sqrt{1 - \left(\frac{R}{CRL} \cdot sin\left(\frac{\pi \cdot \theta_i}{180}\right)\right)^2}\right) \tag{3.6}$$

The cylinder volume (V_{cyl}) and area (A_{cyl}) are calculated from Eq. (3.7) and Eq. (3.8) respectively. For these calculations, the assumption of flat piston crown and cylinder head is adopted.

$$V_{cyl_i} = x_i \cdot \pi \cdot \frac{D^2}{4} + V_c$$
$$V_c = \frac{\pi \cdot \frac{D^2}{4} \cdot S}{CR - 1} \tag{3.7}$$

$$A_{cyl_i} = \pi \cdot D \cdot \left(x_i + \frac{V_c}{\pi \cdot \frac{D^2}{4}} \right) + 2 \cdot \pi \cdot \frac{D^2}{4} \tag{3.8}$$

The piston speed (*Sp [m/°]*) is derived from the derivative of piston displacement as described in Eq. (3.9):

$$Sp_i = \frac{dx_i}{d\theta} = \frac{\pi}{180} \cdot R \cdot sin\left(\frac{\pi \cdot \theta_i}{180}\right) \cdot \left(\frac{R/_{CRL} \cdot cos\left(\frac{\pi \cdot \theta_i}{180}\right)}{\sqrt{1 - \left(\frac{R}{CRL} \cdot sin\left(\frac{\pi \cdot \theta_i}{180}\right)\right)^2}} - 1 \right) \tag{3.9}$$

In the previous expressions, subscript *i* denotes the current calculation step, *θ* corresponds to *CA [° ABDC]*, *R [m]* is the crank radius, *CRL [m]* is the connecting rod length, *D [m]* and *S [m]* are the cylinder bore and stroke respectively, *CR* is the engine compression ratio and V_c *[m^3]* is the cylinder clearance volume.

3.3.5 Calculation of Initial Conditions for Large–Scale, 2–Stroke Engines – Scavenging Model Description

The initial conditions required for the calculations regarding the large–scale, *2*–stroke engines are the trapped charge mass, its chemical composition and temperature at the start of compression, namely when the exhaust valve closes (*EVC*).

The calculation of the initial conditions for this type of engines is a difficult issue because the exhaust phase period is much smaller compared to the one of *4*–stroke engines, thus the scavenging process has to be considered for. The scavenging process is not as effective as the corresponding one in *4*–stroke engines where exhaust gases are displaced by the piston upwards move. Thus, a significant amount of residual exhaust gas (*RG*) remains in the combustion chamber. Moreover, only a part of the delivered fresh air is trapped inside the combustion chamber since an important amount (up to *50%* [216]) is lost during the scavenging procedure. The high amount of *RG* results in an increase of temperature at the intake phase and thus deterioration of engine volumetric efficiency and also decrease of O_2 concentration, which induce deterioration of engine performance. The lower amount of trapped mass also worsens performance. On the contrary, the *RG* behaves as internal *EGR*,

thus it tends to mitigate *NO* formation. Considering the previous, it is deduced that the scavenging procedure in *2*–stroke engines is important since it severely affects performance and NO_x emissions and thus, in the present study, it is simulated using the scavenging model described at next.

To estimate the initial conditions for *2*–stroke engines, a perfect–mixing, non–isothermal scavenging model is used as described in Ref. [9,146] with some modifications. The charge composition, temperature and trapped mass at *EVC* are calculated using an iterative procedure. The in–cylinder charge is assumed to behave as an ideal gas in the following calculations. In these calculations, the in–cylinder volume and pressure at the following *CA* events are utilized: at *EVC*, exhaust valve open (*EVO*) and end of blow down period[2] (*EOBD*). The corresponding volumes are calculated from Eq. (3.7) as described in section 3.3.4 and the corresponding pressures are derived from the in–cylinder measured pressure trace, as the average of the pressure values which correspond to the examined *CA* event and its *2* previous and *2* ahead neighbor values.

At first, the delivery ratio (Λ) is calculated as described in Eq. (3.10) [9]:

$$\Lambda = \frac{mass\ of\ fresh\ air\ delivered}{m_0} \tag{3.10}$$

In the previous relation, "*fresh air mass delivered"* corresponds to the engine's intake ambient air *[kg/cycle]* and m_0 is the reference air mass.

"*fresh air mass delivered"* is calculated as the difference between the exhaust mass (calculated from carbon balance method [8,214,215], see section 3.3.3) and the known fuel mass flow. m_0 is calculated from the state equation for ideal gases using manifold (scavenging) pressure (p_{scav} *[Pa]*) and temperature (T_{scav} *[K]*), ambient air composition (wet air (*MWair,wet [kg/kmole]*), i.e. accounting for the measured air humidity), the cylinder volume at *EVC* (V_{EVC} *[m^3]*) and the number of cylinders (n_{cyl}) as described in Eq. (3.11). $\bar{R} = 8314$ *[J/kmol/K]* is the universal gas constant.

$$m_0 = \frac{p_{scav} \cdot V_{EVC}}{\frac{\bar{R}}{\overline{MW}_{air_{wet}}} \cdot T_{scav}} \cdot n_{cyl} \tag{3.11}$$

As already mentioned, the calculation of the composition of the trapped mass inside the cylinder, which is composed from fresh (ambient) air and residual gas (*RG*), is estimated by incorporating the aforementioned scavenging model. This model suggests that the scavenging efficiency (η_{sc}) is given from Eq. (3.12):

$$\frac{mass\ of\ fresh\ air\ in\ the\ cylinder}{total\ cylinder\ mass} = \eta_{sc}^{k} = 1 - \frac{T_{EVC}^{k-1}}{T_{EOBD}^{k-1}} \cdot e^{-\Lambda} \tag{3.12}$$

[2] blow down period is the period from the exhaust valve opening to the scavenging port opening (*SPO*)

where T_{EVC} *[K]* is the temperature at *EVC* and T_{EOBD} *[K]* is the temperature at *EOBD* period. η_{sc} corresponds to the fraction of trapped mass occupied by ambient air. Superscript *k* corresponds to the current iteration sequence number.

The residual gas fraction (*RG*) is composed from exhaust gas (x_{exh}, y_{exh}, MW_{exh}) derived from ideal combustion (using the cylinder mean equivalence ratio and neglecting dissociation) of the entire fuel amount via the combustion procedure described in section 3.4.5. *RG* mass fraction is calculated via Eq. (3.13):

$$RG^k = 1 - \eta_{sc}^k \tag{3.13}$$

The charge composition and molecular weight (*MW*) are then calculated as described in Eq. (3.14):

$$\begin{aligned} y_j^k &= \eta_{sc}^k \cdot y_{air,j} + RG^k \cdot y_{exh,j} \\ x_j^k &= \frac{y_j^k}{MW_j} \cdot \left(\sum_j \frac{y_j^k}{MW_j} \right)^{-1} \\ MW_{ch}^k &= \sum_j x_j^k \cdot MW_j \end{aligned} \tag{3.14}$$

where *x* is the mole and *y* is the mass fraction of the j^{th} species in the charge, *MW*, y_{air} and y_{exh} are the molecular weight, ambient air and exhaust mass fraction respectively. Subscript *ch* denotes the unburnt charge.

The new temperature of trapped mass at *EVC* is calculated from Eq. (3.15) [146] as follows:

$$T_{EVC}^k = \frac{T_{sc}}{1 - \left(1 - \frac{T_{sc}}{T_{EOBD}^{k-1}}\right) \cdot e^{-\Lambda}} \tag{3.15}$$

where T_{sc} *[K]* and T_{EOBD} *[K]* are the temperatures at inlet manifold and *EOBD* period respectively.

The trapped mass (m_{EVC}^k *[kg]*) is calculated from the state equation for ideal gases as described in Eq. (3.16):

$$m_{EVC}^k = \frac{p_{EVC} \cdot V_{EVC}}{\frac{\bar{R}}{MW_{ch}^k} \cdot T_{EVC}^k} \tag{3.16}$$

where $\bar{R} = 8314$ *[J/kmol/K]* is the universal gas constant, *p [Pa]* and *V[m^3]* are the cylinder pressure and volume at *EVC*.

Then, the charge mass at *EVO* (m_{EVO}) is calculated as the sum of trapped mass at *EVC* (m_{EVC}) and the injected fuel mass in each cylinder (*[kg/cycle]*), which is calculated from Eq. (3.4) in section 3.3.2, assuming negligible mass losses due to blow–by effect.

Afterwards, the mass at *EOBD* (m_{EOBD}) is calculated via Eq. (3.19) [146], which is derived from the first thermodynamic law assuming adiabatic process, zero back flow into the cylinder at blow–down period and constant specific heats as described in Eq. (3.17), in combination with the differential form of the equation of state, as described in Eq. (3.18):

$$dQ = dH - V \cdot dp \overset{adiab.}{\Longrightarrow} V \cdot dp = dH = m \cdot c_p \cdot dT \Rightarrow m \cdot dT = \frac{V}{cp} \cdot dp \tag{3.17}$$

$$\begin{gathered} \frac{dp}{p} + \frac{dV}{V} = \frac{R \cdot T}{p \cdot V} \cdot dm + \frac{m \cdot R}{p \cdot V} \cdot dT = \frac{dm}{m} + \frac{R}{cp} \cdot \frac{dp}{p} \Rightarrow \\ \left(1 - \frac{R}{c_p}\right) \cdot \frac{dp}{p} + \frac{dV}{V} = \frac{dm}{m} \Rightarrow \\ \frac{1}{\gamma} \cdot \int_{EVO}^{EOBD} \frac{dp}{p} + \int_{EVO}^{EOBD} \frac{dV}{V} = \int_{EVO}^{EOBD} \frac{dm}{m} \end{gathered} \tag{3.18}$$

$$\begin{gathered} m_{EOBD}^{k} = m_{EVO}^{k} \cdot (V_{EOBD}/V_{EVO}) \cdot (p_{EOBD}/p_{EVO})^{1/\gamma(x_{exh}, T_{EOBD}^{k-1})} \\ \gamma = \frac{cp^{k-1}}{cp^{k-1} - R} \end{gathered} \tag{3.19}$$

In the previous expressions, *cp [J/kg/K]*, *γ*, *R [J/kg/K]* are the specific heat capacity at constant pressure, isentropic exponent and gas constant ($R = \bar{R}/MW_{exh}$) of the exhaust gas respectively. *cp/R* is calculated from NASA polynomial approximation [180] as described in Appendix d.

Thereafter, the updated value of T_{EOBD} is calculated from Eq. (3.20):

$$T_{EOBD}^{k} = \frac{p_{EOBD} \cdot V_{EOBD}}{\frac{\bar{R}}{MW_{exh}} \cdot m_{EOBD}^{k}} \tag{3.20}$$

The iterative procedure continues until the value of *RG* converges.

3.3.6 Calculation of Initial Conditions for Large–Scale 4–Stroke Engines

For *4*–stroke, large–scale, *DI* Diesel engines, the composition of the charge at the start of compression is assumed to be identical to the ambient air because the *RG* is significantly lower when compared to *2*–stroke engines since the scavenging efficiency is considerably higher [9]. The calculation of the temperature at compression initiation (T_{IVC}), namely at intake valve closure (*IVC*), is a difficult issue due to lack of measurements or validated predicting models for engines of this scale. According to the literature and experience, the temperature of the trapped charge mass at the start of compression phase, namely at *IVC*, is higher than T_{sc} because the incoming air is heated from the cylinder wall and the *RG* retained in the chamber from the previous combustion cycle. However, this temperature increase is relatively low because the wall and *RG* temperature variation with engine power is small.

Nonetheless, wall and *RG* temperatures are slightly increased with engine power. Furthermore, stationary engines, which are used for power generation, operate at a constant speed and hence the effect of this parameter on the initial temperature of trapped mass is lower and thus can be neglected. Considering the previous, in the present work and for the specific engine type, T_{IVC} was estimated using a linear correlation which involves T_{sc} and engine power (P) as described in Eq. (3.21):

$$T_{IVC} = T_{sc} + 30 + 30 \cdot \frac{P}{P_N} \tag{3.21}$$

where P_N in the engine nominal power. After the calculation of T_{IVC}, the trapped mass at the start of compression is calculated using the ambient air composition, the cylinder volume and measured pressure at *IVC* via the equation of state for ideal gases.

3.3.7 Calculation of Initial Conditions for Automotive 4–Stroke Engines

The automotive engines examined herein correspond to a passenger car and a truck. Both are *DI* Diesel engines using common rail fuel injection, supercharging and *EGR* system. The passenger car engine also uses pilot fuel injection. The measurement data for these engines were obtained from detailed laboratory measurements. The data utilized for the determination of initial conditions are:

- the pressure trace diagram of the "average" (representative) cylinder,
- engine speed,
- intake air mass flow,
- fuel mass flow,
- fuel *H/C* malar ratio,
- *EGR* mass fraction,
- residual gas (*RG*) mass fraction,
- intake manifold pressure and
- ambient temperature and relative humidity or humidity in [g water/kg dry air].

The required initial conditions are the unburnt charge mass and composition before combustion initiation. The composition of the unburnt charge (zone) is assumed to remain unchanged from *IVC* to *SOC*. The in–cylinder trapped mass during an engine cycle ($m_{tr}[kg] = \dot{m}_{tr}\left[\frac{kg}{cycle}\right] \cdot 1[cycle]$) and its composition are calculated using the intake air flow rate ($\dot{m}_{IA}$ *[kg/h]*), *EGR* and *RG* mass fractions and fuel composition (*H/C*) which are provided as input data. The trapping efficiency is assumed equal to unity (realistic for *4*–stroke engines) thus the delivered mass (in intake manifold: $\dot{m}_{IM}$*[kg/h]*) equals to the trapped

mass, which is calculated from Eq. (3.22) where n_{cyl} is the number of cylinders and N is the engine speed *[rpm]*:

$$\begin{aligned} \dot{m}_{tr} &= \dot{m}_{IM} + \dot{m}_{RG} \\ \dot{m}_{IM} &= \dot{m}_{IA} + \dot{m}_{EGR} \\ \dot{m}_{EGR} &= EGR \cdot \dot{m}_{IM} \\ \dot{m}_{RG} &= RG \cdot \dot{m}_{IM} \\ m_{tr} &= \frac{\dot{m}_{IA}}{n_{cyl} \cdot N \cdot 30} \cdot \frac{1 + RG}{1 - EGR} \end{aligned} \tag{3.22}$$

The composition of *EGR* and *RG* gases is assumed identical to the one of exhaust gas which is derived from ideal combustion using the cylinder mean equivalence ratio according to the combustion concept described in section 3.4.5. Then, the final composition of the charge is calculated, using *EGR*, *RG* and ambient air fractions and their composition as described in Eq. (3.23):

$$\begin{aligned} FA &= \frac{\dot{m}_{IA}}{\dot{m}_{tr}} \\ EGR &= \frac{\dot{m}_{EGR}}{\dot{m}_{tr}} \\ RG &= \frac{\dot{m}_{RG}}{\dot{m}_{tr}} \\ y_{ch_j} &= FA \cdot y_{air,j} + (EGR + RG) \cdot y_{exh,j} \\ x_{ch_j} &= \frac{y_{ch_j}}{MW_j} \cdot \left(\sum_j \frac{y_{ch_j}}{MW_j} \right)^{-1} \\ MW_{ch} &= \sum\nolimits_j x_{ch_j} \cdot MW_j \end{aligned} \tag{3.23}$$

where *FA* denotes the fresh air mass fraction, subscript *ch* corresponds to the trapped charge and *j* to the species considered, which in this case are the O_2, N_2, CO_2 and H_2O.

3.4 Heat Release Rate and Fuel Burnt Rate Calculation

3.4.1 Importance of the Heat Release Rate Analysis

In the present study the heat release rate (*HRR*) is calculated from the first thermodynamic law using the in–cylinder measured pressure trace (experimental *HRR*). The analysis of the experimental *HRR* contributes to the emergence of information for the combustion mechanism which is directly reflected in the measured in–cylinder pressure trace as described in section 3.2.1. Other researchers use simulation models to predict the *HRR* and

from this they calculate the pressure trace. However, by this way the aforementioned advantageous feature of directness does not exist.

The experimental *HRR* provides useful information for the combustion events taking place inside the combustion chamber such as start of main combustion, detection of smaller combustion events due to pilot or post injection, distinguishing of the premixed (if exists) and diffusion phase, provides the position (*CA*) of *SOC*, maximum *HRR* and *EOC*. Moreover, *HRR* provides an overview of combustion evolution inside the cylinder which is essential during combustion optimization procedures for the improvement of engine performance and emissions control. In general, the *HRR* provides a realistic representation for the combustion mechanism.

The fuel burnt rate is directly obtained from the division of *HRR* with the fuel lower hating value (*LHV*), assuming ideal combustion efficiency, which is very close to reality especially for Diesel engines. Namely, the fuel fraction burnt in each *CA* interval is calculated. The proposed model makes use of a time–*CA* discretization of the burnt fuel to generate combustion zones at each instant. Furthermore, the cumulative *HR* (*CHR*) diagram and burnt fuel fraction can be created. In these diagrams the evolution of combustion is also depicted, namely the *SOC*, *COC*, *EOC*, slope of the curve, etc. An indicative schematic description of the net and gross *HRR* and *CHR* is depicted in Fig. 3.1. The fuel burnt at each *CA* instant and the cumulative fuel burnt is depicted in Fig. 3.2:

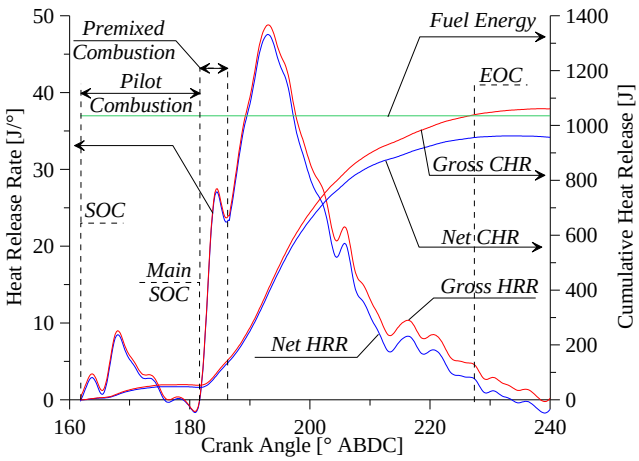

Figure 3.1: Net and gross HRR, CHR and the provided combustion information.

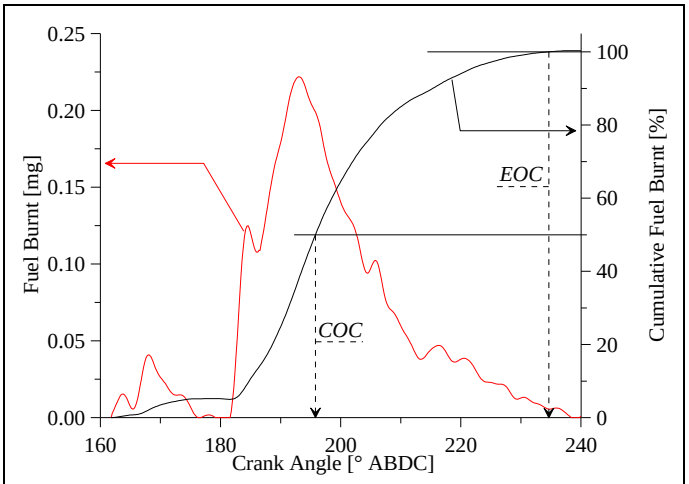

Figure 3.2: Fuel mass burnt and percentage of the total (cumulative) burnt fuel at each CA.

In the section below, the method followed for the *HRR* calculation is presented.

3.4.2 Analytical Description of the Heat Release Rate Model

The *HRR* model used in the present work is a single–zone, zero–dimensional, thermodynamic model which makes use of the actual in–cylinder pressure trace. After smoothing of the measured pressure trace, as described in section 3.2.3, it is utilized in the calculation of the experimental *HRR* using the first thermodynamic law, combustion chemistry, cylinder geometry (volume), initial conditions of the trapped charge and a semi–empirical correlation for the heat exchange between the cylinder charge and wall.

The *HRR* analysis is valid only during combustion. Thus the *SOC* and *EOC* have to be calculated. For this reason, an initial estimation of the *SOC* is attained directly from the pressure trace as described in section 3.4.4. Nevertheless, the analysis showed that the model for the estimation of initial *SOC* usually locates *SOC* slightly earlier than the actual one. Hence, the *HRR* calculations begin from this initial *SOC* value by applying the first thermodynamic law assuming constant charge mass and composition. At the time when the heat term (see Eq. (3.29)) becomes positive, namely when combustion occurs, the actual *SOC* is defined. From that time on the calculations continue until and end of expansion, which is defined as the *CA* where the exhaust valve opens (*EVO*), accounting for combustion and its effect on charge composition. The *EVO* is provided as an input. The *EOC* is calculated finally, with the method described in section 3.4.6.

Initially, the *CA* interval ($\Delta\theta$ *[°]*) is calculated by subtracting two consecutive *CA* values of the provided *CA*–*p* file. The *CA* – pressure points must be equidistance (i.e. $\Delta\theta$ is constant). In addition, the values of *CA* are distinguished in integer calculation steps together with the corresponding variables i.e. pressure, volume, etc.

The initial charge mass and its chemical composition are obtained from the initial conditions calculations described in section 3.3. Moreover, is assumed that during the period from start of compression until *SOC*, the trapped mass remains constant despite the blow–by mass losses which are considered negligible. Furthermore, the charge chemical compo-

sition during this period remains unchanged since no combustion occurs. Hence, before combustion commencement the charge mass and composition is the one determined from the initial conditions. The molecular weight and the total number of moles of the charge, are calculated from Eq. (3.24) and Eq. (3.25) respectively:

$$MW_{ch,i} = \sum_{j} x_{j,i} \cdot MW_j \tag{3.24}$$

$$n_{ch,i} = \frac{m_{ch}}{MW_{ch,i}} \tag{3.25}$$

In the previous expressions *MW [kg/kmol]* is the molecular weight, *x [kmol/kmol]* is the molar fraction of each species comprised in the charge, *m [kg]* is the mass and *n [kmol]* is the number of moles. Subscript *ch* denotes the cylinder's charge, *i* the current *CA* step and *j* the sequence number of each species: (*1*) for O_2, (*2*) for N_2, (*3*) for CO_2, (*4*) for H_2O, (*5*) for *Ar* and (*6*) for SO_2. For the automotive engines only the first four species were taken into account.

The initial temperature of the trapped charge, namely its temperature at the *CA* step just before *SOC*, is calculated via the ideal gas state equation described in Eq. (3.26), using its number of moles (*n*) calculated from Eq. (3.25), the respective combustion chamber volume (see section 3.3.4) and the respective measured pressure.

$$T_i = \frac{p_i \cdot V_i}{n_{ch,i} \cdot \bar{R}} \tag{3.26}$$

In the previous expression, *T [K]* is the temperature, *p [Pa]* is the measured in–cylinder pressure, *V [m^3]* is the cylinder's volume, *n [kmol]* is the number of moles and $\bar{R} = 8314\ {}^{J}/_{kmol\ K}$ is the universal gas constant for ideal gases. Subscript *i* denotes the examined *CA* step.

Then, the specific enthalpy *h [J/kmol]* of each species comprised in the charge (*ch*) is calculated using the charge temperature (*T [K]*) via the *NASA* polynomial approximation [180] (see Appendix d) which is only a function of temperature. A different set of polynomial coefficients corresponds to each species (*j*). The total enthalpy of the mixture (charge) *H [J]* at the current *CA* step (*i*) is calculated from Eq. (3.27) as follows, considering the mole fraction (*x*) of the species comprised in the charge:

$$H_i = n_{ch,i} \cdot h_i = n_{ch,i} \cdot \sum_{j} x_{j,i} \cdot h_{j,i}(T_i) \tag{3.27}$$

As mentioned above, during the period between initial and final estimation of *SOC*, the first thermodynamic law is applied in the cylinder charge as described in the Eq.

(3.28). During this process, the heat exchange between the charge and cylinder wall is neglected and constant charge mass and composition are assumed.

$$\frac{dQ_{N,i}}{d\theta} = \frac{\Delta H_i}{\Delta\theta} - V_i \cdot \left(\frac{dp}{d\theta}\right)_i \tag{3.28}$$

In the previous expression $\frac{dQ_{N,i}}{d\theta}$ is the net *HRR* (*NHRR*), $\Delta H_i = H_i - H_{i-1}$ is the enthalpy variation between two consecutive *CA* steps and $\left(\frac{dp}{d\theta}\right)_i$ is the pressure derivative at the current *CA* step (*i*). When the dQ_N becomes positive for a number of consecutive *CA* steps after the current step, then the final value of *SOC* is determined from a lineal interpolation between steps *i* ($dQ_{N,i}>0$) and *i-1* ($dQ_{N,i-1}<0$) considering that at *SOC* $dQ_{N,SOC}=0$.

The reason for using *NHRR* instead of the gross one, which takes into account the heat exchange through the wall, is that the *SOC* estimation procedure is very sensitive and any introduced inaccuracy from the wall heat–exchange model may induce error on the *SOC* estimation. Furthermore, wall heat–exchange is not significant before combustion commence, since the in–cylinder temperature is lower compared to the developed temperatures during combustion.

Having determined the *SOC* (final estimation), the actual *HRR* calculation initiates. The presented model calculates the *HRR* for each *CA* step via an iterative procedure in order to account for the charge composition variation due to combustion. Then, from the *HRR* the fuel burnt rate is calculated. The procedure, which is described by detailed at next, ceases when the value of the fuel amount burnt at the examined *CA* step converges.

As mentioned, *HRR* is calculated from the first thermodynamic law as described in Eq. (3.29). The enthalpy increase from the fuel injected and enthalpy losses due to leakages and fuel vaporization are neglected, because their contribution is rather small [8], however the heat exchange through cylinder wall is now accounted for.

$$\begin{gathered}\frac{dQ_G}{d\theta} = \frac{dQ_N}{d\theta} + \frac{dQw}{d\theta} \\ \frac{dQ_G}{d\theta} = \frac{dH_{sens}}{d\theta} - V \cdot \frac{dp}{d\theta} + \frac{dQw}{d\theta} \\ \frac{dQ_{G_i}^{\ k}}{d\theta} = \frac{(H_{sens_i}^{\ k} - H_{sens_{i-1}})}{\Delta\theta} - V_i \cdot \left(\frac{dp}{d\theta}\right)_i + \left(\frac{dQw}{d\theta}\right)_i^k\end{gathered} \tag{3.29}$$

In the previous equation $\frac{dQ_G}{d\theta}$ *[J/°]* is the gross (or apparent) *HRR* (*GHRR*) which is acquired from the sum of *NHRR* and head exchange with cylinder wall denoted as $\frac{dQw}{d\theta}$ *[J/°]*. The $\frac{dQw}{d\theta}$ is calculated using the Annand model [139] as described in section 3.4.7. H_{sens} is the sensible enthalpy of the cylinder charge, which is derived when the reference enthalpy $H°$ is subtracted from the total enthalpy *H* as described in Eq. (3.30):

$$H_{sens_i}^{\ k}\left(x_i^k, T_i^k\right) = H_i^k - H°_i^k = H_i^k\left(x_i^k, T_i^k\right) - H_i^k\left(x_i^k, T_{ref}\right) \tag{3.30}$$

where subscript *k* denotes the current iteration for the calculation of H_{sens} at the examined *CA* step *i*. The total enthalpy is calculated from Eq. (3.27). At this point, it is noted that the charge molecular composition (*x*) is determined from combustion chemistry and it varies between iterations due to its dependence of the fuel mass amount (m_f *[kg]*) burnt at each *CA* step. This fuel amount is directly calculated from the *GHRR* as described in Eq. (3.31):

$$m_{f_i}^{\ k} = \frac{dQ_{G_i}^{\ k}}{d\theta} \cdot \Delta\theta \cdot \frac{1}{LHV} \tag{3.31}$$

The combustion of the respective fuel amount at the current *CA* step (*i*), which is described by detail in section 3.4.5, results in a variation of the number of moles *[kmol]* (n_{ch}) and composition (x_j) of the charge at the current *CA* step and iteration. Using the newly calculated n_{ch} and x_j, a new value for the temperature T_i^k is calculated using Eq. (3.26). From this temperature and composition, a new value of $H_{sens_i}^{\ k}\left(x_i^k, T_i^k\right)$ is calculated for the current *CA* step. This procedure continues until convergence.

At the next section the flow chart of the *HRR* model is presented.

3.4.3 Heat Release Rate Model Flow Chart

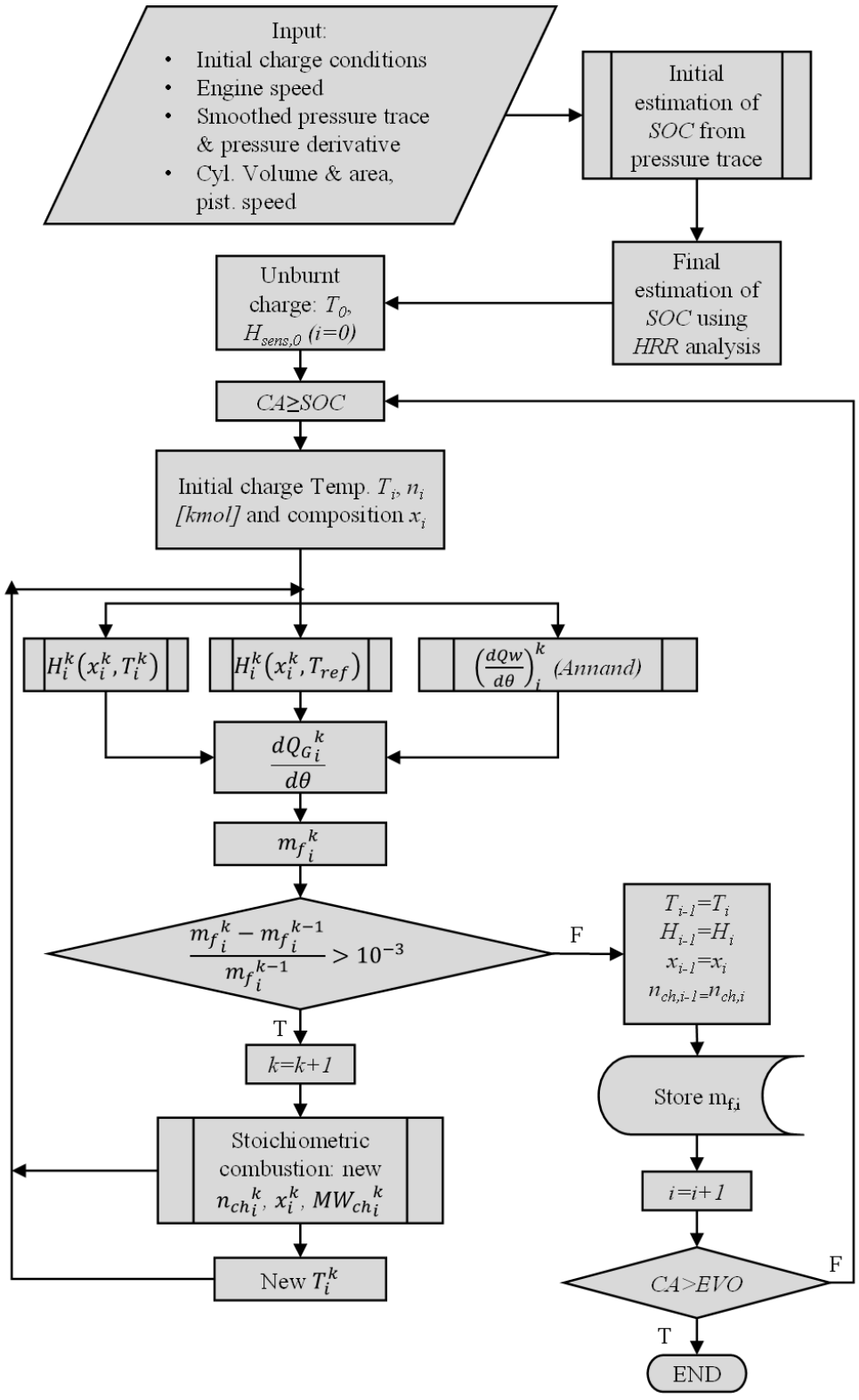

3.4.4 Initial Calculation of Start of Combustion (SOC)

As already mentioned in section 3.4.2, the *HRR* initiates when combustion commences, namely when the injected fuel begins to release its chemical energy. However, due to the pressure measurement noise, the direct estimation of *SOC* from *HRR*, may lead to improper conclusions because in the *HRR* calculations the noise is magnified (due to the use of the pressure derivative, see also section 3.2.3) and can result in positive *HRR* values earlier than the actual *SOC*, especially for cases with retarded fuel injection timing. For this reason, a first estimation of *SOC* is attained directly from the measured pressure trace as described at next.

Considering various studies reported in the literature i.e. [217,218,219] and from the observation of a great number of measured pressure traces (from various types of engines and engine settings (e.g. *SOI* variation)) and their respective derivatives, it was deduced that, after the determination of the appropriate pressure–*CA* – search–window described at next, the premises for the *SOC* at an examined *CA* (*i*) are:

- the variation of second order pressure derivative is ascending, namely: $\left(\frac{d^2p}{d\theta^2}\right)_i > \left(\frac{d^2p}{d\theta^2}\right)_{i-1}$ AND
- the variation of pressure derivative becomes maximum or presents an inflection point (the one that happens earlier, the second one is more common), namely: $\left\{\left(\frac{d^2p}{d\theta^2}\right)_i > \left(\frac{d^2p}{d\theta^2}\right)_{i+1}\right\}\ OR\left\{\left(\frac{d^4p}{d\theta^4}\right)_i \cdot \left(\frac{d^4p}{d\theta^4}\right)_{i-1} < 0\right\}$

The first premise stems from the fact that combustion causes continuously increasing pressure derivative variation $\left(\frac{d}{d\theta}\left(\frac{dp}{d\theta}\right)\right)$, namely making it more positive or less negative $\left(\left(\frac{d^2p}{d\theta^2}\right)_i - \left(\frac{d^2p}{d\theta^2}\right)_{i-1} > 0\right)$. If the first premise is on, then, when the pressure derivative variation becomes maximum $\left(\frac{d^2}{d\theta^2}\left(\frac{dp}{d\theta}\right) = 0\right)$ or presents an inflection point $\left(\frac{d^3}{d\theta^3}\left(\frac{dp}{d\theta}\right) = 0\right)$, is a robust indication that the pressure evolution, which is driven from compression phase, is deviated due to combustion commencement. Katrašnik T., who also uses the $\frac{d^4p}{d\theta^4} = 0$ criterion to detect *SOC*, attempts to provide a physical interpretation correlating the pressure derivative and *HRR*, deducing that the *SOC* occurs when the *HRR* curvature is maximized [218].

The implementation of the proposed method for the initial estimation of *SOC* on four different Diesel engine types is depicted in Fig. 3.3. The pressure derivatives $\left(\frac{d^2p}{d\theta^2}\right)$ and $\left(\frac{d^4p}{d\theta^4}\right)$ are calculated using central finite differences as described in Appendix f.

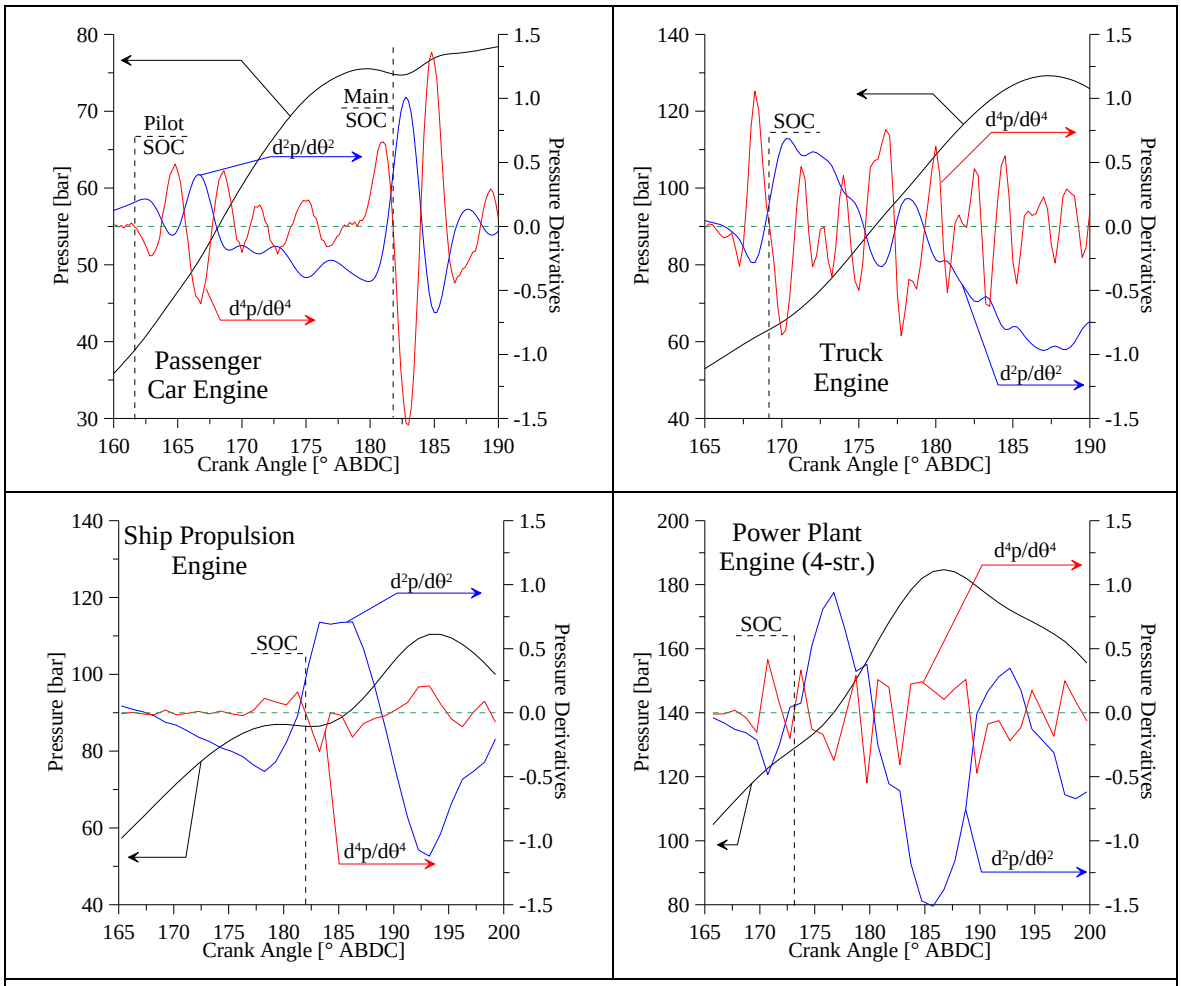

Figure 3.3: Initial estimation of SOC for four operating points of different engine types: upper left: passenger car engine, upper right: truck engine, lower left: 2–str. vessel propulsion engine and lower right: 4–str. constant speed power plant engine.

From the observation of Fig. 3.3, the ability of the proposed methodology for the detection of *SOC* is confirmed. Nevertheless, it is also shown that the aforementioned criteria may be fulfilled at different *CA* events, other than *SOC*, especially at the vicinity on top dead center (*TDC*) and later after the actual *SOC*, mostly due to signal noise. Namely, the proposed methodology provides adequate results if its window of implementation is appropriately determined.

To accomplish this, the following concept is followed for the determination of the *CA* where the calculation should start: The number of stationary points of the pressure trace, namely the local minimums or maximums $\left(\frac{dp}{d\theta}=0\right)$ and inflection points $\left(\frac{d^2p}{d\theta^2}=0\right)$ followed by concave up pressure curve $\left(\frac{d^2p}{d\theta^2}>0\right)$ in a window around *TDC* (e.g. *-10:+30° ATDC*) is obtained, beginning from the left side of *TDC*. If this number is greater than unity (since all the pressure traces have at least one peak – stationary point), is an indication that *SOC* occurs after *TDC*. Therefore the initial *SOC* calculation methodology is implemented

after *TDC*, beginning a step prior the *CA* where the aforementioned number becomes equal to two.

The previous is based on the fact that if the combustion commences after *TDC*, then a local pressure maximum occurs at *TDC* and one at maximum combustion pressure which follows a pressure minimum. This minimum may not occur if combustion commences very late during expansion because peak combustion pressure is not developed. Instead, a negative local minimum of the pressure derivative $\left(\left(\frac{dp}{d\theta}\right)_{min} < 0\right)$ (the pressure derivative is negative because the in–cylinder pressure is descending at the right of *TDC* prior combustion) or an inflection point followed by concave up pressure curve will occur. The last almost always appears in contrast with the first which may not occur, if combustion commences too late during expansion. Finally, if combustion commences too close to *TDC*, initially an inflection point will occur at this point, followed by a concave up pressure curve. The next pressure stationary point (maximum) that will occur, is the one corresponding to the peak combustion pressure.

For the case where the *SOC* occurs before *TDC*, generally, an inflection point of the pressure curve appears $\left(\frac{d^2p}{d\theta^2} = 0\right)$. Specifically a positive local pressure derivative minimum $\left(\left(\frac{dp}{d\theta}\right)_{min} > 0\right)$ occurs prior but close to *TDC*. The last occurs while the pressure derivative, which is positive since pressure always rises at the left of *TDC* $\left(\frac{dp}{d\theta} > 0\right)$ (compression phase), tends to become zero as it approaches *TDC* but suddenly starts to increase due to the combustion event, forming a local pressure derivative minimum $\left(\frac{dp}{d\theta}\right)_{min}$. Thus, the implementation of initial *SOC* estimation methodology should start at this *CA*.

On the other hand, if combustion commences significantly earlier than *TDC* (i.e. *5–10°*) the aforementioned positive local pressure derivative minimum may not occur. In this case the starting *CA* for the *SOC* search–window corresponds to the first *CA* where a change in the slope of pressure derivative is observed, as the *CA* elapses to the right. Particularly, this change corresponds to an inflection point of the pressure curve $\left(\frac{d^2p}{d\theta^2} = 0\right)$ followed by an ascending variation of pressure derivative $\left(\frac{d^2p}{d\theta^2} > 0\right)$, which denotes that the pressure curve is concave up. Apparently, this sudden change of the pressure derivative slope is due to combustion event. This occurs, as already mentioned, while the pressure derivative is positive, since the in–cylinder pressure is always ascending before *TDC*.

According to the starting *CA* calculated above and its position relative to *TDC*, the examined *CA* window is set. In this window, the initial *SOC* estimation methodology is implemented. Specifically, for *SOC* < *TDC* the window is defined from the starting *CA* and *TDC* and for *SOC* ≥ *TDC* from the starting *CA* and the *CA 30°* after *TDC*. The aforementioned pre–process for the determination of the search–window is applied for the determination of main *SOC* and not in the determination procedure of pilot *SOC* (if exists). In this case, the initial *SOC* estimation methodology is implemented several *CA* steps before *TDC*.

Nonetheless, the final value of *SOC* is derived from the *HRR* analysis calculations for the *SOC* determination as described in section 3.4.2. These calculations initiate at the *CA* which corresponds to the initial *SOC* estimation. The aforementioned methodology provides

the ability to the model to accurately and reliably detect *SOC* for a variety of pressure traces (i.e. engine configurations/settings/adjustments) without significant computational time cost.

3.4.5 Single–Zone Combustion Concept

As already mentioned in section 3.4.2 the *HRR* model used in the present study is a single–zone, zero dimensional one, which means that the temperature of the charge is uniform throughout the closed cycle. Furthermore, after combustion commencement, the combustion products, produced from the instantaneous elementary fuel (m_{f_i} *[kg]*) combustion which corresponds to the current *CA* interval, are added to the cylinder charge and are homogenized with the remaining unburnt charge. The combustion of each elementary fuel amount is assumed ideal and stoichiometric (*Φ=1*) as described in Eq. (3.32), neglecting chemical dissociation effects. Here, it is noted that, according to this concept, at the *EOC* the charge composition, i.e. exhaust gas composition, is the one that would has been obtained if the total fuel was burnt with the cylinder global equivalence ratio $\Phi\left(\Phi = \frac{m_f}{m_{tr}} \cdot \left(\frac{m_{tr}}{m_f}\right)_{st}\right)$. The number of moles of O_2 ($\nu_{O_2} \cdot m_{f_i}$) which is required for the stoichiometric oxidation of the fuel at each *CA* step and the number of moles derived from the oxidation reaction, namely the combustion products (CO_2, H_2O, SO_2, N_2), are calculated via the mole balance of the monoatomic species. Thereafter, the number of moles of the cylinder charge (n_{ch}) is determined from the sum of its number of moles at the previous *CA* step and the number of moles of the resulted products at the current *CA* step (*i*), subtracting the O_2 number of moles used for the combustion as described in Eq. (3.33). The mole (*x*) and mass (*y*) fractions of the chemical species comprised in the charge and their molecular weight (MW_{ch}) at the current *CA* step are calculated from Eq. (3.34).

$$C_m H_n S_p O_q N_r + \nu_{O_2} O_2 \rightarrow mCO_2 + \frac{n}{2} H_2O + pSO_2 + \frac{r}{2} N_2$$
$$\nu_{O_2} = \left(m + \frac{n}{4} + p - \frac{q}{2}\right) \tag{3.32}$$

$$n_{ch_i}^{\,k} = n_{\mathrm{ch}_{i-1}} + \left(m + \frac{n}{2} + p + \frac{r}{2} - \nu_{O_2}\right) \cdot m_{f_i}^{\,k} = n_{\mathrm{ch}_{i-1}} + \left(\frac{n}{4} + \frac{r}{2} - \frac{q}{2}\right) \cdot m_{f_i}^{\,k} \tag{3.33}$$

$$x_{j_i}^{\,k} = \frac{n_{j_i}^{\,k}}{n_{ch_i}^{\,k}}$$
$$MW_{ch_i}^{\,k} = \sum_j x_{j_i}^{\,k} \cdot MW_j \tag{3.34}$$
$$y_{j_i}^{\,k} = x_{j_i}^{\,k} \cdot \frac{MW_j}{MW_{ch_i}^{\,k}}$$

In the previous expressions, subscripts *m, n, p, q, r [kmol/kg fuel]* correspond to the *C, H, S, O, N* content of the fuel respectively, derived from the available fuel mass fraction *[kg/kg]*

divided by the molecular weight *MW [kg/kmol]* of the respective species. v_{O2} *[kmol* O_2*/kg fuel]* is the oxygen stoichiometric coefficient determined from the fuel composition (see Eq. (3.32)). Subscript *j* denotes the species sequence number, *ch* the cylinder charge, *i* the current *CA* step and superscript *k* is the sequence number of the current iteration loop for the elementary fuel mass (m_{f_i}) calculation (see Eq. (3.31) in section 3.4.2).

3.4.6 End of Combustion Estimation

The *CA* where the combustion ceases i.e. the end of combustion (*EOC*) is a significant parameter because it has an effect on the results of both, *HRR* and *NO* models. However, its detection is a difficult issue due to the high signal noise, which appears on pressure trace and hence *HRR*, late in expansion phase where combustion ends.

The estimated value of *EOC* and injected fuel mass, which is an input, are determinant factors for the *GHRR* calculation because they affect the calculation of combustion duration and coefficient α used for the calculation the heat transfer through the cylinder wall as described in section 3.4.7.

The combustion duration and *CA* step determine the number of combustion zones formed and considered. Hence, an early *EOC* estimation results in less zones and hence less *NO* is formed. On the contrary, overestimation of combustion duration, e.g. due to signal noise, results in interpretation of this noise as combustion overestimating the number of combustion zones and hence *NO* formation.

Moreover, underestimation or overestimation of the combustion duration induces greater or smaller values for coefficient α respectively. This coefficient corresponds proportionally to the amount of heat exchange through cylinder wall. It is noted that this coefficient, which is derived from *HRR* analysis, is also used in the calculation of zone temperature in the *NO* model. The heat losses through cylinder wall affect the final temperature of each zone and thus *NO* formation. Namely, overestimation of coefficient α causes underestimation of temperature and hence *NO* and underestimation of coefficient α causes overestimation temperature and hence *NO* formation.

For the reasons mentioned previously, the *EOC* should be approached with the maximum possible accuracy. To manage this, the net *HRR* (*NHRR [J/°]*) is utilized. *EOC* is located at the *CA* where the *NHRR* is reduced significantly and becomes parallel to the horizontal axis. The proposed methodology initiates at the *CA* where the *85%* of the maximum cumulative net *HR* (*CNHR*) value has been occurred. From this point on, the *NHRR* value at the current *CA* step is further smoothed using the moving average method as shown in the following Eq. (3.35):

$$NHRR_{s_i} = \frac{1}{2 \cdot W_s + 1} \sum_{l=-W_s}^{l=W_s} NHRR_{i+l} \tag{3.35}$$

where W_s is the number of neighbor points at the left and right of the examined point *i*, ($2W_s+1$) is the smoothing window and subscript *s* denotes the smoothed values. When the

NHRR value of the examined point ($NHRR_{s_i}$) becomes less than a threshold, which is defined as a percentage (i.e. *3%*) of the maximum *NHRR*, then the smoothing procedure continues for a specific number of *CA* steps. Then, the average ($NHRR_{s_{aver}}$ *[J/°]*) of these smoothed *NHRR* values (i.e. $NHRR_s$), including the examined one (*i*) (i.e. the first point), is calculated as described in Eq. (3.36):

$$NHRR_{s_{aver}} = \frac{1}{W_{aver}} \sum_{l=i}^{l=i+W_{aver}-1} NHRR_{s_l} \tag{3.36}$$

where W_{aver} is the smoothing window. When this average becomes less than the *NHRR* threshold defined above, then the fluctuation (standard deviation based on sample) of the $NHRR_s$ values (see Eq. (3.35)), comprised in the average window (W_{aver}), around their average value ($NHRR_{s_{aver}}$), is calculated from Eq. (3.37):

$$STDV_s = \sqrt{\frac{\sum_{l=i}^{l=i+W_{aver}-1}\left(NHRR_{s_l} - NHRR_{s_{aver}}\right)^2}{W_{aver}-1}} \tag{3.37}$$

When this fluctuation becomes less than *50%* of the average value, namely $STDV_s < 0.5 \cdot NHRR_{s_{aver}}$, it is considered that the examined point (*i*) corresponds to *EOC*.

3.4.7 Heat Exchange through the Cylinder Wall – Annand Model Description

In the present work, the Annand model [8,9,139,140] was used for the calculation of heat exchange between the in–cylinder charge and cylinder wall. This model was chosen because it is widely used in the field due to the adequate results that provides but its most important advantage is the simplicity of its implementation, and the lower calibration effort and input parameters that requires when compared to other models [220] i.e. Woschni model [162].

The Annand formula used for the calculation of heat exchange to the cylinder wall $\frac{dQw}{d\theta}$ *[J/°]* at each *CA* step (*i*), which is then used to Eq. (3.29), is described from Eq. (3.38):

$$\left(\frac{dQw}{d\theta}\right)_i = \frac{A_{cyl_i}}{6 \cdot N} \cdot \left[a \cdot \frac{k_i}{D} \cdot {Re_i}^b \cdot (T_i - T_w) + c \cdot \sigma \cdot \left({T_i}^4 - T_w^4\right)\right]$$
$$Re = \frac{Sp_i \cdot D. \rho_i}{\mu_i} \tag{3.38}$$

where A_{cyl} *[m²]* is the cylinder area at the current *CA* step (*i*), *N [rpm]* is the engine speed, *D [m]* is the cylinder diameter, *Re* is the Reynolds number, *T [K]* and T_w *[K]* are the charge/zone and wall temperatures respectively and σ is the Stefan Boltzmann constant for radiation heat exchange (σ*=5.6704·10⁻⁸ [W/m² K⁴]*). Thermal conductivity (*k [W/m/K]*) and dynamic viscosity (μ *[Pa s]*) of each species (*j*) comprised in the mixture, are calculated

from NASA polynomial approximations [221] which are functions of temperature (see Appendix e). In addition, the *k* and μ of the mixture are calculated via Eq. (3.39) and Eq. (3.40) respectively which have been derived from Refs. [222,223]:

$$k_i = \frac{\sum_j x_{j,i} \cdot k_{j,i} \cdot MW_j^{1/3}}{\sum_j x_{j,i} \cdot MW_j^{1/3}} \tag{3.39}$$

$$\mu_i = \frac{\sum_j x_{j,i} \cdot \mu_{j,i} \cdot MW_j^{1/2}}{\sum_j x_{j,i} \cdot MW_j^{1/2}} \tag{3.40}$$

In the previous expression, *x* is the mole fraction of the species denoted with subscript *j*. For the Reynolds (*Re*) number calculation, the mean piston speed *Sp [m/s]* was used as proposed in Ref. [9]. Mixture density ρ *[kg/m^3]* was calculated as the quotient of the charge/zone mass and cylinder/zone volume at the current *CA* step (*i*). The parameters *A, k,* μ*, Sp,* ρ*, T, Re* vary with *CA*. The mean wall temperature is assumed constant at *450 K* during the entire closed cycle since it does not fluctuate more than *5 – 10 [K]* [8,224,101,225], while α*, b* and *c* are calibration constants. The values of *b* and *c* were kept constant using statistical values reported in the literature [8,9,225,146,143,226]: i.e. ***b=0.75*** for the entire closed cycle, ***c=0*** and ***c=0.576*** before and after *SOC*.

Finally, coefficient $\boldsymbol{\alpha}$ is calculated using a modified false position, root finding method (*regula falsi*) [227], which is described by detail in Appendix g, in order to satisfy the constraint described in Eq. (3.41), assuming that the total amount of injected fuel is completely burnt.

$$\begin{aligned} m_{f\,cyl} &= \frac{1}{LHV} \cdot \sum_{i=SOC}^{EOC} \left(\frac{dQ_N}{d\theta} + \frac{dQw}{d\theta} \right)_i \cdot \Delta\theta \\ m_{f\,cyl} &= \frac{1}{LHV} \cdot \sum_{i=SOC}^{EOC} \left(\frac{dQ_G}{d\theta} \right)_i \cdot \Delta\theta \end{aligned} \tag{3.41}$$

In the previous expression, *LHV [J/kg]* is the lower heating value of the fuel. The sum term represents the cumulative gross *HR* (*CGHR*) which is calculated from Eq. (3.29) and is composed from the cumulative net *HR* (*CNHR*) and the heat exchange through the cylinder wall. *EOC* corresponds to the *CA* that combustion ends which has been determined with the method described in section 3.4.6. Finally, m_f *[kg/cycle]* is the known amount of

fuel injected per engine cycle in the examined cylinder. This procedure is schematically presented in Fig. 3.4:

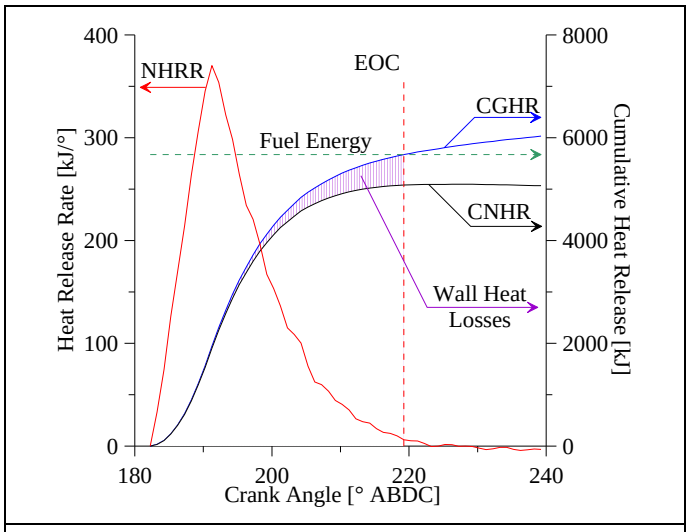

Figure 3.4: Determination of "α" coefficient from HR analysis and the known injected fuel amount.

The total engine fuel flow rate is distributed to the cylinders proportionally to their respective *CNHR* at *EOC*, according to the approach described in section 3.3.2. Thus, if pressure measurements are available for all cylinders, a different α coefficient is calculated for each cylinder. Otherwise, the coefficient α corresponds to the available "average" (representative) cylinder. As already mentioned in section 3.4.6, the calculated coefficient α, from the *HR* analysis, along with the default coefficients *b* and *c* are also utilized in the *NO* model in the zone temperature calculation. Apparently, regarding the unburnt zone, coefficient *c*, which corresponds to the radiation heat transfer, is always zero throughout the entire engine cycle.

It is also noted that due to the *HRR* noise (derived from pressure signal) and/or inaccurate fuel flow rate input data, coefficient α may be miscalculated. This has an effect on zone temperature calculation and hence *NO* formation. Regarding tail–pipe *NO* emissions predictions, the aforementioned effect is noticeable when the *NO* absolute values and the slop of the *NO* trend are considerably low. Even negative values of α can arise. To prevent the latest abnormality, when its value drops below a threshold (i.e. *0.01*) then the threshold value is imposed to α.

Nevertheless, the investigation has revealed that the approach followed for the heat exchange between the zone and cylinder wall (i.e. the use of α coefficient which has been derived from the *HRR* analysis) slightly improves the *NO* trend for most of the cases examined, when compared to the use of a constant α coefficient.

Here it is also mentioned that the average α coefficient for the large–scale engines examined is *0.32* and for the automotive engine examined is *0.26*. These values are similar to the ones reported in the relevant literature [8,9,225,146,143,226].

3.5 Description of the Proposed Nitric Oxide Model

3.5.1 Presentation of the Model's Concept

The proposed model is a simplified zero–dimensional, physical–based, semi–empirical, pseudo–multi–zone one which aims to predict Diesel engine NO_x emissions. To accomplish this, it makes use of the in–cylinder measured pressure trace, basic cylinder geometry and operating parameters (i.e. speed, fuel and exhaust flow, etc.).

Initially, the measured pressure trace is processed as described in section 3.2. Thereafter, the initial conditions of the in–cylinder charge at initiation of combustion are calculated accounting for the in–cylinder residual gas (*RG*), *EGR* rate, intake air mass flow rate and engine speed as described in section 3.3. Then, a *HRR* analysis is conducted using the measured pressure trace of each cylinder or the corresponding one of the "average" (representative) cylinder, from which the fuel burn rate, *SOC*, *EOC*, etc. are derived as described comprehensively in section 3.4. Then, the *NO* model is implemented from *SOC* until exhaust valve opening (*EVO*).

The concept of the model is depicted in Fig. 3.5. The solid stars represent the combustion zone generation. The first zone is generated at the *SOC*. Each zone is determined from the elementary fuel mass burnt at the corresponding *CA* step as defined from the combustion rate shown in Fig. 3.6 (derived from *HRR*, see section 3.4.2) and from the requisite amount of unburnt charge mass. This mass is determined using an empirical correlation which provides the zone equivalence ratio (Φ_z) and is described by detailed in section 3.5.8. After its generation, the zone continues being expanded or compressed (depends on the current in–cylinder pressure derivative) inside the engine cylinder, in parallel with the generation or evolution of the other existing zones until *EVO*, having its own history of chemical composition, temperature and volume, as shown in Fig. 3.7, 3.8 and 3.9 respectively. The individual zones are considered internally homogeneous. Zone temperature is calculated using the first thermodynamic law accounting for the heat exchange between the zone and cylinder wall. Each zone contributes to *NO* formation, after its generation and until the end of the closed engine cycle. The *NO* inside each zone is calculated kinetically via the extended Zeldovich mechanism [29,30]. Moreover, a chemical dissociation scheme [228] is implemented (described in section 3.5.6), which provides the equilibrium composition. The equilibrium composition is required for the *NO* formation mechanism. Chemical dissociation results in zone temperature decrease. An indicative image of the chemical composition history in a specific zone is depicted in Fig. 3.10. The pressure of all zones is assumed uniform at every *CA* and equal to the respective measured one. After the end of combustion (*EOC*), zone generation ceases but the existing zones continue to evolve up to *EVO*. The expanding/compressing zones are depicted in Fig. 3.5 as empty squares. Through this approach, the *NO* history of each zone is obtained (i.e. *NO* vs. *CA*) as shown in Fig. 3.11. The sum of the *NO* amounts formed inside the existing zones at each *CA* step, provides the in–cylinder *NO* history as shown in Fig. 3.12. Therefore, the sum of *NO* amounts inside each zone at *EVO*,

provides the *NO* contribution of the examined cylinder in the engine's tail–pipe *NO* emissions.

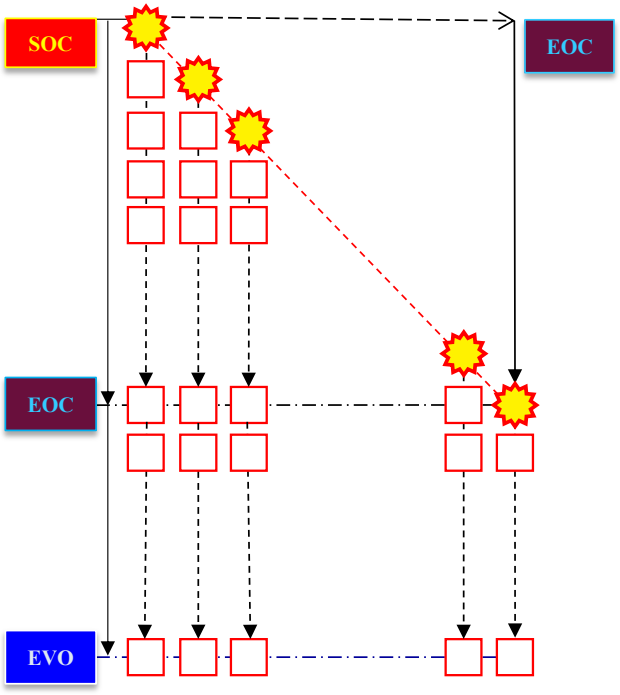

Figure 3.5: The concept of the proposed NO model – Zone generation and evolution.

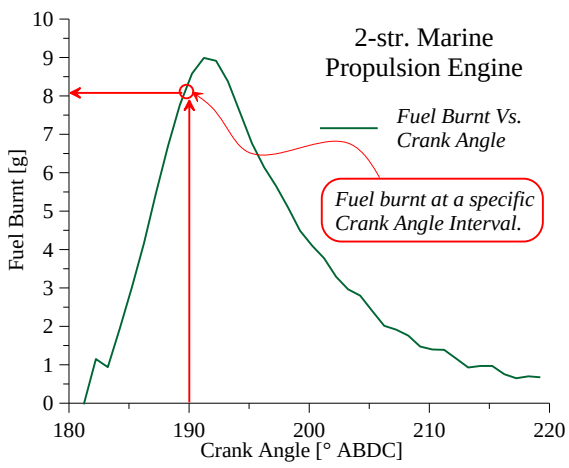

Figure 3.6: Calculation of the fuel burnt at a specific crank angle interval of the examined cylinder.

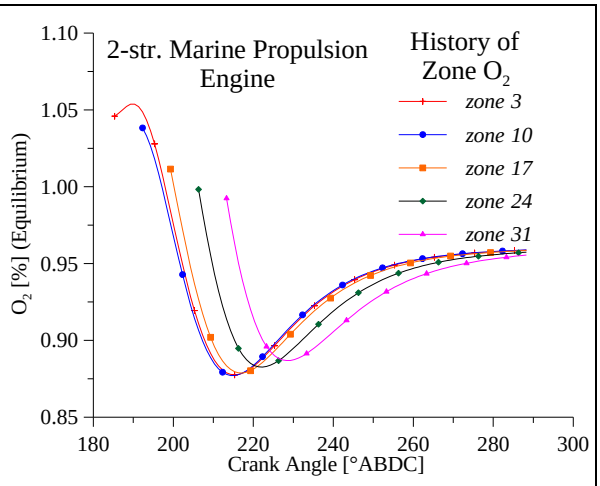

Figure 3.7: Zone oxygen (O_2) history during the period from the zone generation up to EVO.

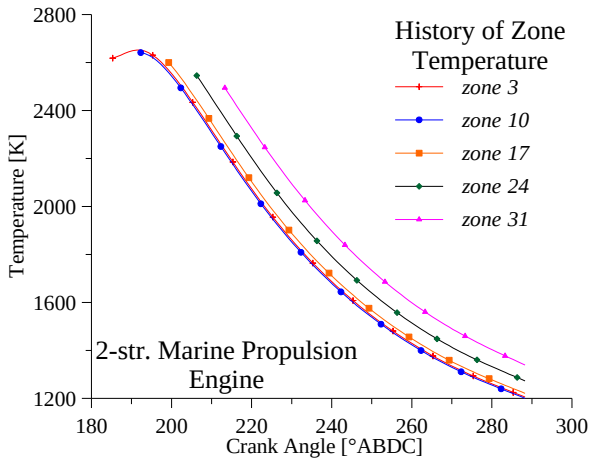

Figure 3.8: Zone temperature history during the period from the zone generation up to EVO.

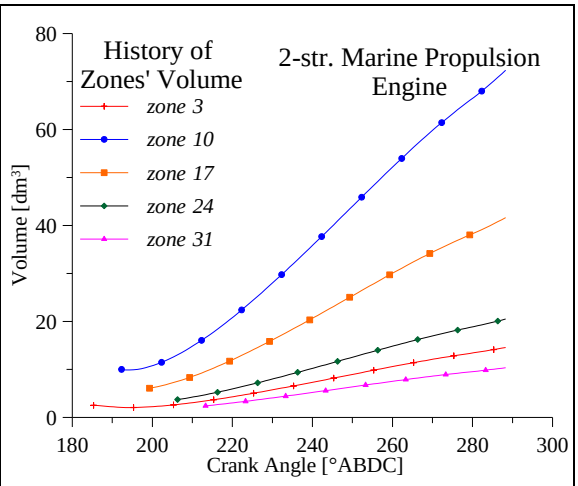

Figure 3.9: Zone volume history during the period from the zone generation up to EVO.

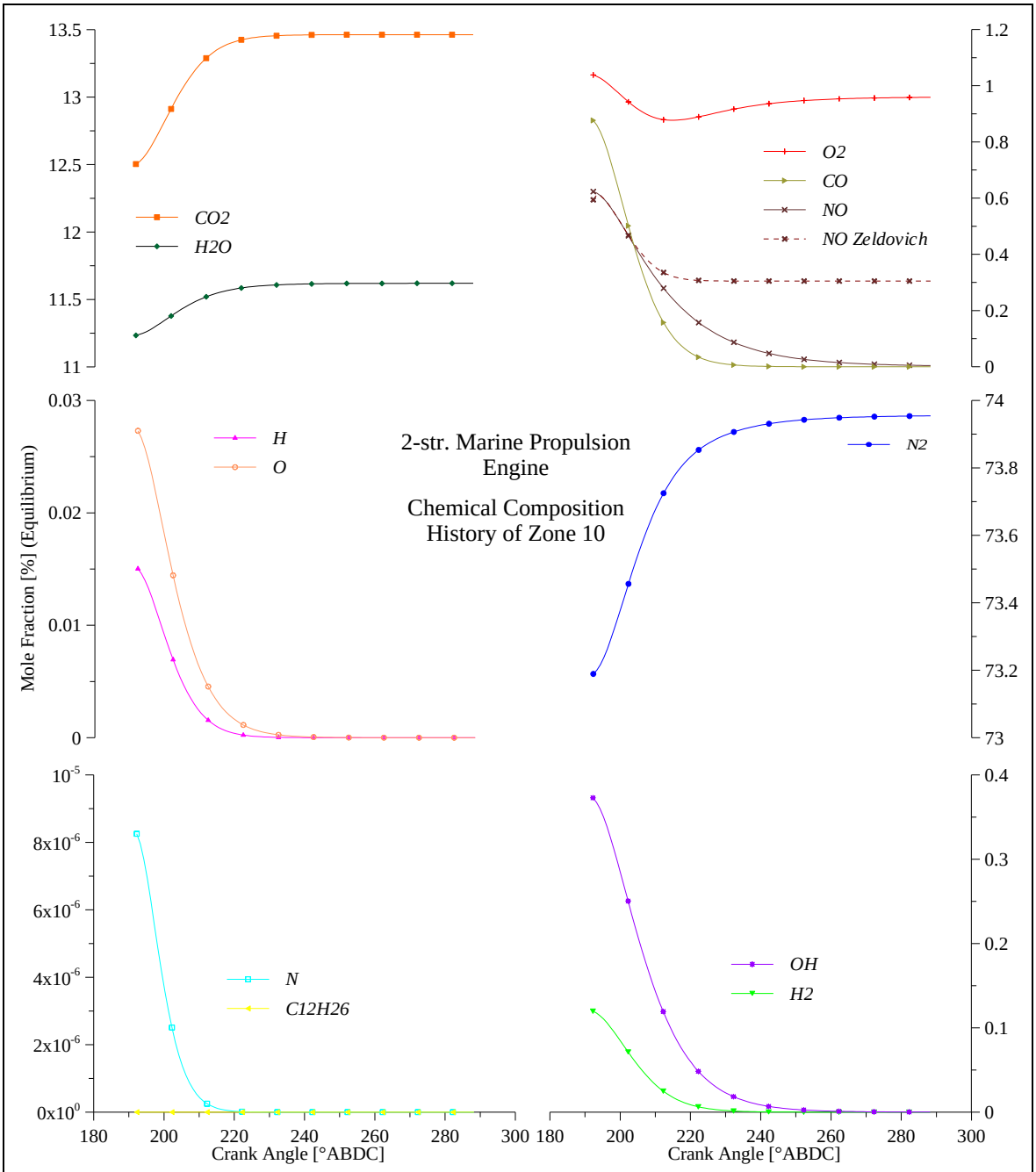

Figure 3.10: Chemical composition history of a specific zone from the time of its generation up to EVO.

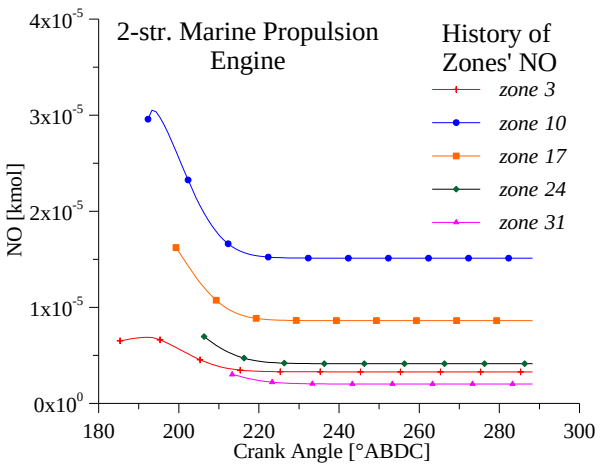

Figure 3.11: NO history inside the zones during the period from their generation up to EVO.

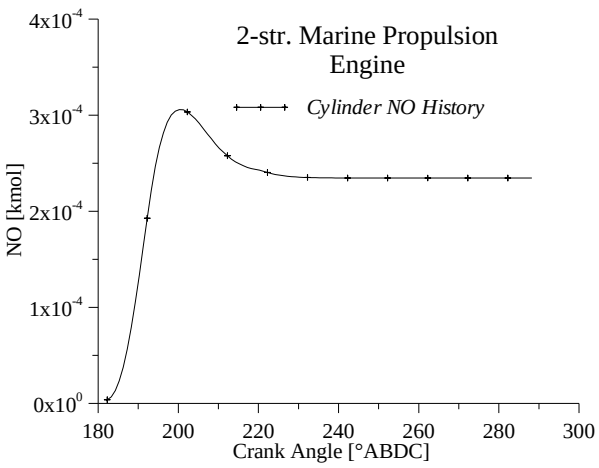

Figure 3.12: Overall in–cylinder NO history as crank angle elapses.

In the following sections, the mathematical treatment of the processes taking place inside the unburnt zone and combustion zones is comprehensively presented.

3.5.2 Unburnt Zone Evolution inside the Combustion Chamber

The unburnt zone is the source from which the generating combustion zones obtain the requisite amount of unburnt charge, for the combustion of the attributed fuel amount to each zone. As already mentioned in section 3.4.2 (see Eq. (3.31)) and schematically described in Fig. 3.6 of section 3.5.1, this fuel amount is calculated via *HRR* analysis. Nevertheless, the unburnt charge does not consist only of ambient air but also residual or recirculated exhaust gases. Hence, its chemical composition has to be calculated. Moreover, the temperature of the unburnt zone, at each *CA* step, is a requisite for the calculation of the combustion temperature for the generating zone, since it constitutes the temperature of reactants. The considerations about the calculation of unburnt zone composition and temperature are analyzed at next.

As in *HRR* model (section 3.4.2), the mass and composition of the trapped charge (unburnt zone) in the combustion chamber are assumed to remain unchanged during the period of compression initiation (*2–str.*: *EVC*, *4–str.*: *IVC*) until the moment just before *SOC* (i.e. *SOC-1*), neglecting blow–by mass loss and considering complete mixing of the fresh air with residual or recirculated gases, which is close to reality. The calculations for the initial conditions are described by detail in section 3.3. Moreover, the chemical composition of the unburnt zone is assumed constant for the entire closed cycle since mixing and heat exchange with the combustion zones is not considered for. Furthermore, charge composition remains constant since chemical dissociation does not take place inside the unburnt zone due to its low temperature. When combustion commences, at each *CA* interval, a part of the unburnt zone mass (or mole amount) participates in combustion (denoted later in Eq. (3.43) as n_{out}). Its magnitude depends on the corresponding fuel amount burnt at the examined *CA* interval, which has been determined from *HRR*, and the zone equivalence ratio (Φ_z), which is calculated using an empirical correlation as described in section 3.5.8. The pressure of unburnt zone is equal to the prevailing in–cylinder pressure at the current *CA*. The unburnt zone

volume ($V\ [m^3]$) is determined as the difference of the total cylinder volume (Eq. (3.7)) and the sum of the volumes of the existing combustion zones as described in Eq. (3.42):

$$V_{ub_i} = V_{cyl_i} - \sum_{z=1}^{i-SOC+1} V_{b_z} \tag{3.42}$$

where subscript *i* denotes the *CA* step, *ub* the unburnt zone, *b* the burning zones, *cyl* the cylinder, *z* the zone sequence number and *SOC* is the *CA* step that combustion commences.

The temperature of the unburnt zone, which is used as reactants' temperature in the calculations of combustion zone generation, is calculated at each *CA* step (*i*) via the first thermodynamic law, using an iterative procedure (superscript *k* denotes the iteration sequence number) until the unburnt zone enthalpy converges, using Eqs. (3.43) and (3.45):

$$h_i^k = \frac{n_{i-1} \cdot h_{i-1} + dp_i \cdot \frac{\left(V_{ub_{i-1}} + V_{ub_i}\right)}{2} - n_{out} \cdot \frac{\left(h_{i-1} + h_i^{k-1}\right)}{2} - dQw_i^k}{n_i} \tag{3.43}$$

$$n_i = n_{i-1} - n_{out}$$

In the previous expression, $h\ [J/kmol]$ is the enthalpy of the unburnt zone, which is calculated via Eq. (3.44) using its chemical composition (*x*) and the enthalpies of the comprised species, denoted with subscript *j*, which are calculated via NASA polynomials [180] (see Appendix d) using the unburnt zone temperature. The number of moles ($n\ [kmol]$) comprised in the unburnt zone volume (V_{ub_i}) is determined from the difference between the number of moles of the previous *CA* step (*ι-1*) and the mole amount transferred (n_{out}) from the unburnt zone to the newly generated combustion zone at the current *CA* step (*ι*). The initial value of *n* (n_0) is derived from the trapped mass and its composition $\left(n_0 = \frac{m_{tr}}{MW_{ch}}\right)$, which have been calculated as described in section 3.3.

$$h_i^k = \sum\nolimits_j x_{j_i} \cdot h_{j_i}\left(T_{ub_i}^{\ k}\right) \tag{3.44}$$

Furthermore, $dQw\ [J]$ $\left(dQw = \frac{dQw}{d\theta} \cdot \Delta\theta\right)$ corresponds to the heat exchange with the cylinder walls, which is calculated using the Annand model described by detail in section 3.4.7. However, in order to approach the zone–cylinder interface with greater physical consistency, the following modification to the Annand formula has been established: the current cylinder area $Acyl_i\ [m^2]$ is multiplied with $\frac{V_{ub_i}^{\ k}}{Vcyl_i}$ [109] to fairly represent the equivalent interface area.

The unburnt zone temperature T_{ub} is calculated via a Newton–Raphson iterative methodology [229] as described in Eq. (3.45):

$$T_{ub_i}^{\ k} = T_{ub_i}^{\ k-1} - \frac{h_i^k - h_i^{k-1}}{cp_i^{k-1}} \tag{3.45}$$

where *cp [J/kmol/K]* is the specific heat capacity at constant pressure $\left(cp = \left(\frac{dh}{dT}\right)_p\right)$ of the unburnt zone, which is calculated from Eq. (3.46) using the unburnt zone composition (*x*) and the *cp* of the comprised species, denoted with subscript *j*. The *cp* of each species is calculated via NASA polynomials [180] (see Appendix d) using the unburnt zone temperature.

$$cp_i^{k-1} = \sum_j x_{j_i} \cdot cp_{j_i}\left(T_i^{k-1}\right) \tag{3.46}$$

The initial value of the unburnt zone temperature ($T_{ub,0}$ *[K]*), namely at the *CA* step just before *SOC* (i.e. *SOC-1*, *i=SOC* in Eq. (3.43)), is calculated using the cylinder volume (V_0 *[m^3]*) and pressure (p_0 *[Pa]*) at this point, the in–cylinder trapped mass (m_{tr} *[kg]*) and its molecular weight (MW_{ch} *[kg/kmol]*) (initial conditions) as calculated in section 3.3, via the equation of state as described in Eq. (3.47):

$$T_{ub_0} = \frac{p_0 \cdot V_{cyl_0}}{m_{tr} \cdot \frac{\bar{R}}{MW_{ch}}} \tag{3.47}$$

3.5.3 Combustion Zone Generation

According to the literature [14,8,9,143,30,31] the accurate prediction of NO_x emissions depends strongly on the realistic estimation of the local conditions (i.e. temperature, species concentration) inside the combustion chamber. However, these conditions are mainly controlled from the air–fuel mixing and combustion mechanism. Based on this consideration, the combustion procedure, is divided into zones to fairly represent the actual temperature and composition distribution inside the combustion chamber.

Each combustion zone (denoted by subscript *z*) is formed from the fuel amount burnt at the respective *CA* step (denoted by subscript *i*), as determined from the *HRR* analysis described in section 3.4.2 and shown in Figs. 3.5 and 3.6, and the corresponding unburnt zone charge amount. The generated zone forms an independent, closed thermodynamic system inside which the amount of the attributed fuel burns instantaneously within the specific *CA* step. There is no interaction between the individual zones which have their own temperature, volume, composition and *NO* history. Thus, the total zone mass (fuel + unburnt charge) remains constant throughout the cycle. Moreover, the pressure of the existing zones is constant and equal to the measured one at the current *CA* step.

The temperature of the combustion zone – combustion products temperature (*Tp [K]*) – is calculated via the first thermodynamic law using an iterative procedure (superscript *k* denotes the iteration number) which includes a Newton–Raphson methodology [229] as described in Eq. (3.48). The procedure ceases when *Tp* converges.

$$Tp_{z_i}^{\ k} = Tp_{z_i}^{\ k-1} - \frac{hp_{z_i}^{\ k-1} - hr_{z_i} + dqw_{z_i}^{\ k-1} - V_{z_i}^{\ k-1} \cdot dp_i/m_z}{cp_{z_i}^{\ k-1}} \tag{3.48}$$

In the previous expression, the specific heat capacity at constant pressure (*cp [J/kg/K]*) is assumed to represent the derivative (*f'(T)*) of the function (*f(T)*) to be zero (*f(T)*≡numerator of the second term at the right hand side of Eq. (3.48)), since zone reactants' enthalpy (*hr [J/kg]*) is known and the last two terms are less important compared to zone products' enthalpy (*hp [J/kg]*). Thus $f'(T) = \frac{df(T)}{dT} \cong \frac{dhp}{dT} = cp$.

Zone chemical composition before and after combustion, which is used in combination with unburnt zone temperature – reactants temperature (T_i) – and combustion temperature (*Tp*) for the calculation of zone reactants' and products' enthalpy respectively, is derived from the chemical reaction (combustion) between the fuel and requisite unburnt charge, as described in section 3.5.5. In addition, regarding zone composition after combustion, chemical dissociation of the ideal combustion products, which are: O_2 or $C_{12}H_{26}$ (fuel), N_2, CO_2 and H_2O, is accounted for. The chemical dissociation process, which is a function of pressure, temperature and ideal combustion products' mole fraction, provides the final, equilibrium composition of the combustion products as described in section 3.5.6.

Zone enthalpy before combustion, namely reactants enthalpy (*hr*), is the one determined for the unburnt zone at the current *CA* step, which is calculated using the method described in section 3.5.2., however divided by the unburnt charge molecular weight to convert it in *[J/kg]* units. The zone enthalpy after combustion (*hp [J/kg]*) is calculated from Eq. (3.49) using the final equilibrium composition of the zone and the enthalpies of the comprised combustion products (h_j *[J/kmol]*). These enthalpies are calculated via the NASA polynomials [180] (see Appendix d) using the combustion zone temperature *Tp*.

$$hp_{z_i}^{k-1} = \sum_j \frac{x_{j,z_i}}{MW_j} \cdot h_{j_i}\left(Tp_{z_i}^{k-1}\right) \tag{3.49}$$

Similarly, the specific heat capacity at constant pressure (*cp [J/kg/K]*) of the zone is calculated from Eq. (3.50) using the zone final equilibrium composition and the specific heats of the comprised combustion products (cp_j *[J/kmol/K]*), which are calculated via the NASA polynomials [180] (see Appendix d) using the combustion zone temperature *Tp*.

$$cp_{z_i}^{k-1} = \sum_j \frac{x_{j,z_i}}{MW_j} \cdot cp_{j_i}\left(Tp_{z_i}^{k-1}\right) \tag{3.50}$$

For the initiation of the iteration method (*k=1*) described above (Eq. (3.48) – (3.50)), the initial value of the combustion temperature (*Tp*) is set arbitrary to *2200 [K]* (selected relatively close to the expected values of adiabatic flame temperature for faster convergence).

The enthalpies, *hr* and *hp* are converted into *[J/kg]* using the molecular weight of the reactants' and products' mixture respectively, because in the first thermodynamic law (see Eq. (3.48)) calculations, the total enthalpies $\left(H\,[J] = m[kg] \cdot h[\frac{J}{kg}]\right)$ have to be used. However, due to the assumption that the mass of each zone is constant throughout the closed cycle, regarding Eq. (3.48), the mass term is finally eliminated. Zone mass (*m [kg]*) is calculated as the sum of fuel burnt at the examined *CA* and the entrained unburnt charge at the

time of its generation. Zone volume is calculated using the state equation for ideal gas as described in Eq. (3.51):

$$V_{z_i}^{k-1}[m^3] = \frac{m_z \cdot \bar{R} \cdot Tp_i^{k-1}}{p_i \cdot MW_{z_i}^{k-1}} \tag{3.51}$$

Moreover, referring to Eq. (3.51) and Eq. (3.48), *p [Pa]* is the measured cylinder pressure, *dp [Pa]* is the pressure differential $\left(\frac{dp}{d\theta} \cdot \Delta\theta\right)$ and *dqw [J/kg]* is the wall heat exchange differential $\left(\frac{\frac{dQw}{m_z}}{d\theta} \cdot \Delta\theta\right)$ calculated with Annand model which have been described in section 3.4.7. For the Annand model used, the same rationale with the unburnt zone was adopted (section 3.5.2), namely, the cylinder area $Acyl_i$ is multiplied with $\frac{V_{z_i}^{k-1}}{Vcyl_i}$ [109] to fairly represent the equivalent interface area between the zone and the wall. As with unburnt zone, the coefficient α used in Annand formula is the one estimated from the *HRR* analysis. The remaining coefficients (*b*, *c*) are kept constant as declared in section 3.4.7.

3.5.4 Combustion Zone Evolution inside the Combustion Chamber

After its generation, the zone continues to expand or compress (depending on the current in–cylinder pressure derivative) inside the combustion chamber up to *EVO*. At each *CA* step, the values of volume (*V [m³]*), chemical composition (*x*), number of moles (*n [kmol]*), molecular weight (*MW [kg/kmol]*), enthalpy (*h [J/kmol]*) and temperature (*T [K]*) of the examined zone are calculated from an iterative procedure using a concept similar to the one used for the unburnt zone (section 3.5.2), however herein the chemical dissociation is accounted for, since the zone temperature is significantly increased for noticeable time after *SOC*. The zone enthalpy is calculated from Eq. (3.52) and its temperature via the Newton–Raphson [229] iterative method as described in Eq. (3.53):

$$h_{z_i}^{k} = \frac{n_{z_{i-1}} \cdot h_{z_{i-1}} + dp_i \cdot \frac{\left(V_{z_{i-1}} + V_{z_i}^{k}\right)}{2} - dQw_{z_i}^{k}}{n_{z_i}^{k}}$$

$$V_{z_i}^{k} = \frac{m_z \cdot \bar{R} \cdot Tp_i^{k}}{p_i \cdot MW_{z_i}^{k}} \tag{3.52}$$

$$n_{z_i}^{k} = \frac{m_z}{MW_{z,i}^{j}}$$

$$MW_{z,i}^{j} = \sum\nolimits_j x_{z,j_i}^{k} \cdot MW_j$$

$$T_{z_i}^{k} = T_{z_i}^{k-1} - \frac{h_{z_i}^{k} - h_{z_i}^{k-1}}{cp_{z_i}^{k-1}} \tag{3.53}$$

where superscript *k* denotes the iteration sequence number, *z* the zone sequence number and *i* the current *CA* step. The specific heat capacity at constant pressure is denoted with *cp*

[J/kmol/K] and it corresponds to the enthalpy derivative $\left(\left(\frac{dh}{dT}\right)_p\right)$. Zone volume ($V\ [m^3]$) is calculated from equation of state as shown in Eq. (3.52). The initial values for the iteration procedure are derived from the final values of the previous *CA* step (*i-1*) for each existing zone. Moreover, the wall heat exchange term $\left(\frac{dQw}{d\theta}\cdot\Delta\theta\right)$ is calculated as in the case of combustion zone generation, which has been already described in section 3.5.3. The iteration procedure ceases when the zone temperature (*T*) converges.

3.5.5 Calculation of Zone Composition before and after Combustion

The calculation of the chemical composition inside the zone during its formation is attained by the implementation of the combustion mechanism of *C–H–S–O–N* system described in Eq. (3.54):

$$C_mH_nS_pO_qN_r + \frac{\nu_{O_2}}{\Phi}\left(O_2 + \sum_j \frac{x_{j,ch}}{x_{O_2,ch}}M_j\right) \rightarrow mCO_2 + \frac{n}{2}H_2O + pSO_2 + \frac{r}{2}N_2$$
$$+ \frac{\nu_{O_2}}{\Phi}\left((1-\Phi)O_2 + \sum_j \frac{x_{j,ch}}{x_{O_2,ch}}M_j\right) \tag{3.54}$$
$$\nu_{O_2} = \left(m + \frac{n}{4} + p - \frac{q}{2}\right)$$

where M_j and $x_{j,ch}$ are the j^{th} species in the entrained unburnt charge into the zone and its mole fraction respectively and ν_{O2} *[kmol/kg fuel]* is the O_2 stoichiometric coefficient calculated according to the composition of the fuel used. The reacting unburnt charge comprises ambient air and residual or/and recirculating exhaust gases. The mole fractions of the comprised species considered are obtained from the unburnt zone (see section 3.3). The fractions *m, n, p, q* and *r [kmol/kg fuel]* are defined from the available mass fraction of *C, H, S, O* and *N* in the fuel used, divided by the respective molecular weight. Φ_z is the theoretical local equivalence ratio used in the combustion zones calculations at the time of their formation. This value is not the actual in–cylinder mean equivalence ratio but a theoretical value which is obtained from an empirical correlation which is presented in section 3.5.8. For rich mixtures, stoichiometric combustion is assumed ($\Phi_z = 1$) and the excess fuel vapor is treated as one of the ideal combustion products. The excess fuel is then dissociated into its compounds (section 3.5.6) in the final combustion products composition calculation. In this study, $C_{12}H_{26}$ is used to represent the fuel chemical type. This consideration is not absolutely appropriate, however is adopted due to the absence of the actual fuel chemical type. The fuel chemical type is used to find its molecular weight and its corresponding number of moles. The number of fuel moles is significantly lower compared to the number of moles of the other species comprised in the zone reactants or products thus its contribution to mixture's number of moles and molecular weight is rather small. Different chemical types for the representation of fuel can be used such as $C_{16}H_{34}$ for Diesel fuel and $C_{25}H_{52}$ for heavy fuel oil. The procedure for the calculation of zone mass and composition is presented at next.

Initially, the mass (*m [kg]*) of the zone is calculated from Eq. (3.55):

$$m_z = \left(\frac{AFR_{ST}}{\Phi} + 1\right) \cdot m_{f_i}$$
$$AFR_{ST} = \frac{\nu_{O_2} \cdot MW_{O_2}}{y_{ch_{O_2}}} \tag{3.55}$$

where AFR_{st} is the stoichiometric unburnt–charge to fuel ratio. This ratio depends on the fuel composition and unburnt–charge oxygen (O_2) content. $y_{ch,O2}$ is the O_2 mass fraction of the unburnt charge (*ch*) and m_f *[kg]* is the fuel burnt at the current *CA* step (*i*) calculated from Eq. (3.31).

The composition of zone contents (reactants) before combustion (x_{reac}) is calculated using the entrained unburnt charge composition (*x*) and the comprised fuel amount, as described in the Eq. (3.56):

$$n_{z,reac} = \frac{m_f}{MW_f} + \frac{m_{ch}}{MW_{ch}}$$
$$x_{j,reac} = \frac{x_j \cdot \frac{m_{ch}}{MW_{ch}}}{n_{z,reac}} \tag{3.56}$$
$$x_{fuel,reac} = \frac{\frac{m_f}{MW_f}}{n_{z,reac}}$$

Zone composition (products) after combustion (before dissociation) is derived using the conservation equations that describe the aforementioned combustion mechanism (see Eq.(3.54)), as shown in Eqs. (3.57) – (3.63):

$$n_{z,prod,O_2} = \nu_{O_2} \cdot \left(\frac{1}{\Phi} - 1\right) \cdot m_{f_i} \quad for\ \Phi \leq 1$$
$$n_{z,prod,O_2} = 0\ for\ \Phi > 1 \tag{3.57}$$

$$n_{z,prod,N_2} = \left(\frac{r}{2} + \frac{\nu_{O_2}}{\Phi} \cdot \frac{x_{N_2,ch}}{x_{O_2,ch}}\right) \cdot m_{f_i} \tag{3.58}$$

$$n_{z,prod,CO_2} = \left(m + \frac{\nu_{O_2}}{\Phi} \cdot \frac{x_{CO_2,ch}}{x_{O_2,ch}}\right) \cdot m_{f_i} \tag{3.59}$$

$$n_{z,prod,H_2O} = \left(\frac{n}{2} + \frac{\nu_{O_2}}{\Phi} \cdot \frac{x_{HO_2,ch}}{x_{O_2,ch}}\right) \cdot m_{f_i} \tag{3.60}$$

$$n_{z,prod,Ar} = \left(\frac{\nu_{O_2}}{\Phi} \cdot \frac{x_{Ar,ch}}{x_{O_2,ch}}\right) \cdot m_{f_i} \tag{3.61}$$

$$n_{z,prod,SO_2} = \left(p + \frac{\nu_{O_2}}{\Phi} \cdot \frac{x_{SO_2,ch}}{x_{O_2,ch}}\right) \cdot m_{f_i} \tag{3.62}$$

In the previous expressions (Eq. (3.58) – (3.62)), if combustion is fuel rich ($\Phi > 1$) then, as already mentioned, combustion is considered to be stoichiometric ($\Phi = 1$, since no additional oxidizer entrains into the zone after its generation) and the excess amount of fuel is assumed to be mixed with the zone combustion products and its mole amount is calculated from Eq. (3.63). This amount is then used in the chemical dissociation mechanism (see section 3.5.6) for the calculation of the final composition of the combustion products (i.e. zone composition).

$$n_{z,prod,C_{12}H_{26}} = \frac{\Phi - 1}{MW_f} \quad for\ \Phi > 1 \tag{3.63}$$

The mole fractions of the ideal combustion products (x_{prod}) comprised in the examined zone are calculated by the division of their corresponding number of moles with the total number of moles comprised in the zone.

Here, it is noted that from this point on, only the substances $C_{12}H_{26}$, O_2, N_2, CO_2 and H_2O are used as ideal combustion products to feed the chemical dissociation scheme in order to calculate the final equilibrium composition of the examined zone, considering negligible concentration of *Ar* and SO_2. This scheme is described in the section below.

3.5.6 Chemical Dissociation Scheme

As mentioned, the calculation of the combustion zone temperature, during its formation and evolution, involves chemical dissociation of combustion products. This mechanism results in noticeable decrease of combustion temperature, since most of the dissociation reactions are endothermic. The proposed model makes use of a chemical dissociation scheme [230,228,147] which involves *12* species which are identified from a specific sequence number as follows: *(1)* O_2 for fuel lean or *(12)* $C_{12}H_{26}$ for fuel rich mixture, *(2)* N_2, *(3)* CO_2, *(4)* H_2O, *(5) H*, *(6)* H_2, *(7) N*, *(8) NO*, *(9) O*, *(10) OH*, *(11) CO*. According to this scheme, it is assumed that dissociation reactions eventually comes into chemical equilibrium. This assumption is valid for the most of the species considered, because there reaction times are significantly lower compared to the processes taking place inside the combustion chamber of Diesel engines.

For the calculation of the equilibrium concentrations of the aforementioned species in every zone at each *CA* step, the five (*1 – 5*) mole conservation equations (see Eq. (3.65)) describing the combustion for the *C–H–O–N* system presented in Eq. (3.64) are used, in combination with the seven chemical dissociation reactions described in Table 3.1.

$$\begin{aligned}&\left(x_{12,r}^0 \cdot C_{12}H_{26} + x_{1,r}^0 \cdot O_2 + x_{2,r}^0 \cdot N_2 + x_{3,r}^0 \cdot CO_2 + x_{4,r}^0 \cdot H_2O\right) \cdot n_r \rightarrow \\ &\rightarrow \left(x_{1,p} \cdot O_2 + x_{2,p} \cdot N_2 + x_{3,p} \cdot CO_2 + x_{4,p} \cdot H_2O + x_{5,p} \cdot H + x_{6,p} \cdot H_2 + \right. \\ &\left. + x_{7,p} \cdot N + x_{8,p} \cdot NO + x_{9,p} \cdot O + x_{10,p} \cdot OH + x_{11,p} \cdot CO\right) \cdot n_p \end{aligned} \tag{3.64}$$

$$\begin{aligned}&A = \frac{n_r}{n_p} \\ &(\mathbf{1}.)\ \boldsymbol{C}\text{:}\ \ A \cdot \left(12 \cdot x_{12,r}^0 + x_{3,r}^0\right) = x_{3,p} + x_{11,p} \\ &(\mathbf{2}.)\ \boldsymbol{H}\text{:}\ \ A \cdot \left(26 \cdot x_{12,r}^0 + 2 \cdot x_{4,r}^0\right) = 2 \cdot x_{4,p} + x_{5,p} + 2 \cdot x_{6,p} + x_{10,p} \\ &(\mathbf{3}.)\ \boldsymbol{O}\text{:}\ \ A \cdot \left(2 \cdot x_{1,r}^0 + 2 \cdot x_{3,r}^0 + x_{4,r}^0\right) = \\ &= 2 \cdot x_{1,p} + 2 \cdot x_{3,p} + x_{4,p} + x_{8,p} + x_{9,p} + x_{10,p} + x_{11,p} \\ &(\mathbf{4}.)\ \boldsymbol{N}\text{:}\ \ A \cdot 2 \cdot x_{2,r}^0 = 2 \cdot x_{2,p} + x_{7,p} + x_{8,p} \\ &(\mathbf{5}.)\ \sum_{j=1}^{12} x_j = 1 \end{aligned} \tag{3.65}$$

In the previous expressions, *x* is the mole fraction of each species in the reactants and products denoted with subscript *r* and *p* respectively and *n [kmol]* is number of moles. The initial values for this calculation, denoted with the superscript *0*, are taken from the estimated mole fractions assuming that ideal combustion takes place. The calculation of these values is attained using the Eq. (3.57) – (3.60) and (3.63) presented in section 3.5.5. If combustion is fuel rich ($\Phi > 1$) then the excess fuel is dissociated into its components thus its concentration in the final equilibrium products is zeroth ($x_{12,p} = 0$). In this case, as discussed in section 3.5.4, the aforementioned initial values are calculated considering stoichiometric combustion ($\Phi = 1$). Apparently, for fuel lean ($\Phi < 1$) and stoichiometric combustion,

the fuel fraction in both products and reactants of the reaction described in Eq. (3.62) is zeroth ($x_{12,r} = x_{12,p} = 0$). According to the above, *12* unknown parameters occur: *11* concentrations (x_1 or x_{12} and $x_2 - x_{11}$) and the number of products' mole (n_p). Hence, seven additional equations must be used among with the five aforementioned conservation equations (Eq. (3.65)). Thus, seven chemical dissociation reactions are used for the solution of the system which provides the equilibrium composition of the mixture. These reactions are demonstrated in Table 3.1:

Chemical Reactions
$\frac{1}{2}H_2 \leftrightarrow H$
$\frac{1}{2}O_2 \leftrightarrow O$
$\frac{1}{2}N_2 \leftrightarrow N$
$2H_2O \leftrightarrow 2H_2 + O_2$
$H_2O \leftrightarrow OH + \frac{1}{2}H_2$
$CO_2 + H_2 \leftrightarrow H_2O + CO$
$H_2O + \frac{1}{2}N_2 \leftrightarrow H_2 + NO$
P=p_i[bar]/1bar: normalized in–cylinder pressure

Table 3.1: Chemical reactions used in the chemical dissociation of the combustion products scheme.

To utilize the considered chemical reactions of Table 3.1, the assumption of equilibrium was adopted, as mentioned. Thus, the equations derived from the definition of the corresponding equilibrium constants (*Kp*) and from the calculated *Kp* values via Gibbs free energy minimization method (using NASA polynomials [180] (see Appendix d) for the calculation of Gibbs free energy), were utilized (see Table 3.2).

Constant *Kp* for each reaction is defined from Eq. (3.66) [8,231]:

$$Kp = \prod_j \left(\frac{p_j}{p_0}\right)^{\nu_{j,p}-\nu_{j,r}} = \frac{\left(p_{1,p}/p_0\right)^{\nu_{1,p}} \cdot \left(p_{2,p}/p_0\right)^{\nu_{2,p}} \cdot \cdots \left(p_{11,p}/p_0\right)^{\nu_{11,p}}}{\left(p_{1,r}/p_0\right)^{\nu_{1,r}} \cdot \left(p_{2,r}/p_0\right)^{\nu_{2,r}} \cdot \cdots \left(p_{11,r}/p_0\right)^{\nu_{11,r}}} \qquad (3.66)$$

The previous equation is converted in Eq. (3.68), according to the Dalton's law for ideal gases which postulates that the pressure of the mixture (p) equals with the sum of partial pressures of its comprised species (p_j) as described in Eq. (3.67):

$$p = \sum_j p_j$$
$$p_j = x_j \cdot p \Rightarrow x_j = \frac{p_j}{p} \tag{3.67}$$

$$Kp = \left(\frac{p}{p_0}\right)^{\sum_j (\nu_{j,p} - \nu_{j,r})} \cdot \prod_j x_j^{\nu_{j,p} - \nu_{j,r}} =$$
$$= \frac{\left(\frac{p}{p_0}\right)^{\nu_{1,p} + \nu_{2,p} + \cdots + \nu_{11,p}}}{\left(\frac{p}{p_0}\right)^{\nu_{1,r} + \nu_{2,r} + \cdots + \nu_{11,r}}} \cdot \frac{x_{1,p}^{\nu_{1,p}} \cdot x_{2,p}^{\nu_{2,p}} \cdot \ldots x_{11,p}^{\nu_{11,p}}}{x_{1,r}^{\nu_{1,r}} \cdot x_{2,r}^{\nu_{2,r}} \cdot \ldots x_{11,r}^{\nu_{11,r}}} \tag{3.68}$$

where the ratio p/p_0 is the normalized pressure, p *[Pa]* is the current cylinder pressure and $p_0 = 10^5$ *[Pa]* is the reference pressure.

Constant *Kp* for each reaction of Table 3.1 is calculated according to the Gibbs free energy minimization method described at next. The definition of Gibbs free energy (*G [J]*) is provided from Eq. (3.69):

$$G(T, p) \triangleq H(T) - T \cdot S(T, p) \tag{3.69}$$

where *H [J]* is enthalpy, *S [J/K]* in entropy and *T [K]* is temperature. According to the ideal gas assumption, Gibbs free energy and entropy are functions of temperature and pressure (p) in contrast to enthalpy, which is only a function of temperature.

The combination of the following equations provides the correlation between the variation of Gibbs free energy and chemical potential μ *[J/kmol]* for a variation of the number of moles (*dn [kmol]*) of each species (j) comprised in the mixture:

- first thermodynamic law including the term of chemical energy due to the species interactions in the mixture as shown in Eq. (3.71),
- state function of entropy (*S [J/K]*) described in Eq. (3.70),

- differentiation of Gibbs free energy as shown in Eq. (3.73) and accompanied with the following assumptions:
- constant pressure (*dp = 0*),
- constant temperature (*dT = 0*),
- zero useful work (i.e. non $p \cdot dV$) exchange ($dW_t = 0$),
- ideal gas consideration for the mixture components and
- reversible (*rev*) process.

The aforementioned correlation is shown in Eq. (3.74).

$$dS = \left(\frac{\delta Q}{T}\right)_{rev} \Rightarrow \delta Q = T \cdot dS \tag{3.70}$$

$$dH = \delta Q + V \cdot dp + \sum_j \mu_j \cdot dn_j \ , \ \ dp = 0 \tag{3.71}$$

$$\delta Q = dH - \sum_j \mu_j \cdot dn_j = \ T \cdot dS \tag{3.72}$$

$$\begin{gathered} dG = dH - T \cdot dS - S \cdot dT \ , \ \ dT = 0 \\ dG = dH - T \cdot dS = \sum_j \mu_j \cdot dn_j \end{gathered} \tag{3.73}$$

$$(dG)_{p,T,rev} = \sum_j \mu_j \cdot dn_j \tag{3.74}$$

At chemical equilibrium, the variation of Gibbs free energy (*dG [J]*) is minimized i.e. becomes zero, as shown in Eq. (3.75):

$$(dG)_{p,T,rev} = \sum_j \mu_j \cdot \left(\nu_{j,p} - \nu_{j,r}\right) \cdot \delta\xi = 0 \tag{3.75}$$

where $\delta\xi$ is the differential of the extent of reaction, ν is the stoichiometric coefficient of the j^{th} species (ν corresponds to the chemical reaction that the examined species (*j*) participates into– see Table 3.1) and μ *[J/kmol]* is the chemical potential, which is identical to the partial molar Gibbs function (*g [J/kmol]*) for constant pressure (*p*), temperature (*T*) and species (*l*, other than *j*). μ is defined from Eq. (3.76):

$$\mu_j = g_j = \left(\frac{\partial G}{\partial n_j}\right)_{p,T,n_l(l \neq j)} \tag{3.76}$$

Considering the following Eqs. (3.77) and (3.78) for the determination of molar entropy (*s [J/kmol/K]*) and enthalpy (*h [J/kmol]*) of ideal gas in combination with Gibbs free

energy definition described in Eq. (3.69), the partial molar Gibbs function (*g [J/kmol]*) can be defined from Eq. (3.79).

$$s_j = s^0{}_j + \int_{T_0}^{T} \frac{cp_j(T)}{T} \cdot dT - \bar{R} \cdot \ln\left(\frac{p_j}{p_0}\right) \tag{3.77}$$

$$h_j = h^0{}_j + \int_{T_0}^{T} cp_j(T) \cdot dT \tag{3.78}$$

$$g_j = h_j - T \cdot s_j$$

$$g_j = h^0{}_j + \int_{T_0}^{T} cp_j(T) \cdot dT - T \cdot s^0{}_j - T \cdot \int_{T_0}^{T} \frac{cp_j(T)}{T} \cdot dT + T \cdot \bar{R} \cdot ln\left(\frac{p_j}{p_0}\right)$$

$$g^0{}_j = h^0{}_j + \int_{T_0}^{T} cp_j(T) \cdot dT - T \cdot s^0{}_j - T \cdot \int_{T_0}^{T} \frac{cp_j(T)}{T} \cdot dT \tag{3.79}$$

$$\Rightarrow g_j = g^0{}_j + T \cdot \bar{R} \cdot \ln\left(\frac{p_j}{p_0}\right)$$

In the previous expressions, superscript *0* on entropy and enthalpy term denotes the standard–state values which are defined at reference temperature (T_0 *=298.15 [K]*) and pressure ($p_0 = 10^5$ *[Pa]*) [180], *cp [J/kmol/K]* is the specific heat capacity at constant pressure, g^0 *[J/kmol]* is the molar Gibbs free energy at standard–state (^{0}) pressure ($p_j = p_0$) and p_j *[Pa]* is the partial pressure. The subscript *j* denotes the sequence number of the species comprised in the mixture.

From the combination of Eqs. (3.75), (3.76) and (3.79) the Eq. (3.80) is derived:

$$\sum\nolimits_j \left(g^0{}_j + \bar{R} \cdot T \cdot \ln\left(\frac{p_j}{p_0}\right)\right) \cdot \left(\nu_{j,p} - \nu_{j,r}\right) = 0 \tag{3.80}$$

and after some mathematical processing the above expression is converted to Eq. (3.81):

$$\sum\nolimits_j \ln\left(\frac{p_j}{p_0}\right)^{\nu_{j,p}-\nu_{j,r}} = -\sum\nolimits_j \frac{g^0{}_j \cdot \left(\nu_{j,p} - \nu_{j,r}\right)}{\bar{R} \cdot T} = -\frac{\Delta G^0}{\bar{R} \cdot T} = \ln(Kp) \tag{3.81}$$

In the present study, the equilibrium constants *Kp* are calculated, using Eq. (3.82) derived from Eq. (3.81).

$$Kp(T) = e^{-\frac{\Delta G^0(T)}{\bar{R} \cdot T}} = e^{-\frac{G_p^0(T) - G_r^0(T)}{\bar{R} \cdot T}} = e^{-\sum_j \frac{g^0{}_j(T) \cdot \left(\nu_{j,p} - \nu_{j,r}\right)}{\bar{R} \cdot T}} \tag{3.82}$$

where ΔG^0 *[J]* is the Gibbs free energy change at standard–state (^{0}) pressure (p_0) of the examined reaction, which is a function of temperature (T) and of stoichiometric coefficients of the participating species. The dimensionless ratio $\frac{g^0{}_j(T)}{\bar{R}\cdot T}$ is calculated using NASA polynomials [180] (see Appendix d) as described in Eq. (3.83) for the current zone temperature (T), for each species (j) which participates in the examined chemical reaction.

At this point, it must be clarified that NASA polynomials are only functions of temperature. Particularly, the polynomial for the calculation of entropy (s), of each species, calculates the entropy at standard–state pressure (p_j=p_0), thus the term $\left(\ln\left(\frac{p_j}{p_0}\right)\right)$ of Eq. (3.77) becomes zero, namely it calculates only the part of the entropy that is independent from pressure $\left(s^0{}_j + \int_{T_0}^{T} \frac{cp_j(T)}{T}\cdot dT\right)$ [232]. Thus, the Gibbs free energy polynomial (f_g) is derived from the combination of NASA polynomials for entropy (f_s) and enthalpy (f_h) calculation (see Appendix d). The polynomial (f_g) for the calculation of g^0 is described in Eq. (3.83) presented below, which has been derived from Eq. (3.79). Hence, the use of this polynomial (f_g) provides the Gibbs free energy (g^0) for standard–state pressure (p_0) at any temperature (T).

$$f_{h_j}^{NASA}(T) \equiv \frac{h_j}{\bar{R}\cdot T}(T) = \frac{h^0{}_j + \int_{T_0}^{T} cp_j(T)\cdot dT}{\bar{R}\cdot T}$$

$$f_{s_j}^{NASA}(T) \equiv \frac{s_j}{\bar{R}}(T) = \frac{s^0{}_j + \int_{T_0}^{T} \frac{cp_j(T)}{T}\cdot dT}{\bar{R}} \tag{3.83}$$

$$f_{g_j}^{NASA}(T) \equiv \frac{g^0{}_j}{\bar{R}\cdot T}(T) = \frac{h_j}{\bar{R}\cdot T}(T) - \frac{s_j}{\bar{R}}(T) = f_{h_j}^{NASA}(T) - f_{s_j}^{NASA}(T)$$

After the calculation of g^0 (see Eq. 3.83) for each species (j) via the Gibbs minimization method described above, the equilibrium constants *Kp* of the chemical dissociation reactions presented in Table 3.1, can be now calculated from Eq. (3.82). These reactions and the calculation of the corresponding *Kp* are demonstrated in the first and third column of

Table 3.2 respectively. Each equilibrium constant *Kp* has been defined from Eq. (3.68) accounting for the stoichiometry of the respective chemical reaction and is demonstrated in the second column of Table 3.2:

Chemical reaction	Equilibrium Constant definition (Eq. **(3.68)**)	Equilibrium Constant Calculation (Eq. **(3.82)**)
$\frac{1}{2}H_2 \leftrightarrow H$	$K_{p1} = \sqrt{P} \cdot \frac{x_H}{\sqrt{x_{H_2}}}$	$K_{p1} = e^{-\frac{g^0{}_H - \frac{1}{2} \cdot g^0{}_{H_2}}{\bar{R} \cdot T}}$
$\frac{1}{2}O_2 \leftrightarrow O$	$K_{p2} = \sqrt{P} \cdot \frac{x_O}{\sqrt{x_{O_2}}}$	$K_{p2} = e^{-\frac{g^0{}_O - \frac{1}{2} \cdot g^0{}_{O_2}}{\bar{R} \cdot T}}$
$\frac{1}{2}N_2 \leftrightarrow N$	$K_{p3} = \sqrt{P} \cdot \frac{x_N}{\sqrt{x_{N_2}}}$	$K_{p3} = e^{-\frac{g^0{}_N - \frac{1}{2} \cdot g^0{}_{N_2}}{\bar{R} \cdot T}}$
$2H_2O \leftrightarrow 2H_2 + O_2$	$K_{p4} = P \cdot \frac{x_{O_2} \cdot \left(x_{H_2}\right)^2}{\left(x_{H_2O}\right)^2}$	$K_{p4} = e^{-\frac{2 \cdot g^0{}_{H_2} + g^0{}_{O_2} - 2 \cdot g^0{}_{H_2O}}{\bar{R} \cdot T}}$
$H_2O \leftrightarrow OH + \frac{1}{2}H_2$	$K_{p5} = \sqrt{P} \cdot \frac{x_{\mathrm{OH}} \cdot \sqrt{x_{H_2}}}{x_{H_2O}}$	$K_{p5} = e^{-\frac{g^0{}_{OH} + \frac{1}{2} \cdot g^0{}_{H_2} - g^0{}_{H_2O}}{\bar{R} \cdot T}}$
$CO_2 + H_2 \leftrightarrow H_2O + CO$	$K_{p6} = \frac{x_{H_2O} \cdot x_{\mathrm{CO}}}{x_{CO_2} \cdot x_{H_2}}$	$K_{p6} = e^{-\frac{g^0{}_{H_2O} + g^0{}_{CO} - g^0{}_{CO_2} - g^0{}_{H_2}}{\bar{R} \cdot T}}$
$H_2O + \frac{1}{2}N_2 \leftrightarrow H_2 + NO$	$K_{p7} = \sqrt{P} \cdot \frac{x_{H_2} \cdot x_{NO}}{x_{H_2O} \cdot \sqrt{x_{N_2}}}$	$K_{p7} = e^{-\frac{g^0{}_{H_2} + g^0{}_{NO} - g^0{}_{H_2O} - \frac{1}{2} \cdot g^0{}_{N_2}}{\bar{R} \cdot T}}$

Table 3.2: Definition and calculation of equilibrium constants (Kp) via Gibbs minimization method. Normalized pressure: $P=p_{cyl}/p_0$, $p_0=10^5$ Pa.

After the calculation of the equilibrium constants, seven nonlinear equations are formed (2nd column of Table 3.2) for the mixture equilibrium composition calculation. These equations are formed when the right term of the respective equations of the second and third column of Table 3.2 are equated. These equations among with the five conservation equations describing the combustion for the *C–H–O–N* system (Eq. (3.65)), comprise a nonlinear system of *12* equations. This system, after some mathematical processing (i.e. linearization, reduction, etc.), is solved using the Newton–Raphson method [233]. The detailed description of the computational methodology followed for the solution of the aforementioned system is presented analytically in Ref. [147] and [234].

As already mentioned, the dissociation scheme is implemented in order to introduce the effect of dissociation in zone temperature, namely the temperature decrease and additionally, to calculate the equilibrium composition of the zone, which is used with the calculated zone temperature and volume to calculate the *NO* formation inside the zone. The procedure for the *NO* formation calculation is described in the section below.

3.5.7 Nitric Oxide Formation Mechanism

According to literature [14,8,9,30,38] and existing experience, thermal *NO* is the predominant component of NO_x, especially for the high–temperature diffusion flame occurring in Diesel engines. Although the NO_2/NO_x ratio may range from *10–30%* for low loads in Diesel engines [8], the proposed model calculates only the number of moles of *NO* produced in an engine cycle, assuming that this is representative of total NO_x.

Hence, regarding the examined automotive engines (*4*–stroke), the predicted mass amount of *NO [mg/cycle]* per engine cycle, is directly compared to the available *NO [ppmv]* experimental measurements which are converted into mass per cycle units *[mg/cycle]*. This conversation is accomplished via Eq. (3.84) using the available measured engine speed (*N [rpm]*), intake air ($\dot{m}_{IA}$) and fuel mass ($\dot{m}_f$) flow rates, or exhaust mass flow rate *[kg/h]* which are input data (obtained from engine map of are calculated from respective models). The estimated exhaust gas composition, namely its molecular weight (MW_{exh} *[kg/kmol]*) which is calculated from Eq. (3.23) in section 3.3.7, is also used in Eq. (3.84).

$$NO\left[\frac{mg}{cycle}\right] = NO[ppmv] \cdot \frac{MW_{NO}}{MW_{exh}} \cdot \frac{\left(\dot{m}_{IA} + \dot{m}_{f\,eng}\right)}{30 \cdot N} \tag{3.84}$$

Furthermore, regarding the large–scale Diesel engines, *IMO* regulations [46] refer to NO_x absolute values in *[g/kWh]* units in wet basis where nitric oxides are expressed to equivalent NO_2. This consideration is based on the fact that finally all *NO* will be converted into NO_2 in the atmosphere with the same proportion as described in Eq. (3.85):

$$2 \cdot NO + O_2 \rightarrow 2 \cdot NO_2 \tag{3.85}$$

According to this rationale, the extracted results for *NO [kmol/cycle]* are multiplied with the NO_2 molecular weight (MW_{NO2} *[kg/kmol]*) to transform them into equivalent NO_x *[g/cycle]*. Then, they are compared to the measured NO_x *[ppmv]* which are also converted to mass per engine cycle units *[g/cycle]* in wet basis, as described in Eq. (3.86) using the fuel flow rate *[kg/h]*, exhaust gas composition, engine speed and ambient conditions to estimate the exhaust mass flow rate $\dot{m}_{exh}$ *[kg/h]* via the carbon balance method as proposed by *IMO* [46] and described in Appendix a.

$$NO_x\left[\frac{g}{cycle}\right] = NO_x[ppmv] \cdot 10^{-3} \cdot \frac{MW_{NO_2}}{MW_{exh}} \cdot \frac{str. \cdot \dot{m}_{exh}}{120 \cdot N} \tag{3.86}$$

In the previous expression, *str.* is the number of strokes for an engine cycle i.e. *2* for *2*–stroke and *4* for *4*–stroke engines and the molecular weight of the exhaust gas (MW_{exh} *[kg/kmol]*) which is approximated from the measured exhaust composition (O_2, CO_2, *CO*, NO_x, SO_2, H_2O).

Nonetheless, for simplicity, *IMO* [46] proposed a semi–empirical concept to transform dry NO_x from *[ppmv]* to *[g/h]*. Additionally, if the NO_x measurement is in dry basis, *IMO* suggests the multiplication of NO_x with a "dry to wet (*kwr2*)" correction factor. This concept is presented in Appendix b. The transformed measured NO_x (wet) values are converted from *[g/h]* to *[g/cycle]* according to Eq. (3.87):

$$NO_x\left[\frac{g}{cycle}\right] = NO_x\left[\frac{g}{h}\right] \cdot \frac{str.}{120 \cdot N} \tag{3.87}$$

As mentioned in section 3.5.6, chemical equilibrium of the dissociated combustion products is assumed because the majority of the chemical reactions considered have relatively low characteristic reaction time (fast reactions) compared to the processes taking

place inside the combustion chamber of a Diesel engine. Nonetheless, this assumption may not be satisfactory late during expansion where the in–cylinder charge temperature is significantly decreased. However, this fact slightly affects the final *NO* amount since *NO* levels "freeze" early at expansion stroke [30]. On the contrary, nitrogen oxide (*NO*) rarely reaches equilibrium due to the long time required for its formation. Hence, *NO* formation is kinetically controlled [8,30,31]. Thus, chemical kinetics are used for the calculation of *NO* concentration in the zone. Lavoie et al [30] suggested a scheme which includes the extended Zeldovich mechanism (thermal *NO* mechanism) [29] and *NO* formation from the N_2O mechanism. The chemical reactions that participate in this scheme are shown in Table 3.3:

Chemical Reaction	Reaction Number
$O + N_2 \leftrightarrow NO + N$	(1)
$N + O_2 \leftrightarrow NO + O$	(2)
$N + OH \leftrightarrow NO + H$	(3)
$\mathrm{H} + N_2O \leftrightarrow N_2 + OH$	(4)
$\mathrm{O} + N_2O \leftrightarrow N_2 + O_2$	(5)
$\mathrm{O} + N_2O \leftrightarrow 2NO$	(6)

Table 3.3: Chemical reactions for NO formation. 1 – 3: Extended Zeldovich mechanism, 4 – 6: "N_2O" mechanism.

According to this scheme, the concentrations of O_2, N_2, *H*, *O* and *OH* in the flame are close to chemical equilibrium. The *NO*, *N* and N_2O concentrations are obtained from their chemical kinetics equations which represent the variation of the examined species concentration ($[M_j]$ *[kmol/m^3]*) with time (*dt*). This variation, for each one of the aforementioned substances is defined from the difference between the reaction rates (*R*) of forward (R^+: formation) and reverse (R^-: dissipation) reactions of Table 3.3 multiplied with the stoichiometry coefficient (ν) of the examined substance (j= *NO*, *N* and N_2O) and reaction (r=*1,2,…6*) as described in Eq. (3.88):

$$\frac{d[M_j]}{dt} = \sum_r \nu_{j,r} \cdot (R_r^+ - R_r^-) \tag{3.88}$$

The reaction rate (*R*) of a specific reaction is given from Eq. (3.89):

$$R_r^+ = k_r^+ \cdot \prod_{j(form)} \left[M_{j(form),r}\right]^{\nu_{j(form),r}}$$

$$R_r^- = k_r^- \cdot \prod_{j(diss)} \left[M_{j(diss),r}\right]^{\nu_{j(diss),r}} \tag{3.89}$$

$$R_r^{eq} = k_r^+ \cdot \prod_{j(form)} \left[M_{j(form),r}\right]_{eq}^{\nu_{j(form),r}} = k_r^- \cdot \prod_{j(diss)} \left[M_{j(diss),r}\right]_{eq}^{\nu_{j(diss),r}}$$

where k *[m^3/kmol/s]* is the forward (+) and reverse (-) reaction rate constant of each reaction (r=*1,2…6*) of Table 3.3 and M_j denotes the species that participate in the respective reaction, where *form* denotes formation and *diss* dissipation of the examined species and finally superscript and subscript *eq* denotes equilibrium.

If the reaction rates of Eq. (3.89) substitute the respective ones in Eq. (3.88) considering equilibrium only for O_2, N_2, H, O and OH, then the following Eqs. (3.90), (3.91) and (3.92) are extracted for the variation of NO, N and N_2O concentrations with time, respectively:

$$\frac{d[NO]}{dt} = k_1^+ \cdot [O]_{eq} \cdot [N_2]_{eq} + \left(k_2^+ \cdot [N]_{eq} \cdot [O_2]_{eq} + k_3^+ \cdot [N]_{eq} \cdot [OH]_{eq}\right) \cdot \frac{[N]}{[N]_{eq}} + 2 \cdot k_6^+ \cdot [O]_{eq} \cdot [N_2O]_{eq} \cdot \frac{[N_2O]}{[N_2O]_{eq}} - \left(k_1^- \cdot [NO]_{eq} \cdot [N]_{eq} \cdot \frac{[N]}{[N]_{eq}} + k_2^- \cdot [NO]_{eq} \cdot [O]_{eq} + k_3^- \cdot [NO]_{eq} \cdot [H]_{eq}\right) \cdot \frac{[NO]}{[NO]_{eq}} - 2 \cdot k_6^- \cdot [NO]_{eq}^2 \cdot \left(\frac{[NO]}{[NO]_{eq}}\right)^2 \tag{3.90}$$

$$\frac{d[N]}{dt} = k_1^+ \cdot [O]_{eq} \cdot [N_2]_{eq} + \left(k_2^+ \cdot [NO]_{eq} \cdot [O]_{eq} + k_3^+ \cdot [NO]_{eq} \cdot [H]_{eq}\right) \cdot \frac{[NO]}{[NO]_{eq}} - \left(k_1^- \cdot [NO]_{eq} \cdot [N]_{eq} \cdot \frac{[NO]}{[NO]_{eq}} + k_2^- \cdot [O_2]_{eq} \cdot [N]_{eq} + k_3^- \cdot [OH]_{eq} \cdot [N]_{eq}\right) \frac{[N]}{[N]_{eq}} \tag{3.91}$$

$$\frac{d[N_2O]}{dt} = k_4^+ \cdot [N_2]_{eq} \cdot [OH]_{eq} + k_5^+ \cdot [N_2]_{eq} \cdot [O_2]_{eq} + k_6^+ \cdot [NO]_{eq}^2 \cdot \left(\frac{[NO]}{[NO]_{eq}}\right)^2 - \left(k_4^- \cdot [H]_{eq} \cdot [N_2O]_{eq} + k_5^- \cdot [O]_{eq} \cdot [N_2O]_{eq} + k_6^- \cdot [O]_{eq} \cdot [N_2O]_{eq}\right) \cdot \frac{[N_2O]}{[N_2O]_{eq}} \tag{3.92}$$

When the equilibrium reaction rates are introduced in the previous expressions and $\frac{[NO]}{[NO]_{eq}}$, $\frac{[N]}{[N]_{eq}}$ and $\frac{[N_2O]}{[N_2O]_{eq}}$ are substituted with the symbols $\boldsymbol{\alpha}$, $\boldsymbol{\beta}$ and $\boldsymbol{\gamma}$ respectively, then Eqs. (3.90) – (3.92) are converted into Eq. (3.93) – (3.95) respectively:

$$\frac{d[NO]}{dt} = R_1^{eq} + \left(R_2^{eq} + R_3^{eq}\right) \cdot \beta + 2 \cdot R_6^{eq} \cdot \gamma - \left(R_1^{eq} \cdot \beta + R_2^{eq} + R_3^{eq} + 2 \cdot R_6^{eq} \cdot \alpha\right) \cdot \alpha \tag{3.93}$$

$$\frac{d[N]}{dt} = R_1^{eq} + \left(R_2^{eq} + R_3^{eq}\right) \cdot \alpha - \left(R_1^{eq} \cdot \alpha + R_2^{eq} + R_3^{eq}\right) \cdot \beta \tag{3.94}$$

$$\frac{d[N_2O]}{dt} = R_4^{eq} + R_5^{eq} + R_6^{eq} \cdot \alpha^2 - \left(R_4^{eq} + R_5^{eq} + R_6^{eq}\right) \cdot \gamma \tag{3.95}$$

As reported in Ref. [30], rough estimates of the magnitude of the terms in equations (3.93), (3.94) and (3.95) indicate that the relaxation times [3] [235] for Eq. (3.94) and (3.95) are several orders of magnitude shorter than that of equation (3.93). Hence, it is appropriate to assume steady–state concentrations for *N* and *N₂O*, namely $\frac{d[N]}{dt} = \frac{d[N_2O]}{dt} = 0$. This can be further justified from the fact that the activation energy for oxidation of *N* atoms is small and when there is sufficient O_2, as in a fuel–lean flame, the rate of consumption of free *N* atoms becomes equal to the rate of its formation and therefore a quasi–steady state assumption can be established. This assumption is valid for most combustion cases except in extremely fuel–rich combustion conditions [32]. According to the last assumption $\left(\frac{d[N]}{dt} = \frac{d[N_2O]}{dt} = 0\right)$, the coefficients β and γ are eliminated from Eq. (3.93) using Eq. (3.94) and (3.95) and thus Eq. (3.93) is converted to the following Eq. (3.96) which describes the *NO* formation:

$$\frac{d[NO]}{dt} = 2 \cdot (1 - \alpha^2) \cdot \left(\frac{R_1^{eq}}{1 + \alpha \cdot \frac{R_1^{eq}}{R_2^{eq} + R_3^{eq}}} + \frac{R_6^{eq}}{1 + \alpha \cdot \frac{R_6^{eq}}{R_4^{eq} + R_5^{eq}}} \right) \tag{3.96}$$

where the first term in the large brackets corresponds to the extended Zeldovich mechanism (reactions 1 – 3 of Table 3.3) and the second one (reactions 4 – 6 of Table 3.3) to the *N₂O* mechanism which uses the *N₂O* as an intermediary.

As revealed from the investigation presented in Ref. [30], most of *NO* is formed via the extended Zeldovich mechanism except the cases with lean mixtures at low temperatures. The last is not the usual case for Diesel engines during combustion except at low load operation or/and very high *ERG* rate, and late during exhaust phase where the *N₂O* mecha-

[3] Relaxation time is the lagging time required for a chemical reaction to reach the new equilibrium position after the application of a sudden change (i.e. temperature, pressure, etc.) on it and is related to its reaction rate constants (k^+ and k^-).

nism may become dominant. However, the last does not affect significantly the *NO* calculation since both mechanisms are very slow and effectively frozen, generally earlier than the time where the N_2O mechanism would become important.

Therefore, in the present work, only the extended Zeldovich mechanism is taken into account. This was decided after a comparison between the results derived from the implementation of both methods: the aforementioned method, which includes both mechanisms and the simplified one, which includes only extended Zeldovich mechanism. The comparison revealed that both mechanisms provide quite similar results. Hence, only the extended Zeldovich mechanism was utilized since it requires lower computational cost while providing decent predictions. In addition, more detailed NO_x formation mechanisms [38,39,40,41] were not examined because they introduce high complexity, increase sensitivity and computational time of the system.

At next, the *NO* formation mechanism used to calculate the number of moles of *NO [kmol]* in each zone (*z*) and *CA* step (*i*) is outlined in Eq. (3.97) which is derived from Eq. (3.96):

$$\left(\frac{dNO}{d\theta}\right)_{z_i} = \left(\frac{d[NO]}{dt}\right)_{z_i} \cdot V_{z_i} \cdot \frac{dt}{d\theta} = 2 \cdot (1-\alpha^2) \cdot \frac{R_1^{eq}}{1+\alpha \cdot \frac{R_1^{eq}}{R_2^{eq}+R_3^{eq}}} \cdot \frac{V_{z_i}}{6 \cdot N} \qquad (3.97)$$

where $V\ [m^3]$ is the volume of the current zone (*z*) calculated as described in sections 3.5.3 and 3.5.4, *N [rpm]* is the engine speed which is assumed constant throughout the cycle and $R^{eq}\ [kmol/m^3/s]$ are the equilibrium reaction rates defined from Eq.(3.89) using the chemical equilibrium compositions $[\,]_{eq} \equiv \frac{M_j}{V_{z_i}}\ [kmol/m^3]$ of the comprised species, which have been calculated from the dissociation scheme, as described in section 3.5.6, and the respective reaction rate constants ($k\ [m^3/kmol/s]$) which are derived from the comprehensive experimental studies of R. K. Hanson and S. Salimian presented in Ref. [236]. The equilibrium reaction rates used in the proposed model are shown in Table 3.4:

Chemical Reaction	R^{eq} [kmol/m^3/s]	k [m^3/kmol/s]
$O + N_2 \leftrightarrow NO + N$	$k_1^+ \cdot [O]_{eq} \cdot [N_2]_{eq}$	$k_1^+ = 1.8 \cdot 10^{11} \cdot e^{-\frac{38370}{T}}$
$N + O_2 \leftrightarrow NO + O$	$k_2^+ \cdot [N]_{eq} \cdot [O_2]_{eq}$	$k_2^+ = 1.8 \cdot T \cdot 10^7 \cdot e^{-\frac{4680}{T}}$
$N + OH \leftrightarrow NO + H$	$k_3^+ \cdot [N]_{eq} \cdot [OH]_{eq}$	$k_3^+ = 7.1 \cdot 10^{10} \cdot e^{-\frac{450}{T}}$

Table 3.4: Equilibrium reaction rates used in NO formation mechanism used in the proposed model.

The instantaneous amount of *NO [Kmol]* formed in each zone is derived from the integration of Eq. (3.97) as *CA* elapses up to exhaust valve opening (*EVO*), using the Euler method [237] described in Eq. (3.98):

$$(NO)_{z_i}^{k} = (NO)_{z_i}^{k-1} + \left(\frac{dNO}{d\theta}\right)_{z_i}^{k-1} \cdot \frac{\Delta\theta}{k\_max} \quad , k = 1,2,\cdots k\_max$$
$$(NO)_{z_i}^{0} = (NO)_{z_{i-1}}^{k\_max} \tag{3.98}$$

where the *CA* interval ($\Delta\theta$) has been divided into *k_max* smaller equidistance steps $\left(\frac{\Delta\theta}{k\_max}\right)$ for better accuracy and to avoid divergence of the final (*k=k_max*) predicted *NO* value which is derived from the iteration procedure described in Eq. (3.98) where superscript *k* denotes the iteration sequence number. Regarding the examined zone, denoted with subscript *z*, the initial *NO* value $\left((NO)_{z_i}^{0}\right)$ required for the calculation of *NO* at the current *CA* step, denoted with subscript *i*, is the final *NO* value $\left((NO)_{z_{i-1}}^{k\_max}\right)$ calculated at the previous *CA* step (*i-1*). The $\frac{dNO}{d\theta}$ term is calculated from Eq. (3.97) using the equilibrium concentrations and reaction rate constants presented in Table 3.4, which have been calculated using the current zone temperature T_{z_i} *[K]* at the current *CA* step (*i*).

Following the previously described procedure, the *NO* formation history of each zone is obtained. To calculate the total *NO* formation history in the combustion chamber, the calculated *NO* amounts of all existing zones (see also Fig. 3.5 for interpretation of the term "existing") are summed at each *CA* step (*i*) as shown in Eq. (3.99):

$$(NO)_i = \sum_{z=1}^{i-SOC+1} (NO)_{z_i}^{k\_max} \quad , i = SOC \cdots EOC$$
$$(NO)_i = \sum_{z=1}^{EOC-SOC+1} (NO)_{z_i}^{k\_max} \quad , i = EOC+1 \cdots EVO \tag{3.99}$$

Apparently, the total *NO [kmol]* at *EVO* is calculated from Eq. (3.99) as the sum of the *NO* from all zones at this point i.e. $(NO)_{EVO}$.

3.5.8 Calculation of the Zone Equivalence Ratio Φ

As already mentioned is section 3.5.1 and 3.5.5, the zone equivalence ratio (Φ_z) and the fuel mass attributed to each zone, determine the total zone mass and affect its chemical composition, volume and temperature. These parameters have a significant effect on *NO* formation inside the zone as explained in section 3.5.7.

In the present work a constant zone equivalence ratio (Φ_z) was assumed for all zones. Although this concept does not correspond to the actual case of *DI* Diesel engines, it has been adopted for low complexity and computational cost reasons.

To evaluate the validity of this assumption (i.e. constant Φ_z), a sensitivity analysis has been conducted to examine its effect on tailpipe *NO* values. For this reason, a detailed

investigation was conducted to examine *NO* variation with Φ_z. This investigation revealed that the Φ used in the combustion mechanism during zone generation is very important for the *NO* calculation because it introduces high sensitivity to the model. This is demonstrated in the following Fig. 3.13 where the variation of the ratio between the calculated and measured *NO* (or NO_x representing equivalent NO_2) with Φ_z variation is depicted, indicatively, for four different engine types:

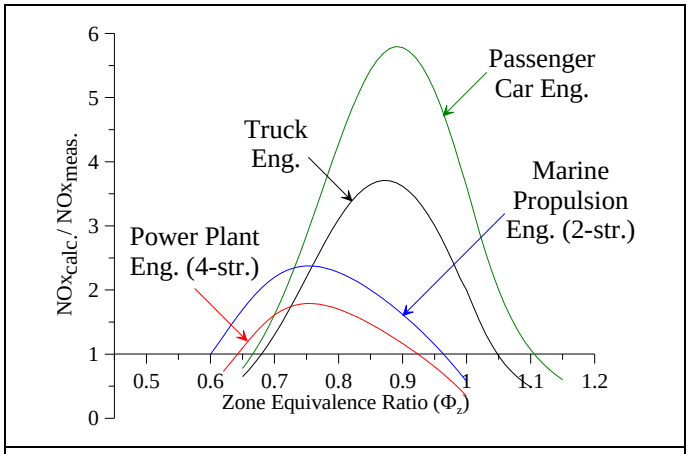

Figure 3.13: Variation of the ratio of calculated and measured NO_x with zone equivalence ratio Φ_z for four different engine types: passenger car engine with pilot injection, truck engine, 2–str. vessel propulsion engine and 4–str. constant speed power plant engine. For the first two engines NOx represent NO and for the last two, NO_x represent equivalent NO_2.

As shown in Fig. 3.13, tailpipe NO_x variation with zone Φ is similar for the engine types examined. Furthermore, the sensitivity of the model to Φ_z is obvious according to the gradient of the curves, especially for the automotive engines. The main reason for this, is the very low absolute values of *NO* emitted from these engines compared to the large–scale ones. Another important reason is the different trapped mass calculation approaches followed for each category, which have been described in sections 3.3.5 – 3.3.7. Namely, the magnitude of the bell–curve of Fig. 3.13 strongly depends on the estimated amount of trapped mass (m_{tr}). This amount is a determinant factor for the initial temperature of unburnt zone ($T_{ub,0}$) as described in Eq. (3.47) of section 3.5.2. From this equation, it is obvious that the augmentation of the trapped mass induce unburned zone temperature decrease and hence combustion zone temperature decrease and vice versa. According to this and from the observation of Fig.

3.14, it can be inferred that the sensitivity of the proposed model to Φ_z is intensified with the decrease of trapped mass and hence with the increase of unburnt charge temperature.

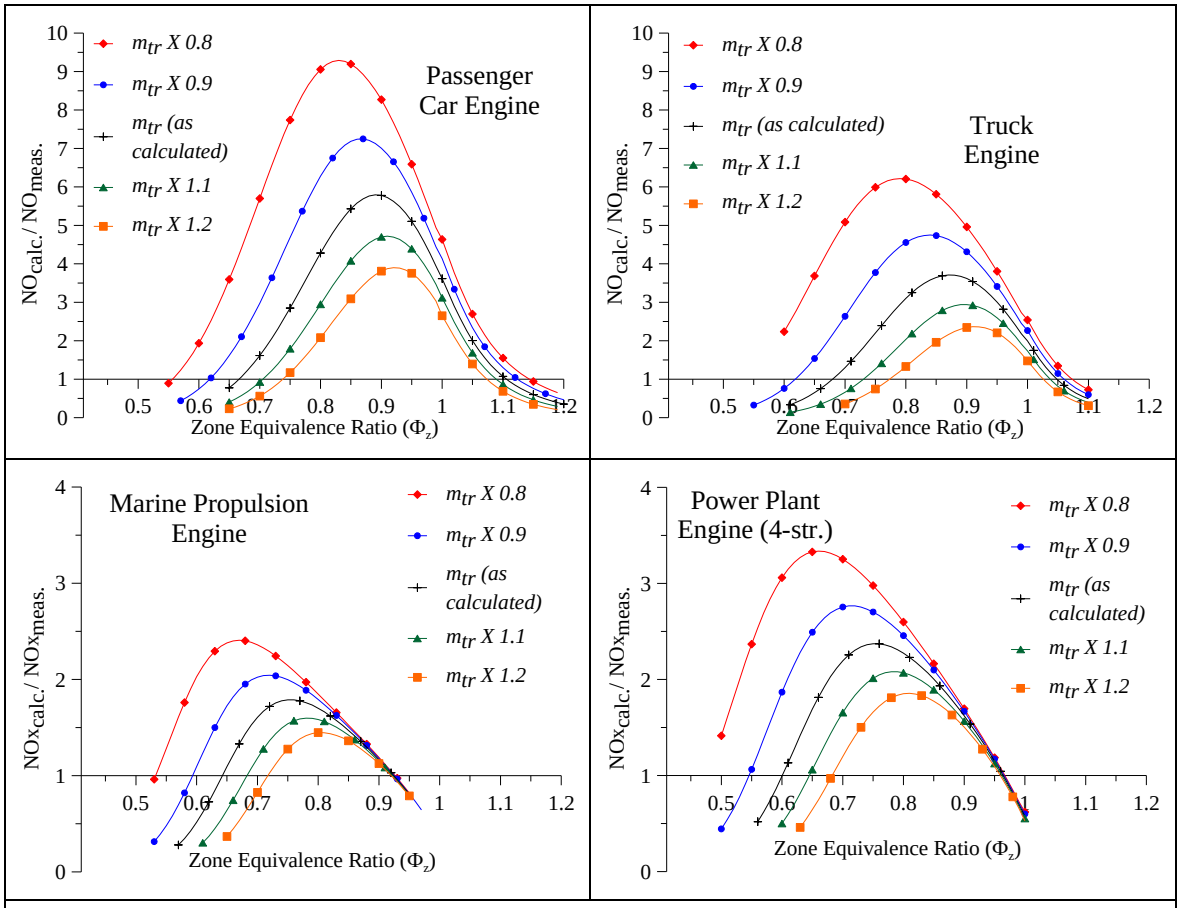

Figure 3.14: Variation of the ratio of calculated to measured NO_x with zone equivalence ratio Φ_z and trapped mass amount for four different engine types: upper left: passenger car engine, upper right: truck engine, lower left: 2–str. marine propulsion engine and lower right: 4–str. constant speed power plant engine. For the first two engines NOx represent NO and for the last two, NO_x represent equivalent NO_2.

Furthermore, regarding Fig. 3.13 and 3.14, it is clearly shown that the calculated *NO* presents a maximum for equivalence ratios (Φ) in the fuel lean region not far from stoichiometry, which is in accordance with the literature [8]. This is explained as follows: Very low Φ means high fraction of "cold" unburnt charge amount in the mixture, hence the combustion temperature will be relatively lower compared to the most favorable *NO* formation case. This is the case when the mixture becomes less fuel lean and approaches stoichiometry, where ideal combustion occurs and oxygen concentration is adequately high but there is not exorbitant "cold" unburnt charge in the mixture to absorb heat and decrease the temperature as in the cases of lower Φ. On the contrary, as the mixture becomes richer, even before stoichiometry ($\Phi=1$), despite the ideal combustion and the temperature increase, the oxygen concentration decreases resulting in lower *NO*. For stoichiometric and fuel rich mixture ($\Phi>1$) inside the zone, the oxygen for *NO* formation is derived only from the dissociation of the combustion products (see Table 3.1), since the oxygen derived from the entrained unburnt charge has been completely consumed from the combustion process. After combustion, no further oxidizer entrainment from the unburnt zone to the combustion zones occurs. Hence the fractions of oxygen (O & O_2) and also N_2, N and OH participating in the *NO* formation used (see Table 3.4), are continually decreasing because the increasing fractions of the products, derived from the dissociation of the excess fuel, are taking their place. The

last also affects the dissociation reactions' equilibrium constants (see Table 3.2) and thus the final equilibrium composition. Moreover, late during expansion, as temperature decreases further, the production of oxygen through the dissociation effect is diminishing. To provide a schematic representation of the previous justification, in Fig. 3.15, the variation of the equilibrium mole fractions of O_2, O, OH, N, N_2 (which are participating in extended Zeldovich mechanism – see section 3.5.7) with zone equivalence ratio Φ and CA time is indicatively depicted for the tenth zone generated in the combustion chamber of a large–scale *2*–

stroke marine propulsion engine. In Fig. 3.15, the variation of the kinetically formed *NO* is also depicted.

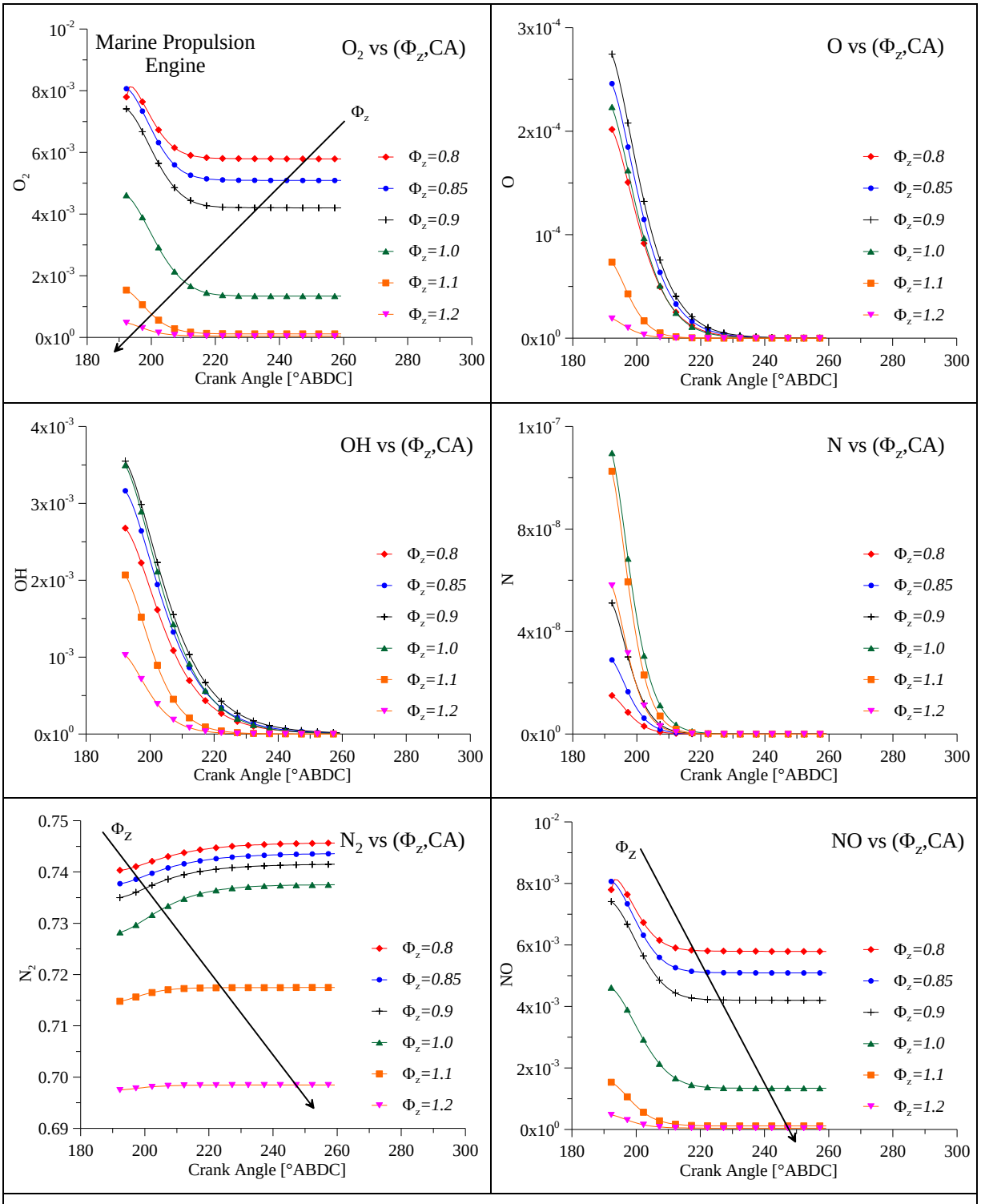

Figure 3.15: Variation of the equilibrium mole fractions of O_2, O, OH, N, N_2 and kinetically formed NO, for a specific zone (i.e. zone 10 which is generated at the 10th CA step after SOC).

Nonetheless, the most important observation of Fig. 3.13, is the occurrence of two ideal values of zone Φ_z that provide optimum results, namely $\frac{calc.NO}{meas.NO} = 1$, called Φ^*. The Φ^* value, for each test case examined, was derived directly from the process depicted in Fig. 3.13, using the modified false position, root finding method (*regula falsi*) [227] described in Appendix g. In order to estimate the ideal value (Φ^*) of zone equivalence ratio (Φ_z) for each

operating point, an empirical correlation is introduced. This correlation involves typical engine operating parameters and values derived from the measured cylinder pressure processing and *HHR* analysis.

The empirical/statistical correlation for the estimation of Φ_z (calculated only once for an engine cycle) emerged from a multiple regression analysis using numerous engine operating parameters and special parameters derived from the processing of pressure trace and *HRR* analysis in order to correlate them with Φ^*. The data for this analysis have been derived from all test cases examined. Some of the examined parameters are demonstrated in Table 3.5:

S/N	Parameter Definition	S/N	Parameter Definition
1	$p_{amb}[bar]/1[bar]$	8	$\theta_{comb.max}/TDC$
2	$T_{amb}[°C]/25[°C]$	9	SOC_{main}/TDC
3	$p_{compr.start}/p_{amb}$	10	$\theta_{HRR\ max}/TDC$
4	$p_{SOC_{main}}/p_{amb}$	11	$\Phi_{eng.overall}$
5	$p_{comb.max}/p_{SOC_{main}}$	12	$\Phi_{cyl.overall}$
6	$p_{comb.max}/p_{amb}$	13	$S_p/S_{p_{ref}}$
7	COC/TDC	14	P/P_{ref}

Table 3.5: The engine operating parameters and special parameters of the measured pressure trace and HRR diagram used in the multiple regression analysis to evaluate their correlation with zone equivalence ratio Φ_z.

In the previous table, p is the pressure, θ is the *CA* after bottom dead center (*ABDC* $\equiv 0^{+}°$), P and S_p are the engine brake power and mean piston speed respectively. P_{ref} corresponds to the nominal brake power regarding large–scale engines and to the maximum brake power output regarding the automotive engines. $S_{p,ref}$ has been defined equal to *10 [m/s]*. SOC_{main}, *COC* and *TDC* (*TDC≡180° CA ABDC*) are the *CA* of start of main combustion, center of combustion and top dead center respectively *ABDC*. Subscripts *compr. start* denotes the *CA [°ABDC]* where the compression initiates, namely intake valve closure (*IVC*) for *4*–stroke engines and exhaust valve closure (*EVC*) for *2*–stroke engines, *comb. max* denotes the *CA [°ABDC]* where the maximum pressure occurs after combustion commencement and *HRR max* denotes the *CA [°ABDC]* where the maximum *HRR* occurs. p is the absolute in–cylinder pressure $\Phi_{eng.\ overall}$ and $\Phi_{cyl.\ overall}$ is the mean engine and cylinder equivalence ratio respectively. The last two are defined in Eq. (3.100):

$$\Phi_{eng.overall} = \frac{\dot{m}_{f\,eng}}{\dot{m}_{IA}} \cdot \frac{\nu_{O_2} \cdot MW_{O_2}}{y_{amb\,O_2}}$$
$$\Phi_{cyl.overall} = \frac{m_{f\,cyl}}{m_{tr}} \cdot AFR_{st} \qquad (3.100)$$

where $\dot{m}_{f_{eng}}$ and $\dot{m}_{IA}$ are the engine's fuel and ambient air mass flow rates *[kg/h]* respectively, ν_{O2} *[kmol/kg fuel]* is the O_2 stoichiometric coefficient calculated from Eq. (3.32) for the fuel used as described in section 3.4.5, MW_{O2} is the molecular weight of O_2, $y_{amb_{O_2}} = 0.232$ is the typical mass fraction of O_2 in ambient air, $m_{f_{cyl}}$ and m_{tr} are the burnt fuel and trapped unburnt charge mass *[kg]* in the cylinder during an engine cycle respectively. $m_{f_{cyl}}$ is calculated from Eq. (3.41) in section 3.4.7 and m_{tr} is calculated as described in section 3.3.

As revealed from the aforementioned analysis, only the "*right-side*" Φ^* value (see Fig. 3.13) can be associated with some of the parameters of Table 3.5. This is convenient for the following reasons:

- The Extended Zeldovich *NO* formation mechanism used in the present model, is commonly considered valid/reliable for combustion near stoichiometry. This is not deviate significantly from reality since during *NO* formation, the local Φ is close to stoichiometry (stoichiometric diffusion flame [15]).
- Furthermore, the "*left-side*" Φ^* value (see Fig. 3.13) is close to the cylinder overall mean equivalence ratio ($\Phi_{cyl.,overall}$). This is a shortcoming, because for Φ values less than $\Phi_{cyl.,overall}$, the calculation concept followed (see section 3.5.1) collapses. This is caused from the assumption of constant Φ for all zones during the entire engine closed cycle. Hence, if $\Phi < \Phi_{cyl.,overall}$, the available unburnt charge will not be enough to form the total of the resulting zones during combustion of the injected fuel which have been distributed to these zones. Then, the mass for the unburnt zone will unlikely become zero and the calculation procedure will be terminated. Additionally, even if Φ is slightly greater than $\Phi_{cyl.,overall}$, convergence issues may occur.
- Moreover, as shown in Fig. 3.14, the "*right-side*" Φ^* has smaller sensitivity to the trapped mass amount compared to the "*left-side*" one.

Then, an elimination procedure was adopted to disqualify the parameters which are correlated less with the "*right-side*" Φ^* in order to simplify the polynomial for zone Φ calculation, minimize the introduced error sources and keep low the number of the required inputs. This procedure was performed using the *F* and *t* test [238] and also *AIC* and *BIC* models [239,240] via computer statistical programs [241,242,243], intending to keep as less parameters as possible without significant deterioration of the coefficient of determination (R^2).

When the previous procedure was completed, the experimental data from all test cases of the remaining parameters demonstrated in Table 3.6, were utilized through a multiple regression analysis in order to be correlated with Φ^*. From this analysis a lineal polynomial for the prediction of the suitable zone equivalence ratio (Φ_z) was derived. The acquired polynomial is an empirical correlation which calculates the Φ_z as a function of these parameters. The significance of the chosen parameters is evident since they provide information for the quality and quantity of fuel/unburnt–charge mixture preparation and other important characteristics of combustion such as ignition timing, combustion duration and combustion evolution, which are mainly affected/determined from the mixture evolution in the cylinder.

These characteristics are critical for the description of combustion and hence *NO* formation, especially for the Diesel cycle.

S/N	Parameter Definition
1	$p_{compr.start}/p_{amb}$
2	$p_{SOC_{main}}/p_{amb}$
3	$p_{comb.max}/p_{SOC_{main}}$
4	COC/TDC
5	$\Phi_{eng.overall}$
6	$S_p/S_{p_{ref}}$
7	P/P_{ref}

Table 3.6: The chosen parameters that the statistical analysis indicates as the most effective on zone equivalence ratio Φ_z.

1. The first (*1*) parameter of Table 3.6 indicates the effect of the supercharger (intake manifold pressure).
2. The second (*2*) parameter provides information for the effective compression of the trapped charge inside the cylinder before combustion initiation.
3. The third (*3*) parameter indicates the grade of pressure rise (pressure derivative) due to the combustion event (which strongly affects *NO* formation) and is related with the injection timing, by comparing the pressure at the commencement of combustion ($p_{SOC_{main}}$) against peak combustion pressure ($p_{comb.\max}$).
4. The fourth (*4*) parameter provides information for the temporal evolution of the combustion during the engine cycle (i.e. combustion duration).
5. The fifth (*5*) parameter provides information for the overall engine intake ambient air supply with respect to the injected amount of fuel.
6. The sixth (*6*) parameter introduces the effect of piston speed (engine speed), which is related with the in–cylinder charge perturbation (which contributes in fuel–air mixing) and the available time for NO_x formation.
7. Finally, the seventh (*7*) parameter introduces the effect of engine load.

In general, the aforementioned parameters provide information for the quality and quantity of fuel–unburnt charge mixture preparation, ignition timing and the developed pressures and temperatures inside the cylinder, which have a significant effect on *NO* formation.

The final multiple regression analysis was conducted using a weighted (bisquare) least squares robust–fit regression method using a computer program [242]. The extracted polynomial is described in Eq. (3.101) and it is determined from two sets of coefficients

demonstrated in Table 3.7, one for each category, automotive and large–scale Diesel engines.

$$\Phi_z = c_0 + c_1 \cdot \left(\frac{p_{compr.start}}{p_{amb}}\right)^{-1} + c_2 \cdot \left(\frac{p_{SOC_{main}}}{p_{amb}}\right)^{-1} + c_3 \cdot \frac{p_{comb.max}}{p_{SOC_{main}}} + \\ + c_4 \cdot \frac{COC}{TDC} + c_5 \cdot \Phi_{eng.overall} + c_6 \cdot \frac{S_p}{S_{p_{ref}}} + c_7 \cdot \frac{P}{P_{ref}} \tag{3.101}$$

Polynomial Coefficients	Automotive Engines	Large–Scale Engines
c_0	2.2978E+00	1.2186E+00
c_1	-5.4755E-01	1.8397E-01
c_2	3.1672E+01	-4.7380E+00
c_3	-2.2693E-01	-1.2459E-01
c_4	-1.2151E+00	-1.3805E-01
c_5	1.8754E-01	1.0553E-01
c_6	2.4215E-01	7.6885E-02
c_7	6.0551E-03	-7.7165E-02

Table 3.7: The coefficients of the polynomial for the prediction of zone equivalence ratio Φ_z for automotive and large–scale Diesel engines.

The root mean square error (*RMSE*) between the polynomial predictions Φ_z and target Φ^*, which is calculated from Eq. (3.102), is *1.47%* for the automotive engines and *1.49%* for the large–scale Diesel engines.

$$RMSE\ [\%] = \sqrt{\frac{1}{M} \cdot \sum_{t=1}^{M} \left(\Phi_{z_t} - {\Phi^*}_t\right)^2} \cdot 100 \tag{3.102}$$

In the previous expression, *M* is the total number of the test cases comprised in the sample and *t* is the sequence number of each one of them.

The use of the aforementioned empirical correlation, significantly improves qualitative the model's results for the NO_x emissions when compared to the use of an arbitrary constant Φ_z (e.g. $\Phi_z = 1$) or the average of the actual suitable Φ^* (i.e. $\Phi_z = \overline{\Phi^*}$) which have been also examined. However, when the model is implemented on a different engine, despite the adequate trend prediction, the calculated absolute NO_x values, may have noticeable divergence from the experimental ones. Thus to improve the results quantitatively, the raw calculated values should corrected using a single scaling factor (*SF*) for each engine design. This is discussed in section 3.5.10.

At this point, it should be noted that even though the statistical analysis conducted herein provides a strong indication that the aforementioned parameters correlate well with

zone equivalence ratio Φ_z, further validation of the extracted correlation is required, by making use of a greater range of engine configurations, operating points and engine types, to come into general conclusions.

As mentioned, a different set of the coefficients ($c_0 - c_7$) of Eq. (3.101) is used for the two engine categories examined, i.e. automotive and large–scale engines. This can be attributed to the differences in geometrical and operational characteristics of the examined types of engines which directly or indirectly affect the in–cylinder conditions and combustion evolution and hence NO_x formation. The most important of them are the following:

- Engine magnitude, cylinder volume, intake air and injected fuel amount.
- Engine speed which is much lower in large–scale engines.
- Fuel injection technology. The automotive engines use common rail system while the specific large–scale engines examined in the present work, use jerk type fuel pumps with a plunger moving in a matched barrel [55], commonly, one for each cylinder.
- Fuel type. Large–scale engines use heavy–fuel oil (for the test cases examined) while automotive engines uses ultra–low sulfur Diesel fuel.
- Type of engine cycle (*2/4* stroke) and scavenging method. The majority of the large–scale engines examined are *2*–stroke in contrast to the automotive engines which are *4*–stroke.
- Supercharging method. Pulse pressure for the automotive engines and constant pressure for the large–scale ones.
- The automotive engines are optimized/designed for low emissions (e.g. use *EGR* system, special injectors for low emissions, etc.) to comply with the much stricter legislation limits compared to the respective ones for the large–scale engines.
- Finally, in automotive engines combustion chamber design (e.g. geometry of the piston bowl, cylinder head, etc.), fuel injection and valve timing strategies, are much more complicated/advanced compared to the respective ones of large–scale engines used in ships and power plants.

Nevertheless, a plausible question arises: why the aforementioned parameters were not directly correlated with the raw NO_x measurements? To answer this question, an investigation was conducted to create a totally empirical correlation for NO_x predictions. This investigation revealed that the empirical correlation, derived from a multiple regression analysis similar to the one applied for the determination of Φ_z, provides adequate results for only a small part of the examined operating points. In most cases fails to capture the trend and moreover, it presents very high sensitivity to the input parameters resulting in unacceptable NO_x predictions.

In the section below, a synoptic flow–chart of the proposed NO_x model is presented.

3.5.9 The Flow–Chart of the Proposed NO_x Model

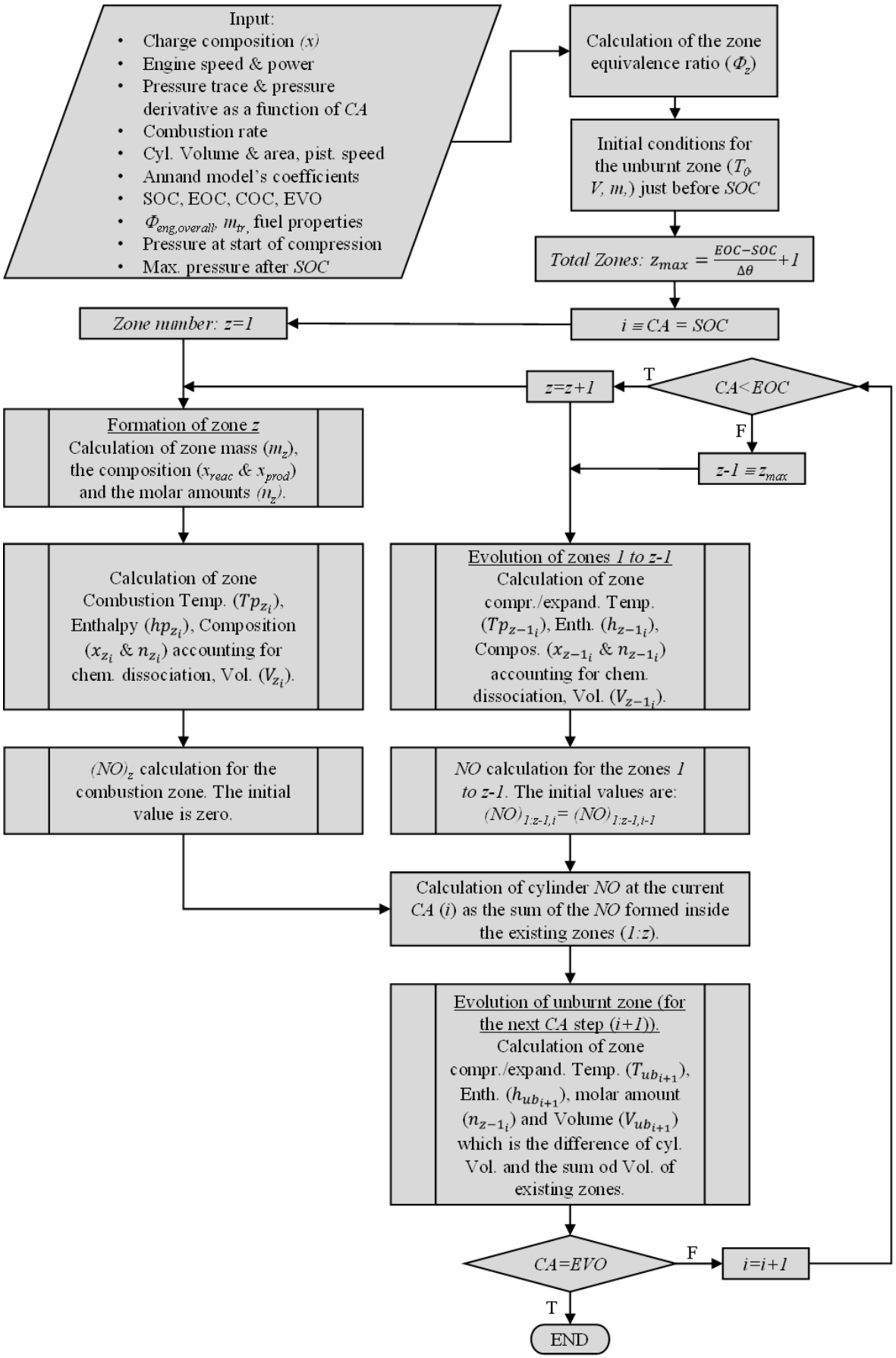

3.5.10 Calibration of the NO_x Model

Although the model captures the trend of *NO* formed in the automotive engines examined, when engine power, *SOI*, *EGR*, injection and manifold pressure vary and the trend of NO_x formed in the large–scale engines examined, when engine power and injection timing vary, a percentage diversion of the predicted absolute values from the respective measured ones may exist. To compensate this, a scaling factor (*SF*) is applied on the calculated values, as described in Eq. (3.103) to optimize the results quantitatively. This factor is constant and unique for each engine and is calculated from the ratio of the measured and calculated *NO*, at a specific operating point (calibration point (*c*)) as described in Eq. (3.104):

$$calibr.NOx_{eng,i} = calc.NOx_{eng,i} \cdot SF_{eng} \tag{3.103}$$

$$SF_{eng} = \frac{meas.NOx_{eng,i=c}}{calc.NOx_{eng,i=c}} \tag{3.104}$$

where subscripts *i* and *eng* denote the operating point and the examined engine respectively. Particularly, for the large–scale engines, the *SF* is calculated as the measured NO_x at the higher available load point. This point (*70–90*% of nominal engine power) was chosen because it has the highest weighting factor in the test cycles defined by *IMO Annex VI regulation 13* for NO_x [46] emissions and also, it is close to the actual operating point of most marine engines.

For the examined large–scale engines, the *SF* ranges from *0.79* to *1.39* with an average value at *1.02* and standard deviation at *16%*. However, no *SF* was used for the automotive engines for the following reasons:

1. The average relative error was close to unity.
2. The results are acceptable even without calibration.
3. High fluctuation of relative error.
4. High relative error of some cases (due to the much lower absolute *NO* emissions values compared to the large–scale engines).
5. The automotive engines operate in wide range on engine map (engine speed/load) without any specified frequency. Thus, the select of a specific calibration point (as for the marine engines case) could not be justified.

Hence, if an arbitrary calibration point is chosen, due to the aforementioned reasons *3* and *4*, there is a high possibility to select an inadequate point (e.g. with relative error far from the average one or a very high relative error) and therefore seriously deteriorate the results.

The extracted results from the model, after calibration, are presented in the next chapter.

Chapter 4 APPLICATION OF THE PROPOSED MODEL

4.1 Model Application on Large–Scale Diesel Engines

4.1.1 Description of the Test Engines

For the validation and evaluation of the proposed NO_x prediction model, measurements from two different engine categories were used: marine and stationery large–scale *DI* Diesel engines and automotive *DI* Diesel engines. In the present section, the implementation of the model on the engines of the first category is presented. The model was implemented on sixteen different large–scale Diesel engines. The experimental data were acquired from measurements attained on–board and in real–time from *NTUA* internal combustion engine (*ICE*) laboratory research group. The examined engines are categorized into *2* and *4*–stroke, used for propulsion and power generation on ships and for power generation on power plants in Greek Islands. All engines are supercharged and the intake air is cooled from a sea–water heat exchanger. The examined engines use jerk type fuel pumps [55] one for each cylinder. The *2*–stroke engines use a uniflow scavenging system with an exhaust head–valve. The basic geometric and operating features of the examined engines are presented in Table 4.1 [56]:

Engine	Cyl. Numb.	Bore [mm]	Stroke [mm]	Comp. Ratio	Nom. Pow. [kW]	Nom. Speed [rpm]	Cycle	Application
A	9	600	1650	18.5	14840	143	2–str.	Pow. Gen.
B	9	600	1650	18.5	14840	143	2–str.	Pow. Gen.
C	7	500	2000	17.9	11080	127	2–str.	Ship Prop.
D	7	600	2400	17.9	16640	105	2–str.	Ship Prop.
E	7	600	2400	17.9	16640	105	2–str.	Ship Prop.
F	12	980	2660	18.5	68340	94	2–str.	Ship Prop.
G	7	840	2400	18.3	28350	102	2–str.	Ship Prop.
H	7	980	2660	18.5	40040	94	2–str.	Ship Prop.
I	6	700	2800	17.9	18620	91	2–str.	Ship Prop.
J	7	600	1650	18.0	11500	143	2–str.	Pow. Gen.
K	6	400	1770	18.0	6810	146	2–str.	Ship Prop.
L	7	600	2400	17.9	15810	105	2–str.	Ship Prop.
M	7	225	300	13.1	905	720	4–str.	Ship Gen.
N	7	210	320	17.0	1120	720	4–str.	Ship Gen.
O	7	270	380	15.9	2310	720	4–str.	Ship Gen.
P	12	460	580	14.5	12600	500	4–str.	Pow. Gen.

Table 4.1: The examined large–scale engines and their basic engine geometry and operation data.

4.1.2 Test Cases Examined

In the present study, *18* measurement sets taken from *16* large–scale, *DI* Diesel engines, presented in Table 4.1, were utilized for the evaluation of the proposed model on NO_x predictions for large–scale engines. The total number of the test cases examined herein is *89.* As mentioned in section 4.1.1, the measurements (i.e. pressure trace acquisition, etc.) were performed by *NTUA ICE* laboratory research team using in–house software and hardware. The measurement procedure was completed in a period of *~18* months. The NO_x measurements for the aforementioned engines were taken at various engine loads and start of injection (*SOI*) timings. Here, it is clarified that for marine propulsion engines, the load variation corresponds directly to engine speed variation since the engine power follows the propeller law, namely the engine speed determines the engine load. On the contrary, for stationary engines, namely the power generators, engine speed is constant and hence the engine power is defined from generator power (load) demands. *SOI* was modified using the variable injection timing (*VIT*) [55] system whenever available. The effect of fuel change from heavy fuel oil (*HFO*) to Diesel fuel oil (*DFO*) on NO_x emission was also examined for a specific engine (Engine A, measurement 2_b). The test cases examined are summarized in Table 4.2 [56]:

Meas. set	Engine	Numb. of test points	Speed	VIT variation
1	A	6	Const.	Yes
2_a	A	12	Const.	Yes
2_b	A	5	Const.	No
3	B	6	Const.	Yes
4	C	4	Var.	No
5	D	5	Var.	No
6	E	4	Var.	No
7	F	4	Var.	No
8	G	6	Var.	Yes
9	H	6	Var.	Yes
10	I	2	Var.	No
11	J	3	Const.	No
12	K (o/b)[4]	4	Var.	No
13	K (s/t)[5]	4	Var.	No
14	L	4	Var.	No
15	M	3	Const.	No
16	N	4	Const.	No
17	O	4	Const.	No
18	P	3	Const.	No

Table 4.2: The outline of the test cases examined regarding large–scale engines.

[4] o/b: real time on board measurements
[5] s/t: bench measurements of the engine which are recorded in shop–test reports

The pressure trace acquisition, pegging and transformation from time to crank angle (*CA*) domain was attained using an in–house diagnostic system which has been designed and developed by Prof. D. T. Hountalas [209,210,138,132]. The procedure has been briefly described in section 3.2.2. The system was also used for the estimation of engine power and engine fuel consumption after the processing of the measured data. This methodology has been *MARPOL* type approved [208]. These two parameters along with the resulting exhaust gas mass flow derived from the carbon balance methodology, are used to convert NO_x concentration, which is measured in *[ppm]* units, into absolute values (*[g/kWh]*, *[g/kg fuel]*) with the methodology proposed by *IMO* [46] and described in Appendix a, b and c. Additionally, as mentioned in section 3.5.7, exhaust mass flow rate and engine speed are used by the means of Eq. (3.86) to convert the measured NO_x from *[ppm]* to *[g/cycle]*. The carbon balance method used herein (demonstrated in Appendix a and described in *IMO Annex VI regulation 13* [46]), makes use of the estimated fuel flow rate and the measured exhaust emissions concentrations to calculate the exhaust flow. The exhaust emissions (O_2, CO_2, CO, NO_x, SO_2, H_2O) were measured using the *MARPOL* type approved [244] portable analyzer "*Testo 350 maritime*".

In the sections below, the ability of the proposed model to capture the variation of NO_x with engine power and *SOI* variation is presented. Furthermore, the NO_x emissions are presented in *[g/cycle]* units because the NO_x formation tendency is more clear compared to the use of *[g/kg fuel]* or/and *[g/kWh]*. Furthermore, regarding model's results, the presentation in *[g/cycle]*, minimizes the effect of the calculation error derived from the power and fuel consumption estimation.

4.1.3 NO_x Variation with Engine Power

In the present section, the ability of the proposed model to capture the trend of NO_x emissions with engine power (i.e. engine load) variation and adequately approach the measured NO_x absolute values, is evaluated. Thus, the model is implemented on all large–scale engines presented in Table 4.1.

4.1.3.1 Stationary Power Plant Engines

Initially the results for the power plant engines are presented. For Engine A, which is a *2*–stroke, constant speed stationary power generation engine, two measurement sets were available derived at different periods with different engine adjustments and ambient condi-

tions. Hence, slightly different NO_x amounts for the respective operating points were recorded. For this reason both sets were examined and the results are depicted in Fig. 4.1 and Fig. 4.2 respectively:

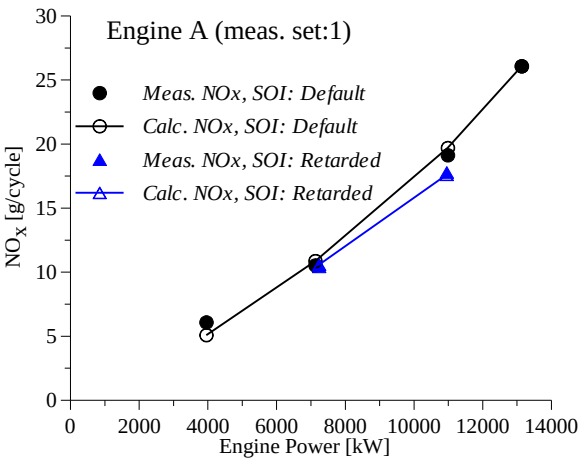

Figure 4.1: First set of measurements for Engine A. Calculated and measured NO_x vs. engine power for two different SOI settings.

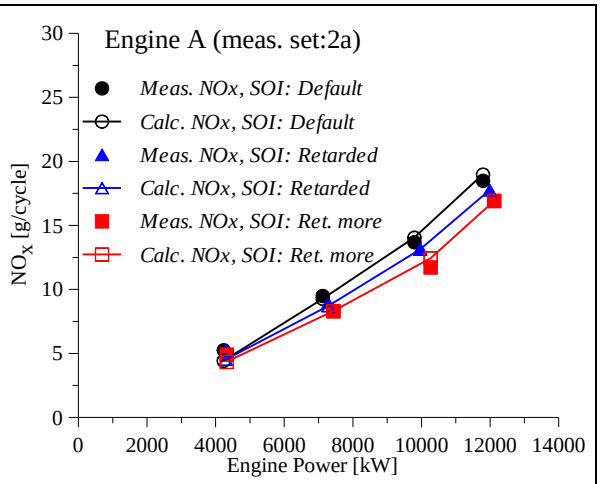

Figure 4.2: Second set of measurement (2_a) for Engine A. Calculated and measured NO_x vs. engine power for three different SOI settings.

Engine B is of the same type with A and located at the same power plant. The calculated and measured NO_x emissions of Engine B are depicted in Fig. 4.3. In these graphs (Fig. 4.1 – 4.3), the effect of the *SOI* variation on NO_x emissions is also presented. As shown, despite the relatively small decrease of NO_x with *SOI* retard, the proposed model is able to capture this variation.

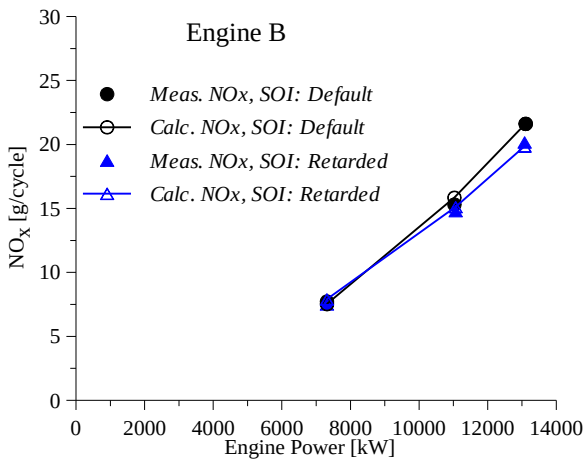

Figure 4.3: Calculated and measured NO_x vs. engine power for two different SOI settings for Engine B.

In Fig. 4.4 and Fig. 4.5 are shown respectively the results for Engine J, which is of the same type with Engine A and B (having two cylinders less) and for a *4*–stroke (Engine P) Diesel unit, both located at another power plant in a Greek Island. The outcome from these figures is that the model manages to capture NO_x variation with engine power for both engines (J and P). Additionally, from Fig. 4.1, Fig. 4.2, Fig. 4.3 and Fig. 4.4 which depicts the results for the stationary, constant speed, *2*–stroke engines, an increase of NO_x with engine power *~2 g/cycle* per *MW* is observed. On the other hand, the respective variation for

the constant speed, *4*–stroke engine depicted in Fig. 4.5 is *~1.1 g/cycle* per *MW*. As shown, the model captures the trends and absolute NO_x values adequately:

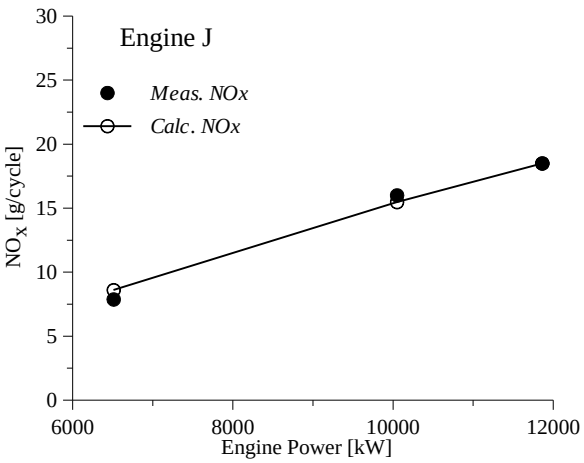

Figure 4.4: Calculated and measured NO_x vs. engine power for Engine J.

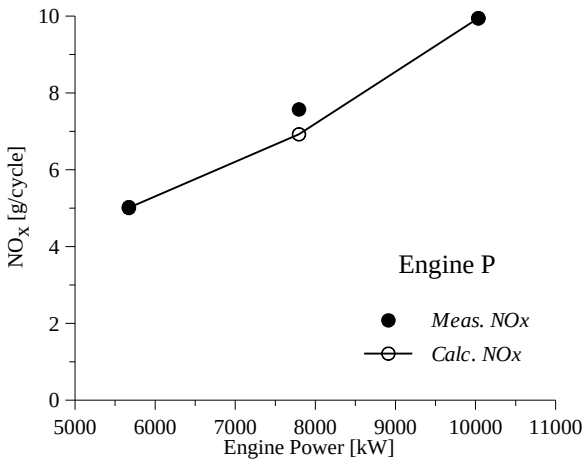

Figure 4.5: Calculated and measured NO_x vs. engine power for Engine P.

4.1.3.2 Marine 2–Stroke Main Engines

At next, the results extracted from the implementation of the proposed model on the marine main (propulsion) engines examined are demonstrated and discussed. In Fig. 4.6 the results for Engines D, E and L are presented. These engines are *2*–stroke ship propulsion ones (marine main engines), of the same type, installed on different vessels.

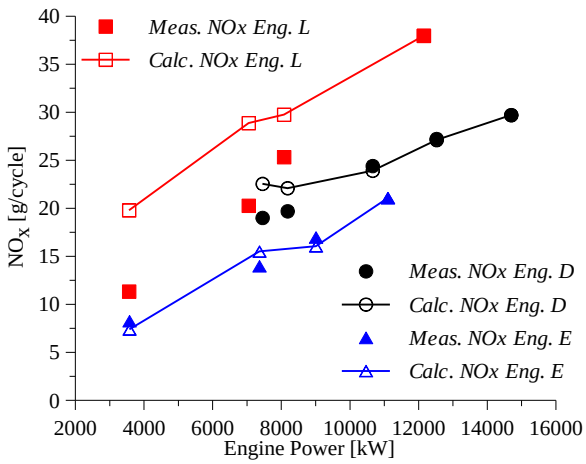

Figure 4.6: Calculated and measured NO_x vs. engine power for Engines D, E, and L.

Observing Fig. 4.6, it is shown that the respective exhaust NO_x values of the engines examined differ. However, NO_x increase with engine power for Engine D and E is similar i.e. *~1.5* and *1.7 g/cycle* per *MW* respectively in contrast to Engine L which presents a steeper variation *~3.1 g/cycle* per *MW*. This difference in trend is probably attributed to the engine setting/adjustment (e.g. *SOI*, effective compression ratio, etc.), fuel type used and ambient conditions (ambient temperature, pressure, humidity, sea water temperature). Although NO_x trend prediction is acceptable, a significant deviation of absolute NO_x values is

observed regarding Engine L (see Fig. 4.6). This is mainly due to the selection of the calibration point. Regarding Engine D, the slight deviation of the NO_x trend at low load is due to the inaccurate estimation of the zone Φ from the respective empirical correlation ((3.101)) resulted from the inaccurate determination of some of its input data. The last stems mostly from the pressure trace signal noise and its improper smoothing.

In Fig. 4.7, two different sets of measurements for Engine K are provided: on–board measurements and measurements acquired at test–bench during the shop–test procedure. For the second case, only performance measurements were acquired while NO_x values were taken from the corresponding "parent engine"[6] *NO_x–file* from which the test conditions were quite similar.

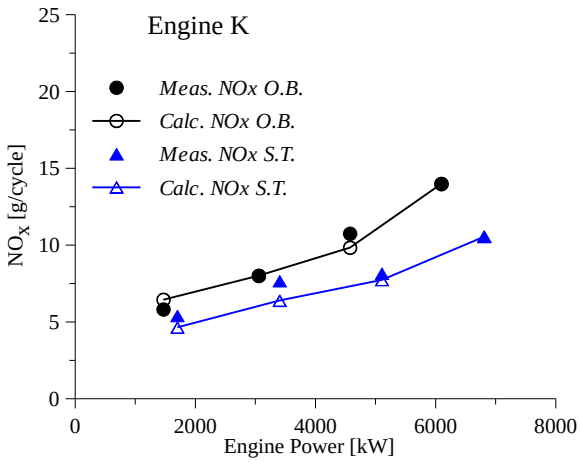

Figure 4.7: Calculated and measured NO_x vs. engine power for Engine K for on–board (O.B.) and for shop–test measurements (S.T.).

The observation of Fig. 4.7 indicates a steeper variation of NO_x with engine power for the first case *~1.8 g/cycle* per *MW* compared to the second one which is *0.9 g/cycle* per *MW*. The differences in trend and in exhaust NO_x values are to be expected because they depend strongly on the application, current engine settings and ambient conditions. However, the model manages to capture the NO_x trend for each engine because it makes use of the actual combustion characteristics provided from the measured pressure trace.

In Fig. 4.8 – 4.12 the results derived from the application of the proposed model on Engines C and F – I are shown. These are also *2*–stroke ship main engines. From these figures, it is observed a variation of NO_x with engine power *~1.1 g/cycle* per *MW* for Engine C, *~2.1 g/cycle* per *MW* for F and J, *~2.3 g/cycle* per *MW* for G and *~2.8 g/cycle* per *MW* for H and I. Specifically in Fig. 4.11, the increase of NO_x due to *SOI* advance for engine H is

[6]"Parent engine" is a test engine with the same major geometry and operation characteristics with the examined engine. The experimental emissions and performance measurements of the "parent engine" are recorded on the respective *NO_x–file*.

also demonstrated. As revealed, the model captures the NO_x trend and absolute values satisfactorily.

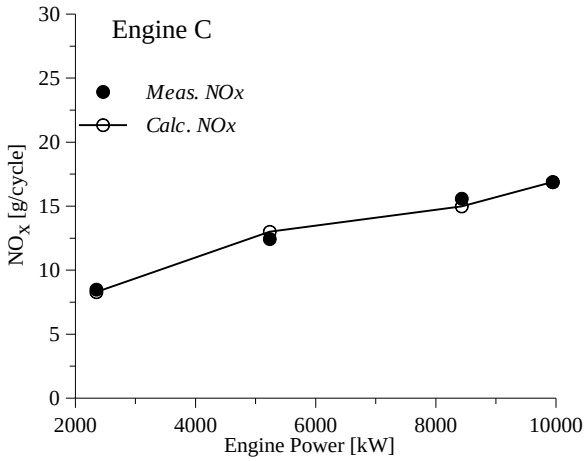

Figure 4.8: Calculated and measured NO_x vs. engine power for Engine C.

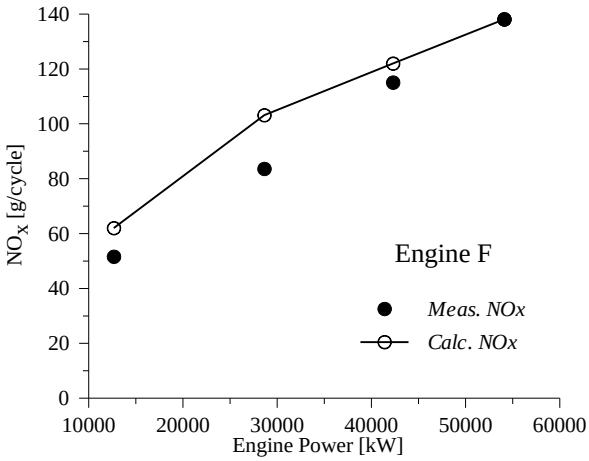

Figure 4.9: Calculated and measured NO_x vs. engine power for Engine F.

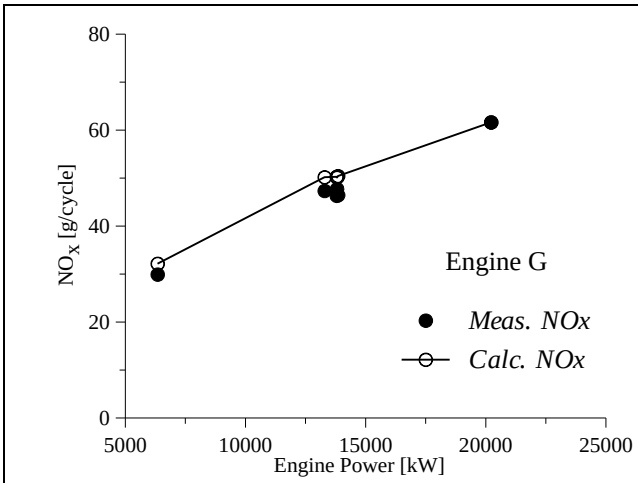

Figure 4.10: Calculated and measured NO_x vs. engine power for Engine G.

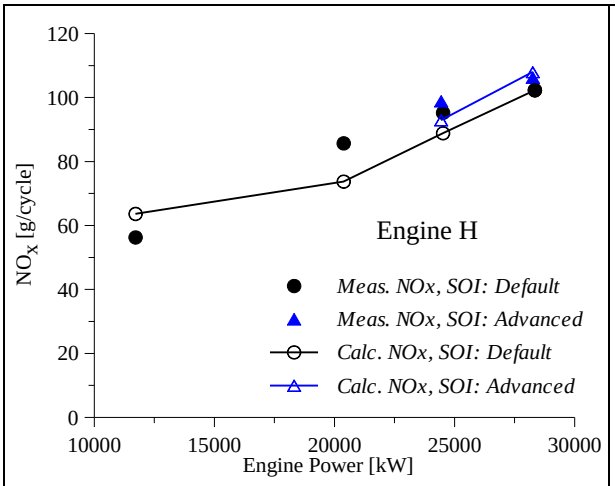

Figure 4.11: Calculated and measured NO_x vs. engine power for engine H for two different SOI settings.

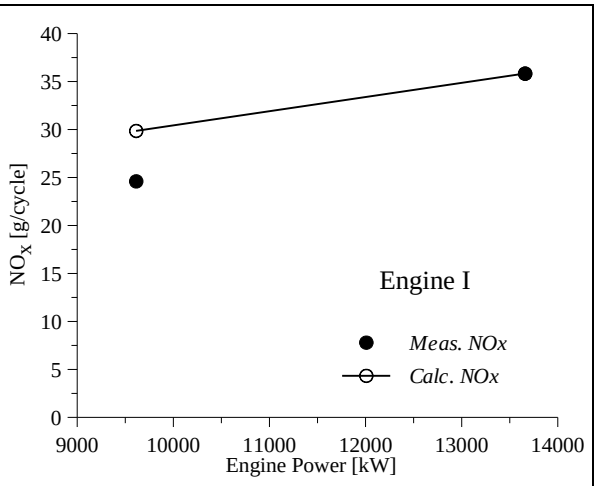

Figure 4.12: Calculated and measured NO_x vs. engine power for Engine I.

4.1.3.3 Marine 4–Stroke Auxiliary Engines

In Fig. 4.13 – 4.15 are presented the results for three *4*–stroke, constant speed, *DI* Diesel auxiliary engines which are established on different vessels and used for power generation (Engines M, N, O respectively). The observation of these figures indicates a variation of NO_x with engine power of about *~0.5 g/cycle* per *MW*. The lower slope compared to the ones of the main (propulsion) engines (*2*–stroke) is attributed to the fact that the auxiliary engines are of different design and type (i.e. *4*–stroke, having significantly higher engine operating speed which remains constant with load and have lower displacement volume), different injection strategy, etc. From Fig. 4.13 – 4.15, the ability of the proposed model to capture both, trends and absolute values for this type of engines, is also proven.

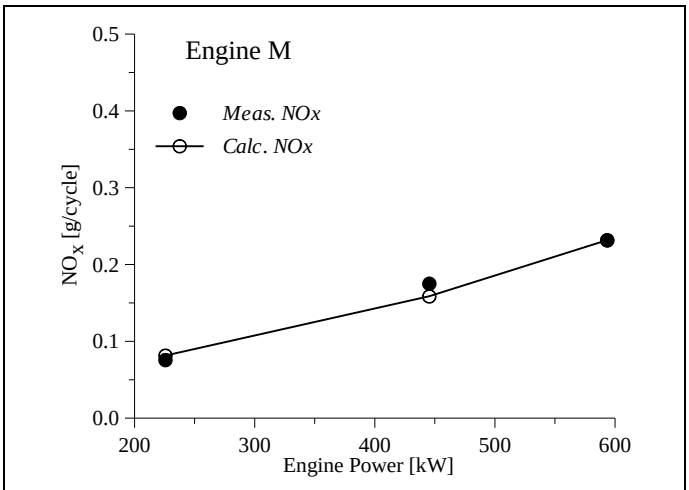

Figure 4.13: Calculated and measured NO_x vs. engine power for Engine M.

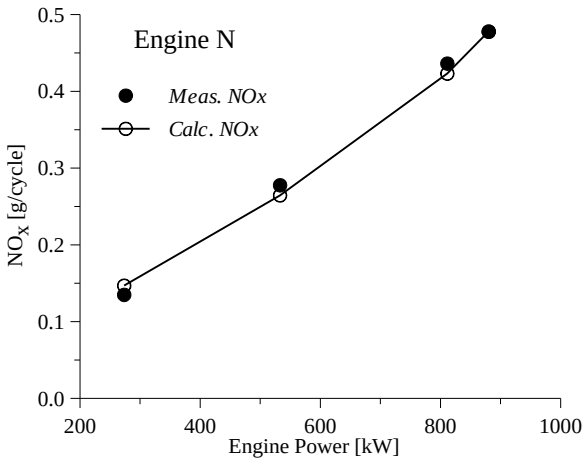

Figure 4.14: Calculated and measured NO_x vs. engine power for Engine N.

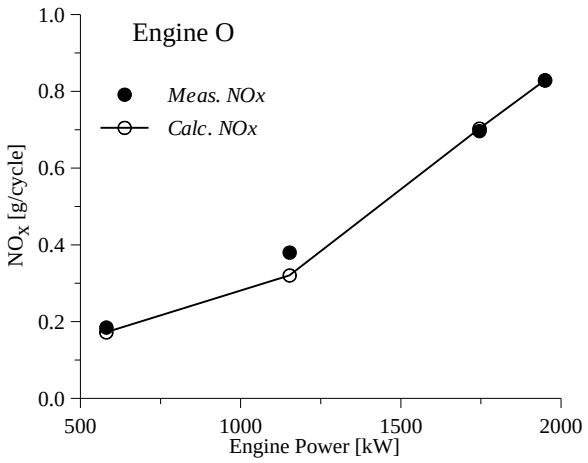

Figure 4.15: Calculated and measured NO_x vs. engine power for Engine O.

The general conclusion from the observation of Fig. 4.1 – 4.15 is the almost linear variation of NO_x with engine power but with a different gradient. It is also clear that the model is able to predict the trend of NO_x with engine load for both, *2* and *4*–stroke engines. Furthermore, for the majority of the test cases, the absolute NO_x values are approached satisfactorily.

4.1.4 Evaluation of Model Capability to Predict NO_x with the Start Of fuel Injection (SOI) Variation

It is widely recognized that *SOI* has a strong effect on NO_x emissions. *SOI* is an important parameter because of its effect on peak combustion pressure and brake specific fuel consumption. For most marine and stationary applications a *VIT* system [55] is used to adjust the *SOI*, with minimum effort and vary it according to engine power or speed. For this reason, the capability of the model to capture the effect of *SOI* on NO_x emissions is examined by detail in this section.

The calculated NO_x emissions are compared against the measured ones as *SOI* varies. However, in the following figures, the variation of NO_x with start of combustion (*SOC*) is presented. The *SOC* values, which are directly derived from the pressure trace and *HRR* analysis, presented in section 3.4, are used instead of the injection timings (*SOI*), which were not directly available, assuming that any variation in *CA* of injection timing, induces the same corresponding variation in *SOC*.

Herein, measurements from both, stationary and marine applications are used. Specifically, measurements from two *2*–stroke stationary Diesel engines (Engine A and B) used for power generation and two *2*–stroke Diesel ship propulsion engines (Engine G and H) are utilized.

4.1.4.1 Stationary 2–stroke, power plant engines

The results for the stationary *2*–stroke, power plant engines (constant speed) are depicted in Fig. 4.16 – 4.18. For these engines, the *SOI* was retarded up to ~*3 °CA* at various engine loads. The results reveal an almost linear variation (reduction) of NO_x with *SOI* retard.

The average variation of NO_x is *~-3%* per *°CA*. From these figures, is observed that the slope becomes slightly steeper with the increase of engine load. As shown a good agreement between the measured and predicted NO_x values is achieved.

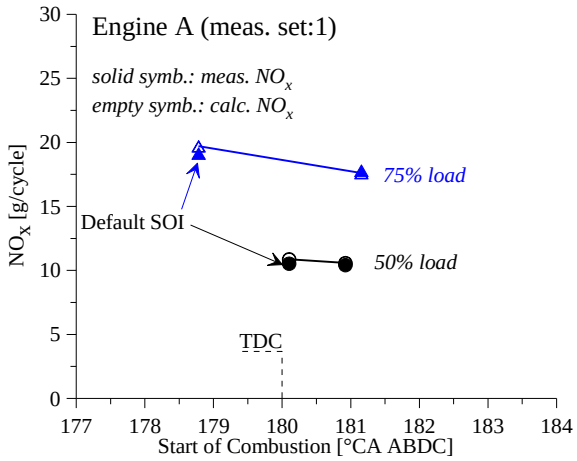

Figure 4.16: Calculated and measured NO_x vs. SOC for Engine A: 1st measurement set.

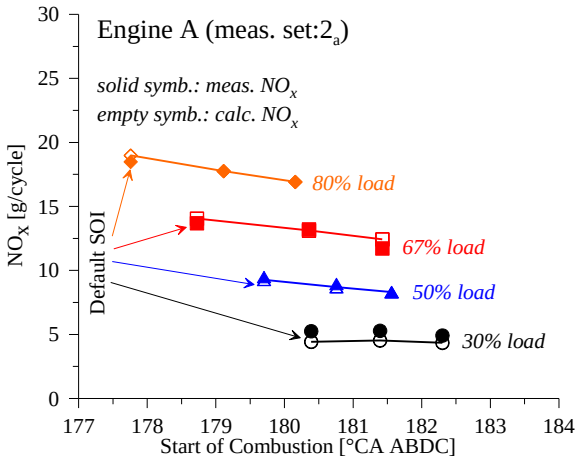

Figure 4.17: Calculated and measured NO_x vs. SOC for Engine A: 2nd measurement set (2_a).

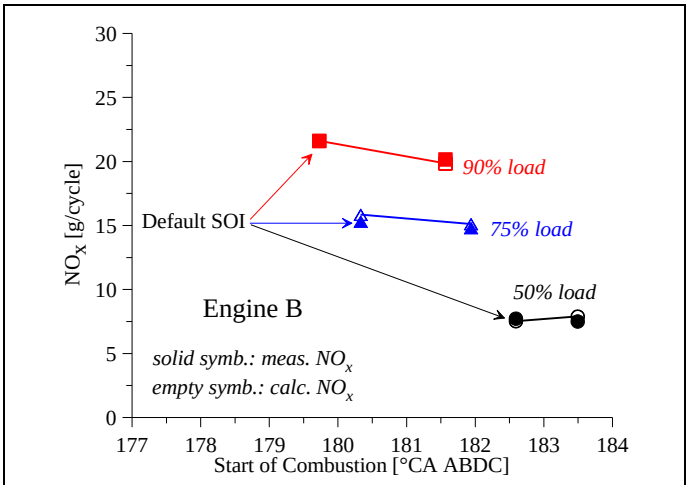

Figure 4.18: Calculated and measured NO_x vs. SOC for Engine B.

4.1.4.2 Marine 2–stroke main engines

The results for the marine Diesel Engines G and H (variable speed) are depicted in Fig. 4.19 and 4.20 respectively. From the observation of Fig. 4.19, regarding Engine G, it can be deduced that the variation of NO_x with *SOI* is negligible for the *SOI* variation range examined. The experimental data reveal that for a *SOI* retard of *~0.7°*, NO_x is reduced by *~3%*. On the other hand, advancing *SOI* by *~0.3°* and *~0.6°* from the default injection timing, a *~3%* and *~1%* NO_x reduction is induced respectively (compared to the NO_x at default injection timing). The reason for NO_x reduction in both cases, advance and retard is that the maximum combustion pressure decreases slightly, which reveals possible additional variation of other engine operating parameters. Unlikely, for the specific case, the model fails to capture the NO_x variation when *SOI* is retarded, possibly due to the very small NO_x variation

and differences in operating conditions. Furthermore, it should be noted that, for the specific case, the variation of *SOI* is too low to derive safe conclusions.

For Engine H, a NO_x increase of ~7% per ^oCA of *SOI* advance is observed for both loads examined. As shown in Fig. 4.20 the model manages to adequately capture the NO_x trend, however a constant divergence in absolute values at lower load is observed.

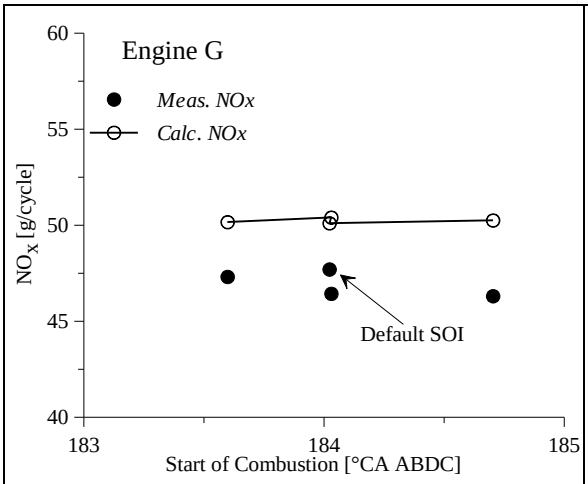

Figure 4.19: Calculated and measured NO_x vs. SOC for Engine G.

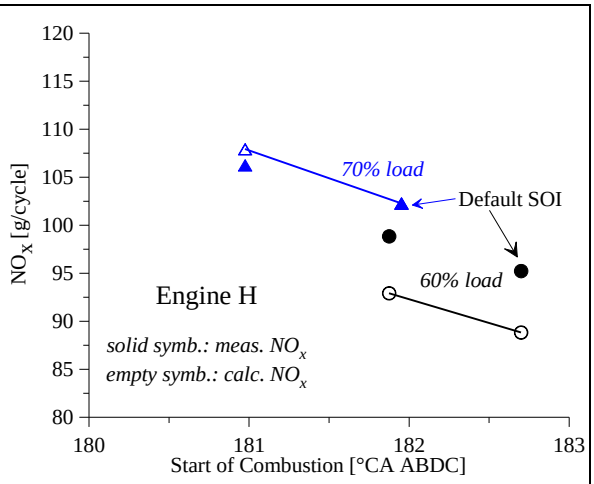

Figure 4.20: Calculated and measured NO_x vs. SOC for engine H.

As shown in the Fig. 4.16 – 4.20, for the majority of test cases, the model captures the trend of NO_x with *SOC* for the test cases examined, despite the fact that the actual variation of NO_x, in some cases, is very low.

4.1.5 NO_x Variation with Change of Fuel Type from HFO to DFO

Herein, the variation of NO_x emissions when the fuel changes from *HFO* to *DFO* (ultra–low sulfur diesel fuel oil) during engine operation is examined. This is important considering the present demand to operate engines in emission control emission areas (*ECAS*)

using low sulfur fuels. These measurements were taken in the same session (2^{nd} measurement set (2_b)) with the ones of *VIT* variation of Engine A (see Table 4.2). In Fig. 4.21, the variation of NO_x against *DFO* content in the fuel is depicted:

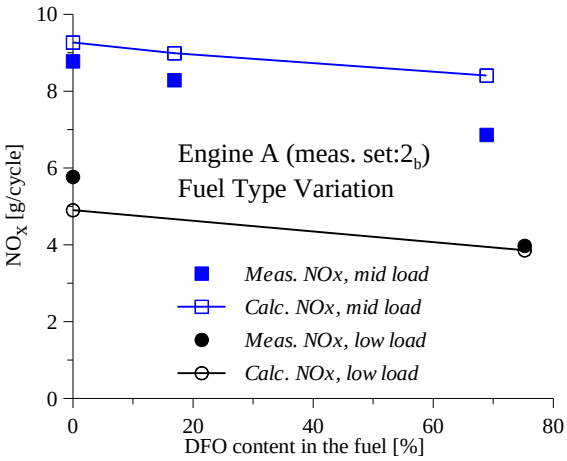

Figure 4.21: Calculated and measured NO_x vs. DFO content in the fuel for Engine A.

At this point, is mentioned that in the specific case the measurements were initiated, while the engine was operated using fuel consisting 100% of *HFO*. Following, a number of measurements were conducted during the transition from *HFO* to *DFO* operation, in order to evaluate the effect of the fuel switching on the engine performance and exhaust emissions. During the transition period it was assumed that the two fuels were completely mixed and homogenized forming an equivalent fuel (mixture of *HFO* and *DFO*) [245].

From Fig. 4.21, the ability of the model to capture the trend and adequately approach the absolute values of NO_x, as the mass percentage of the *DFO* in the fuel augments and the respective mass fraction of *HFO* decreases, is evident. The variation is approximately linear. The NO_x decrease is *~3%* per *10% DFO* content increase in the fuel for the mid–load and *~4%* per *10% DFO* content increase in the fuel for the low–load. The model accomplishes decent NO_x predictions, because it makes use of the actual *HRR* derived from the measured in–cylinder pressure trace.

The decrease of NO_x emissions with the augmentation of *DFO* content in the fuel is mainly a result of better ignitability of *DFO* fuel and hence shorter ignition delay period and thus limited high temperature premixed combustion. Moreover the *DFO* fuel consists less nitrogen compared to *HFO*, thus the fuel NO_x formation mechanism is also limited, despite the fact that its contribution in total NO_x is rather small. Moreover, as explained later, when the *DFO* content augments, the *SOI* is retarded resulting in further NO_x reduction. *SOI* retard appears to be the main cause for the observed NO_x reduction

In Fig. 4.22, is depicted the variation of *SOC* (in *°CA*) with the augmentation of *DFO* content in the fuel, derived from the processing of the "average cylinder" pressure trace. This trace is derived from averaging of the corresponding raw pressure traces of all engine cylinders. As shown in the Fig. 4.22, the *SOC*, is retarded with the augmentation of *DFO*

content in the fuel resulting in lower peak pressures and mean in–cylinder temperatures and thus lower NO_x formation.

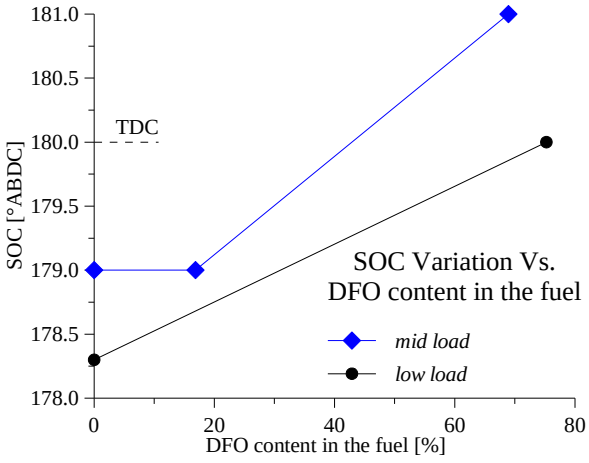

Figure 4.22: Average SOC variation vs. DFO content in the fuel for Engine A.

The *SOC* retard is due to the fuel injection retard. This is addressed to the fuel injection system characteristics and fuel physical properties, which are explained as follows:

The fuel injection system of the specific engine uses jerk type fuel injection pumps, one for each cylinder, with a plunger reciprocating in a matched barrel [55]. The reciprocating plunger has a vertical, helical crevice on its interface with the matched barrel. The position at which the crevice is aligned to the barrel's spill hole, determined from the position of the fuel rack, determines the fuel mass that will be compressed and injected to the combustion chamber.

During the upwards move of the plunger, the barrel's volume ($V\ [m^3]$) decreases and hence the pressure ($p\ [Pa]$) of the trapped fuel mass ($m\ [kg]$) increases. When the fuel pressure overtake a pressure threshold where the injector needle lifts, the injection process initiates. It is noted that the position of the plunger inside the barrel (and hence the barrel volume) is directly coupled (cam controlled) with the position of the engine's crank shaft and thus piston position with respect to *TDC*.

The fuel properties have an impact on the aforementioned fuel injection process. Specifically, due to the higher compressibility of *DFO* when compared to *HFO*, as the *DFO* content in the fuel augments during the transition period from *HFO* to *DFO*, causes a fuel compressibility increase (which means that the fuel becomes more compressible, namely for a specific pressure occupies less volume). Thus, the trapped fuel volume must be further decreased in order to acquire the adequate pressure for the injection initiation. This is also justified from the definition of fluid compressibility ($\beta\ [Pa^{-1}]$) provided in Eq. (4.1). Therefore, the plunger should be moved further upwards to achieve the required fuel pressure for injection initiation. This corresponds to a new, retarded *CA* piston position where the injector needle lifts. Hence, fuel injection, regarding *CA*, is retarded. The injection retard with the

increase of fuel compressibility has been also revealed from various investigations in *DI* Diesel engines where a variety of fuel blends were examined [246,247,248].

$$\beta = -\frac{1}{v}\cdot\frac{\partial v}{\partial p}\Big|_T = -\rho\cdot\frac{\partial\, {}^1/_\rho}{\partial p}\Big|_T = -\frac{1}{V}\cdot\frac{\partial V}{\partial p}\Big|_T\Big|_m = -\frac{\rho}{m}\cdot\frac{\partial V}{\partial p}\Big|_T\Big|_m \qquad (4.1)$$

In addition, viscosity directly affects the amount of fuel that leaks through the plunger back to the fuel pump (plunger–barrel clearance and spill hole) and through the needle to the fuel injection nozzle. High viscosity fuels lead to reduced fuel losses during the injection process compared to lower viscosity fuels, resulting in a faster evolution of pressure and thus an advance in fuel injection timing [246]. On the contrary, lower viscosity causes a less rapid pressure rise within the pump and thus injection is retarded [248]. For the examined case, the fuel viscosity is decreased with the augmentation of the *DFO* content in the fuel, due to the lower viscosity of *DFO* compared to *HFO*. This, contributes to the fuel injection timing retard. Although that the viscosity of the *HFO* is significantly decreased due to the heating of the fuel in higher temperature compared to the cases where *DFO* is used, the difference between the kinematic viscosity of the examined fuels remains noticeable as also shown in Fig. 4.23 [249].The heating of the *HFO* is applied in order to facilitate its flow in the fuel circulation and injection system.

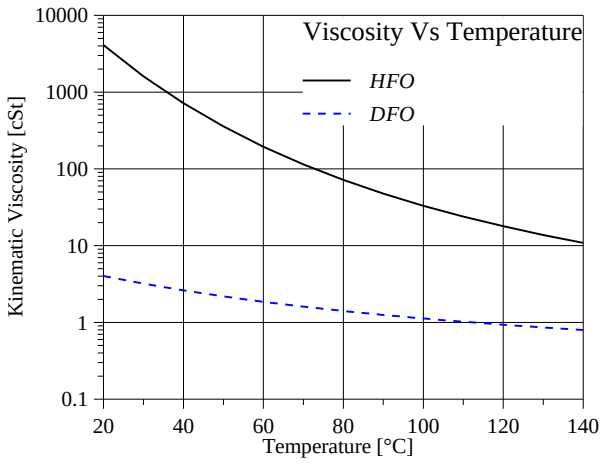

Figure 4.23: Kinematic viscosity variation with temperature for the reference fuels used (DFO and HFO).

Furthermore, considering constant engine power output and apparently constant engine speed, the fuel density (ρ *[kg/m^3]*) is decreased as the fuel *DFO* content augments, due to the lower density of *DFO* compared to *HFO* and thus the volumetric fuel flow should be increased to retain the mass flow constant. On the contrary, the fuel mass flow and hence volume flow should be decreased due to the augmentation of *LHV* with the increase of the *DFO* content in the fuel, since the *LHV* of *DFO* is slightly higher than the one of *HFO*. Nevertheless, the fuel racks position increase (which have been recorded during the measurement session), indicates that the actual fuel volume flow eventually increases. This should

cause an injection advance[7] instead of a retard, if the fuel compressibility was remaining constant. Also, the fuel ignitibility is increased as the *DFO* content in the fuel augments, since *DFO* has higher/better ignitibility than *HFO*. This should cause shorter ignition delay period and hence advanced of *SOC*. However, the fuel injection retard, deduced from the *SOC* retard (from the observation of *HRR* diagrams), indicates that the dominant fuel property that finally affects the *SOI*, is the fuel compressibility and viscosity.

From the literature [248,250,251] is known that the compressibility (β) for a given hydrocarbon liquid fuel, decreases with increasing pressure at constant temperature (T) and increases with increasing temperature at constant pressure. The compressibility is strongly dependent on the rigidity of the molecular shape, determined from the fuel molecular structure, and is decreased as the rigidity augments [251]. In addition, the fuel compressibility is increased with decreasing density (see also Eq. (4.1)), because a less dense fluid possesses more free space to be consumed during compression [250].

The effect of the *DFO* content in the fuel on the in–cylinder pressure and mean temperature, *HRR* and cumulative combustion rate[8] of the average cylinder (derived from

[7] For constant engine speed, higher volumetric flow from the fuel pump corresponds to lower plunger position at *SOI* and hence lower piston position regarding *TDC* and thus fuel injection timing advance.
[8] The cumulative combustion rate is acquired from the ratio of cumulative gross heat release (*CGHR*) at the examined instance divided with the *CGHR* at the end of combustion (*EOC*).

averaging of the respective measurements of each cylinder) is depicted in Fig. 4.24 and 4.25, for mid–load and low–load respectively:

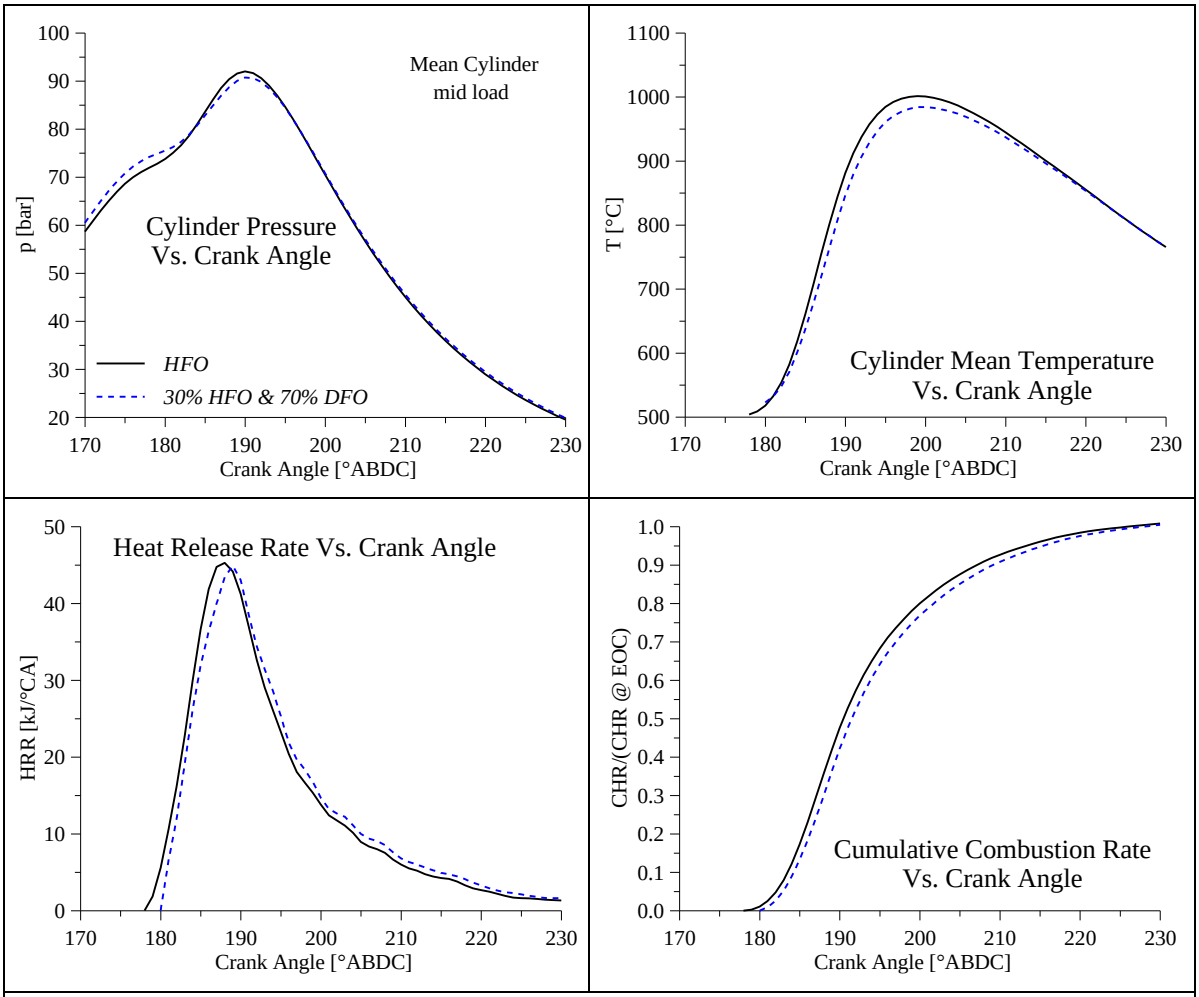

Figure 4.24: In–cylinder pressure (upper left), mean temperature (upper right), HRR (lower left) and cumulative combustion rate (lower right) vs. DFO content in the fuel for mid–load for Engine A.

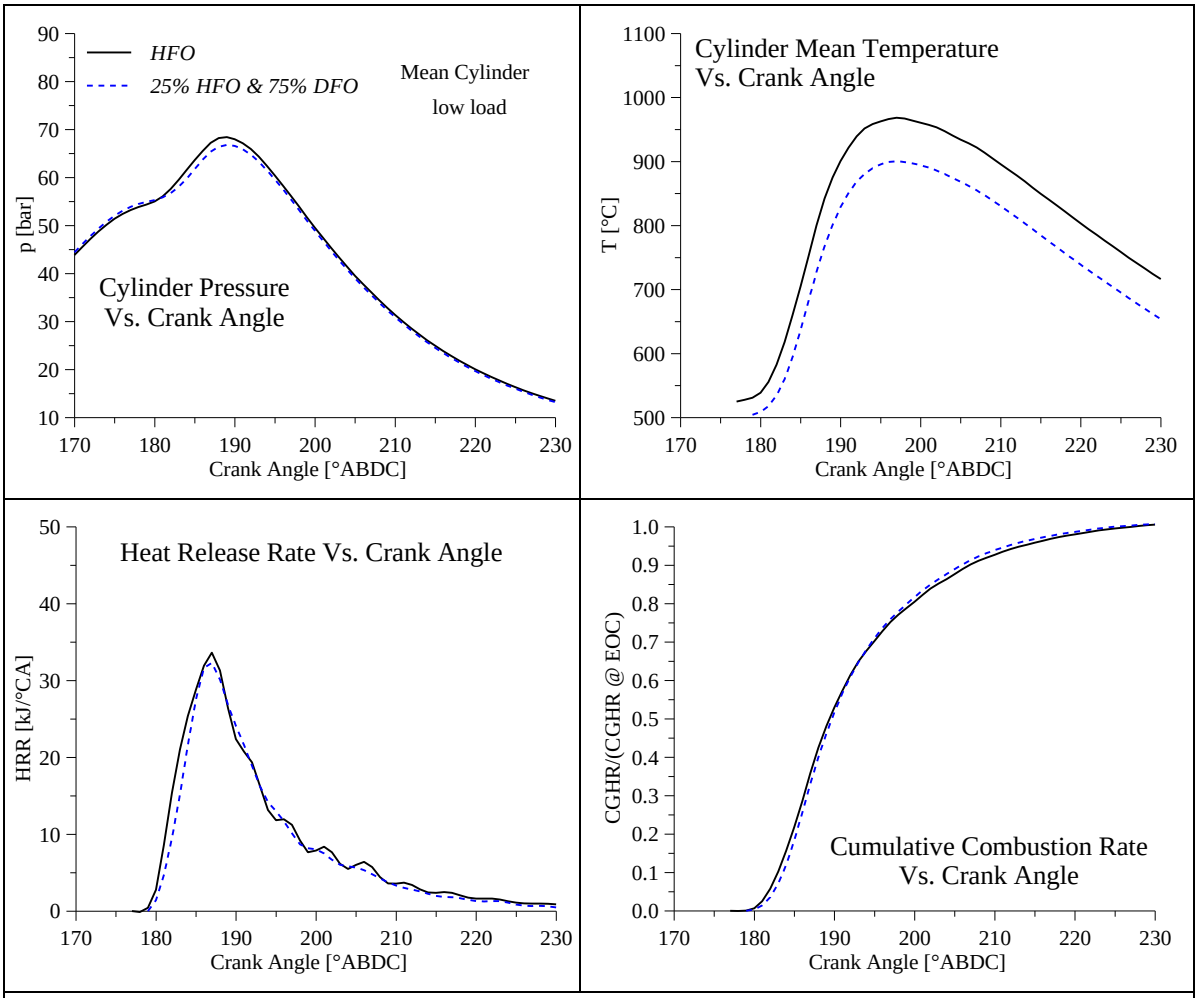

Figure 4.25: In–cylinder pressure (upper left), mean temperature (upper right), HRR (lower left) and cumulative combustion rate (lower right) vs. DFO content in the fuel for low–load for Engine A.

From the observation of Fig. 4.24 and 4.25, the effect of fuel *DFO* content is revealed. Due to the *SOC* retard, a decrease of the in–cylinder pressure is caused and the *HRR* diagram is shifted to the right. The interpretation of the last is that the combustible mixture is burnt under lower pressures (i.e. later in the cycle) and hence the derived temperatures are lower resulting lower NO_x formation. Moreover, as it can be observed, the slopes of the *HRR* and combustion rate diagrams at the first stages of combustion (i.e. some *°CA* after *SOC* and up to the *CA* of the maximum *HRR* occurrence), are slightly decreased as the fuel *DFO* content increases. This is probably attributed to the improved fuel ignitability with the increase of its *DFO* content which mitigates the effect of premixed (rapid) combustion. These, along with a slight increase of trapped mass, cause temperature reduction and thus result in less NO_x formation.

The trapped mass increase is reflected on the compression pressure increase of the in–cylinder pressure trace. This increase corresponds to intake air mass flow increase which is depicted in Fig. 4.26 where the specific intake air mass flow variation is presented, in *[kg/kWh]* units to compensate any load variation during the measurement, as the *DFO* content in the fuel augments. A possible explanation for this, is the following: Since the combustion has shifted to the right, when the exhaust valve opens, the turbine is fed with

higher enthalpy gas, thus turbocharger power increases resulting in higher scavenging air pressure and thus intake air flow. This was observed during the experimental procedure.

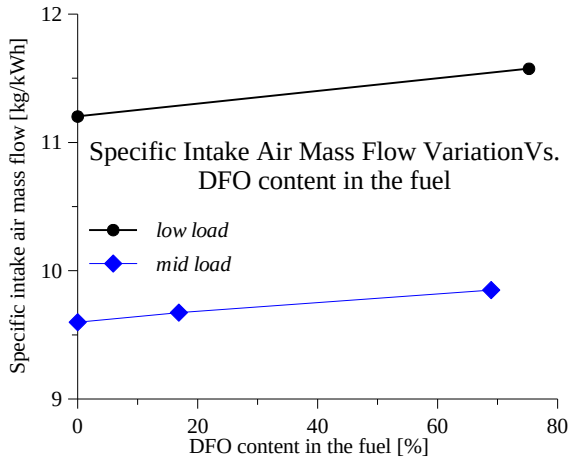

Figure 4.26: Specific Intake air mass flow vs. DFO content in the fuel for low and mid–load for Engine A.

4.1.6 Overall Results and Statistical Analysis

In the present section, the comparison between the NO_x predictions from the implementation of the model on the large–scale engines and the respective measured ones, is demonstrated. The overall comparison between calculated (after calibration) and measured NO_x absolute values is depicted in Fig. 4.27:

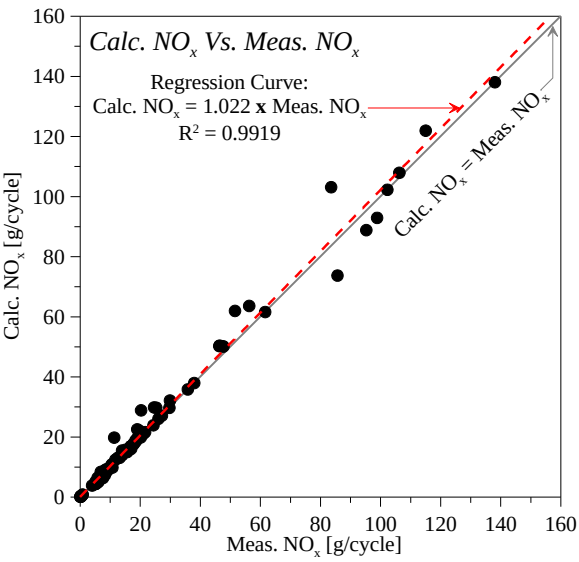

Figure 4.27: Comparison of calculated against measured NO_x values for the entire range of the available measurements for large–scale engines.

From Fig. 4.27, where the measured and calculated NO_x values corresponding to the total of the *89* test cases examined, it is shown that the model is capable to adequately

predict the NO_x absolute values for various large–scale engine as the engine load and injection timing (i.e. *VIT*) vary. The regression between calculated and measured NO_x values provides the relation between them, which is given in Eq. (4.5):

$$Calc.NO_x = 1.022 \cdot Meas.NO_x \qquad R^2 = 0.9919 \tag{4.2}$$

The gradient of the above relation (*1.022*) is closed to unity which means that model predicts adequately the measured absolute NO_x for the most cases examined. Also, the acquired coefficient of determination (R^2) is satisfactorily close to unity, which indicates that the regression is proper.

At next, the statistical analysis for the total of test cases (*i*) examined (*89*) is provided, to evaluate the model's predictions. For this purpose, the absolute ($Error_{ABS}$) and relative error ($Error_{REL}$ *[%]*) between the calculated NO_x values obtained from the proposed model, after calibration (*calibr.*NO_x, see Eq. (4.3)) and the respective measured ones (*meas.*NO_x), are calculated from Eq. (4.3) and (4.4) correspondingly:

$$ERROR_{ABS_i} = calibr.NOx_i - meas.NOx_i \tag{4.3}$$

$$ERROR_{REL_i} = \frac{calibr.NOx_i - meas.NOx_i}{meas.NOx_i} \cdot 100 \tag{4.4}$$

The absolute error is calculated in three forms, namely in *[g/cycle]*, *[g/kWh]* and *[g/kg fuel]* units. The last two and mainly *[g/kWh]* are commonly used in industry and field applications.

The percentage of test cases of which their corresponding error lies into a specific error zone, is demonstrated in Table 4.3:

Test Cases	rel. error (±)	abs. error (±)		
[%]	[%]	[g/cycle]	[g/kg fuel]	[g/kWh]
24	0–0	0–0.0	0–0.5	0–0.1
49	0–5	0–0.5	0–2.5	0–0.5
74	0–10	0–1.0	0–6.8	0–1.3
85	0–15	0–3.5	0–9.9	0–1.9
93	0–20	0–7.0	0–13.6	0–2.6
98	0–25	0–10.4	0–15.4	0–3.1

Table 4.3: Relative and absolute error analysis of the model's predictions for the large–scale engines examined.

As shown in Table 4.3, about *74%* of the test cases examined present a relative error in the ±*10%* error zone and absolute error in the zone of ±*1.0 [g/cycle]*, ±*6.8 [g/kg fuel]* and ±*1.3 [g/kWh]*. Moreover, almost for all cases, the relative error does not exceed ±*25%*. Here is emphasized that the values presented in Table 4.3 are strongly affected from the

selected *SF* (i.e. calibration point) for each engine. For the examined large–scale engines, the calibration was attained on the highest available load for the reasons already explained in section 3.5.10. However, an optimum *SF* could be selected for minimal divergence between the calculated and measured absolute NO_x values.

Possible error sources for the test cases examined are the following:

1. Primary measurement error.
2. Improper processing of measured data.
3. Estimation error of fuel consumption, power output and exhaust mass flow rate.
4. *HRR* analysis and consequently fuel burning rate error.
5. *SOC*, *COC* and *EOC* estimation error.
6. Numerical errors (i.e. smoothing, rounding, integrating, differentiation, etc.).
7. Sensitivity of the model to the parameter "Φ_z" (zone equivalence ratio).

4.2 Model Application on Automotive Engines

4.2.1 Description of the Test Engines

In the current study, the proposed model is applied on two different type of automotive Diesel engines: a heavy–duty truck engine (Engine D1) and a light–duty passenger car engine (Engine D2) to evaluate its ability to predict *NO* emissions. Both engines are supercharged, *4*–stroke engines, using a common–rail, direct injection (*DI*) fuel system and exhaust gas recirculation (*EGR*) system for emissions control. The passenger car engine uses pilot fuel injection. The basic geometry data of the test engines examined herein, are summarized in Table 4.4:

	Engine A	Engine B
Number of Cylinders	6	4
Bore [mm]	102	88
Stroke [mm]	130	88.4
Connecting Rod Length [mm]	215	149
Compression Ratio	18.5	18.0
Displacement Volume [lt]	6.37	2.15
Inlet Valve Close [° ATDC]	-171	-123
Exhaust Valve Open [° ATDC]	121	135
Maximum Brake Power Output	205kW@2300 rpm	92kW@4200 rpm

Table 4.4: The automotive test engines examined and their basic engine geometry.

4.2.2 Test Cases Examined

In the present work, numerous measurements were used to evaluate the ability of the proposed model to predict *NO* emissions from automotive engines. The experimental measurements were obtained from the research facilities of *AVL* and *ETH* during cooperation under an *EU* funded project. Unlike the test cases of large–scale engines, for the automotive engines, *NO* emission measurements where available and for this reason the extracted results from the model were not transformed from *NO* to equivalent NO_x. Similarly to large–scale

engines (see section 4.1.2), the measured and calculated *NO* values are presented in *[mg/cycle]* because their tendency with the examined parameters is more obvious and interpretable.

The examined operating points for Engine D1 are categorized as follows:

1. The operating points corresponding to the Extended European Stationary Cycle (*EESC*) covering a wide range of engine operating conditions. The *EESC* includes seven load points for five engine speed cases (*1400–2200 rpm*), namely a total of *35* operating points. The *EESC* operating points are depicted in Fig 4.28:

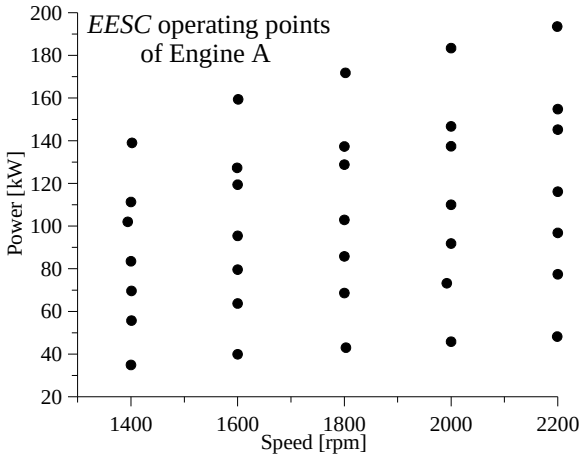

Figure 4.28: The Extended European Stationary Cycle (EESC) operating points of the truck engine (Engine D1)

As for the mid–speed and mid–load engine operation (*1800 rpm* and *86 kW*) the following cases are examined:

2. *SOI* variation from *-20* to *+10 ºCA ATDC.*
3. *EGR* variation from *2* to *18%*.
4. Fuel injection pressure variation from *1000* to *1400 bar.*
5. Inlet manifold pressure variation from *1.3* to *2 bara.*

For Engine D2, the following parameters are varied at three engine operating points, namely: *2000 rpm* and *29.4 kW, 2500 rpm* and *18.3 kW* and *2500 rpm* and *31.4 kW*:

1. *EGR* variation from *0* to *25%.*
2. Fuel injection pressure variation from *500* to *1000 bar.*
3. *SOI* variation from *-10* to *6º ATDC.*
4. Inlet manifold pressure variation from *1.1* to *1.7 bara.*

For the previous automotive engines, a total of *132* operating points were examined, *60* of which are attributed to Engine D1 and *72* to Engine D2.

4.2.3 Heavy–Duty Truck Diesel Engine (Engine D1)

4.2.3.1 Prediction of NO Emissions for the Extended European Stationary Cycle (EESC)

In the present section, the results extracted from the proposed model from its application on various operating points of Engine D1 as determined by the *EESC* are presented.

The operating points of this cycle are determined from engine load and speed. The *SOI*, *EGR*, fuel injection pressure and intake manifold (boost) pressure settings were obtained from the engine *ECU* (default settings). The comparison of calculated and measured *NO* values, in *[mg/cycle]*, against engine power for various speeds from *1400 – 2200 rpm*, according to the *EESC* (see Fig. 4.28), is presented in Fig. 4.29 – 4.33.

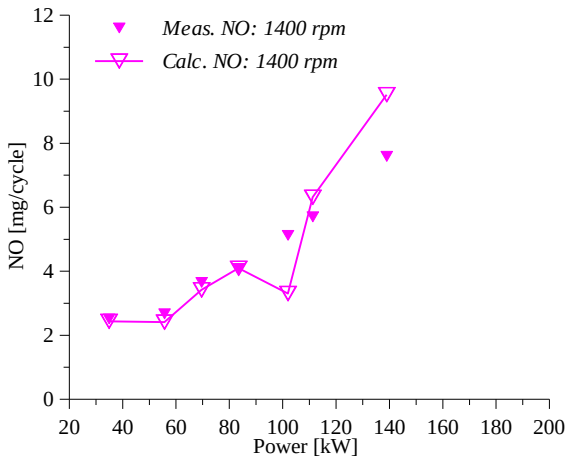

Figure 4.29: NO variation with engine load at 1400 rpm for Engine D1.

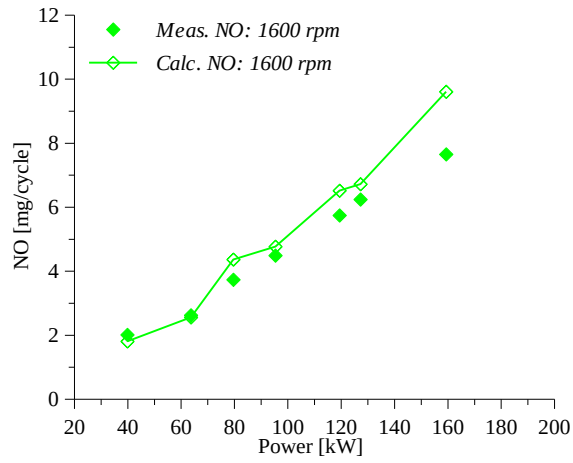

Figure 4.30: NO variation with engine load at 1600 rpm for Engine D1.

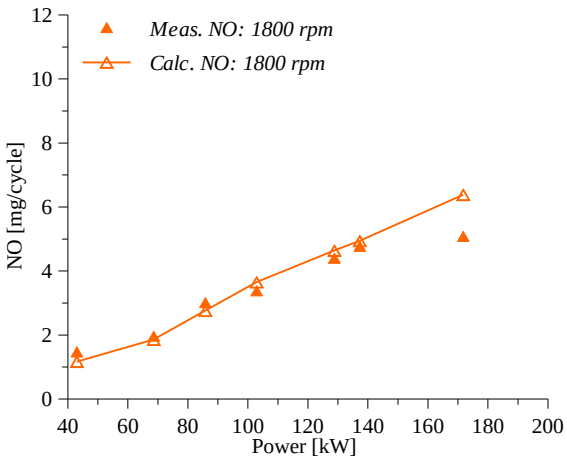

Figure 4.31: NO variation with engine load at 1800 rpm for Engine D1.

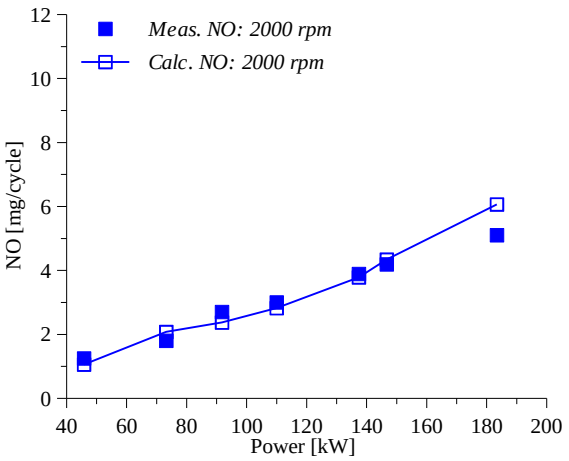

Figure 4.32: NO variation with engine load at 2000 rpm for Engine D1.

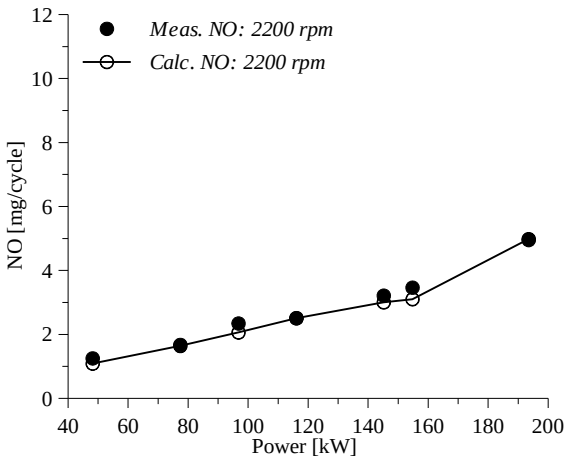

Figure 4.33: NO variation with engine load at 2200 rpm for Engine D1.

The observation of Fig. 4.29 – 4.33 shows that the proposed model captures the trend of *NO* variation with engine power. *NO* trend is approximately linear and ranges between *~2* and *5 mg/cycle* per *100kW* and decreases as engine speed increases. The model also captures absolute values adequately, however a diversion for some of the calculated values is observed. This is due to the error introduced in the model from possible uncertainties in input data of some operating points, such as air flow, *EGR* rate, in–cylinder pressure, etc. which are affecting the initial conditions (i.e. reactants temperature and charge composition at *SOC*).

Additionally, an important source of error is the inaccurate estimation of *EOC* from the model and hence combustion duration miscalculation. This error stems from the relatively high noise of the measured pressure diagram at the last part of expansion phase. The increased combustion duration results in *NO* overestimation because more, high temperature, combustion zones (which do not correspond to actual combustion but noise) are created. Moreover, the overestimation of *EOC* results in underestimation of the coefficient α used in Annand heat exchange model (see section 3.4.7) and hence the heat losses from the combustion zones to the cylinder wall are also underestimated resulting in higher zone temperature and therefore higher *NO* formation.

The *EOC* overestimation is more intense at highest engine load as depicted in Fig. 4.29 –4.32. Indicatively, in Fig. 4.34 is depicted the *NHRR*, from which the *EOC* is calculated (see section 3.4.6), for the lowest and highest engine load at *1800 rpm* (see Fig. 4.31). The higher noise in the high load *NHRR* diagram is evident.

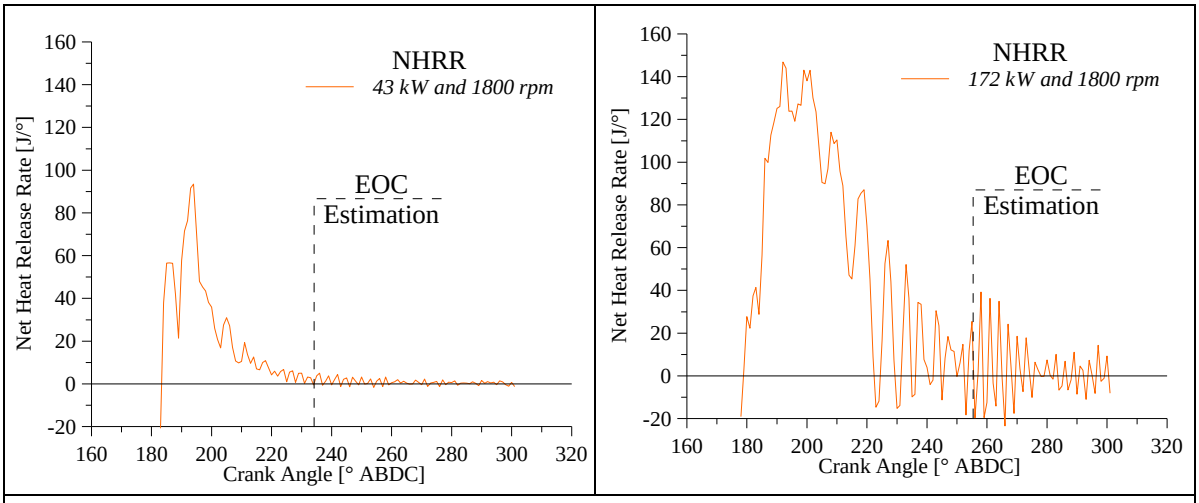

Figure 4.34: NHRR of the lowest and highest operating point at 1800 rpm for Engine D1. Uncertainty in *EOC estimation.*

Additionally, uncertain input data such as in–cylinder trapped mass and pressure at *SOC* result in incorrect estimation of unburnt charge temperature at *SOC* (see Eq. (3.47)), which severely affects the combustion zone temperature and hence *NO* formation. This is important since *NO* formation presents high sensitivity (exponential) to temperature according to the calculation method used (see section 3.5.7). For this reason, high relative error occurs, especially for the low *NO* absolute values.

For instance, considering engine operation at *1400 rpm* and *102 kW*, which is depicted in Fig. 4.29, the *NO* prediction presents a noticeable divergence. This is caused from the unburnt zone temperature underestimation, which is about *50 [K]*, as shown in the following Fig. 4.35:

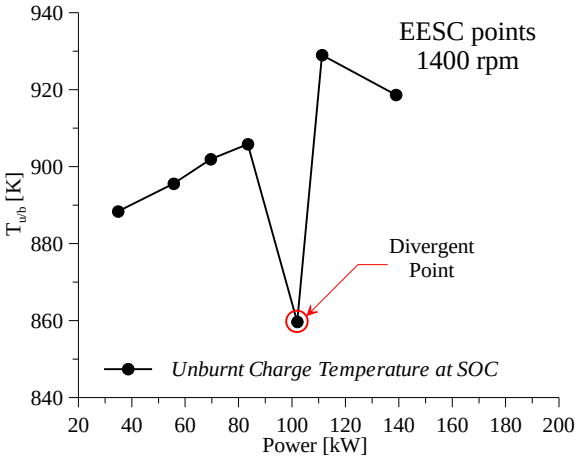

Figure 4.35: Temperature of unburnt zone at SOC with engine power at 1400 rpm for Engine D1.

This underestimation is due to the lower in–cylinder pressure and higher trapped mass values at *SOC* (see Eq. (3.47)) compared to the ones expected according to their general trend against engine power as shown in Fig. 4.36:

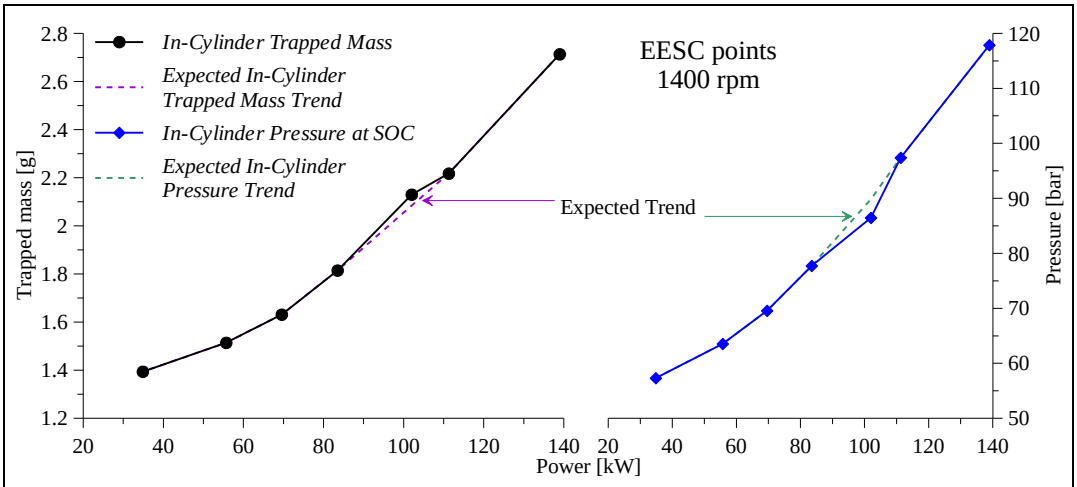

Figure 4.36: In–cylinder pressure and trapped mass of unburnt zone at SOC with engine power at 1400 rpm for Engine D1.

The investigation for the specific operating point revealed that, if the corresponding in–cylinder pressure and trapped mass had the expected values, as demonstrated in Fig. 4.36, the *NO* trend for engine operation at *1400 rpm* (see Fig. 4.29) would be significantly improved.

4.2.3.2 NO Variation with Engine Settings

In the present section, the model's ability to capture the *NO* variation for different engine settings namely *SOI*, *EGR* rate, fuel injection pressure and intake manifold pressure variation, is examined. The comparison between the calculated *NO* from the model and the respective measured values, is depicted correspondingly for each engine setting variation in Fig. 4.37 – 4.40:

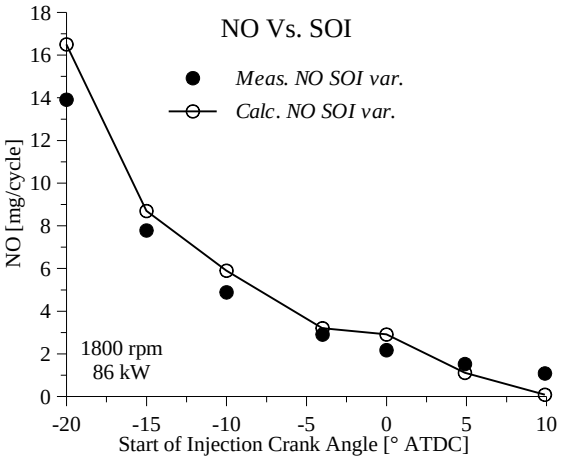

Figure 4.37: NO variation with SOI setting at 1800 rpm & 86 kW for Engine D1.

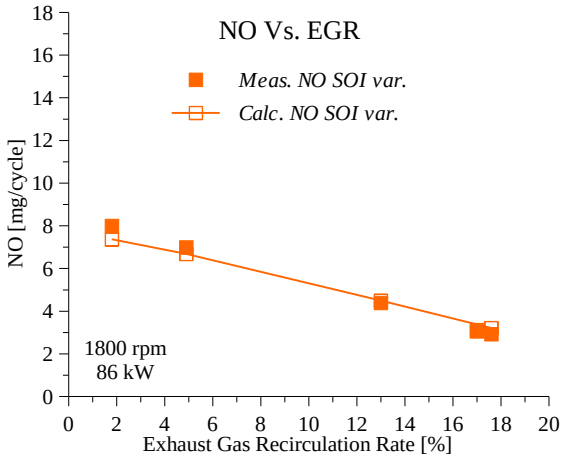

Figure 4.38: NO variation with EGR rate at 1800 rpm & 86 kW for Engine D1.

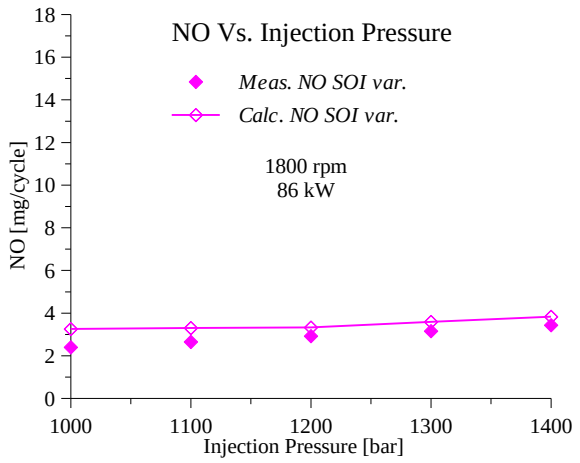

Figure 4.39: NO variation with fuel injection pressure at 1800 rpm & 86 kW for Engine D1.

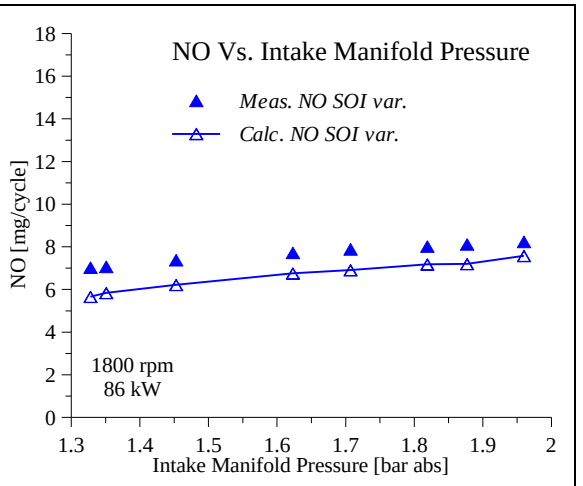

Figure 4.40: NO variation with intake manifold pressure at 1800 rpm & 86 kW for Engine D1.

From Fig. 4.37 – 4.40 is revealed that the model is capable to capture the trend of *NO* with *SOI*, *EGR* rate, injection pressure and intake manifold pressure variation. The model also accomplishes to adequately approach the *NO* absolute values.

As shown in Fig. 4.37, *NO* is exponentially reduced when the start of fuel injection (*SOI*) is retarded, as expected. Referring to Fig. 4.38, the increase of *EGR* rate induces lineal *NO* reduction *~0.3 mg/cycle* (or *4%*) per *1% EGR*. Furthermore, the observation of Fig. 4.39 reveals that injection pressure increase induce a linear increase of *NO ~0.3 mg/cycle* (or *~8%*) per *100 bar*. Regarding Fig. 4.40, a linear increase of *NO* with intake manifold (boost) pressure increase *~0.2 mg/cycle* (or *~2%*) per *0.1 bar* is observed.

Referring to *NO* predictions with *SOI* variation, for the most advanced *NO* is noticeably overestimated and for the most retarded *SOI* is underestimated. This error, which is not significantly affect the *NO* trend, is mostly attributed to the inaccurate estimation of zone Φ values (with respect to the expected ones) calculated from the empirical correlation described in Eq. (3.101) (see section 3.5.8).

4.2.3.3 Overall Results and Statistical Analysis

At next, the overall *NO* predictions provided from the proposed model are compared to the respective measured values as shown in Fig. 4.41:

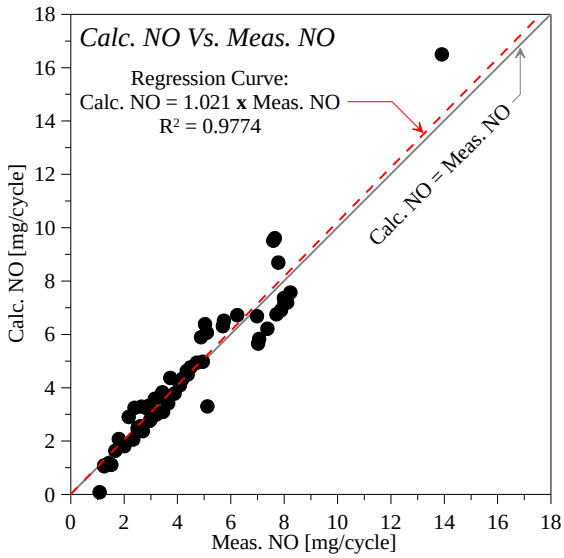

Figure 4.41: Overall Comparison between Calculated and Measured NO for Engine D1.

From the observation of Fig. 4.41, where the measured and calculated *NO* values corresponding to the total of the *60* operating points of Engine *D1* are examined, is shown that the model, is capable to adequately predict the *NO* absolute values for various engine operating conditions and engine settings, even without calibration (see section 3.5.10). The regression between calculated and measured *NO* values provides the relation between them, which is given in Eq. (4.5):

$$Calc.NO = 1.021 \cdot Meas.NO$$
$$R^2 = 0.9774 \tag{4.5}$$

The gradient of the above relation (*1.021*) is closed to unity which means that model's predictions approach adequately the measured absolute values. Also, the acquired coefficient of determination (R^2) is satisfactorily close to unity, which indicates that the regression is proper.

In addition, the absolute and relative error of model's *NO* predictions is calculated using Eq. (4.3) and (4.4) respectively as presented in section 4.1.6. The absolute error is calculated in *[mg/cycle]*, *[g/kWh]* and *[g/kg fuel]*. The percentage of the test cases for which

their corresponding error lies inside a specific error zone, for Engine D1, is presented in Table 4.5:

Test Cases	rel. error (±)	abs. error (±)		
[%]	[%]	[mg/cycle]	[g/kg fuel]	[g/kWh]
5	0–1	0–0.0	0–0.0	0–0.0
22	0–5	0–0.2	0–0.4	0–0.1
42	0–10	0–0.3	0–0.9	0–0.2
68	0–15	0–0.7	0–1.9	0–0.4
83	0–20	0–1.0	0–2.8	0–0.6
87	0–25	0–1.1	0–2.8	0–0.6
93	0–30	0–1.4	0–3.4	0–0.7
98	0–40	0–2.0	0–4.0	0–0.9

Table 4.5: Relative and absolute error analysis of the model's predictions for Engine D1.

As clearly shown in the above table, almost the entire test cases present maximum relative error up to *±40%*. Furthermore, *83%* of the examined cases present maximum relative error up to *±20%* and maximum absolute error up to *±1.0 mg/cycle*, *±2.8 g/kg fuel* and *±0.6 g/kWh* which are satisfactory for the specific application. It is emphasized that no *SF* was used for calibration. Although the relative error for some test cases is noticeable, the most important is the proven ability of the model to capture the *NO* trends with engine operating parameters variation (as shown in Figs. in sections 4.2.3.1 and 4.2.3.2).

The higher relative error compared to the large–scale engines (see sections 4.1.6, 4.2.3.1 and 4.2.3.2) is due to the much lower absolute *NO* values of automotive engines, namely, the low denominator value induces high ratio (relative error) value (see Eq. (4.4)).

Among others, which have already described in section 4.1.6, the error stems from the possible inaccurate input data and also from the quality of pressure diagram and its special characteristics, which are utilized in the correlation for the calculation of zone equivalence ratio (Φ_z see section 3.5.8) and the calculation of unburnt in–cylinder charge temperature. The last two, as revealed, introduce high sensitivity to the model which is still a drawback.

4.2.4 Light–Duty Automotive Diesel Engine (Engine D2)

4.2.4.1 NO Variation with EGR

In the present section, the model's ability to capture the *NO* variation as *EGR* rate varies is examined. The extracted results from the model, for three different engine operating

points of Engine *D2*, are compared to the respective measured *NO* values as demonstrated in the Fig. 4.42 – 4.44:

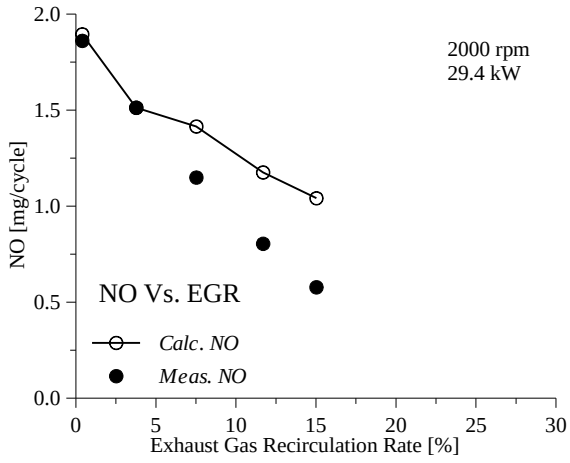

Figure 4.42: NO variation with EGR rate at 2000 rpm & 29.4 kW for Engine D2.

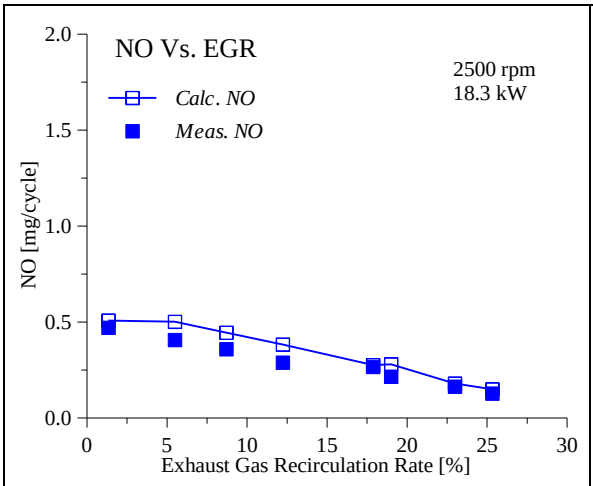

Figure 4.43: NO variation with EGR rate at 2500 rpm & 18.3 kW for Engine D2.

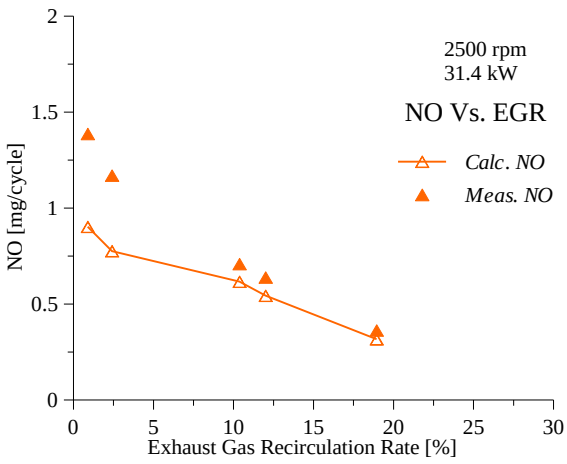

Figure 4.44: NO variation with EGR rate at 2500 rpm & 31.4 kW for Engine D2.

As shown in the Fig. 4.42 – 4.44, the model manages to predict the trend of *NO* variation with *EGR* rate. This trend is descending and approximately linear. Its slope becomes steeper with engine load increase (see Fig. 4.43 and 4.44) and engine speed decrease (see Fig. 4.44 and 4.42).

Referring to Fig. 4.42, where the test case of the high load (*29.4 kW*) and lowest speed (*2000 rpm*) is depicted, the *NO* decrease is *~0.09 mg/cycle* (or *~5%*) per *1% EGR* rate. For higher speed (*2500 rpm, 31.4 kW*, see Fig. 4.44), this variation is decreased to *~0.06 mg/cycle* (or *~4%*) per *1% EGR* rate. Finally, the aforementioned variation is even lower *~0.01 mg/cycle* (or *~3%*) per *1% EGR* rate for the lowest load (*2500 rpm, 18.3 kW*) as shown in Fig. 4.43. It is also noticeable that the calculated *NO* values are quite close to the measured ones for the most cases examined, despite the low absolute values which make prediction even more challenging.

The underestimation of *NO* at *2500 rpm, 31.4 kW* and lowest *EGR* rates (see Fig. 4.44) is mostly attributed to the earlier *EOC* positioning (regarding *CA*) and higher *a* coefficient (used in heat exchange model – see section 3.4.7) estimation from the model. The first leads to a lower number of combustion zones formation (see section 3.4.6) and the second results in overestimation of heat losses through the cylinder wall and thus lower zone temperatures. Both cause *NO* formation underestimation,

Nonetheless, it is noted that the most important is to capture the trend of *NO* as *EGR* rate varies. The high relative error is mainly due to the very low *NO* absolute values especially when compared to the *NO* emitted from the large–scale Diesel engines (see section 4.1).

4.2.4.2 NO Variation with Fuel Injection Pressure

The model ability to estimate tail–pipe *NO* with fuel injection pressure variation was also examined. The obtained results and their comparison with the respective measured *NO* values, for three different engine operating points of Engine D2, are depicted in Fig. 4.45 – 4.47:

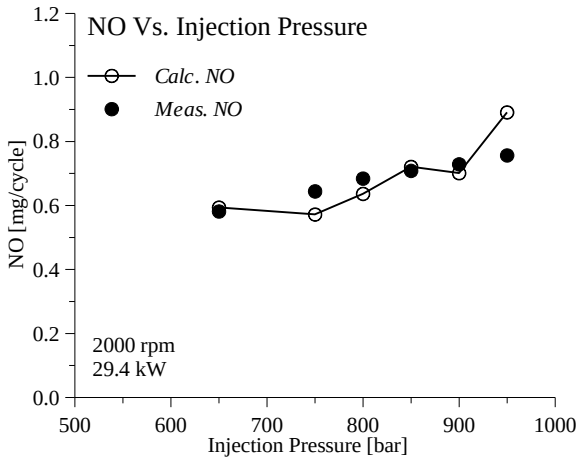

Figure 4.45: NO variation with fuel injection pressure at 2000 rpm & 29.4 kW for Engine D2.

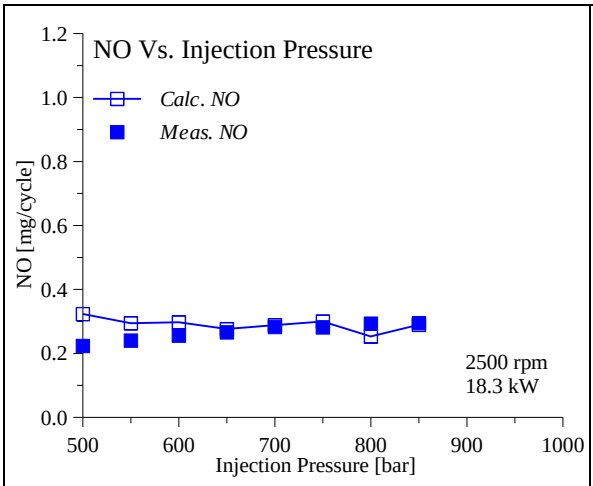

Figure 4.46: NO variation with fuel injection pressure at 2500 rpm & 18.3 kW for Engine D2.

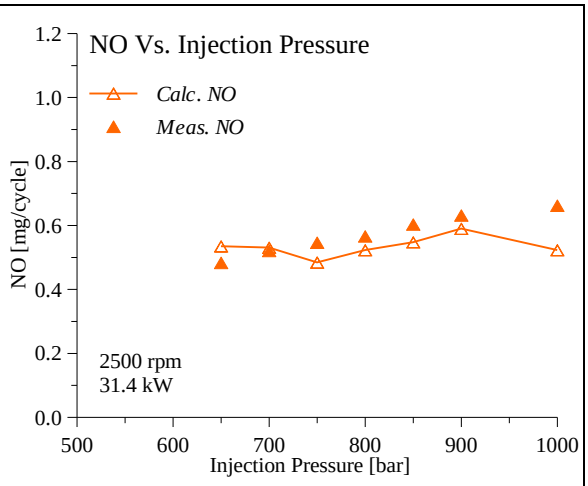

Figure 4.47: NO variation with fuel injection pressure at 2500 rpm & 31.4 kW for Engine D2.

As shown in Figs. 4.45 – 4.47, the model approaches fairly well the *NO* trend which is approximately linear and slightly ascending as the injection pressure rises. For engine operation at *2000 rpm* and *29.4 kW*, which is depicted in Fig. 4.45, the *NO* increase with injection pressure is *~0.06 mg/cycle* (or *~8%*) per *100 bar*. Nonetheless, the *NO* trend at *2500 rpm* is not ideally captured as shown in Fig. 4.46 – 4.47, despite the fact that the absolute calculated *NO* values are sufficiently close to the measured ones. The divergence is mainly observed at lower injection pressures where the absolute *NO* values are very low. The low absolute *NO* values and the small variation of measured *NO* with injection pressure increase (at the examined pressure range) is the most possible explanation for the poor correspondence of the model to injection pressure variation at lower injection pressures. Moreover, small inaccuracies in input data also cause observable divergences, again due to the low absolute *NO* values.

For instance, regarding engine operation at *2500 rpm* and *31.4kW* (see Fig. 4.47), where an increase of *NO* with injection pressure of *~0.05 mg/cycle* (or *~8%*) per *100 bar* is observed, for the operating point with injection pressure at *1000 bar*, a significant underestimation of *NO* is observed. This is explained as follows: For the specific operating point, the *EGR* rate is *1%* greater compared to the points with lower injection pressure where *EGR* rate is constant (*~13.7%*). Moreover, fuel and air mass flow rates are also greater about *5%* and *3%* respectively. The previous are demonstrated schematically in Fig. 4.48. These result in an underestimation of *NO* formation at this operating point. However, these variations are not reflected on the measured *NO* value of the specific point, which indicates possible inaccurate input data or variation within the measurement error. As mentioned in section 4.2.3.1, when the value of fuel flow used is greater than actual, the model overestimates the wall heat losses (see Eq. (3.38) in section 3.4.7) and hence underestimates the zones temperature (see Eq. (3.48) and (3.53) in sections 3.5.3 and 3.5.4 respectively) resulting in lower *NO*. Moreover, the increased value of air mass flow induces higher trapped mass and hence lower

initial temperature of the unburnt zone resulting lower temperature of the combustion zones and therefore lower *NO* formation.

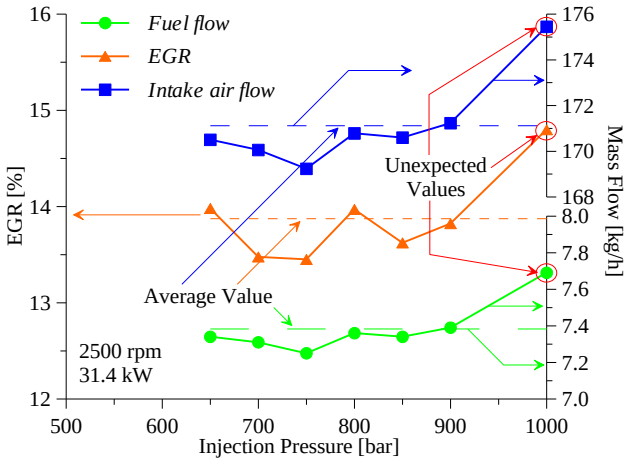

Figure 4.48: Investigation for the consistency of the input data, at 2500 rpm & 31.4 kW for Engine D2.

Finally, referring to engine operation at *2500 rpm* and *18.3 kW* (see Fig. 4.46), where the increase of *NO* with injection pressure is *~0.02 mg/cycle* (or *~7%*) per *100 bar*, for the lower injection pressure cases, the calculated *NO* trend does not follow the experimental one ideally. The analysis of the experimental input data, which is schematically demonstrated in Fig. 4.49, revealed that fuel flow rate slightly increases when injection pressure varies from *500* to *600 bar* regardless the constant power output. This is in contrast to experience since the increase of injection pressure increases efficiency and thus decreases fuel consumption for constant power output. This is an indication of inaccurate measured fuel mass flow rate data, which is used as an input. Small errors in these data are to be expected since they are normal during the experimental measurement procedure. However, they can affect the calculated *NO* values resulting in diverging predictions. As previously mentioned, the use of decreased fuel flow results in underestimation of zone heat losses and hence overestimation of zone temperature resulting in higher *NO* formation. Furthermore, the *EGR* rate at *500* to *700 bar* is approximately *1%* lower than the one at higher fuel injection pressures, which also induces higher *NO* than expected. It is hence confirmed that, de-

spite the small differences of fuel mass flow and *EGR* rate, their effect on model's predictions is more significant compared to the effect of injection pressure, especially when referring at the very low absolute *NO* values of the specific test case.

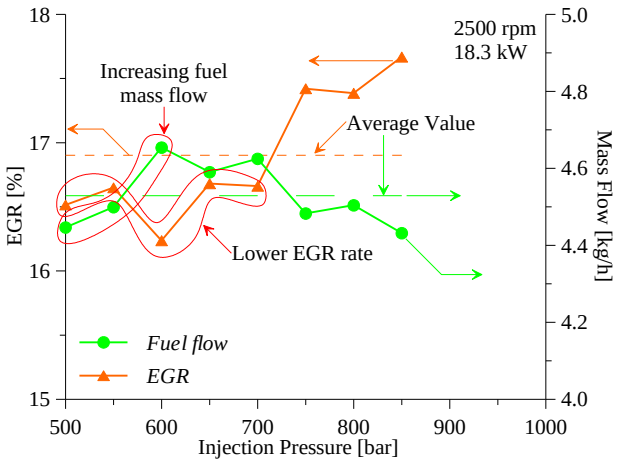

Figure 4.49: Input data analysis at 2500 rpm & 18.3 kW for Engine D2.

For the previous two cases, where model's results were not considered satisfactory, in order to confirm that the input data is the cause of the inaccurate *NO* predictions, they were substituted with the ones corresponding to the expected values (i.e. average values as shown in Fig. 4.48) and then the model's predictions were significantly improved. Nevertheless, it is clarified that the presented results in Figs. 4.45 – 4.49 are the ones extracted using the original input data.

4.2.4.3 NO Variation with SOI Setting

In this section, model's ability to predict *NO* variation with *SOI* setting is examined. In Fig. 4.50 – 4.52 is depicted the variation of calculated and measured *NO* against *SOI* setting for three different engine operating points of Engine D2:

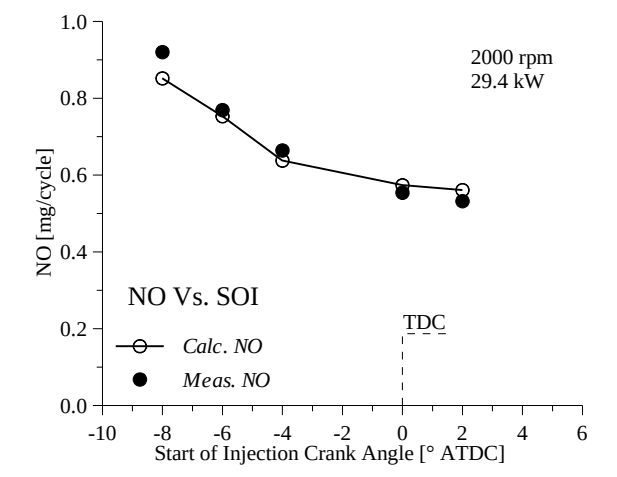

Figure 4.50: NO variation with SOI setting at 2000 rpm & 29.4 kW for Engine D2.

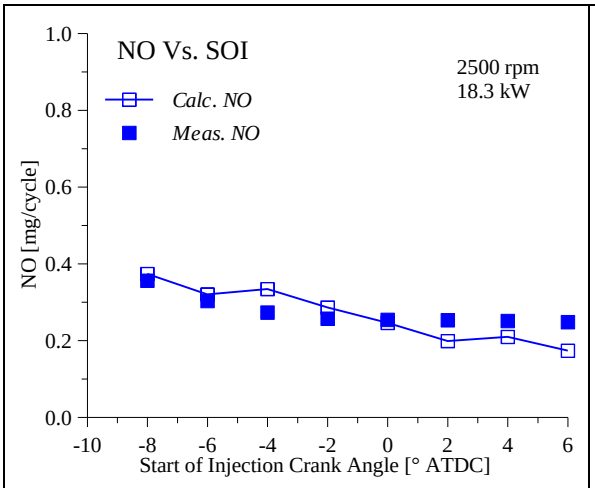

Figure 4.51: NO variation with SOI setting at 2500 rpm & 18.3 kW for Engine D2.

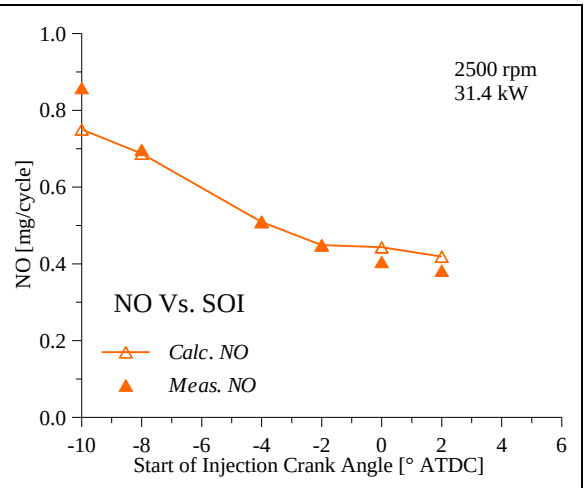

Figure 4.52: NO variation with SOI setting at 2500 rpm & 31.4 kW for Engine D2.

From the observation of Fig. 4.50 – 4.52, the ability of the model to predict *NO* trend with *SOI* variation, is clearly proven. Absolute *NO* values are also adequately calculated.

As shown, for the higher loads (*29.4 & 31.4 kW* depicted in Fig. 4.50 and 4.52 respectively), the decrease of *NO* with *SOI* (injection retard) is more intense *~0.04 mg/cycle* (or *4–5%* correspondingly) per *°CA*. On the other hand, the engine speed does not affect the slop significantly.

With reference to engine operation at *2500 rpm* and *18.3 kW*, which is depicted in Fig. 4.51, both *NO* variation (*~0.01 mg/cycle* (or *2%*) per *°CA*) and absolute values are considerably low. For this reason, the model cannot capture precisely the measured *NO* tendency despite the fact that it achieves to approach the absolute values satisfactorily.

This is justified (as already mentioned in section 4.2.4.2) from the fact that in some cases, small variations of the input data used in the model's calculations, such as *SOC*, *EOC*, *a* (used in heat transfer model), etc., may be more influencing than the variation of the examined parameter (e.g. *SOI*), especially when its variation does not affect the absolute tail–pipe *NO* values significantly. Therefore, even small errors (normal) of the input data may deteriorate the predicted *NO* tendency against the examined operating parameter. These errors are mainly stemmed from the pressure signal noise and improper smoothing intensity.

For instance the main *SOC* may be miscalculated (due to the pressure derivatives method used for its determination, where pressure signal noise is magnified even more, see also section 3.2.3). Hence the number, magnitude and initial temperature of the zones can be miscalculated providing inaccurate *NO* predictions. For example, earlier *CA* positioning of *SOC* due to the aforementioned noise, results in generation of more combustion zones (which correspond to *HRR* noise and not to actual zones), having higher temperatures promoting *NO* formation (more important than the increased number of zones) since their generation begins closer to *TDC* (higher reactants' and therefor products' temperatures).

Furthermore, inaccurate *SOC* estimation induces improper determination of the center of combustion (*COC*), pressure at *SOC* ($p_{SOC\ main}$) and, for the cases where $p_{SOC\ main} \equiv p_{comb.\ max}$ (i.e. late *SOC* cases where during combustion is not developed greater pressure than

the corresponding one at *SOC*), of the value of maximum combustion pressure ($p_{comb.\ max.}$). These parameters introduce additional error because they result in improper calculation of zone equivalence ratio (Φ_z) via Eq. (3.101) as described in section 3.5.8.

Moreover, inaccurate estimation of *SOC* and *EOC*, resulted from the *HRR* noise, leads to improper estimation of net *HRR* (see Eqs. (3.28) and (3.29) is section 3.4.2) and hence of α coefficient used for heat exchange between the zones and cylinder wall (see section 3.4.7). The last results in zone temperature miscalculation (see sections 3.5.3 and 3.5.4) and therefore *NO* is underestimated/overestimated.

4.2.4.4 NO Variation with Intake Manifold Pressure

Finally, in the current section the model was tested regarding its ability to predict *NO* against intake manifold (boost) pressure variation. The comparison between measured and calculated *NO* values, for three different engine operating points of Engine *D2*, are demonstrated in the following Figs. 4.53 – 4.55:

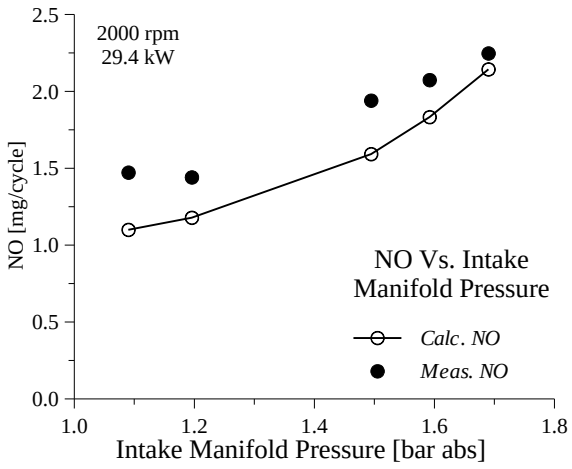

Figure 4.53: NO variation with intake manifold pressure at 2000 rpm & 29.4 kW for Engine D2.

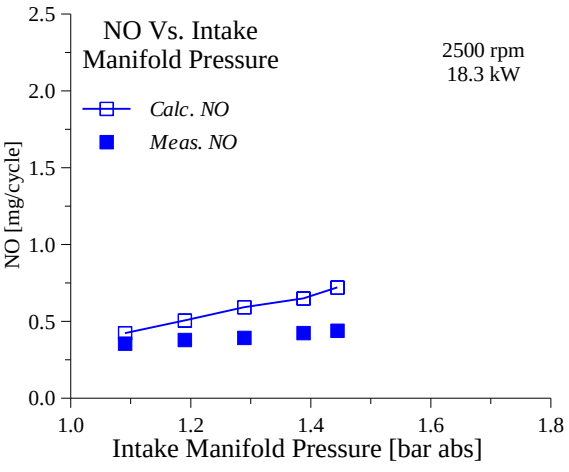

Figure 4.54: NO variation with intake manifold pressure at 2500 rpm & 18.3 kW for Engine D2.

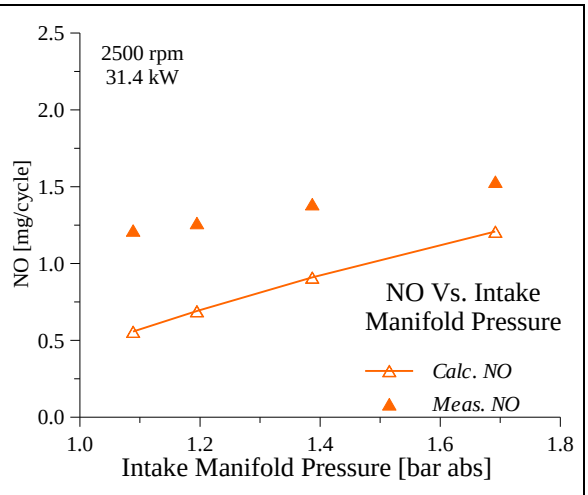

Figure 4.55: NO variation with intake manifold pressure at 2500 rpm & 31.4 kW for Engine D2.

The observation of Figs. 4.53 – 4.55 reveals model's ability to approach fairly well the trend of *NO* with intake manifold pressure variation despite the small differences in *NO* absolute values. In general, the *NO* trend is practically linear and acceding as intake manifold pressure increases. Its slope decreases when engine speed increases (see Fig. 4.53 and 4.55) and increases when engine load increases (see Fig. 4.54 and 4.55). Namely, for engine operation at *2000 rpm* and *29 kW* the gradient is *~0.14 mg/cycle* (or *~6%*) per *0.1bar* (see Fig. 4.53), at *2500 rpm* and *31.4 kW* is *~0.05 mg/cycle* (or *~3%*) per *0.1bar* (see Fig. 4.55) and at *2500 rpm* and *18.3 kW* is *~0.02 mg/cycle* (or *~5%*) per *0.1 bar* (see Fig. 4.54).

As previously mentioned in the present chapter, the divergence observed between the calculated and measured *NO* values is mostly attributed to the following:

- very low *NO* absolute values resulting in magnification of relative error (see Eq. (4.4) in section 4.1.6),
- miscalculation of heat–exchange α coefficient, *SOC*, *EOC*, etc. due to signal noise,
- uncertainties in experimental input data such as fuel and air flow rates and
- no *SF* (i.e. calibration) was used for the automotive engines, which could reduce the absolute error in some cases, for the reasons already described in section 3.5.10.

4.2.4.5 Overall Results and Statistical Analysis

Considering the previous analysis for the passenger car *DI* Diesel engine (Engine *D2*), presented in sections 4.2.4.1 – 4.2.4.4, where the ability of the proposed model to predict the variation of tail–pipe *NO* emissions against various engine settings was investigated, herein, the statistical analysis of the extracted results for the total of the *72* test cases examined, is presented.

Initially, the calculated tail–pipe *NO* emissions, corresponding to the total of the *72* test cases of Engine *D2* examined, are compared to the respective measured values as shown in Fig. 4.56:

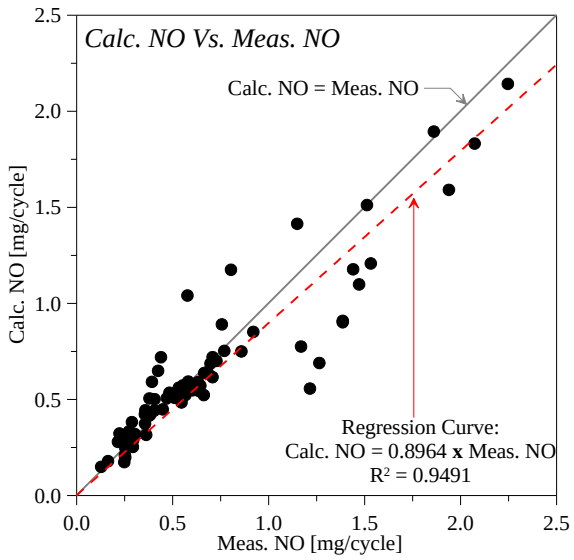

Figure 4.56: Overall comparison between calculated and measured NO for Engine D2.

From Fig. 4.56, it is revealed that the proposed model is capable to predict the *NO* absolute values satisfactory for various engine operation and settings, even without calibration. The regression between calculated and measured *NO* values provides the relation between them, which is given in Eq. (4.6):

$$Calc.NO = 0.8964 \cdot Meas.NO \qquad R^2 = 0.9491 \tag{4.6}$$

The gradient of the previous relation (*0.8964*) is closed to unity which confirms that model's predictions approach the measured absolute values adequately. Also, the acquired coefficient of determination (R^2) is satisfactorily close to unity, which indicates that the regression is proper.

Furthermore, the absolute and relative errors of model's *NO* predictions are calculated using Eq. (4.3) and (4.4) respectively, as presented in section 4.1.6. The absolute error is calculated in *[g/cycle]*, *[g/kWh]* and *[g/kg fuel]*. The percentage of test cases for which their corresponding error lies inside a specific error zone, for Engine D2, is presented in Table 4.6:

Test Cases	rel. error (±)	abs. error (±)		
[%]	[%]	[mg/cycle]	[g/kg fuel]	[g/kWh]
1	0	0–0.00	0–0.0	0–0.0
26	0–5	0–0.02	0–0.3	0–0.1
43	0–10	0–0.04	0–0.5	0–0.1
57	0–15	0–0.07	0–0.9	0–0.2
67	0–20	0–0.09	0–1.1	0–0.3
78	0–25	0–0.14	0–2.2	0–0.5
79	0–30	0–0.20	0–2.2	0–0.5
89	0–35	0–0.35	0–3.4	0–0.8
93	0–50	0–0.45	0–4.2	0–1.0

Table 4.6: Relative and absolute error analysis of the model's predictions for Engine D2.

As clearly shown in Table 4.6, almost the entire test cases (*~93%*), of Engine D2, their maximum relative error does not overcome the *±50%*. Furthermore, *67%* of the examined cases present maximum relative error up to *±20%* and maximum absolute error up to *±0.09 mg/cycle*, *±1.1 g/kg fuel* and *±0.3 g/kWh* which are satisfactory for the specific application. Similarly to the previously examined engine (*D1*), no *SF* was used for the calibration (i.e. quantitative optimization of the extracted results) for the reasons already described in section 3.5.10. Nevertheless, the most important was to reveal the model's ability to capture trends.

Here, it is emphasized that high relative error is mainly attributed to the very low *NO* absolute values because they magnify the relative error ratio (since they are used as denominators (see Eq. (4.4)).

As already comprehensively described in sections 4.2.4.1 – 4.2.4.4, an error is introduced from the pressure signal noise and possible inaccuracies in input data (e.g. primary measurement error). Moreover, due to pressure signal noise, the pressure trace and *HRR* characteristics such as p_{comb_max}, $p_{SOC,main}$, *COC*, etc., which are utilized in the correlation for the determination of zone equivalence ratio (Φ_z see section 3.5.8), may altered or misallocated resulting in miscalculation of Φ_z. Inaccurate approach of Φ_z, which determines the unburnt charge amount consisted in the zones, severely affects zone mass, volume and temperature and hence *NO* formation (see Eq. (3.97) and Table 3.4). The effect of the aforementioned error sources was verified by a thorough investigation.

Additionally, error is also derived from possible inaccuracy of measured intake air mass flow rate resulting in in–cylinder trapped mass miscalculation. The last results in miscalculation of unburnt in–cylinder charge temperature and therefore miscalculation of combustion zones temperature at the time step of their generation and consequently during their evolution throughout the closed engine cycle. Apparently, zone temperature miscalculation leads inevitably to inaccurate *NO* predictions. Furthermore, the combination of improper calculation of Φ_z and trapped mass may lead to convergence errors. As revealed from the investigation (sensitivity analysis) on both automotive engines *D1* and *D2* and also on the large–scale engines (see sections 3.5.8), the last two parameters (Φ_z and trapped mass), introduce high sensitivity to the model, which should be compensated via future work.

4.3 NO_x Formation History inside the Combustion Chamber

4.3.1 Introduction

As mentioned in section 3.5.1, the proposed model can calculate the number of *NO* moles formed inside each combustion zone at every *CA* step. Thus the *NO* formation history in each combustion zone can be obtained. The in–cylinder *NO* history during an engine cycle is derived from the sum of the *NO* moles comprised in the existing zones at each *CA* calculation step. In the present section, this model's feature is demonstrated. However, no experimental data for the *NO* formation during an engine cycle was available. For this reason the extracted formation trend could not be verified experimentally. Nevertheless, the provided results can be utilized for *NO* formation analysis by conducting parametric investigations.

These investigations intend to reveal the effect of various parameters (e.g. scavenging pressure, effective compression ratio, injection strategy, boost pressure, *EGR* and *RG* fractions, etc.) on the evolution of actual pressure and *HR* inside the cylinder during an engine cycle and hence the *NO* formation history during the engine cycle, from which the tail–pipe NO_x are eventually derived. This feature provides the potentials for the model to be used, after further development, in research and optimization studies for *NO* emissions control.

In the following paragraphs, is indicatively presented, for some of the examined engines (see sections 4.1.1 and 4.2.1), the *NO* formation history inside the combustion chamber during an engine cycle against engine parameters variation. Moreover, along with the *NO* history inside the combustion chamber, the in–cylinder pressure evolution, combustion rate and other parameters history during an engine cycle are depicted, since they are determinant factors for the NO_x formation. Also, this presentation indicates the basic philosophy of the model, namely the use of in–cylinder pressure trace to calculate *HRR* and from this the NO_x formation history and finally the tail–pipe NO_x (i.e. NO_x at *EVO*).

4.3.2 NO_x Formation History with Load Variation

4.3.2.1 Large–Scale DI Diesel Engines

In the present paragraph is indicatively presented a schematic description of the *NO* formation history inside the combustion chamber during an engine cycle of some of the large–scale *DI* Diesel engines examined in the present dissertation (see section 4.1.1).

In Fig. 4.57 is indicatively depicted the *NO* formation history for the highest and lowest available load operating points for four large–scale engines with different characteristics. Specifically, the results derived from the model implementation on a *2*–stroke stationary engine established in a power plant on Chios Island (Engine A), a *4*–stroke stationary engine established in a power plant on Paros Island (Engine P), a *2*–stroke marine main

engine (Engine H) and a *4*–stroke constant speed marine auxiliary engine (Engine N), are demonstrated in Fig. 4.57.

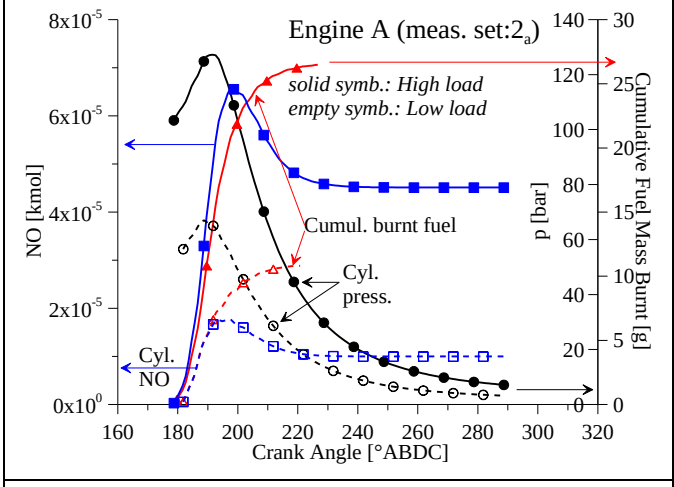

2–str. stationary, constant speed DI Diesel engine established in a power plant.

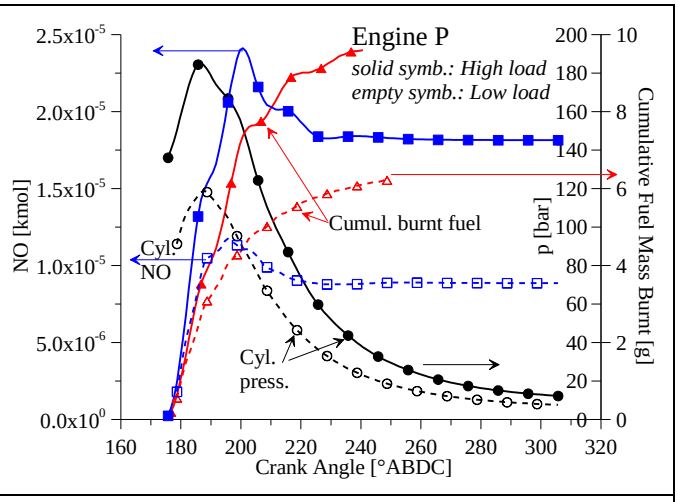

4–str. stationary, constant speed DI Diesel engine established in a power plant.

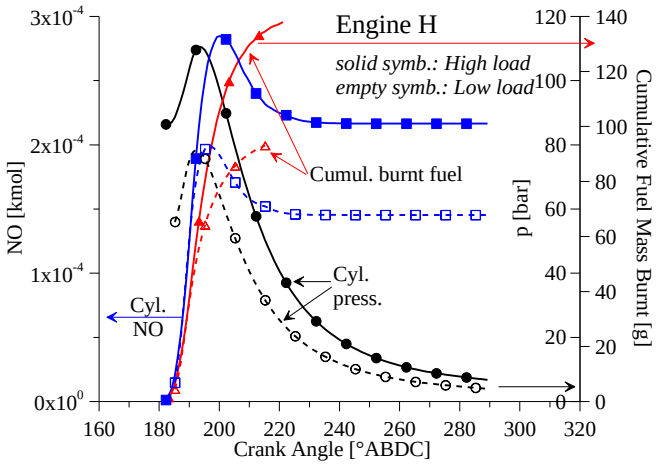

2–str. marine propulsion DI Diesel main engine.

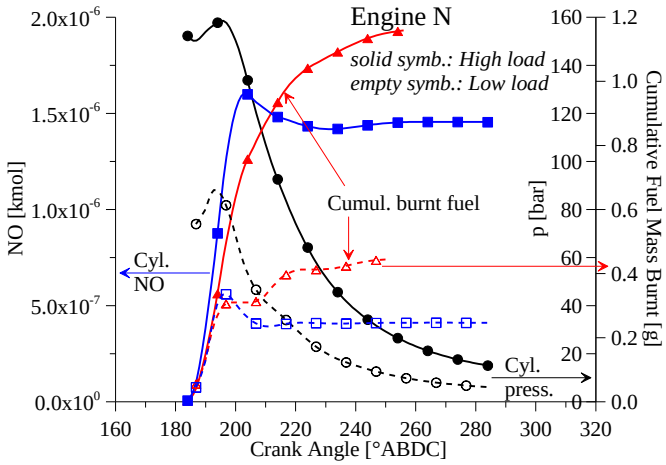

4–str. marine constant speed DI Diesel auxiliary engine.

Figure 4.57: NO formation history inside the combustion chamber along with pressure evolution in the cylinder and cumulative fuel mass burnt in the combustion chamber during an engine cycle against engine load variation.

As shown in Fig. 4.57, the *NO* formation is increased with load as expected. The *NO* amount as *CA* time elapses is proportional to the corresponding burnt fuel (which is calculated from *HRR* analysis). The *NO* formation continues after the *EOC*, however with much lower rate since, due to the lower temperature and oxygen availability during expansion phase, *NO* formation rate "freezes", as clearly shown in Fig. 4.57.

As already mentioned in section 3.5.1, the cylinder *NO* formed at a specific *CA* step is derived from the sum of the *NO* formed inside the existing zones at this time instance.

Thus the form of *NO* formation history curve is determined from the sum of zone *NO* formation history curves as shown in Fig. 4.58:

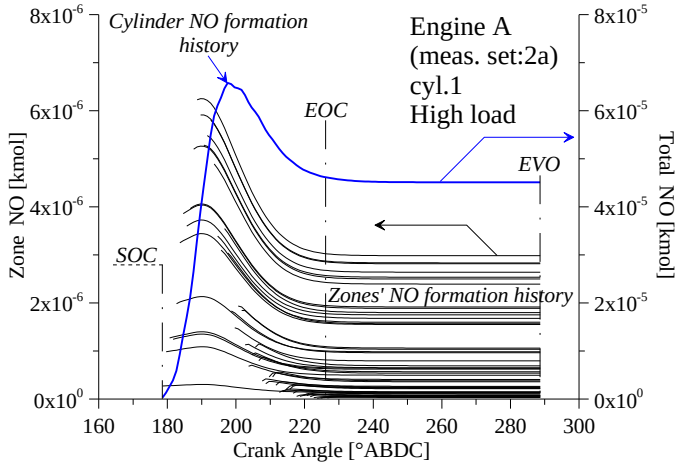

Figure 4.58: NO formation histories of the combustion zones (49) and cumulative NO formation inside the combustion chamber during an engine cycle.

The form of these curves (see Fig. 4.58) depends mostly from the *CA* time in the cycle at which the zone has been generated and from the magnitude (number of moles) of the zone. The number of moles comprised in the zone is determined from the burnt fuel amount attributed to the zone (as determined from *HRR* analysis), the selected zone Φ and the zone composition.

The *CA* time where a zone is generated is important for the following reasons: At first, as already mentioned, the fuel amount burnt (assumed instantaneously) at a specific *CA* is attributed to the zone generated at this *CA* time step. Another reason is the temperature of the unburnt zone which depends on the in–cylinder pressure and unburnt zone mass at the examined *CA* step. This temperature serves as the reactants temperature during combustion inside the generated zone and has a determinant role to the final zone combustion temperature used in *NO* formation calculations. The derived combustion temperature is then used, as the initial value to calculate the zone temperature at the next *CA* step, as the zone is evolving up to the *EVO*. Hence, the unburnt zone temperature at the time of a zone generation has a significant impact on the temperature history of this zone. Furthermore, the in–cylinder pressure and pressure derivative, which correspond to the *CA* time that the zone is generated, affect the equilibrium composition (e.g. O_2, *O*, *OH*, etc.) used in the *NO* formation mechanism (see section 3.5.7), and the temperature of the unburnt and newly generated zone since they are participating in the temperature calculations (i.e. first thermodynamic law). The zone volume, which is a function of *CA* time (among others), is also a significant factor since it affects the *NO* formation calculations as shown in Eq. (3.97).

An indicative representation of the zone *3* and *30* history of *NO* formation, zone temperature and volume, in–cylinder pressure, instantaneous fuel mass burnt at each *CA* interval and the unburnt zone temperature, is depicted in Fig. 4.59. In addition, the histories of the species composition participating in the *NO* formation mechanism used (see section 3.5.7) are depicted in Fig. 4.60, in order to evaluate their effect on *NO* formation history.

The depicted results have been derived from the implementation of the model on the first cylinder of a *2*–stroke stationary *DI* Diesel engine when operating at the highest load.

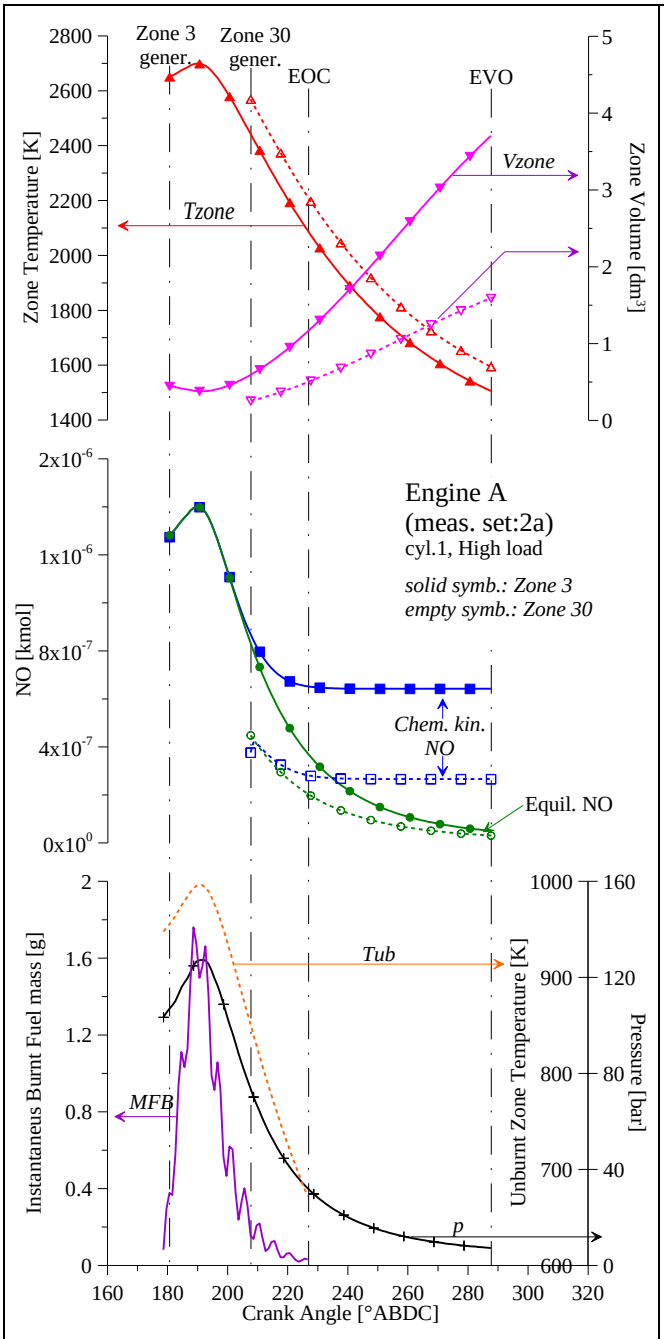

Figure 4.59: History of combustion zone 3 and 30 inside the combustion chamber during an engine cycle. Comparison between the equilibrium and actual (kinetically control) NO mole amount.

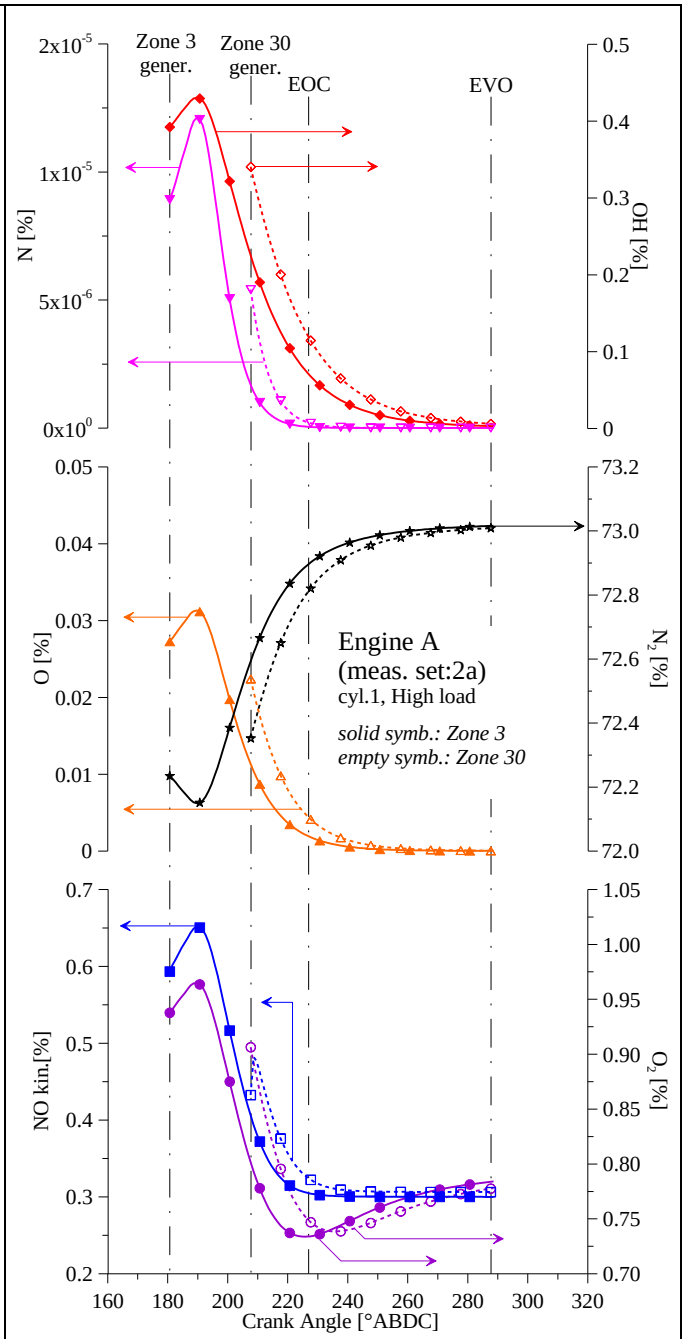

Figure 4.60: History of the species composition (that participates in NO formation mechanism) of combustion zone 3 and 30 inside the combustion chamber during an engine cycle.

In Fig. 4.59, is also shown the comparison between the equilibrium *NO* and actual *NO* calculated using chemical kinetics (Zeldovich mechanism). As is clearly shown, the latest "freezes" when the temperature drops under a threshold (the lower oxygen availability also contributes to the *NO* formation "freeze") in contrast to equilibrium *NO*.

The peak occurrence on the cylinder *NO* formation history (see Fig. 4.57 and 4.58) results from the fact that in some cases, the zones which follow the initial ones (at the first stages of combustion) present higher *NO* formation. Hence a peak is observed which is due

to the peak occurrence of the firstly generated zones, since the cylinder *NO* formation history is resulted from the sum of zones history at each *CA* step.

In addition, as observed in Fig. 4.59, at the zone generation and shortly after, where the temperature is significantly high, the *NO* formation calculated using chemical kinetics, approaches equilibrium (namely follows the equilibrium *NO* formation history). The *NO* formation equilibrium composition trend is similar with the temperature evolution trend (see also section 3.5.6 and Table 3.2). This is justified from the fact that as higher are the temperatures, the kinetically controlled reactions are becoming faster and the chemical reaction time is diminished significantly, thus the *NO* formation can approach equilibrium [228].

Furthermore, regarding the species that participate in Zeldovich *NO* formation mechanism (see Table 3.3), and specifically O_2, *O*, *OH* and *N*, their composition also follows the temperature evolution trend, and is steeply diminished as temperature descents during expansion as shown in Fig. 4.60. Therefore, the descending zone temperature is the main reason for the observed *NO* formation "freeze" because it has a significant impact on reaction rate constants of the *NO* formation mechanism and on the concentrations of species participating in this mechanism.

4.3.2.2 Heavy–Duty Automotive DI Diesel Engine

In the following graphs (Fig. 4.61–4.65) is depicted the *NO* formation history inside the combustion chamber along with the in–cylinder pressure evolution and the elementary fuel burnt at each *CA* interval, which have been derived from the implementation of the proposed model on the heavy–duty truck engine examined in the present work. The depicted results correspond to the highest and lowest load operating points of the five available engine speed cases.

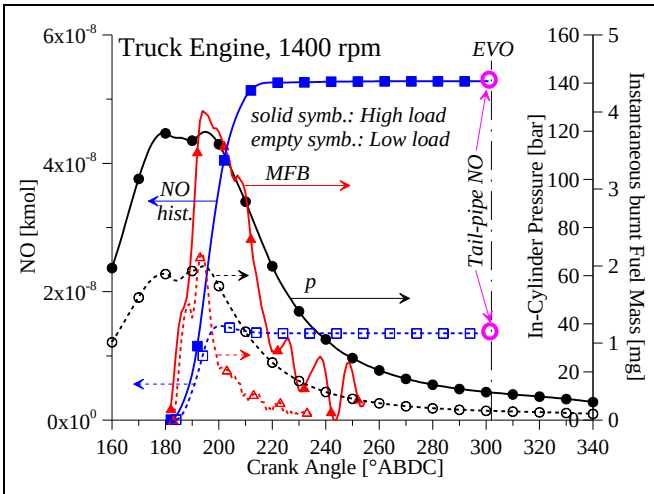

Figure 4.61: NO formation history inside the combustion chamber during an engine cycle along with the in–cylinder pressure evolution and fuel amount burnt at each CA step for Engine D1 at 1400 rpm and high and low load.

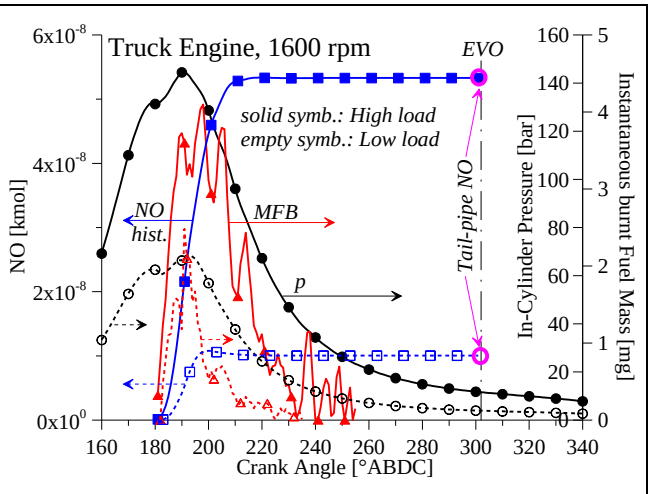

Figure 4.62: NO formation history inside the combustion chamber during an engine cycle along with the in–cylinder pressure evolution and fuel amount burnt at each CA step for Engine D1 at 1600 rpm and high and low load.

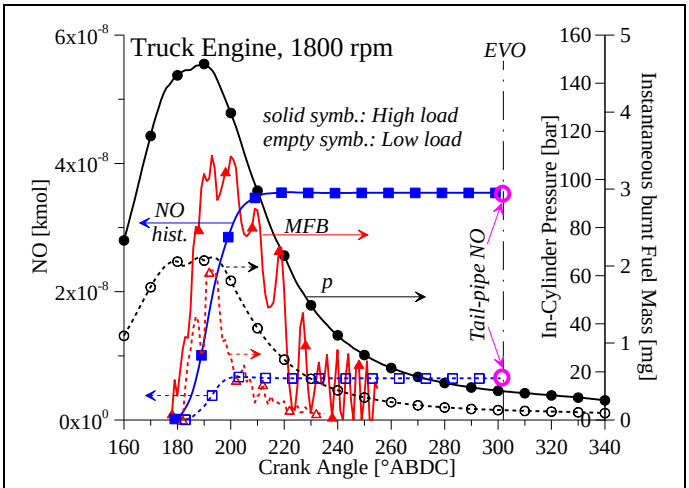

Figure 4.63: NO formation history inside the combustion chamber during an engine cycle along with the in–cylinder pressure evolution and fuel amount burnt at each CA step for Engine D1 at 1800 rpm and high and low load.

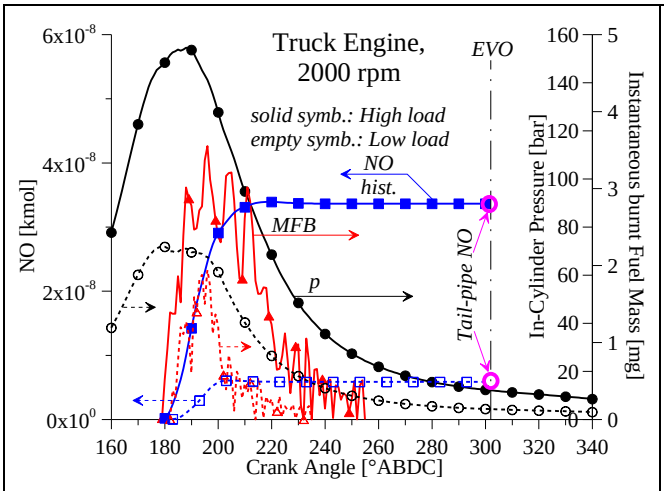

Figure 4.64: NO formation history inside the combustion chamber during an engine cycle along with the in–cylinder pressure evolution and fuel amount burnt at each CA step for Engine D1 at 2000 rpm and high and low load.

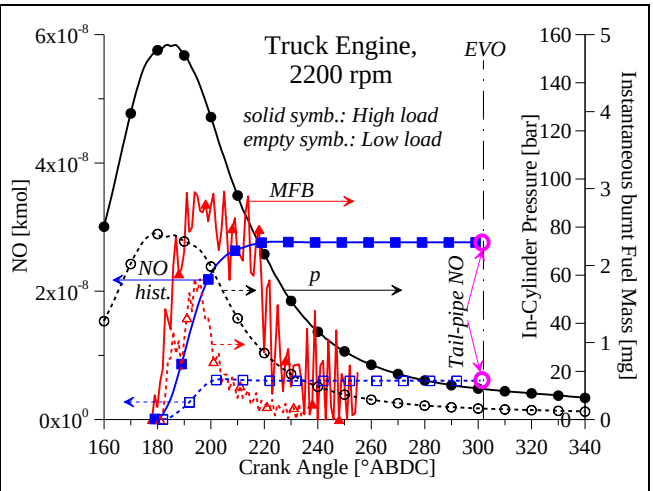

Figure 4.65: NO formation history inside the combustion chamber during an engine cycle along with the in–cylinder pressure evolution and fuel amount burnt at each CA step for Engine D1 at 2200 rpm and high and low load.

From Fig. 4.61–4.65 is observed that the *NO* formation is more intense at the initial stages of combustion where the largest amount of fuel is burnt and the temperatures are significantly high. Furthermore, as mentioned in section 4.2.3.1, the intensity of *NO* formation is reduced as engine speed increases, which is mostly attributed to the lower available time (i.e. in *ms*) that the chemical species remain in *NO* formation favorable conditions. This is possibly also the reason for the growing gap of *NO* between the lower and higher load as the engine speed decreases.

4.3.2.3 Light–Duty Automotive DI Diesel Engine

In Fig. 4.66 and 4.67 are depicted the *NO* histories for the high and low load which have been derived from the implementation of the model on the light–duty passenger car

engine examined in the present work. Along with the *NO* history, the in–cylinder pressure evolution, elementary fuel burnt at each *CA* interval (Fig. 4.66), average zone temperature (mass weighted) and the cumulative zone mass (Fig. 4.67). The average zone temperature is calculated from Eq. (4.7):

$$T_{zone,aver_i} = \frac{\sum_{z=1}^{z=i-SOC+1} m_{z_i} \cdot T_{z_i}}{\sum_{z=1}^{z=i-SOC+1} m_{z_i}} \tag{4.7}$$

where *m [kg]* and *T [K]* correspond to mass and temperature respectively and subscripts *i* and *z* correspond to the examined *CA* step and zone sequence number respectively.

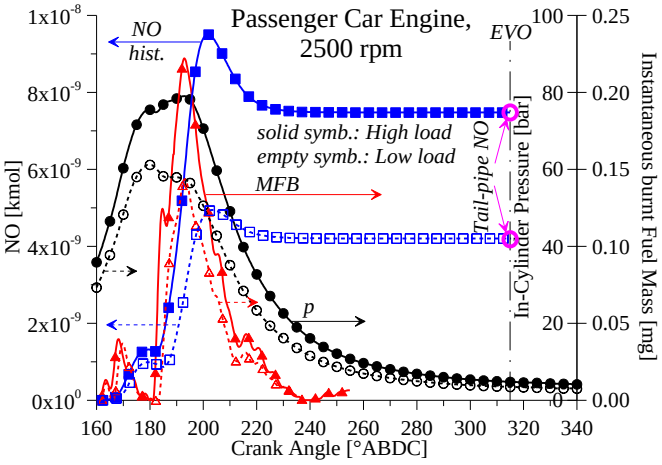

Figure 4.66: NO formation history inside the combustion chamber during an engine cycle along with the in–cylinder pressure evolution and fuel amount burnt at each CA step for engine D2 at 2500 rpm and high and low load.

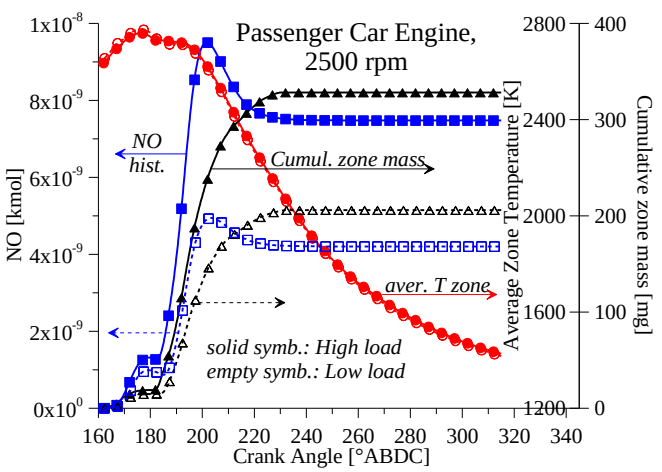

Figure 4.67: NO formation history along with the average zone temperature and cumulative zone mass for engine D2 at 2500 rpm and high and low load.

As shown in Fig. 4.66 and 4.67 the *NO* formation intensity is higher for the highest load as expected. This is mostly attributed to the amount of fuel mass burnt at each *CA* time instance and the derived zone mass amount rather than the zone average temperature in the specific case. The last is justified observing Fig. 4.67 where is clearly shown that the zone weighted average temperatures for high and low loads are quite similar. As mentioned in previous sections, the zone temperature history is strongly dependent on the initial conditions before *SOC*, which determine the unburnt zone initial temperature (reactants' temperature). For the examined case and higher load, the reactants temperature is slightly lower compared to the respective one of low load operating point. This is because, although the higher compression pressure at higher load, the trapped mass is significantly higher resulting in lower reactants temperature and hence lower zone temperatures.

4.3.3 NO_x Formation History with SOI Variation

4.3.3.1 Large–Scale DI Diesel Engines

The *NO* histories inside the combustion chamber during an engine cycle as the *SOI* setting varies for two large–scale *DI* Diesel engines, one constant speed stationary engine (Engine A) and one vessel main engine (Engine H) are depicted in Fig. 4.68. Referring

to Engine A, the *SOI* has been retarded about *3 °CA* and for Engine H, the *SOI* has been advanced about *0.5 °CA*.

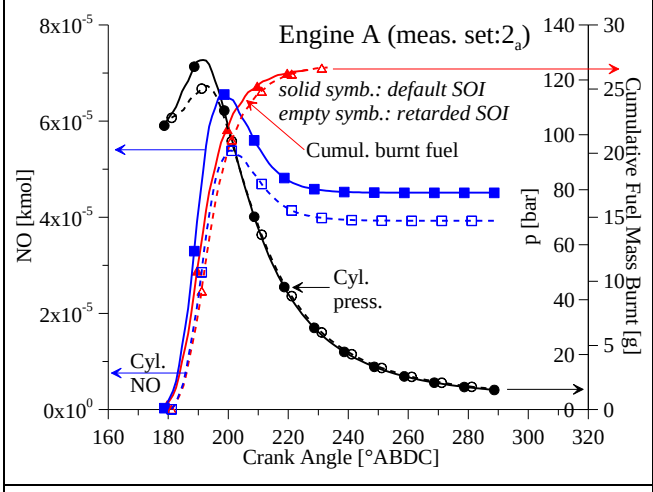

2–str. stationary, constant speed DI Diesel engine established in a power plant.

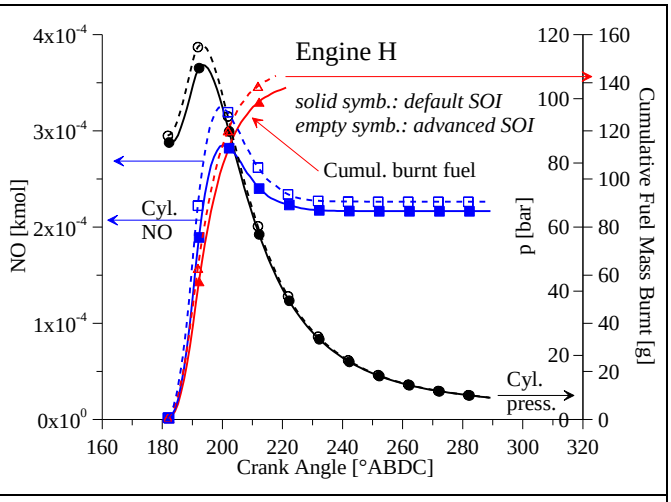

2–str. ship propulsion DI Diesel main engine.

Figure 4.68: NO formation history inside the combustion chamber along with pressure evolution in the cylinder and cumulative fuel mass burnt in the combustion chamber during an engine cycle against SOI variation.

From the observation of Fig. 4.68, the effect of *SOI* on *NO* formation history is evident. As the fuel injection initiates later in the cycle, the *NO* formation is reduced. This is apparently due to the lower temperatures developed, since the combustion initiates later in the cycle and hence is evolving under lower in–cylinder pressures. This is confirmed from Fig. 4.69 where the weighted zone temperature $\left(\frac{Temp_{zone.} \times Mass_{zone}}{Mass_{cyl.}}\right)$ history of three zones generated at three different *CA* events (i.e. at specific *°CA ABDC*) is depicted. As revealed from Fig. 4.69, the zone temperature is reduced with *SOI* retard resulting in lower *NO* formation. In order to account for both factors that affect the absolute *NO* amount formed, zone temperature and mass, the mass weighted temperature was used herein.

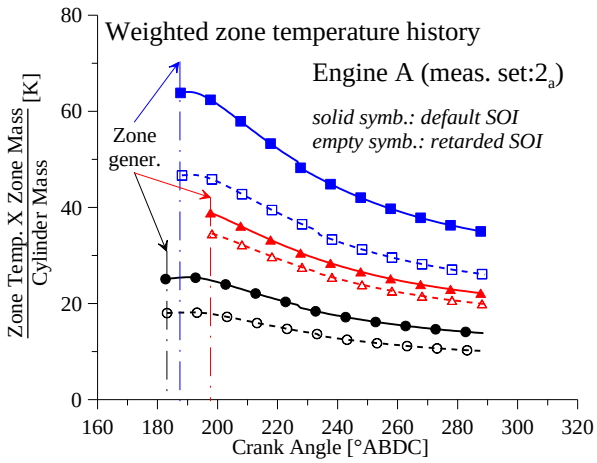

Figure 4.69: Weighted zone temperate history against SOI variation of the zones generated at 3 specific CA steps during an engine cycle at the high load of Engine A.

4.3.3.2 Heavy–Duty Automotive DI Diesel Engine

In Fig. 4.70 are depicted the results from the implementation of the model on the heavy–duty truck engine at *1800 rpm* and *86 kW* operation to examine the *NO* formation history against *SOI* variation. Here, are presented indicatively the results only for three different *SOI* settings for presentation clarity. Thus in Fig. 4.70 are depicted the *NO* formation histories along with the in–cylinder pressure evolution, cumulative fuel burnt mass and weighted average zone temperature (see Eq. (4.7)) for the following cases: *SOI=-15°*, *-4°* and *+5° ATDC*.

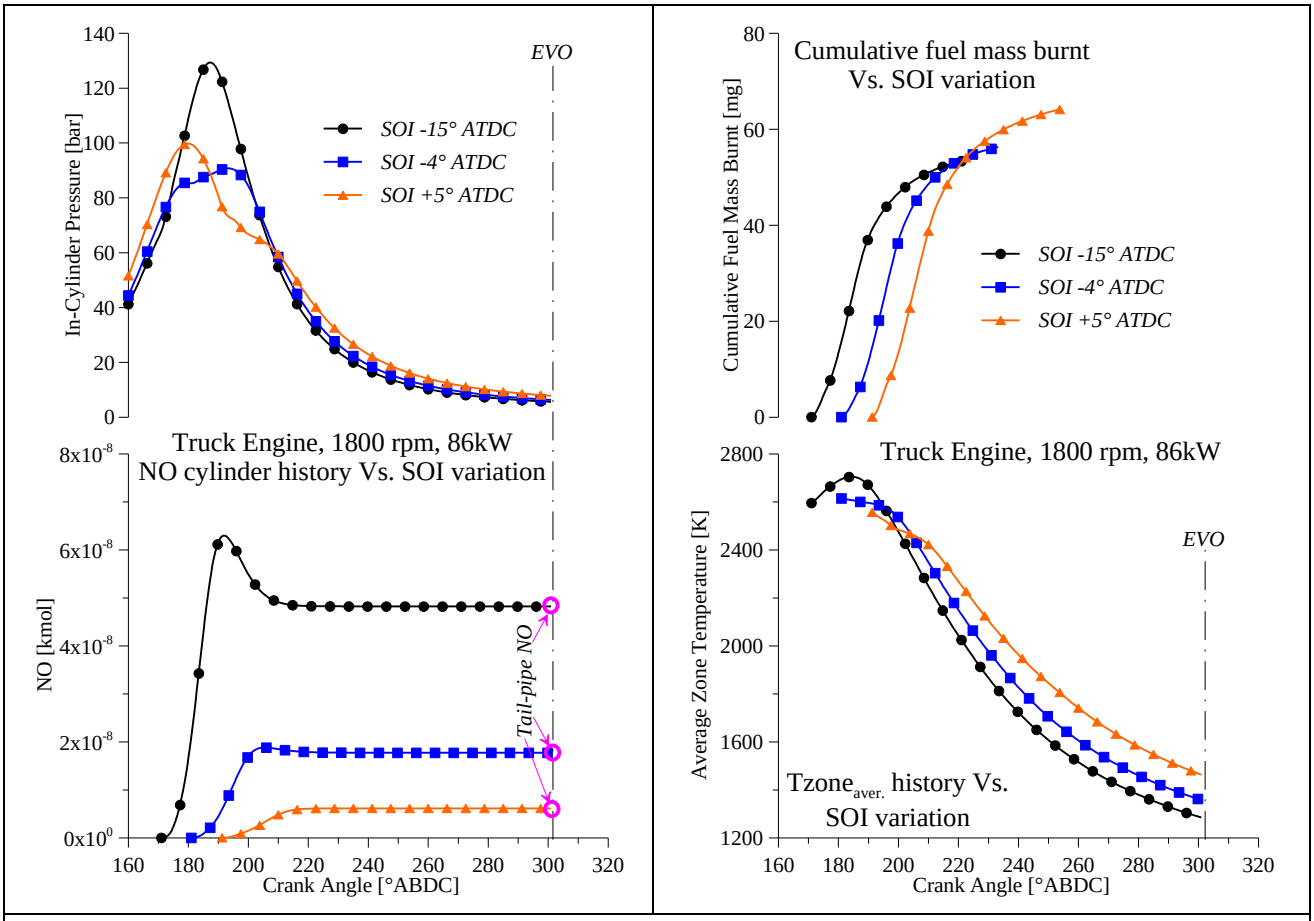

Figure 4.70: NO formation history inside the combustion chamber along with the pressure evolution in the cylinder (at the left), cumulative fuel mass burnt during an engine cycle and the average zone temperature (at the right) against SOI variation for Engine D1 at 1800 rpm and 86 kW operation.

From the observation of Fig. 4.70 the mitigation of the *NO* formation intensity as the fuel is injected later in the cycle is obvious. It is also revealed that although the average zone temperature becomes higher later in expansion as the *SOI* is retarded, the higher developed temperatures at the first stages of combustion as the *SOI* is advanced, are much more important regarding *NO* formation, since this mechanism is exponentially dependent on temperature (see Table 3.4 in section 3.5.7). Moreover, at these higher temperatures the chemical dissociation of the combustion products is intensified hence the concentrations of the species participating in the *NO* formation mechanism (see Table 3.3 in section 3.5.7) are significantly increasing, resulting in higher *NO* amounts.

The time period (in *ms*) that the combustion products remain in a high temperature regime is critical for *NO* formation. As soon as the temperature drops under a temperature

threshold, the *NO* formation "freezes" up to the *EVO* event. For instance, regarding the most advanced *SOI* setting, due to the longest time period that the combustion products remain in high temperatures, after the steep increase of *NO*, the *NO* formation rate becomes negative resulting *NO* reduction. The last persists because although the temperature drops, is still higher than the "freezing" threshold.

4.3.3.3 Light–Duty Automotive DI Diesel Engine

The *NO* formation history inside the combustion chamber during an engine cycle, for the passenger car engine, for different engine *SOI* settings is depicted in Fig. 4.71. In Fig. 4.71 are indicatively depicted the results derived from the application of the proposed model on the aforementioned engine at *2000 rpm* and *2500 rpm* and mid–load. The *SOI* settings correspond to *-15°*, *-4°* and *+2° ATDC.*

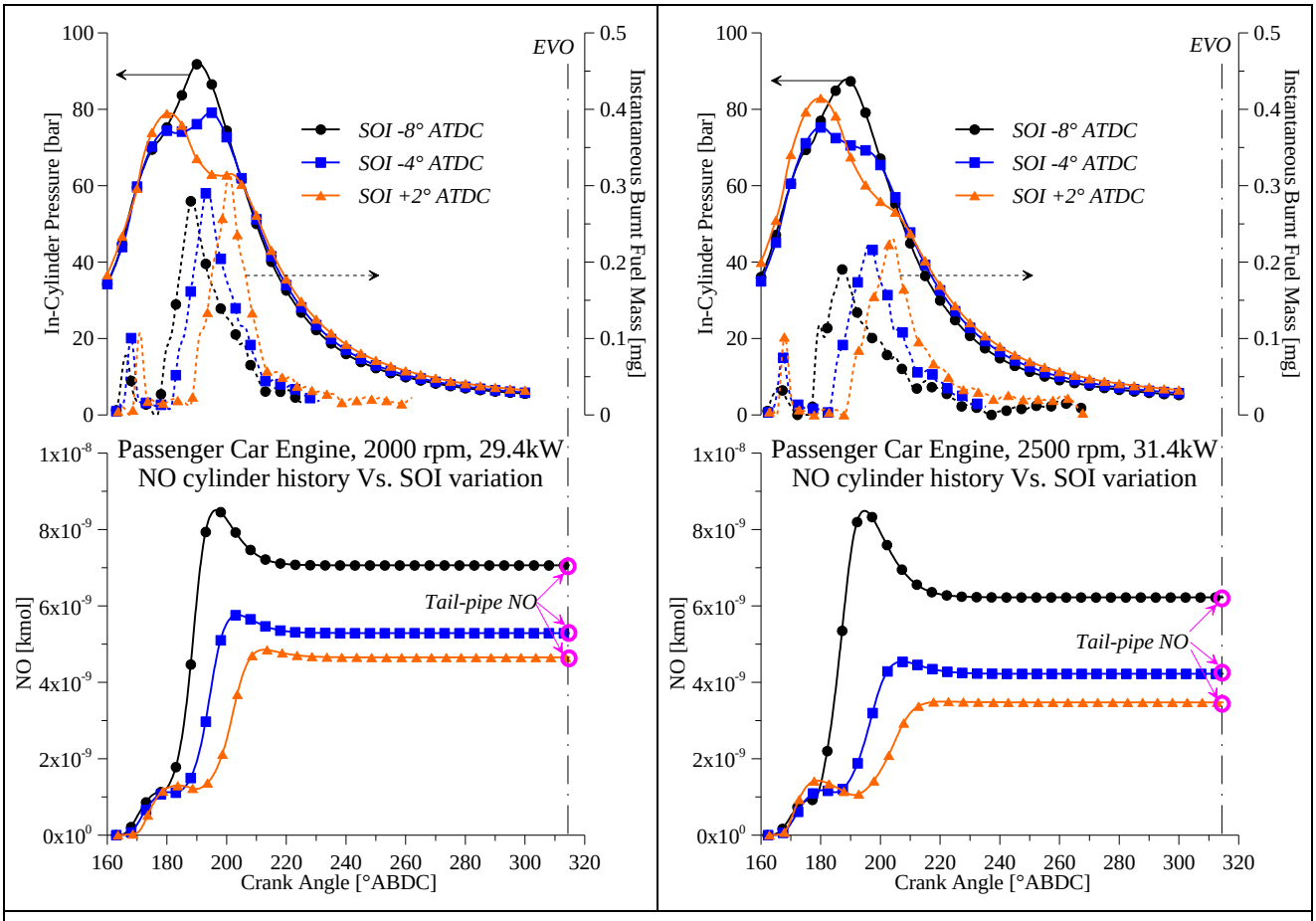

Figure 4.71: NO formation history inside the combustion chamber along with the pressure evolution in the cylinder and instantaneous fuel burnt mass during the cycle against SOI variation for Engine D2 at 2000 rpm and 29.4 kW (at the left) and 2500 rpm and 31.4 kW (at the right).

As shown in Fig. 4.71, the *NO* formation inside the combustion chamber is reduced as the *SOI* is retarded. The reasons for this variation have been already explained in section 4.3.3.1and 4.3.3.2. Here it is noted that the *NO* formation occurs also during the pilot combustion, even if its intensity is significantly lower. In addition, it can be observed that the *NO* formation intensity is diminished as the engine speed increases especially for the most retarded *SOIs*. This is attributed to the lower time (in *ms*) that the combustion products remain in high temperature regimes, as the engine speed increases.

4.3.4 NO_x Formation History with EGR Rate Variation

4.3.4.1 Heavy–Duty Automotive DI Diesel Engine

In Fig. 4.72 are depicted the results from the implementation of the model on the heavy–duty truck engine at *1800 rpm* and *86 kW* operation to examine the *NO* formation history against *ERG* rate variation. Here, are presented indicatively only the results for three different *EGR* rates for presentation clarity. Thus in Fig. 4.72 are depicted the *NO* formation histories along with the in–cylinder pressure evolution, zone average O_2 and *O* concentrations and weighted average zone temperature (see Eq. (4.7)) for the following cases: *ERG~2%*, *13%* and *18%*.

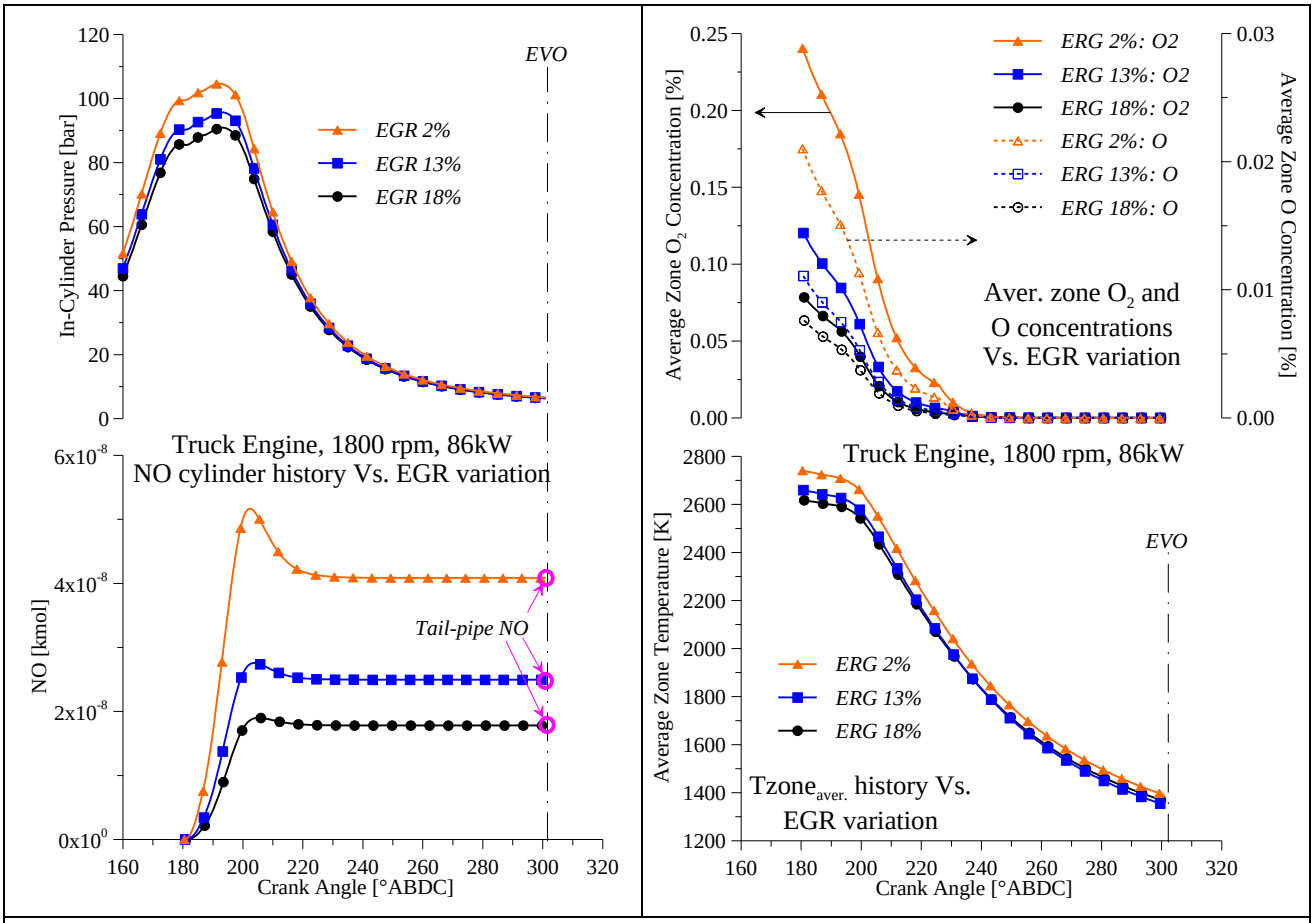

Figure 4.72: NO formation history inside the combustion chamber along with pressure evolution in the cylinder (at the left), average zone O_2 and O concentrations and temperature during an engine cycle (at the right) against EGR variation for Engine D1 at 1800 rpm and 86 kW operation.

As shown in Fig. 4.72 the *NO* formation intensity is reduced with the increase of *EGR* rate as expected. The last is resulted from the lower temperatures developed during the cycle and lower oxygen concentrations. The temperature becomes lower with *EGR* increase because the heat capacity of the charge (*EGR* + *RG* + ambient air) is increased, the oxygen availability is decreased and more heat is absorbed during the dissociation of the *EGR* gas components (see also section 1.4.2.5). Observing Fig. 4.72, the decrease of weighted average zone temperature (see Eq. (4.7)) and average zone equilibrium concentrations of O_2 and *O* as *EGR* rate increases is evident. The average zone equilibrium concentrations of O_2 and *O* are diminishing as the *CA* time elapses because, due to the descending temperatures, the

dissociation of the combustion products (from which the O_2 and O, comprised in the zone, are derived) becomes less intensive.

It is emphasized that for the present cases, the zone Φ, which has been provided from the empirical correlation described in Eq. (3.101), is slightly greater that stoichiometry (i.e. $\Phi > 1$). Hence the O_2 and O comprised in the zone are only derived from the chemical dissociation of the products of ideal combustion (see section 3.5.8), since no further air entrainment occurs after the zone formation, according to the model's concept. Moreover is highlighted that the reactants composition, used in zone combustion and determined from the *EGR* and *RG* fractions (taken into account in the model's calculations), affects the composition of combustion products and hence *NO* formation.

In addition, the observed decreasing compression pressure (see Fig. 4.72) is justified as follows: The specific engine uses high pressure *EGR* system and a fixed geometry turbine. Thus, by increasing the *EGR* rate, the exhaust gas amount that feeds the turbine decreases resulting lower compression pressures and charge trapped mass. The lower compression pressure results in lower combustion pressures and hence lower *NO* formation.

4.3.4.2 Light–duty automotive DI Diesel engine

The variation of *NO* formation history with *EGR* rate for the passenger car engine is depicted, along with the in–cylinder pressure evolution, weighted average zone temperature (see Eq. (4.7)) and average zone oxygen concentrations, in Fig. 4.73. In Fig. 4.73 are presented indicatively only the results derived from the implementation of the model for three different *EGR* settings for engine operation at *2500 rpm* and *18.3 kW*. The depicted test cases correspond to the following: *ERG~1%*, *12%* and *25%*.

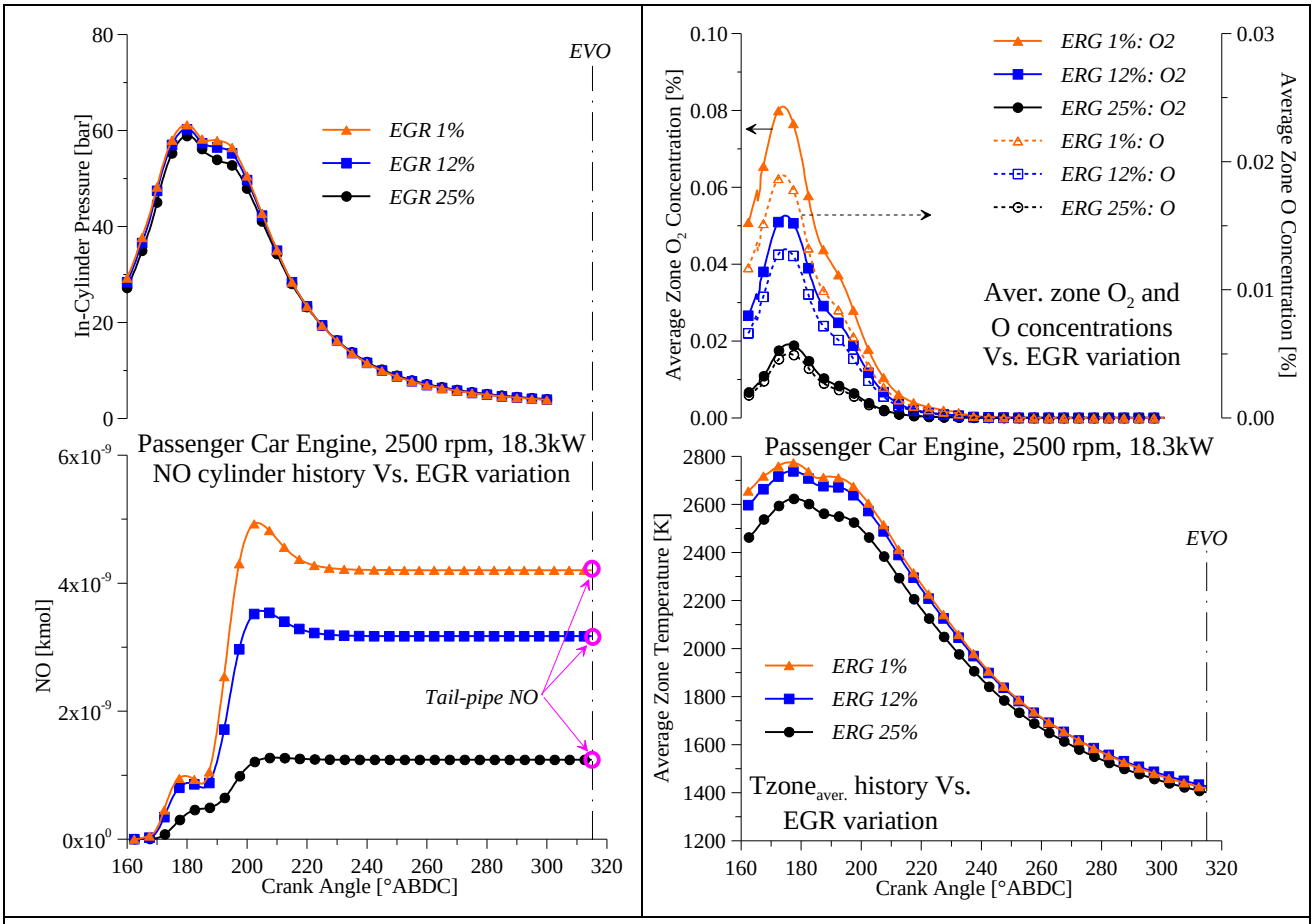

Figure 4.73: NO formation history inside the combustion chamber along with pressure evolution in the cylinder (at the left), average zone O_2 and O concentrations and temperature during an engine cycle (at the right) against EGR variation for Engine D2 at 2500 rpm and 18.3 kW operation.

From the observation of Fig. 4.73, the diminishing *NO* formation inside the combustion chamber during the engine cycle when the *EGR* rate is increased is evident. This is because the increasing amount of *EGR* gasses results in lower temperatures and oxygen concentrations as already explained in section 4.3.4.1.

4.3.5 NO_x Formation History with Fuel Injection Pressure Variation

4.3.5.1 Heavy–Duty Automotive DI Diesel Engine

In Fig. 4.74 are depicted the results from the implementation of the model on the heavy–duty truck engine at *1800 rpm* and *86 kW* operation to examine the *NO* formation history against fuel injection pressure (rail pressure) variation. In the present section, only the results for three different injection pressure settings are indicatively presented. Thus in Fig. 4.74 are depicted the *NO* formation histories along with the in–cylinder pressure evolution, instantaneous fuel mass burnt at each *CA* step, cumulative zone mass (sum of zones'

mass at each *CA* step) and weighted average zone temperature (see Eq. (4.7)) for the following cases: *pInj.=1000 bar*, *1200 bar* and *1400 bar*.

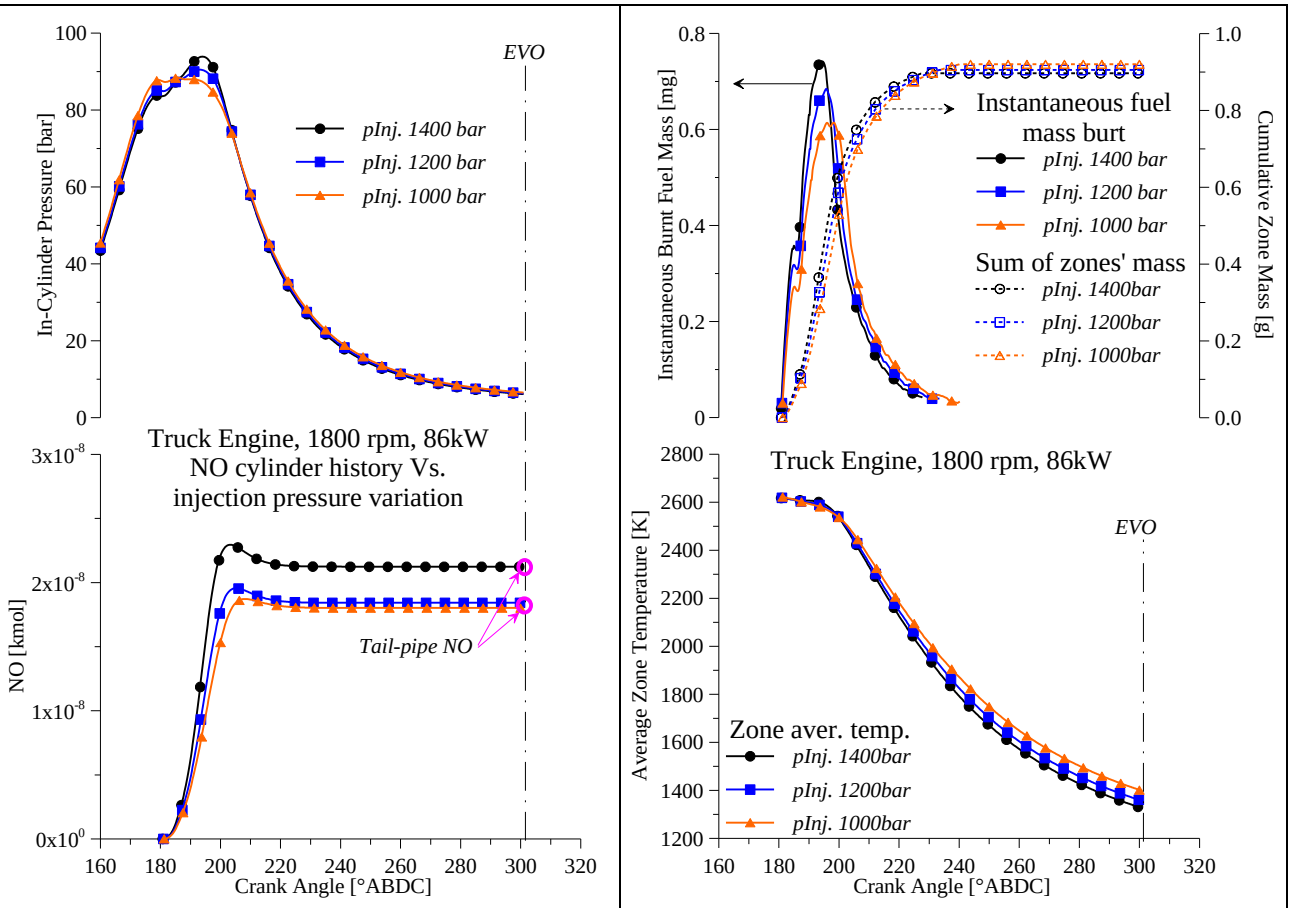

Figure 4.74: NO formation history inside the combustion chamber along with the pressure evolution in the cylinder (at the left), instantaneous fuel mass burnt during the engine cycle, cumulative zone mass and weighted average zone temperature history (at the right) against fuel injection pressure variation for Engine D1 at 1800 rpm and 86 kW operation.

As shown in Fig. 4.74 the *NO* formation increases as fuel injection pressure increases, however not significantly when compared to the corresponding *NO* formation variation with *SOI* and *EGR* rate (see section 4.3.3.2and 4.3.4.1 respectively). From Fig. 4.74 it can also be observed an increase of in–cylinder peak pressure with fuel injection pressure increase. Furthermore, it is shown that as the injection pressure increases, more fuel is burned earlier in the cycle (i.e. closer to the highest pressure/temperature part of the cycle). Moreover, the slope of the cumulative zone mass is stepper as the injection pressure increases which indicates combustion duration shortening (i.e. the same energy amount is released in a shorter *CA* interval, closer to the *CAs* where the highest pressure/temperature conditions in the cycle are prevailing). Due to the aforementioned reasons, *NO* formation increase with injection pressure. Namely, although the weighted average zone temperature (see Eq. (4.7)) does not vary significantly (at temperatures greater than *2000 K* which have a significant effect *NO* formation), the *NO* formation increase with injection pressure is attributed to the increasing amount of mixture burnt near the highest pressure/temperature part of the engine cycle (i.e. close to *SOC* and *TDC*). The increase of injection pressure results in more efficient fuel atomization/vaporization/mixing and hence lower ignition delay and faster combustion. This is the reason that a greater amount of combustion products is gathered at the highest pressure/temperature part of the cycle resulting in higher number of *NO* moles.

4.3.5.2 Light–Duty Automotive DI Diesel Engine

In Fig 4.75 are depicted the *NO* formation histories inside the combustion chamber during an engine cycle, indicatively for three different fuel injection pressure settings of the passenger car engine. The depicted results have been derived from the implementation of the proposed model on the aforementioned engine at *2000 rpm* and *2500 rpm* and mid–load for the following injection pressure settings: *650 bar*, *800 bar* and *900 bar*.

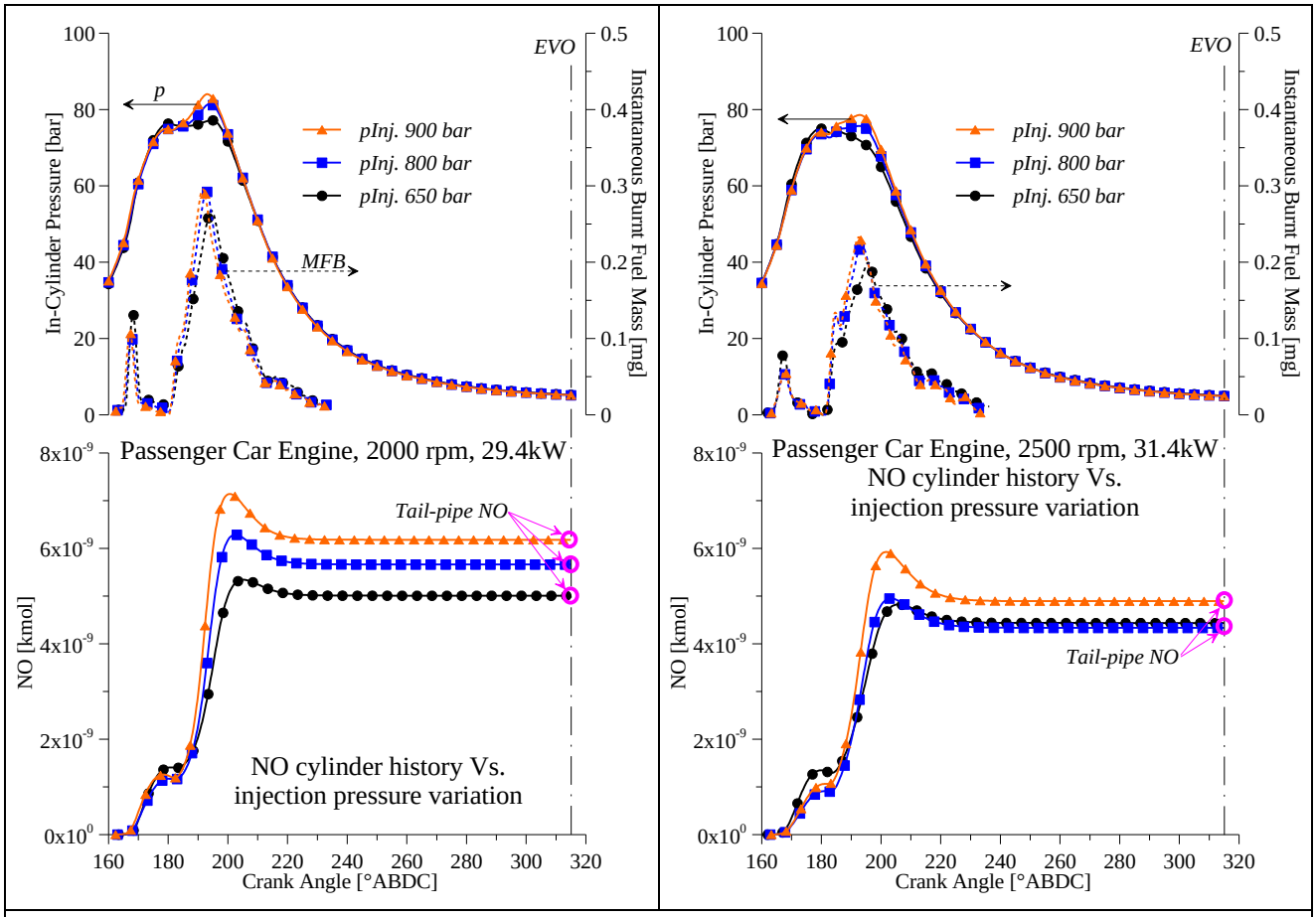

Figure 4.75: NO formation history inside the combustion chamber along with the pressure evolution in the cylinder and instantaneous fuel burnt mass during the cycle against fuel injection pressure variation for Engine D2 at 2000 rpm and 29.4 kW (at the left) and 2500 rpm and 31.4 kW (at the right).

From the observation of Fig 4.75, is revealed that the *NO* formation inside the combustion chamber during the engine cycle is increased with injection pressure increase. Furthermore, as shown in Fig 4.75 higher peak pressures are developed with the increase of injection pressure resulting in higher temperatures. The last in combination with the increasing combustion of fuel mass amount (energy release) and hence the increasing charge mass amount closer to the high pressure/temperature part of the cycle (due to the combustion duration shortening as explained in section 4.3.6.1), resulting in increasing *NO* formation. Comparing the *NO* formation for different engine speeds, it is observed that *NO* formation is reduced as the engine speed increases and also the effect of injection pressure is waning. This is due to the less time (in *ms*) available for *NO* formation (also see section 4.3.3.3).

4.3.6 NO_x Formation History with Intake Manifold Pressure Variation

4.3.6.1 Heavy–Duty Automotive DI Diesel Engine

The results derived from the implementation of the model on the heavy–duty truck engine at *1800 rpm* and *86 kW* operation to examine the *NO* formation history against intake manifold pressure (boost pressure) variation are presented in Fig. 4.76. Only the results for three different intake manifold pressure settings are indicatively presented herein. In Fig. 4.76 are depicted the *NO* formation histories along with the in–cylinder pressure evolution, instantaneous fuel mass burnt at each *CA* step, cumulative zone mass (sum of zones' mass at each *CA* step), weighted average zone temperature (see Eq. (4.7)) and zone average O_2 concentration history for the following cases: *pIM=1.3 bar*, *1.6 bara* and *1.9 bar* (absolute pressure).

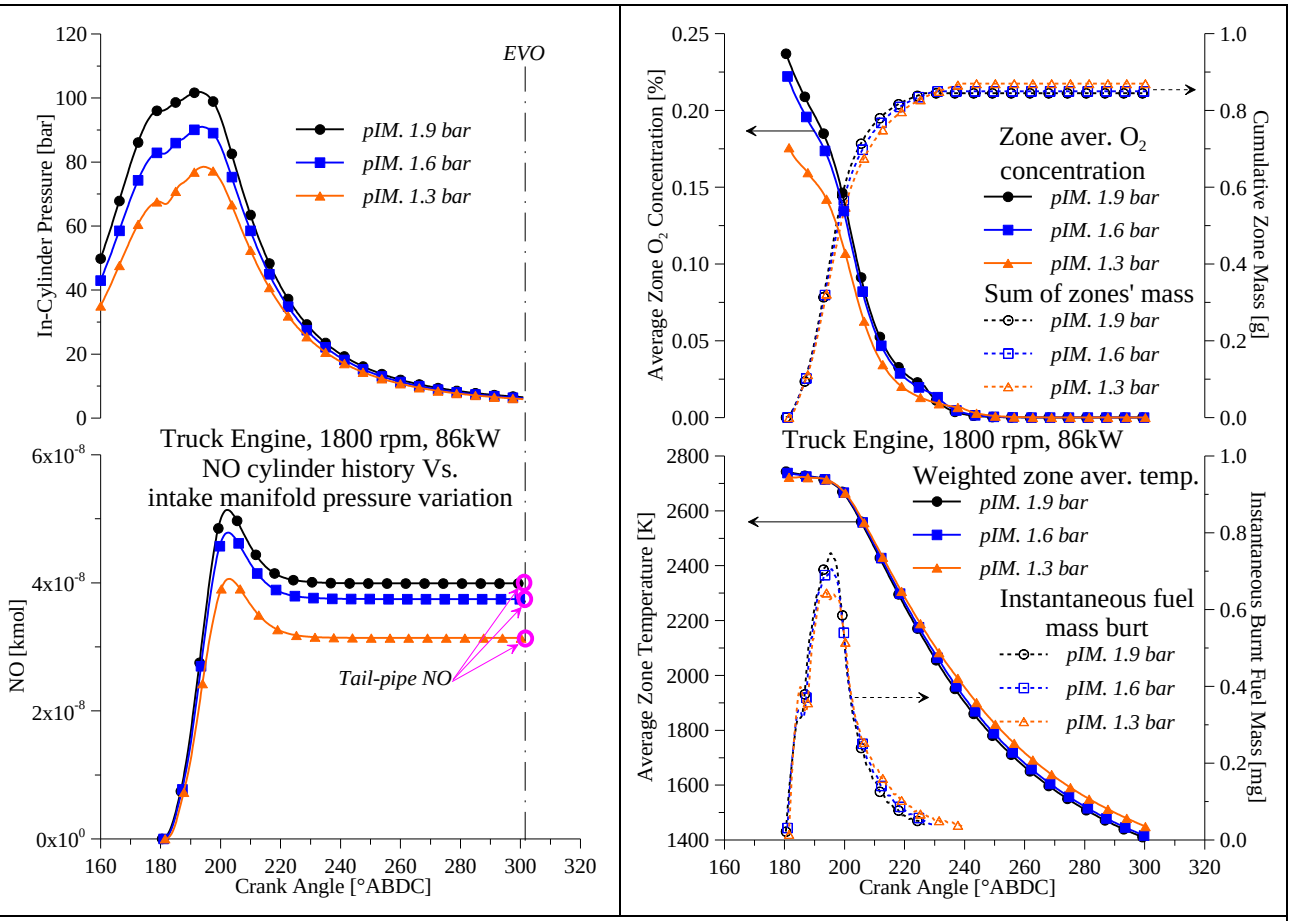

Figure 4.76: NO formation history inside the combustion chamber along with the pressure evolution in the cylinder (at the left), instantaneous fuel mass burnt during the cycle, cumulative zone mass, weighted average zone temperature and average zone O_2 concentration history (at the right) against intake manifold pressure variation for Engine D1 at 1800 rpm and 86 kW operation.

As shown in Fig. 4.76, the *NO* formation increases with intake manifold pressure. It can also be observed a significant increase of in–cylinder pressure as intake manifold pressure increases. The increase of in–cylinder pressure also affects the O_2 formation via combustion products dissociation (see Table 3.2 in section 3.5.6) and hence the average zone O_2 concentration is increased.

Furthermore, it is revealed that as the intake manifold pressure increases, the fuel is burned faster, thus greater amounts of mixture are combusted close to the highest pressure/temperature regions of the cycle (i.e. the first stages of combustion). Moreover, the slope of the cumulative zone mass becomes stepper as the intake manifold pressure increases which indicates combustion duration shortening (i.e. the same mixture amount is combusted in a shorter *CA* interval, closer to the *CA*s where the highest pressure/temperature conditions in the cycle are prevailing).

Although the weighted average zone temperature does not vary significantly (at temperatures greater than *2000 K* which have a significant effect *NO* formation), the *NO* formation increase with intake manifold pressure is attributed to the increasing amount of mixture burnt near the highest pressure/temperature part of the engine cycle. In addition, the increase of intake manifold pressure results in higher trapped charge temperature and hence lower ignition delay, faster combustion and higher developed in–cylinder pressures (the last results in highest thermal efficiency) and higher local temperatures. The highest mass amount of mixture combusted at the highest pressure/temperature part of the engine cycle and the higher O_2 concentrations due to the increasing in–cylinder pressure, are the major reasons for the *NO* formation increase with intake manifold pressure.

4.3.6.2 Light–Duty Automotive DI Diesel Engine

Finally in Fig. 4.77 are depicted the *NO* formation histories along with in–cylinder pressure evolution and O_2 concentration and weighed average zone temperature (see Eq. (4.7)) histories inside the combustion chamber during an engine cycle, indicatively for three different intake manifold pressure (boost pressure) settings of the passenger car engine. The depicted results have been derived from the implementation of the proposed model on the

aforementioned engine at *2000 rpm* and *2500 rpm* and mid–load engine operation for the following intake manifold pressure settings: *1.1 bar*, *1.2 bar* and *1.7 bar* (absolute pressure).

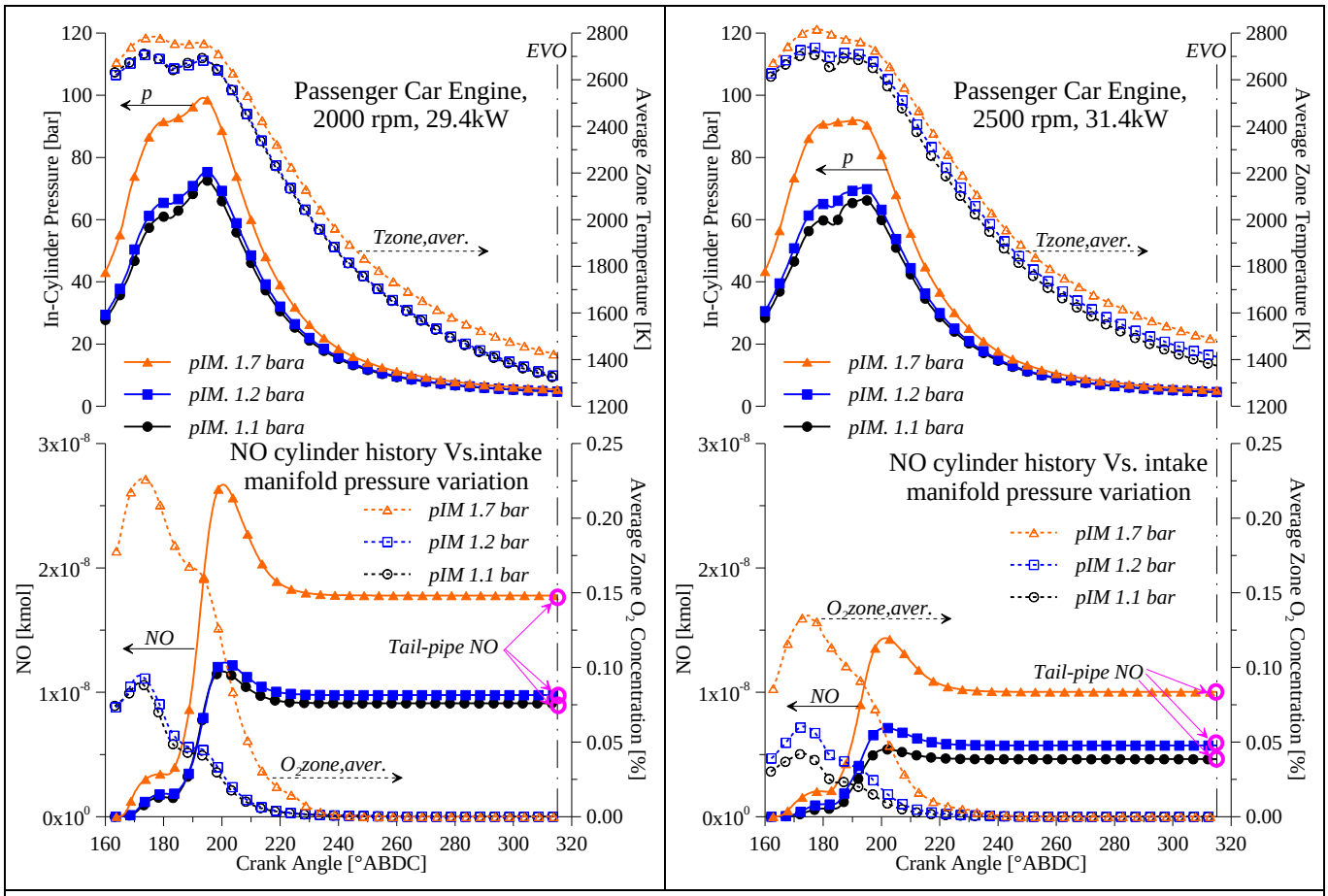

Figure 4.77: NO formation history inside the combustion chamber along with the pressure evolution in the cylinder, weighted average zone temperature and average zone O_2 concentration against intake manifold pressure variation for Engine D2 at 2000 rpm and 29.4 kW (at the left) and 2500 rpm and 31.4 kW (at the right).

Observing Fig. 4.77, it is revealed that *NO* formation increases with intake manifold pressure. This increase is due to the increase of the in–cylinder pressure, local temperatures, O_2 availability (from combustion products dissociation) and combustion shortening (in *CA* time), namely a greater mass amount is combusted at the highest pressure/temperature part of the engine cycle as explained in section 4.3.6.1. Furthermore, from the observation of Fig. 4.77, it is deduced that the effect of intake manifold pressure becomes weaker with the increase of engine speed despite the higher average zone temperature developed at *2500 rpm* engine operation. As mentioned in previous sections, the main reason for the last is the less available time for *NO* formation as engine speed increases.

4.3.7 General Outcomes Regarding NO Formation History inside the Combustion Chamber

One of the targets of the present work was the development of a model which can be used for investigations regarding *NO* formation inside the combustion chamber during the engine cycle. As revealed from the previous sections 4.3.2–4.3.6, the model is capable

to provide an image of the formation history of total and zone (local) *NO* inside the combustion chamber. This image has not been experimentally validated yet however is in concordance with the relevant literature/theory [8,108,152,182].

Furthermore, from this investigation, it has been revealed that the model is capable to capture the effect of engine load and speed, *SOI*, *EGR* rate, fuel injection pressure and intake manifold pressure on *NO* formation and assist to its physical interpretation. This capability stems from the use of the measured in–cylinder pressure trace, actual engine operating conditions/characteristics (e.g. trapped mass composition which is affected from *EGR* rate and *RG* fraction, engine speed, etc.) and its strong physical base. Thus, the proposed model, after further development, it can be utilized in optimization studies for NO_x control.

4.4 Evaluation of Model Computational Time

4.4.1 Parameters Affecting Model Computational Time

One of the major targets of the present study (section 1.5) is to keep the computational time as low as possible preserving at the same time the physical consistency. The low computational cost target is currently partially fulfilled, even though the proposed NO_x model provide results in a period of a few seconds and for some cases, even lower than a second. However, after additional development and improvement of the model, it could provide results in the time scale of the engine cycle. In order to detect the most influencing parameters for the computational time of the proposed model, an investigation involving model parameters sensitivity analysis was conducted. This investigation has indicated that the parameters affecting the computational time the most are the following:

1. Zone equivalence ratio Φ_z.
2. Crank angle calculation step.
3. Integration step used in the NO_x integration calculation.
4. Number of engine cylinder used in the calculation.
5. Amount of in–cylinder trapped mass.
6. Computer system computational power.

The aforementioned sensitivity analysis for the above parameters is presented in the following sections 4.4.2 – 4.4.7. In these sections the presented results are derived from the analysis conducted on four, randomly chosen, operating points, each one derived from the following four different engine types: truck engine (*D1*), passenger car engine (*D2*), vessel propulsion *2*–stroke engine (*H*) and constant speed *4*–stroke power station engine (*P*). These engines have been presented in the previous sections: 4.2.1 for automotive and 4.1.1 large–scale engines. In the present investigation, when the effect on computational time of a specific parameter is investigated, the remaining of the aforementioned parameters sustain their default values (the ones used for the NO_x prediction in Chapter 4).

At this point, it is noted that the computational time mentioned in the next sections includes the time of pressure trace and input data reading, smoothing of the pressure signal, heat release rate (*HRR*) calculations, pressure trace and *HRR* special characteristics detection

and NO_x model implementation. The last is the most time consuming. Furthermore, it is clarified that the computational time is the *CPU* (central processing unit) time[9].

4.4.2 Zone Equivalence Ratio (Φ_z) Effect

As shown in section 3.5.8, the proposed NO_x model presents high sensitivity to the zone equivalence ratio (Φ_z) parameter. Moreover, as shown in Fig. 4.78, where the effect of the Φ_z parameter on computational time for four different engine types is depicted, this parameter has a significant effect on calculation time.

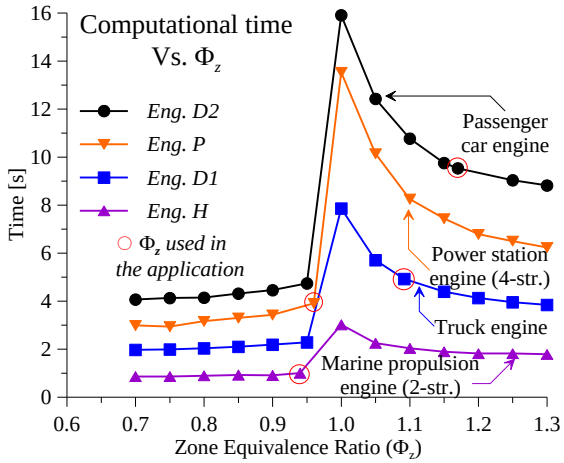

Figure 4.78: Computational time against zone equivalence ratio (Φ_z) parameter for four engine types.

Observing Fig. 4.78, it is revealed that the computational time slightly increases as Φ_z increases in the fuel lean region ($\Phi_z < 1$) and exponentially decreases, approaching asymptotically a minimum value, as Φ_z increases in the fuel rich region ($\Phi_z > 1$). However, in the lean region ($\Phi_z < 1$), computational time remains always lower than the minimum value of the fuel rich region. The intensive discontinuity at $\Phi_z = 1$, where the maximum computational time occurs, is evident. The aforementioned tendency is due to the time required for the convergence of the chemical equilibrium sub–model which has an important impact on the zone temperature calculation methodology (see sections 3.5.3 and 3.5.4). As observed, close to stoichiometry ($\Phi_z = 1$) the equilibrium composition and temperature require more time to converge. This problem could be solved with program optimization, with the use of more efficient system solving methods and/or by adopting different/improved chemical schemes for the composition calculation.

4.4.3 Crank Angle Calculation Step Effect

In the present section, is examined the effect of the crank angle (*CA*) calculation step on the total execution time. In Fig. 4.79, is depicted the variation of computational time

[9]*CPU* time is the time that the *CPU* requires to run the program exclusively. The other procedures running on the *PC* do not have an impact on it.

when the magnitude of the calculation *CA* step is increased for four different engine types. It is noted that the first value (most left) in the horizontal axis is the default *CA* step.

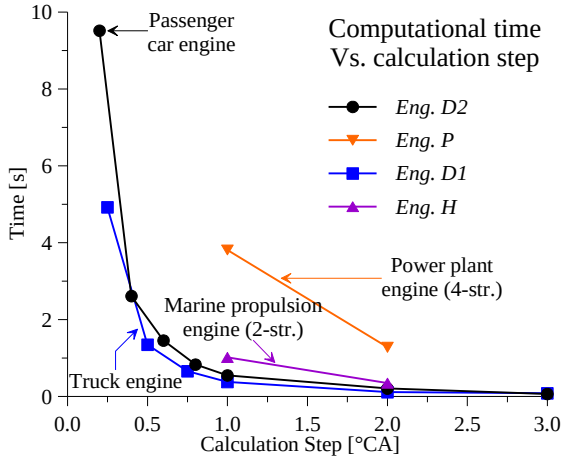

Figure 4.79: Computational time against crank angle calculation step for four engine types.

As clearly shown in Fig. 4.79, computational time steeply decreases as *CA* step is increased. The most important is that the relative error between calculated and measured NO_x values (see Eq. (4.4) in section 4.1.6), before calibration, does not significantly vary as shown in Fig. 4.80. Nonetheless, when the magnitude of *CA* step is excessive, the model fails to detect some of the pressure trace characteristics such as the *SOC* and *EOC*, maximum combustion pressure etc. and thus the model is not able to proceed to reliable calculations. This is the reason that in Fig. 4.79, for the large–scale engines, the results are not presented for *CA* step greater than *2°*. From the previous, it is inferred that an optimum calculation step can be selected to minimize computational time without significant deterioration of NO_x predictions.

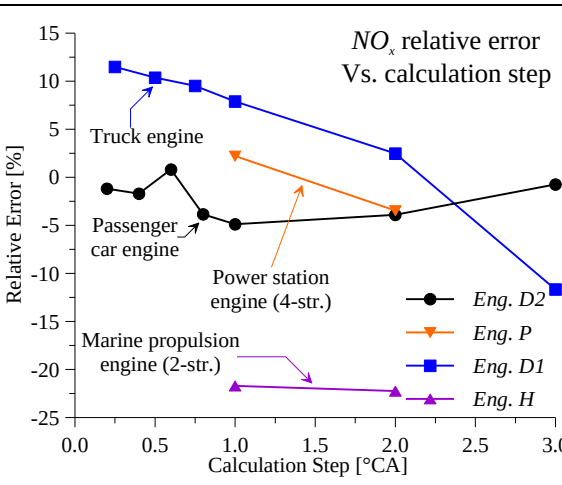

Figure 4.80: NO_x relative error (before calibration) against crank angle calculation step for four engine types.

4.4.4 NO_x Integration Calculation Step Effect

Herein, the effect of NO_x integration calculation step on the computational time is examined. The integration step is determined from the number of divisions of the *CA*

interval defined from two consecutive *CA* steps (see section 3.5.7). Apparently, this integration step influences only the NO_x sub–model. In Fig. 4.81, the effect of the number of divisions of the *CA* interval on the calculation time for four different engine types is demonstrated. The default *CA* step used in the depicted test cases, corresponds to the first value (most left, i.e. zero divisions) in the horizontal axis of Fig. 4.79 as already mentioned in section 4.4.3.

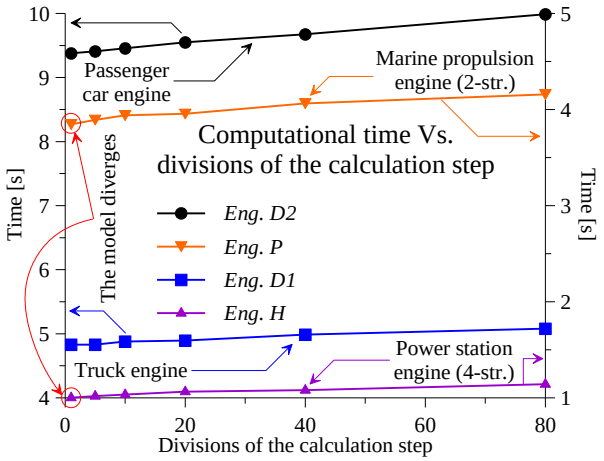

Figure 4.81: Computational Time against NO_x integration calculation step for four engine types.

The observation of Fig. 4.81 indicates that NO_x integration step has a minor effect (if it is not excessively small) on the total computational time which is slightly increased as the *CA* step is divided in more sub–steps (i.e. NO_x integration step). However, greater number of *CA* divisions (i.e. integration steps) shields the model from divergence and provides more accurate integration. On the other hand, a large integration step, may lead to inaccurate NO_x predictions, even in divergence, especially when the computational *CA* step is large. For instance, the model diverges when the integration step is equal with *1° CA*, namely *0* divisions, for both of the large–scale (Engine *H* and *P*) depicted in Fig. 4.81 and noted with a circle. Therefore, the highest possible (which does not cause divergence) integration step should be used to achieve minimum computational time.

4.4.5 Cylinder Number Effect

In the present section the effect of the number of engine cylinders used in the calculations on the computational time is examined. This effect is presented in Fig. 4.82. In this figure, in contrast to Fig. 4.78 – 4.81, only the two large–scale engines (Engine *H* and

P) are depicted since for the automotive engines (*D1* and *D2*) only measurements from the average/representative cylinder were available.

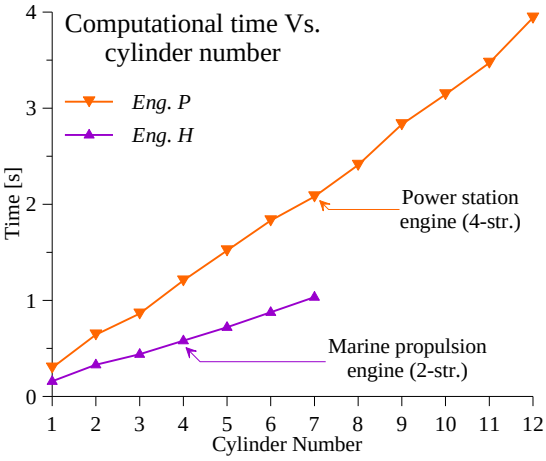

Figure 4.82: Computational time against the number of engine cylinder used, for two engine types.

In Fig. 4.82, it is clearly shown the linear increase of computational time with the number of engine cylinders as expected. Moreover, the relative error (before calibration) does not significantly affected. The last indicates that only one representative cylinder may be used in order to reduce computational time. Nonetheless, especially for the large–scale engines, sometimes is important to examine the emissions of each cylinder separately since they may have different adjustments and/or, some of them may present wear or disoperation which could affect *NO* formation.

4.4.6 Trapped Mass Amount Effect

The trapped mass amount inside the cylinder is also an important parameter affecting the computational time because in combination with the chosen zone equivalence ratio (Φ_z) has a significant impact in model's convergence. The last is explained as follows: the in–cylinder trapped mass corresponds to the initial mass amount of unburnt zone, namely just before combustion initiation. When combustion commences, the unburnt zone mass is gradually consumed since at each *CA* calculation step during combustion event, a part of it, the magnitude of which is determined from the selected Φ_z and the attributed fuel mass at the examined *CA* step, is used to form a combustion zone, as comprehensively described in sections 3.5.1 – 3.5.3. Thus, for a specific Φ_z, if the trapped mass is underestimated, the unburnt zone temperature, which coincides with combustion zone reactants' temperature, will be high and excessively higher later during combustion as its mass decreases. For this reason, the iterative procedure, used for the calculation of combustion zone temperature (see sections 3.5.3 – 3.5.4), require more time to converge, as observed. This is confirmed from

the observation of Fig. 4.83 where the variation of computational time against the percentage of the trapped mass amount which actually was used, is depicted.

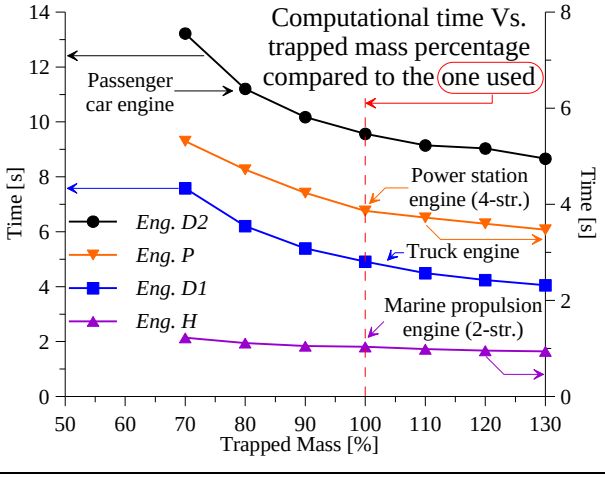

Figure 4.83: Computational time against the trapped mass percentage compared to the mass amount used, for four engine types.

From Fig. 4.83, it is revealed that computational time decreases significantly as the amount of trapped mass increases. Furthermore, regarding automotive engines (*D1* and *D2*) the relative error is severely affected from trapped mass miscalculation since it affects unburnt zone and hence reactants temperature. On the contrary, for large–scale engines (*H* and *P*) the relative error variation is less sensitive due to the higher absolute NO_x values compared to the respective ones of the automotive engines. The relative error between calculated and measured NO_x values (see Eq. (4.4) in section 4.1.6) as the trapped mass varies, for the four engine types examined herein, is depicted in Fig. 4.84:

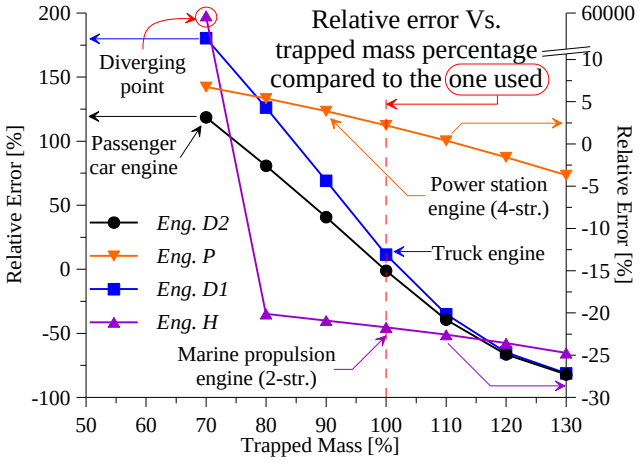

Figure 4.84: Relative error against the trapped mass percentage compared to the one used for four engine types.

Moreover, in Fig. 4.84 is also indicated that significant underestimation of trapped mass in the cylinder results in divergence of the predicted NO_x values.

Nevertheless, the present investigation, aims to reveal that the value of trapped mass amount has an impact on the total computational time affecting the convergence time of the iterative processes comprised in the model's calculations.

4.4.7 Computer System Power Effect

In the present section is examined, indicatively, the effect of the computer system power on the computational time. This was managed by running the model on personal computers (*PC*) with different specifications. Herein, the term "computer power" mostly corresponds to the number of processor threads, frequency (i.e. speed) of *CPUs* and *RAM* memory and speed. In the following Table 4.7 the basic specifications of the *PCs* used are presented in ascending "computer power" order.

PC	Processor Frequency [GHz]	Number of Processor Threads [ ]	RAM memory [Gbyte]	RAM speed [MHz]
1	2.53	1	0.5	533
2	2.00	2	2	800
3	2.00	2	4	1333
4	2.30	2	4	800
5	1.80	4	6	1600
6	1.80	4	8	1600
7	3.10	4	4	1333
8	2.50	4	6	1600
9	2.20	8	6	1333
10	2.80	8	6	1333
11	2.93	8	8	1333

Table 4.7: The basic specifications of the PCs used to run the proposed model.

In Fig. 4.85, is depicted the computational time (*CPU* time – see section 4.4.1) required from the proposed model to provide final results when it runs on each *PC*:

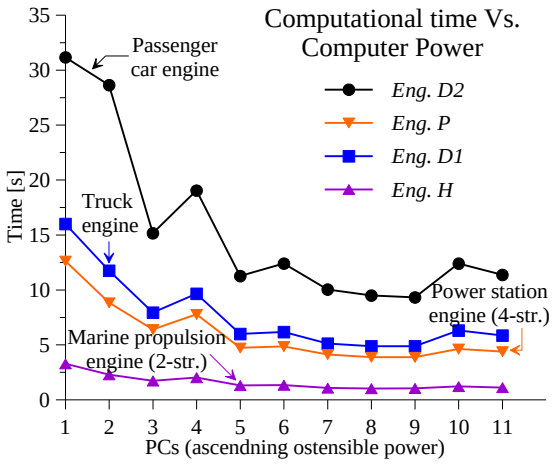

Figure 4.85: Computational time against computer power for four engine types.

From the observation of Fig. 4.85 (see also Table 4.7) is obvious that the computational time is generally decreased as computer specifications are improved (ostensible "computer power" increase) as expected. It is noted that, the order of magnitude of execution time varies for each engine type because the run settings (i.e. *CA* step, NO_x integration step, Φ, cylinder number, etc.), which have an impact on computational time (see sections 4.4.2–4.4.6), differ. The reason that the trend presents some fluctuation, is that the computational time depends not only from the parameters of Table 4.7 but also on a number of parameters such as the *CPU* stage of development, architecture of the *CPU*, number of *CPU* arithmetic units, storage unit speed, cache memory, memory management from the operating system, etc. It should be noted that the number of *CPUs* (i.e. threads) does not affect the computational time of the specific model, since its algorithm is serial and it has not been parallelized yet.

Chapter 5 SUMMARY AND CONCLUSIONS

5.1 Summary

The objective of the study described in the present dissertation is the development and evolution of a simulation tool which can provide fast and reliable predictions for NO_x exhaust emissions and formation history inside the combustion chamber of *DI* Diesel engines by using the in–cylinder measured pressure trace. For this reason, a semi–empirical, multi–zone, thermodynamic model has been developed. The source code of the proposed model was composed from the author using the FORTRAN programming language [252].

The motivation for this study emerged from the requirement of Diesel engine manufacturers and end–users for simple solutions to assist the effort for the NO_x control, monitoring and verification. This requirement stems from the demand for compliance to the current strict and future even stringent regulations for NO_x limits, which have been prescribed from national and international organizations and adopted from governments worldwide. A great number of nations have adopted these regulations in their legislation, realizing the adverse effects of NO_x emissions on human health and environment.

Considering that one of the most significant source of NO_x emissions is the tail–pipe exhaust gases from passenger cars (especially in crowded cities), automotive transportation (e.g. trucks), marine transportation and power generation in isolated areas and that the majority of the engines used for these applications are Diesel, the proposed model is focusing in this category of reciprocating internal combustion engines. Hence, the proposed model has been validated and evaluated using measurements derived from a passenger car light–duty Diesel engine, a truck heavy–duty Diesel engine and various large–scale Diesel engines of both types, *2* and *4*–stroke used for vessel propulsion (main engines) and power generation (auxiliary engines) and also in power plants in Greek Islands.

In order to investigate and analyze the existing knowledge in the field of computational *NOx* emission prediction tools, a comprehensive literature review has been conducted. From this investigation, the interest for simplified but also accurate and reliable simulation models has been revealed. These models have been extensively studied, analyzed and evaluated in order to define the areas of improvement. The advantageous features of the existing models in combination with new innovative concepts introduced in the present work, were then composed and optimized to develop a new NO_x prediction model, oriented for real–time applications. The proposed model aims to cope with the downsides of the existing models/concepts such as the high computational cost, complexity, calibration effort, low range of implementation and reliability, difficulty of handling, etc.

After the literature review, the proposed NO_x model and its sub–models have been thoroughly analyzed. At first, the measured in–cylinder pressure processing is described in brief. The determination of initial conditions (e.g. composition of the trapped mass accounting for the *EGR* and *RG* fractions) that are required for *HRR* and NO_x sub–models, follows. Regarding *2*–stroke engines, a new, modified perfect–mixing, non–isothermal scavenging

model was introduced for the determination of the initial conditions (temperature, trapped mass and its composition). Then the *HRR* analysis is demonstrated. In this analysis a single–zone concept was adopted, which uses the measured in–cylinder pressure trace, ideal combustion chemistry, Annand concept for heat exchange between the cylinder wall and in–cylinder charge, new methodologies for the determination of *SOC* and *EOC* and determination of the apparent combustion rate (i.e. the fuel amount burnt at each *CA* interval assuming instantaneous combustion). The last was utilized at next in the NO_x sub–model which distributes the elementary fuel amounts into combustion zones.

The number of zones is determined from the engine cycle – crank angle (*CA*) discretization and combustion duration (in °*CA*). After its generation, each zone is evolving during the closed engine cycle and is treated as individual thermodynamic system having its own history of temperature, volume, composition and *NO* formation while assuming pressure homogeneity inside the cylinder at each instance, which corresponds to the measured one. The temperature and volume of each zone (generating, evolving or unburnt) are calculated using the first thermodynamic law, accounting for the heat exchange through cylinder wall and the number of moles variation, without adopting any constant pressure and volume process assumptions. Moreover, the composition of the zones at the time of their generation was calculated using combustion chemistry, the zone equivalence ratio Φ_z (which is other than the mean Φ), and a chemical equilibrium scheme to calculate the equilibrium composition of the products and to account for the temperature decrease due to the endothermic chemical reactions of dissociation. This scheme was also implemented to calculate the composition of the zone while is being compressed/expanded throughout the cycle. The composition of the unburnt zone was assumed unchanged. Obviously, the NO_x is formed only in the combustion zones (at generation and evolution) and is calculated using a NO_x kinetics scheme based on the extended Zeldovich thermal *NO* mechanism. This mechanism uses as inputs the zone temperature, volume, equilibrium composition and the *NO* amount from the previous step. Thereby, the *NO* history of each zone is provided, but also the in–cylinder *NO* history (i.e. *NO* formed at each instance) from the sum of *NO* comprised in the existing zones at the current *CA* time step. This, provides the potential for investigating *NO* formation during the engine cycle. At the end of the closed engine cycle, namely when exhaust valve opens, this sum corresponds to the tail–pipe exhaust NO_x emissions.

To optimize qualitatively the model results, an empirical correlation for the calculation of the equivalence ratio used in zones' combustion (Φ_z) was developed. It is noted that, the value of Φ_z remains constant for the entire close cycle. However its value alternates for different operating points since is a lineal function of typical engine operating parameters and values derived from the measured cylinder pressure processing and *HHR* analysis. Moreover, to optimize the results quantitatively, a single scaling factor (*SF*) was used for each large–scale engine examined, which however, for the test cases examined, was relatively close to unity. The *SF* is derived from calibration on a single operating point. It is also noted that for the automotive engines examined, no calibration using *SF* was used, since the extracted results (absolute *NO* values) were adequate.

The model was implemented on various types of supercharged, *DI* Diesel engines for various engine configurations and settings variation. The test engine types and the corresponding test parameters which were used to evaluate the model's ability to predict NO_x

emissions, but most importantly NO_x trends with the variation of these parameters, were the following:

1. Two large–scale, *2*–stroke, constant speed, power generation engines established in Chios island. Variation of engine load, fuel injection timing and fuel type change from *HFO* to *DFO* (during engine operation).
2. One large–scale, *2*–stroke constant speed, power generation engine established in Paros Island. Variation of engine load.
3. One large–scale, *4*–stroke constant speed, power generation engine established in Paros Island. Variation of engine load.
4. Nine large–scale, *2*–stroke, low speed marine propulsion engines (main engines). Variation of engine speed/load and for two of them, variation of fuel injection timing.
5. Three large–scale, *4*–stroke, constant speed engines, established in ships for power generation (auxiliary engines). Variation of engine load.
6. A heavy–duty truck engine equipped with common rail fuel injection. Variation of engine load for various engine speed cases, as determined from the Extended European Stationary Cycle (*EESC*). For a particular engine speed and load: variation of fuel injection timing, *EGR* rate, fuel injection pressure and intake (boost) pressure.
7. A passenger car engine, equipped with common rail fuel injection and pilot injection. Variation of *EGR* rate, fuel injection pressure, fuel injection timing and intake (boost) pressure.

The implementation of the proposed model on these engines has provided encouraging results, revealing its capability to adequately predict the measured NO_x emissions and also capture the trend of NO_x variation as the engine parameters and settings vary. As shown, the model can also provide information for the *NO* formation history inside the combustion chamber during the engine cycle. The most important is that it accomplishes to provide reliable results, with low computational cost, for different engine types without significant calibration effort. Thus, after additional development, it can be utilized in research and practical field.

5.2 Justification of the Dissertation

From numerous scientific studies and extensive research, it has been deduced that NO_x pollution has hazardous effects on human health and environment. This is worldwide recognized thus, the governments of the developed countries have set strict limits for NO_x emissions. Among others, the internal combustion engine (*ICE*) industry is a major contributor to NO_x pollution. Hence is obligated, from the legislation, to significantly reduce NO_x emissions presently and in the near future. The future limits are continually tighten, where in some cases, the imposed from the legislation decrease comes up to *~95%*! For this reason the *ICE* manufacturers and end–users are seeking for efficient methods to control NO_x emissions in order to quarantine their presence in the markets, increase their competitiveness and avoid the high fines, severe sanctions and boycott.

To face the legislation for the NO_x emissions limits the *ICE* industry makes use of various methods/technologies for NO_x abatement. These methods/technologies are divided into two categories: primary (in–cylinder) and secondary (exhaust after–treatment) methods.

The implementation of the primary methods objects to locally limit the oxygen availability and lowering the temperatures developed in the combustion chamber which favor NO_x formation. The secondary methods aim to chemically or/and catalytically dissipate the NO_x comprised in the exhaust gases. Thus, these methods, alone or in combination, can significantly reduce NO_x emissions from Diesel engines (which is the *ICE* examined in the present work) up to more than *90%*.

It is mentioned that the secondary methods, namely exhaust after–treatment technologies, are more efficient. However, these technologies, induce a significant space and weight penalty and also present high installation and operating cost. Alternatively and/or supplementary, the primary methods should be used. These methods are advantageous because they do not present the drawbacks of the after–treatment technologies and in some cases, can be directly implemented on existing engines by applying low cost retrofits. However, their implementation requires extensive research involving the use of both, computational and experimental techniques.

Considering the previous, *ICE* industry is focusing on the use of primary (in–cylinder) measures, which alone or combined, can provide adequate NO_x reduction. These measures can also reduce the demands from after–treatment devices in cases where these are used. Therefore, increasing effort should be given (considering the cost) to reduce as much as possible NO_x emissions using primary measures. To assist the development and operating process and minimize the cost, *ICE* manufacturers and end–users are involving simulation tools, in combination with experimental research, to contribute to the effort for the enhancement of design development and efficiency optimization during actual operation (i.e. real–time/close–loop control) and to control NO_x emissions with the least possible fuel penalty.

For this reason, researchers have developed a variety of models from detailed *CFD* to very simple empirical/statistical ones to support this effort. However, as revealed, the *CFD* and *3D* spray phenomenological models present high computational cost and complexity despite the fact that they can provide a robust physical image of the processes taking place inside the combustion chamber. On the other hand, simple models (i.e. totally empirical) are very fast and can be ideal for specific applications but unfortunately are reliable only inside their calibration range. For these reasons, extensive research has been conducted for the development of semi–empirical models, which have the physical background, in order to be fast, reliable and valid in a wide range of engine configurations and operating conditions.

The majority of this type of models make use of multi–zone approaches, namely the in–cylinder charge is discretized into zones (two of more) to fairly represent the inhomogeneity of Diesel engine combustion process. They also use basic thermodynamics, combustion chemistry, empirical and semi–empirical/phenomenological correlations to describe the in–cylinder processes. Furthermore, in some cases the in–cylinder measured (or calculated) pressure trace and *HRR* analysis are used. Each one of these models has its special characteristics, advantages and disadvantages.

The proposed model, which falls into the last mentioned category, aims to use only basic thermodynamics, combustion chemistry and simple but representative thermal NO_x formation mechanism in combination with a simplified empirical concept. Furthermore, in order to maintain the concept of the proposed model simple with the features of low computational cost, low calibration effort and easy handling, high versatility and wide implementation range, are not involved complicated semi–empirical/phenomenological correlations for air entrainment, fuel vaporization mixing, mass and heat transfer, etc. which are used from similar models. The effect of the previous is compensated from the utilization of the measured pressure trace on which the proposed model is based on.

The utilization of the measured in–cylinder pressure in the calculation of combustion rate via *HRR* analysis and the use of actual pressure in the NO_x model calculations, is a robust model feature since it provides, directly or indirectly, useful information for the processes taking place inside the cylinder where the NO_x is formed. Namely, the evolution of the closed engine thermodynamic cycle is directly reflected in the pressure trace and the derived *HRR*. Moreover, the most important is that the complex mechanisms describing these processes, the modeling of which is very complicated, has high computational cost and contains many uncertainties in its calculation, can be indirectly accounted for via the use of the actual in–cylinder pressure. Some of these mechanisms are the following:

- charge flow,
- turbulence,
- spray formation,
- penetration,
- break–up,
- spreading,
- fuel atomization, vaporization and mixing with the unburnt charge,
- combustion and dissociation reactions,
- flame propagation and quenching,
- leakages,
- heat losses,
- etc.

In addition, the effect of engine geometry is also implicitly accounted for.

5.3 Conclusions of the Dissertation

Considering the previous justification for the elaboration of the present dissertation based on the *ICE* industry demand for the deployment of efficient tools to assist on the effort for NO_x abatement, a new simplified, multi–zone, semi–empirical model for NO_x prediction has been developed. The model combines physical and empirical model concepts and utilizes the in–cylinder pressure trace to provide the tail–pipe NO_x emissions and formation history during an engine cycle. The model has been extensively validated on various types of *DI* Diesel engines, as follows:

1. *2* and *4*–stroke engines.
2. Automotive engines:
   - heavy–duty and

- light–duty.

3. Large–scale engines:
   - marine propulsion (main engines),
   - marine auxiliary engines and
   - stationary power plant engines.
4. Regarding engine speed:
   - low, mid and high speed and
   - constant and variable speed.

The model ability to capture the NO_x variation trend and *NO* formation history inside the combustion chamber during an engine cycle when engine parameters vary was also examined. The examined engine parameters/settings were the following:

1. Engine speed and load.
2. Fuel type.
3. Exhaust gas recirculation (*EGR*) rate.
4. Start of injection (*SOI*) timing
5. Fuel injection pressure.
6. Intake manifold (boost) pressure.

A total of *89* operating points for large–scale engines and *132* for automotive engines were utilized for model validation and evaluation. From the results, the model's ability to adequately approach the measured NO_x absolute values but most importantly, to predict the NO_x trend with the variation of the aforementioned parameters/settings, has been presented. As for absolute NO_x emissions values, after calibration at a single operating point for each large–scale engine examined using a scaling factor (*SF*) – multiplier and without any calibration for the examined automotive engines, the model manages to predict NO_x with a relative error in the vicinity of $\pm 20\%$ for the majority of the test cases examined, for all types of engines considered.

Nevertheless, the relative error, as shown, is sometimes misleading because very low measured NO_x values induce high ratios (i.e. high relative error). This is justified when the relative error ratios of the test cases corresponding to the large–scale engines are compared against the ones of the light–duty engine which emits much lower amounts of NO_x. Namely, the *74%* of the large–scale engines test cases presents a relative error up to $\pm 10\%$ in contrast to the light–duty engine where the *43%* of its test cases lies in the error zone of $\pm 10\%$. Moreover, high relative error can result from other sources such as:

1. In–cylinder pressure primary measurement error, e.g. signal noise, pegging, etc.
2. Improper smoothing of the pressure trace, i.e. under or over–smoothing.
3. *HRR* processing and analysis.
4. Inaccurate input data (normal), i.e. *EGR* rate, fuel mass flow, intake manifold conditions.
5. Uncertain calculated trapped mass due to uncertainties in input data such as air mass flow or exhaust gas composition.
6. Computational errors (e.g. convergence, rounding, *CA* and zonal discretization, etc.).
7. Choice of the calibration point.

Furthermore, the computational time of the model was analyzed. The algorithm can provide results in a period from *10 s* to *1 s* (depends on the test case) when executed on a *PC*. However, this time period can be significantly reduced after simplification modifications of the model. The parameters that mostly effect model's run time are the following:

1. Number of iterative procedures.
2. Convergence criteria of the iterative procedures.
3. Zonal discretization, i.e. crank angle calculation step.
4. Zone equivalence ratio.
5. Trapped mass.
6. Number of cylinders considered.
7. Solver of the non–linear system for the calculation of zone composition.
8. Integration step of *NO* calculation procedure.
9. The precision of numbers used in the computation, i.e. single/double/quadruple floating–point representation format.
10. Potential/power of the computer system used (e.g. *PC*).

Finally, considering the potentials of the model developed in the present work, namely its ability to reliably predict the NO_x variation when engine parameters and settings are varied and to adequately approach the absolute NO_x values as well, for various engine types, in a considerably low computational cost, the proposed model, after additional development and validation, can be proposed for the following applications:

1. Real–time monitoring of NO_x emissions on vessels, power plants, locomotives, trucks, etc.
2. NO_x prediction at operating points required by *IMO Annex VI regulation 13* that cannot be measured, in order to complete the NO_x report/certificate.
3. Real–time and on–line NO_x emissions monitoring of vessel engines since on–line in–cylinder pressure measurement is now feasible.
4. NO_x emissions verification procedures, e.g. verification of the provided NO_x specifications (i.e. from the manufacturer), etc.
5. Prediction of NO_x emission deviation, from the certified/regulated values (e.g. from legislation), of an in–service engine, as the engine operating conditions vary.
6. NO_x sensor check for faults/malfunction (e.g. due to fouling) by comparing its measurements with the model's results.
7. Support the development/operation/real–time control and optimization of the in–cylinder (primary) NO_x abatement techniques (e.g. model–base control).
8. Contribution to the management of NO_x after–treatment systems (e.g. close–loop control, etc.).
9. Contribution to the field of engine research, development and optimization regarding NO_x control on existing engines (i.e. improvement of injection strategy, *EGR* rate, boost pressure, etc.).

5.4 Novelty Features of the Present Dissertation

Despite the fact that a variety of semi–empirical, multi–zone models have been developed in the past, herein a new concept is adopted, with new additions and novelty features. Existing knowledge, as presented in the relevant literature, new methodologies/strategies developed and comprehensive statistical analysis of a large amount of engines and experimental data, were composed to create a versatile simulation tool for the prediction of NO_x emissions from a wide range of *DI* Diesel configurations. The new, innovative and novelty features of the present work are the following:

1. A new simplified multi–zone concept was adopted for the calculation of the following:
   - tail–pipe *NO* (or equivalent NO_x) emissions,
   - *NO* formation history inside the cylinder during the closed engine thermodynamic cycle,
   - zone temperature, volume, chemical composition history during the closed engine cycle,
   - weighted average zone temperature, average zone composition and cumulative zone mass evolution during the engine cycle and
   - average cylinder temperature and chemical composition history.
2. The model makes use of the measured in cylinder pressure, on which the effects of the mechanisms taking place inside the cylinder are reflected on, directly or indirectly, to calculate, via a detailed *HRR* analysis, the elementary fuel amount burnt at each *CA* interval. The *HRR* analysis combines the first thermodynamic law and combustion chemistry and also accounts for the heat exchange with cylinder wall, actual charge composition (i.e. ambient air, *ERG* and *RG* gases) and cylinder basic geometry.
3. The combustion rate (derived from *HRR*) is discretized according to a *CA* step into individual autonomous zones which evolve throughout the engine cycle following physical laws. By this way, the combustion and evolution of each elementary fuel amount burnt at a specific *CA* interval can be investigated separately. This feature can be useful in NO_x control optimization investigations (e.g. fuel injection strategy, *EGR* rate, etc.).
4. A new approach is used for the calculation of the zone equivalence ratio Φ_z. Φ_z is calculated using an empirical/statistical correlation which involves typical engine operating parameters and values derived from the measured in–cylinder pressure processing and *HHR* analysis. Its value is calculated only once for each engine operating point and remains constant throughout the engine cycle. This feature minimizes model complexity, computational cost and calibration effort and adds versatility to the model.
5. Despite its simplified structure the proposed model sustains a strong physical base and in combination with the use of actual engine data and especially of the measured in–cylinder pressure, provide to the model directness, reliability and versatility.

6. Low calibration effort is required in order to improve quantitatively the model's results. Particularly, only a single multiplier was used for each large–scale engine (which was practically close to unity), in order to correct the raw calculated NO_x values. This multiplier, called scaling factor (*SF*), is simply derived from calibration on a single operating.

7. From the literature review, is revealed that for the first time a NO_x emissions simulation model was applied on such a large number of engine types, operating points and engine adjustments/settings.

8. Furthermore, in order to accurately and reliably locate the start of combustion (*SOC*) for various types/forms of in–cylinder pressure traces, a new methodology was developed for the determination of the *CA* step where the combustion commences (*SOC*). This methodology has successfully estimated the *SOC* for a variety of pressure traces corresponding to different engine types and engine adjustments/settings.

9. A new methodology was developed for the determination of end of combustion (*EOC*) using the *NHRR* by processing the tail of the diagram using additional smoothing and statistical technics.

10. A new, fast methodology was developed for the determination "α" coefficient used in the calculations of heat exchange through the cylinder wall.

11. Regarding *2*–stroke engines, a new simplified scavenging model was developed and used to calculate the initial conditions (trapped charge mass, temperature and *RG* mass fraction) at the start of compression, i.e. at exhaust valve closure (*EVC*).

5.5 Future Work

Despite the adequate predictions of *NO* (or equivalent NO_x) emissions that the proposed model can provide, the prospective exists for further improvement after additional development, in order to enhance its reliability, minimize the computational cost and enrich/expand its potentials.

For the enhancement of model reliability and versatility, the following modifications/additions can be employed:

1. Regarding NO_x formation calculations, additional formation mechanisms should be employed such as the N_2O–intermediate pathway. This mechanism becomes important at low–temperature combustion ($T < 1800$ *K*), e.g. in high–*EGR* combustion and low–temperature combustion (*LTC*) engines. Furthermore, considering that the fuel–bound nitrogen content in the heavy fuel oil (*HFO*), used in large–scale engines, is noticeable, the fuel NO_x formation mechanism should be employed, although its contribution is rather small, in order to account fuel's contribution to NO_x formation. The use of more complicated NO_x formation schemes, which involve numerous chemical reactions and chemical kinetics considerations, can provide more representative NO_x emissions. However, the use of these

schemes will increase the computational cost disproportionately with the grade of the results improvement.

2. As revealed from the investigation, the correct determination of the *HRR* and hence combustion rate, *TDC*, *SOC*, *COC*, *EOC*, pressure at start of compression and main *SOC*, maximum combustion pressure, etc. is crucial for the *NO* model calculations, since their miscalculation induce significant error in the model's results. Thus, the raw pressure signal should be appropriately filtered. In the present work, Savitzky–Golay filter was used with a constant width smoothing window. However, more effective digital filters can be used to achieve more intensive smoothing in regions with higher noise (e.g. late in expansion phase) but lighter smoothing is sensitive regions such as in the vicinity of *TDC*, *SOC* and maximum combustion pressure in order to avoid useful information loss. This can be managed by filtering the pressure signal using reconfigurable filters (variable smoothing window and weighting factors). Moreover, dada driven methods (e.g. wavelet, furrier, etc.) can be employed to analyze the pressure trace and contribute to signal interpretation, namely to acquire information for its specific characteristics (e.g. *SOC*) and also, to detect the noise frequencies in an effort to develop and use the suitable signal filters.
3. Despite the fact that the empirical correlation for the zone equivalence ratio Φ_z was derived from an extensive statistical investigation, further validation is proposed in the future on additional engine configurations and operating points. Moreover, the use of nonlinear polynomials should be examined. Also additional investigation is proposed in order to examine the possibility of enrichment or modification of the proposed correlation accounting for new parameters.
4. In order to enhance the model's physical background, investigations for new semi–empirical correlations may be conducted. For instance, a new correlation could provide a variable Φ_z during the engine cycle to represent, with better physical consistency, the mean actual zonal/local Φ. In Diesel engines, the mixture composition becomes from very fuel rich at the start of combustion to very lean as combustion evolves and close to stoichiometry late in combustion/expansion phase. This concept can be approached using a sigmoid function. Nonetheless, the coefficients and shape factors of such a function, should be determined via a thorough investigation using experimental and/or simulation data from relevant in–cylinder studies.
5. To further simplify the model's concept, minimize computational time and sensitively to parameter α used for heat exchange through cylinder wall process, is proposed to use an empirical concept instead of Annand's model for the heat exchange between zones and cylinder wall. For instance, a constant percentage of zone's fuel energy could be considered as a heat loss. Alternatively, an empirical correlation could be used to determine this percentage, using as independent variables the engine geometry and/or engine operating parameters such as piston position/speed, engine load, etc.

For the diminution of the model computational time, the following measures are proposed:

1. As already mentioned, the enthalpies (*h*), constant pressure specific heat capacities (*cp*) and Gibbs free energy (g^0) (and from this, equilibrium constants (*Kp*)) are calculated using the NASA polynomial approximations which are functions of temperature and composition. These polynomials are used numerous times during an engine cycle because they participate in many calculation processes, many of which are embedded in iterative computations. Hence, the use of these polynomials increases the computational cost. Thus, thermodynamic maps (JANAF tables) for each participating species may be used for the calculation of *h*, *cp* and g^0 instead of the aforementioned polynomials. However, this methodology require efficient memory and database management in order to be adequately fast.
2. Adoption of simplifications/assumptions (isentropic, adiabatic, isobaric variations, etc.) for the thermodynamic procedures. In the proposed model these assumptions were not adopted to sustain a strong physical background. However, the implementation of these assumptions will affect the quality of the extracted results and cause convergence issues due to inconsistencies that may occur during zone temperature and volume calculation (e.g. very low temperatures, negative volumes, etc.).
3. During model calculations, a large number of matrices/arrays computations are carried out, which however are executed in serial mode. Therefore, the parallelization of the algorithm is suggested, which will significantly decrease the computational cost. This conversion can be attained by using parallel programing protocols/methods such as *MPI*, *openMP*, *KUDA*, etc. Apparently, in order to utilize the time reduction ability of the parallelized algorithm, it should be run on a computational system using multiple central processing units (*CPUs*) or graphics processing units (*GPUs*), etc.
4. Programming and memory management optimization can also contribute to the computational time diminution.
5. Considering the number of iteration procedures, the use of looser convergence criteria will noticeably decrease computational time, but will also increase the risk for unforeseen divergences.
6. The algorithm of the proposed model is composed using double–precision (*64 bit*) computations. If single–precision (*32 bit*) is used instead, the computational time would be significantly decreased, since the processing and memory demands would be lower. However, this measure may result in deterioration of the results and convergence problems. The last, can be generally overtaken by using appropriate numerical methodologies.
7. One of the most time consuming procedures carried out during model calculations, is the solution of the non–linear system for the calculation of zone equilibrium composition. Herein, this system is solved, after linearization and reduction, by using the Gauss elimination method. Faster technics may be employed, such as LU decomposition, in order to decrease computational time.
8. The computational cost can obviously reduce by using advanced computer system hardware, i.e. faster *RAM* and permanent storage memory (i.e. solid state drives),

faster *CPUs*, contemporary *CPU* architecture and stage of development, *CPUs* with high number of arithmetic units, fast and high capacity cache memory, fast system bus, etc.

9. Another interesting perspective to reduce computational time, is to break the algorithm into parts and embed each part/procedure (i.e. sub–model, or group of sub–models) in a separate specialized standalone computational system. These systems would be coupled under a manager controller. Such computational systems are the application specific integrated circuits (*ASICs*) systems and the field programmable gate arrays (*FPGAs*) which are much faster than a *PC* since they are design for the specific application (e.g. do not use operating system).

In the future, the proposed model can be enriched with additional sub–models/systems in order to be able to be implemented autonomously in research and practical applications. The suggested new sub–models/systems could be the following:

1. In–cylinder pressure signal acquisition and pegging system.
2. Filtering of the analog pressure signal using the appropriate hardware (i.e. analog low–pass filters).
3. Thermodynamic model or electromechanical system for the determination of *TDC* and therefore synchronization of pressure signal with *CA*.
4. Simplified, simulation single–zone model for the prediction of pressure trace for the cases where the corresponding measured one is not available. Ideally, this model should have the capabilities to account for the variations in engine settings, e.g. *SOI*, *EGR* rate, injection pressure and boost pressure, etc.
5. Model for the estimation of fuel mass flow or ideally, system for its direct measurement.
6. Model in conjunction with the use of sensors (e.g. that measure intake pressure, temperature, exhaust O_2, etc.) for the estimation of intake air mass flow.
7. Model for the estimation of initial conditions at intake manifold (e.g. open cycle simulation) or system for their direct measurement or combination of both.

Nonetheless, the potential exists for the proposed model, to be integrated to existing, well validated software and hardware systems used for engine performance and emissions analysis, diagnosis and control.

5.6 Publications

During the period of this doctoral study the following papers were published:

1. Hountals D. T., Savva N. , and Papagiannakis R. G., "Development of a new physically based semi–empirical NO_x model using the measured cylinder pressure.", in *THIESEL 2010 Conference on Thermo-and Fluid Dynamic Processes in Diesel Engines*, Valencia, Spain, pp. 341–356, Sept. 14–17, 2010.
2. Savva N. S. and Hountalas D. T., "Detailed evaluation of a new semi–empirical multi–zone NO_x model by application on various Diesel engine configurations.", *SAE paper*, Apr. 2012, 2012-01-1156.

3. Provataris S. , Savva N. S., and Hountalas D. T., "Detailed evaluation of a new semi-empirical two–zone nox model by application on various Diesel engine configurations.", in *Proceedings of the Spring Technical Conference of the ASME Internal Combustion Engine Division.*, Torino, pp. 727-743, May 6–9, 2012.
4. Savva N. S. and Hountalas D. T., "Evolution and application of a pseudo-multi-zone model for the prediction of NO_x emissions from large-scale Diesel engines at various operating conditions.", *Energy Conversion and Management*, vol. 85, pp. 373–388, Sept. 2014.

Furthermore, the following paper have been submitted to an international journal and is currently under review:

1. Savva N. S. and Hountalas D. T., " Implementation of a Nitric Oxide (NO) semi–empirical, multi–zone model on a heavy and a light–duty DI Diesel engine.", *Under Review*.
2. Savva N. S., Raptotasios S. I., Zovanos G. N., Sakellaridis N. F., Hountalas D. T., "Investigation of fuel switching (HFO to DFO) on a large–scale, two–stroke Diesel engine: effect on performance and emissions.", *Under Review*.

REFERENCES

[1] Diesel, R., "A process for producing motive work from the combustion of fuel.", Patent No. GB189207241 A, 1892.

[2] Diesel, R., "diesel.", Patent No. US542846 A, Aug. 26, 1895.

[3] Diesel, R., "Vorrichtung zum anlässen von Viertakt-verbrennungskraftmaschinen durch umwandlung derselben in zweltakt-druckluftmachinen.", Munchen, Patent No. 86633, Apr. 27, 1896.

[4] Diesel, R., "Internal-combustion engine.", Patent No. US608845 A, Aug. 9, 1898.

[5] Jääskeläinen, H. (2013, Nov.) Early History of the Diesel Engine. [Online]. https://www.dieselnet.com/tech/diesel_history.php#diesel

[6] Kyrtatos, N.P., *Σημαντικά θέματα έρευνας και εξέλιξης στους ναυτικούς κινητήρες Diesel*. Athens, Greece: NTUA, 1993.

[7] Ishii, Y., Brooks, C., Pedersen, P.S., Hill, S.R., Wilson, K., and Craig, P.H., "A half century with marine diesel engines. Discussion.", *IMarE*, vol. 109, pp. 33-45, 1997, 1358-3956.

[8] Heywood, J.B., *Internal Combustion Engine Fundamentals.* New York, USA: McGraw-Hill, 1988, ISBN: 0071004998.

[9] Heywood, J.B. and Sher, E., *The Two-Stroke Cycle Engine*. Philadelphia, USA: Taylor & Francis, 1999, ISBN: 1560328312.

[10] Watson, N. and Janota, M.S., *Turbocharging the internal combustion engine*. London, UK: MacMillan, 1982, ISBN: 0333242904.

[11] Curran, H.J., Gaffuri, P., Pitz, W.J., and Westbrook, C.K., "A comprehensive modeling study of n-heptane oxidation.", *Combustion and Flame*, vol. 114, no. 1-2, pp. 149-177, 1998, No. 0010-2180.

[12] Caroline, G.L. (2014) Spray physics and engine research Lab. [Online]. http://www.spherelab.gatech.edu/

[13] Merker, G.P., Schwarz, C., and Teichmann, R., *Combustion engines development: mixture formation, combustion, emissions and simulation.* Berlin Heidelberg: Springer, 2012, ISBN: 978-3-642-02951-6.

[14] Ferguson, R.C., *Internal combustion engines: Applied thermosciences.* New York, USA: John Wiley, 1986, ISBN: 0471881295.

[15] Dec, J.E., "A Conceptual Model of DI Diesel Combustion Based on Laser-Sheet Imaging", *SAE Paper*, 1997, No. 970873.

[16] Flynn, P.F., Durrett, R.P., Hunter, G.L., zur Loye, A.O., Akinyemi, O.C., Dec, J.E., and Westbrook, C.K., "Diesel combustion: an integrated view combining laser diagnostics, chemical kinetics, and empirical validation.", *SAE Paper*, 1999, No. 1999-01-0509.

[17] Dembinski, H.W.R., "Flow measurements using combustion image velocimetry in diesel engines." Department of Machine Design, KTH, Stockholm, Sweden, Licentiate thesis ISSN: 1400-1179, 2012.

[18] Rakopoulos, C.D. and Hountalas, D.T., *Καύση – Ρύπανση Εμβολοφόρων Μ.Ε.Κ., Ε.Μ.Π.* Athens, Greece, 1998.

[19] Openstax CNX. [Online]. http://cnx.org/contents/39ed05df-dbef-4151-ae87-0e0646f82462@1

[20] Hernandez, J., Lapuerta, M., and Perez-Collado, J., "A combustion kinetic model for estimating diesel engine NOx emissions.", *Combustion Theory and Modelling*, vol. 10, no. 4, pp. 639-657, Jan. 2006, DOI: 10.1080/13647830600632758.

[21] Turns, S.R., *An introduction to combustion: Concepts and applications.*, 3rd ed. New York, USA: McGraw-hill, 1996, ISBN: 978-0-07-338019-3.

[22] Pipho, M.J..K.D.B..&.Z.D.D., "NO2 formation in a Diesel engine.", *SAE paper*, 1991, DOI: 10.4271/910231, No. 910231.

[23] Stone, R., *Introduction to internal combustion engines.*, 3rd ed. London: Macmillan, 1999.

[24] Rakopoulos, C.D. and Giakoumis, E.G., *Diesel engine transient operation*. London, UK: Springer, 2009, vol. 5, ISBN: 978-1-84882-374-7.

[25] Dimaratos, A.M., "Διερεύνηση των εκπομπών ρύπων κατά τη μεταβατική λειτουργία κινητήρων Diesel." Mechanical Engineering School, NTUA, Athens, Greece, Greece, Doctoral Dissertation 2011.

[26] DieselNet. (2010, Mar.) Gaseous Emissions. [Online]. https://www.dieselnet.com/tech/emi_gas.php

[27] Glassman, I. and A., Y.R., "Environmental combustion considerations. Formation and reduction of nitrogen oxides.", in *Combustion*, 4th ed. San Diego, USA, US: Elsevier, 2008, ch. 8C, pp. 417-441, ISBN: 978-0-12-088573-2.

[28] Zeldovich, Y.B., "The oxidation of nitrogen in combustion and explosions.", *Acta Physiochimica USSR*, vol. 21, no. 4, pp. 577-628, 1946.

[29] Zeldovich, Y.B., Frank-Kamenetskii, D., and Sadovnikov, P., "Oxidation of nitrogen in combustion.", *Publishing House of the Acad of Sciences of USSR*, vol. 21, no. 4, pp. 577-628, 1947.

[30] Lavoie, G.A., Heywood, J.B., and Keck, J.C., "Experimental and theoretical study of nitric oxide formation in internal combustion engines.", *Combustion Science and Technology*, vol. 1, no. 4, pp. 313-326, 1970.

[31] Cakir, H., "Nitric Oxide Formation in Diesel Engines." , in *IMechE*, vol. 188, pp. 477-483, 1974, DOI: 10.1243/PIME_PROC_1974_188_057_02.

[32] Fluent Inc., "Modeling pollutant formation - NOx formation", in *FLUENT 6.3 user's guide.*, 2006, ch. 20, pp. 20.1-20.25.

[33] Dec, J.E., "Advanced compression-ignition engines—understanding the in-cylinder processes.", *Proceedings of the Combustion Institute*, vol. 32, no. 2, pp. 2727–2742, 2009, DOI: 10.1016/j.proci.2008.08.008.

[34] Tomeczek, J. and Gradon, B., "The role of nitrous oxide in the mechanism of thermal nitric oxide formation within flame temperature range. Combustion science and technology.", *Combustion Science and Technology*, vol. 125, no. 1-6, pp. 159-180, Mar. 1997, DOI: 10.1080/00102209708935658.

[35] Mellor, A.M., Mello, J.P., Duffy, K.P., Easley, W.L., and Faulkner, J.C., "Skeletal mechanism for NOx chemistry in diesel engines.", *SAE Paper*, May 1998, DOI: 10.4271/981450, No. 981450.

[36] Arrègle, J., López, J.J., Guardiola, C., and Moni, C., "On board NOx prediction in diesel engines: a physical approach", in *Automotive Model Predictive Control*. London, UK: Springer, 2010, ch. 2, pp. 25-36, ISBN: 1849960704.

[37] Fenimore, C.P., "Formation of nitric oxide in premixed hydrocarbon flames.", *Symposium (International) on Combustion*, vol. 13, no. 1, pp. 373–380, 1971, DOI: 10.1016/S0082-0784(71)80040-1.

[38] Miller, J.A. and Bowman, C.T., "Mechanism and modeling of nitrogen chemistry in combustion.", *Progress in Energy and Combustion Science*, vol. 15, no. 4, pp. 287-338, 1989, DOI: dx.doi.org/10.1016/0360-1285(89)90017-8.

[39] Drake, M.C. and Blint, R.J., "Calculations of NOx formation pathways in propagating laminar, high pressure premixed CH4/air flames.", *Combustion science and technology*, vol. 75, pp. 261-285, 1991.

[40] Drake, M.C. and Blint, R.J., "Relative importance of nitric oxide formation mechanisms in laminar opposed-flow diffusion flames.", *Combustion and Flame*, vol. 83, no. 1-2, pp. 185-203, Jan. 1991, DOI: 10.1016/0010-2180(91)90212-T.

[41] Miller, R., Davis, G., Lavoie, G., Newman, C., and Gardner, T., "A super-extended Zel'dovich mechanism for NOx modeling and engine calibration", *SAE Paper*, 1998, DOI: 10.4271/980781.

[42] Lawrence, M.G. and Crutzen, P.J., "Influence of NO(x) emissions from ships on tropospheric photochemistry and climate.", *Nature*, vol. 402, no. 6758, pp. 167-170, November 1999, DOI: 10.1038/46013.

[43] Kampa, M. and Castanas, E., "Human health effects of air pollution.", *Environmental Pollution*, vol. 151, no. 2, pp. 362–367, Jan. 2008, DOI: 10.1016/j.envpol.2007.06.012.

[44] US-EPA. (2002) Clear skies. [Online]. http://www.epa.gov/clearskies/pdfs/overview.pdf

[45] UN. United nations environment program. [Online]. http://www.unep.org/tnt-unep/toolkit/pollutants/Nitrogen.html

[46] IMO, "Revised MARPOL Annex VI-Resoloution MEPC.176(58) & MEPC.177(58)" 2008.

[47] IMO. (2014) Nitrogen Oxides (NOx) - Regulation 13. [Online]. http://www.imo.org/OurWork/Environment/PollutionPrevention/AirPollution/Pages/Nitrogen-oxides-%28NOx%29-%E2%80%93-Regulation-13.aspx

[48] EU-EEA. Environmental policy document catalogue. [Online]. http://www.eea.europa.eu/policy-documents#c5=all&c0=0&b_start=0

[49] DieselNet. (2010, Jan) Emission Standards-European Union. [Online]. https://www.dieselnet.com/standards/eu/

[50] US-EPA. (2012, Nov.) Federal Emission Standards. [Online]. http://www.epa.gov/otaq/standards/allstandards.htm

[51] DieselNet. Emission Standards. [Online]. https://www.dieselnet.com/standards/

[52] De Risi, A., Donateo, T., and Laforgia, D., "Optimization of the combustion chamber of direct injection diesel engines.", *SAE Paper*, Mar. 2003, DOI: 10.4271/2003-01-1064, No. 2003-01-1064.

[53] Gray, C., "A review of variable engine valve timing.", *SAE Paper*, 1988, DOI: 10.4271/880386, No. 880386.

[54] Hara, S., Suga, S., Watanabe, S., and Nakamura, M., "Variable valve actuation systems for environmentally friendly engines.", *Hitachi Review*, vol. 58, no. 7, pp. 319-324, 2009.

[55] Marko, V. Operational Information: The MAN B&W MC Engine VIT Fuel Pump. [Online]. http://www.marinediesels.info/2_stroke_engine_parts/Other_info/MANBW_VIT_pump.htm

[56] Savva, N.S. and Hountalas, D.T., "Evolution and application of a pseudo-multi-zone model for the prediction of NOx emissions from large-scale diesel engines at various operating conditions.", *Energy Conversion and Management*, vol. 85, pp. 373-388, Sept. 2014, DOI: 10.1016/j.enconman.2014.05.103.

[57] Demmerle, R. and Heim, K., "Evolution of the Sulzer RT-flex common rail system." , in *24th CIMAC World Congress on Combustion Engine Technology*, Kyoto, JP, 2004.

[58] Wärtsilä, "The Sulzer RT-flex common-rail system described." VK marine library, 2004. [Online]. ftp://vk.od.ua/20011.pdf.

[59] Simelius, M., "Next steps in exhaust emissions control for Wärtsilä low-speed engines.", *Wärtsilä technical journal: indetail*, no. 1, pp. 34-37, 2007.

[60] Schnellmann, L., "Advanced technologies for improved engine efficiencies and lower emissions." , in *FFCA East Coast*, New York, 2008.

[61] Goldsworthy, L., "Design of ship engines for reduced emissions of oxides of nitrogen." , in *Engineering a Sustainable Future Conference*, 2002.

[62] Marko, V. The Miller cycle and emissions reduction. [Online]. http://www.marinediesels.info/2_stroke_engine_parts/Other_info/miller_cycle.htm

[63] Gonca, G., Sahin, B., Parlak, A., Ust, Y., Ayhan, V., Cesur, İ., and Boru, B., "Theoretical and experimental investigation of the Miller cycle diesel engine in terms of performance and emission parameters.", *Applied Energy*, vol. 138, pp. 11-20, Jan. 2015, DOI: 10.1016/j.apenergy.2014.10.043.

[64] Serrano, J.R., Arnau, F.J., Dolz, V., Tiseira, A., Lejeune, M., and Auffret, N., "Analysis of the capabilities of a two-stage turbocharging system to fulfil the US2007 anti-pollution directive for heavy duty diesel engines.", *Journal of Automotive Technology*, vol. 9, no. 3, pp. 277-288, Jun. 2008, DOI: 10.1007/s12239-008-0034-5, No. 1229-9138.

[65] MAN Diesel and Turbo, "MAN Diesel & Turbo introduces the two-stage turbocharging with new TCX generation." Copenhagen, Denmark, Press release 2010. [Online]. http://www.mandieselturbo.com/files/news/filesof14755/6510-0183%20PR%20Two-stage%20Turbocharging.pdf.

[66] Steffens, D., "The Diesel Engine and the Environment." , in *Dynamic positioning conference*, Houston, 2003.

[67] MAN B&W, "Exhaust gas emission control today and tomorrow: Application on MAN B&W Two-stroke marine Diesel engines." Copenhagen, Presentation 2010. [Online]. http://www.mandieselturbo.com/files/news/filesof11539/Exhaust%20Gas%20Emission.htm.pdf.

[68] MAN Diesel and Turbo, "Humid Air Motor: Technology for green profits" Brochure 2011. [Online]. http://www.mandieselturbo.com/files/news/filesof15316/HAM_PS_Brochure_May2011.pdf.

[69] Sarvi, A., Kilpinen, P., and Zevenhoven, R., "Emissions from large-scale medium-speed diesel engines: 3. Influence of direct water injection and common rail.", *Fuel Processing Technology*, vol. 90, no. 2, pp. 222-231, February 2009, DOI: dx.doi.org/10.1016/j.fuproc.2008.09.003, ISSN: 0378-3820.

[70] Armas, O., Ballesteros, R., Martos, F.J., and Agudelo, J.R., "Characterization of light duty Diesel engine pollutant emissions using water-emulsified fuel.", *Fuel*, vol. 84, no. 7-8, pp. 1011-1018, May 2005, DOI: 10.1016/j.fuel.2004.11.015.

[71] Khan, M.Y., Abdul Karim, Z.A., Hagos, F.Y., Aziz, R.A., and Tan, I.M., "Current trends in water-in-diesel emulsion as a fuel.", *The Scientific World Journal*, 2014, DOI: http://dx.doi.org/10.1155/2014/527472, No. 527472.

[72] Bedford, F., Rutland, C., Dittrich, P., Raab, A., and Wirbeleit, F., "Effects of direct water injection on DI Diesel engine combustion.", *SAE Paper*, Oct. 2010, DOI: 10.4271/2000-01-2938, No. 2000-01-2938.

[73] Takasaki, K., Takaishi, T., Ishida, H., and Tayama, K., "Direct water injection to Improve Diesel spray combustion." , in *ASME 2003 Internal Combustion Engine Division Spring Technical Conference.*, Salzburg, Austria, pp. 27-34, May 2003, DOI: 10.1115/ICES2003-0554, ISBN: 0-7918-3678-9.

[74] Murotani, T., Hattori, K., Sato, E., Chryssakis, C., Babajimopoulos, A., and Assanis, D.N., "Simultaneous reduction of NOx and soot in a heavy-duty Diesel engine by instantaneous mixing of fuel and water.", *SAE Paper*, Apr. 2007, DOI: 10.4271/2007-01-0125, No. 2007-01-0125.

[75] Axelsson, M., "Introduction of water to reduce NOx." KTH, Stockholm, Sweden, Master thesis 2009.

[76] Skeltved, O., "System solutions for exhaust gas emissions." , in *CIMAC NMA*, Norway, 2010.

[77] Zamboni, G. and Capobianco, C., "Experimental study on the effects of HP and LP EGR in an automotive turbocharged diesel engine.", *Applied Energy*, vol. 94, pp. 117–128, Jun. 2012, DOI: 10.1016/j.apenergy.2012.01.046.

[78] Maiboom, A., Tauzia, X., and He´tet, J., "Experimental study of various effects of exhaust gas recirculation (EGR) on combustion and emissions of an automotive direct injection diesel engine.", *Energy*, vol. 33, no. 1, pp. 22-34, Jan. 2008, DOI: 10.1016/j.energy.2007.08.010.

[79] Ladommatos, N., Abdelhalim, S., Zhao, H., and Hu, Z., "The dilution, chemical, and thermal eEffects of exhaust gas recirculation on Diesel engine emissions - Part 4: Effects of carbon dioxide and water vapour.", *SAE Paper*, 1997, DOI: 10.4271/971660, No. 971660.

[80] Tomazic, D. and Pfeifer, A., "Cooled EGR - A must or an option for 2002/04.", *SAE Paper*, Mar. 2002, DOI: 10.4271/2002-01-0962, No. 01-0962.

[81] Hawley, J.G., Wallace, F.J., Cox, A., Horrocks, R.W., and Bird, G.L., "Reduction of steady state NOx levels from an automotive diesel engine using optimised VGT/EGR schedules.", *SAE Paper*, 1999, No. 1999-01-0835.

[82] Zheng, M., Reader, G.T., and Hawley, G.J., "Diesel engine exhaust gas recirculation–a review on advanced and novel concepts.", *Energy Conversion and Management*, vol. 45, no. 6, pp. 883–900, Apr. 2004, DOI: 10.1016/S0196-8904(03)00194-8.

[83] Hansen, J.P., Kaltoft, J., Flemming, B., Gortz, J., Pedersen, M., and Underwood, C., "Reduction of SO2, NOx and Particulate Matter from Ships with Diesel Engines." Danish EPA, Copenhagen, Denmark, 978-87-93026-57-5, 2014. [Online]. http://www2.mst.dk/Udgiv/publications/2014/03/978-87-93026-57-5.pdf.

[84] Forzatti, P., "Present status and perspectives in de-NOx SCR catalysis.", *Applied Catalysis A: General*, vol. 222, no. 1-2, pp. 221–236, Dec. 2001, DOI: 10.1016/S0926-860X(01)00832-8.

[85] Lloyd's Register of Shipping, "Emissions of nitrogen oxides from marine Diesel engines: Questions and answers." London, 2002. [Online]. www.lr.org.

[86] Hitachi Zosen Corporation. (2014, Oct.) SCR system for marine Engines received world's first approval from MAN Diesel & Turbo. [Online]. http://www.hitachizosen.co.jp/english/release/2014/10/001433.html

[87] Alano, E., Jean, E., Perrot, Y., Brunel, J.P., Ferrand, N., Ferhan, M., and Pajot, K., "Compact SCR for passenger cars.", *SAR Paper*, 2011, DOI: 10.4271/2011-01-1318, No. 2011-01-1318.

[88] Fogel, S., Doronkin, D.E., Høj, J.W., Gabrielsson, P., and Dahl, S., "Combination of Ag/Al2O3 and Fe-BEA for High-Activity catalyst system for H2-assisted NH3-SCR of NO x for light-duty Diesel car applications.", *Topics in Catalysis*, vol. 56, no. 1-8, pp. 14-18, Feb. 2013, DOI: 10.1007/s11244-013-9921-8.

[89] Johnson, T.V., "Review of diesel emissions and control", *International Journal of Engine*, vol. 10, no. 5, pp. 275-285, Oct. 2009, DOI: 10.1243/14680874JER04009.

[90] Canova, M., Midlam-Mohlera, S., Pisu, P., and Soliman, A., "Model-based fault detection and isolation for a diesel lean NOx trap aftertreatment system.", *Control Engineering Practice*, vol. 18, no. 11, pp. 1307-1317, Nov. 2010, DOI: 10.1016/j.conengprac.2009.10.004.

[91] Hiroyasu, H., "Diesel engine combustion and its modeling." , in *Proceedings of 1st International Symposium on Diagnostics and Modeling of Combustion in internal Combustion Engines.*, Tokyo, Japan, pp. 53-75, 1985.

[92] Jung, D. and Assanis, D.N., "Multi-zone DI diesel spray combustion model for cycle simulation studies of engine performance and emissions.", *SAE Paper*, 2001, DOI: 10.4271/2001-01-1246, No. 2001-01-1246.

[93] Rakopoulos, C.D., Antonopoulos, K.A., Rakopoulos, D.C., and Hountalas, D.T., "Multi-zone modeling of combustion and emissions formation in DI diesel engine operating on ethanol–diesel fuel blends.", *Energy Conversion and Management*, vol. 49, no. 4, pp. 625-643, April 2008, DOI: dx.doi.org/10.1016/j.enconman.2007.07.035.

[94] Lamaris, V.T., Hountalas, D.T., Zannis, T.C., and Glaros, S.E., "Development and validation of a multi-zone combustion model for predicting performance characteristics and NOx emissions in large scale two-stroke diesel engines." , in *ASME International Mechanical Engineering Congress and Exposition*, vol. 3, Florida, USA, pp. 317-327, 2009, DOI: 10.1115/IMECE2009-11382, No. IMECE2009-11382.

[95] GT-SUITE, "Engine performance application manual." Gamma Technologies, 2009.

[96] Reitz, R.D. and Rutland, C.J., "Development and testing of diesel engine CFD models.", *Progress in Energy and Combustion Science*, vol. 21, no. 2, pp. 173-196, 1995, DOI: 10.1016/0360-1285(95)00003-Z.

[97] Kilpinen, P., "Optimization of a simplified sub-model for NO emission prediction by CFD in large 4-stroke marine diesel engines.", *Fuel Processing Technology*, vol. 91, no. 2, pp. 218-228, February 2010, DOI: dx.doi.org/10.1016/j.fuproc.2009.10.001, ISSN: 0378-3820.

[98] Coda Zabetta, E. and Kilpinen, P., "Improved NOx submodel for in-cylinder CFD simulation of low-and medium-speed compression ignition engines.", *Energy & fuels*, vol. 15, no. 6, pp. 1425-1433, 2001.

[99] Li, G. and Sapsford, S.M., "CFD simulation of HSDI engine combustion using VECTIS." Ricardo Consulting Engineer's Ltd., Shoreham-by-Sea, UK, 2003.

[100] Kosmadakis, G.M., Rakopoulos, C.D., Demuynck, J., De Paepe, M., and Verhelst, S., "CFD modeling and experimental study of combustion and nitric oxide emissions in hydrogen-fueled spark-ignition engine operating in a very wide range of EGR rates.", *International Journal of Hydrogen Energy*, vol. 37, no. 14, pp. 10917–10934, Jul. 2012, DOI: 10.1016/j.ijhydene.2012.04.067.

[101] Arsie, I., Genova, F.D., Pianese, C., Rizzo, G., Sorrentino, M., Caraceni, A., Cioffi, P., and Flauti, G., "A Single-Zone Model for Combustion and NOx Simulation in Common-Rail Multi-Jet Diesel Engines." , in *6th International Conference on Engines for Automobile*, 2003.

[102] Yasar, H., Soyhan, H.S., Walmsley, H., Head, B., and Sorusbay, C., "Double-Wiebe function: An approach for single-zone HCCI engine modeling.", *Applied Thermal Engineering*, vol. 28, no. 11-12, pp. 1284-1290, August 2008, DOI: dx.doi.org/10.1016/j.applthermaleng.2007.10.014.

[103] Awad, S., Varuvel, E.G., Loubar, K., and Tazerout, M., "Single zone combustion modeling of biodiesel from wastes in diesel engine.", *Fuel*, vol. 106, pp. 558-568, April 2013, DOI: dx.doi.org/10.1016/j.fuel.2012.11.051.

[104] Muric, K., Stenlaas, O., and Tunestal, P., "Zero-dimensional modeling of NOx formation with least squares interpolation.", *International Journal of Engine Research*, Oct. 2013, DOI: 10.1177/1468087413495843.

[105] Provataris, S., Savva, N.S., and Hountalas, D.T., "Detailed evaluation of a new semi-empirical two-zone NOx model by application on various diesel engine configurations." , in *Proceedings of the Spring Technical Conference of the ASME Internal Combustion Engine Division.*, Torino, pp. 727-743, May 6-9, 2012, DOI: 10.1115/ICES2012-81101.

[106] Scappin, F., Sigurður, S.H., Haglind, F., Andreasen, A., and Larsen, U., "Validation of a zero-dimensional model for prediction of NOx and engine performance for electronically controlled marine two-stroke diesel engines.", *Applied Thermal Engineering*, vol. 37, pp. 344-352, May 2012, DOI: dx.doi.org/10.1016/j.applthermaleng.2011.11.047, ISSN: 1359-4311.

[107] Wilhelmsson, C., Tunestål, P., Widd, , and Johansson, R., "A physical two-Zone NOx model intended for embedded implementation.", *SAE paper*, 2009, DOI: 10.4271/2009-01-1509, No. 2009-01-1509.

[108] Engell, R., "Combustion diagnostics by means of multizone heat release analysis and NO calculation.", *SAE Paper*, 1998, DOI: 10.4271/981424, No. 981424.

[109] Weisser, G.A., "Modelling of combustion and nitric oxide formation for medium-speed DI Diesel engines: a comparative evaluation of zero-and three-dimensional approaches." ETH, Zurich, Doctoral dissertation 2001.

[110] Goldsworthy, L., "Real time model for oxides of nitrogen emissions from a slow speed marine diesel.", *Journal of Marine Engineering and Technology*, vol. 2003, no. 2, pp. 3-12, March 2003.

[111] Andersson, M., Johansson, B., Hultqvist, A., and Noehre, C., "A predictive real time NOx model for conventional and partially premixed Diesel combustion.", *SAE parer*, 2006, DOI: 10.4271/2006-01-3329, No. 2006-01-3329.

[112] Borkowski, T., "Assessment of large bore marine engine cylinder pressures to estimate nox emission.", *Journal of KONES Powertrain and Transport*, vol. 13, no. 2, 2006.

[113] Diotallevi, F., "Development of a multi-zone model for NOx formation in Diesel engines." KTH, Stockholm, Sweden, Master Thesis MMK 2007:55 MFM109, 2007.

[114] Maiboom, A., Tauzia, X., Shah, S.R., and Hétet, J., "New Phenomenological Six-Zone Combustion Model for Direct-Injection Diesel Engines.", *Energy & Fuels*, vol. 23, no. 2, pp. 690-703, 2009, DOI: 10.1021/ef800735d.

[115] Seykens, X.L.J., "Development and validation of a phenomenological diesel engine combustion model." Eindhoven University of Technology, Eindhoven, The Netherlands, Doctoral Dissertation 2010.

[116] Finesso, R. and Spessa, E., "A real time zero-dimensional diagnostic model for the calculation of in-cylinder temperatures, HRR and nitrogen oxides in diesel engines.", *Energy Conversion and Management*, vol. 79, pp. 498-510, March 2014, DOI: http://dx.doi.org/10.1016/j.enconman.2013.12.045.

[117] Xue, X. and Caton, J., "Nitric oxide and soot emissions determined from a multi-zone thermodynamic direct-injection diesel engine combustion model.", *International Journal of Engine Research*, vol. 15, no. 2, pp. 135-152, Feb. 2014, DOI: 10.1177/1468087412466253.

[118] Hirsch, M., Oppenauer, K., and del Re, L., "Dynamic Engine Emission Models.", in *Automotive Model Predictive Control*.: Springer, 2010, ch. 5, pp. 73-78.

[119] Sequenz, H. and Isermann, R., "Emission model structures for an implementation on engine control units." , in *18th IFAC World Congress*, Milano, pp. 11851-11856, 2011.

[120] Guardiola, C., Pla, B., Blanco-Rodriguez, D., and Eriksson, L., "A computationally efficient Kalman filter based estimator for updating look-up tables applied to NOx estimation in diesel engines.", *Control Engineering Practice*, vol. 21, no. 11, pp. 1455-1468, Nov. 2013, DOI: dx.doi.org/10.1016/j.conengprac.2013.06.015.

[121] Arrègle, J., Lopez, J., Guardiola, C., and Monin, C., "Sensitivity Study of a NOx Estimation Model for On-Board Applications.", *SAE Paper*, 2008, DOI: 10.4271/2008-01-0640.

[122] Asprion, J., Chinellato, O., and Guzzella, L., "A fast and accurate physics-based model for the NOx emissions of Diesel engines.", *Applied Energy*, vol. 103, pp. 221-233, March 2013, DOI: 10.1016/j.apenergy.2012.09.038.

[123] Asprion, J., Chinellato, O., and Guzzella, L., "Optimisation-oriented modelling of the NOx emissions of a Diesel engine", *Energy Conversion and Management*, vol. 75, pp. 61-73, November 2013, DOI: dx.doi.org/10.1016/j.enconman.2013.05.039.

[124] Kowalski, J. and Tarelko, W., "NOx emission from a two-stroke ship engine. Part 1: Modeling aspect.", *Applied Thermal Engineering*, vol. 29, no. 11-12, pp. 2153-2159, August 2009, DOI: dx.doi.org/10.1016/j.applthermaleng.2008.06.032.

[125] Guardiola, C., López, J.J., Martín, J., and García-Sarmiento, D., "Semiempirical in-cylinder pressure based model for NOX prediction oriented to control applications.", *Applied Thermal Engineering*, vol. 31, no. 16, pp. 3275-3286, November 2011, DOI: dx.doi.org/10.1016/j.applthermaleng.2011.05.048.

[126] Park, W., Lee, J., Min, K., Yu, J., Park, S., and Cho, S., "Prediction of real-time NO based on the in-cylinder pressure in Diesel engines.", *Proceedings of the Combustion Institute*, vol. 34, no. 2, pp. 3075-3082, 2013.

[127] Husted, H., Kruger, D., Fattic, G., Ripley, G., and Kelly, E., "Cylinder pressure-based control of pre-mixed diesel combustion.", *SAE Paper*, Apr. 2007, DOI: 10.4271/2007-01-0773, No. 2007-01-0773.

[128] Cremers, J.J.F.G., "Beginnings for cylinder pressure based control." TUE, Eindhoven, Master thesis No. WVT 2007.16, 2007. [Online]. http://w3.tue.nl/fileadmin/wtb/ct-pdfs/Master_Theses/AfstudeerverslagRaymondCremers.pdf.

[129] Toth, D., Shaw, T., Wlodarczyk, M., and Cummings, C., "Cylinder head gasket with integrated combustion pressure sensors for advanced engine controls.", *SAE Paper*, Apr. 2011, DOI: 10.4271/2011-01-0938, No. 2011-01-0938.

[130] (2014) Ship-technology.com. [Online]. http://www.ship-technology.com/contractors/propulsion/lehmann/

[131] Kongsberg Maritime, "Engine diagnostics and emission monitoring." Brochure 2014. [Online]. http://www.km.kongsberg.com/ks/web/nokbg0397.nsf/AllWeb/64E9841D6B44E4B4C12579EB00433B64/$file/Kongsberg-Engine-Performance-Systems.pdf?OpenElement.

[132] Hountalas, D.T., Papagiannakis, R.G., Zovanos, G.N., and Antonopoulos, A.K., "Comparative evaluation of various methodologies to account for the effect of load variation during cylinder pressure measurement of large scale two-stroke diesel engines.", *Applied Energy*, vol. 113, pp. 1027-1042, January 2014, http://dx.doi.org/10.1016/j.apenergy.2013.08.036.

[133] Carlucci, A.P., Laforgia, D., Motz, S., Saracino, R., and Wenzel, S.P., "Advanced closed loop combustion control of a LTC diesel engine based on in-cylinder pressure signals.", *Energy Conversion and Management*, vol. 77, pp. 193-207, Jan. 2014, DOI: 10.1016/j.enconman.2013.08.054.

[134] Hiroyasu, H., Kadota, T., and Arai, M., "Development and use of a spray combustion modeling to predict diesel engine efficiency and pollutant emissions: Part 1 combustion modeling.", *Bulletin of JSME*, vol. 26, pp. 569-575, 1983, DOI: 10.1299/jsme1958.26.569, no. 214.

[135] Kouremenos, D.A., Rakopoulos, C.D., and Hountalas, D.T., "Multi-zone combustion modeling for the prediction of pollutants emissions and performance of DI diesel engines.", *SAE Parer*, Feb. 1997, DOI: 10.4271/970635, No. 970635.

[136] Hountalas, D.T., Kouremenos, D.A., Mavropoulos, G.C., Binder, K.B., and Schwarz, V., "Multi-Zone combustion modelling as a tool for DI Diesel engine development-application for the effect of Injection pressure", *SAE Paper*, 2004, DOI: 10.4271/2004-01-0115, No. 2004-01-0115.

[137] Hountalas, D.T., Zovanos, G.N., Sakellarakis, D., and Antonopoulos, A.K., "Validation of Multi-Zone Combustion Model Ability to Predict Two Stroke Diesel Engine Performance and NOx Emissions Using on Board Measurements." , in *ASME 2012 Internal Combustion Engine Division Spring Technical Conference*, Torino, Italy, pp. 47-60, 2012, DOI: 10.1115/ICES2012-81100.

[138] Hountalas, D.T., Antonopoulos, A.K., Zovanos, G.N., and Papagiannakis, R.G., "Evaluation of a New Diagnostic Technique to Detect and Account for Load Variation during Cylinder Pressure Measurement of Large-Scale Four-Stroke Diesel Engines.", *SAE Paper*, 2012, DOI: 10.4271/2012-01-1342, No. 2012-01-1342.

[139] Annand, W.J.D., "Heat transfer in the cylinders of reciprocating internal combustion engines.", *Proceedings of the Institution of Mechanical Engineers*, vol. 177, no. 1, pp. 973-996, 1963, DOI: 10.1243/PIME_PROC_1963_177_069_02.

[140] Annand, W.J.D. and Ma, T.H., "Instantaneous Heat Transfer Rates to the Cylinder Head Surface of a Small Compression-Ignition Engine." , in *Proceedings of the Institution of Mechanical Engineers*, vol. 185, pp. 976-987, 1970, DOI: 10.1243/PIME_PROC_1970_185_110_02.

[141] Amsden, A.A., Butler, T.D., O'Rourke, P.J., and Ramshaw, J.D., "KIVA-A comprehensive model for 2-D and 3-D engine simulations.", *SAE Paper*, 1985, No. 850554.

[142] Nishida, K.a.H.H., "Simplified three-dimensional modelling of mixture formation and combustion in a D.I. diesel engine.", *SAE Paper*, 1989, No. 890269.

[143] Ramos, J.I., *Internal combustion engine modeling.*, 1st ed. New York: Hemisphere, 1989, ISBN: 0891161570.

[144] Glauert, M.B., "The wall jet.", *Journal of Fluid Mechanics*, pp. 625-643, 1956.

[145] Borman, G.L. and Johnson, J.H., "Unsteady vaporization histories and trajectories of fuel drops injected into swirling air.", *SAE Paper*, Jan. 1962, DOI: 10.4271/620271, No. 620271.

[146] Benson, R.S. and Whitehouse, N.D., *Internal combustion engines.*, 1st ed. Oxford, UK: Pergamon Press, 1979, ISBN: 08022717.

[147] Rakopoulos, C.D., Hountalas, D.T., Tzanos, E.I., and Taklis, G.N., "A fast algorithm for calculating the composition of diesel combustion products using an eleven species chemical equilibrium scheme.", *Advances in Engineering Software*, vol. 19, no. 2, pp. 109-119, 1994, DOI: 10.1016/0965-9978(94)90064-7.

[148] Callahan, T.J., Ryan, T.W., Dietzmann, H., and Waytulonis, R., "The effects of discrete transients in speed and load on diesel engine exhaust emissions.", *SAE Paper*, Feb. 1985, DOI: 10.4271/850109, No. 850109.

[149] Andersson, P., "Models for predicting the NOx exhaust pollutants in a Diesel engine." Lund university and Saab-Scania, Lund, Diploma paper 1989.

[150] Lavoie, G.A. and Blumberg, P.N., "Measurements of NO emissions from a stratified charge engine: comparison of theory and experiment.", *Combustion Science and Technology*, vol. 8, no. 1-2, pp. 25-37, 1973, No. 0010-2202.

[151] Toof, J.L., "A model for the prediction of thermal, prompt, and fuel NOx emissions from combustion turbines.", *Journal of engineering for gas turbines and power*, vol. 108, no. 2, pp. 340-347, 1986, No. 0742-4795.

[152] Gartner, U., Hohenberg, G., Daudel, H., and Oelschlegel, H., "Development and Application of a Semi – Empirical NOx Model to Various HD Diesel Engines." , in *Thiesel 2002 Conference on thermo and Fluid Dynamic Processes in Diesel Engines*, Valencia, Spain, 2002.

[153] Wu, K.J. and Peterson, R.C., "Correlation of nitric oxide emission from a diesel engine with measured temperature and burning rate.", *SAE Paper*, Oct. 1986, DOI: 10.4271/861566, No. 861566.

[154] Plee, S.L. and Ahmad, T., "Relative roles of premixed and diffusion burning in Diesel combustion.", *SAE Paper*, Oct. 1983, DOI: 10.4271/831733, No. 831733.

[155] Peterson, R. and Wu, K., "The effect of operating conditions on flame temperature in a diesel engine.", *SAE Paper*, Oct. 1986, DOI: 10.4271/861565.

[156] Horrocks, R., "Control of NOx emissions from diesel engines using exhaust gas re-circulation." BURA, London, PhD Thesis 2001. [Online]. http://bura.brunel.ac.uk/handle/2438/6625.

[157] CD-adapco, "STAR-CD v4.10 Methodology" 2009. [Online]. http://www.cd-adapco.com/products/star-cd%C2%AE.

[158] Kee, R.J., Rupley, F.M., Miller, J.A., and II, C., "A Fortran chemical kinetics package for the analysis of gas-phase chemical kinetics." Sandia National Laboratories, Livermore, No. SAND89-8009B, 1996.

[159] D'Ambrosio, S., Finesso, R., Fu, L., Mittica, A., and Spessa, E., "A control-oriented real-time semi-empirical model for the prediction of NOx emissions in diesel engines.", *Applied Energy*, vol. 130, pp. 265–279, Jun. 2014, DOI: 10.1016/j.apenergy.2014.05.046.

[160] Timoney, D.J., Desantes, J.M., Hernandes, L., and Lyons, C.M., "The development of a semi–empirical model for rapid NOx concentrations evaluation using measured in cylinder pressure in Diesel engines.", *IMechE, Part D: J. Automobile Engineering*, vol. 219, no. 5, pp. 621-631, 2005, DOI: 10.1243/095440705X11095.

[161] Payri, F., Arrègle, J., López, J.J., and Mocholí, E., "Diesel NOx modeling with a reduction mechanism for the initial NOx coming from EGR or re-entrained burned gases.", *SAE Paper*, Apr. 2008, DOI: 10.4271/2008-01-1188, No. 2008-01-1188.

[162] Woschni, G., "A universally applicable equation for the instantaneous heat transfer coefficient in the internal combustion engine.", *SAE Paper*, 1967, DOI: 10.4271/670931, No. 670931.

[163] Bazari, Z., "A DI Diesel combustion and emission predictive capability for use in cycle simulation.", *SAE Paper*, Feb. 1992, DOI: 10.4271/920462, No. 920462.

[164] Olikara, C. and Borman, G.L., "A computer program for calculating properties of equilibrium combustion products with some applications to IC engines.", *SAE Paper*, Feb. 1975, DOI: 10.4271/750468, No. 750468.

[165] Nüesch, M., "Prozeßrechnungsprogramm für Dieselmotoren mit und ohne Aufladung." LVV, Internal report 1987.

[166] Petzold, L.R., "Description of DASSL: A differential/algebraic system solver." Sandia National Labs, Livermore, CA (USA), No. SAND-82-8637, CONF-820810-21, 1982.

[167] Grill, M., Chiodi, M., Berner, H.J., and Bargende, M., "Calculating the thermodynamic properties of burnt gas and vapor fuel for user-defined fuels.", *MTZ worldwide*, vol. 68, no. 5, pp. 30-35, May 2007.

[168] Lapuerta, M., Hernández, J.J., and Armas, O., "Kinetic modelling of gaseous emissions in a diesel engine.", *SAE Paper*, Oct. 2000, DOI: 10.4271/2000-01-2939, No. 2000-01-2939.

[169] Murayama, T., Miyamoto, N., Sasaki, S., and Kojima, N., "The relation between nitric oxide formation and combustion process in diesel engines." , in *12th International Congress on Combustion Engines, CIMAC*, vol. B, Tokyo, pp. 1-23, 1977.

[170] Naber, J. and Siebers, D., "Naber, J. D., & Siebers, D. L. (1996). Effects of gas density and vaporization on penetration and dispersion of diesel sprays.", *SAE Paper*, Feb. 1996, DOI: 10.4271/960034, No. 960034.

[171] Bowman, C.T., "Kinetics of pollutant formation and destruction in combustion.", *Progress in Energy and Combustion Science*, vol. 1, pp. 33-45, 1975.

[172] Kramlich, J.C. and Linak, W.P., "Nitrous oxide behavior in the atmosphere, and in combustion and industrial systems.", *Progress in Energy and Combustion Science*, vol. 20, no. 2, pp. 149-202, 1994, DOI: 10.1016/0360-1285(94)90009-4.

[173] Wilhelmsson, C., Tunestål, P., and Johansson, B., "Model based engine control using ASICs: A virtual heat release sensor." , in *Les Rencontres Scientifiques de l'IFP: "New Trends in Engine Control, Simulation and Modelling"*, 2006, No. 538189.

[174] Ricou, F.P. and Spalding, D.B., "Measurements of entrainment by axisymmetrical turbulent jets.", *Journal of fluid mechanics*, vol. 11, no. 01, pp. 21-32, Aug. 1961, DOI: dx.doi.org/10.1017/S0022112061000834.

[175] Arrègle, J., López, J.J., García, J.M., and Fenollosa, C., "Development of a zero-dimensional Diesel combustion model. Part 1: Analysis of the quasi-steady diffusion combustion phase.", *Applied Thermal Engineering*, vol. 23, no. 11, pp. 1301–1317, Aug. 2003, DOI: 10.1016/S1359-4311(03)00079-6.

[176] Siebers, D.L., "Scaling liquid-phase fuel penetration in diesel sprays based on mixing-limited vaporization.", *SAE Paper*, Mar. 1999, DOI: 10.4271/1999-01-0528, No. 1999-01-0528.

[177] Siebers, D.L., Higgins, B., and Pickett, L.M., "Flame lift-off on direct injection diesel fuel jets: Oxygen concentration effects.", *SAE Paper*, Mar. 2002, DOI: 10.4271/2002-01-0890, No. 2002-01-0890.

[178] Barba, C., Burkhardt, C., Boulouchos, K., and Bargende, M., "A phenomenological combustion model for heat release prediction in high speed DI diesel engines with common-rail injection.", *SAE Paper*, Oct. 2000, DOI: 10.4271/2000-01-2933.

[179] Ericson, C., Westerberg, B., Andersson, M., and Egnell, R., "Modelling diesel engine combustion and NOx Formation for model based control and simulation of engine and exhaust after-treatment systems.", *SAE Paper*, Apr. 2006, DOI: 10.4271/2006-01-0687, No. 2006-01-0687.

[180] McBride , B.J., Zehe, M.J., and Gordon, S., "NASA Glenn Coefficients for Calculating Thermodynamic Properties of Individual Species." NASA, Cleveland, Ohio, No. NASA/TP—2002-211556, 2002.

[181] Miyamoto, N., Chikahisa, T., Murayama, T., and Sawyer, R., "Description and analysis of diesel engine rate of combustion and performance using Wiebe's functions.", *SAE Paper*, Feb. 1985, DOI: 10.4271/850107, No. 850107.

[182] Goldsworthy, L., "Reduced kinetics schemes for oxides of nitrogen emissions from a slow-speed marine diesel engine.", *Energy & fuels*, vol. 17, no. 2, pp. 450-456, Feb. 2003, DOI: 10.1021/ef020172c.

[183] Blair, G.P., "Scavenging the two stroke engine.", in *Design and simulation of two-stroke engines.* USA: SAE, 1996, ch. 3, pp. 211-281, ISBN: 1-56091-685-0.

[184] Goldsworthy, L., "Simulating primary control measures for oxides of nitrogen emissions in a slow speed marine diesel engine." , in *Sea Australia*, Sydney, 2000.

[185] Zabetta, E.C., Kilpinen, P., Hupa, M., Ståhl, K., Leppälahti, J., Cannon, M., and Nieminen, J., "Kinetic modeling study on the potential of staged combustion in gas turbines for the reduction of nitrogen oxide emissions from biomass IGCC plants.", *Energy & Fuels*, vol. 14, no. 4, pp. 751-761, Jun. 2000, DOI: 10.1021/ef9901591, No. 0887-0624.

[186] Zabetta, E.C. and Kilpinen, P., "Improved NOx submodel for in-cylinder CFD simulation of low- and medium-speed compression ignition engines.", *Energy & Fuels*, vol. 15, no. 6, pp. 1425–1433, Oct. 2001, DOI: 10.1021/ef010062q.

[187] Cui, Y., Deng, K., and Wu, J., "A direct injection diesel combustion model for use in transient condition analysis.", *Proceedings of the Institution of Mechanical Engineers, Part D: Journal of Automobile Engineering*, vol. 215, no. 9, pp. 995-1004, Sept. 2001, No. 0954-4070.

[188] Hountals, D.T., Savva, N., and Papagiannakis, R.G., "Development of a new physically based semi-empirical NOx model using the measured cylinder pressure." , in *THIESEL 2010 Conference on Thermo-and Fluid Dynamic Processes in Diesel Engines*, Valencia, Spain, pp. 341-356, Sept. 14-17, 2010.

[189] Savva, N.S. and Hountalas, D.T., "Detailed evaluation of a new semi-empirical multi-zone NOx model by application on various Diesel engine configurations.", *SAE paper*, Apr. 2012, DOI: 10.4271/2012-01-1156, No. 2012-01-1156.

[190] Savva, N.S. and Hountalas, D.T., "Implementation of a Nitric Oxide (NO) semi–empirical, multi–zone model on a heavy and a light–duty DI Diesel engine.", *UNDER REVIEW*.

[191] Antonopoulos, A., "Ανάπτυξη και εξέλιξη τεχνικών μέτρησης και επεξεργασίας λειτουργικών μεγεθών κινητήρων Diesel από τον θάλαμο καύσης και τον άξονα μετάδοσης της ισχύος με σκοπό την διάγνωση." NTUA, Athens, Doctoral Dissertation 2013.

[192] KISTLER. (2013) KISTLER sensors. [Online]. http://www.kistler.com/gr/en/category/Sensors+and+Transmitter/Pressure/PSEPR/?reload=true

[193] Hountalas, D.T. and Anestis, A., "Effect of pressure transducer position on measured cylinder pressure diagram of high speed diesel engines.", *Energy Conversion and Management*, vol. 39, no. 7, pp. 589–607, May 1998, DOI: 10.1016/S0196-8904(97)10009-7.

[194] Shi, S.X. and Sheng, H.Z., "Numerical simulation and digital signal processing in measurements of cylinder pressure of internal combustion engines." , in *Proceedings of the Institution of Mechanical Engineers International Conference on Computers in Engine Technology*, vol. 20, pp. 211-218, 1987.

[195] Payri, F., Lujan, J.M., Martin, J., and Abbad, A., "Digital signal processing of in-cylinder pressure for combustion diagnosis of internal combustion engines.", *Mechanical Systems and Signal Processing*, vol. 24, no. 6, pp. 1767–1784, Aug. 2010, DOI: 10.1016/j.ymssp.2009.12.011.

[196] Chang, H., Zhang, Y., and Chen, L., "An applied thermodynamic method for correction of TDC in the indicator diagram and its experimental confirmation.", *Applied Thermal Engineering*, vol. 25, no. 5, pp. 759-768, Apr. 2005, DOI: 10.1016/j.applthermaleng.2004.07.016.

[197] Wang, X.B., Deng, K.Y., He, F.Z., and Zhou, Z.H., "A thermodynamics model for the compression and expansion process during the engine's motoring and a new method for the determination of TDC with simulation technique.", *Applied Thermal Engineering*, vol. 27, no. 11-12, pp. 2003–2010, Aug. 2007, DOI: 10.1016/j.applthermaleng.2006.12.012.

[198] Antonopoulos, A. and Hountalas, D., "Identification and correction of the error induced by the sampling method used to monitor cylinder pressure of reciprocating internal combustion engines.", *SAE Paper*, Apr. 2012, DOI: 10.4271/2012-01-1155, No. 2012-01-1155.

[199] Lee, K., Yoon, M., and Sunwoo, M., "A study on pegging methods for noisy cylinder pressure signal.", *Control Engineering Practice*, vol. 16, no. 8, pp. 922–929, Aug. 2008, DOI: 10.1016/j.conengprac.2007.10.007.

[200] Davis, R.S. and Patterson, G.J., "Cylinder pressure data quality checks and procedures to maximize data accuracy.", *SAE Paper*, 2006, DOI: 10.4271/2006-01-1346.

[201] Ceviz, M.A., Çavuşoğlu, B., Kaya, F., and Öner, İ.V., "Determination of cycle number for real in-cylinder pressure cycle analysis in internal combustion engines.", *Energy*, vol. 36, no. 5, pp. 2465–2472, May 2011, DOI: 10.1016/j.energy.2011.01.038.

[202] Savitzky, A. and Golay, M.J., "Smoothing and differentiation of data by simplified least squares procedures.", *Analytical Chemistry*, vol. 36, no. 8, pp. 1627-1639, 1964.

[203] Maurya, K.R., Pal, D.D., and Agarwal, A.K., "Digital signal processing of cylinder pressure data for combustion diagnostics of HCCI engine.", *Mechanical Systems and Signal Processing*, vol. 36, no. 1, pp. 95-109, 2013.

[204] Madden and Hannibal, H., "Comments on the Savitzky-Golay convolution method for least-squares-fit smoothing and differentiation of digital data.", *Analytical Chemistry*, vol. 50, no. 9, pp. 1383-1386, 1978.

[205] Gorry, P.A., "General least-squares smoothing and differentiation by the convolution (Savitzky-Golay) method.", *Analytical Chemistry*, vol. 62, no. 6, pp. 570-573, 1990.

[206] Shayler, P.J., Wiseman, M.W., and Ma, T., "Improving the determination of mass fraction burnt.", *SAE Paper*, 1990, DOI: 10.4271/900351, No. 900351.

[207] Press, W.H., Teuklosky, S.A., and Vetterling, W.T., "Savitzky-Golay Smoothing Filters", in *Numerical Recipes in Fortran 77*.: Press Syndicate of the Univ. of Cambridge, 1997, ch. 14.8, pp. 644-649, ISBN: 0-521-43064-x.

[208] Germanischer Lloyd (GL) , "Type approval certificate No 37 974 – 12 HH." 2012.

[209] Hountalas, D.T., "Prediction of marine diesel engine performance under fault conditions.", *Applied Thermal Engineering*, vol. 20, no. 18, pp. 1753-1783, December 2000, DOI: dx.doi.org/10.1016/S1359-4311(00)00006-5.

[210] Lamaris, V.T. and Hountalas, D.T., "A general purpose diagnostic technique for marine diesel engines– Application on the main propulsion and auxiliary diesel units of a marine vessel.", *Energy Conversion and Management*, vol. 51, no. 4, pp. 740-753, April 2010, DOI: dx.doi.org/10.1016/j.enconman.2009.10.031.

[211] Desantes, J.M., Galindo, J., Guardiola, C., and Dolz, V., "Air mass flow estimation in turbocharged diesel engines from in-cylinder pressure measurement.", *Experimental Thermal and Fluid Science*, vol. 34, no. 1, pp. 37-47, Jan. 2010, DOI: 10.1016/j.expthermflusci.2009.08.009.

[212] Youssef, B., Guillemin, F., Le Solliec, G., and Corde, G., "In cylinder trapped mass estimation in diesel engines using cylinder pressure measurements." , in *Control Applications (CCA), 2011 IEEE International Conference on*, Denver, CO, pp. 561-566, 2011, DOI: 10.1109/CCA.2011.6044475, No. 1457710625.

[213] ISO 5167-1:2003, Measurement of fluid flow by means of pressure differential devices inserted in circular cross-section conduits running full -- Part 1: General principles and requirements., 2003, Stage: 90.93 (2014-02-14).

[214] ISO 8178-1:2006, Reciprocating internal combustion engines -- Exhaust emission measurement -- Part 1: Test-bed measurement of gaseous and particulate exhaust emissions., 2006, Stage: 90.92 (2013-07-24).

[215] ISO 8178-2:2008, Reciprocating internal combustion engines -- Exhaust emission measurement -- Part 2: Measurement of gaseous and particulate exhaust emissions under field conditions., 2008, Stage: 90.93 (2013-07-22).

[216] Rakopoulos, C.D., "Πραγματικός κύκλος λειτουργίας εμβολοφόρων κινητήρων.", in *Αρχές Εμβολοφόρων M.E.K.* Athens, Greece: Fountas, 2001, ch. 5, 960-330-423-9.

[217] School, D.J., "Method for detecting and regulating the start of combustion in an internal combustion engine.", US, Patent No. 006840218B2, Jan. 11, 2005.

[218] Katrašnik, T., Trenc, F., and Oprešnik, S.R., "A new criterion to determine the start of combustion in Diesel engines." , in *ASME*, vol. 128, pp. 928-933, Oct. 2006, DOI: 10.1115/1.2179471.

[219] Luján, J.M., Bermúdez, V., Guardiola, C., and Abbad, A., "A methodology for combustion detection in diesel engines through in-cylinder pressure derivative signal.", *Mechanical Systems and Signal Processing*, vol. 24, no. 7, pp. 2261-2275, Oct. 2010, DOI: 10.1016/j.ymssp.2009.12.012.

[220] Borman, G. and Nishiwaki, K., "Internal-combustion engine heat transfer.", *Progress in Energy and Combustion Science*, vol. 13, no. 1, pp. 1-46, 1987.

[221] Roger, A.S., "Transport coefficients for the NASA Lewis chemical equilibrium program." NASA, Cleveland, Ohaio, 1995.

[222] Katz, D.L., *Handbook of natural gas engineering.* New York: McGraw-Hill, 1959, ISBN: 007033384X.

[223] TEMA, *Standards of the Tubular Exchanger Manufacturers Association.*, 7th ed. New York, 10591, USA, 1988.

[224] Anatone, M. and Cipollone, R., "Contribution in Calculating the Thermal Fields in Internal Combustion Engines Components.", *SAE Paper*, 1996, DOI: 10.4271/961127.

[225] Rakopoulos, C.D., Rakopoulos, D.C., Mavropoulos, G.C., and Giakoumis, E.G., "Experimental and theoretical study of the short term response temperature transients in the cylinder walls of a diesel engine at various operating conditions.", *Applied Thermal Engineering*, vol. 24, no. 5-6, pp. 679-702, April 2004, DOI: dx.doi.org/10.1016/j.applthermaleng.2003.11.002.

[226] Rakopoulos, C.D., Antonopoulos, K.A., and Rakopoulos, D.C., "Experimental heat release analysis and emissions of a HSDI diesel engine fueled with ethanol–diesel fuel blends.", *Journal of Energy*, vol. 32, no. 10, pp. 1791-1808, Oct. 2007, DOI: 10.1016/j.energy.2007.03.005.

[227] Hamming, R.W., "Modified false position", in *Numerical Methods for Scientists and Engineers*. New York, USA: Dover Publications, 1973, ch. 4.5, pp. 65-67, ISBN: 0-486-65241-6.

[228] Way, R.J.B., "Methods for determination of composition and thermodynamic properties of combustion products for internal combustion engine calculation." , in *Proceedings of the Institution of Mechanical Engineers*, vol. 190, pp. 687-697, 1976, DOI: 10.1243/PIME_PROC_1976_190_073_02.

[229] Hamming, R.W., "Newton's Method", in *Numerical Methods for Scientists and Engineers*, 2nd ed. New York, USA: Dover Publications, 1962,1973, ch. 4.6, pp. 68-70, ISBN: 0-486-65241-6.

[230] Vickland, C.W., Strange, F.M., Bell, R.A., and Starkman, E.S., "A consideration of the high temperature thermodynamics of internal combustion engines.", *SAE Paper*, 1962, DOI: 10.4271/620564.

[231] Glassman, I. and A., Y.R., "Chemical thermodynamics and flame temperatures – Free energy and the equilibrium constants.", in *Combustion*, 4th ed. San Diego, US: Elsevier, 2008, ch. 1C, pp. 8-16, ISBN: 978-0-12-088573-2.

[232] Eriksson, L., "Documentation for the CHemical Equilibrium Program Package CHEPP" Vehicular Systems, Linköping University, Linköping, 2000.

[233] Press, W.H., Teuklosky, S.A., and Vetterling, W.T., "Newton-Raphson method for nonlinear systems of equations.", in *Numerical Recipes in Fortran 77*.: Press Syndicate of the Univ. of Cambridge, 1997, ch. 9.6, pp. 372-375, ISBN: 0-521-43064-x.

[234] Michos, K.N., "Αριθμητική προσομοίωση καύσης και εκπομπής μονοξειδίου του αζώτου κινητήρων Otto αέριων βιοκαυσίμων: ενεργειακή και εξεργειακή ανάλυση." NTUA, Athens, Dissertation 2010.

[235] Atkins, P. and Paula, J., "The rates of chemical reactions", in *Atkins' pysical chemistry*, 9th ed. New York, USA: W. H. Freeman and Company, 2006, ch. 22, pp. 791-829, ISBN: 0-7167-8759-8.

[236] Hanson, R.K. and Salimian, S., "Survey of Rate Constants in H/N/O Systems.", *Combustion Chemistry*, p. 341, 1984.

[237] Hamming, R.W., "The numerical solution", in *Numerical Methods for Scientists and Engineers*. New York, USA: Dover Publications, 1973, ch. 22.3, pp. 382-386, ISBN: 0-486-65241-6.

[238] Seber, G.F. and Lee, A.J., *Linear regression analysis.*, 2nd ed. Hoboken, New Jersey, USA: John Wiley & Sons, 2012, ISBN: 978-1-118-27442-2.

[239] Burnham, P.K. and Anderson, D.R., "Multimodel inference: Understanding AIC and BIC in model selection.", *Sociological Methods & Research*, vol. 33, no. 2, pp. 261-304, November 2004, DOI: 10.1177/0049124104268644.

[240] Venables, W.N. and Smith, D.M., *An Introduction to R.*: CRAN, 2013.

[241] "Excel 2013: Analysis Toolpack" Microsoft, 2013.

[242] "MATLAB" MathWorks, 2011.

[243] The R Core Team, *R: A Language and Environment for Statistical Computing: Reference Index.*, 2013.

[244] Germanischer Lloyd (GL), "Type approval certificate No 59 488 – 08 HH." 2008.

[245] Savva, N.S., Raptotasios, S.J., Zovanos, G.N., Sakellaridis, N.F., and Hountalas, D.T., "Investigation of fuel switching (HFO to DFO) on a large–scale, two–stroke Diesel engine: effect on performance and emissions.", *UNDER REVIEW*.

[246] Boehman, A.L., Morris, D., Szybist, J., and Esen, E., "The impact of the bulk modulus of diesel fuels on fuel injection timing.", *Energy & Fuels*, vol. 18, no. 6, pp. 1877-1882, Oct. 2004, DOI: 10.1021/ef049880j.

[247] Seykens, X.L.J., Somers, L.M.T., and Baert, R.S.G., "Modeling of common rail fuel injection system and influence of fluid properties on injection process." , in *VAFSEP2004*, Dublin, Ireland, 6-9 Jul. 2004.

[248] Lapuerta, M., Agudelo, J.R., Prorok, M., and Boehman, A.L., "Bulk modulus of compressibility of diesel/biodiesel/HVO blends.", *Energy & Fuels*, vol. 26, no. 2, pp. 1336-1343, 2012, DOI: dx.doi.org/10.1021/ef201608g.

[249] ASTM D341, "Standard Practice for Viscosity-Temperature Charts for Liquid Petroleum Products" ASTM International, West Conshohocken, ICS: 75080, 2009. [Online]. http://www.astm.org/DownloadStandardA.html?ASTM%20HC=ASTM&DESIGNATION=D341&AdID=&Split=&Campaign=Individual%20Standards%207&gclid=Cj0KEQiAz7OlBRDErsTx47LKz-8BEiQAY0OlYgfxtBjjM_GPNgi1XejeJCqRyiNdGNRmkLzOV080UXAaAo_X8P8HAQ.

[250] Bridgman, P.W., *Physics of high pressure.* London, UK: G. Bell and Sons, 1952.

[251] Cutler, W.G., McMickle, R.H., Webb, W., and Schiessler, R.W., "Study of the compressions of several high molecular weight hydrocarbons.", *The Journal of Chemical Physics*, vol. 29, no. 4, pp. 727-740, 1958, DOI: dx.doi.org/10.1063/1.1744583.

[252] Intel, FORTRAN Composer XE, 2011.

[253] Kuhn, T., Mowll, D., Wirbeleit, F., and Willand, J., "Optimization of the valve lift strategy during the acceleration of a diesel engine using WAVE and DOE." , in *4th International Ricardo Software Users Conference*, Detroit, 2000.

APPENDIX

a. Calculation of Exhaust Mass Flow with Carbon Balance Method

Herein, the carbon balance method used for the exhaust mass flow ($\dot{m}_{exh}$) on wet basis calculation and therefore intake air mass flow ($\dot{m}_{air}$) calculation, in *[kg/h]*, is presented. This method is obtained from *IMO Annex 13* (revised *Annex VI*) [46]. The inputs of the method are:

1. Fuel mass flow ($\dot{m}_{fuel}$ *[kg/h]*) (measured or calculated).
2. Fuel mass composition (Y *[%]*): carbon (*C*), hydrogen (*H*), nitrogen (*N*) and oxygen (*O*) mass content, i.e. *kg C/kg fuel*.
3. Humidity ratio of the intake air (*H [g water/kg dry air]*).
4. Exhaust gas composition, particularly: dry CO_2 ($X_{CO2exh,d}$ *[%]* vol.), dry *CO* ($x_{COexh,d}$ *[ppmv]*), wet *HC* ($x_{HCexh,w}$ *[ppmv]*).
5. Ambient air CO_2 concentration ($X_{CO2amb,d}$ *[%]* vol. = *0.03%*).

$$\dot{m}_{exh} = \dot{m}_{fuel} \cdot \left(\left(\frac{1.4 \cdot Y_C^2}{\frac{\left(\frac{1.4 \cdot Y_C}{f_c} + 0.08936 \cdot Y_H - 1\right) \cdot \frac{1}{1.293} + f_{fd}}{f_c^2} + 0.08936 \cdot Y_H - 1} \right) \cdot \left(1 + \frac{H}{10^3}\right) + 1 \right)$$

$$H = min(H_a; H_{SC})$$

$$H_a = \frac{6.22 \cdot p_a \cdot R_a}{p_b - 0.01 \cdot p_a \cdot R_a}$$

$$p_a = (4.856884 + 0.2660089 \cdot T_a + 0.01688919 \cdot T_a^2 - 7.477123 \cdot 10^{-5} \cdot T_a^3 + 8.10525 \cdot 10^{-6} \cdot T_a^4 - 3.115221 \cdot 10^{-8s} \cdot T_a^5) \cdot \frac{101.32}{760}$$

$$H_{SC} = \frac{622 \cdot p_{SC}}{p_c - p_{SC}}$$

$$f_{fd} = -0.055593 \cdot Y_H + 0.008002 \cdot Y_N + 0.0070046 \cdot Y_O$$

$$f_c = \left(X_{CO2_{exh,d}} - X_{CO2_{amb,d}}\right) \cdot 0.5441 + \frac{x_{CO_{exh,d}}}{18522} + \frac{x_{HC_{exh,w}}}{17355}$$

$$\dot{m}_{air} = \dot{m}_{exh} - \dot{m}_{fuel}$$

where f_c is called carbon factor, f_{fd} is the fuel specific constant for the dry exhaust, which is calculated by the sum of the additional volumes of the combustion of the fuel elements, H_a is the intake air humidity ratio, H_{SC} is the humidity ratio of the scavenging air in *g* water per *kg* dry air, p_a *[kPa]* is the saturation vapor pressure of the intake air, R_a *[%]* is the relative

humidity of the intake air, p_b *[kPa]* is the total barometric pressure, p_{SC} *[kPa]* is the saturation vapor pressure of the charge air and p_c *[kPa]* is the charge air (scavenging) pressure. The temperature (T_a *[°C]*) used in the p_a calculation is the one measured at the same physical location as the measurements for p_b and R_a [46].

b. Conversion of NO_x from [ppmv] Dry to [g/h] Wet / IMO Concept

If the NO_x emissions are not measured on a wet basis, namely are measured in dry basis (after moisture removal from the sample) in volume *ppm* (*ppmv*), the measured concentration shall be converted to a wet basis. This is managed by multiplying the raw NO_x dry measurement with the "dry to wet" correction factor (k_{rw2}), which is calculated for raw exhaust gas as shown in the following correlation, where the units for *CO*, CO_2 and H_2 concentrations (X) are in *[%]*. The specific factor is used when the carbon balance method is used for the calculation of exhaust flow. The corrections used in other cases and further details can be found in Ref. [46]. After the conversion of the NO_x concentration in wet basis, it is multiplied with exhaust mass flow and the empirical coefficient u_{NOx} to be converted in *[g/h]*. The u_{NOx} coefficient is the ratio between density of NO_x and density of exhaust gas, assuming the following: typical fuel oil composition, combustion with $\lambda=2$ ($\Phi=0.5$), wet air, *273 K* and *101.3 kPa* [46].

$$k_{wr2} = \left[1 + a \cdot 0.005 \cdot \left(X_{CO2_{exh,d}} + X_{CO_{exh,d}}\right) - 0.01 \cdot X_{H2,d} + k_{w2} - \frac{p_r}{p_b}\right]^{-1}$$

$$a = 11.9164 \cdot \frac{Y_H}{Y_C}$$

$$X_{H2,d} = \frac{0.5 \cdot a \cdot X_{CO_{exh,d}} \cdot \left(X_{CO2_{exh,d}} + X_{CO_{exh,d}}\right)}{X_{CO_{exh,d}} + 3 \cdot X_{CO2_{exh,d}}}$$

$$k_{w2} = \frac{1.608 \cdot H_a}{1000 + 1.608 \cdot H_a}$$

$$NO_{x_{wet}} = NO_{x_{dry}} \cdot k_{wr2}$$

$$\dot{m}_{NO_{x_{wet}}} = u_{NO_x} \cdot NO_{x_{wet}} \cdot \dot{m}_{exh}$$

$$u_{NO_x} = 0.001586, for\ \lambda = 2, wet\ air, 273\ K\ and\ 101.3\ kPa$$

where p_b *[kPa]* is the total barometric pressure and p_r *[kPa]* is the water vapor pressure after cooling bath. Herein, p_r is taken equal with *0.76 [kPa]* which corresponds to a cooling bath temperature of *3°C*. H_a is the absolute humidity of intake air, in g water per kg dry air, which can be calculated as shown in Appendix a. $NO_{x_{wet}}$ is in *[ppmv]* units, $\dot{m}_{exh}$ *[kg/h]* is the exhaust mass flow in wet basis as calculated in Appendix a and $\dot{m}_{NO_{x_{wet}}}$ *[g/h]* is the NO_x mass flow in wet basis.

c. Conversion of NO_x [g/h] Wet to [g/kWh] and [g/kg fuel]

Usually, in the legislation forms or certificates, the limits for NO_x emissions are provided in reduced form, namely in *[g/kWh]* or *[g/kg fuel]* units, for easiness in comparison and supervision. For this reason the conversion of NO_x (wet) emissions from *[g/h]* (see Appendix b) to [g/kWh] and [g/kg fuel] is demonstrated at next:

$$\dot{m}_{NO_{x_{wet}}}\left(\frac{g}{kWh}\right) = \frac{\dot{m}_{NO_{x_{wet}}}\left(\frac{g}{h}\right)}{P(kW)}$$

$$\dot{m}_{NO_{x_{wet}}}\left(\frac{g}{kg\ fuel}\right) = \frac{\dot{m}_{NO_{x_{wet}}}\left(\frac{g}{h}\right)}{\dot{m}_{fuel}\left(\frac{kg}{h}\right)}$$

$$or\ \dot{m}_{NO_{x_{wet}}}\left(\frac{g}{kg\ fuel}\right) = \frac{\dot{m}_{NO_{x_{wet}}}\left(\frac{g}{h}\right)}{bsfc\left(\frac{g}{kWh}\right)\cdot\frac{P(kW)}{1000\left(g/_{kg}\right)}}$$

where $P\ [kW]$, $\dot{m}_{fuel}\ [kg/h]$ and *bsfc* are the engine power, fuel mass flow and brake specific fuel consumption during measurement. It is noted that, particularly for NO_x emissions, for the completion of the respective emission certificate, a humidity correction factor (i.e. k_{hd} [46]) should also be applied to reduce the NO_x to a reference ambient humidity, since ambient humidity has a considerable impact on NO_x emissions. However, the target of the current study in not to compare the engines NO_x emissions with the legislation limits but to evaluate the ability of the proposed model to predict NO_x for the actual ambient and engine conditions. Hence, this correction is not applied.

d. NASA Polynomials for Constant Pressure Specific Heat Capacity, Enthalpy and Entropy

In this section, the polynomials used for the calculation of the constant pressure specific heat capacity (*cp [J/kmol/K]*), enthalpy (*h [kJ/kmol]*) and entropy (*s [J/kmol/K]*), as proposed by NASA Glenn Research Center [180] are described as follows:

$$\left(\frac{cp(T)}{\bar{R}}\right)_j = a_{1_j}\cdot T^{-2} + a_{2_j}\cdot T^{-1} + a_{3_j} + a_{4_j}\cdot T + a_{5_j}\cdot T^2 + a_{6_j}\cdot T^3 + a_{7_j}\cdot T^4$$

$$\left(\frac{h(T)}{\bar{R}\cdot T}\right)_j = -a_{1_j}\cdot T^{-2} + a_{2_j}\cdot ln(T)\cdot T^{-1} + a_{3_j} + a_{4_j}\cdot\frac{T}{2} + a_{5_j}\cdot\frac{T^2}{3} + a_{6_j}\cdot\frac{T^3}{4} + a_{7_j}\cdot\frac{T^4}{5} + b_{1_j}\cdot T^{-1}$$

$$\left(\frac{s(T)}{\bar{R}}\right)_j = -a_{1_j}\cdot\frac{T^{-2}}{2} - a_{2_j}\cdot T^{-1} + a_{3_j}\cdot ln(T) + a_{4_j}\cdot T + a_{5_j}\cdot\frac{T^2}{2} + a_{6_j}\cdot\frac{T^3}{3} + a_{7_j}\cdot\frac{T^4}{4} + b_{2_j}$$

where $T\ [K]$ is the gas temperature, $\bar{R} = 8314.472\ [J/kmol\ K]$ is the universal gas constant of ideal gas and *a* and *b* are the polynomial constants for each species denoted with subscript *j*. The values of these coefficients are derived from fitting of experimental data using least

squares methodologies. Furthermore, each coefficient is defined from two constant values, the first is valid for temperatures equal or lower than *1000 [K]* and the second for temperatures greater than *1000 [K]*. Here it is noted that enthalpy *h(T)* and entropy *s(T)* are obtained by integrating the $c_p(T)$ and $c_p(T)/T$, respectively, with respect to *T*. Particularly for entropy (*s*), the result provided form the respective polynomial corresponds only to the part of entropy which is a function of temperature and not to the one which corresponds to pressure variation (see Eq. (3.77) in section 3.5.6) [232]. Furthermore, it should be clarified that the calculation of enthalpy (*h*) using the corresponding polynomial provides the total enthalpy, namely the sum of reference and sensible enthalpy.

Apparently, to calculate the *cp*, *h* and *s* of a mixture (*mix*), their values for each species comprised in the mixture for the examined temperature are calculated at first and then are summed up proportionally with their molar fraction in the mixture as follows (see also Eq. (3.49) and (3.50) in section 3.5.3):

$$cp_{mix} = R \cdot \sum_j x_j \cdot \left(\frac{cp}{R}\right)_j$$

$$h_{mix} = R \cdot T \cdot \sum_j x_j \cdot \left(\frac{h}{R \cdot T}\right)_j$$

$$s_{mix} = R \cdot \sum_j x_j \cdot \left(\frac{s}{R}\right)_j$$

The values of the polynomials coefficients, for each one of the species considered, are demonstrated in the following tables (at next page) for both temperature cases, less or equal than *1000 [K]* and greater than *1000 [K]*:

NASA Polynomials Coefficients for T ≤ 1000K					
species	O_2	N_2	CO_2	H_2O	H
MW [kg/kmol]	31.99880	28.01340	44.00950	18.01528	1.00794
Coefficients a_1	-3.425563420E+04	2.210371497E+04	4.943650540E+04	-3.947960830E+04	0.000000000E+00
Coefficients a_2	4.847000970E+02	-3.818461820E+02	-6.264116010E+02	5.755731020E+02	0.000000000E+00
Coefficients a_3	1.119010961E+00	6.082738360E+00	5.301725240E+00	9.317826530E-01	2.500000000E+00
Coefficients a_4	4.293889240E-03	-8.530914410E-03	2.503813816E-03	7.222712860E-03	0.000000000E+00
Coefficients a_5	-6.836300520E-07	1.384646189E-05	-2.127308728E-07	-7.342557370E-06	0.000000000E+00
Coefficients a_6	-2.023372700E-09	-9.625793620E-09	-7.689988780E-10	4.955043490E-09	0.000000000E+00
Coefficients a_7	1.039040018E-12	2.519705809E-12	2.849677801E-13	-1.336933246E-12	0.000000000E+00
Coefficients b_1	-3.391454870E+03	7.108460860E+02	-4.528198460E+04	-3.303974310E+04	2.547370801E+04
Coefficients b_2	1.849699470E+01	-1.076003744E+01	-7.048279440E+00	1.724205775E+01	-4.466828530E-01
species	H_2	N	NO	O_2	OH
MW [kg/kmol]	2.01588	14.00670	30.00610	15.99940	17.00734
Coefficients a_1	4.078323210E+04	0.000000000E+00	-1.143916503E+04	-7.953611300E+03	-1.998858990E+03
Coefficients a_2	-8.009186040E+02	0.000000000E+00	1.536467592E+02	1.607177787E+02	9.300136160E+01
Coefficients a_3	8.214702010E+00	2.500000000E+00	3.431468730E+00	1.966226438E+00	3.050854229E+00
Coefficients a_4	-1.269714457E-02	0.000000000E+00	-2.668592368E-03	1.013670310E-03	1.529529288E-03
Coefficients a_5	1.753605076E-05	0.000000000E+00	8.481399120E-06	-1.110415423E-06	-3.157890998E-06
Coefficients a_6	-1.202860270E-08	0.000000000E+00	-7.685111050E-09	6.517507500E-10	3.315446180E-09
Coefficients a_7	3.368093490E-12	0.000000000E+00	2.386797655E-12	-1.584779251E-13	-1.138762683E-12
Coefficients b_1	2.682484665E+03	5.610463780E+04	9.098214410E+03	2.840362437E+04	2.991214235E+03
Coefficients b_2	-3.043788844E+01	4.193905036E+00	6.728725490E+00	8.404241820E+00	4.674110790E+00
species	CO	$C_{12}H_{26}$	Ar	SO_2	
MW [kg/kmol]	28.01010	170.33484	39.94810	64.06440	
Coefficients a_1	1.489045326E+04	-1.583387502E+07	0.000000000E+00	-5.310842140E+04	
Coefficients a_2	-2.922285939E+02	2.318455011E+05	0.000000000E+00	9.090311670E+02	
Coefficients a_3	5.724527170E+00	-1.301084838E+03	2.500000000E+00	-2.356891244E+00	
Coefficients a_4	-8.176235030E-03	3.729278890E+00	0.000000000E+00	2.204449885E-02	
Coefficients a_5	1.456903469E-05	-5.271624900E-03	0.000000000E+00	-2.510781471E-05	
Coefficients a_6	-1.087746302E-08	3.786419430E-06	0.000000000E+00	1.446300484E-08	
Coefficients a_7	3.027941827E-12	-1.083032706E-09	0.000000000E+00	-3.369070940E-12	
Coefficients b_1	-1.303131878E+04	-1.147286089E+06	-7.453750000E+02	-4.113752080E+04	
Coefficients b_2	-7.859241350E+00	7.267799460E+03	4.379674910E+00	4.045512519E+01	

NASA Polynomials Coefficients for T > 1000K						
species		O_2	N_2	CO_2	H_2O	H
MW [kg/kmol]		31.99880	28.01340	44.00950	18.01528	1.00794
Coefficients	a_1	-1.03793902E+06	5.87712406E+05	1.17696242E+05	1.03497210E+06	6.07877425E+01
	a_2	2.34483028E+03	-2.23924907E+03	-1.78879148E+03	-2.41269856E+03	-1.81935442E-01
	a_3	1.81973204E+00	6.06694922E+00	8.29152319E+00	4.64611078E+00	2.50021182E+00
	a_4	1.26784758E-03	-6.13968550E-04	-9.22315678E-05	2.29199831E-03	-1.22651286E-07
	a_5	-2.18806799E-07	1.49180668E-07	4.86367688E-09	-6.83683048E-07	3.73287633E-11
	a_6	2.05371957E-11	-1.92310549E-11	-1.89105331E-12	9.42646893E-11	-5.68774456E-15
	a_7	-8.19346705E-16	1.06195439E-15	6.33003659E-16	-4.82238053E-15	3.41021020E-19
	b_1	-1.68901093E+04	1.28321042E+04	-3.90835059E+04	-1.38428651E+04	2.54748640E+04
	b_2	1.73871651E+01	-1.58664003E+01	-2.65266928E+01	-7.97814851E+00	-4.48191777E-01
species		H_2	N	NO	O_2	OH
MW [kg/kmol]		2.01588	14.00670	30.00610	15.99940	17.00734
Coefficients	a_1	5.60812801E+05	8.87650138E+04	2.23901872E+05	2.61902026E+05	1.01739338E+06
	a_2	-8.37150474E+02	-1.07123150E+02	-1.28965162E+03	-7.29872203E+02	-2.50995728E+03
	a_3	2.97536453E+00	2.36218829E+00	5.43393603E+00	3.31717727E+00	5.11654786E+00
	a_4	1.25224912E-03	2.91672008E-04	-3.65603490E-04	-4.28133436E-04	1.30529993E-04
	a_5	-3.74071619E-07	-1.72951510E-07	9.88096645E-08	1.03610459E-07	-8.28432226E-08
	a_6	5.93662520E-11	4.01265788E-11	-1.41607686E-11	-9.43830433E-12	2.00647594E-11
	a_7	-3.60699410E-15	-2.67722757E-15	9.38018462E-16	2.72503830E-16	-1.55699366E-15
	b_1	5.33982441E+03	5.69735133E+04	1.75031766E+04	3.39242806E+04	2.01964021E+04
	b_2	-2.20277477E+00	4.86523151E+00	-8.50166909E+00	-6.67958535E-01	-1.10128234E+01
species		CO	$C_{12}H_{26}$	Ar	SO_2	
MW [kg/kmol]		28.01010	170.33484	39.94810	64.06440	
Coefficients	a_1	4.61919725E+05	-3.43056026E+06	2.01053848E+01	-1.12764012E+05	
	a_2	-1.94470486E+03	-1.98034819E+04	-5.99266107E-02	-8.25226138E+02	
	a_3	5.91671418E+00	9.21342378E+01	2.50006940E+00	7.61617863E+00	
	a_4	-5.66428283E-04	9.02395447E-03	-3.99214116E-08	-1.99932761E-04	
	a_5	1.39881454E-07	-2.21997358E-06	1.20527214E-11	5.65563143E-08	
	a_6	-1.78768036E-11	2.77046319E-10	-1.81901558E-15	-5.45431661E-12	
	a_7	9.62093557E-16	-1.37207320E-14	1.07857664E-19	2.91829410E-16	
	b_1	-2.46626108E+03	4.38186988E+04	-7.44993961E+02	-3.35130869E+04	
	b_2	-1.38741311E+01	-5.24819104E+02	4.37918011E+00	-1.65577609E+01	

e. Calculation of Gas Properties (k, μ) using NASA Polynomials

Thermal conductivity (*k [W/m/K]*) and dynamic viscosity (μ *[Pa s]*) of each species *j*, is calculated via NASA polynomial approximations [221], which account only for the effect of gas temperature. These polynomials are presented at next:

$$k_j = exp\left(A_{c_j} \cdot ln(T) + B_{c_j} \cdot T^{-1} + C_{c_j} \cdot T^{-2} + D_{c_j}\right)$$

$$\mu_j = exp\left(A_{dv_j} \cdot ln(T) + B_{dv_j} \cdot T^{-1} + C_{dv_j} \cdot T^{-2} + D_{dv_j}\right)$$

where *A*, *B*, *C*, and *D* are the polynomial coefficients and the subscripts *c* and *dv* denote conductivity and dynamic viscosity respectively. Each coefficient is defined from two constant values, the first is valid for temperatures equal or lower than *1000 [K]* and the second for temperatures greater than *1000 [K]*. These polynomials provide the *k* and μ in *[W/cm/K* x *10^{-6}]* and *[g/cm/s* x *10^{-6}]* units. Thus the extracted values of *k* and μ are multiplied with *10^{-4}* and *10^{-7}* correspondingly in order to convert them into *[W/m/K]* and *[Pa s]* respectively. The *k* and μ of the mixture are calculated using the Eq. (2.39) and (2.40) [222,223] described in section 3.4.7. The values of the polynomials coefficients, for each one of the species considered, are demonstrated in the following tables for both temperature cases, less or equal than *1000 [K]* and greater than *1000 [K]*:

NASA Coefficients for conductivity (*k*) polynomial							
		T ≤ 1000K					
species		O_2	N_2	CO_2	H_2O	Ar	SO_2
MW [kg/kmol]		31.99880	28.01340	44.00950	18.01528	39.94810	64.06440
Coefficients	A_c	0.77238828	0.85372829	0.51435424	1.13229910	0.60968928	0.61476551
	B_c	6.9293259	105.1866500	-474.4462600	-512.1386700	-70.8922490	-564.0929500
	C_c	-5900.85180	-12299.75300	31295.93000	99913.49800	584.20624	49580.78700
	D_c	1.22029650	0.48299104	3.41287390	-0.52900911	1.93371520	2.39400640
		T > 1000K					
Coefficients	A_c	0.90875998	0.88506520	0.67510355	0.50036257	0.69075463	0.53617558
	B_c	289.86028	134.69656	-112.83945	-1719.42890	62.67606	-694.13085
	C_c	-79180.433	-11386.420	-69132.618	387590.610	-25667.413	75304.908
	D_c	0.068622859	0.236100080	2.041278700	4.755867000	1.266418900	3.041200200

NASA Coefficients for dynamic viscosity (μ) polynomial							
		T ≤ 1000K					
species		O_2	N_2	CO_2	H_2O	Ar	SO_2
MW [kg/kmol]		31.99880	28.01340	44.00950	18.01528	39.94810	64.06440
Coefficients	A_{dv}	0.6091618	0.62526577	0.51137258	0.49966928	0.61205763	0.53157084
	B_{dv}	-52.244847	-31.779652	-229.51321	-697.84297	-67.714354	-295.89873
	C_{dv}	-599.74009	-1640.7983	13710.678	88274.722	190.4066	21224.84
	D_{dv}	2.0410801	1.7454992	2.7075538	3.0878979	2.1588272	2.5975549
		T > 1000K					
Coefficients	A_{dv}	0.72216486	0.87395209	0.63978285	0.5896333	0.69357334	0.60783098
	B_{dv}	175.50839	561.52222	-42.637076	-538.75152	70.953943	-192.83581
	C_{dv}	-57974.816	-173948.09	-15522.605	54745.23	-28386.007	7823.2002
	D_{dv}	1.0901044	-0.39335958	1.6628843	2.3409644	1.4856447	1.9811072

f. Finite Differences for the Calculation of Pressure Derivatives

The second $\left(\frac{d^2p}{d\theta^2}\right)$ and fourth $\left(\frac{d^4p}{d\theta^4}\right)$ derivatives of the pressure with respect to θ are demonstrated at next. These derivatives schemes were used in the determination of the start of combustion (*SOC*). The following equations are implemented when the measuring sampling rate is constant. Namely the crank angle intervals determined from two consecutive measurements of pressure are constant (equidistance) throughout the cycle.

$$\left(\frac{d^2p}{d\theta^2}\right)_i = \frac{-p_{i+2} + 16 \cdot p_{i+1} - 30 \cdot p_i + 16 \cdot p_{i-1} - p_{i-2}}{12 \cdot (\Delta\theta)^2}$$

$$\left(\frac{d^4p}{d\theta^4}\right)_i = \frac{p_{i+2} - 4 \cdot p_{i+1} + 6 \cdot p_i - 4 \cdot p_{i-1} + p_{i-2}}{(\Delta\theta)^4}$$

In the previous expressions *p [Pa]* is pressure, *θ [°]* is the crank angle and subscript *i* denotes the current calculation step. $\left(\frac{d^2p}{d\theta^2}\right)$ is calculated using fourth order accuracy central finite differences and $\left(\frac{d^4p}{d\theta^4}\right)$ is calculated using second order accuracy central finite differences. For $\left(\frac{d^4p}{d\theta^4}\right)$, second order accuracy was used in order to shorten the calculation time but also for practical reasons, namely less pressure values are required (*5* instead of *7*) and the number of required pressure values is equal to the one required for $\left(\frac{d^2p}{d\theta^2}\right)$ calculation. The first derivative of the pressure was directly calculated during the pressure trace smoothing procedure using Savitzky–Golay filter as described in section 3.2.3.

g. Modified False Position Method for Root Finding

The modified false position method is based on false position method but eliminates the undesirable feature of the one–sited approach [227]. This method, is essentially a linear interpolation method where the values that define the interval that the root lies in, vary at each iteration step according to the sign of the root estimation of the previous step, until final convergence. This method was used to calculate coefficient "*α*" used in the Annand correlation for the calculation of heat exchange with the wall (see section 3.4.7) and to find the optimum Φ values which were utilized in the statistical procedure for the determination of the empirical correlation for the calculation of zone Φ^* (see section 3.5.8). At next the flow–chart of the aforementioned method is demonstrated. Referring to the flow–chart, x_0 is the sought root, namely the value which zeros *y* ($y_0=f(x_0)=0$), *f* is a function of the independent variable *x*, *a* and *b* are the left and right initial limits where the x_0 lies in, determined by the user. It is emphasized that the success of this method depends from the appropriate determination of the initial values of *a* and *b*. Ideally, these values should enclose x_0, namely $y(a) \cdot y(b) < 0$, however the last is not imperative.

For the calculation of heat exchange coefficient "*α*" ($x=\alpha$) the function *f* corresponds to the difference between the measured fuel amount and the fuel amount provided by the heat release sub–model (presented in section 3.4) which uses as an input the examined

coefficient α (see also section 3.4.7). When this function becomes approximately zero, then the correct coefficient α is obtained.

For the calculation of the actual Φ^* ($x=\Phi^*$) value (see also section 3.5.8)) the function f corresponds to the difference between the measured NO_x and calculated NO_x using the NO_x sub–model (presented in section 3.5) which uses as an input the examined Φ^* (see also section 3.5.8). When this function becomes approximately zero, then the actual Φ^* where the calculated NO_x is very close to measured one, is obtained.

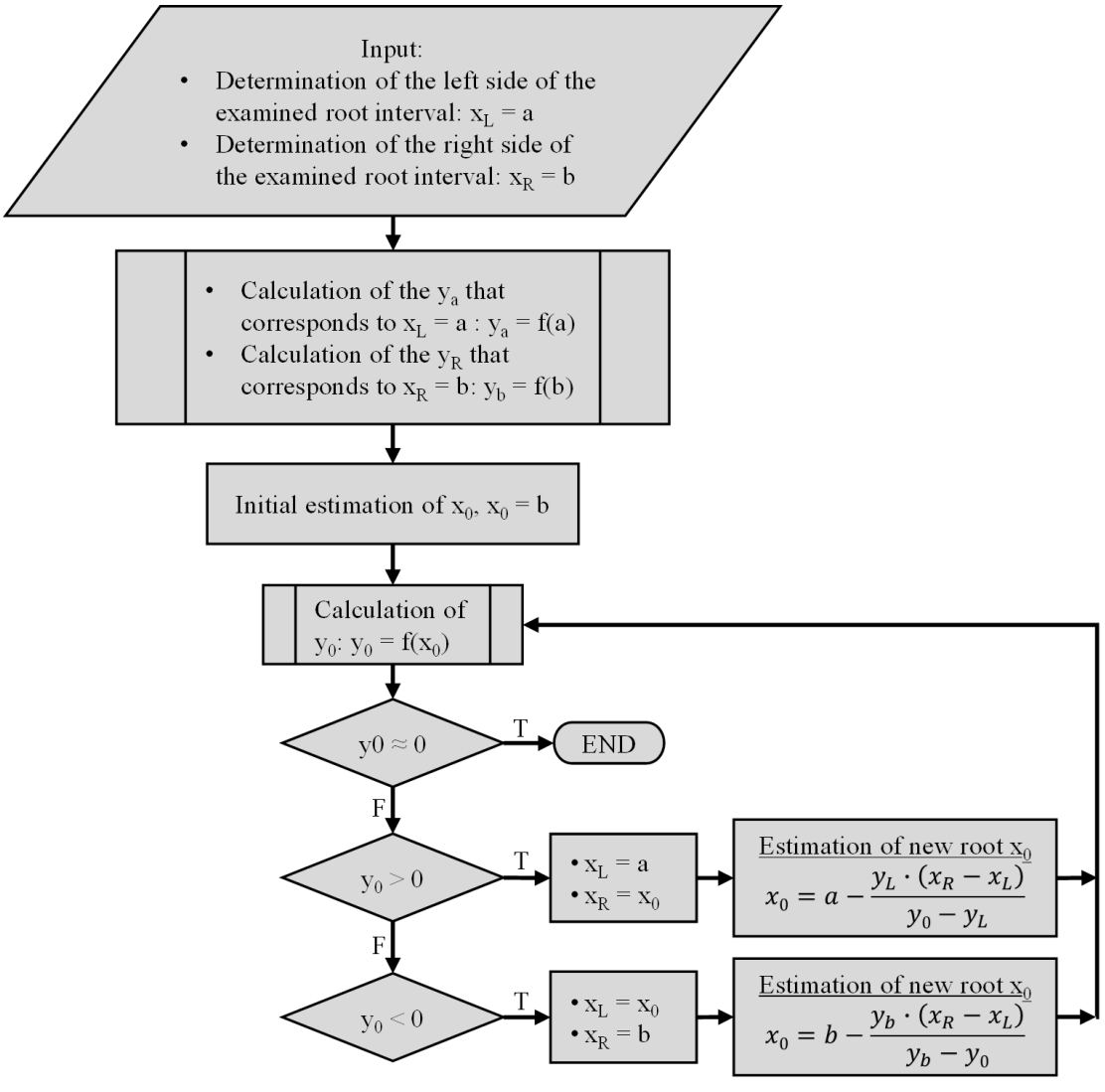

Flow–chart of the modified false position method for root finding.

CURRICULUM VITAE

Curriculum Vitae

Personal information

First name / Surname	**Nikolaos Savva**
Address(es)	(Permanent): 29, Kyparissas str., 4107, Limassol, Cyprus. (Term): 6A, Kokkinopoulou str., 15773, Athens, Greece.
Telephone(s)	+30–2107723528 Mobile: +30-69 77081172 +357–25728861 +357-99 310531
E–Mail	nichosavv@hotmail.com
Nationality	Cypriot
Date of birth	26th of January 1986
Gender	Male

Education and training

Dates	*January 2010 until today*
Title of qualification	Ph.D. doctoral degree.
Principal subjects	Research in the field of Reciprocating Internal Combustion Engines emphasising on large–scale ship main and auxiliary engines and power–plant engines, 2 and 4–stroke) and automotive *DI* Diesel engines. Thermodynamic and thermochemical analysis of the combustion procedures taking place inside the combustion chamber. Utilization of measured in–cylinder pressure for engine cycle analysis, diagnosis and pollutant emissions prediction. Development and application of simplified, semi–empirical, thermodynamic models, which utilize the in–cylinder pressure, for the simulation of combustion process in order to examine the influence of various operating parameters and engine settings/adjustments on engine performance and exhaust emissions. The developed models are oriented for real–time/model–based/closed loop control. Performance, emissions and in–cylinder pressure measurements on large–scale Diesel engines. Assisting in the teaching of the course "Internal Combustion Engines" provided from the School of Mechanical Engineering of NTUA. Until now, four scientific papers of my study have been published, one is under review and one is under preparation. I have presented one of my works is SAE international congress (April 2012, Detroit, USA).

Dissertation subject	"Development and evaluation of a semi–empirical, multi–zone, thermodynamic model for the estimation of Nitric Oxide emissions and formation history in Diesel engines using the measured cylinder pressure trace." (At the moment, the final dissertation text is under review from my supervisor.)
Supervisor	NTUA Professor Hountalas T. Dimitrios.
Funding	My doctoral program was funded from Alexander S. Onassis Public Benefit Foundation, which was provided me with a four year full scholarship –1st Oct. 2010 – 30th Sept. 2014), and from State Scholarship Foundation of Cyprus, which was provided me with a three year complementary scholarship.
Name of the organisation providing the education	National Technical University of Athens (NTUA), School of Mechanical Engineering, Thermal Engineering Department, Internal Combustion Engines Lab.
Dates	*October 2004 to October 2009*
Title of qualification awarded	Five–year Diploma with a master certificate in Mechanical Engineering.
Principal subjects/occupational skills covered	Specialization in the field of Energy. The basic fields covered by this Diploma are the following: maths, physics, mechanics, computational methods and programming, optimization, thermodynamics and thermochemistry, fluid dynamics, heat and mass transfer, internal and external combustion engines, power plants, energy production and energy management, environment and pollution, emission prediction and control, renewable sources of energy, air conditioning, cooling/refrigeration, logistics, production management, mechanical design (plan), measurements and statistics, engineering of mechanics, construction, materials, turbo machinery, compressors, turbines, pumps, pipe lines, electromechanical engines, electronics, etc. I have elaborated my diploma thesis under the supervision of Professor Hountalas T. Dimitrios at the Internal Combustion Engines Lab of Mechanical Engineering School of NTUA. Thesis subject**:** Development of a semi–empirical model for the estimation of nitric oxide (NO) emissions from Diesel engines by using the in–cylinder pressure diagram at various operating conditions.
Name of the organization providing the education	National Technical University of Athens (NTUA), School of Mechanical Engineering, Thermal Engineering Department.
Level in national or international classification	Diploma grade: 8.5/10 – this grade is calculated as the sum of the 80% of the average of the grades of all courses (a total of 65) and of 20% of the diploma thesis grade, which was graded with 10/10. I have been ranked 7th between the 190 graduates of my graduation year – 2009). I had also approved with annual monetary awards from the School for excellent performance.

Dates	*21st of July 2008 to 5th of September 2008*
Practical Exercise / Internship	Practical exercise as a student (working student) at a power–plant of the Electrical Authority of Cyprus – EAC) under the supervision of NTUA Steam Boilers and Thermal Plants Lab.
Principal subjects/occupational skills covered	Observing, training and participating to the activities of engineers and technicians of EAC. I was placed in all departments of the station – Chemical, Electrical, Instrument and Control, Central Control) but mostly at the Mechanical Engineering department. Observation of the construction of the two new combined–cycle power units. In this period, I came in contact with a lot of engineers and technicians who transmitted me some of their knowledge and experience in the field of power generation and power plant operation. I had also experienced the practical implementation of the relevant courses that I had followed during my studies in the university.
Name of the organisation providing the training	Electrical Authority of Cyprus, Vasilikos Power Station.
Dates	*July 2003 to June 2004*
Military Service	I have served my military service in Cyprus in the National Guard (Artillery).
Dates	June 2003
Been accepted in University	Participation to the Pancyprian University Entrance Examinations, from which I gained a place in the School of Mechanical Engineering of the National Technical University of Athens, first personal choice, with a five–year scholarship from the State Scholarship Foundation of Cyprus, due to the excellent average grade of my lyceum degree.
Dates	*September 2000 to June 2003*
Title of qualification awarded	Lyceum degree.
Name of the organisation providing the education	Lanitio Lyceum B' (Limassol, Cyprus).
Level in national or international classification	Grade of the Degree: 19.75/20 (Excellent).

Personal skills and competences	
Mother tongue	**Greek**
Other language	**English**

Self–assessment	**Understanding**				**Speaking**				**Writing**	
European level (*)	Listening		Reading		Spoken interaction		Spoken production			
English	C1	Proficient user	C2	Proficient user	B2	Independent user	B2	Independent user	C2	Proficient user

(*) Common European Framework of Reference for Languages

Computer skills and competences	**Operating Systems:** Windows, MacOS, Linux, Unix. **Programming:** FORTRAN (excellent skills), MATLAB (good skills). **Simulation:** GT–Power (basic skills). **Design Software:** Auto–CAD (basic skills). **Word Processing Software:** MS Office (excellent skills), Open Office, LaTeX. **Internet Software:** internet browsers and applications.
Other skills and competences	**Sports / hobbies:** Basketball, Swimming, Cycling, Running, Windsurfing, Sailing.
Social skills and competences	Spirit of collaboration inside a team, through the participation in the basketball team of Anagennisis Yermasoyias (2001–2003, Cyprus).
Driving licence	European car and motorcycle driving licence (categories AM, A1, A, B1, B, BE).
Offshore sailing licence	I attended the offshore sailing course from 1/11/2007 to 22/12/2007 in offshore sailing school yachting club of Kalamaki and graduated from it successfully.

References	
Name	Dr. Hountalas T. Dimitrios
Title	NTUA Professor.
Affiliation	NTUA, Mechanical Engineering School, Internal Combustion Engine Lab.
Address	Heroon Polytechniou 9, 15780 Zografou, Athens, Greece.
Telephone	0030–210 772–1259
E–mail	dx1961@central.ntua.gr
Name	Dr.–Ing. Karellas Sotirios
Title	NTUA Associate Professor.
Affiliation	NTUA, Mechanical Engineering School, Steam Boilers and Thermal Plants Lab.
Address	Heroon Polytechniou 9, 15780 Zografou, Athens, Greece.
Telephone	0030–210 772–2810
E–mail	sotokar@mail.ntua.gr
Reference Letters	Available upon request.

ΕΘΝΙΚΟ ΜΕΤΣΟΒΙΟ ΠΟΛΥΤΕΧΝΕΙΟ
ΣΧΟΛΗ ΜΗΧΑΝΟΛΟΓΩΝ ΜΗΧΑΝΙΚΩΝ
ΤΟΜΕΑΣ ΘΕΡΜΟΤΗΤΑΣ
ΕΡΓΑΣΤΗΡΙΟ ΜΗΧΑΝΩΝ ΕΣΩΤΕΡΙΚΗΣ ΚΑΥΣΗΣ

Ανάπτυξη και Αξιολόγηση Ημι–εμπειρικού Θερμοδυναμικού Πολυζωνικού Μοντέλου για την Εκτίμηση των Εκπομπών Οξειδίου του Αζώτου και του Ιστορικού του Σχηματισμού τους σε Κινητήρες Ντίζελ από το Μετρημένο Διάγραμμα Πίεσης του Θαλάμου Καύσης.

ΔΙΔΑΚΤΟΡΙΚΗ ΔΙΑΤΡΙΒΗ

Σάββα Σ. Νικόλαου

Διπλ. Μηχανολόγου Μηχανικού ΕΜΠ

ΤΡΙΜΕΛΗΣ ΣΥΜΒΟΥΛΕΥΤΙΚΗ ΕΠΙΤΡΟΠΗ:

1. Δ.Θ. Χουντάλας, Καθ. ΕΜΠ (Επιβλέπων)
2. Κ.Δ. Ρακόπουλος, Καθ. ΕΜΠ
3. Μ.Α. Φούντη, Καθ. ΕΜΠ

ΕΠΤΑΜΕΛΗΣ ΕΞΕΤΑΣΤΙΚΗ ΕΠΙΤΡΟΠΗ:

1. Δ.Θ. Χουντάλας, Καθ. ΕΜΠ (Επιβλέπων)
2. Κ.Δ. Ρακόπουλος, Καθ. ΕΜΠ
3. Μ.Α. Φούντη, Καθ. ΕΜΠ
4. Κ.Α. Αντωνόπουλος, Καθ. ΕΜΠ
5. Ε.Γ. Γιακουμής, Αν. Καθ. ΕΜΠ
6. Σ. Καρέλλας, Αν. Καθ. ΕΜΠ
7. Ρ.Γ. Παπαγιαννάκης , Αν. Καθ. Σχ. Ικάρων

Αθήνα, Ιούνιος 2015

ΕΥΧΑΡΙΣΤΙΕΣ

Στην παρούσα διδακτορική διατριβή αναπτύχθηκε ένα απλό, ημιεμπειρικό, πολυζωνικό, θερμοδυναμικό μοντέλο για την εκτίμηση των οξειδίων του αζώτου και του ιστορικού του σχηματισμού τους σε κινητήρες ντίζελ χρησιμοποιώντας το μετρημένο διάγραμμα πίεσης του κυλίνδρου και αξιολογήθηκε η ικανότητα του εφαρμόζοντάς το σε διάφορους τύπους κινητήρων Diesel. Η διατριβή αυτή εκπονήθηκε κατά τη διάρκεια της περιόδου Ιανουάριος 2010 και Ιανουάριος 2015 στο Εργαστήριο Μηχανών Εσωτερικής Καύσης της Σχολής Μηχανολόγων Μηχανικών του Εθνικού Μετσόβιου Πολυτεχνείου.

Σε αυτό το σημείο , θα ήθελα να εκφράσω την ευγνωμοσύνη μου στο κοινωφελές Ίδρυμα Αλέξανδρος Ωνάσης για την παροχή τετραετούς πλήρους υποτροφίας (1 Οκτωβρίου 2010 - 30 Σεπτεμβρίου του 2014). Επίσης θα ήθελα να ευχαριστήσω το ίδρυμα κρατικών υποτροφιών Κύπρου που μου παρείχε τριετή συμπληρωματική υποτροφία. Χωρίς αυτή τη χρηματοδότηση, δεν θα ήμουν σε θέση να διεξάγω αυτή την διδακτορική διατριβή.

Επιπλέον, θα ήθελα να εκφράσω την εκτίμηση και την ευγνωμοσύνη μου στον επιβλέποντα μου, Καθηγητή Δημήτριο Χουντάλα που με καθοδήγησε καθ' όλη τη διάρκεια αυτής της έρευνας, παρέχοντας μου χρήσιμες πληροφορίες, εξειδικευμένες συμβουλές και κατευθυντήριες γραμμές που πηγάζουν από την πολυετή εμπειρία του και τη βαθιά του γνώση στον τομέα των κινητήρων εσωτερικής καύσης. Επίσης, μου παρείχε πληθώρα πειραματικών δεδομένων τα οποία προέκυψαν από τη συνεργασία του με ερευνητικούς οργανισμούς, κατασκευαστές κινητήρων και από μετρήσεις πραγματικού χρόνου σε πλοία και σταθμούς παραγωγής ηλεκτρικής ενέργειας .

Επίσης, πολλές ευχαριστίες αποδίδονται στα μέλη της Συμβουλευτικής Επιτροπής του Διδακτορικού μου προγράμματος, τον Καθηγητή Κωνσταντίνο Ρακόπουλο και την Καθηγήτρια Μαρία Φουντή για την πολύτιμη βοήθειά που μου προσέφεραν.

Τέλος, θα ήθελα να ευχαριστήσω τους συναδέλφους και φίλους μου: Σακελλαρίδη Νικόλαο, Ραπτοτάσιο Σπυρίδων, Ζοβάνο Γεώργιο, Αντωνόπουλο Αντώνη και Δημάρατο Αθανάσιο για τη συμβολή τους σε αυτή την έρευνα προσφέροντας μου την επιστημονική τους γνώμη και για τις εποικοδομητικές συνομιλίες που είχαμε στον τομέα της έρευνας μας.

Σάββα Νικόλαος

Αθήνα, Απρίλιος, 2015

ΠΕΡΙΛΗΨΗ

Ο σκοπός της παρούσας διδακτορικής διατριβής είναι η ανάπτυξη και αξιολόγηση ενός απλού, ημιεμπειρικού, πολυζωνικού, θερμοδυναμικού μοντέλου για την πρόβλεψη των εκπομπών του οξειδίου του αζώτου (NO_x), καθώς και του ιστορικού του σχηματισμού τους μέσα στον θάλαμο καύσης, κατά τη διάρκεια του κλειστού κύκλου λειτουργίας των κινητήρων Diesel άμεσου ψεκασμού (*DI*).

Το κίνητρο για αυτή την εργασία είναι οι απαιτήσεις της βιομηχανίας κατασκευής και χρήσης κινητήρων εσωτερικής καύσης, για τον έλεγχο των εκπομπών ρύπων. Αυτή η ανάγκη προέκυψε λόγω των αυστηρών νομοθετικών πλαισίων που υιοθετήθηκαν από τις κυβερνήσεις παγκοσμίως. Ο τομέας των κινητήρων *DI* Diesel επηρεάζεται σημαντικά από αυτές τις νομοθεσίες επειδή χρησιμοποιείται ευρέως στις θαλάσσιες και επίγειες μεταφορές, σε εφαρμογές βαρέος τύπου στη βιομηχανία, στην παραγωγή ηλεκτρικής ενέργειας σε απομακρυσμένες/απομονωμένες περιοχές και σε επιβατικά οχήματα. Ειδικότερα για τα επιβατικά οχήματα, οι κινητήρες Diesel κερδίζουν σημαντικό έδαφος στην αγορά έναντι των βενζινοκινητήρων τα τελευταία χρόνια. Επίσης, ένας από τους πιο σημαντικούς ρύπους που δύναται να περιοριστεί σε αυτούς τους τομείς, είναι τα οξείδια του αζώτου (NO_x). Για αυτούς τους λόγους, στην εργασία αυτή, ο συγγραφέας εστιάζει στο πεδίο του ελέγχου των NO_x σε κινητήρες *DI* Diesel στοχεύοντας στην ανάπτυξη λογισμικού το οποίο θα μπορεί να συνεισφέρει στην έρευνα και εφαρμογή των τεχνολογιών για τη μείωση των εκπεμπόμενων NO_x.

Έτσι, σε αυτή την εργασία, αναπτύχθηκε και αξιολογήθηκε ένα νέο μοντέλο εκτίμησης των εκπομπών NO_x από τους κινητήρες *DI* Diesel. Το προτεινόμενο μοντέλο χρησιμοποιεί τα γεωμετρικά χαρακτηριστικά, το μετρημένο δυναμοδεικτικό διάγραμμα και βασικές λειτουργικές παραμέτρους του κινητήρα. Αρχικά αξιοποιεί το δυναμοδεικτικό διάγραμμα για την εκτίμηση του ρυθμού καύσης του καυσίμου. Από αυτό, δημιουργείται μια χρονική κατανομή του καιόμενου καυσίμου στον κλειστό κύκλο λειτουργίας. Στη συνέχεια, τα στοιχειώδη ποσά καυσίμου που έχουν καεί διαδοχικά σε κάθε χρονική στιγμή αποδίδονται σε αυτόνομες ζώνες ακολουθώντας μια πολυζωνική προσέγγιση. Το ποσό της απαιτούμενης άκαυστης γόμωσης που εισέρχεται σε κάθε ζώνη, για να πραγματοποιηθεί η καύση, καθορίζεται από τον λόγο ισοδυναμίας καυσίμου/αέρα της ζώνης. Αυτή η παράμετρος υπολογίζεται με μια εμπειρική σχέση, η οποία εξάχθηκε στα πλαίσια αυτής της εργασίας, και λαμβάνεται ως σταθερή για όλες τις ζώνες. Αυτή η σχέση εμπλέκει λειτουργικές παραμέτρους του κινητήρα και στοιχεία που προκύπτουν από την ανάλυση των αντίστοιχων διαγραμμάτων πίεσης και ρυθμού έκλυσης θερμότητας. Κάθε ζώνη, μετά τον σχηματισμό της, συμπεριφέρεται ως κλειστό θερμοδυναμικό σύστημα και εξελίσσεται μέσα στο θάλαμο καύσης έχοντας το δικό της ιστορικό χημικής σύστασης, θερμοκρασίας και όγκου ενώ η πίεση αντιστοιχεί σε αυτήν του κυλίνδρου την τρέχουσα χρονική στιγμή. Το ποσό των NO_x που σχηματίζεται σε κάθε ζώνη, υπολογίζεται χρησιμοποιώντας τον μηχανισμό Extended Zeldovich. Το σύνολο των εκπομπών NO_x στην εξαγωγή του κινητήρα υπολογίζεται από το άθροισμα των NO_x της κάθε ζώνης όταν ανοίγει η βαλβίδα εξαγωγής. Σύμφωνα με αυτό το

σενάριο, το μοντέλο μπορεί επίσης να παρέχει το ιστορικό του σχηματισμού των NO_x (της κάθε ζώνης και συνολικά) μέσα στον θάλαμο καύσης.

Το προτεινόμενο μοντέλο έχει επικυρωθεί και αξιολογηθεί σε διάφορους τύπους υπερπληρωμένων κινητήρων *DI* Diesel όπως δίχρονων κινητήρων μεγάλης κλίμακας που χρησιμοποιούνται στην πρόωση πλοίων και στην παραγωγή ηλεκτρικής ενέργειας, τετράχρονων κινητήρων μεγάλης κλίμακας που χρησιμοποιούνται στα πλοία για ηλεκτροδότηση και σε σταθμούς παραγωγής ισχύος και τετράχρονων κινητήρων οχημάτων βαρέος και ελαφρού τύπου, αξιοποιώντας ένα σύνολο *221* μετρημένων περιπτώσεων λειτουργίας. Αυτές, αντιστοιχούν σε διάφορα σημεία λειτουργίας που καθορίζονται από διαφορετικές παραμέτρους και ρυθμίσεις του κινητήρα. Έτσι, μπορεί να εξεταστεί η ικανότητα του μοντέλου να προβλέπει τις απόλυτες τιμές των NO_x, για κάθε εξεταζόμενη περίπτωση και να ακολουθεί την επίδραση της μεταβολής αυτών των παραμέτρων στο σχηματισμό των NO_x. Οι παράμετροι που εξετάζονται είναι οι ακόλουθες: ισχύς και ταχύτητα του κινητήρα, είδος καυσίμου, χρονισμός και πίεση έγχυσης, ποσοστό ανακυκλοφορίας καυσαερίου (*EGR*) και πίεση αέρα σάρωσης.

Όπως αποκαλύπτεται από την εφαρμογή του μοντέλου σε ένα εκτεταμένο εύρος τύπων μηχανών και σημείων λειτουργίας, το μοντέλο είναι ικανό να προβλέψει τις εκπομπές NO_x με ικανοποιητική ακρίβεια, για την πλειονότητα των περιπτώσεων που εξετάστηκαν. Σημαντικότερο είναι το ότι μπορεί να προβλέψει την τάση μεταβολής των NO_x με την μεταβολή διάφορων παραμέτρων του κινητήρα. Αυτό, κατορθώνεται για διαφορετικούς τύπους κινητήρων χωρίς ιδιαίτερη δυσκολία στη βαθμονόμηση, αφού χρησιμοποιείται μόνο ένας απλός πολλαπλασιαστής για κάθε κινητήρα, για τη διόρθωση των αποτελεσμάτων που εξαγάγει το μοντέλο. Ακόμα ένα σημαντικό πλεονέκτημα του προτεινόμενου μοντέλου είναι το χαμηλό υπολογιστικό του κόστος. Τα προαναφερθέντα, δίνουν μια ενθαρρυντική ένδειξη για χρήση του μοντέλου στην έρευνα, ανάπτυξη και βελτιστοποίηση των κινητήρων *DI* Diesel στο πεδίο της μείωσης των NO_x, ελέγχου των NO_x σε πραγματικό χρόνο, συνεχούς παρακολούθησης των εκπεμπόμενων NO_x, κ.λπ. Στη συνέχεια παρουσιάζεται η εκτεταμένη περίληψη του κάθε κεφαλαίου.

ΕΚΤΕΤΑΜΕΝΗ ΠΕΡΙΛΗΨΗ

Κεφάλαιο 1 ΕΙΣΑΓΩΓΗ

Κινητήρες Diesel

Το πρώτο κεφάλαιο της διατριβής ξεκινά με μια σύντομη ιστορική περιγραφή των κινητήρων Diesel τονίζοντας τα πλεονεκτήματά τους τα οποία είναι τα ακόλουθα: υψηλός βαθμός απόδοσης (μέχρι και *55%*), υψηλή ανθεκτικότητα, αξιοπιστία, ευελιξία, ροπή στον άξονα, μεγάλη διάρκεια ζωής, δυνατότητα χρήσης διάφορων χαμηλού κόστους καυσίμων, κ.λπ. Λόγω αυτών, οι κινητήρες αυτοί χρησιμοποιούνται ευρέως στον τομέα των μεταφορών (δηλ. επιβατικά και φορτηγά οχήματα, τρένα, πλοία, κ.λπ.), στη βαριά βιομηχανία (εργοστάσια, λατομεία, ορυχεία, κ.λπ.) και στην ηλεκτροπαραγωγή (απομακρυσμένες/απομονωμένες περιοχές, μηχανές έκτακτης ανάγκης). Ενδεικτικά αναφέρεται ότι ποσοστό άνω του 95% των κινητήρων στην ναυτιλία είναι Diesel [6,7].

Ωστόσο ο κινητήρας Diesel παραμένει σημαντικός ρυπαντής, ειδικότερα όσο αφορά τις εκπομπές NO_x και σωματιδίων (*PM*). Για να ξεπεραστεί αυτό το μειονέκτημα, οι ερευνητές και οι μηχανικοί εργάζονται εντατικά στην βελτιστοποίηση των διαδικασιών της καύσης, με σκοπό την αύξηση της απόδοσης του κινητήρα και μείωσης των εκπεμπόμενων ρύπων, έτσι ώστε να μπορούν να ανταποκριθούν στη συνεχή αυστηροποίηση των κανονισμών για περιορισμό των ρύπων (EURO V/VI (*EU*), Stage III/IV (*EU*), TIER II/III (*IMO*), κ.λπ.).

Στη συνέχεια του κεφαλαίου αυτού, περιγράφονται οι διαδικασίες που εξελίσσονται στον θάλαμο καύσης από την έναρξη της έγχυσης του καυσίμου μέχρι το τέλος της καύσης και οι αιτίες σχηματισμού των NO_x.

Θερμοδυναμικές Διαδικασίες, Καύση και Σχηματισμός NOx στους Κινητήρες Diesel

Οι επικρατούντες τύποι κινητήρων Diesel που χρησιμοποιούνται σήμερα είναι οι δίχρονοι και οι τετράχρονοι. Οι δίχρονοι χρησιμοποιούνται σε μεγάλης κλίμακας εφαρμογές (πλοία, σταθμοί παραγωγής ενέργειας) ενώ οι τετράχρονοι χρησιμοποιούνται στην αυτοκινητοβιομηχανία, στη βαριά βιομηχανία, στα τρένα και σε μικρότερες εφαρμογές ηλεκτροπαραγωγής. Η ουσιαστική διαφορά στον θερμοδυναμικό κύκλο των τύπων αυτών έγκειται στις φάσεις της εισαγωγής του αέρα και της εξαγωγής του καυσαερίου, δηλαδή της διαδικασίας σάρωσης/εναλλαγής αερίων, η οποία καθορίζει τη μάζα και τη σύσταση της παγιδευμένης γόμωσης. Ωστόσο, οι διαδικασίες που διαδραματίζονται κατά τη διάρκεια του κλειστού κύκλου είναι πανομοιότυπες.

Για τους κινητήρες Diesel, η διαδικασία της έγχυσης καυσίμου είναι καθοριστικής σημασίας διότι οδηγεί την εξέλιξη της καύσης μέσα στον θάλαμο καύσης, η οποία επηρεάζει τον σχηματισμό ρύπων και τις επιδόσεις του κινητήρα. Το ανυψωμένης πίεσης, από την αντλία καυσίμου, υγρό καύσιμο εγχέεται στον θάλαμο καύσης μέσω ειδικού εγχυτήρα σε μορφή δέσμης μικρών σταγονιδίων όπως φαίνεται στο Σχ. 1.1. Εισχωρεί μέσα στο θάλαμο καύσης, ατμοποιείται και αναμειγνύεται με τη γόμωση του κυλίνδρου, μέρος της οποίας εισροφάται στη δέσμη καυσίμου, ωθούμενο από την ορμή της δέσμης και την κίνηση/ροή της γόμωσης. Στη συνέχεια, όταν οι συνθήκες γίνουν κατάλληλες το καύσιμο αντιδρά με τον οξειδωτή (O_2) ακολουθώντας πολύ πολύπλοκους μηχανισμούς διασπώμενων διακλαδώσεων αλυσίδας [11] οι οποίοι προκαλούν την αυτανάφλεξη του καυσίμου. Η χρονική περίοδος μεταξύ της έναρξης της έγχυσης (*SOI*) και της καύσης (*SOC*) καλείται καθυστέρηση ανάφλεξης.

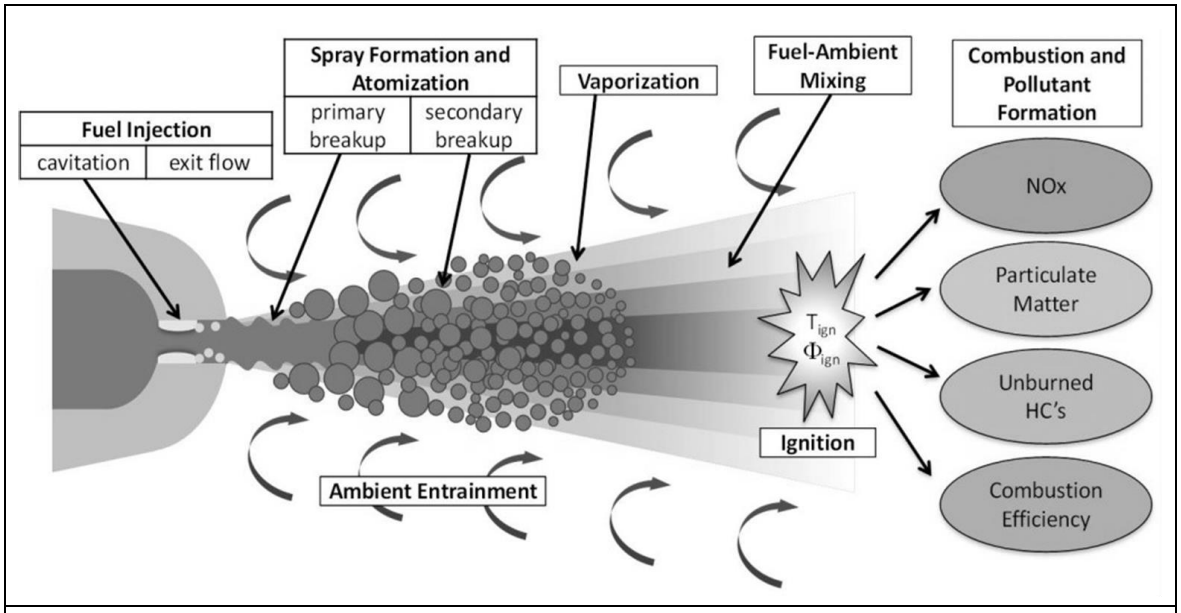

Σχήμα 1.1: Σχηματική περιγραφή των φυσικών διεργασιών που λαμβάνουν χώρα στο θάλαμο καύσης κατά την έγχυση πριν την ανάφλεξη [12].

Στους κινητήρες *DI* Diesel η καύση εξελίσσεται ταυτόχρονα με την διείσδυση της δέσμης καυσίμου και σχηματισμού του μείγματος. Μόνο ένα μικρό ποσοστό του καυσίμου σχηματίζει ομοιογενές μείγμα με τον αέρα κατά τη διάρκεια της καθυστέρησης ανάφλεξης. Αυτό, μετά την ανάφλεξη, καίγεται σχεδόν αμέσως (προαναμεμειγμένη καύση). Στη συνέχεια, ο σχηματισμός του αναφλέξιμου μείγματος και η καύση εξελίσσονται ταυτόχρονα. Έτσι η καύση ελέγχεται από τη διαδικασία του σχηματισμού του μείγματος (καύση διάχυσης) [13]. Λόγω της βαθμιαίας προετοιμασίας του αναφλέξιμου μείγματος παράλληλα με την καύση, η διαδικασία αυτή χαρακτηρίζεται από έντονη ανομοιογένεια (θερμοκρασίας και σύστασης). Οι κινητήρες Diesel γενικά λειτουργούν με φτωχά σε καύσιμο μείγματα, ωστόσο η άμεση έγχυση καυσίμου οδηγεί σε δημιουργία περιοχών μείγματος από πολύ πλούσιες σε πολύ φτωχές. Μια ενδεικτική απεικόνιση της στρωμάτωσης του μείγματος στη δέσμη καυσίμου παρουσιάζεται στο Σχ. 1.2 [15] με σκοπό την κατανόηση των διεργασιών

που συμβαίνουν κατά την καύση στους κινητήρες αυτούς. Η στρωμάτωση αυτή οδηγεί αναπόφευκτα στο σχηματισμό ρυπαντών και ειδικότερα αιθάλης και NO_x [13] όπως φαίνεται στο Σχ. 1.2.

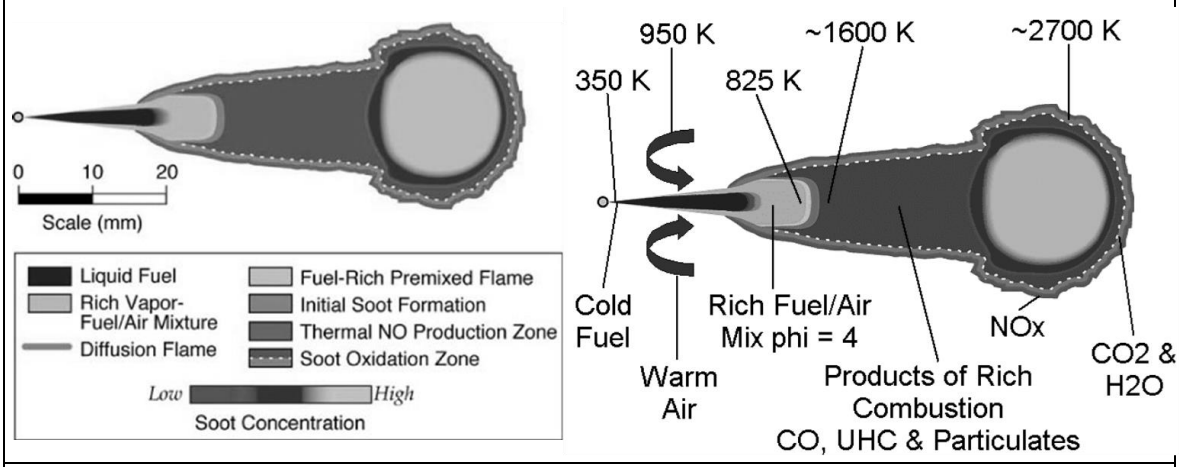

Σχήμα 1.2: Μοντέλο καύσης για κινητήρες Diesel σύμφωνα με τον Dec [15].

Η διαδικασία της καύσης στους κινητήρες Diesel, διαιρείται σε τέσσερα στάδια: την καθυστέρηση ανάφλεξης, την προαναμεμειγμένη καύση, την καύση διάχυσης και την τελική φάση της καύσης ελεγχόμενη από τις χημικές αντιδράσεις [8,13,14]. Ενδεικτικά, στο Σχ. 1.3, απεικονίζεται το διάγραμμα ρυθμού έκλυσης θερμότητας (*HRR*) και οι διάφορες φάσεις της καύσης, μαζί με το δυναμοδεικτικό διάγραμμα και τη μέση θερμοκρασία του κυλίνδρου κατά την καύση για τον κινητήρα ενός επιβατικού οχήματος:

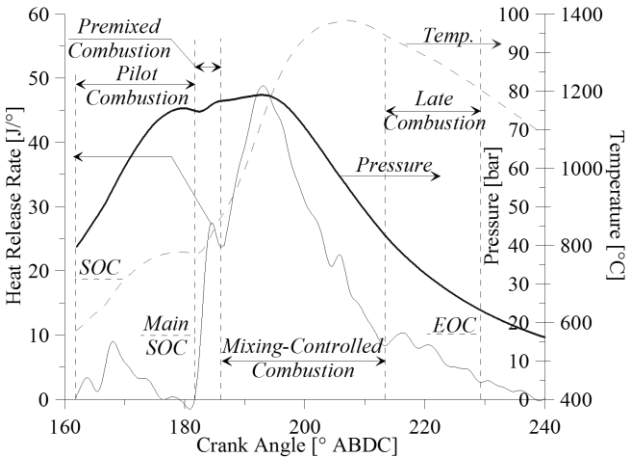

Σχήμα 1.3: Διάγραμμα HRR και οι φάσεις της καύσης μαζί με το δυναμοδεικτικό διάγραμμα και το διάγραμμα μέσης θερμοκρασίας για κινητήρα Diesel επιβατικού οχήματος.

Οι πιο σημαντικοί ρύποι που σχηματίζονται στους κινητήρες Diesel είναι τα NO_x και η αιθάλη [8,14,18]. Στην παρούσα εργασία εξετάζονται μόνο οι εκπομπές NO_x. Τα NO_x είναι χημικές ενώσεις του αζώτου (N) και του οξυγόνου (O). Ωστόσο, οι πιο σημαντικοί τύποι NO_x που σχηματίζονται στο θάλαμο καύσης είναι το μονοξείδιο του αζώτου (NO), το νιτρώδες οξείδιο (N_2O) και το διοξείδιο του αζώτου (NO_2).

Το μονοξείδιο του αζώτου (*NO*) αποτελεί το μεγαλύτερο ποσοστό των NO_x, συνήθως περισσότερο του *90%*. Ωστόσο, για τη λειτουργία του κινητήρα σε πολύ χαμηλά φορτία, όπου υπάρχει μεγάλη διαθεσιμότητα αέρα, ο σχηματισμός των NO_2 μπορεί να φτάσει μέχρι *10 – 30%* [8]. Ωστόσο, στα μεσαία και υψηλά φορτία και κατά την μεταβατική λειτουργία, οι ποσότητες N_2O, NO_2 και άλλων NO_x πλην των *NO*, είναι αμελητέες [8,23,24,25].

Ο σχηματισμός των NO_x στον θάλαμο καύσης των κινητήρων Diesel χαρακτηρίζεται από υψηλή πολυπλοκότητα. Ωστόσο, διάφοροι απλοί μηχανισμοί έχουν προταθεί για την μοντελοποίησή του. Οι πιο ευρέως αναγνωριζόμενοι και χρησιμοποιούμενοι μηχανισμοί είναι οι ακόλουθοι:

1. Σχηματισμός θερμικών NO_x.
2. Σχηματισμός NO_x από τα ενδιάμεσα N_2O.
3. Σχηματισμός άμεσων NO_x.
4. Σχηματισμός NO_x από το καύσιμο.

Ο κυρίαρχος από αυτούς τους μηχανισμούς είναι αυτός των θερμικών NO_x. Οι άλλοι μηχανισμοί έχουν μικρότερη συνεισφορά. Τα θερμικά NO_x σχηματίζονται στο μέτωπο της φλόγας αλλά και στα πολύ θερμά καυσαέρια που προκύπτουν μετά την καύση [8,27]. Ο μηχανισμός αυτός, καθορίζεται από χημικές αντιδράσεις, ισχυρά εξαρτώμενες από τη θερμοκρασία. Καλείται μηχανισμός Extended Zeldovich και περιγράφεται από τις Εξ. (1.1) – (1.3):

$$O + N_2 \leftrightarrow NO + N \tag{1.1}$$

$$N + O_2 \leftrightarrow NO + O \tag{1.2}$$

$$N + OH \leftrightarrow NO + H \tag{1.3}$$

Ο μηχανισμός αυτός ελέγχεται από χημική κινητική και εξαρτάται σημαντικά από τις τοπικές συγκεντρώσεις N_2 και ειδικότερα O_2, την τοπική θερμοκρασία και τον χρόνο παραμονής σε υψηλές θερμοκρασίες, δηλ. άνω των *1800 K* όπου είναι εντονότερος ο σχηματισμός NO_x. Όταν οι θερμοκρασίες στον κύλινδρο αρχίζουν να πέφτουν, π.χ. κατά τη φάση της εκτόνωσης, ο σχηματισμός των NO_x μειώνεται και έτσι η συγκέντρωσή τους στον κύλινδρο «παγώνει».

Δυσμενείς Συνέπειες από τις Εκπομπές NO_x

Στη συνέχεια παρουσιάζονται οι δυσμενείς συνέπειες από τη ρύπανση λόγω των NO_x στην ανθρώπινη υγεία και το περιβάλλον [40,41]. Αυτές οι συνέπειες ώθησαν τις κυβερνήσεις παγκοσμίως να αυστηροποιήσουν τα όρια εκπομπών ρύπων από τους κινητήρες. Οι σημαντικότερες από τις συνέπειες αυτές παρατίθενται πιο κάτω [43,44,45]:

1. Μείωση της λειτουργίας των πνευμόνων με αποτέλεσμα τη δυσκολία στην αναπνοή και άλλα συμπτώματα.
2. Συμπτώματα στο αναπνευστικό σύστημα, όπως βρογχίτιδα, επιδεινούμενος βήχας και πόνοι στο στήθος.

3. Αυξημένης συχνότητας και σοβαρότητας περιστατικά του αναπνευστικού συστήματος, όπως επιδείνωση άσθματος και ευαισθησία στις αναπνευστικές λοιμώξεις, που έχουν ως αποτέλεσμα αυξημένες εισαγωγές στα νοσοκομεία και τις πρώτες βοήθειες.
4. Χρόνιες φλεγμονές και μη ανατρέψιμες δομικές αλλαγές στους πνεύμονες, όπου η επαναλαμβανόμενη έκθεση, μπορεί να οδηγήσει σε πρόωρη γήρανσή τους καθώς και άλλες πνευμονολογικές ασθένειες όπως οίδημα στους πνεύμονες και πνευμονικό εμφύσημα.
5. Ερεθισμός του αναπνευστικού συστήματος, των ματιών και του δέρματος, πονοκέφαλοι, απώλεια όρεξης, διάβρωση των δοντιών, ναυτία, σοβαρή καθυστέρηση ανάπτυξης των παιδιών, ακόμα και καρκίνο.
6. Αύξηση της οξύτητας του επιφανειακού νερού και συνεπώς μείωση της βιοποικιλότητας και εξόντωση των ψαριών.
7. Καταστροφή των δασών μέσω των άμεσης επίδρασης στα των φυτών και της αύξησης της οξύτητας του εδάφους.
8. Καταστροφή των δασικών οικοσυστημάτων, δέντρων, καλλωπιστικών φυτών και των καλλιεργειών λόγω του σχηματισμού τοξικού νέφους.
9. Συνεισφορά στον παράκτιο ευτροφισμό, σκοτώνοντας ψάρια και οστρακοειδή.
10. Συνεισφορά στη μειωμένη ορατότητα (περιφερειακή ομίχλη) και ειδικά σε πολυσύχναστες πόλεις με μεγάλη κυκλοφορία, όπου η ατμόσφαιρα γίνεται αποπνικτική.
11. Επιτάχυνση της φθοράς των μνημείων, κτιρίων, και άλλων πέτρινων και μεταλλικών κατασκευών.

Όρια για τις εκπομπές NO_x

Ακολουθεί η παρουσίαση των ορίων για τις εκπομπές NO_x που έχουν υιοθετηθεί από πολλά κράτη. Επίσης παρουσιάζεται το ποσοστό μείωσής τους από τα προηγούμενα στα σημερινά ή από τα σημερινά στα μελλοντικά όρια.

Για τους κινητήρες που είναι εγκατεστημένοι σε σκάφη, ισχύος άνω των *130 kW*, ο International Maritime Organization (*IMO*) έχει θέσει αυστηρά όρια για τις εκπομπές NO_x (*regulation 13, Annex VI*), τα οποία παρουσιάζονται στον Πίνακα 1.1 [46,47]:

Σειρά	Ημ/νία κατασκευής του πλοίου, πριν ή μετά την	Όρια για τις συνολικές εκπομπές από τον σταθμισμένο κύκλο [g/kWh] n: ονομαστική ταχύτητα του κινητήρα [rpm]		
		$n < 130$	$130 \leq n \leq 1999$	$n \geq 2000$
I	1 Ιανουαρίου 2000	17.0	$45 \cdot n^{-0.2}$	9.8
II	1 Ιανουαρίου 2011	14.4	$44 \cdot n^{-0.23}$	7.7
III	1 Ιανουαρίου 2016*	3.4	$9 \cdot n^{-0.2}$	2.2
Μείωση από σειρά II σε III [%]		76	~80	71

* Θέμα για τεχνική επισκόπηση, αυτή η ημ/νία μπορεί να καθυστερήσει, κανον. 13.10.

Πίνακας 1.1: Σειρά I, II and III: όρια NO_x για μηχανές σκαφών ισχύος άνω των 130 kW.

Τα όρια για τις εκπομπές NO_x που έχει θέσει η ευρωπαϊκή ένωση (*EU*) για διάφορους κινητήρες Diesel, που αντιστοιχούν στις πιο πρόσφατες οδηγίες (*EURO IV–VI, Stage II–IV* (2002/80/EC, 715/2007, 2005/55/EC, 595/2009, 2002/88/EC, 2010/26/EU, 2010/22/EU), κ.λπ.) [48], παρουσιάζονται στον Πίνακα 1.2 [49].

Τύπος Κινητήρα	EURO IV	EURO V	EURO VI	Μείωση ορίων από EURO IV σε VI
	2005	2009	2014	
	NO_x [g/km]	NO_x [g/km]	NO_x [g/km]	[%]
Επιβατικά οχήματα Diesel	0.25	0.18	0.08	68
Ελαφρά εμπορικά οχήματα Diesel (<1305 kg)	0.25	0.18	0.08	68
Ελαφρά εμπορικά οχήματα Diesel (1305–1760 kg)	0.33	0.235	0.105	68
Ελαφρά εμπορικά οχήματα Diesel (1760–3500 kg)	0.39	0.28	0.125	68
Ελαφρά εμπορικά οχήματα Diesel (3.5–12 tonnes)	-	0.28	0.125	-
	2005	2008	2013	
	NO_x [g/kWh]	NO_x [g/kWh]	NO_x [g/kWh]	[%]
Βαρέος τύπου κινητήρες Diesel	3.5	2.0	0.4	89
	Stage II	Stage III B	Stage IV	Μείωση ορίων από Stage II σε IV
	2001/2/3/4	2011/12/13	2014	
	NOx [g/kWh]	NOx [g/kWh]	NOx [g/kWh]	[%]
Μη οδικοί κινητήρες Diesel ($130 \leq P \leq 560$)	6	2.0	0.4	93
Μη οδικοί κινητήρες Diesel ($75 \leq P < 130$)	6	3.3	0.4	93
Μη οδικοί κινητήρες Diesel ($37 \leq P < 75$)	7	3.3	0.4	94
Μη οδικοί κινητήρες Diesel ($18 \leq P < 37$)	8	4.7(incl. HC)-		-

Πίνακας 1.2: Όρια εκπομπών NO_x κινητήρων Diesel στην Ευρωπαϊκή Ένωση.

Στη συνέχεια παρουσιάζονται στον Πίνακα 1.3 τα τρέχοντα/μελλοντικά και τα προηγούμενα όρια τα οποία έχουν οριστεί από το Environmental Protection Agency (*EPA*) των Ηνωμένων Πολιτειών [50].

Τύπος Κινητήρα	Προηγούμενα	Τρέχοντα και μελλοντικά		Ποσοστό μείωσης
	NO_x [g/kWh]	Year	NO_x [g/kWh]	[%]
Οδικοί, βαρέος τύπου κινητήρες Diesel και κινητήρες αστικών λεωφορείων	2.98	2007+	0.15	95
Μη οδικοί κινητήρες Diesel: P≥560kW	9.20	2015+	3.50	62
Μη οδικοί κινητήρες Diesel: P<560kW	9.20	2015+	0.40	96
Μη οδικοί κινητήρες Diesel: P≥560kW (για ηλεκτροπαραγωγά ζεύγη)	9.20	2011+	0.67	93
Κινητήρες τρένων (Line haul)	4.10	2015+	0.97	76
Κινητήρες τρένων (Switch)	3.73	2015+	0.97	74

Πίνακας 1.3: Προηγούμενα και τρέχοντα/μελλοντικά όρια εκπομπών NO_x για κινητήρες Diesel στις Ηνωμένες Πολιτείες.

Από τους πιο πάνω πίνακες, φαίνεται καθαρά το μεγάλο ποσοστό της μείωσης των ορίων για τις εκπομπές NO_x που φθάνει μέχρι και *96%*. Οι περισσότερες ανεπτυγμένες χώρες έχουν ενσωματώσει τα όρια αυτά στις αντίστοιχες νομοθεσίες τους ή έχουν ορίσει παρόμοιους κανονισμούς.

Τεχνικές Λύσεις για την μείωση των NO_x

Για την επίτευξη αυτών των ορίων έχουν προταθεί πολλές τεχνολογίες οι οποίες ήδη εφαρμόζονται ή είναι σε κάποιο στάδιο ανάπτυξης. Οι τεχνολογίες αυτές χωρίζονται στις πρωτογενείς και τις δευτερογενείς. Οι δευτερογενείς τεχνολογίες είναι αυτές που περιορίζουν τα NO_x των καυσαερίων, μετά την εξαγωγή του κυλίνδρου. Οι πιο γνωστές είναι η selective catalytic reduction (*SCR*) και η lean NO_x trap (*LNT*). Οι πρωτογενείς τεχνολογίες/μέθοδοι σκοπεύουν στον έλεγχο των NO_x μέσα στο θάλαμο καύσης, δηλαδή ελέγχοντας το σχηματισμό τους. Οι πιο σημαντικές από αυτές τις τεχνολογίες/μεθόδους είναι: Τροποποίηση της στρατηγικής έγχυσης του καυσίμου, τροποποίηση του χρονισμού και ανύψωσης των βαλβίδων, βελτιστοποίηση του σχεδιασμού των ακόλουθων: εγχυτήρων, βαλβίδων και του θαλάμου καύσης, ανακυκλοφορία καυσαερίων (*EGR*), άμεση έγχυση νερού (*DWI*) στο θάλαμο καύσης, εσωτερικό *EGR* – υδρόψυκτο κατάλοιπο καυσαερίου (WaCoReG), ύγρανση του αέρα σάρωσης, ανάμειξη νερού/καυσίμου, υιοθέτηση του σεναρίου υπερπλήρωσης Miller και μείωση της θερμοκρασίας του αέρα σάρωσης (π.χ. με χρήση υπερπλήρωσης με ενδιάμεση ψύξη).

Οι πρωτογενείς μέθοδοι, στις περιπτώσεις που μπορούν να εφαρμοστούν, υπερτερούν των δευτερογενών, παρόλο που αυτές μπορούν να επιτύχουν μεγαλύτερα ποσοστά

μείωσης, γιατί δεν παρουσιάζουν το μειονέκτημα του υψηλού κόστους εγκατάστασης και λειτουργίας, του μεγάλου βάρους και του απαιτούμενου χώρου. Ωστόσο, η εφαρμογή τους απαιτεί εκτεταμένη πειραματική και υπολογιστική έρευνα.

Λαμβάνοντας τα πιο πάνω υπόψη, οι εταιρίες που κατασκευάζουν ή χρησιμοποιούν κινητήρες Diesel, αναζητούν αποδοτικές μεθόδους για τον έλεγχο των εκπομπών NO_x ώστε να μπορέσουν να συμμορφωθούν με τους αυστηρούς κανονισμούς, αλλά χωρίς την επιδείνωση των επιδόσεων του κινητήρα, προκειμένου να διατηρήσουν την θέση τους στις αγορές, να αυξήσουν την ανταγωνιστικότητά τους και να αποφύγουν πρόστιμα, κυρώσεις και περιορισμούς.

Υπάρχουν πολλές λύσεις για να επιτευχθεί ένα ικανοποιητικό ισοζύγιο επιδόσεων/απόδοσης του κινητήρα και εκπεμπόμενων ρύπων, διατηρώντας τους ρύπους από τα καυσαέρια εντός των νομοθετικών ορίων. Αυτές οι λύσεις μπορεί να περιλαμβάνουν πρωτογενή ή δευτερογενή μέτρα ή ένα συνδυασμό και των δύο. Ωστόσο, η ανάπτυξη, η εξέλιξη και η εφαρμογή τους απαιτούν εκτεταμένη έρευνα. Παρόλα αυτά, οι πειραματικές μεθόδοι έρευνας είναι σε πολλές περιπτώσεις και ειδικά στους κινητήρες μεγάλης κλίμακας (λόγω του μεγέθους τους), πολύ δαπανηρές και χρονοβόρες. Συνεπώς, μπορούν να αξιοποιηθούν μοντέλα προσομοίωσης για να ενισχύσουν αυτή την έρευνα, παρέχοντας ταχύτατες και αξιόπιστες προβλέψεις με χαμηλό κόστος για διάφορες συνθήκες λειτουργίας του κινητήρα. Έτσι, μοντέλα προσομοίωσης μπορούν να χρησιμοποιηθούν σε αυτό το πεδίο έρευνας, στην ανάπτυξη και σχεδιασμό πειραμάτων (*DOE*), φυσική ερμηνεία και άμεση εποπτεία των διεργασιών που διαδραματίζονται μέσα στον κύλινδρο, βελτιστοποίηση του σχεδιασμού σχετικών μηχανικών μερών του κινητήρα και των λειτουργικών του χαρακτηριστικών. Επιπλέον, μπορούν να χρησιμοποιηθούν στον έλεγχο πραγματικού χρόνου και κλειστού βρόχου καθώς επίσης και στη βελτιστοποίηση της λειτουργίας των πρωτογενών και δευτερογενών τεχνολογιών/μεθόδων για τον περιορισμό των εκπομπών ρύπων, παρακολούθηση και επικύρωση/επαλήθευση, σε πραγματικό χρόνο (π.χ. εν–πλω), της απόδοσης και των εκπομπών του κινητήρα, συμπλήρωση πιστοποιητικών για τις εκπομπές ρύπων σύμφωνα με τη νομοθεσία, κ.λπ.

Ο Ρόλος των Μοντέλων Προσομοίωσης στην Προσπάθεια περιορισμού των Εκπομπών NO_x

Πολλά μοντέλα προσομοίωσης έχουν προταθεί, τα οποία διαπραγματεύονται τις φυσικές και θερμοχημικές διεργασίες που λαμβάνουν χώρα μέσα στον κύλινδρο του κινητήρα. Αυτά τα μοντέλα διακρίνονται σε δύο κύριες κατηγορίες: τα μηδενδιάστατα και πολυδιάστατα. Τα μηδενδιάστατα μοντέλα χωρίζονται περαιτέρω σε καθαρά εμπειρικά, φαινομενολογικά και θερμοδυναμικά. Ο συνδυασμός αυτών αντιστοιχεί στα ημιεμπειρικά μοντέλα. Τα προηγούμενα μοντέλα μπορούν να διακριθούν σε μονοζωνικά (ομοιογενής γόμωση), διζωνικά (καμένη και άκαυτη ζώνη) και πολυζωνικά (περαιτέρω διακριτοποίηση της γόμωσης). Τα πολυδιάστατα μοντέλα, συνήθως αντιστοιχούν σε μοντέλα υπολογιστικής ρευστοδυναμικής (*CFD*) και σε τρισδιάστατα (*3D*) φαινομενολογικά μοντέλα δέσμης.

Τα πιο επιτυχημένα από αυτά τα μοντέλα είναι τα πολυζωνικά, *3D*, φαινομενολογικά μοντέλα δέσμης και τα αντίστοιχα *CFD* συνδυασμένα με λεπτομερή σχήματα χημικής κινητικής. Αυτά τα μοντέλα επιχειρούν να προσομοιώσουν τις πραγματικές διαδικασίες

που λαμβάνουν χώρα στο εσωτερικό του κυλίνδρου παρέχοντας λεπτομερείς πληροφορίες για τις συνθήκες μέσα στον κύλινδρο χωρικά και χρονικά. Παρά τα αξιόπιστα αποτελέσματα που μπορούν να εξαγάγουν, και οι δύο τύποι μοντέλων και ειδικά τα *CFD* έχουν σημαντικά αυξημένο υπολογιστικό κόστος που εξακολουθεί να είναι σημαντικό μειονέκτημα σε εφαρμογές έρευνας αλλά και σε πρακτικές εφαρμογές. Επιπλέον, έχουν σχετικά υψηλή πολυπλοκότητα, ευαισθησία στις αρχικές ή συνοριακές συνθήκες και απαιτείται σημαντική προσπάθεια για τη βαθμονόμησή τους. Όλα αυτά περιορίζουν τη δυνατότητα χρήσης τους σε εφαρμογές πραγματικού χρόνου ή άλλες πρακτικές εφαρμογές. Επίσης, αυτοί οι δύο τύποι μοντέλων χρειάζονται ακριβή προφίλ εγχύσεως για την εξαγωγή αντιπροσωπευτικών αποτελεσμάτων [95]. Αντίθετα, τα μηδενδιάστατα, μονοζωνικά μοντέλα [101,102,103,104] δεν παρουσιάζουν τέτοιο υπολογιστικό κόστος και πολυπλοκότητα, αλλά λόγω της μονοζωνικής τους δομής παρέχουν μόνο τις μέσες συνθήκες του θαλάμου καύσης. Με αυτό τον τρόπο, η ανομοιογένεια της γόμωσης και συνεπώς η διάκριση σε περιοχές υψηλών θερμοκρασιών, που καθορίζουν τον τοπικό σχηματισμό των NO_x, δεν μπορούν να ληφθούν υπόψη. Για να αντισταθμιστεί αυτή η αδυναμία, σε αυτά τα μοντέλα εισάγονται εμπειρικές σχέσεις, προκειμένου να μπορέσουν να παρέχουν επαρκή αποτελέσματα. Για να ξεπεραστεί το θέμα της ομοιογένειας, πρέπει να χρησιμοποιηθούν μηδενδιάστατα, διζωνικά [105,106,107] ή πολυζωνικά μοντέλα [108] – [117]. Εναλλακτικά, πλήρως εμπειρικά [118,119,120] ή ημιεμπειρικά μοντέλα [121] – [126] μπορούν να χρησιμοποιηθούν λόγω της απλής τους δομής και του χαμηλού τους υπολογιστικού κόστους. Εντούτοις, αυτά τα στατιστικά μοντέλα, απαιτούν εκτεταμένη βάση πειραματικών δεδομένων για την ορθή βαθμονόμησή τους, αλλά ακόμα και έτσι, βρίσκουν δυσκολίες στο να κάνουν προβλέψεις έξω από το εύρος στο οποίο βαθμονομήθηκαν, λόγω έλλειψης φυσικού υπόβαθρου.

Προκειμένου να ενισχυθεί η προγνωστική ικανότητα των μοντέλων προσομοίωσης, συνιστάται η εισαγωγή, ως δεδομένα εισόδου, πραγματικών χαρακτηριστικών των διεργασιών που λαμβάνουν χώρα στο εσωτερικό του κυλίνδρου. Έτσι, πολλοί ερευνητές έχουν υιοθετήσει τη χρήση του μετρημένου δυναμοδεικτικού διαγράμματος, στο οποίο αντανακλώνται άμεσα ή έμμεσα οι διαδικασίες στο εσωτερικό του κυλίνδρου που οδηγούν ή συμβάλλουν στο σχηματισμό NO_x. Ως εκ τούτου, η χρήση του δυναμοδεικτικού διαγράμματος σε πειραματικές και πραγματικού χρόνου εφαρμογές προσθέτει στα μοντέλα αυτά τη δυνατότητα να συλλάβουν, αναφορικά με τη φυσική του προβλήματος, τις διάφορες μεταβολές στο εσωτερικό του κυλίνδρου σε διάφορα σημεία λειτουργίας και για διαφορετικούς τύπους κινητήρων. Επίσης, οι εν–πλω/πραγματικού χρόνου μετρήσεις της πίεσης του κυλίνδρου είναι πλέον συνήθης πρακτική για τους κινητήρες μεγάλης κλίμακας για ανίχνευση βλαβών και γενικά για διάγνωση. Ακόμα, καθώς το κόστος των αισθητήρων πίεσης πέφτει, θα είναι επίσης δυνατή η χρησιμοποίησή τους στον τομέα της αυτοκινητοβιομηχανίας, όπως σε εφαρμογές πραγματικού χρόνου [127] – [133]. Ωστόσο, ακόμα και αν η άμεση μέτρηση της πίεσης δεν είναι δυνατή, μπορεί να χρησιμοποιηθεί εναλλακτικά, δυναμοδεικτικό διάγραμμα που να έχει προκύψει από ένα απλό, γρήγορο, μονοζωνικό μοντέλο που είναι επαρκώς επικυρωμένο.

Κίνητρο και Στόχος της Διατριβής

Λαμβάνοντας υπόψη τη ζήτηση της βιομηχανίας για τις τεχνολογίες ελέγχου των εκπομπών ρύπων και στοχεύοντας στη συμμόρφωση με τη νομοθεσία για τον περιορισμό τους, διερευνώντας τις διαθέσιμες τεχνολογίες για τον έλεγχό τους, μελετώντας την υπάρχουσα βιβλιογραφία και τα διάφορα προγράμματα για τον έλεγχο και τη βελτίωση των εν λόγω τεχνολογιών με τη χρήση μοντέλων προσομοίωσης, λαμβάνοντας υπόψη τη δυνατότητα διαθεσιμότητας του δυναμοδεικτικού διαγράμματος και το γεγονός ότι τα NO_x είναι από τους σημαντικότερους ελεγχόμενους ρύπους των κινητήρων Diesel, ο συγγραφέας της παρούσας διατριβής, αποφάσισε να αναπτύξει ένα απλοποιημένο, ημιεμπειρικό, πολυζωνικό, θερμοδυναμικό μοντέλο για την εκτίμηση των εκπομπών NO_x και του ιστορικού του σχηματισμού τους σε κινητήρες Diesel, με χρήση του μετρημένου δυναμοδεικτικού διαγράμματος. Προκειμένου να αξιολογηθεί αυτό το μοντέλο, χρησιμοποιήθηκε ένα ευρύ φάσμα συνθηκών λειτουργίας και ρυθμίσεων του κινητήρα, για διαφορετικούς τύπους κινητήρων.

Συνεπώς, ο στόχος της παρούσας διατριβής είναι η ανάπτυξη και αξιολόγηση μοντέλου προσομοίωσης για την πρόβλεψη του NO_x που εκπέμπεται από τους κινητήρες Diesel, στοχεύοντας στα ακόλουθα:

1. Μείωση του κόστους έρευνας, σχεδιασμού και των πειραμάτων.
2. Συνεισφορά στην κατανόηση/επίβλεψη του σχηματισμού των *NO* κατά τη διάρκεια του κύκλου λειτουργίας του κινητήρα και συνεπώς στον αποδοτικό περιορισμό του.
3. Εκτίμηση των εκπομπών NO_x, για διάφορους τύπους κινητήρων, καθώς οι παράμετροι/ρυθμίσεις του κινητήρα τροποποιούνται.
4. Παρακολούθηση/επικύρωση σε πραγματικό χρόνο των εκπομπών NO_x.

Τα βασικά χαρακτηριστικά του προτεινόμενου μοντέλου είναι τα ακόλουθα:

1. Απλή δομή και σενάριο.
2. Χαμηλές υπολογιστικές απαιτήσεις, γρήγορη εξαγωγή αποτελεσμάτων.
3. Ισχυρό φυσικό υπόβαθρο.
4. Αξιοποίηση του μετρημένου δυναμοδεικτικού διαγράμματος.
5. Συνδυασμός με εμπειρικές/στατιστικές προσθήκες για βέλτιστα αποτελέσματα.
6. Ευρύ φάσμα εφαρμογής με χαμηλό κόπο βαθμονόμησης.
7. Ευελιξία στην εφαρμογή.

Κεφάλαιο 2 ΕΠΙΣΚΟΠΗΣΗ ΒΙΒΛΙΟΓΡΑΦΙΑΣ – ΔΙΑΘΕΣΙΜΑ ΜΟΝΤΕΛΑ ΠΡΟΒΛΕΨΗΣ NO_X

Στο δεύτερο κεφάλαιο παρουσιάζεται εκτενής ανασκόπηση της διεθνούς βιβλιογραφίας σχετικά με τα μοντέλα προσομοίωσης που χρησιμοποιούνται για την πρόβλεψη των εκπομπών NO_x. Τα μοντέλα αυτά κατηγοριοποιούνται εδώ, στις ακόλουθες τρεις κατηγορίες ανάλογα με την πολυπλοκότητα, την αξιοπιστία και το υπολογιστικό τους κόστος:

1. Πολυζωνικά, τρισδιάστατα (*3D*) φαινομενολογικά.
2. Μονοζωνικά, καθαρά εμπειρικά και ημιεμπειρικά.
3. Μηδενδιάστατα, ημιεμπειρικά/φαινομενολογικά, πολυζωνικά, θερμοδυναμικά.

Έμφαση δόθηκε στην τελευταία κατηγορία, στην οποία εμπίπτει το προτεινόμενο μοντέλο.

Πολυζωνικά, Τρισδιάστατα (*3D*) Φαινομενολογικά Μοντέλα

Η βασική διαφορά της πρώτης κατηγορίας με τις άλλες δύο είναι η γεωμετρική/χωρική (*3D*) θεώρηση της δέσμης καυσίμου και της φλόγας. Αυτά τα μοντέλα έχουν το πλεονέκτημα της προσέγγισης της φυσικής της εξέλιξης του ψεκασμού και της φλόγας στο εσωτερικό του θαλάμου καύσης με τρόπο που είναι κοντά στην πραγματικότητα. Έτσι, μετά από βαθμονόμηση, μπορούν να παρέχουν χρήσιμες πληροφορίες για τις διεργασίες εντός του κυλίνδρου, που μπορούν να χρησιμοποιηθεί για τη βελτιστοποίηση της απόδοσης του κινητήρα και των εκπομπών ρύπων. Ωστόσο, τα μοντέλα αυτά έχουν σχετικά υψηλό υπολογιστικό κόστος και αυξημένη πολυπλοκότητα, αλλά είναι σημαντικά ταχύτερα από τα αντίστοιχα *CFD*. Επίσης είναι πιο ευέλικτα, όταν χρησιμοποιούνται σε συνδυασμό με άλλα μοντέλα, π.χ. μοντέλα υπερπλήρωσης κ.λπ., για παράδειγμα, σε διερευνήσεις βελτιστοποίησης που χρησιμοποιούν πειράματα με μοντέλα προσομοίωσης (*DOE*).

Τα μοντέλα αυτά, κάνουν χρήση του ρυθμού έγχυσης καυσίμου για να προσομοιώσουν τη δέσμη καυσίμου στο εσωτερικό του θαλάμου καύσης. Το εγχεόμενο καύσιμο χωρίζεται σε πολλαπλούς διακριτούς όγκους, που ονομάζονται ζώνες. Οι ζώνες αυτές εξελίσσονται στο χώρο και το χρόνο, σύμφωνα με ένα μοτίβο ψεκασμού (π.χ. *3D* διακριτοποίηση κώνου) και σύμφωνα με την εξέλιξη της δέσμης στο χρόνο. Οι επιβαλλόμενοι γεωμετρικοί περιορισμοί του κυλίνδρου λαμβάνονται, επίσης, υπόψη. Επιπλέον, τα θερμοχημικά χαρακτηριστικά της κάθε ζώνης καθορίζονται μέσω αυτής της πολυζωνικής προσέγγισης που συνοδεύεται από ημιεμπειρικές/φαινομενολογικές συσχετίσεις που περιγράφουν: τα χαρακτηριστικά της δέσμης καθώς εξελίσσεται εντός του κυλίνδρου (μήκος διάσπασης, γωνία και διείσδυση της δέσμης, μέγεθος των σταγονιδίων, ρυθμός ατμοποίησης και ανάμιξης, κ.λπ.), τη ροή αέρα από τις βαλβίδες ή τις θυρίδες, την προετοιμασία του αναφλέξιμου μείγματος, την ανάπτυξη και σβέση της φλόγας διάχυσης, τη ροή της γόμωσης του κυλίνδρου, τις χημικές αντιδράσεις, κ.λπ. Από αυτή την προσέγγιση μπορούν να εκτιμηθούν η απόδοση του κινητήρα (δηλ. κατανάλωση καυσίμου, ισχύς, κ.λπ.) και οι εκπομπές ρύπων (δηλ. NO_x,

SO_x, *CO_x*, *HC*, *PM*, κ.λπ.). Μερικά από αυτά τα μοντέλα μπορούν να βρεθούν σε αυτές τις αναφορές [91,95,134,135,136].

Μονοζωνικά, Εμπειρικά και Ημιεμπειρικά Μοντέλα

Για να αντιμετωπίσουν το υψηλό υπολογιστικό κόστος και την πολυπλοκότητα που παρουσιάζει η προηγούμενη κατηγορία μοντέλων, πολλοί ερευνητές έχουν αναπτύξει πιο απλοϊκά μοντέλα, όπως καθαρά εμπειρικά/στατιστικά και μονοζωνικά εμπειρικά και ημιεμπειρικά. Αυτά τα μοντέλα είναι εξαιρετικά γρήγορα και κατάλληλα για εφαρμογές πραγματικού χρόνου/εν–πλω και εφαρμογές ελέγχου κλειστού βρόχου, όμως, λόγω έλλειψης φυσικού υπόβαθρου, είναι έγκυρα/αξιόπιστα μόνο μέσα στο εύρος βαθμονόμησής τους και για τον συγκεκριμένο τύπο κινητήρα που έχουν σχεδιαστεί. Επίσης απαιτείται εκτεταμένη βαθμονόμηση για να προκύψουν αξιόπιστα αποτελέσματα. Κάποια από αυτά τα μοντέλα μπορούν να βρεθούν σε αυτές τις αναφορές [41,121,122,125,126,148,149,152,150], [151,153,159,160].

Μηδενδιάστατα, Ημιεμπειρικά/Φαινομενολογικά, Πολυζωνικά, Θερμοδυναμικά

Για να αντιμετωπίσουν τα μειονεκτήματα των δύο προαναφερθεισών κατηγοριών μοντέλων, ορισμένοι ερευνητές έχουν κάνει προσπάθειες για την ανάπτυξη ενός τύπου μοντέλου που συνδυάζει τα πλεονεκτήματα και των δύο αυτών κατηγοριών. Αυτός ο τύπος μοντέλου αντιστοιχεί στα μηδενδιάστατα, πολυζωνικά, ημιεμπειρικά/ φαινομενολογικά, θερμοδυναμικά μοντέλα. Αυτά τα μοντέλα χρησιμοποιούν τουλάχιστον δύο ζώνες για την προσομοίωση των διαδικασιών εντός του κυλίνδρου. Ωστόσο, η διακριτοποίηση δεν περιλαμβάνει γεωμετρική, *3D* μοντελοποίηση της δέσμης καυσίμου ή του χώρου στο εσωτερικό του θαλάμου καύσης, αν και λαμβάνει υπόψη τους περιορισμούς που επιβάλλονται από τη γεωμετρία του. Αντί αυτού, το περιεχόμενο του κυλίνδρου διαχωρίζεται σε ζώνες οι οποίες εξελίσσονται καθώς ο χρόνος παρέρχεται, ακολουθώντας φυσικούς ή φαινομενολογικούς νόμους (π.χ. θερμοδυναμική, κ.λπ.). Ο διαχωρισμός σε ζώνες, κάθε μια από τις οποίες καθορίζεται από ένα αντίστοιχο τμήμα του περιεχομένου του κυλίνδρου και των φυσικών και χημικών του ιδιοτήτων, εισάγει το σενάριο της ανομοιογένειας εντός του κυλίνδρου. Για να βελτιωθούν οι προβλέψεις τους, τα μοντέλα αυτά μπορεί επίσης να χρησιμοποιούν το μετρημένο ή εκτιμημένο δυναμοδεικτικό διάγραμμα, ανάλυση του ρυθμού έκλυσης θερμότητας ή/και εμπειρικές/στατιστικές ή ημιεμπειρικές συσχετίσεις. Τα χαρακτηριστικά αυτά, τα καθιστούν ικανά να προβούν σε αξιόπιστες προβλέψεις για ένα ευρύ φάσμα τύπων κινητήρων και σημείων λειτουργίας. Λόγω της απλής δομής τους και της φυσικής τους βάσης, είναι πολύ γρήγορα και αξιόπιστα, και συνεπώς ικανά να χρησιμοποιηθούν στην έρευνα αλλά και σε πρακτικές εφαρμογές. Ορισμένα από αυτά τα μοντέλα περιγράφονται σε αυτές τις αναφορές [106] – [115], [156,20,179].

Εδώ επισημαίνεται ότι ανάμεσα στο νέο σενάριο και τα νέα χαρακτηριστικά του προτεινόμενου μοντέλου, πολλά χαρακτηριστικά από τα υπάρχοντα μοντέλα και καινοτόμες ιδέες από άλλους ερευνητές υιοθετήθηκαν, εξελίχθηκαν και συνδυάστηκαν, έτσι ώστε να συντεθεί ένα αξιόπιστο και γρήγορο μοντέλο για τις εκπομπές *NO_x*.

Κεφάλαιο 3 ΑΝΑΠΤΥΞΗ ΤΟΥ ΠΡΟΤΕΙΝΟΜΕΝΟΥ ΜΟΝΤΕΛΟΥ

Το προτεινόμενο μοντέλο αναπτύχθηκε και επικυρώθηκε μέσα από πολλά στάδια εξέλιξης [188,189,56,190]. Η τελική του μορφή παρουσιάζεται αναλυτικά σε αυτό το κεφάλαιο. Αρχικά περιγράφεται η διαδικασία μέτρησης και επεξεργασίας του δυναμοδεικτικού διαγράμματος. Ακολουθεί ο υπολογισμός των αρχικών συνθηκών που χρησιμοποιούνται στο μοντέλο του ρυθμού έκλυσης θερμότητας και στο μοντέλο NO_x. Στη συνέχεια, περιγράφεται αναλυτικά η μεθοδολογία που ακολουθήθηκε για τον υπολογισμό:

- Του ρυθμού έκλυσης θερμότητας.
- Της μεταφοράς θερμότητας με τα τοιχώματα του κυλίνδρου
- Της αρχής και του τέλους της καύσης.
- Του ρυθμού καύσης.
- Του μοντέλου NO_x το οποίο αναλύεται:
- Στην κύρια ιδέα και το σενάριο που ακολουθήθηκε για τις καμένες και τη άκαυστη ζώνη.
- Στα υπό–μοντέλα που χρησιμοποιήθηκαν στον υπολογισμό των NO_x, δηλαδή αυτό της χημικής διάστασης (για τον υπολογισμό της σύστασης ισορροπίας) και του μηχανισμού Extended Zeldovich (υπολογισμός των θερμικών NO_x, δηλ. NO).
- Στη μεθοδολογία για τη βαθμονόμηση του μοντέλου.

Πλεονεκτήματα από τη Χρήση του Δυναμοδεικτικού Διαγράμματος

Το θεμελιώδες χαρακτηριστικό του προτεινόμενου μοντέλου είναι το ότι κάνει χρήση του μετρημένου δυναμοδεικτικού διαγράμματος. Το δυναμοδεικτικό διάγραμμα είναι ένα ισχυρό εργαλείο για τον μηχανικό, γιατί παρέχει σημαντικές πληροφορίες για τους μηχανισμούς που λαμβάνουν χώρα στο εσωτερικό του κυλίνδρου του κινητήρα. Η πίεση, η θερμοκρασία και η χημική σύσταση της γόμωσης στο εσωτερικό του θαλάμου καύσης, τα οποία οδηγούν το σχηματισμό των NO_x, προσδιορίζονται από αυτούς τους μηχανισμούς οι οποίοι περιλαμβάνουν τη συμπίεση, ανάμειξη καυσίμου–αέρα, καύση, εκτόνωση κ.λπ. [8,14]. Οι παραπάνω μηχανισμοί επηρεάζονται άμεσα από τις αρχικές συνθήκες της γόμωσης, τη γεωμετρία του κινητήρα, τη μεταφορά θερμότητας με τα τοιχώματα του κυλίνδρου, τις διαρροές προς τον στροφαλοθάλαμο, την τύρβη της γόμωσης, το προφίλ και το χρονισμό της έγχυσης καυσίμου κ.λπ. Ως εκ τούτου, η χρήση του μετρημένου δυναμοδεικτικού διαγράμματος προσθέτει στο μοντέλο τη δυνατότητα να λαμβάνει υπόψη τους σημαντικότερους παράγοντες που επηρεάζουν την καύση και συνεπώς τον σχηματισμό των NO_x. Αυτό είναι σημαντικό επειδή οποιαδήποτε μεταβολή αυτών των παραγόντων θα επηρεάσει άμεσα την πίεση μέσα στον κύλινδρο και ως εκ τούτου το αποτέλεσμα της μεταβολής αυτής στα NO_x, μπορεί να συλληφθεί από το μοντέλο.

Επιπλέον, μπορούν να ληφθούν απευθείας από το δυναμοδεικτικό διάγραμμα σημαντικές πληροφορίες όπως η πίεση συμπίεσης, η μέγιστη πίεση καύσης, η γωνία έναρξης της καύσης, κ.λπ. Επίσης, μετά από μαθηματική επεξεργασία, μπορεί να χρησιμοποιηθεί για τον υπολογισμό της ενδεικνυόμενης ισχύος του κινητήρα, της μέσης ενδεικνυόμενης πίεσης και του ρυθμού έκλυσης θερμότητας (*HRR*).

Η μέτρηση του δυναμοδεικτικού διαγράμματος γίνεται με τη χρήση ειδικών αισθητήρων πίεσης (πιεζοηλεκτρικοί αισθητήρες) [191]. Το λαμβανόμενο σήμα ενισχύεται, μετατρέπεται σε ψηφιακό μέσω αναλογοψηφιακού μετατροπέα και το σήμα/τάση αντιστοιχίζεται σε πίεση. Για να αξιοποιηθεί το σήμα αυτό, πρέπει να αντιστοιχιστεί και να συγχρονιστεί με τη γωνία στροφάλου (*CA*). Για να επιτευχθεί αυτό, το σημείο του δυναμοδεικτικού που αντιστοιχεί στο άνω νεκρό σημείο (*TDC*) πρέπει να εντοπιστεί με τη μέγιστη δυνατή ακρίβεια. Αυτό μπορεί να γίνει με χρήση επαγωγικού αισθητήρα τοποθετημένου στον σφόνδυλο του κινητήρα [25] ή εναλλακτικά με χρήση θερμοδυναμικών μεθόδων [196,197]. Επίσης, για να συγχρονιστεί ο χρονισμός της γωνίας στροφάλου (θέση εμβόλου) με τον ρυθμό δειγματοληψίας της πίεσης μπορεί να χρησιμοποιηθεί ειδικό σύστημα που μετράει τη γωνία στροφάλου (*CA* encoder) ταυτόχρονα με την πίεση του κυλίνδρου ή εναλλακτικά μετατρέποντας το πεδίο του χρόνου, στο οποίο γίνεται η μέτρηση της πίεσης, στο πεδίο της γωνίας στροφάλου υποθέτοντας σταθερές στροφές μέσα στον κύκλο. Τέλος, υπάρχουν πολλές μέθοδοι για την πρόσδεση της μετρούμενης πίεσης που σκοπό έχει τον υπολογισμό της απόλυτης πίεσης (π.χ. κάνοντας χρήση της μετρημένης πίεσης σάρωσης), που μπορούν να βρεθούν στη βιβλιογραφία [199].

Στην παρούσα εργασία εξετάστηκε μόνο η λειτουργία κινητήρα σε μόνιμη κατάσταση. Έτσι, για κάθε σημείο λειτουργίας, το τελικό δυναμοδεικτικό διάγραμμα του κάθε κυλίνδρου προκύπτει από τον μέσο όρο των περίπου *20–100* διαδοχικών κύκλων του κινητήρα ανάλογα με την εφαρμογή (υψηλότερος αριθμός για υψηλότερες στροφές) [191,194,200,201] στοχεύοντας στην απομείωση του σφάλματος που οφείλονται σε θόρυβο του σήματος, κυκλική διακύμανση και σφάλματα δειγματοληψίας. Τα τελικά δυναμοδεικτικά διαγράμματα του συνόλου των κυλίνδρων μπορούν να χρησιμοποιηθούν για πιο λεπτομερή ανάλυση. Εναλλακτικά μπορεί να γίνει χρήση του δυναμοδεικτικού διαγράμματος ενός αντιπροσωπευτικού κυλίνδρου ο οποίος χαρακτηρίζεται ως «μέσος κύλινδρος», υποθέτοντας ότι οι άλλοι κύλινδροι έχουν παρόμοια συμπεριφορά.

Σε αυτή τη μελέτη, η προαναφερθείσα διαχείριση του σήματος πίεσης, για τις περιπτώσεις των κινητήρων μεγάλης κλίμακας, επιτεύχθηκε με τη χρήση καλά επικυρωμένου διαγνωστικού εργαλείου που αναπτύχθηκε στο εργαστήριο μηχανών εσωτερικής καύσης του *ΕΜΠ* [209,210,138,132]. Οι μετρήσεις αυτές, ελήφθησαν σε πραγματικό χρόνο ή/και εν–πλω από την ερευνητική ομάδα του εργαστηρίου. Για τις περιπτώσεις που αφορούν στους οδικούς κινητήρες, τα τελικά δυναμοδεικτικά διαγράμματα ελήφθησαν από την *AVL* και το *ETH* κατά τη διάρκεια συνεργασίας υπό ευρωπαϊκό πρόγραμμα. Αυτές οι μετρήσεις ελήφθησαν υπό ελεγχόμενες εργαστηριακές συνθήκες και η προεπεξεργασία τους έγινε από τον πάροχο.

Στη συνέχεια, αναλόγως της κατάστασης του δυναμοδεικτικού διαγράμματος και της παραγώγου του, δηλαδή της έντασης και συχνότητας του περιεχόμενου θορύβου, το δυναμοδεικτικό διάγραμμα πρέπει να φιλτραριστεί. Σε αυτή την εργασία χρησιμοποιήθηκε το χαμηλοπερατό φίλτρο Savitzky–Golay [202].

Η μέθοδος αυτή, χρησιμοποιεί συντελεστές βαρύτητας για τα σημεία μέσα στο παράθυρο του φίλτρου που χρησιμοποιούνται για τον υπολογισμό της εξομαλυμένης τιμής του εξεταζόμενου σημείου. Η χρήση αυτών των συντελεστών (συντελεστές συνέλιξης) είναι ακριβώς ισοδύναμη με την προσαρμογή των δεδομένων με χρήση πολυωνύμου. Επίσης, μπορεί να ληφθεί απευθείας από το αφιλτράριστο δυναμοδεικτικό διάγραμμα το αντίστοιχο διάγραμμα της παραγώγου του εξομαλυμένο. Ο υπολογισμός των συντελεστών αυτού του φίλτρου βασίζεται στην παλινδρόμηση πολυωνύμου με χρήση της μεθόδου των ελαχίστων τετραγώνων. Το πλάτος του παραθύρου φιλτραρίσματος επιλέχθηκε έτσι ώστε να δίνει ικανοποιητικής ποιότητας διαγράμματα παραγώγου της πίεσης και ρυθμού έκλυσης θερμότητας. Ο αλγόριθμος που χρησιμοποιήθηκε στην παρούσα εργασία βασίζεται στις κατευθυντήριες γραμμές της αναφοράς [207].

Δεδομένα Εισόδου

Στη συνέχεια αναφέρονται τα δεδομένα εισόδου και οι προκαταρτικοί υπολογισμοί που απαιτούνται για το προτεινόμενο μοντέλο. Το πιο σημαντικό στοιχείο εισόδου στο μοντέλο *NO* είναι ο ρυθμός καύσης (δηλ. το μέρος του καυσίμου που καίγεται σε κάθε χρονική στιγμή), το οποίο υπολογίζεται χρησιμοποιώντας το δυναμοδεικτικό διάγραμμα, τα ακόλουθα βασικά γεωμετρικά χαρακτηριστικά του κινητήρα όπως:

- τον αριθμό των κυλίνδρων,
- τη διάμετρο του κυλίνδρου,
- τη διαδρομή του εμβόλου,
- το μήκος του διωστήρα,
- την ακτίνα στροφάλου,
- το λόγος συμπίεσης,
- τον τύπο του κινητήρα: δίχρονος ή τετράχρονος,
- τη γωνία στροφάλου στην αρχή της συμπίεσης,
- τη γωνία στροφάλου στο άνοιγμα της βαλβίδας εξαγωγής

και τα ακόλουθα λειτουργικά χαρακτηριστικά του κινητήρα όπως:

- τις στροφές του κινητήρα,
- την παροχή μάζας καυσίμου,
- την παροχή μάζας αέρα εισόδου ή καυσαερίων,
- το ποσοστό ανακυκλοφορίας καυσαερίου (*EGR*),
- τη θερμοκρασία στην πολλαπλή εισαγωγής και
- την πίεση στην πολλαπλή εισαγωγής.

Για να μπορεί το μοντέλο να δώσει ικανοποιητικά αποτελέσματα οι αρχικές συνθήκες πριν την έναρξη της καύσης πρέπει να καθοριστούν με ακρίβεια. Οι συνθήκες αυτές είναι η παγιδευμένη μάζα στον κύλινδρο και η χημική της σύσταση.

Όσον αφορά στο καύσιμο, η κατώτερη θερμογόνος δύναμη (*LHV*) και η χημική του σύσταση κατά μάζα (άνθρακας *C*, υδρογόνο *H*, θείο *S*, οξυγόνο *O* και άζωτο *N*), χρησιμοποιούνται εμμέσως στους υπολογισμούς των αρχικών συνθηκών αλλά και αργότερα στους βασικούς υπολογισμούς των μοντέλων του *HRR* και *NO*.

Όσον αφορά στις μεγάλης κλίμακας μηχανές, η παροχή καυσίμου υπολογίστηκε με επικυρωμένο [208] διαγνωστικό σύστημα (που αναπτύχθηκε στο εργαστήριο μηχανών εσωτερικής καύσης του *ΕΜΠ*) [209,210,138,132] και χρησιμοποιώντας αυτό, τη σύσταση του καυσίμου και τη μετρημένη σύσταση καυσαερίου, υπολογίζεται η παροχή αέρα *[kg/h]* μέσω της μεθόδου ισοζυγίου άνθρακα [46]. Για τους οδικούς κινητήρες που εξετάστηκαν, χρησιμοποιήθηκαν οι τιμές των παροχών που προέκυψαν από εργαστηριακές μετρήσεις (με χρήση ογκομετρικού παροχόμετρου).

Ειδικά για τους κινητήρες μεγάλης κλίμακας, όπου μετρήθηκαν τα δυναμοδεικτικά όλων των κυλίνδρων, θα πρέπει να γίνει κατανομή της ροής καυσίμου του κινητήρα σε κάθε κύλινδρο. Αυτό είναι επιτακτική ανάγκη δεδομένου ότι, κάθε κύλινδρος μπορεί να έχει διαφορετική κατανάλωση καυσίμου. Λαμβάνοντας αυτό υπόψη, υιοθετήθηκε η ακόλουθη απλή μεθοδολογία για την κατανομή της συνολικής ροής του καυσίμου στους κυλίνδρους: Υπολογίζεται η σωρευτική καθαρή (χωρίς να λαμβάνονται υπόψη οι απώλειες θερμότητας) έκλυση θερμότητας (*CNHR*) κατά τη διάρκεια του κύκλου για κάθε κύλινδρο χρησιμοποιώντας το αντίστοιχο δυναμοδεικτικό διάγραμμα. Επίσης, από την ανάλυση του ρυθμού έκλυσης θερμότητας εντοπίζεται το τέλος της καύσης (*EOC*) όπως περιγράφεται πιο κάτω. Ακολούθως, οι τιμές των *CNHR* στο *EOC* του κάθε κυλίνδρου προστίθενται προκειμένου να υπολογιστεί η συνολική καθαρή έκλυση θερμότητας που αντιστοιχεί στο εγχεόμενο καύσιμο. Στη συνέχεια, υπολογίζεται ο λόγος μεταξύ του *CNHR* στο *EOC* και του συνολικού για κάθε κύλινδρο. Η αντίστοιχη μάζα καυσίμου που εγχέεται σε κάθε κύλινδρο υπολογίζεται στη συνέχεια από τον πολλαπλασιασμό αυτού του λόγου με το συνολικό εγχεόμενο καύσιμο. Παρόλο που η μεθοδολογία αυτή αγνοεί τις απώλειες θερμότητας από τα τοιχώματα, παρέχει επαρκείς ενδείξεις για τη διανομή του καυσίμου στους κυλίνδρους. Επίσης, η συνολική παροχή αέρα κατανέμεται στους κυλίνδρους με την ίδια μεθοδολογία, δηλ. πολλαπλασιάζοντάς την με τον αντίστοιχο λόγο (σύμφωνα με τον πιο πάνω υπολογισμό) κάθε κυλίνδρου.

Ειδικότερα για τους δίχρονους κινητήρες μεγάλης κλίμακας, οι αρχικές συνθήκες, δηλ. η παγιδευμένη μάζα στον κύλινδρο, η χημική της σύσταση και η θερμοκρασία στην έναρξη της συμπίεσης, δηλαδή στο κλείσιμο της βαλβίδας εξαγωγής (*EVC*) υπολογίζονται με τη χρήση ενός μοντέλου σάρωσης. Η χρήση μοντέλου σάρωσης έγινε, επειδή σε αυτού του τύπου τις μηχανές η διαδικασία απόπλυσης είναι πλημμελής σε σχέση με την αντίστοιχη στους τετράχρονους και συνεπώς το παραμένον καυσαέριο είναι αυξημένο. Αυτό επηρεάζει τη σύσταση και τη θερμοκρασία της γόμωσης και συνεπώς την απόδοση του κινητήρα και τις εκπομπές ρύπων.

Το μοντέλο σάρωσης που χρησιμοποιήθηκε είναι πλήρους ανάμειξης, μη ισοθερμικό και προέρχεται από τις αναφορές [9,146] εισάγοντας κάποιες τροποποιήσεις. Σε αυτό το μοντέλο, η γόμωση θεωρείται ότι συμπεριφέρεται ως ιδανικό αέριο στους υπολογισμούς του μοντέλου. Σε αυτούς τους υπολογισμούς χρησιμοποιούνται, επίσης, ο όγκος και η πίεση του κυλίνδρου σε τρία σημεία: στο κλείσιμο της βαλβίδας εξαγωγής (*EVC*), στο άνοιγμα της βαλβίδας εξαγωγής (*EVO*) και στο τέλος της εκτόνωσης όταν οι θυρίδες εισαγωγής αποκαλύπτονται (*SPO*). Οι πιέσεις προέρχονται από το μετρημένο δυναμοδεικτικό διάγραμμα, ως ο μέσος όρος των τιμών πιέσεων της γειτονικής περιοχής του εκάστοτε εξεταζόμενου σημείου.

Αρχικά υπολογίζεται ο λόγος διανομής αέρα (*Λ*) όπως περιγράφεται στην Εξ. (0.1) [9]:

$$\Lambda = \frac{mass\ of\ fresh\ air\ delivered}{m_0} \tag{0.1}$$

όπου ο "*fresh air mass delivered" [kg/cycle]* αντιστοιχεί στον αέρα περιβάλλοντος που εισέρχεται σε κάθε κύλινδρο και m_0 είναι η μάζα αέρα αναφοράς που υπολογίζεται στη θερμοκρασία και πίεση που επικρατεί στην πολλαπλής εισαγωγής και τον όγκο του κυλίνδρου στο *EVC*.

Ο βαθμός απόδοσης σάρωσης (η_{sc}) του κυλίνδρου υπολογίζεται από την Εξ. (3.2):

$$\frac{mass\ of\ fresh\ air\ in\ the\ cylinder}{total\ cylinder\ mass} = \eta_{sc}^k = 1 - \frac{T_{EVC}^{k-1}}{T_{SPO}^{k-1}} \cdot e^{-\Lambda} \tag{3.2}$$

όπου οι θερμοκρασίες είναι σε *[K]*. Ο η_{sc} αντιστοιχεί στο κλάσμα της παγιδευμένης μάζας που καταλαμβάνεται από αέρα περιβάλλοντος. Ο εκθέτης *k* υποδεικνύει τον αύξοντα αριθμό της επανάληψης. Το υπόλοιπο κλάσμα είναι το παραμένον καυσαέριο (*RG*), του οποίου η σύσταση (x_{exh}, y_{exh}, MW_{exh}) υπολογίζεται θεωρώντας ιδανική καύση χρησιμοποιώντας τον μέσο λόγο ισοδυναμίας του κυλίνδρου και παραλείποντας τα προϊόντα της χημικής διάστασης. Η κλάσμα μάζας του *RG* υπολογίζεται από την Εξ. (3.3):

$$RG^k = 1 - \eta_{sc}^k \tag{3.3}$$

Στη συνέχεια υπολογίζεται η σύσταση και το μοριακό βάρος (*MW*) της γόμωσης σύμφωνα με την Εξ. (3.4):

$$\begin{aligned} y_j^k &= \eta_{sc}^k \cdot y_{air,j} + RG^k \cdot y_{exh,j} \\ x_j^k &= \frac{y_j^k}{MW_j} \cdot \left(\sum_j \frac{y_j^k}{MW_j} \right)^{-1} \\ MW_{ch}^k &= \sum\nolimits_j x_j^k \cdot MW_j \end{aligned} \tag{3.4}$$

όπου *x* και *y* είναι η σύσταση κατά mole και κατά μάζα αντίστοιχα του στοιχείου *j* της γόμωσης (*ch*), οι δείκτες *air* και *exh* υποδεικνύουν τον ατμοσφαιρικό αέρα και τα καυσαέρια αντίστοιχα.

Η νέα θερμοκρασία της παγιδευμένης μάζας στο *EVC* υπολογίζεται από την Εξ. (3.5) [146]:

$$T_{EVC}^k = \frac{T_{sc}}{1 - \left(1 - \frac{T_{sc}}{T_{SPO}^{k-1}}\right) \cdot e^{-\Lambda}} \tag{3.5}$$

όπου οι θερμοκρασίες είναι σε *[K]* και *Tsc* είναι η θερμοκρασία σάρωσης. Η παγιδευμένη μάζα (m_{EVC}^{k} *[kg]*) υπολογίζεται με την Εξ. (3.6):

$$m_{EVC}^{k} = \frac{p_{EVC} \cdot V_{EVC}}{\frac{\bar{R}}{MW_{ch}^{k}} \cdot T_{EVC}^{k}} \tag{3.6}$$

όπου $\bar{R} = 8314$ *[J/kmol/K]*, *p [Pa]* και *V*[m^3] είναι ο όγκος και η πίεση του κυλίνδρου στο *EVC*.

Κατόπιν, η μάζα φορτίου στο *EVO* (m_{EVO}) υπολογίζεται ως το άθροισμα της παγιδευμένης μάζας στο *EVC* και της εγχεόμενης μάζας καυσίμου. Μετά, υπολογίζεται η μάζα στο *SPO* (m_{SPO}) μέσω της Εξ. (3.7) [146]:

$$\begin{gathered} m_{SPO}^{k} = m_{EVO}^{k} \cdot (V_{SPO}/V_{EVO}) \cdot (p_{SPO}/p_{EVO})^{1/\gamma(x_{exh}, T_{SPO}^{k-1})} \\ \gamma = \frac{cp^{k-1}}{cp^{k-1} - R} \end{gathered} \tag{3.7}$$

όπου , *cp [J/kg/K]*, *γ*, *R [J/kg/K]* είναι η ειδική θερμοχωρητικότητα σε σταθερή πίεση, ο ισεντροπικός εκθέτης και η σταθερά του καυσαερίου ($R = \bar{R}/MW_{exh}$) αντιστοίχως. Ο λόγος *cp/R* υπολογίζεται από πολυωνυμικές προσεγγίσεις [180].

Εν τέλει, η καινούρια τιμή της T_{SPO} υπολογίζεται από την Εξ. (3.8):

$$T_{SPO}^{k} = \frac{p_{EOBD} \cdot V_{EOBD}}{\frac{\bar{R}}{MW_{exh}} \cdot m_{EOBD}^{k}} \tag{3.8}$$

Η επαναληπτική διαδικασία συνεχίζεται μέχρι να συγκλίνει σε μια τελική τιμή το *RG*.

Για τους τετράχρονους κινητήρες μεγάλης κλίμακας, η σύσταση της γόμωσης στην έναρξη της συμπίεσης θεωρείται ταυτόσημη με εκείνη του αέρα περιβάλλοντος, επειδή το *RG* είναι σημαντικά χαμηλότερο σε σύγκριση με τους δίχρονους κινητήρες, δεδομένου ότι ο βαθμός απόδοσης σάρωσης είναι σημαντικά υψηλότερος [9]. Η θερμοκρασία στην έναρξη της συμπίεσης (T_{IVC}), δηλαδή όταν η βαλβίδα εισαγωγής κλείνει (*IVC*) υπολογίζεται από την Εξ. (3.9) θεωρώντας ότι αυτή είναι αυξημένη σε σχέση με τη θερμοκρασία σάρωσης (T_{sc}) ανάλογα με το φορτίο του κινητήρα (P/P_N).

$$T_{IVC} = T_{sc} + 30 + 30 \cdot \frac{P}{P_N} \tag{3.9}$$

όπου *P* είναι η ισχύς του κινητήρα και P_N η αντίστοιχη ονομαστική. Αφού υπολογιστεί η T_{IVC}, η παγιδευμένη μάζα κατά την έναρξη της συμπίεσης υπολογίζεται χρησιμοποιώντας τη σύνθεση του ατμοσφαιρικού αέρα, τον όγκο και την πίεση του κυλίνδρου στο *IVC* μέσω της καταστατικής εξίσωσης των τέλειων αερίων.

Όπως έχει ήδη αναφερθεί, τα δεδομένα των μετρήσεων που αφορούν στους οδικούς κινητήρες που εξετάστηκαν λήφθησαν από εργαστηριακές μετρήσεις. Τα στοιχεία που αξιοποιούνται για τον προσδιορισμό των αρχικών συνθηκών για αυτούς τους κινητήρες είναι τα ακόλουθα:

- το δυναμοδεικτικό διάγραμμα του «μέσου» κυλίνδρου (αντιπροσωπευτικού),
- οι στροφές του κινητήρα,
- η παροχή μάζας αέρα,
- η παροχή μάζας καυσίμου,
- η μοριακή αναλογία *H/C* καυσίμου,
- το ποσοστό *EGR*,
- το κλάσμα μάζας *RG*,
- η πίεση στην πολλαπλή εισαγωγής και
- οι συνθήκες περιβάλλοντος.

Οι απαιτούμενες αρχικές συνθήκες είναι η μάζα και η σύσταση της άκαυστης γόμωσης ακριβώς πριν από την έναρξη της καύσης (*SOC*). Η σύσταση της άκαυστης γόμωσης (ζώνης) θεωρείται αμετάβλητη από το *IVC* μέχρι το *SOC*. Η παγιδευμένη μάζα στον κύλινδρο, κατά τη διάρκεια ενός κύκλου, ($m_{tr}[kg] = \dot{m}_{tr}\left[\frac{kg}{cycle}\right] \cdot 1[cycle]$) και η σύστασή του υπολογίζονται χρησιμοποιώντας την παροχή αέρα εισαγωγής ($\dot{m}_{IA}$ *[kg/h]*), τα κλάσματα μάζας *EGR* και *RG* και την κατά μάζα σύσταση του καυσίμου (*H/C*), τα οποία δίνονται ως δεδομένα εισόδου. Ο βαθμός απόδοσης παγίδευσης θεωρείται ίσος με τη μονάδα (ρεαλιστικό για τετράχρονους κινητήρες), η παρεχόμενη μάζα αέρα στην πολλαπλή εισαγωγής ($\dot{m}_{IM}$*[kg/h]*) ισούται με αυτήν που παγιδεύεται, η οποία υπολογίζεται από την Εξ. (3.10) όπου n_{cyl} είναι ο αριθμός των κυλίνδρων και *N* είναι οι στροφές του κινητήρα *[rpm]*:

$$m_{tr} = \frac{\dot{m}_{IA}}{n_{cyl} \cdot N \cdot 30} \cdot \frac{1 + RG}{1 - EGR} \tag{3.10}$$

Η σύσταση των αερίων του *EGR* και *RG* θεωρείται ταυτόσημη με αυτήν των καυσαερίων η οποία προέρχεται από ιδανική καύση με χρήση του μέσου λόγου ισοδυναμίας του κυλίνδρου. Στη συνέχεια, η τελική σύνθεση της γόμωσης υπολογίζεται χρησιμοποιώντας τα κλάσματα μάζας των *EGR, RG* και αέρα του περιβάλλοντος και τη σύστασή τους, όπως περιγράφεται στην Εξ (3.11):

$$FA = \frac{\dot{m}_{IA}}{\dot{m}_{tr}}, \qquad EGR = \frac{\dot{m}_{EGR}}{\dot{m}_{tr}}, \qquad RG = \frac{\dot{m}_{RG}}{\dot{m}_{tr}}$$

$$y_{ch_j} = FA \cdot y_{air,j} + (EGR + RG) \cdot y_{exh,j}$$

$$x_{ch_j} = \frac{y_{ch_j}}{MW_j} \cdot \left(\sum_j \frac{y_{ch_j}}{MW_j} \right)^{-1} \tag{3.11}$$

$$MW_{ch} = \sum_j x_{ch_j} \cdot MW_j$$

όπου *FA* υποδηλώνει το κλάσμα μάζας φρέσκου αέρα, ο δείκτης *ch* αντιστοιχεί στη γόμωση και ο *j* στα χημικά στοιχεία τα οποία είναι το O_2, N_2, CO_2 and H_2O.

Μοντέλο Ρυθμού Έκλυσης Θερμότητας (HRR)

Στη συνέχεια αναλύεται το μοντέλο του ρυθμού έκλυσης θερμότητας (*HRR*). Το *HRR* παρέχει χρήσιμες πληροφορίες σχετικά με την καύση όπως, ο καθορισμός της έναρξης της κύριας καύσης, η ανίχνευση των μικρότερων γεγονότων καύσης που οφείλονται σε πιλοτική έγχυση ή μετέγχυση, διάκριση της προαναμεμειγμένης (αν υπάρχει) από την καύση διάχυσης, παρέχει τη θέση (*CA*) του μέγιστου *HRR* του *SOC, COC* και του *EOC*. Επιπλέον, το *HRR* προσφέρει μια εποπτεία της εξέλιξης της καύσης στο θάλαμο που είναι ουσιαστική για τις διαδικασίες βελτιστοποίησης της καύσης για τη βελτίωση της απόδοσης και τον έλεγχο των εκπομπών του κινητήρα. Το σημαντικότερο όμως είναι η δυνατότητα άμεσου υπολογισμού του ρυθμού καύσης, δηλαδή της ποσότητας του καυσίμου που καίγεται κάθε στιγμή, ο οποίος προκύπτει από τη διαίρεση του *HRR* με την κατώτερη θερμογόνο ικανότητα του καυσίμου (*LHV*). Το προτεινόμενο μοντέλο κάνει χρήση μιας χρονικής διακριτοποίησης του καμένου καυσίμου για τη δημιουργία ζωνών καύσης σε κάθε στιγμή.

Το μοντέλο *HRR* που χρησιμοποιείται εδώ, είναι ένα μονοζωνικό, μηδενδιάστατο θερμοδυναμικό μοντέλο που υπολογίζει το *HRR* με τον πρώτο θερμοδυναμικό νόμο χρησιμοποιώντας το μετρημένο δυναμοδεικτικό διάγραμμα (πειραματικό *HRR*). Λόγω του ότι η ανάλυση του *HRR* έχει νόημα μόνο από την αρχή (*SOC*) έως το τέλος της καύσης (*EOC*), τα σημεία αυτά πρέπει να υπολογιστούν πρώτα. Έτσι η αρχική τιμή του *SOC* υπολογίζεται απευθείας από το δυναμοδεικτικό διάγραμμα όπως θα αναλυθεί στη συνέχεια. Η τελική του τιμή προκύπτει από το διάγραμμα του καθαρού *HRR (NHRR)*. Μετά τον τελικό καθορισμό του *SOC*, το *EOC* υπολογίζεται από το διάγραμμα του καθαρού *HRR* (*NHRR*) όπως επίσης θα αναλυθεί στη συνέχεια.

Το μοριακό βάρος *MW [kg/kmol]* και ο συνολικός αριθμός των mole (*n [kmol]*) της γόμωσης, υπολογίζονται από την Εξ. (3.12) και Εξ. (3.13) αντιστοίχως:

$$MW_{ch,i} = \sum_j x_{j,i} \cdot MW_j \tag{3.12}$$

$$n_{ch,i} = \frac{m_{ch}}{MW_{ch,i}} \tag{3.13}$$

Στις προηγούμενες σχέσεις, *x [kmol/kmol]* είναι το μοριακό κλάσμα του κάθε χημικού στοιχείου που περιέχεται στη γόμωση και *m [kg]* είναι η μάζα της γόμωσης. Πριν το ξεκίνημα της καύσης τα *x* και *m* καθορίζονται από τις αρχικές συνθήκες. Ο δείκτης *ch* υποδεικνύει τη γόμωση, ο *i* το τρέχον βήμα *CA* και ο *j* τον αύξοντα αριθμό του στοιχείου: (*1*) για το O_2, (*2*) για το N_2, (*3*) για CO_2, (*4*) για το H_2O, (*5*) για το *Ar* και (*6*) για το SO_2. Για τους οδικούς κινητήρες μόνο τα τέσσερα πρώτα στοιχεία χρησιμοποιήθηκαν.

Η αρχική θερμοκρασία της γόμωσης *T [K]*, δηλαδή η θερμοκρασία ένα βήμα πριν το *SOC*, υπολογίζεται από την καταστατική εξίσωση του τέλειου αερίου όπως περιγράφεται στην Εξ. (3.14):

$$T_i = \frac{p_i \cdot V_i}{n_{ch,i} \cdot \bar{R}} \tag{3.14}$$

όπου, *p [Pa]* και *V [m^3]* είναι η μετρημένη πίεση και ο όγκος του κυλίνδρου αντίστοιχα.

Κατόπιν, υπολογίζεται η ειδική ενθαλπία h_i *[J/kmol]* της γόμωσης χρησιμοποιώντας τη θερμοκρασία T_i μέσω πολυωνυμικών προσεγγίσεων [180]. Ένα διαφορετικό σύνολο συντελεστών του πολυωνύμου αντιστοιχεί σε κάθε χημικό στοιχείο (*j*). Έτσι, η συνολική ενθαλπία του μείγματος (γόμωση) H_i *[J]* στο τρέχον υπολογιστικό βήμα δίνεται από την Εξ. (3.15):

$$H_i = n_{ch,i} \cdot h_i = n_{ch,i} \cdot \sum_j x_{j,i} \cdot h_{j,i}(T_i) \tag{3.15}$$

Το μοντέλο υπολογίζει το *HRR* για κάθε υπολογιστικό βήμα γωνίας στροφάλου (*CA*) μέσω μιας επαναληπτικής διαδικασίας, προκειμένου να ληφθεί υπόψη η μεταβολή της σύστασης της γόμωσης εξαιτίας της καύσης.

Όπως αναφέρθηκε, το *HRR* υπολογίζεται από τον πρώτο θερμοδυναμικό νόμο, όπως περιγράφεται στην Εξ. (3.16). Η ενθαλπική αύξηση από το εγχεόμενο καύσιμο και οι απώλειες ενθαλπίας που οφείλονται σε διαρροές και την ατμοποίηση του καυσίμου έχουν αμεληθεί, γιατί η συμβολή τους είναι μάλλον μικρή [8], ωστόσο, η μεταφορά θερμότητας μέσω των τοιχωμάτων του κυλίνδρου λαμβάνεται υπόψη.

$$\begin{gathered} \frac{dQ_G}{d\theta} = \frac{dH_{sens}}{d\theta} - V \cdot \frac{dp}{d\theta} + \frac{dQw}{d\theta} \\ \frac{dQ_G{}_i^k}{d\theta} = \frac{(H_{sens}{}_i^k - H_{sens_{i-1}})}{\Delta\theta} - V_i \cdot \left(\frac{dp}{d\theta}\right)_i + \left(\frac{dQw}{d\theta}\right)_i^k \end{gathered} \tag{3.16}$$

Στις πιο πάνω σχέσεις, το $\frac{dQ_G}{d\theta}$ *[J/°]* είναι το μεικτό (ή φαινομενικό) *HRR* (*GHRR*) το οποίο προκύπτει από το άθροισμα του καθαρού *HRR* (*NHRR*) και της θερμότητας που μεταφέρεται μέσω των τοιχωμάτων του κυλίνδρου που συμβολίζεται ως $\frac{dQw}{d\theta}$ *[J/°]*. Το $\frac{dQw}{d\theta}$ υπολογίζεται με τη φόρμουλα που πρότεινε ο Annand [139] η οποία αναλύεται στη συνέχεια. H_{sens} είναι η αισθητή ενθαλπία της γόμωσης του κυλίνδρου, η οποία προέρχεται όταν η ενθαλπία αναφοράς $H°$ αφαιρεθεί από την ολική ενθαλπία H όπως περιγράφεται στην Εξ. (3.17):

$$H_{sens}{}_i^k\left(x_i^k, T_i^k\right) = H_i^k - H°_i^k = H_i^k\left(x_i^k, T_i^k\right) - H_i^k\left(x_i^k, \mathrm{T} = 298.15\right) \tag{3.17}$$

Όπου ο εκθέτης *k* δηλώνει την τρέχουσα επανάληψη για τον υπολογισμό του H_{sens}. Η συνολική ενθαλπία υπολογίζεται από την Εξ. (3.15). Σημειώνεται ότι η μοριακή σύσταση (*x*) της γόμωσης καθορίζεται από τη χημεία της καύσης και αλλάζει μεταξύ των επαναλήψεων,

λόγω της εξάρτησής της από την ποσότητα της μάζας του καυσίμου (m_f *[kg]*) που καίγεται σε κάθε βήμα *CA*. Αυτή η μάζα καυσίμου υπολογίζεται απευθείας από το φαινομενικό/πειραματικό *HRR* όπως περιγράφεται στην Εξ. (3.18):

$$m_{f_i}^{\ k} = \frac{dQ_{G_i}^{\ k}}{d\theta} \cdot \Delta\theta \cdot \frac{1}{LHV} \tag{3.18}$$

Χρησιμοποιώντας τις νέες τιμές των n_{ch} και x_j που προέκυψαν λόγω της καύσης, υπολογίζεται νέα τιμή για τη θερμοκρασία T_i^k χρησιμοποιώντας την Εξ. (3.14). Από αυτή τη θερμοκρασία και σύσταση, μια νέα τιμή για την $H_{sens_i}^{\ k}\left(x_i^k, T_i^k\right)$ υπολογίζεται στο εξεταζόμενο βήμα *CA*. Αυτή η διαδικασία τερματίζεται όταν η τιμή του καιγόμενου καυσίμου στο εξεταζόμενο βήμα *CA* συγκλίνει.

Λόγω του θορύβου που εμπεριέχεται στο σήμα της μετρημένης πίεσης, η άμεση εκτίμηση της *SOC* από το *HRR*, μπορεί να οδηγήσει σε λάθος συμπεράσματα, διότι στους υπολογισμούς του *HRR* ο θόρυβος μεγεθύνεται και θα μπορούσε να προκαλέσει θετικές τιμές του *HRR* νωρίτερα από το πραγματικό *SOC*, ειδικά σε περιπτώσεις με καθυστερημένη έγχυση καυσίμου. Για το λόγο αυτό, η πρώτη εκτίμηση του *SOC* επιτυγχάνεται απευθείας από το μετρημένο δυναμοδεικτικό διάγραμμα, με τρόπο που περιγράφεται στη συνέχεια.

Εντοπισμός της Έναυσης

Λαμβάνοντας υπόψη τη βιβλιογραφία π.χ. [217,218,219] και από παρατηρήσεις διάφορων τύπων δυναμοδεικτικών διαγραμμάτων και των αντίστοιχων παραγώγων τους, συνάχθηκε ότι οι προϋποθέσεις για την εμφάνιση του *SOC* στην εξεταζόμενη γωνία στροφάλου (*CA*) είναι:

- η μεταβολή της δεύτερης παραγώγου της πίεσης να είναι αύξουσα, δηλαδή: $\left(\frac{d^2p}{d\theta^2}\right)_i > \left(\frac{d^2p}{d\theta^2}\right)_{i-1}$ ΚΑΙ
- Η μεταβολή της παραγώγου $\left(\frac{d}{d\theta}\left(\frac{dp}{d\theta}\right)\right)$ γίνεται μέγιστη $\left(\frac{d^2}{d\theta^2}\left(\frac{dp}{d\theta}\right) = 0\right)$ ή παρουσιάζει σημείο καμπής $\left(\frac{d^3}{d\theta^3}\left(\frac{dp}{d\theta}\right) = 0\right)$: $\left\{\left(\frac{d^2p}{d\theta^2}\right)_i > \left(\frac{d^2p}{d\theta^2}\right)_{i+1}\right\}$ $'H$ $\left\{\left(\frac{d^4p}{d\theta^4}\right)_i \cdot \left(\frac{d^4p}{d\theta^4}\right)_{i-1} < 0\right\}$

Λόγω του ότι τα κριτήρια αυτά μπορεί να ικανοποιούνται και σε άλλες *CA* και ειδικότερα στην περιοχή του άνω νεκρού σημείου (*TDC*) κυρίως λόγω θορύβου, το παράθυρο στο οποίο δύναται να βρίσκεται το *SOC* πρέπει να καθοριστεί ορθά πριν την εφαρμογή της προαναφερθείσας μεθοδολογίας. Αυτό επιτυγχάνεται ως εξής: Μετριέται ο αριθμός των τοπικών ακροτάτων του δυναμοδεικτικού διαγράμματος $\left(\frac{dp}{d\theta} = 0\right)$ και των σημείων καμπής $\left(\frac{d^2p}{d\theta^2} = 0\right)$ που η καμπύλη πίεσης έχει τα κοίλα προς τα άνω $\left(\frac{d^2p}{d\theta^2} > 0\right)$ μέσα σε ένα παράθυρο γύρω από το *TDC* (π.χ. *-10:+30° ATDC*), ξεκινώντας από τα αριστερά του *TDC*. Αν αυτός ο αριθμός είναι μεγαλύτερος από τη μονάδα (δεδομένου ότι όλα τα δυναμοδεικτικά διαγράμματα έχουν τουλάχιστον μία κορυφή–τοπικό μέγιστο), αποτελεί ένδειξη ότι το *SOC*

εμφανίζεται μετά το *TDC*. Ως εκ τούτου, η αρχική μεθοδολογία υπολογισμού *SOC*, υλοποιείται μετά το *TDC*, ξεκινώντας ένα βήμα *CA* πριν από εκείνο όπου ο προαναφερόμενος αριθμός γίνεται ίσος με δύο.

Για την περίπτωση που το *SOC* εμφανίζεται πριν το *TDC*, γενικά ένα σημείο καμπής ή πιο συγκεκριμένα ένα θετικό τοπικό ελάχιστο της παραγώγου της πίεσης $\left(\left(\frac{dp}{d\theta}\right)_{min} > 0\right)$ εμφανίζεται πριν ή πολύ κοντά στο *TDC*. Έτσι, σε αυτό το σημείο (*CA*) πρέπει να εκκινήσει η εφαρμογή της μεθόδου για την αρχική εκτίμηση του *SOC*. Από την άλλη, η αντίστοιχη γωνία (*CA*) εκκίνησης, για τις περιπτώσεις που η καύση ξεκινά αρκετά νωρίτερα από το *TDC* (δηλ. *5–10°*), ορίζεται εκεί που παρατηρείται αλλαγή στην κλίση της παραγώγου της πίεσης, καθώς η *CA* αυξάνει προς τα δεξιά. Πιο συγκεκριμένα, αυτή η αλλαγή αντιστοιχεί σε ένα σημείο καμπής του δυναμοδεικτικού $\left(\frac{d^2p}{d\theta^2} = 0\right)$ ακολουθούμενο από αύξουσα μεταβολή της παραγώγου της πίεσης $\left(\frac{d^2p}{d\theta^2} > 0\right)$, το οποίο υποδεικνύει ότι η καμπύλη της πίεσης έχει τα κοίλα προς τα άνω.

Αν η θέση εκκίνησης (αριστερό άκρο) της μεθόδου για την αρχική εκτίμηση του *SOC* βρίσκεται πριν το *TDC* τότε το δεξιό άκρο του παραθύρου αντιστοιχεί στο *TDC*, ενώ αν βρίσκεται μετά το *TDC* τότε το δεξιό άκρο ορίζεται *30° CA* μετά το *TDC*. Παρόλα αυτά, η τελική τιμή του *SOC* καθορίζεται από το σημείο που το *NHRR* ξενικά να γίνεται θετικό. Οι υπολογισμοί για το *NHRR*, ξεκινούν από την υπολογισθείσα αρχική τιμή του *SOC*.

Στοιχειομετρία της Καύσης

Μετά την έναρξη της καύσης, τα προϊόντα της, που προέκυψαν από την στιγμιαία καύση του στοιχειώδους καυσίμου που αντιστοιχεί στο τρέχον διάστημα *CA*, προστίθενται στη γόμωση του κυλίνδρου και ομογενοποιούνται. Η καύση της κάθε στοιχειώδους ποσότητας καυσίμου θεωρείται ιδανική και στοιχειομετρική όπως περιγράφεται στην Εξ.(3.19), αμελώντας την επίδραση τις χημικής διάστασης. Ο αριθμός των mole του O_2 ($\nu_{O_2} \cdot m_{f_i}$) που απαιτούνται για τη στοιχειομετρική οξείδωση του καυσίμου σε κάθε βήμα *CA* και ο αριθμός των mole που προέρχονται από την αντίδραση οξείδωσης, δηλαδή τα προϊόντα καύσης (CO_2, H_2O, SO_2, N_2), υπολογίζονται με ισοζύγιο των μονοατομικών στοιχείων. Στη συνέχεια, ο αριθμός των mole της γόμωσης του κυλίνδρου (n_{ch}) προσδιορίζεται ως το άθροισμα του αριθμού των mole στο προηγούμενο βήμα και του αριθμού των mole των προϊόντων που παράχθηκαν στο τρέχον βήμα, αφαιρώντας τον αριθμό των mole του O_2 που χρησιμοποιήθηκαν για την καύση, όπως περιγράφεται στην Εξ. (3.20). Τα κλάσματα mole (x) και μάζας

(*y*) των στοιχείων που εμπεριέχονται στη γόμωση και το μοριακό της βάρος στο τρέχον βήμα *CA* (*i*) υπολογίζονται από την Εξ. (3.21).

$$C_m H_n S_p O_q N_r + \nu_{O_2} O_2 \rightarrow mCO_2 + \frac{n}{2} H_2O + pSO_2 + \frac{r}{2} N_2$$
$$\nu_{O_2} = \left(m + \frac{n}{4} + p - \frac{q}{2}\right) \tag{3.19}$$

$$n_{ch_i}^{\ k} = n_{\mathrm{ch}_{i-1}} + \left(m + \frac{n}{2} + p + \frac{r}{2} - \nu_{O_2}\right) \cdot m_{f_i}^{\ k} = n_{\mathrm{ch}_{i-1}} + \left(\frac{n}{4} + \frac{r}{2} - \frac{q}{2}\right) \cdot m_{f_i}^{\ k} \tag{3.20}$$

$$x_{j_i}^{\ k} = \frac{n_{j_i}^{\ k}}{n_{ch_i}^{\ k}}$$
$$MW_{ch_i}^{\ k} = \sum\nolimits_j x_{j_i}^{\ k} \cdot MW_j \tag{3.21}$$
$$y_{j_i}^{\ k} = x_{j_i}^{\ k} \cdot \frac{MW_j}{MW_{ch_i}^{\ k}}$$

Στην πιο πάνω έκφραση, οι δείκτες *m, n, p, q, r [kmol/kg fuel]* αντιπροσωπεύουν το περιεχόμενο του καυσίμου σε *C, H, S, O, N* αντίστοιχα και υπολογίζονται από τη διαίρεση των αντίστοιχων κλασμάτων μάζας *[kg/kg]* του καυσίμου και του μοριακού βάρους (*MW [kg/kmol]*) του αντίστοιχου στοιχείου (*j*). ν_{O2} *[kmol* O_2*/kg fuel]* είναι ο στοιχειομετρικός συντελεστής οξυγόνου που προσδιορίζεται από τη σύνθεση του καυσίμου (βλ. Εξ. (3.19)). Ο εκθέτης *k* υποδηλώνει τον αύξοντα αριθμό της επανάληψης της υπολογιστικής διαδικασίας για τον υπολογισμό της μάζας του καυσίμου.

Εντοπισμός του Τέλους της Καύσης

Η ορθή εκτίμηση του *EOC* είναι σημαντική για τα μοντέλα του *HRR* και NO_x διότι επηρεάζει τη διάρκεια της καύσης και τον συντελεστή απωλειών θερμότητας, έτσι πρέπει να προσεγγίζεται με όσο το δυνατό μεγαλύτερη ακρίβεια. Αυτό επιτυγχάνεται με τη χρήση του καθαρού *HRR* (*NHRR [J/°]*), δηλαδή παραλείποντας τον όρο της μεταφοράς θερμότητας από τα τοιχώματα του κυλίνδρου. Το *EOC* εντοπίζεται στην *CA* όπου το *NHRR* μειώνεται σημαντικά και γίνεται παράλληλο προς τον οριζόντιο άξονα. Η προτεινόμενη μεθοδολογία ξεκινά στην *CA*, όπου εμφανίζεται το *85%* της μέγιστης τιμής του σωρευτικού καθαρού *HR* (*CNHR*). Από αυτό το σημείο και μετά, η τιμή του *NHRR* στο τρέχον βήμα *CA* εξομαλύνεται περαιτέρω χρησιμοποιώντας τη μέθοδο «moving average», όπως φαίνεται στην Εξ. (3.22):

$$NHRR_{s_i} = \frac{1}{2 \cdot W_s + 1} \sum_{l=-W_s}^{l=W_s} NHRR_{i+l} \tag{3.22}$$

όπου ($2W_s+1$) είναι το παράθυρο δειγμάτων για την εξομάλυνση και ο δείκτης *s* υποδεικνύει τις εξομαλυνόμενες τιμές. Όταν το εξεταζόμενο σημείο ($NHRR_{s_i}$) είναι μικρότερο από ένα κατώφλι (*3%* του $NHRR_{max}$), τότε υπολογίζεται ο μέσος όρος ($NHRR_{s_{aver}}$) και η τυπική απόκλιση ενός αριθμού από τις ακόλουθες διαδοχικές τιμές του *NHRR* ($NHRR_s$). Αν ο μέσος όρος αυτών των τιμών $NHRR_{s_{aver}}$, συμπεριλαμβανομένου του πρώτου, δηλ. του $NHRR_{s_i}$, είναι μικρότερος από αυτό το κατώφλι ή η τυπική απόκλιση αυτών των τιμών γίνει μικρότερη από το *20%* του $NHRR_{s_{aver}}$, τότε η διαδικασία τερματίζεται και το τρέχον βήμα *CA* (*i*) αντιστοιχεί στο *EOC*.

Μοντέλα Συναλλαγής Θερμότητας

Για τη μεταφορά θερμότητας $\frac{dQw}{d\theta}$ *[J/°]* μέσω των τοιχωμάτων του κυλίνδρου, τόσο στο μοντέλο του *HR* όσο και για το μοντέλο του *NO*, χρησιμοποιήθηκε το μοντέλο του Annand [8,9,139,140]. Το μοντέλο αυτό περιγράφεται στην Εξ. (3.23):

$$\left(\frac{dQw}{d\theta}\right)_i = \frac{A_{cyl_i}}{6 \cdot N} \cdot \left[a \cdot \frac{k_i}{D} \cdot {Re_i}^b \cdot (T_i - T_w) + c \cdot \sigma \cdot \left({T_i}^4 - T_w^4\right)\right]$$
$$Re = \frac{Sp_i \cdot D. \rho_i}{\mu_i} \tag{3.23}$$

όπου A_{cyl} *[m^2]* είναι η συνολική επιφάνεια του θαλάμου καύσης στο τρέχον βήμα (*i*), *N [rpm]* είναι οι στροφές του κινητήρα, *D [m]* η διάμετρος του κυλίνδρου, *Re* ο αριθμός Reynolds, *T [K]* και T_w *[K]* είναι η θερμοκρασία της γόμωσης/ζώνης και των τοιχωμάτων αντίστοιχα και σ είναι η σταθερά του Stefan Boltzmann (σ*=5.6704*10^{-8} [W/m^2 K^4]*). Η θερμική αγωγιμότητα (*k [W/m/K]*) και η δυναμική συνεκτικότητα (μ *[Pa s]*) του κάθε χημικού στοιχείου (*j*) που περιέχεται στο μείγμα, υπολογίζονται με πολυωνυμικές προσεγγίσεις [221] που είναι συναρτήσεις της θερμοκρασίας. Τα *k* και μ του μείγματος υπολογίζονται μέσω των Εξ. (3.24) και Εξ. (3.25) αντιστοίχως, οι οποίες λήφθησαν από τις αναφορές [222,223].

$$k_i = \frac{\sum_j x_{j,i} \cdot k_{j,i} \cdot {MW_j}^{1/3}}{\sum_j x_{j,i} \cdot {MW_j}^{1/3}} \tag{3.24}$$

$$\mu_i = \frac{\sum_j x_{j,i} \cdot \mu_{j,i} \cdot {MW_j}^{1/2}}{\sum_j x_{j,i} \cdot {MW_j}^{1/2}} \tag{3.25}$$

Για τον υπολογισμό του αριθμού Reynolds (*Re*) χρησιμοποιήθηκε η μέση ταχύτητα του εμβόλου *Sp [m/s]* [9]. Η πυκνότητα του μείγματος ρ *[kg/m^3]* υπολογίζεται ως ο λόγος της μάζας της γόμωσης/ζώνης και του όγκου του κυλίνδρου/ζώνης στο τρέχον βήμα *CA* (*i*). Οι παράμετροι *A, k,* μ*, Sp,* ρ*, T, Re* μεταβάλλονται σε κάθε βήμα. Η μέση θερμοκρασία των τοιχωμάτων θεωρήθηκε σταθερή στους *450 K* [8,224,101,225]. Οι τιμές των σταθερών *b* και *c* διατηρούνται σταθερές δηλ. *b=0.75* για όλο το κλειστό κύκλο, *c=0* and *c=0.576* πριν

και μετά το *SOC* [8,9,225,146,143,226]. Εν τέλει, η σταθερά $\boldsymbol{\alpha}$ βαθμονομείται χρησιμοποιώντας μια τροποποιημένη μορφή της μεθόδου εσφαλμένης θέσης (*regula falsi*) [227] προκειμένου να ικανοποιήσει τον περιορισμό που περιγράφεται στην Εξ. (3.26).

$$m_{f\,cyl} = \frac{1}{LHV} \cdot \sum_{i=SOC}^{EOC} \left(\frac{dQ_N}{d\theta} + \frac{dQw}{d\theta} \right)_i \cdot \Delta\theta$$
$$m_{f\,cyl} = \frac{1}{LHV} \cdot \sum_{i=SOC}^{EOC} \left(\frac{dQ_G}{d\theta} \right)_i \cdot \Delta\theta \quad (3.26)$$

Στην πιο πάνω σχέση, *LHV* είναι η κατώτερη θερμογόνος ικανότητα του καυσίμου, ο όρος του αθροίσματος αντιστοιχεί στο *CGHR* το οποίο υπολογίζεται με την Εξ. (3.16) και m_f *[kg/cycle]* είναι η ποσότητα του εγχεόμενου καυσίμου ανά κύκλο στον κύλινδρο, η οποία είναι δεδομένη.

Αν είναι διαθέσιμα τα δυναμοδεικτικά όλων των κυλίνδρων τότε μπορεί να υπολογιστεί διαφορετικός συντελεστής *α* για κάθε κύλινδρο. Ο υπολογισθείς με αυτό τον τρόπο συντελεστής *α*, μαζί με τους σταθερούς συντελεστές *b* και *c* χρησιμοποιούνται επίσης και στο μοντέλο *NO* στον υπολογισμό της θερμοκρασίας των ζωνών. Προφανώς, όσον αφορά στην άκαυστη ζώνη, ο συντελεστής *c* (μεταφορά θερμότητας με ακτινοβολία) είναι πάντοτε μηδενικός κατά τη διάρκεια του κύκλου.

Μοντέλο υπολογισμού των NO

Στη συνέχεια, το μοντέλο *NO* εφαρμόζεται από το *SOC* μέχρι το άνοιγμα της βαλβίδας εξαγωγής (*EVO*). Το σκεπτικό του μοντέλου απεικονίζεται στο Σχ. 3.1. Τα αστέρια αντιστοιχούν στη γέννηση των ζωνών. Η πρώτη ζώνη δημιουργείται στο *SOC*. Κάθε ζώνη προσδιορίζεται από τη στοιχειώδη μάζα καυσίμου που καίγεται στο αντίστοιχο διάστημα *CA*, όπως καθορίστηκε από τον ρυθμό καύσης, όπως φαίνεται στο Σχ. 3.2 καθώς και από την απαιτούμενη αντίστοιχη ποσότητα μάζας άκαυστης γόμωσης. Αυτή η μάζα προσδιορίζεται χρησιμοποιώντας μια εμπειρική συσχέτιση που παρέχει τον λόγο ισοδυναμίας της ζώνης (*Φ*), η οποία θα αναλυθεί στη συνέχεια. Μετά τη δημιουργία της, η ζώνη συνεχίζει να εξελίσσεται μέσα στον κύλινδρο παράλληλα με τη δημιουργία/εξέλιξη των άλλων ζωνών μέχρι το *EVO*, έχοντας το δικό της ιστορικό χημικής σύστασης, θερμοκρασίας και όγκου. Οι ζώνες θεωρούνται εσωτερικά ομοιογενείς. Ο υπολογισμός της θερμοκρασίας κάθε ζώνης βασίζεται στον πρώτο θερμοδυναμικό νόμο, λαμβάνοντας υπόψη τη μεταφορά θερμότητας μεταξύ ζώνης και τοιχωμάτων του κυλίνδρου. Κάθε ζώνη συμβάλλει στο σχηματισμό *NO* από τη δημιουργία της, μέχρι το *EVO*. Τα *NO* μέσα σε κάθε ζώνη υπολογίζονται με τον μηχανισμό Extended Zeldovich [29,30]. Ο υπολογισμός της σύστασης ισορροπίας γίνεται με τη βοήθεια ενός σχήματος χημικής διάστασης [228]. Η πτώση της θερμοκρασίας λόγω της χημικής διάστασης λαμβάνεται υπόψη. Η πίεση όλων των ζωνών θεωρείται ομοιόμορφη σε κάθε *CA* και ισούται με την αντίστοιχη μετρούμενη. Μετά το τέλος της καύσης (*EOC*), η παραγωγή ζωνών τερματίζεται αλλά οι υπάρχουσες ζώνες συνεχίζουν να εξελίσσονται μέχρι το *EVO*. Οι εξελισσόμενες ζώνες απεικονίζονται στο Σχ. 3.1 ως κενά τετράγωνα. Μέσω αυτής της προσέγγισης, το ιστορικό *NO* κάθε ζώνης υπολογίζεται (δηλαδή το *NO* vs.

CA) όπως φαίνεται στο Σχ. 3.3. Το άθροισμα των ποσών *NO* που σχηματίστηκε στις υπάρχουσες ζώνες σε κάθε χρονικό βήμα *CA* παρέχει το ιστορικό *NO* του κυλίνδρου, όπως φαίνεται στο Σχ. 3.4. Συνεπώς, το άθροισμα των *NO* της κάθε ζώνης στο *EVO* παρέχει τη συνεισφορά του εξεταζόμενου κυλίνδρου στις τελικές εκπομπές *NO* του κινητήρα.

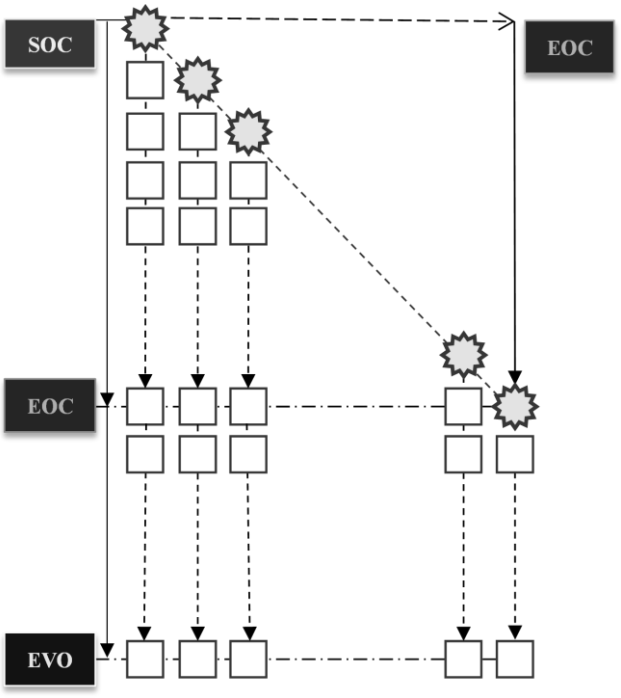

Σχήμα 3.1: Το σενάριο του προτεινόμενου μοντέλου NO – Δημιουργία και εξέλιξη των ζωνών.

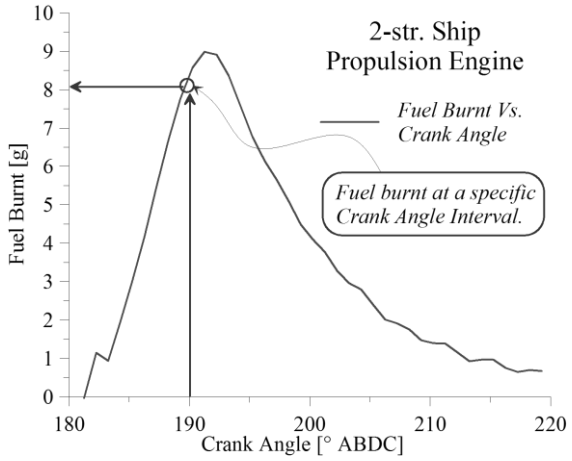

Σχήμα 3.2: Υπολογισμός του καυσίμου που καίγεται σε ένα συγκεκριμένο διάστημα γωνίας στροφάλου.

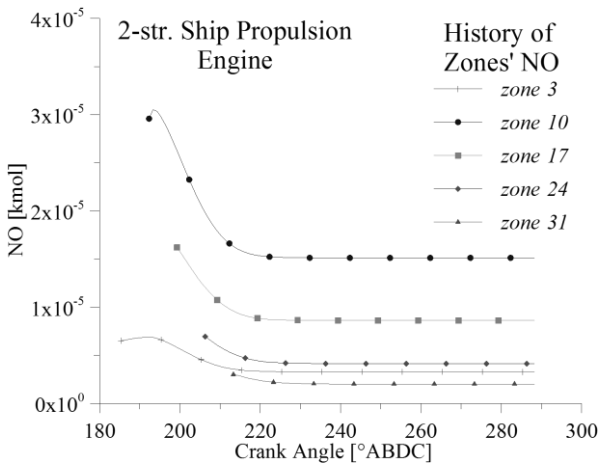

Σχήμα 3.3: Ιστορικό του NO σε συγκεκριμένες ζώνες από τη δημιουργία τους μέχρι το EVO.

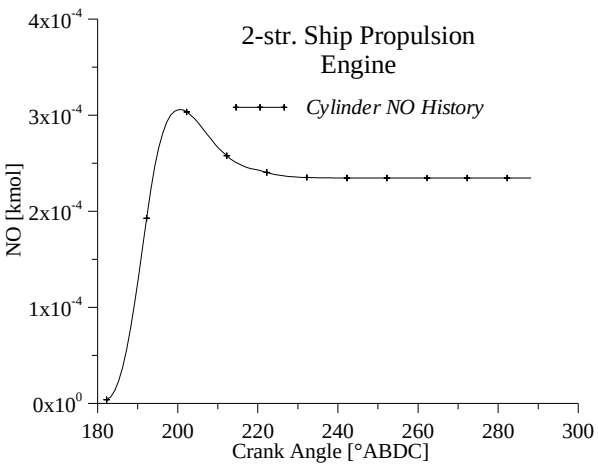

Σχήμα 3.4: Ιστορικό των συνολικών NO μέσα στον κύλινδρο σε συνάρτηση με τη γωνία στροφάλου.

Η άκαυστη ζώνη είναι η πηγή από την οποία οι ζώνες καύσης, κατά τη δημιουργία τους, αντλούν την απαιτούμενη ποσότητα άκαυστης γόμωσης για την καύση του καυσίμου που περιλαμβάνεται σε κάθε ζώνη. Η χημική σύσταση της άκαυστης ζώνης θεωρείται σταθερή σε όλον τον κλειστό κύκλο αφού ούτε ανάμειξη και ανταλλαγή θερμότητας με τις ζώνες καύσης αλλά ούτε και χημική διάσταση των προϊόντων λαμβάνει χώρα. Η πίεση της άκαυστης ζώνης ισούται με την επικρατούσα πίεση εντός του κυλίνδρου στο τρέχον βήμα *CA*. Ο όγκος της ζώνης άκαυστου ($V\ [m^3]$) προσδιορίζεται ως η διαφορά του τρέχοντος όγκου του κυλίνδρου και του αθροίσματος των όγκων των ζωνών καύσης, όπως περιγράφεται στην Εξ. (3.27):

$$V_{ub_i} = V_{cyl_i} - \sum_{z=1}^{i-SOC+1} V_{b_z} \tag{3.27}$$

όπου ο δείκτης *i* συμβολίζει το βήμα *CA*, ο *ub* την άκαυστη ζώνη, ο *b* τις καιόμενες ζώνες, ο *cyl* τον κύλινδρο και ο *z* τον αύξοντα αριθμό της ζώνης.

Η θερμοκρασία της άκαυστης ζώνης, η οποία χρησιμοποιείται ως θερμοκρασία των αντιδρώντων στους υπολογισμούς κατά τη δημιουργία μιας ζώνης καύσης, υπολογίζεται σε κάθε βήμα *CA* (*i*) μέσω του πρώτου θερμοδυναμικού νόμου, χρησιμοποιώντας μια επαναληπτική διαδικασία (ο εκθέτης *k* δηλώνει τον αύξοντα αριθμό της επανάληψης) που εμπεριέχει τις Εξ. (3.28) και (3.29). Η διαδικασία τερματίζεται όταν επιτευχθεί σύγκλιση.

$$h_i^k = \frac{n_{i-1} \cdot h_{i-1} + dp_i \cdot \frac{\left(V_{ub_{i-1}} + V_{ub_i}\right)}{2} - n_{out} \cdot \frac{\left(h_{i-1} + h_i^{k-1}\right)}{2} - dQw_i^k}{n_i} \tag{3.28}$$

$$n_i = n_{i-1} - n_{out}$$

Στην πιο πάνω σχέση, *h [J/kmol]* είναι η ενθαλπία της άκαυστης ζώνης η οποία είναι συνάρτηση της χημικής σύστασης και της θερμοκρασίας της. Ο αριθμός των mole (*n [kmol]*) που εμπεριέχονται στον όγκο της άκαυστης ζώνης (V_{ub_i}) προσδιορίζεται από τη διαφορά

μεταξύ του αριθμού των mole του προηγούμενου βήματος *CA* (*i-1*) και το ποσού που μεταφέρθηκε (n_{out}) από την άκαυστη ζώνη στη ζώνη καύσης που δημιουργείται στο τρέχον βήμα *CA* (*i*).

Το *dQw [J]* $\left(dQw = \frac{dQw}{d\theta} \cdot \Delta\theta\right)$ είναι η συναλλαγή θερμότητας με τα τοιχώματα του κυλίνδρου, η οποία υπολογίζεται χρησιμοποιώντας το μοντέλο του Annand. Ωστόσο, υιοθετήθηκε μια τροποποίηση στη φόρμουλα αυτή, δηλ. η τρέχουσα επιφάνεια του κυλίνδρου $Acyl_i$ $[m^2]$ πολλαπλασιάζεται με $\frac{{V_{ub}}_i^k}{Vcyl_i}$ [109] ώστε να αντιπροσωπεύεται η ισοδύναμη διεπιφάνεια μεταξύ ζώνης και τοιχωμάτων.

Εν τέλει, η θερμοκρασία της άκαυστης ζώνης T_{ub} υπολογίζεται μέσω της μεθόδου Newton–Raphson [229] όπως περιγράφεται στην Εξ. (3.29):

$$ {T_{ub}}_i^k = {T_{ub}}_i^{k-1} - \frac{h_i^k - h_i^{k-1}}{cp_i^{k-1}} \tag{3.29} $$

όπου *cp [J/kmol/K]* η ειδική θερμοχωρητικότητα σε σταθερή πίεση $\left(cp = \left(\frac{dh}{dT}\right)_p\right)$ της άκαυστης ζώνης.

Κατά τη δημιουργία της ζώνης καύσης, η θερμοκρασία της – θερμοκρασία προϊόντων καύσης (*Tp [K]*) – υπολογίζεται με τον πρώτο θερμοδυναμικό νόμο, χρησιμοποιώντας μια επαναληπτική διαδικασία που περιλαμβάνει την μέθοδο Newton-Raphson [229] όπως περιγράφεται στην Εξ. (3.30). Η διαδικασία τερματίζεται όταν η *Tp* συγκλίνει σε μια τιμή. Σημειώνεται ότι η μάζα της κάθε ζώνης παραμένει σταθερή.

$$ {Tp_z}_i^k = {Tp_z}_i^{k-1} - \frac{{hp_z}_i^{k-1} - {hr_z}_i + {dqw_z}_i^{k-1} - {V_z}_i^{k-1} \cdot dp_i/m_z}{{cp_z}_i^{k-1}} \tag{3.30} $$

όπου *hr [J/kg]* και *hp [J/kg]* είναι η ενθαλπία των αντιδρώντων και προϊόντων αντίστοιχα. Η *hr* είναι συνάρτηση της σύστασης και της θερμοκρασίας της άκαυστης ζώνης στο εξεταζόμενο βήμα *CA* (*i*), όπως έχει αναφερθεί. Η υπολογισμός της σύστασης της ζώνης καύσης που χρησιμοποιείται μαζί με την *Tp* στον υπολογισμό της *hp*, θα αναλυθεί στη συνέχεια.

Ο όγκος της ζώνης υπολογίζεται από την καταστατική εξίσωση των τέλειων αερίων, όπως περιγράφεται στην Εξ. (3.31):

$$ {V_z}_i^{k-1}[m^3] = \frac{m_z \cdot \bar{R} \cdot Tp_i^{k-1}}{p_i \cdot {MW_z}_i^{k-1}} \tag{3.31} $$

Στις δύο πιο πάνω σχέσεις, *p [Pa]* είναι η μετρημένη πίεση κυλίνδρου, *dp [Pa]* είναι το διαφορικό της πίεσης $\left(\frac{dp}{d\theta} \cdot \Delta\theta\right)$ και το *dqw [J/kg]* είναι το διαφορικό της μεταφοράς θερμότητας μέσω των τοιχωμάτων του κυλίνδρου $\left(\frac{\frac{dQw}{m_z}}{d\theta} \cdot \Delta\theta\right)$ που υπολογίζεται με το μοντέλο του

Annand, όπου ομοίως με την άκαυστη ζώνη, η επιφάνεια του κυλίνδρου $Acyl_i$ πολλαπλασιάζεται με $\frac{V_{z_i}^{k-1}}{Vcyl_i}$ [109].

Στη συνέχεια, η ζώνη καύσης συνεχίζει να εκτονώνεται ή να συμπιέζεται (ανάλογα με την παράγωγο της πίεσης του κυλίνδρου) σύμφωνα με τον πρώτο θερμοδυναμικό νόμο μέχρι το *EVO*. Συνεπώς, σε κάθε βήμα *CA* (*i*), οι τιμές του όγκου (*V [m³]*), της χημικής σύστασης (*x*), του αριθμού των mole (*n [kmol]*), του μοριακού βάρους (*MW [kg/kmol]*), της ενθαλπίας (*h [J/kmol]*) και της θερμοκρασίας (*T [K]*) της εξεταζόμενης ζώνης (*z*) υπολογίζονται από μια επαναληπτική διαδικασία χρησιμοποιώντας όμοιο σκεπτικό με αυτό της άκαυστης ζώνης, ωστόσο, εδώ η χημική διάσπαση λαμβάνεται υπόψη, δεδομένου ότι η θερμοκρασία της ζώνης είναι σημαντικά αυξημένη. Η ενθαλπία της ζώνης υπολογίζεται από την Εξ. (3.32) και η θερμοκρασία της μέσω της μεθόδου Newton–Raphson [229] όπως περιγράφεται στην Εξ. (3.33):

$$h_{z_i}^{\ k} = \frac{n_{z_{i-1}} \cdot h_{z_{i-1}} + dp_i \cdot \frac{\left(V_{z_{i-1}} + V_{z_i}^{\ k}\right)}{2} - dQw_{z_i}^{\ k}}{n_{z_i}^{\ k}} \tag{3.32}$$

$$T_{z_i}^{\ k} = T_{z_i}^{\ k-1} - \frac{h_{z_i}^{\ k} - h_{z_i}^{\ k-1}}{cp_{z_i}^{\ k-1}} \tag{3.33}$$

Οι αρχικές τιμές για την επαναληπτική διαδικασία προέρχονται από τις τελικές τιμές του προηγούμενου βήματος *CA* (*i-1*). Η διαδικασία τερματίζεται όταν η θερμοκρασία (*T*) συγκλίνει σε μια τιμή.

Η αρχική σύσταση της καμένης ζώνης, η οποία χρησιμοποιείται σαν είσοδος στο υπομοντέλο της χημικής διάστασης για τον καθορισμό της τελικής σύστασης χημικής σύστασης ισορροπίας, υπολογίζεται από την Εξ. (3.34) με ισοζύγιο των mole των μονοατομικών στοιχείων:

$$\begin{aligned} C_m H_n S_p O_q N_r + \frac{\nu_{O_2}}{\Phi}\left(O_2 + \sum_j \frac{x_{j,ch}}{x_{O_2,ch}} M_j\right) \rightarrow mCO_2 + \frac{n}{2}H_2O + pSO_2 + \frac{r}{2}N_2 \\ + \frac{\nu_{O_2}}{\Phi}\left((1-\Phi)O_2 + \sum_j \frac{x_{j,ch}}{x_{O_2,ch}} M_j\right) \\ \nu_{O_2} = \left(m + \frac{n}{4} + p - \frac{q}{2}\right) \end{aligned} \tag{3.34}$$

όπου M_j και $x_{j,ch}$ είναι το j^{th} χημικό στοιχείο της εισερχόμενης στη ζώνη γόμωσης και το αντίστοιχο κλάσμα mole και ν_{O2} *[kmol/kg fuel]* είναι ο στοιχειομετρικός συντελεστής O_2 που υπολογίζεται βάση της σύστασης του καυσίμου που χρησιμοποιήθηκε. Η εισερχόμενη γόμωση αποτελείται από αέρα περιβάλλοντος, παραμένον (*RG*) και ανακυκλοφορούμενο (*EGR*) καυσαέριο. Η θεώρηση είναι όμοια με αυτήν που χρησιμοποιήθηκε στο μοντέλο του *HRR* (βλ. Εξ. (3.21)), μόνο που εδώ η καύση γίνεται με τον θεωρητικό λόγο ισοδυναμίας

της ζώνης Φ_z και όχι τον στοιχειομετρικό. Το Φ_z υπολογίζεται από μια εμπειρική σχέση που θα αναλυθεί στη συνέχεια.

Γνωρίζοντας τη μάζα του καυσίμου (m_f *[kg]*) που αντιστοιχεί σε κάθε ζώνη και το Φ_z, που είναι σταθερό για όλες τις ζώνες, μπορεί να υπολογιστεί η μάζα (*m [kg]*) της ζώνης από την Εξ. (3.35):

$$m_z = \left(\frac{AFR_{ST}}{\Phi} + 1\right) \cdot m_{f_i}$$
$$AFR_{ST} = \frac{\nu_{O_2} \cdot MW_{O_2}}{y_{ch_{O_2}}} \tag{3.35}$$

Όπου AFR_{st} είναι ο στοιχειομετρικός λόγος μάζας άκαυστης γόμωσης και καυσίμου και $y_{ch,O2}$ είναι το κλάσμα μάζας O_2 της άκαυστης γόμωσης (*ch*).

Υπολογισμός του Λόγου Ισοδυναμίας στις Ζώνες

Ο λόγος ισοδυναμίας της ζώνης (Φ_z) καθορίζει τη σύσταση και τον όγκο της. Αυτές οι παράμετροι έχουν σημαντική επίδραση στο σχηματισμό των *NO* μέσα στη ζώνη. Έτσι, διεξήχθη εκτεταμένη έρευνα για τη διερεύνηση της μεταβολής των *NO* με το Φ_z. Αυτή η έρευνα έδειξε ότι το Φ_z που χρησιμοποιείται εισάγει υψηλή ευαισθησία στο μοντέλο. Ωστόσο για συγκεκριμένες τιμές του Φ_z (υποδηλώνονται ως Φ^*), επιτυγχάνεται σύμπτωση μετρημένων και υπολογισμένων τιμών *NO* (ή ισοδύναμων NO_x), δηλ. $\frac{calc.NO}{meas.NO} = 1$. Μετέπειτα, έγινε προσπάθεια συσχέτισης των τιμών Φ^* με λειτουργικές παραμέτρους του κινητήρα και με παραμέτρους που προκύπτουν από την επεξεργασία του δυναμοδεικτικού διαγράμματος και την ανάλυση του *HRR*. Έτσι, χρησιμοποιώντας μεθόδους πολλαπλής παρεμβολής [241,242,243], προέκυψε το ακόλουθο πολυώνυμο για τον υπολογισμό του Φ_z (σταθερό για όλες τις ζώνες), που περιγράφεται στην Εξ. (3.36). Οι συντελεστές του (c_0, c_1, … c_6) παίρνουν αντιστοίχως δύο τιμές, μια για τους οδικούς και μια για τους μεγάλης κλίμακας κινητήρες.

$$\Phi_z = c_0 + c_1 \cdot \left(\frac{p_{compr.start}}{p_{amb}}\right)^{-1} + c_2 \cdot \left(\frac{p_{SOC_{main}}}{p_{amb}}\right)^{-1} + c_3 \cdot \frac{p_{comb.max}}{p_{SOC_{main}}} +$$
$$+ c_4 \cdot \frac{COC}{TDC} + c_5 \cdot \Phi_{eng.overall} + c_6 \cdot \frac{S_p}{S_{p_{ref}}} + c_7 \cdot \frac{P}{P_{ref}} \tag{3.36}$$

Στην πιο πάνω σχέση, *p* είναι η πίεση, *P* και S_p είναι η ισχύς του κινητήρα και η μέση ταχύτητα εμβόλου αντίστοιχα, *TDC [°ABDC]* (*BDC≡0°*) και *COC [°ABDC]* είναι το άνω νεκρό

σημείο και το μέσο της καύσης και $\Phi_{eng.\,overall}$ είναι ο ολικός λόγος ισοδυναμίας του κινητήρα όπως ορίζεται στην Εξ. (3.37):

$$\Phi_{eng.overall} = \frac{\dot{m}_{f_{eng}}}{\dot{m}_{IA}} \cdot \frac{\nu_{O_2} \cdot MW_{O_2}}{y_{amb_{O_2}}} \tag{3.37}$$

όπου $\dot{m}_{f_{eng}}$ και $\dot{m}_{IA}$ είναι η ολική παροχή *[kg/h]* καυσίμου και αέρα περιβάλλοντος του κινητήρα αντίστοιχα και $y_{amb_{O_2}} = 0.232$ είναι το τυπικό κλάσμα μάζας του O_2 του αέρα περιβάλλοντος. Αποδείχθηκε ότι η χρήση αυτής της εμπειρικής σχέσης βελτιώνει ποιοτικά τις προβλέψεις εκπομπών NO_x του μοντέλου.

Μοντέλο Χημικής Διάστασης

Όπως αναφέρθηκε πιο πάνω στον υπολογισμό της θερμοκρασίας της ζώνης καύσης, κατά τον σχηματισμό και την εξέλιξη της, λαμβάνεται υπόψη η χημική διάσπαση των προϊόντων της καύσης. Αυτός μηχανισμός έχει ως αποτέλεσμα την αισθητή μείωση της θερμοκρασίας καύσης, δεδομένου ότι οι περισσότερες από τις αντιδράσεις της είναι ενδόθερμες. Το προτεινόμενο μοντέλο κάνει χρήση ενός συστήματος χημικής διάστασης [230,228,147] που εμπλέκει *12* στοιχεία (*(1)* O_2 για φτωχό σε καύσιμο ή *(12)* $C_{12}H_{26}$ για πλούσιο σε καύσιμο μείγμα, *(2)* N_2, *(3)* CO_2, *(4)* H_2O, *(5) H, (6)* H_2, *(7) N, (8) NO, (9) O, (10) OH, (11) CO*). Σύμφωνα με αυτό το σχήμα υπολογίζεται επίσης η σύσταση χημικής ισορροπίας της κάθε ζώνης καύσης.

Για τον υπολογισμό των συγκεντρώσεων ισορροπίας των προαναφερθέντων στοιχείων σε κάθε ζώνη και σε κάθε βήμα *CA*, χρησιμοποιούνται οι πέντε εξισώσεις διατήρησης των mole που περιγράφουν την καύση για το σύστημα *C–H–O–N*, σε συνδυασμό με επτά αντιδράσεις χημικής διάσπασης.

Για τις αντιδράσεις αυτές υιοθετείται η υπόθεση της χημικής ισορροπίας. Έτσι, αξιοποιούνται οι σχέσεις ορισμού της σταθεράς ισορροπίας (*Kp*) της κάθε αντίδρασης και η υπολογισμένη τιμή του *Kp* μέσω της μεθόδου ελαχιστοποίησης της ελεύθερης ενέργειας Gibbs. Ο *Kp* της κάθε αντίδρασης ορίζεται από την Εξ. (3.38) [8,231]:

$$Kp = \left(\frac{p}{p_0}\right)^{\sum_j \nu_{j,p} - \nu_{j,r}} \cdot \prod_j x_j^{\nu_{j,p} - \nu_{j,r}} =$$

$$= \frac{\left(\frac{p}{p_0}\right)^{\nu_{1,p} + \nu_{2,p} + \cdots + \nu_{11,p}}}{\left(\frac{p}{p_0}\right)^{\nu_{1,r} + \nu_{2,r} + \cdots + \nu_{11,r}}} \cdot \frac{x_{1,p}^{\nu_{1,p}} \cdot x_{2,p}^{\nu_{2,p}} \cdot \ldots x_{11,p}^{\nu_{11,p}}}{x_{1,r}^{\nu_{1,r}} \cdot x_{2,r}^{\nu_{2,r}} \cdot \ldots x_{11,r}^{\nu_{11,r}}} \tag{3.38}$$

όπου ο λόγος p/p_0 είναι η κανονικοποιημένη πίεση, p *[Pa]* είναι η τρέχουσα πίεση του κυλίνδρου και $p_0 = 10^5$ *[Pa]* είναι η πίεση αναφοράς.

Μέσω της μεθόδου ελαχιστοποίησης της ελεύθερης ενέργειας Gibbs, μπορεί να προσδιοριστεί η τιμή του *Kp* όπως περιγράφεται στην Εξ. (3.39):

$$Kp(T) = e^{-\sum_j \frac{g^0{}_j(T)\cdot(\nu_{j,p}-\nu_{j,r})}{\bar{R}\cdot T}} \tag{3.39}$$

Ο αδιάστατος λόγος $\frac{g^0{}_j(T)}{\bar{R}\cdot T}$ υπολογίζεται με τη χρήση πολυωνύμων [180] για τη θερμοκρασία της τρέχουσας ζώνης (*T*) και για κάθε στοιχείο (*j*) που συμμετέχει στην εξεταζόμενη χημική αντίδραση.

Το σύστημα των *12* εξισώσεων και των *12* αγνώστων (*11* συστάσεις και ο αριθμός των mole των προϊόντων), μετά από μαθηματική επεξεργασία, λύνεται με τη μέθοδο Newton–Raphson [233]. Η λεπτομερής περιγραφή της μεθοδολογίας που ακολουθήθηκε περιγράφεται στην αναφορά: [147] και [234].

Αφού υπολογιστεί η σύσταση και η θερμοκρασία της ζώνης το μοντέλο προχωρεί στον υπολογισμό του αριθμού των mole των *NO* που παρήχθησαν σε ένα κύκλο, θεωρώντας ότι είναι αντιπροσωπευτικά του συνόλου των NO_x, το οποίο συνήθως αντιστοιχεί στην πραγματικότητα. Όσον αφορά στους οδικούς κινητήρες, όπου υπήρχαν διαθέσιμες μετρήσεις *NO [ppmv]*, γίνεται απευθείας σύγκριση με τα αποτελέσματα του μοντέλου. Αντίθετα, στους κινητήρες μεγάλης κλίμακας που οι διαθέσιμες μετρήσεις δίνονται σε ισοδύναμο NO_x που αντιστοιχεί σε NO_2 σύμφωνα με την αναφορά [46], οι τιμές *NO* που εξαγάγει το μοντέλο μετατρέπονται σε ισοδύναμο NO_x χρησιμοποιώντας το μοριακό βάρος του NO_2.

Μηχανισμός Σχηματισμού των NOx Zeldovich

Ο μηχανισμός για το σχηματισμό των *NO* θεωρήθηκε ελεγχόμενος από χημική κινητική [8,30,31]. Ο μηχανισμός που χρησιμοποιήθηκε είναι ο Extended Zeldovich [30] [29] του οποίου οι χημικές αντιδράσεις που τον περιγράφουν δίνονται στον Πίνακα 3.1:

Χημική αντίδραση
$O + N_2 \leftrightarrow NO + N$
$N + O_2 \leftrightarrow NO + O$
$N + OH \leftrightarrow NO + H$

Πίνακας 3.1: Χημικές αντιδράσεις του σχηματισμού των NO.

Σύμφωνα με αυτό το σχήμα, οι συγκεντρώσεις των O_2, N_2, *H*, *O* και *OH* μέσα στη ζώνη βρίσκονται σε χημική ισορροπία.

Στη συνέχεια, ο μηχανισμός σχηματισμού των *NO* που χρησιμοποιείται από το παρόν μοντέλο για τον υπολογισμό του αριθμού των mole του *NO [kmol]* σε κάθε ζώνη (*z*) και βήμα *CA* (*i*) συνοψίζεται στην Εξ. (3.40):

$$\left(\frac{dNO}{d\theta}\right)_{z_i} = \left(\frac{d[NO]}{dt}\right)_{z_i} \cdot V_{z_i} \cdot \frac{dt}{d\theta} = 2\cdot(1-\alpha^2)\cdot\frac{R_1^{eq}}{1+\alpha\cdot\frac{R_1^{eq}}{R_2^{eq}+R_3^{eq}}}\cdot\frac{V_{z_i}}{6\cdot N} \tag{3.40}$$

όπου [*NO*] είναι η συγκέντρωση των *NO [kmol/m^3]*, *V [m^3]* ο όγκος της κάθε ζώνης, *N [rpm]* είναι οι στροφές του κινητήρα, *α* είναι ο λόγος $\frac{[NO]}{[NO]_{eq}}$ (όπου ο δείκτης *eq* υποδηλώνει την χημική ισορροπία) και R^{eq} *[kmol/m^3/s]* είναι οι ρυθμοί αντίδρασης ισορροπίας που υπολογίζονται με τη χρήση των συστάσεων χημικής ισορροπίας *[kmol/m^3]* των εμπεριεχομένων στη ζώνη στοιχείων και των αντίστοιχων σταθερών του ρυθμού χημικής ισορροπίας (*k [m^3/kmol/s]*) της κάθε αντίδρασης του Πίνακα 3.1. Οι σταθερές αυτές προέρχονται από τις πειραματικές μελέτες των R. K. Hanson και S. Salimian που παρουσιάζονται στην αναφορά [236]. Το στιγμιαίο ποσό των *NO [Kmol]* που σχηματίζονται σε κάθε ζώνη υπολογίζεται από την ολοκλήρωση της Εξ. (3.40) στον κύκλο (σύμφωνα με το βήμα *CA dθ*), μέχρι το *EVO*, χρησιμοποιώντας τη μέθοδο Euler [237]. Με αυτό τον τρόπο, λαμβάνεται το ιστορικό σχηματισμού του *NO* της κάθε ζώνης. Αθροίζοντας τα *NO* που περιέχονται σε όλες τις ζώνες, σε κάθε χρονικό βήμα *CA* (*i*), προκύπτει το ιστορικό των *NO* του κυλίνδρου. Έτσι στο *EVO* το άθροισμα αυτό δίνει τις τελικές εκπομπές *NO [Kmol]*.

Βαθμονόμηση του Μοντέλου

Παρόλο που το μοντέλο συλλαμβάνει την τάση του *NO* που σχηματίζεται στους οδικούς κινητήρες και στους κινητήρες μεγάλης κλίμακας που εξετάστηκαν, όταν οι λειτουργικές τους παράμετροι ή οι ρυθμίσεις τους τροποποιήθηκαν, εφαρμόστηκε ένας πολλαπλασιαστής κλίμακας (*SF*) (μόνο στους κινητήρες μεγάλης κλίμακας) στις εξαγόμενες από το μοντέλο τιμές, όπως περιγράφεται την Εξ. (3.41) ώστε τα αποτελέσματα να βελτιωθούν ποσοτικά. Αυτός ο πολλαπλασιαστής είναι σταθερός και μοναδικός για κάθε κινητήρα και υπολογίζεται από τον λόγο της μετρημένης και υπολογισμένης τιμής των *NO*, σε ένα συγκεκριμένο σημείο λειτουργίας (σημείο βαθμονόμησης (*c*)), όπως περιγράφεται στην Εξ. (3.42):

$$calibr.NOx_{eng,i} = calc.NOx_{eng,i} \cdot SF_{eng} \tag{3.41}$$

$$SF_{eng} = \frac{meas.NOx_{eng,i=c}}{calc.NOx_{eng,i=c}} \tag{3.42}$$

όπου οι δείκτες *i* και *eng* δηλώνουν το σημείο λειτουργίας και τον εξεταζόμενο κινητήρα αντίστοιχα.

Στους οδικούς κινητήρες που εξετάστηκαν δεν χρησιμοποιείται ο πολλαπλασιαστής αυτός για τη διόρθωση των αποτελεσμάτων, μιας και η μέση τιμή των λόγων μετρημένων προς υπολογισμένων τιμών (Εξ. (3.42)) προσεγγίζει τη μονάδα. Τα αποτελέσματα του μοντέλου παρουσιάζονται στο επόμενο κεφάλαιο.

Κεφάλαιο 4 ΕΦΑΡΜΟΓΗ ΤΟΥ ΠΡΟΤΕΙΝΟΜΕΝΟΥ ΜΟΝΤΕΛΟΥ

Εφαρμογή του Μοντέλου σε Κινητήρες Μεγάλης Κλίμακας

Τα αποτελέσματα από την εφαρμογή του προτεινόμενου μοντέλου παρουσιάζονται στο τέταρτο κεφάλαιο. Αρχικά, εξετάζεται η ικανότητα του μοντέλου να προβλέπει τις εκπομπές NO_x στους κινητήρες μεγάλης κλίμακας, καθώς το φορτίο/στροφές του κινητήρα, η προπορεία έγχυσης καυσίμου και ο τύπος του καυσίμου μεταβάλλονται.

Οι μετρήσεις που χρησιμοποιήθηκαν, λήφθηκαν σε πλοία και σε ηλεκτροπαραγωγούς σταθμούς δύο ελληνικών νησιών [56], σε πραγματικές συνθήκες, από την ερευνητική ομάδα του εργαστηρίου μηχανών εσωτερικής καύσης (*ICE*) του *ΕΜΠ*. Οι μετρήσεις πραγματοποιήθηκαν σε δεκαέξι διαφορετικούς κινητήρες Diesel μεγάλης κλίμακας. Αυτοί οι κινητήρες κατηγοριοποιούνται σε δίχρονους και τετράχρονους, σταθερών και μεταβλητών στροφών. Χρησιμοποιήθηκαν συνολικά *89* περιπτώσεις/σημεία λειτουργίας.

Οι μετρήσεις πραγματοποιήθηκαν με τη χρήση συστήματος συσκευής και λογισμικού που αναπτύχθηκε στο εργαστήριο. Το σύστημα χρησιμοποιήθηκε, επίσης, για την επεξεργασία των μετρημένων δεδομένων, την εκτίμηση της ισχύος και την κατανάλωση καυσίμου του κινητήρα. Η μεθοδολογία που χρησιμοποιήθηκε έχει εγκριθεί από την *MARPOL* [208]. Οι μετρήσεις των αέριων ρύπων (O_2, CO_2, CO, NO_x, SO_2, H_2O) στα καυσαέρια έγιναν με τη βοήθεια του φορητού αναλυτή "*Testo 350 maritime*", ο οποίος είναι επίσης εγκεκριμένος από την *MARPOL* [244].

Στη συνέχεια αξιολογείται η ικανότητα του προτεινόμενου μοντέλου να συλλαμβάνει την τάση των εκπομπών NO_x με τη μεταβολή της ισχύος του κινητήρα (δηλ. του φορτίου), αλλά και να προσεγγίζει επαρκώς τις απόλυτες τιμές των εκπομπών των NO_x για τους κινητήρες μεγάλης κλίμακας.

Αρχικά παρουσιάζονται τα αποτελέσματα για τους κινητήρες των σταθμών παραγωγής ενέργειας οι οποίοι λειτουργούν σε σταθερές στροφές. Για τον κινητήρα Α, ο ο-

ποίος είναι δίχρονος, δύο σειρές μετρήσεων ήταν διαθέσιμες, οι οποίες έγιναν σε διαφορετικές περιόδους με διαφορετικές ρυθμίσεις του κινητήρα και συνθήκες περιβάλλοντος. Τα αποτελέσματα απεικονίζονται στο Σχ. 4.1 και Σχ. 4.2:

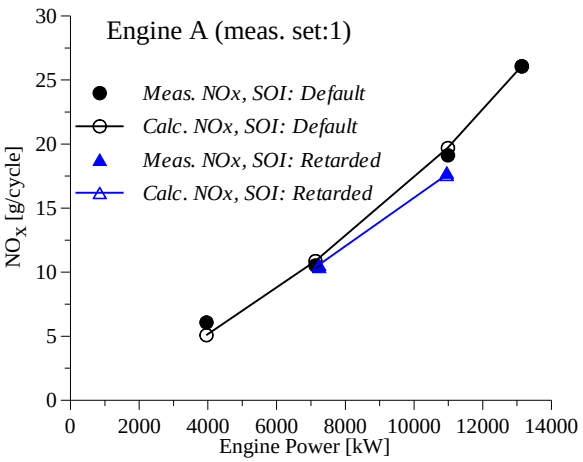

Σχήμα 4.1: Πρώτη σειρά μετρήσεων για τον κινητήρα Α. Υπολογισμένες και μετρημένες τιμές NO_x έναντι της ισχύος του κινητήρα για δύο διαφορετικές ρυθμίσεις προπορείας.

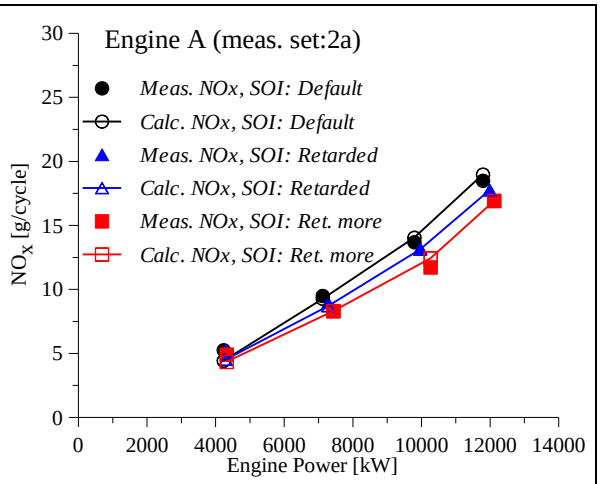

Σχήμα 4.2: Δεύτερη σειρά μετρήσεων (2_a) για τον κινητήρα Α. Υπολογισμένες και μετρημένες τιμές NO_x έναντι της ισχύος του κινητήρα για δύο διαφορετικές ρυθμίσεις προπορείας.

Τα αποτελέσματα για τον κινητήρα Β, ο οποίος είναι του ίδιου τύπου με τον Α, παρουσιάζονται στο Σχ. 4.3. Σε αυτά τα σχήματα φαίνεται ότι, παρά τη μικρή μείωση των NO_x με την καθυστέρηση έγχυσης, το μοντέλο μπορεί να συλλάβει αυτή τη μεταβολή.

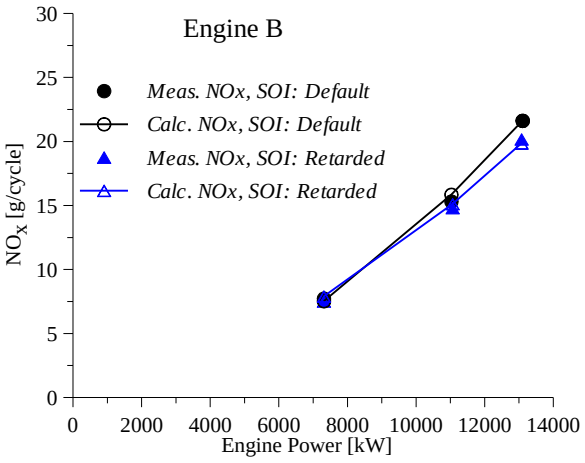

Σχήμα 4.3: Υπολογισμένες και μετρημένες τιμές NO_x έναντι της ισχύος του κινητήρα για δύο διαφορετικές ρυθμίσεις προπορείας για τον κινητήρα Β.

Στο Σχ. 4.4 και Σχ. 4.5 φαίνονται τα αποτελέσματα για τον κινητήρα J, ο οποίος είναι του ίδιου τύπου με τους κινητήρες Α και Β (με δύο κυλίνδρους λιγότερους) και για τον τετράχρονο κινητήρα Ρ. Το συμπέρασμα από αυτά τα σχήματα είναι ότι το μοντέλο κατα-

φέρνει να συλλάβει τη μεταβολή των NO_x με την ισχύ του κινητήρα και για τους δύο κινητήρες (J and P). Επιπλέον, από τα Σχ. 4.1 – 4.5 συνάγεται ότι τα NO_x αυξάνονται ανάλογα με το φορτίο του κινητήρα, όπως αναμενόταν.

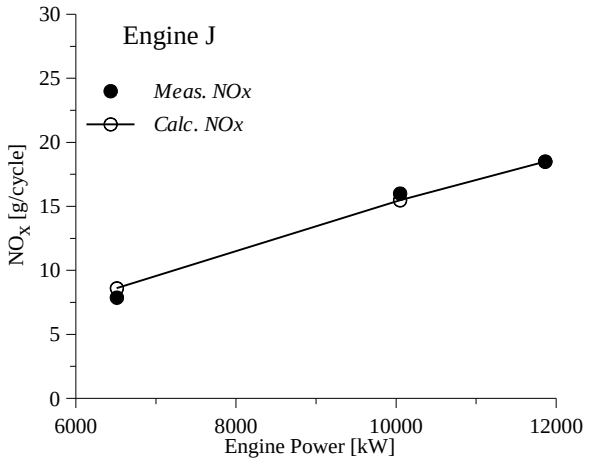

Σχήμα 4.4: Υπολογισμένες και μετρημένες τιμές NO_x έναντι της ισχύος για τον κινητήρα J.

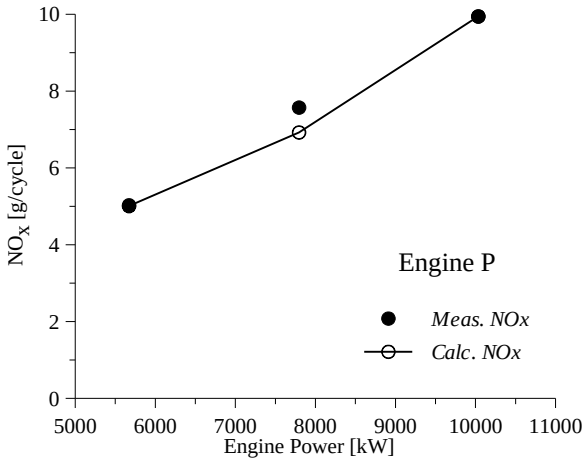

Σχήμα 4.5: Υπολογισμένες και μετρημένες τιμές NO_x έναντι της ισχύος για τον κινητήρα P.

Στη συνέχεια παρουσιάζονται τα αποτελέσματα για τους δίχρονους κινητήρες πρόωσης πλοίων που εξετάστηκαν. Στο Σχ. 4.6 παρουσιάζονται τα αποτελέσματα τριών τέτοιων κινητήρων του ίδιου τύπου (D, E και L) αλλά εγκατεστημένων σε διαφορετικά πλοία. Το Σχ. 4.6, δείχνει ότι παρόλο που οι τιμές των NO_x διαφέρουν για κάθε κινητήρα, η μεταβολή των NO_x έναντι του φορτίου είναι όμοια για τους κινητήρες D και E σε αντίθεση με τον κινητήρα L που παρουσιάζει πιο απότομη μεταβολή. Όπως φαίνεται το μοντέλο μπορεί να συλλάβει αυτές τις μεταβολές ικανοποιητικά.

Στο Σχ. 4.7, δύο διαφορετικές σειρές μετρήσεων για τον κινητήρα K είναι διαθέσιμες: εν–πλω μετρήσεις και μετρήσεις εργαστηρίου (shop–test). Όπως φαίνεται στο Σχ. 4.7 η μεταβολή των NO_x με το φορτίο του κινητήρα στην πρώτη περίπτωση είναι ελαφρώς πιο απότομη. Στη συνέχεια, στα Σχ. 4.8 – 4.12 παρουσιάζονται τα αποτελέσματα της εφαρμογής του μοντέλου στους κινητήρες C και F – I που είναι, επίσης, δίχρονοι κινητήρες πρόωσης πλοίου. Είναι εμφανής η αύξηση των NO_x με την αύξηση του φορτίου αλλά με διαφορετική κλίση αναλόγως της περίπτωσης και του κινητήρα. Ειδικά στο Σχ. 4.11, φαίνεται η αύξηση

των NO_x λόγω αύξησης της προπορείας εγχύσεως του κινητήρα. Όπως αποδεικνύεται το μοντέλο προσεγγίζει ικανοποιητικά τις τάσεις και τις απόλυτες τιμές των πειραματικών NO_x.

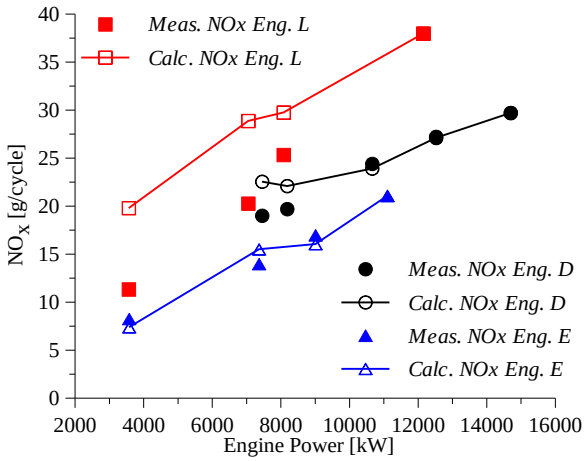

Σχήμα 4.6: Υπολογισμένες και μετρημένες τιμές NO_x έναντι της ισχύος για τους κινητήρες D, E, και L.

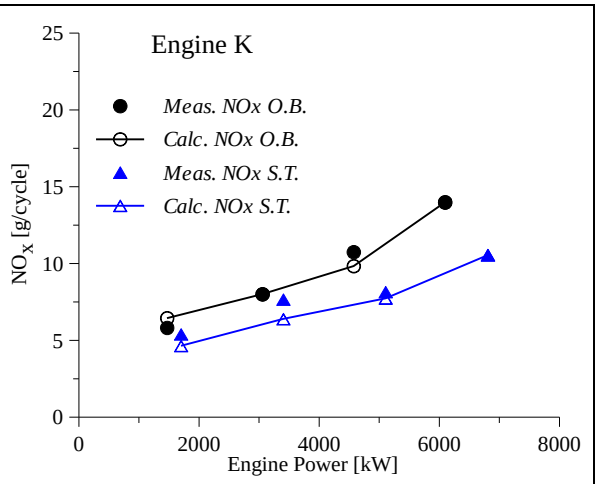

Σχήμα 4.7: Υπολογισμένες και μετρημένες τιμές NO_x έναντι της ισχύος για τον κινητήρα K: μετρήσεις εν–πλω (O.B.) και εργαστηριακές μετρήσεις (S.T.).

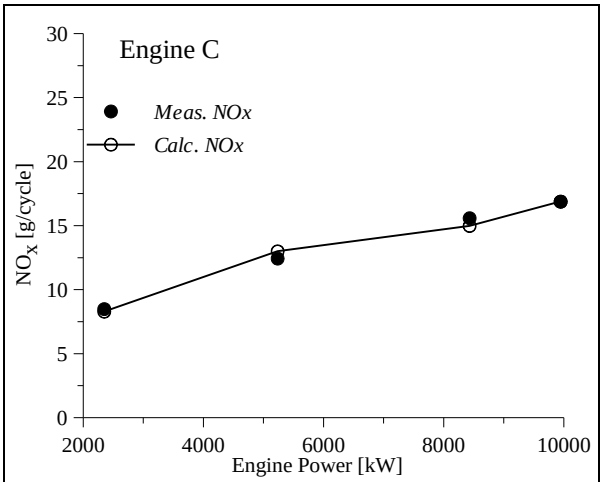

Σχήμα 4.8: Υπολογισμένες και μετρημένες τιμές NO_x έναντι της ισχύος για τον κινητήρα C.

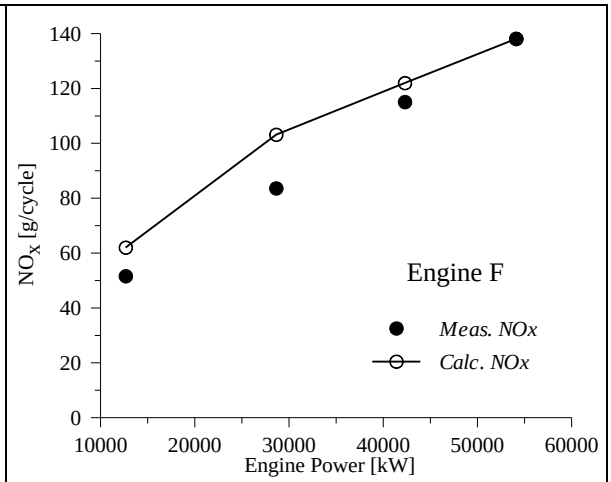

Σχήμα 4.9: Υπολογισμένες και μετρημένες τιμές NO_x έναντι της ισχύος για τον κινητήρα F.

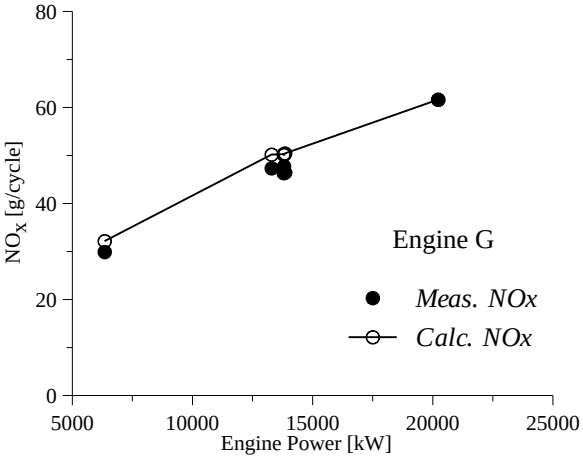

Σχήμα 4.10: Υπολογισμένες και μετρημένες τιμές NO_x έναντι της ισχύος για τον κινητήρα G.

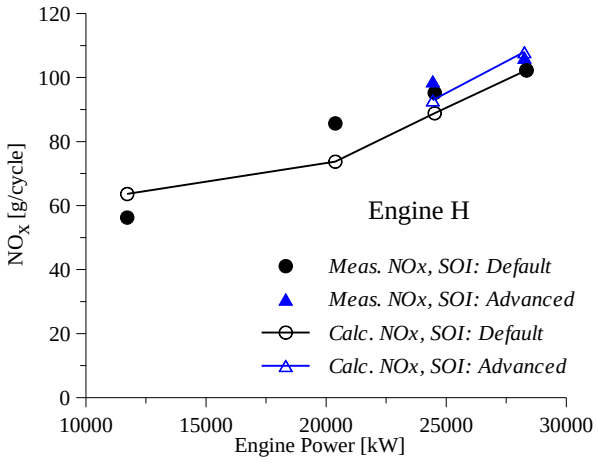

Σχήμα 4.11: Υπολογισμένες και μετρημένες τιμές NO_x έναντι της ισχύος για τον κινητήρα H για δύο διαφορετικές ρυθμίσεις προπορείας.

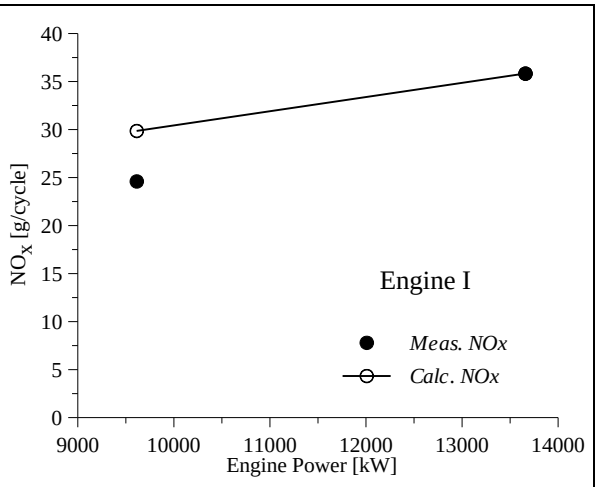

Σχήμα 4.12: Υπολογισμένες και μετρημένες τιμές NO_x έναντι της ισχύος για τον κινητήρα I.

Στο Σχ. 4.13 – 4.15 παρουσιάζονται τα αποτελέσματα για τρεις τετράχρονους κινητήρες Diesel σταθερών στροφών (M, N, O αντίστοιχα) που είναι εγκατεστημένοι σε διαφορετικά πλοία και χρησιμοποιούνται για την παραγωγή ηλεκτρισμού για τις ανάγκες του

πλοίου. Από τα γραφήματα αυτά, αποδεικνύεται η ικανότητα του μοντέλου να συλλαμβάνει και τις τάσεις και τις απόλυτες τιμές για αυτόν τον τύπο κινητήρων.

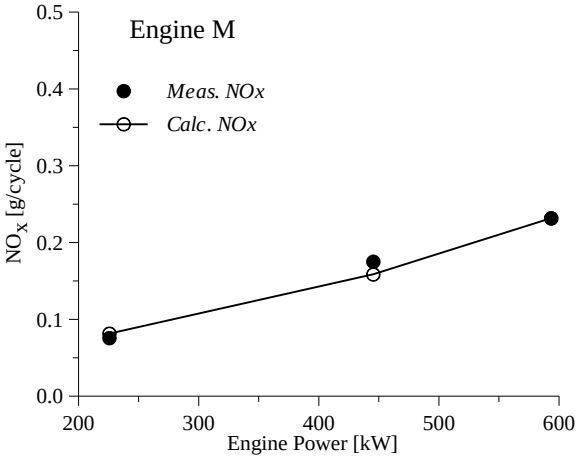

Σχήμα 4.13: Υπολογισμένες και μετρημένες τιμές NO_x έναντι της ισχύος για τον κινητήρα Μ.

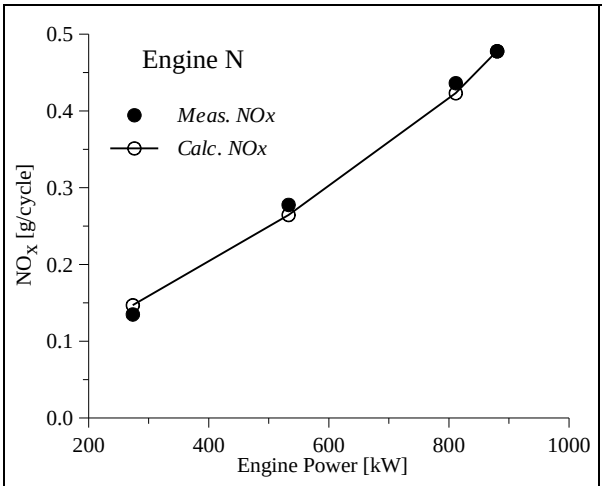

Σχήμα 4.14: Υπολογισμένες και μετρημένες τιμές NO_x έναντι της ισχύος για τον κινητήρα Ν.

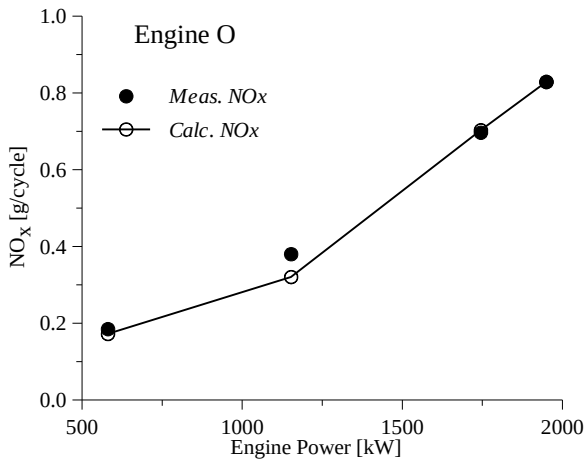

Σχήμα 4.15: Υπολογισμένες και μετρημένες τιμές NO_x έναντι της ισχύος για τον κινητήρα Ο.

Το γενικό συμπέρασμα από την παρατήρηση των Σχ. 4.1 – 4.15 είναι η σχεδόν γραμμική μεταβολή των NO_x με το φορτίο του κινητήρα. Επίσης, αποδεικνύεται η ικανότητα του μοντέλου να προβλέπει τόσο τις τάσεις όσο και τις απόλυτες τιμές των NO_x έναντι του φορτίου του κινητήρα και για τους δύο τύπους κινητήρων που εξετάστηκαν, δηλ. δίχρονους και τετράχρονους.

Στη συνέχεια, εξετάζεται η ικανότητα του μοντέλου να συλλαμβάνει τη μεταβολή του NO_x με την αλλαγή της προπορείας έγχυσης στους κινητήρες μεγάλης κλίμακας. Η μείωση της προπορείας έγχυσης είναι συνήθης πρακτική για τη μείωση των NO_x σε αυτές τις εφαρμογές. Η αλλαγή της προπορείας έγχυσης αντικατοπτρίζεται στην αλλαγή της γωνίας στροφάλου όπου ξεκινά η καύση (*SOC*).

Τα αποτελέσματα για τους δίχρονους κινητήρες ηλεκτροπαραγωγής (σταθερών στροφών) φαίνονται στα Σχ. 4.16 – 4.18. Σε αυτούς τους κινητήρες έχει γίνει καθυστέρηση

έγχυσης (μείωση προπορείας) μέχρι και ~3 ^oCA για διάφορα φορτία. Τα αποτελέσματα υποδεικνύουν μια σχεδόν γραμμική μεταβολή (μείωση) των NO_x με την καθυστέρηση έγχυσης. Παρατηρείται, επίσης, ότι η κλίση αυτής της μεταβολής γίνεται ελαφρώς πιο απότομη με την αύξηση του φορτίου.

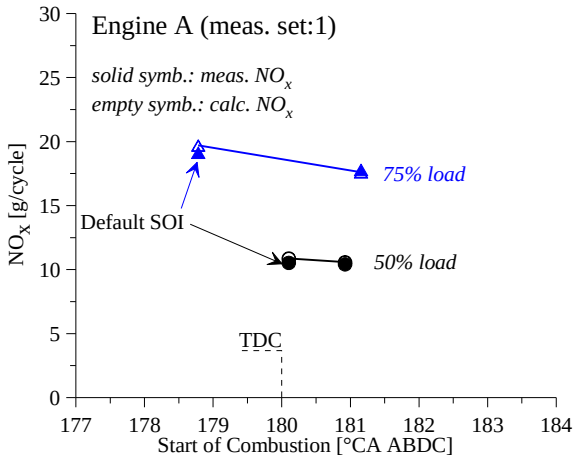

Σχήμα 4.16: Υπολογισμένες και μετρημένες τιμές NO_x έναντι της αρχής της καύσης (SOC) για τον κινητήρα Α: 1η σειρά μετρήσεων.

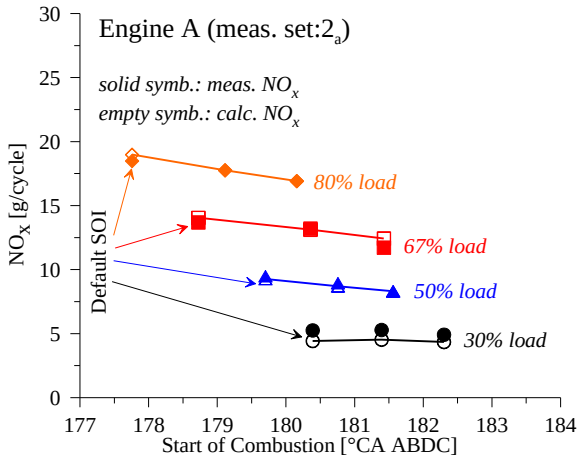

Σχήμα 4.17: Υπολογισμένες και μετρημένες τιμές NO_x έναντι της αρχής της καύσης (SOC) για τον κινητήρα Α: 2η σειρά μετρήσεων (2_a).

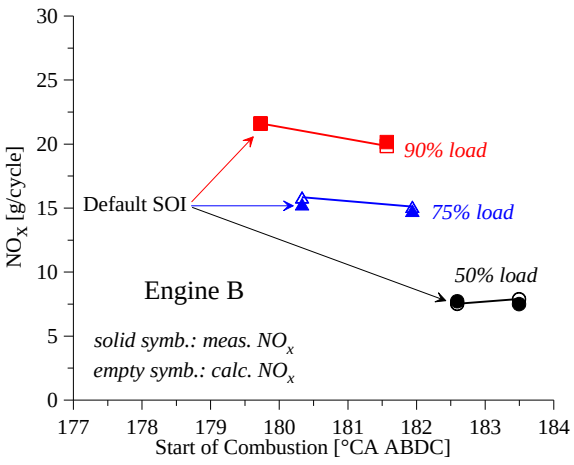

Σχήμα 4.18: Υπολογισμένες και μετρημένες τιμές NO_x έναντι της αρχής της καύσης (SOC) για τον κινητήρα Β.

Τα αποτελέσματα για τους ναυτικούς κινητήρες πρόωσης G και H (μεταβλητών στροφών) απεικονίζονται στο Σχ. 4.19 και 4.20 αντιστοίχως. Από το Σχ. 4.19, φαίνεται πως δεν υπάρχει ουσιαστική μεταβολή των NO_x με την προπορεία έγχυσης. Για τον κινητήρα H

το μοντέλο προσεγγίζει ικανοποιητικά την τάση των NO_x καθώς η προπορεία έγχυσης μεταβάλλεται.

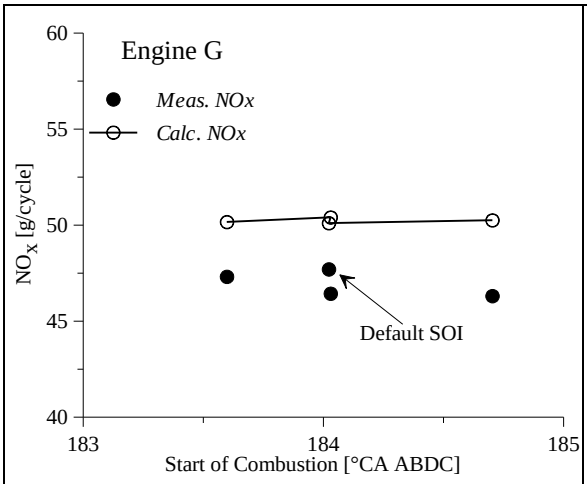

Σχήμα 4.19: Υπολογισμένες και μετρημένες τιμές NO_x έναντι της αρχής της καύσης (SOC) για τον κινητήρα G.

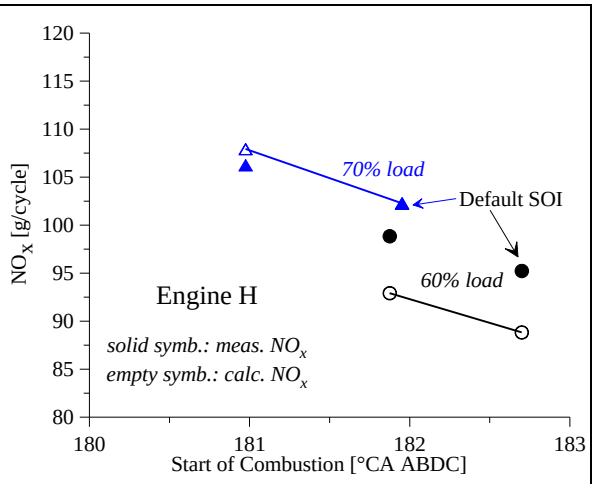

Σχήμα 4.20: Υπολογισμένες και μετρημένες τιμές NO_x έναντι της αρχής της καύσης (SOC) για τον κινητήρα H.

Στη συνέχεια, εξετάζεται η μεταβολή των εκπομπών NO_x όταν ο τύπος του καυσίμου αλλάζει από *HFO* σε *DFO* (κατά τη διάρκεια της λειτουργίας του κινητήρα). Στο Σχ. 4.21, απεικονίζεται η μεταβολή των NO_x με την αύξηση του περιεχομένου του καυσίμου σε *DFO*:

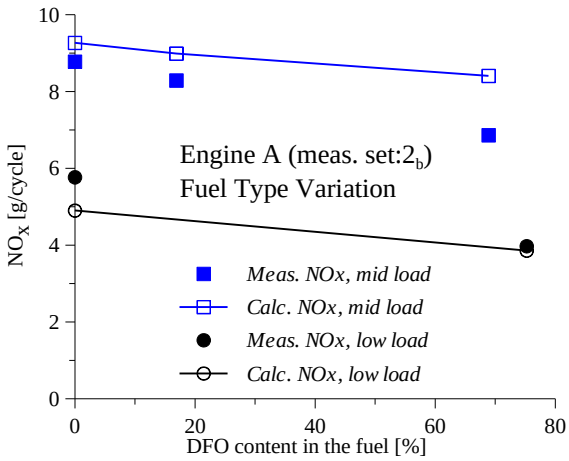

Σχήμα 4.21: Υπολογισμένες και μετρημένες τιμές NO_x έναντι του περιεχομένου του καυσίμου σε DFO στον κινητήρα A.

Από το Σχ. 4.21, αποδεικνύεται η ικανότητα του μοντέλου να προσεγγίζει ικανοποιητικά την τάση και τις απόλυτες τιμές των NO_x, καθώς το κλάσμα μάζας του *DFO* στο καύσιμο αυξάνεται ενώ το αντίστοιχο του *HFO* μειώνεται.

Εν τέλει, παρουσιάζεται η στατιστική ανάλυση του συνόλου (*89*) των περιπτώσεων (*i*) που εξετάστηκαν προκειμένου να αξιολογηθούν τα αποτελέσματα του μοντέλου. Για το λόγο αυτό, υπολογίζεται το απόλυτο ($Error_{ABS}$) και σχετικό σφάλμα ($Error_{REL}$ *[%]*)

μεταξύ των υπολογισμένων από το μοντέλο (*calibr.NO_x*) και των αντίστοιχων μετρημένων τιμών NO_x (*meas.NO_x*), από τις Εξ. (4.1) και (4.2) αντίστοιχα:

$$ERROR_{ABS_i} = calibr.NOx_i - meas.NOx_i \quad (4.1)$$

$$ERROR_{REL_i} = \frac{calibr.NOx_i - meas.NOx_i}{meas.NOx_i} \cdot 100 \quad (4.2)$$

Στον Πίνακα 4.1 παρουσιάζεται το ποσοστό από τις περιπτώσεις που εξετάστηκαν, των οποίων το σφάλμα εμπίπτει σε μια συγκεκριμένη ζώνη σφάλματος:

Περιπτώσεις	Σχετικό σφάλμα (±)	Απόλυτο σφάλμα (±)		
[%]	[%]	[g/cycle]	[g/kg fuel]	[g/kWh]
24	0–0	0–0.0	0–0.5	0–0.1
49	0–5	0–0.5	0–2.5	0–0.5
74	0–10	0–1.0	0–6.8	0–1.3
85	0–15	0–3.5	0–9.9	0–1.9
93	0–20	0–7.0	0–13.6	0–2.6
98	0–25	0–10.4	0–15.4	0–3.1

Πίνακας 4.1: Ανάλυση σχετικού και απόλυτου σφάλματος των αποτελεσμάτων του μοντέλου για τους κινητήρες μεγάλης κλίμακας που εξετάστηκαν.

Όπως φαίνεται στον Πίνακα 4.1, περίπου το *74%* των περιπτώσεων που εξετάστηκαν παρουσιάζουν σχετικό σφάλμα μεταξύ του *±10%* το οποίο θεωρείται ικανοποιητικό.

Εφαρμογή του Μοντέλου σε Οδικούς Κινητήρες

Στη συνέχεια, το μοντέλο εφαρμόστηκε στους ακόλουθους οδικούς κινητήρες Diesel: ένα φορτηγού βαρέος τύπου (D1) και ένα αυτοκινήτου (D2). Και οι δύο αυτοί κινητήρες είναι υπερπληρωμένοι, τετράχρονοι, χρησιμοποιούν σύστημα άμεσης έγχυσης (*DI*) και κοινού αυλού και ανακυκλοφορία καυσαερίων (*EGR*) για τον έλεγχο των εκπομπών NO_x. Επιπλέον, ο κινητήρας του αυτοκινήτου χρησιμοποιεί πιλοτική έγχυση καυσίμου.

Οι μετρήσεις για αυτές τις μηχανές, είναι εργαστηριακές και λήφθηκαν στα πλαίσια ενός ευρωπαϊκού προγράμματος στις εγκαταστάσεις της *AVL* και του *ETH* και χρησιμοποιήθηκαν για την αξιολόγηση του μοντέλου όσον αφορά στις προβλέψεις των εκπομπών *NO* στους οδικούς κινητήρες.

Για τον κινητήρα D1 εξετάστηκαν τα *35* σημεία λειτουργίας που ορίζονται από τον κύκλο Extended European Stationary Cycle (*EESC*) και επιπλέον για το σημείο λειτουργίας μέσου φορτίου και στροφών (*1800 rpm / 86 kW*) εξετάστηκαν τα σημεία (*25*) που προκύπτουν από τη μεταβολή της ρύθμισης του χρονισμού της έγχυσης καυσίμου (*SOI*), του ποσοστού *EGR*, της πίεσης έγχυσης και της πίεσης σάρωσης.

Για τον κινητήρα D2, εξετάστηκαν τα σημεία (*72*) που προκύπτουν από τη μεταβολή της ρύθμισης του χρονισμού της έγχυσης καυσίμου (*SOI*), του ποσοστού *EGR*, της πίεσης έγχυσης και της πίεσης σάρωσης για τα ακόλουθα τρία σημεία λειτουργίας: *2000 rpm* και *29.4 kW*, *2500 rpm* και *18.3 kW* και *2500 rpm* και *31.4 kW*.

Αρχικά παρουσιάζονται τα αποτελέσματα του μοντέλου από την εφαρμογή του στον κινητήρα D1. Πρώτα εξετάζονται τα σημεία λειτουργίας που καθορίζονται από τον κύκλο *EESC*. Η σύγκριση των υπολογισμένων και μετρημένων τιμών των *NO* σε συνάρτηση με το φορτίο του κινητήρα για διάφορες στροφές από *1400 – 2200 rpm*, παρουσιάζεται στα Σχ. 4.22 – 4.26:

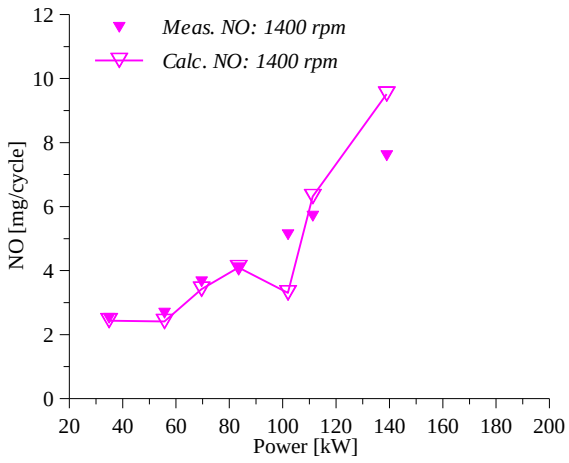

Σχήμα 4.22: Μεταβολή των NO με το φορτίο στις 1400 rpm για τον κινητήρα D1.

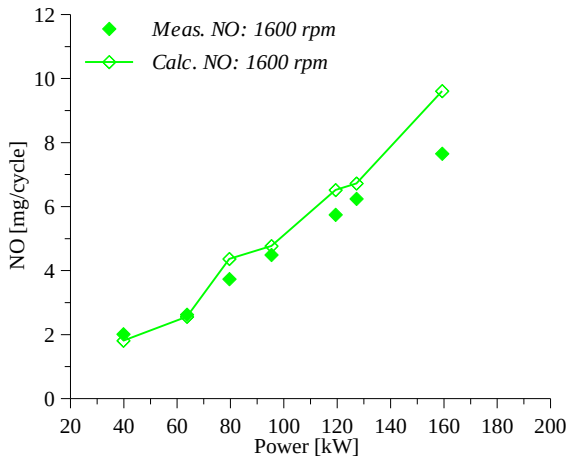

Σχήμα 4.23: Μεταβολή των NO με το φορτίο στις 1600 rpm για τον κινητήρα D1.

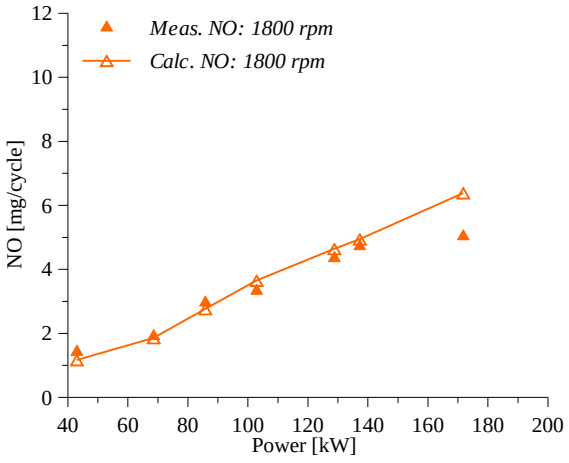

Σχήμα 4.24: Μεταβολή των NO με το φορτίο στις 1800 rpm για τον κινητήρα D1.

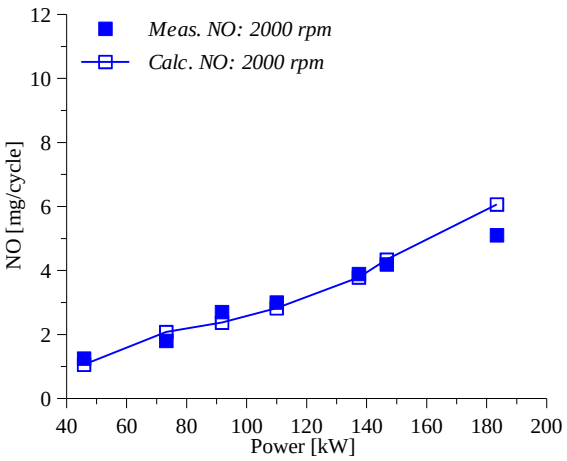

Σχήμα 4.25: Μεταβολή των NO με το φορτίο στις 2000 rpm για τον κινητήρα D1..

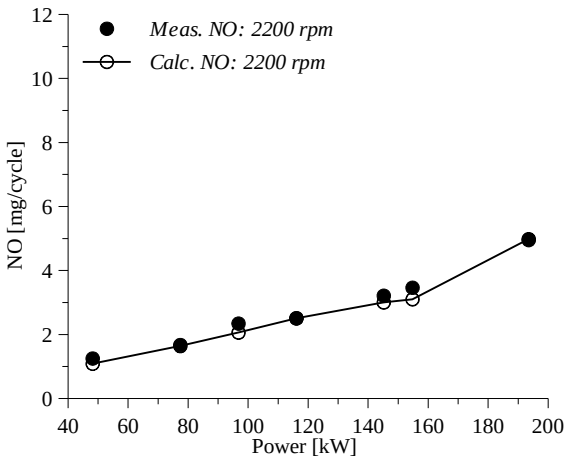

Σχήμα 4.26: Μεταβολή των NO με το φορτίο στις 2200 rpm για τον κινητήρα D1.

Από τα Σχ. 4.22 – 4.26 αποδεικνύεται ότι το προτεινόμενο μοντέλο συλλαμβάνει την τάση της μεταβολής των *NO* με το φορτίο. Η τάση αυτή είναι σχεδόν γραμμική και μειώνεται με την αύξηση της ταχύτητας του κινητήρα. Επίσης, το μοντέλο προσεγγίζει ικανοποιητικά και τις απόλυτες τιμές των *NO* στα περισσότερα σημεία λειτουργίας που εξετάστηκαν.

Στη συνέχεια, εξετάζεται η ικανότητα του μοντέλου να συλλάβει τη μεταβολή του *NO* για διαφορετικές ρυθμίσεις του κινητήρα, δηλ. του *SOI*, του ποσοστού ανακυκλοφορίας καυσαερίων (*EGR*), της πίεσης έγχυσης καυσίμου και της πίεσης αέρα στην πολλαπλή εισαγωγής. Στο Σχ. 4.27– 4.30, απεικονίζεται η σύγκριση των τιμών *NO* όπως υπολογίστηκαν από το μοντέλο, και των αντίστοιχων μετρημένων για τις μεταβολές των προαναφερθεισών παραμέτρων:

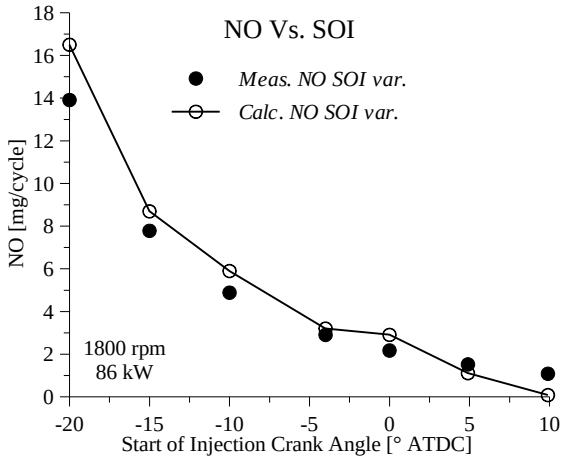

Σχήμα 4.27: Μεταβολή των NO με την ρύθμιση SOI στις 1800 rpm & 86 kW για τον κινητήρα D1.

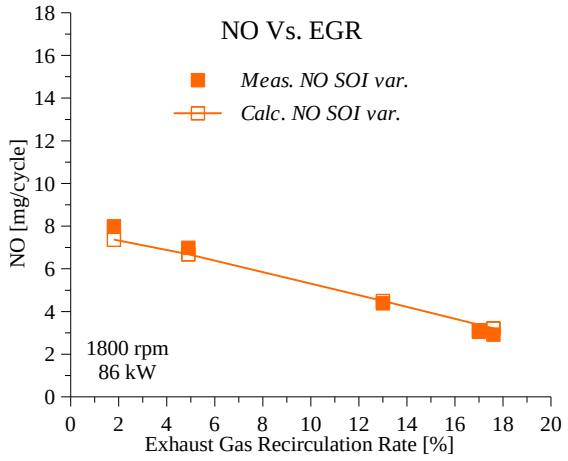

Σχήμα 4.28: Μεταβολή των NO με το ποσοστό EGR στις 1800 rpm & 86 kW για τον κινητήρα D1.

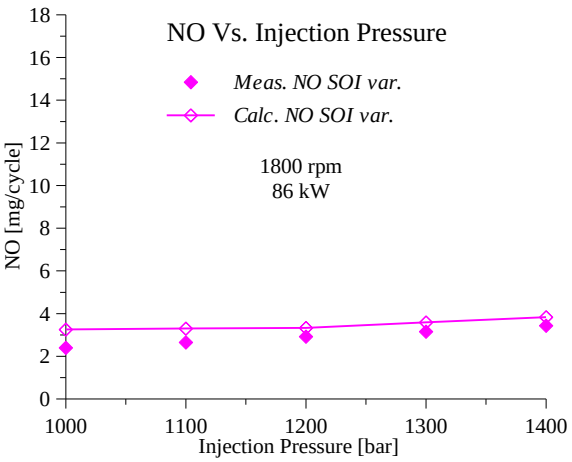

Σχήμα 4.29: Μεταβολή των NO με την πίεση έγχυσης καυσίμου στις 1800 rpm & 86 kW για τον κινητήρα D1.

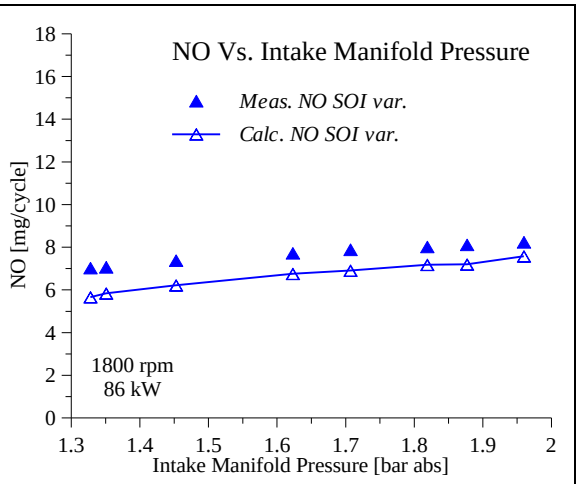

Σχήμα 4.30: Μεταβολή των NO με την πίεση αέρα στην πολλαπλή εισαγωγής στις 1800 rpm & 86 kW για τον κινητήρα D1.

Από τα Σχ. 4.27– 4.30 συνάγεται ότι το μοντέλο είναι ικανό να συλλάβει την τάση των *NO* όταν μεταβάλλεται το *SOI*, το ποσοστό *EGR*, η πίεση έγχυσης καυσίμου και η πίεση στην πολλαπλή εισαγωγής (πίεση σάρωσης). Οι απόλυτες τιμές των *NO* προσεγγίζονται ικανοποιητικά. Όπως φαίνεται στο Σχ. 4.27 οι εκπομπές των *NO* μειώνονται εκθετικά με την καθυστέρηση έγχυσης. Στο Σχ. 4.28, φαίνεται μια γραμμική μείωση των *NO* με την αύξηση του ποσοστού *EGR*. Επιπλέον, στο Σχ. 4.29 φαίνεται ότι η αύξηση της πίεσης έγχυσης προκαλεί μια γραμμική αύξηση των *NO*. Επίσης από το Σχ. 4.30 φαίνεται μια γραμμική αύξηση των *NO* με την αύξηση της πίεσης του αέρα σάρωσης.

Στη συνέχεια υπολογίζεται το απόλυτο και σχετικό σφάλμα (Εξ. (4.1) και (4.2)) των αποτελεσμάτων του μοντέλου για τον κινητήρα D1. Στον Πίνακα 4.2, παρουσιάζεται το ποσοστό από τις περιπτώσεις που εξετάστηκαν, των οποίων το σφάλμα εμπίπτει σε μια συγκεκριμένη ζώνη σφάλματος:

Περιπτώσεις	Σχετικό σφάλμα (±)	Απόλυτο σφάλμα (±)		
[%]	[%]	[mg/cycle]	[g/kg fuel]	[g/kWh]
5	0–1	0–0.0	0–0.0	0–0.0
22	0–5	0–0.2	0–0.4	0–0.1
42	0–10	0–0.3	0–0.9	0–0.2
68	0–15	0–0.7	0–1.9	0–0.4
83	0–20	0–1.0	0–2.8	0–0.6
87	0–25	0–1.1	0–2.8	0–0.6
93	0–30	0–1.4	0–3.4	0–0.7
98	0–40	0–2.0	0–4.0	0–0.9

Πίνακας 4.2: Ανάλυση σχετικού και απόλυτου σφάλματος των αποτελεσμάτων του μοντέλου για τον κινητήρα D1.

Όπως φαίνεται στον Πίνακα 4.2 το *83%* των περιπτώσεων που εξετάστηκαν παρουσιάζουν σχετικό σφάλμα μέχρι *±20%* το οποίο μπορεί να θεωρηθεί ικανοποιητικό για τη συγκεκριμένη εφαρμογή όπου οι απόλυτες τιμές των *NO* είμαι πολύ χαμηλές (ειδικά όταν συγκρίνονται με αυτές των κινητήρων μεγάλης κλίμακας). Εδώ σημειώνεται ότι δεν έγινε βαθμονόμηση (δηλ. χρήση διορθωτικού πολλαπλασιαστή), όπως έγινε στους κινητήρες μεγάλης κλίμακας.

Στη συνέχεια, εξετάζεται ο κινητήρας ελαφρού τύπου (D2) του επιβατικού αυτοκινήτου. Οι υπολογιζόμενες από το μοντέλο τιμές των *NO* καθώς το ποσοστό του *EGR* μεταβάλλεται, για τρία διαφορετικά σημεία λειτουργίας του κινητήρα αυτού, συγκρίνονται με τις αντίστοιχες πειραματικές και παρουσιάζονται στα Σχ. 4.31 – 4.33:

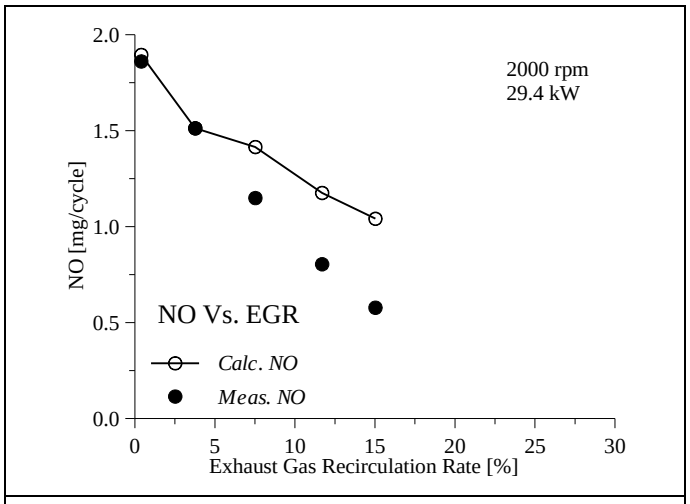

Σχήμα 4.31: Μεταβολή των NO με το ποσοστό EGR στις 2000 rpm & 29.4 kW για τον κινητήρα D2.

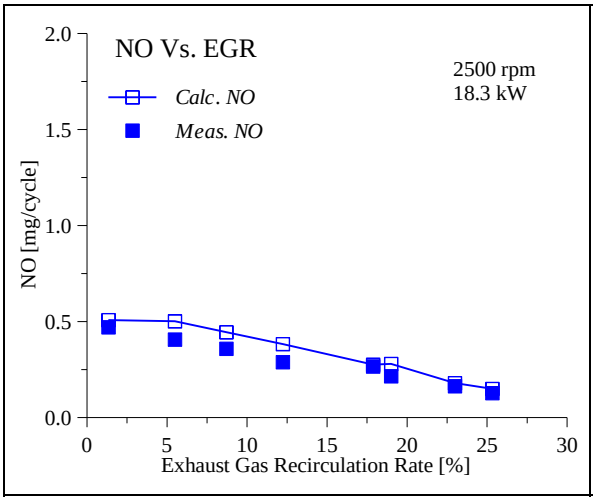

Σχήμα 4.32: Μεταβολή των NO με το ποσοστό EGR στις 2500 rpm & 18.3 kW για τον κινητήρα D2.

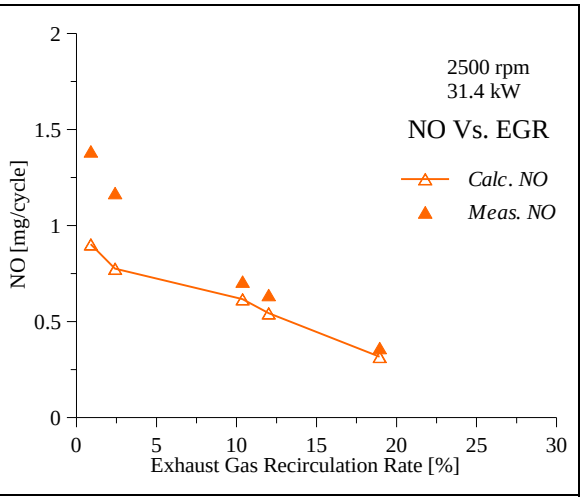

Σχήμα 4.33: Μεταβολή των NO με το ποσοστό EGR στις 2500 rpm & 31.4 kW για τον κινητήρα D2.

Όπως καταδεικνύεται στα πιο πάνω γραφήματα, το μοντέλο επιτυγχάνει να προβλέψει την τάση των *NO* με την μεταβολή του ποσοστού *EGR*. Η τάση αυτή είναι φθίνουσα με την αύξηση του ποσοστού *EGR* και προσεγγιστικά γραμμική. Η κλίση της γίνεται πιο απότομη με την αύξηση του φορτίου (βλ. Σχ. 4.32 και 4.33) και τη μείωση των στροφών του κινητήρα (βλ. Σχ. 4.31 και 4.33).

Η σύγκριση υπολογισμένων και των αντίστοιχων μετρημένων τιμών των εκπομπών *NO*, καθώς η πίεση έγχυσης μεταβάλλεται, για τρία διαφορετικά σημεία λειτουργίας του κινητήρα D2, απεικονίζεται στο Σχ. 4.34 – 4.36:

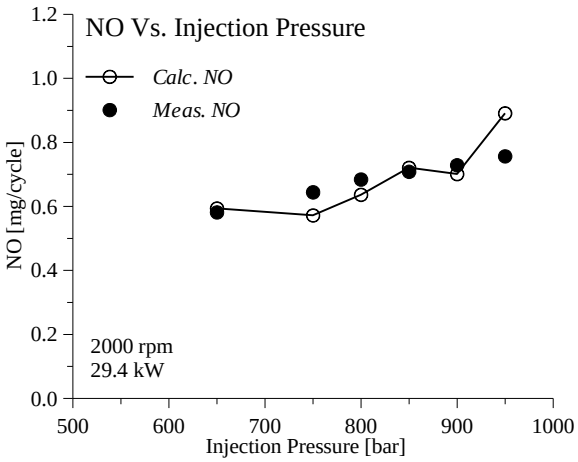

Σχήμα 4.34: Μεταβολή των NO με την πίεση έγχυσης καυσίμου στις 2000 rpm & 29.4 kW για τον κινητήρα D2.

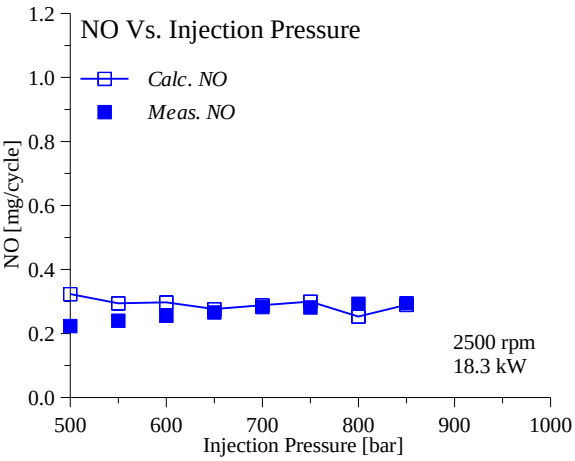

Σχήμα 4.35: Μεταβολή των NO με την πίεση έγχυσης καυσίμου στις 2500 rpm & 18.3 kW για τον κινητήρα D2.

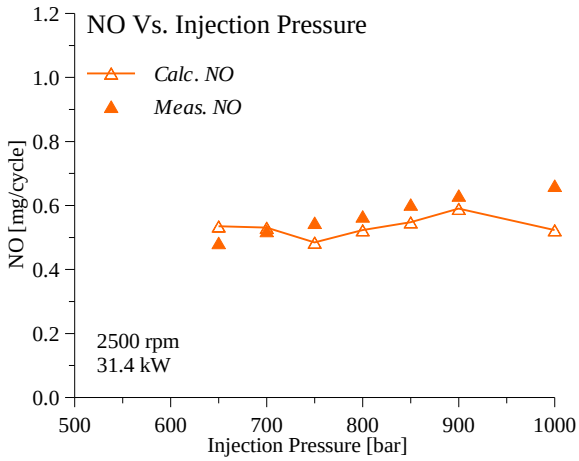

Σχήμα 4.36: Μεταβολή των NO με την πίεση έγχυσης καυσίμου στις 2500 rpm & 31.4 kW για τον κινητήρα D2.

Όπως αποδεικνύεται από τα Σχ. 4.34 – 4.36, το μοντέλο προσεγγίζει αρκετά καλά την τάση των *NO* η οποία είναι προσεγγιστικά γραμμική και ελαφρώς αύξουσα με την αύξηση της πίεσης έγχυσης. Παρόλα αυτά, το μοντέλο αδυνατεί να συλλάβει ιδανικά την τάση των *NO* στις *2500 rpm* όπως φαίνεται στα Σχ. 4.34 – 4.36, παρότι προσεγγίζει πολύ καλά τις απόλυτες τιμές. Αυτό οφείλεται κυρίως στις πολύ μικρές απόλυτες τιμές και στη μικρή μεταβολή των μετρημένων *NO* με την πίεση έγχυσης για το εύρος που εξετάστηκε.

Κατόπιν, γίνεται σύγκριση των υπολογισμένων από το μοντέλο τιμών *NO* με τις αντίστοιχες πειραματικές καθώς ο χρονισμός έγχυσης (*SOI*) μεταβάλλεται, για τρία διαφορετικά σημεία λειτουργίας του κινητήρα D2. Η σύγκριση αυτή παρουσιάζεται στα Σχ. 4.37 – 4.39:

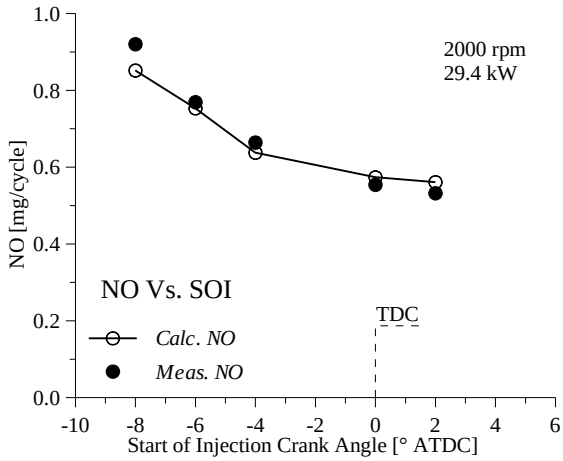

Σχήμα 4.37: Μεταβολή των NO με την ρύθμιση SOI στις 2000 rpm & 29.4 kW για τον κινητήρα D2.

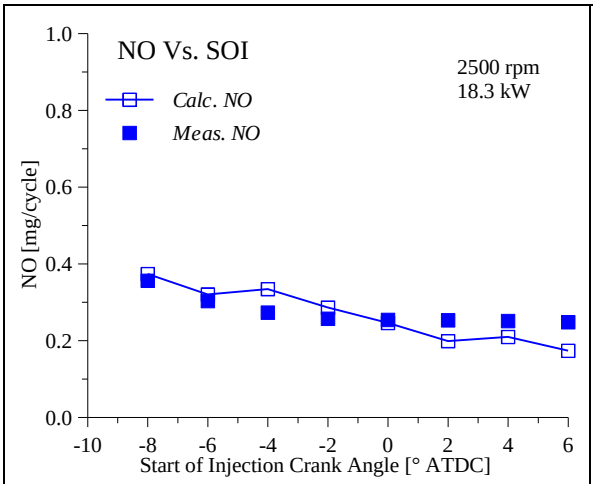

Σχήμα 4.38: Μεταβολή των NO με την ρύθμιση SOI στις 2500 rpm & 18.3 kW για τον κινητήρα D2.

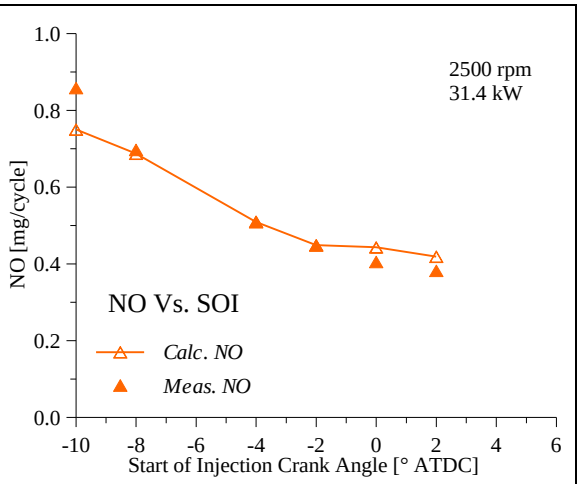

Σχήμα 4.39: Μεταβολή των NO με την ρύθμιση SOI στις 2500 rpm & 31.4 kW για τον κινητήρα D2.

Από τα Σχ. 4.37 – 4.39, αποδεικνύεται η δυνατότητα του μοντέλου να συλλαμβάνει την τάση των *NO* με την μεταβολή του *SOI*. Οι απόλυτες τιμές των *NO*, επίσης, προσεγγίζονται ικανοποιητικά. Όπως φαίνεται, για τα υψηλότερα φορτία η μείωση των εκπομπών *NO* με το *SOI* (μείωση προπορείας) είναι πιο έντονη.

Εν τέλει, στα Σχ. 4.40 – 4.42, απεικονίζεται η σύγκριση των υπολογισμένων από το μοντέλο τιμών των εκπομπών *NO* με τις αντίστοιχες πειραματικές καθώς η πίεση του

αέρα σάρωσης στην πολλαπλή εισαγωγής μεταβάλλεται, για τρία διαφορετικά σημεία λειτουργίας του κινητήρα *D2*:

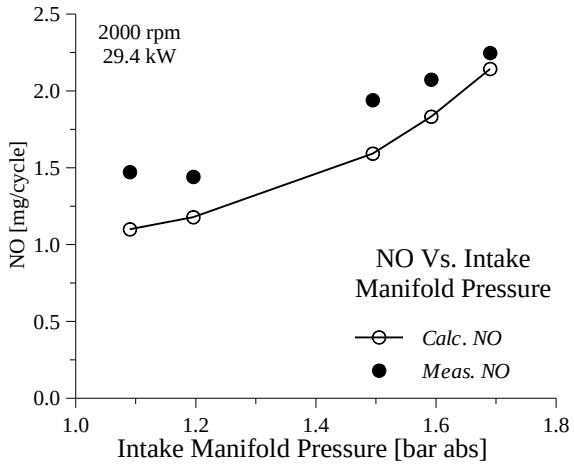

Σχήμα 4.40: Μεταβολή των NO με την πίεση του αέρα στην πολλαπλή εισαγωγής στις 2000 rpm & 29.4 kW για τον κινητήρα D2.

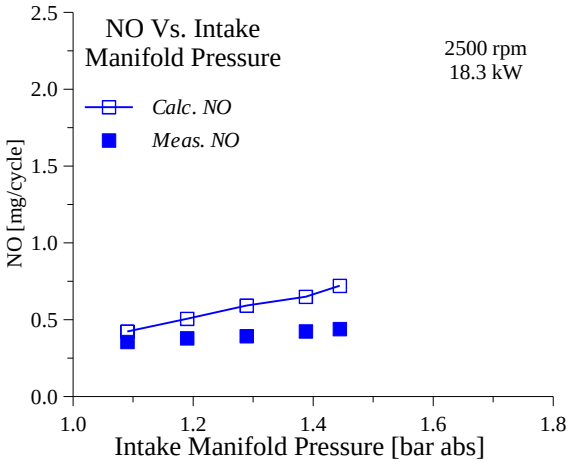

Σχήμα 4.41: Μεταβολή των NO με την πίεση του αέρα στην πολλαπλή εισαγωγής στις 2500 rpm & 18.3 kW για τον κινητήρα D2.

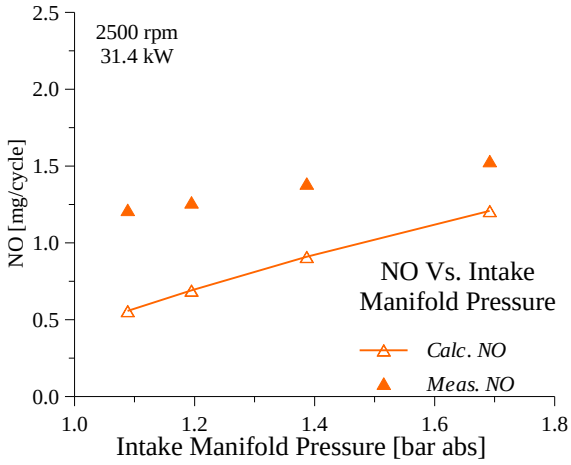

Σχήμα 4.42: Μεταβολή των NO με την πίεση του αέρα στην πολλαπλή εισαγωγής στις 2500 rpm & 31.4 kW για τον κινητήρα D2.

Από τα Σχ. 4.40 – 4.42 αποκαλύπτεται η ικανότητα του μοντέλου να προσεγγίσει ικανοποιητικά την τάση των *NO* με την πίεση του αέρα σάρωσης, παρότι παρατηρείται μια μικρή απόκλιση στις απόλυτες τιμές των *NO*. Η τάση αυτή είναι πρακτικά γραμμική με αύξουσα κλίση καθώς η πίεση του αέρα σάρωσης αυξάνει. Η κλίση αυτή μειώνεται με την αύξηση των στροφών και αυξάνεται με την αύξηση του φορτίου του κινητήρα.

Στη συνέχεια, υπολογίζεται το απόλυτο και σχετικό σφάλμα (Εξ. (4.1) και (4.2)) των αποτελεσμάτων του μοντέλου για τον κινητήρα D2. Στον Πίνακα 4.3, παρουσιάζεται

το ποσοστό από τις περιπτώσεις που εξετάστηκαν, των οποίων το σφάλμα εμπίπτει σε μια συγκεκριμένη ζώνη σφάλματος:

Περιπτώσεις	Σχετικό σφάλμα (±)	Απόλυτο σφάλμα (±)		
[%]	[%]	[mg/cycle]	[g/kg fuel]	[g/kWh]
1	0	0–0.00	0–0.0	0–0.0
26	0–5	0–0.02	0–0.3	0–0.1
43	0–10	0–0.04	0–0.5	0–0.1
57	0–15	0–0.07	0–0.9	0–0.2
67	0–20	0–0.09	0–1.1	0–0.3
78	0–25	0–0.14	0–2.2	0–0.5
79	0–30	0–0.20	0–2.2	0–0.5
89	0–35	0–0.35	0–3.4	0–0.8
93	0–50	0–0.45	0–4.2	0–1.0

Πίνακας 4.3: Ανάλυση σχετικού και απόλυτου σφάλματος των αποτελεσμάτων του μοντέλου για τον κινητήρα D2.

Από τον Πίνακα 4.3 φαίνεται ότι ένα μεγάλο ποσοστό που φτάνει το *67%* των περιπτώσεων που εξετάστηκαν παρουσιάζει σχετικό σφάλμα μέχρι ±*20%* το οποίο μπορεί να θεωρηθεί ικανοποιητικό για τη συγκεκριμένη εφαρμογή. Εδώ σημειώνεται ότι, όπως και στις περιπτώσεις του κινητήρα του φορτηγού, δεν έγινε βαθμονόμηση (δηλ. χρήση διορθωτικού πολλαπλασιαστή).

Όπως αποκαλύπτεται από τις πιο πάνω διερευνήσεις, παρά τα ικανοποιητικά αποτελέσματα στις τάσεις και απόλυτες τιμές των εκπομπών *NO* τόσο στους κινητήρες μεγάλης κλίμακας όσο και στους οδικούς κινητήρες, σε κάποιες από τις περιπτώσεις που εξετάστηκαν παρατηρήθηκαν κάποιες αποκλίσεις. Οι αποκλίσεις αυτές οφείλονται: σε διάφορα σφάλματα, στο σημείο που επιλέχθηκε να γίνει η βαθμονόμηση/διόρθωση (βλ. Εξ. (3.42)) των αποτελεσμάτων και στις πολύ χαμηλές απόλυτες τιμές *NO* ορισμένων περιπτώσεων, οι οποίες προκαλούν μεγέθυνση στο σχετικό σφάλμα (βλ. Εξ. (4.2))

Πιθανές πηγές σφάλματος είναι οι ακόλουθες: σφάλμα πρωτογενούς μέτρησης, επεξεργασία των μετρημένων δεδομένων, σφάλμα εκτίμησης της κατανάλωσης καυσίμου, της ισχύος και της παροχής μάζας καυσαερίου, σφάλματα στην ανάλυση του *HRR* και συνεπώς στον ρυθμό καύσης, στην εκτίμηση του *SOC*, *COC* και *EOC* και επιπλέον, αριθμητικά σφάλματα (π.χ. εξομάλυνση/φιλτράρισμα διαγραμμάτων, στρογγυλοποίηση, ολοκλήρωση, διαφόρηση, κ.λπ.) και σφάλματα από ανακριβή δεδομένα εισόδου (π.χ. ποσοστό *EGR*). Μια άλλη σημαντική πηγή σφάλματος είναι η ευαισθησία του μοντέλου στην παράμετρο «Φ_z», της οποίας η ορθή εκτίμηση εξαρτάται από τον ακριβή καθορισμό των μεταβλητών της. Οι μεταβλητές αυτές υπολογίζονται από την επεξεργασία του δυναμοδεικτικού διαγράμματος, την ανάλυση του *HRR* αλλά και από λειτουργικές παραμέτρους του κινητήρα.

Ιστορικό Σχηματισμού των NO

Όπως αναφέρθηκε, το μοντέλο παρέχει τη δυνατότητα υπολογισμού του ιστορικού του σχηματισμού των *NO* σε κάθε ζώνη καθώς και συνολικά του κυλίνδρου. Παρότι δεν υπήρχαν πειραματικά δεδομένα κατά τη διάρκεια του κλειστού κύκλου για την επικύρωση των αποτελεσμάτων, οι τάσεις του ιστορικού σχηματισμού των *NO* μέσα στον κύλινδρο είναι όμοιες με αντίστοιχες που μπορούν να βρεθούν στη βιβλιογραφία [8,109,153,183]. Αυτή η δυνατότητα επιτρέπει τη χρήση του μοντέλου σε διερεύνησης βελτιστοποίησης και ανάπτυξης σχετικά με τον έλεγχο του σχηματισμού των *NO* κατά τη διάρκεια ενός κύκλου (π.χ. βελτιστοποίηση στρατηγικής έγχυσης, κ.λπ.)

Στη συνέχεια παρουσιάζονται ενδεικτικά στο Σχήμα 4.43, αποτελέσματα για το ιστορικό του σχηματισμού των *NO* στον κύλινδρο για τέσσερεις διαφορετικούς τύπους κι-

νητήρων: ένα δίχρονο και ένα τετράχρονο που χρησιμοποιούνται σε σταθμό παραγωγής ενέργειας, ένα ναυτικό τετράχρονο που χρησιμοποιείται για ηλεκτροπαραγωγή σε πλοία και ένα δίχρονο ναυτικό που χρησιμοποιείται για την πρόωση πλοίου.

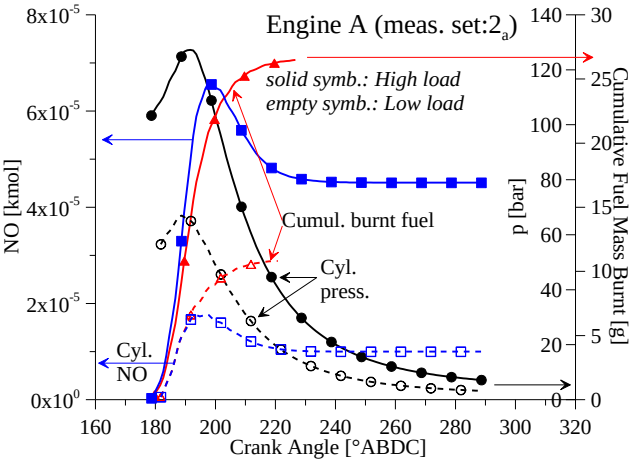

Δίχρονος κινητήρας DI Diesel σταθερών στροφών εγκατεστημένος σε σταθμό παραγωγής ενέργειας.

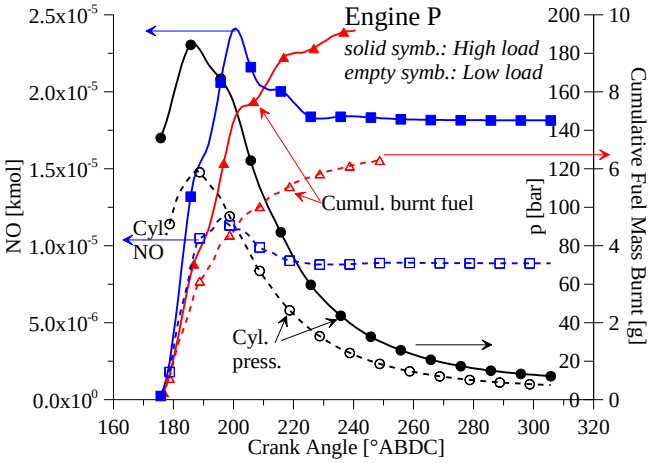

Τετράχρονος κινητήρας DI Diesel σταθερών στροφών εγκατεστημένος σε σταθμό παραγωγής ενέργειας.

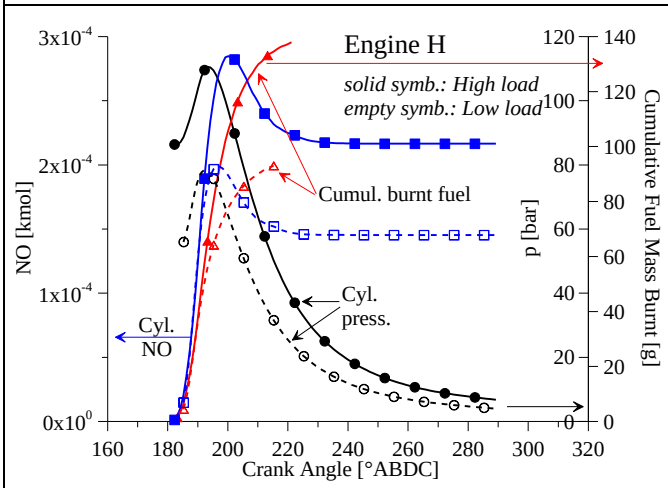

Δίχρονος ναυτικός κινητήρας DI Diesel για την πρόωση πλοίου.

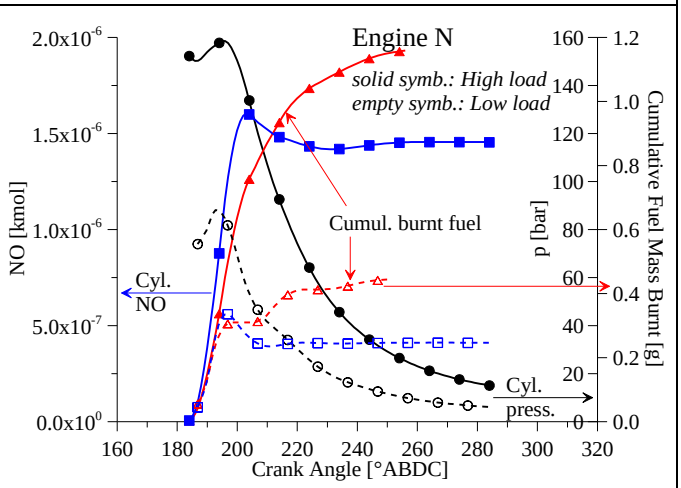

Τετράχρονος ναυτικός κινητήρας DI Diesel σταθερών στροφών για τις ανάγκες ηλεκτροδότησης πλοίου.

Σχήμα 4.43: Ιστορικό σχηματισμού των NO μέσα στο θάλαμο καύσης μαζί με την μεταβολή της πίεσης κυλίνδρου και του αθροιστικού ρυθμού καύσης κατά τη διάρκεια του κλειστού κύκλου σε συνάρτηση με τη μεταβολή του φορτίου του κινητήρα.

Στο Σχήμα 4.43 φαίνεται η επίδραση του φορτίου στο σχηματισμό των *NO*. Όπως αναμένεται ο σχηματισμός των *NO* αυξάνεται με την αύξηση του φορτίου. Επίσης παρατηρείται ότι μετά από κάποιο σημείο, ο σχηματισμός των *NO* «παγώνει», γεγονός που οφείλεται κυρίως στην πτώση της θερμοκρασίας και της διαθεσιμότητας οξυγόνου κατά τη φάση της εκτόνωσης.

Όπως ήδη αναφέρθηκε (Κεφάλαιο 3), το ιστορικό σχηματισμού των *NO* προκύπτει από το άθροισμα των *NO* που σχηματίζονται σε κάθε υπάρχουσα ζώνη κάθε χρονική

στιγμή (γωνία στροφάλου), δηλαδή από άθροισμα των ιστορικών των ζωνών, όπως φαίνεται στο Σχήμα 4.44.

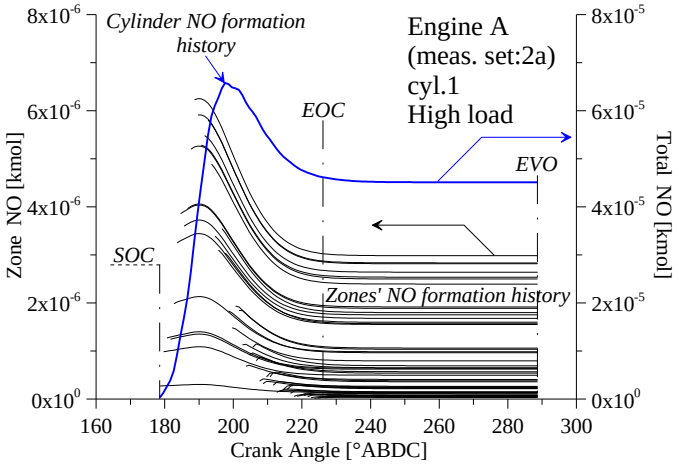

Σχήμα 4.44: Ιστορικό σχηματισμού των NO στις ζώνες (49) και αθροιστικά, το ιστορικό του σχηματισμού των NO στον κύλινδρο κατά τη διάρκεια του κλειστού κύκλου.

Το προτεινόμενο μοντέλο μπορεί να χρησιμοποιηθεί σε διερευνήσεις για την επίδραση διαφόρων παραμέτρων στον σχηματισμό των *NO* όπως η επίδραση της προπορείας

και πίεσης εγχύσεως, πίεσης υπερπλήρωσης, ποσοστού *EGR* κ.λπ. Ενδεικτικά, στο Σχήμα 4.45 παρουσιάζεται η επίδραση της καθυστέρησης έγχυσης στο σχηματισμό *NO*.

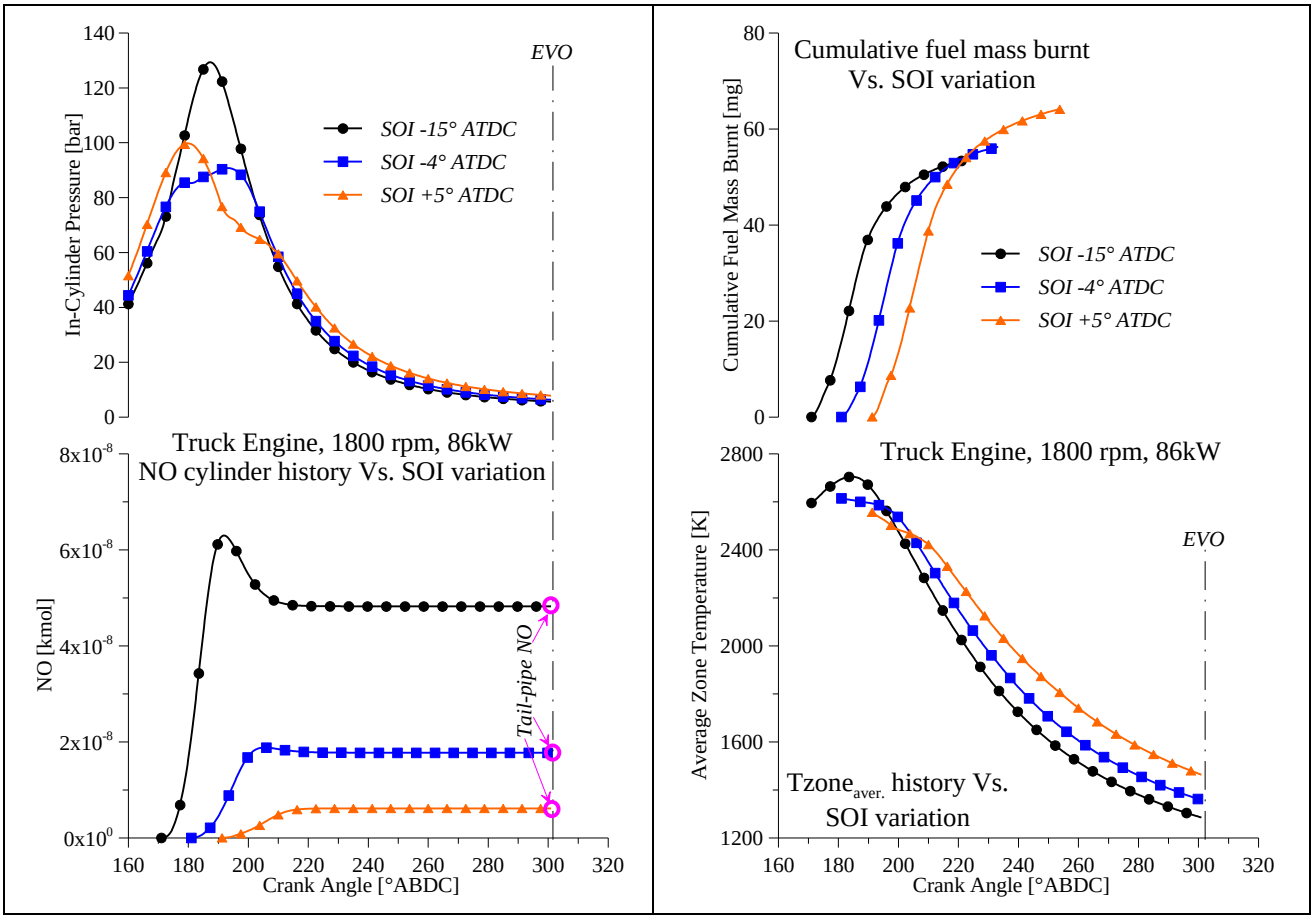

Σχήμα 4.45: Ιστορικό σχηματισμού των NO στο θάλαμο καύσης μαζί με την μεταβολή της πίεσης κυλίνδρου (αριστερά), του αθροιστικού ρυθμού καύσης κατά τη διάρκεια του κλειστού κύκλου και τη μέση (σταθμισμένη με τη μάζα) θερμοκρασία των ζωνών (δεξιά) συναρτήσει της μεταβολής της προπορείας εγχύσεως (SOI) για τον κινητήρα φορτηγού σε λειτουργία 1800 rpm και 86 kW.

Από το Σχήμα 4.45 είναι φανερή η πτώση της πίεσης (αφού ξεκινήσει η καύση) με την καθυστέρηση της έγχυσης. Αυτό μαζί με την συνεπακόλουθη καθυστέρηση έναυσης της καύσης προκαλεί χαμηλότερες θερμοκρασίες ζωνών στα πρώτα στάδια της καύσης (όπου ο σχηματισμός *NO* είναι σημαντικότερος). Επίσης, η καύση μεταφέρεται προς τα δεξιά, δηλαδή μικρότερη μάζα προϊόντων καύσης παραμένει σε συνθήκες υψηλών θερμοκρασιών όπου ευνοείται ο σχηματισμός των *NO*. Ακόμα ο χρόνος που τα προϊόντα της καύσης παραμένουν σε υψηλές θερμοκρασίες μειώνεται. Οι λόγοι αυτοί συντείνουν στη μείωση του σχηματισμού των *NO* με την καθυστέρηση έγχυσης.

Υπολογιστικός Χρόνος

Ένας από τους κύριους στόχους της παρούσας μελέτης είναι να διατηρηθεί ο υπολογιστικός χρόνος όσο το δυνατόν χαμηλότερα, αλλά διατηρώντας ένα ισχυρό φυσικό υπόβαθρο. Ο στόχος του χαμηλού υπολογιστικού κόστους έχει εν μέρει υλοποιηθεί γιατί παρόλο που το προτεινόμενο μοντέλο NO_x παρέχει τα αποτελέσματα σε περίοδο λίγων δευτερολέπτων και σε ορισμένες περιπτώσεις σε χρόνους χαμηλότερους και από δευτερόλεπτο,

υπάρχουν δυνατότητες, μετά από πρόσθετη ανάπτυξη και βελτίωση του μοντέλου, να παρέχει αποτελέσματα στη χρονική κλίμακα του κύκλου μηχανής. Προκειμένου να εντοπιστούν οι παράμετροι που επηρεάζουν σημαντικά τον υπολογιστικό χρόνο του μοντέλου, έγινε ανάλυση ευαισθησίας στις πιο κάτω παραμέτρους:

1. Λόγος ισοδυναμίας της ζώνης Φ_z.
2. Υπολογιστικό βήμα γωνίας στροφάλου (*CA*).
3. Υπολογιστικό βήμα ολοκλήρωσης που χρησιμοποιήθηκε στον υπολογισμό των NO_x.
4. Αριθμός των κυλίνδρων που χρησιμοποιήθηκαν στον υπολογισμό.
5. Ποσότητα της παγιδευμένης μάζας στον κύλινδρο.
6. Υπολογιστική ισχύς του συστήματος.

Από τη διερεύνηση της επίδρασης του Φ_z στον υπολογιστικό χρόνο, αποκαλύφθηκε ότι ο χρόνος αυτός αυξάνεται ελαφρώς με την αύξηση του Φ_z όταν είναι $\Phi_z < 1$ και μειώνεται εκθετικά, προσεγγίζοντας ασυμπτωτικά μια ελάχιστη τιμή, με την αύξηση του Φ_z όταν είναι $\Phi_z > 1$. Ωστόσο, στην περιοχή όπου $\Phi_z < 1$ ο υπολογιστικός χρόνος είναι πάντα χαμηλότερος από αυτή την τιμή. Η μέγιστη τιμή εμφανίζεται στο $\Phi_z = 1$. Αυτή η τάση οφείλεται στο χρόνο που απαιτείται για τη σύγκλιση του υπομοντέλου της χημικής ισορροπίας το οποίο έχει σημαντικό αντίκτυπο στο χρόνο σύγκλισης της μεθόδου υπολογισμού της θερμοκρασίας ζώνης.

Στη συνέχεια διερευνήθηκε η επίδραση του υπολογιστικού βήματος γωνίας στροφάλου (*CA*). Όπως αποκαλύφθηκε, ο υπολογιστικός χρόνος μειώνεται σημαντικά με την αύξηση του βήματος *CA* χωρίς σημαντική επιδείνωση του σχετικού σφάλματος. Βέβαια, όταν το βήμα γίνει υπερβολικά μεγάλο τότε το μοντέλο αποτυγχάνει να φτάσει σε σύγκλιση ή δίνει μη αποδεκτά αποτελέσματα.

Η διερεύνηση έδειξε επίσης ότι η επίδραση του βήματος ολοκλήρωσης (υποδιαιρέσεις του βήματος *CA*) για τον υπολογισμό των NO_x σε κάθε βήμα *CA* στον συνολικό υπολογιστικό χρόνο, είναι σχετικά μικρή (αν το βήμα ολοκλήρωσης δεν είναι υπερβολικά μικρό). Ωστόσο, μεγάλο βήμα ολοκλήρωσης μπορεί να οδηγήσει σε ανακριβείς προβλέψεις NO_x, ακόμα και σε αδυναμία σύγκλισης, ειδικότερα αν το υπολογιστικό βήμα *CA* είναι μεγάλο.

Στη συνέχεια, εξετάστηκε η επίδραση του αριθμού των κυλίνδρων που χρησιμοποιήθηκαν στους υπολογισμούς στον συνολικό υπολογιστικό χρόνο. Όπως αναμενόταν, ο υπολογιστικός χρόνος αυξάνεται γραμμικά με την αύξηση του αριθμού των κυλίνδρων. Ωστόσο το σχετικό σφάλμα δεν μεταβάλλεται σημαντικά, το οποίο υποδεικνύει ότι υπάρχει η δυνατότητα χρήσης μόνο ενός αντιπροσωπευτικού κυλίνδρου στους υπολογισμούς.

Η παγιδευμένη ποσότητα μάζας μέσα στον κύλινδρο επηρεάζει σημαντικά τον υπολογιστικό χρόνο, επειδή, σε συνδυασμό με τον λόγο ισοδυναμίας της ζώνης (Φ_z), επηρεάζουν τη σύγκλιση του μοντέλου. Παρατηρήθηκε ότι, όταν η παγιδευμένη μάζα υποεκτιμάται τότε η θερμοκρασία της άκαυστης ζώνης υπερεκτιμάται και συνεπώς προκαλεί υπερβολικές θερμοκρασίες στις ζώνες καύσης. Όπως παρατηρήθηκε, αυτός είναι ο λόγος που οι επαναληπτικές διαδικασίες που χρησιμοποιούνται στον υπολογισμό της θερμοκρασίας των ζωνών καύσης απαιτούν μεγαλύτερο χρονικό διάστημα για να συγκλίνουν. Όπως αποκαλύφθηκε, ο υπολογιστικός χρόνος μειώνεται σημαντικά με την αύξηση της παγιδευμένης

μάζας. Επίσης, αποκαλύφθηκε ότι μεγάλη υποεκτίμηση της παγιδευμένης μάζας οδηγεί σε αύξηση του σχετικού σφάλματος, ακόμα και σε αδυναμία σύγκλισης.

Στη συνέχεια, εξετάστηκε ενδεικτικά, η επίδραση του χρησιμοποιούμενου υπολογιστικού συστήματος στον υπολογιστικό χρόνο. Στη διερεύνηση αυτή το μοντέλο εφαρμόστηκε σε προσωπικούς υπολογιστές (*PC*) με διαφορετικές προδιαγραφές. Όπως αναμενόταν ο υπολογιστικός χρόνος μειώνεται όσο βελτιώνονται τα χαρακτηριστικά του υπολογιστικού συστήματος. Τα χαρακτηριστικά που φαίνεται να έχουν τη μεγαλύτερη επίδραση είναι το στάδιο ανάπτυξης/εξέλιξης του συστήματος (πόσο σύγχρονο είναι), η ταχύτητα του επεξεργαστή και η ταχύτητα της μνήμης *RAM*.

Κεφάλαιο 5 ΣΥΜΠΕΡΑΣΜΑΤΑ

Στο τελευταίο κεφάλαιο παρουσιάζονται τα τελικά συμπεράσματα αυτής της διατριβής, τα στοιχεία πρωτοτυπίας και οι προτάσεις για μελλοντική εργασία.

Το μοντέλο που αναπτύχθηκε είναι ένα ημιεμπειρικό μοντέλο, το οποίο διακριτοποιεί σε ζώνες το περιεχόμενο του κυλίνδρου ανάλογα με το ρυθμό καύσης, οι οποίες εξελίσσονται στο χρόνο επηρεαζόμενες από τη μεταβολή της πίεσης στο εσωτερικό του κυλίνδρου ακολουθώντας τον πρώτο θερμοδυναμικό νόμο, με σκοπό την πρόβλεψη του ιστορικού των NO_x μέσα στον κύλινδρο και των τελικών εκπομπών των NO_x σε κινητήρες *DI* Diesel. Ο αλγόριθμος του μοντέλου συντέθηκε σε γλώσσα προγραμματισμού FORTRAN.

Το μοντέλο εφαρμόστηκε σε διάφορους τύπους υπερπληρωμένων *DI* Diesel κινητήρων για διάφορες διαμορφώσεις και ρυθμίσεις του κινητήρα. Οι τύποι κινητήρων και οι παράμετροι που εξετάστηκαν είναι:

1. Δύο δίχρονοι κινητήρες μεγάλης κλίμακας, σταθερών στροφών, που χρησιμοποιούνται για ηλεκτροπαραγωγή στη Χίο. Μεταβολή του φορτίου, του χρονισμού έγχυσης και του τύπου του καυσίμου.
2. Ένας δίχρονος και ένας τετράχρονος κινητήρας μεγάλης κλίμακας, σταθερών στροφών, που χρησιμοποιούνται για ηλεκτροπαραγωγή στην Πάρο. Μεταβολή του φορτίου.
3. Εννέα βραδύστροφοι δίχρονοι κινητήρες μεγάλης κλίμακας που χρησιμοποιούνται για πρόωση πλοίων. Μεταβολή των στροφών/φορτίου, και για δύο από αυτές, μεταβολή του χρονισμού έγχυσης καυσίμου.
4. Τρεις τετράχρονοι κινητήρες μεγάλης κλίμακας, σταθερών στροφών που χρησιμοποιούνται για ηλεκτροπαραγωγή σε πλοία. Μεταβολή του φορτίου.
5. Ένας κινητήρας φορτηγού βαρέος τύπου. Μεταβολή φορτίου και στροφών (σύμφωνα με τον κύκλο *EESC*), χρονισμού και πίεσης έγχυσης καυσίμου, ποσοστού *EGR* και πίεσης αέρα σάρωσης.
6. Ένας κινητήρας αυτοκινήτου ελαφρού τύπου. Μεταβολή του χρονισμού και πίεσης έγχυσης καυσίμου, ποσοστού *EGR* και πίεσης αέρα σάρωσης.

Για την επικύρωση και αξιολόγηση του μοντέλου χρησιμοποιήθηκε ένα σύνολο *89* σημείων λειτουργίας για τους κινητήρες μεγάλης κλίμακας και *132* σημείων για τους οδικούς κινητήρες. Αναφορικά με τις απόλυτες τιμές των NO_x, μετά από βαθμονόμηση σε ένα μοναδικό σημείο λειτουργίας για κάθε κινητήρα, χρησιμοποιώντας ένα διορθωτικό συντελεστή (*SF*) – πολλαπλασιαστή (μόνο στους κινητήρες μεγάλης κλίμακας), το μοντέλο καταφέρνει να προβλέψει τα NO_x με σχετικό σφάλμα μέχρι $\pm 20\%$ για την πλειονότητα των περιπτώσεων και για όλους τους τύπους κινητήρων που εξετάστηκαν. Επιπλέον, ο υπολογιστικός χρόνος κυμάνθηκε, αναλόγως της εξεταζόμενης περίπτωσης, από *10 s* μέχρι και *1 s* όταν ο αλγόριθμος εκτελείται σε ένα σύγχρονο *PC*. Ωστόσο υπάρχουν δυνατότητες για μείωση του χρόνου αυτού.

Τα αποτελέσματα από την εφαρμογή του μοντέλου σε αυτές τις μηχανές είναι ενθαρρυντικά, αφού όπως αποκαλύφθηκε είναι ικανό να προβλέπει επαρκώς τις μετρημένες τιμές των NO_x και επίσης, να συλλαμβάνει την τάση μεταβολής τους καθώς οι παράμετροι και οι ρυθμίσεις του κινητήρα μεταβάλλονται. Το πιο σημαντικό είναι ότι καταφέρνει να παρέχει αξιόπιστα αποτελέσματα με χαμηλό υπολογιστικό κόστος, για διαφορετικούς τύπους κινητήρων με χαμηλές απαιτήσεις βαθμονόμησης. Έτσι, μετά από πρόσθετη ανάπτυξη, μπορεί να χρησιμοποιηθεί στην έρευνα αλλά και στο πρακτικό πεδίο.

Το μοντέλο μπορεί να προταθεί για να συνεισφέρει στην έρευνα και ανάπτυξη αλλά και στη λειτουργία και έλεγχο των τεχνικών και τεχνολογιών για τη μείωση των εκπομπών από τους κινητήρες *DI* Diesel.

Ωστόσο η ανάπτυξή τους απαιτεί εκτεταμένη έρευνα η οποία έχει μεγάλο οικονομικό κόστος, απαιτεί χρόνο και κόπο ειδικά αν βασίζεται μόνο σε πειραματικές διερευνήσεις. Επίσης ο έλεγχος και η παρακολούθηση της λειτουργίας τους σε πραγματικό χρόνο γίνεται άμεση ανάγκη τα τελευταία χρόνια λόγω και της αυστηροποίησης των τοπικών και διεθνών κανονισμών για τους ρύπους. Για τους λόγους αυτούς οι κατασκευαστές και χρήστες *ICE* εμπλέκουν εργαλεία προσομοίωσης σε συνδυασμό με πειραματική διερεύνηση, ώστε να ενισχυθεί ο σχεδιασμός και η ανάπτυξη και να βελτιωθεί η απόδοση λειτουργίας των τεχνολογιών για τον περιορισμό των εκπομπών NO_x, αλλά την ίδια ώρα, στοχεύοντας στο βέλτιστο δυνατό ισοζύγιο NO_x, αιθάλης και κατανάλωσης καυσίμου (*bsfc*). Αυτά αποτέλεσαν το κίνητρο για την ανάπτυξη ενός μοντέλου NO_x με δυνατότητες αξιόπιστης πρόβλεψης.

Για το σκοπό αυτό, το μοντέλο που αναπτύχθηκε έχει φυσικό υπόβαθρο και χρησιμοποιεί το μετρημένο δυναμοδεικτικό διάγραμμα το οποίο παρέχει με αμεσότητα σημαντικές πληροφορίες για την εξέλιξη της καύσης και συνεπώς τον σχηματισμό των NO_x μέσα στον κύλινδρο. Οι πολύπλοκοι μηχανισμοί της καύσης, των οποίων η μοντελοποίηση είναι ιδιαίτερα δύσκολη και απαιτεί μεγάλο υπολογιστικό κόστος, μπορούν να ληφθούν άμεσα υπόψη με τη χρήση της μετρημένης πίεσης του κυλίνδρου. Επιπρόσθετα, με τη χρήση του μετρημένου δυναμοδεικτικού διαγράμματος, η επίδραση της γεωμετρίας του κινητήρα λαμβάνεται υπόψη έμμεσα.

Εν τέλει, λαμβάνοντας υπόψη τις δυνατότητες του μοντέλου, δηλαδή την ικανότητά του να προβλέπει αξιόπιστα και με χαμηλό υπολογιστικό κόστος τις εκπομπές των NO_x και την τάση μεταβολής τους καθώς οι παράμετροι ή/και οι ρυθμίσεις του κινητήρα μεταβάλλονται για διάφορους τύπους κινητήρων, μπορεί να προταθεί, μετά από περαιτέρω ανάπτυξη και βελτιστοποίηση, για χρήση στις ακόλουθες εφαρμογές:

1. Παρακολούθηση σε πραγματικό χρόνο των εκπομπών NO_x σε πλοία και σταθμούς παραγωγής ενέργειας.
2. Πρόβλεψη των NO_x σε σημεία λειτουργίας που απαιτούνται από τον κανονισμό «*IMO Annex VI regulation 13*», στα οποία δεν είναι δύσκολο να γίνουν μετρήσεις, προκειμένου να συμπληρωθεί το αντίστοιχο πιστοποιητικό NO_x.
3. Άμεση παρακολούθηση των εκπομπών NO_x σε πλοία με απευθείας σύνδεση (online), αφού η άμεση μέτρηση του δυναμοδεικτικού και η απευθείας δικτυακή σύνδεση είναι σήμερα εφικτή.

4. Διαδικασίες επαλήθευσης για τις εκπομπές NO_x, π.χ. επαλήθευση των προδιαγραφών NO_x (π.χ. εκείνων που δίνει ο κατασκευαστής) ή επαλήθευση/σύγκριση μετρήσεων εκπομπών NO_x.
5. Πρόβλεψη της απόκλισης των εκπομπών NO_x από τις τιμές των ορίων που καθορίζονται από τους κανονισμούς για ένα εν λειτουργία κινητήρα, εάν μεταβληθούν οι συνθήκες λειτουργίας του.
6. Υποστήριξη της ανάπτυξης, λειτουργίας και ελέγχου και βελτιστοποίησης σε πραγματικό χρόνο των πρωτογενών μέτρων για μείωση των εκπομπών NO_x (π.χ. model–base control).
7. Συνεισφορά στη διαχείριση των δευτερογενών μέτρων για μείωση των εκπομπών NO_x (π.χ. closed–loop control).
8. Συνεισφορά στο πεδίο της έρευνας, ανάπτυξης και βελτιστοποίησης υπάρχοντος κινητήρα αναφορικά με τις εκπομπές NO_x (π.χ. βελτιστοποίηση της στρατηγικής έγχυσης, ποσοστού *EGR*, κ.λπ.).

Σε αυτή την εργασία συνδυάστηκαν στοιχεία από τη σχετική βιβλιογραφία, καινούριες μεθοδολογίες και εκτενής στατιστική ανάλυση πειραματικών δεδομένων, με σκοπό τη δημιουργία ενός νέου χρήσιμου εργαλείου προσομοίωσης για την πρόβλεψη των εκπομπών NO_x από κινητήρες *DI* Diesel. Το νέο μοντέλο συνδυάζει επιτυχώς φυσικούς νόμους και εμπειρικές/στατιστικές συσχετίσεις με μια απλοποιημένη δομή, παρέχοντας αξιόπιστες προβλέψεις εκπομπών NO_x και μεγάλο εύρος εφαρμογής όσο αφορά τους τύπους κινητήρων και συνθηκών/ρυθμίσεων λειτουργίας. Στη συνέχεια παρουσιάζονται τα στοιχεία πρωτοτυπίας της παρούσας διατριβής:

1. Ένα νέο, απλοποιημένο πολυζωνικό σενάριο υιοθετήθηκε για τον υπολογισμό των εκπομπών *NO* (ή ισοδύναμου NO_x) και του ιστορικού του σχηματισμού τους στο εσωτερικό του κυλίνδρου κατά τη διάρκεια του κλειστού θερμοδυναμικού κύκλου, χωρίς να χρησιμοποιούνται πολύπλοκες φαινομενολογικές σχέσεις στους υπολογισμούς.
2. Στους υπολογισμούς που πραγματοποιούνται στο μοντέλο, χρησιμοποιείται η μετρημένη πίεση του κυλίνδρου και ο ρυθμός έκλυσης θερμότητας (υπολογίζεται με τη χρήση του μετρημένου δυναμοδεικτικού), πάνω στα οποία αντικατοπτρίζεται η επίδραση των μηχανισμών που εξελίσσονται στον κύλινδρο και επηρεάζουν άμεσα ή έμμεσα το μηχανισμό σχηματισμού των NO_x.
3. Μια νέα προσέγγιση χρησιμοποιήθηκε για τον προσδιορισμό του λόγου ισοδυναμίας Φ_z που χρησιμοποιείται στους υπολογισμούς της ζώνης. Το Φ_z έχει σημαντικό αντίκτυπο στην καύση και συνεπώς στη χημική σύσταση και θερμοκρασία της ζώνης.
4. Από την ανασκόπηση της βιβλιογραφίας, προκύπτει ότι για πρώτη φορά ένα μοντέλο προσομοίωσης για τις εκπομπές NO_x εφαρμόστηκε σε ένα τέτοιο μεγάλο αριθμό τύπων κινητήρων, σημείων λειτουργίας και διαμορφώσεων κινητήρα.
5. Το μοντέλο έχει μικρές απαιτήσεις βαθμονόμησης προκειμένου να βελτιωθούν ποσοτικά τα αποτελέσματα που εξαγάγει. Συγκεκριμένα, χρησιμοποιείται μόνο ένας πολλαπλασιαστής για κάθε κινητήρα (μόνο στους κινητήρες μεγάλης κλίμακας) προκειμένου να διορθωθούν οι υπολογισμένες τιμές NO_x.
6. Μια νέα μεθοδολογία αναπτύχθηκε για τον προσδιορισμό της έναρξης της καύσης (*SOC*). Όπως αποκαλύφθηκε, ο προσδιορισμός του *SOC*, που είναι μια εντελώς αυτοματοποιημένη διαδικασία, ήταν ακριβής για σχεδόν όλα τα σημεία λειτουργίας που εξετάστηκαν.

7. Μια νέα μεθοδολογία ακολουθήθηκε για τον προσδιορισμό του τέλους της καύσης (*EOC*) από την επεξεργασία της ουράς του διαγράμματος *HRR* χρησιμοποιώντας επιπρόσθετη εξομάλυνση και στατιστικές τεχνικές.
8. Όσον αφορά στους δίχρονους κινητήρες, ένα νέο μοντέλο σάρωσης χρησιμοποιήθηκε για τον υπολογισμό των αρχικών συνθηκών (παγιδευμένη μάζα γόμωσης, η σύνθεση και η θερμοκρασία της και το κλάσμα μάζας *RG*) κατά την έναρξη της συμπίεσης.

Παρά τις επαρκείς προβλέψεις των εκπομπών *NO* (ή ισοδύναμου NO_x) που το προτεινόμενο μοντέλο μπορεί να παρέχει, υπάρχει η προοπτική για περαιτέρω βελτίωσή του μετά από επιπλέον ανάπτυξη προκειμένου να ενισχυθεί η αξιοπιστία του, να ελαχιστοποιηθεί το υπολογιστικό του κόστος και να εμπλουτιστούν/επεκταθούν οι δυνατότητές του.

Για την ενίσχυση της αξιοπιστίας και ευελιξίας του μοντέλου, οι ακόλουθες τροποποιήσεις/προσθήκες μπορούν να υιοθετηθούν:

1. Αναφορικά με τον υπολογισμό των NO_x μπορούν να εισαχθούν επιπρόσθετοι μηχανισμοί σχηματισμού NO_x όπως ο μηχανισμός μέσω των ενδιάμεσων N_2O ο οποίος γίνεται σημαντικός σε χαμηλές θερμοκρασίες ($T < 1800\ K$) και ο μηχανισμός σχηματισμού NO_x από το άζωτο του καυσίμου, ο οποίος μπορεί να συνεισφέρει σημαντικά σε περιπτώσεις χρήσεως βαρέος καυσίμου (*HFO*) που χρησιμοποιείται στους ναυτικούς κινητήρες και σε αυτούς που χρησιμοποιούνται στην ηλεκτροπαραγωγή. Επίσης, μπορούν να χρησιμοποιηθούν ακόμα πιο πολύπλοκοι μηχανισμοί και να εισαχθούν θεωρήσεις χημικής κινητικής για περισσότερα στοιχεία/αντιδράσεις.
2. Λόγω της μεγάλης σημαντικότητας της χρήσης του δυναμοδεικτικού διαγράμματος στους υπολογισμούς του μοντέλου είναι σημαντικό, η εξομάλυνσή του να γίνει ορθά προκειμένου να απαλειφθεί ο θόρυβος αλλά και να μην χαθεί χρήσιμη πληροφορία. Στην παρούσα μελέτη χρησιμοποιήθηκε το φίλτρο Savitzky–Golay με σταθερό πλάτος του παραθύρου εξομάλυνσης. Ωστόσο, για πιο ακριβή/αξιόπιστα αποτελέσματα, μπορούν να χρησιμοποιηθούν πιο αποδοτικά φίλτρα μεταβαλλόμενης, μέσα στη διάρκεια ενός κύκλου, έντασης και πλάτους παραθύρου εξομάλυνσης.
3. Όπως αποκαλύφθηκε από τη διερεύνηση, ο λόγος ισοδυναμίας των ζωνών Φ_z είναι καθοριστικής σημασίας για το μοντέλο και μπορεί να χρησιμοποιηθεί σαν ρυθμιστής του μοντέλου που μπορεί να βελτιώσει ποιοτικά τα αποτελέσματα. Για τον υπολογισμό του χρησιμοποιήθηκε μια εμπειρική συσχέτιση. Παρά το γεγονός ότι αυτή η συσχέτιση προήλθε από μια διεξοδική στατιστική διερεύνηση, απαιτείται περαιτέρω επικύρωσή της με χρήση ακόμα περισσότερων πειραματικών περιπτώσεων. Επιπλέον, θα πρέπει να εξεταστεί η χρήση πιο πολύπλοκων πολυωνύμων (αντί της γραμμικής που χρησιμοποιείται εδώ) και επίσης θα μπορούσε να γίνει διερεύνηση με σκοπό να εξεταστεί η πιθανότητα εμπλουτισμού ή τροποποίησης της συσχέτισης αυτής λαμβάνοντας υπόψη νέες παραμέτρους.
4. Προκειμένου να ενισχυθεί η φυσική του μοντέλου όσον αφορά στον προσδιορισμό του Φ_z, μπορεί να εισαχθεί μια νέα συσχέτιση που θα παρέχει μεταβλητή τιμή στο Φ_z κατά τη διάρκεια του κύκλου του κινητήρα (σε αντίθεση με το παρόν

όπου το Φ_z είναι σταθερό) ώστε να αντιπροσωπεύει, με μεγαλύτερη συνέπεια φυσικής, το μέσο πραγματικό τοπικό Φ, το οποίο καθορίζει τη σύσταση του μείγματος καυσίμου/αέρα. Αυτή η σύσταση μετατρέπεται από πολύ πλούσια σε καύσιμο στην αρχή της καύσης, σε πολύ φτωχή όπως εξελίσσεται η καύση και παραμένει κοντά στην στοιχειομετρία αργά στη φάση καύσης/εκτόνωσης. Το σκεπτικό αυτό μπορεί να προσεγγιστεί χρησιμοποιώντας μια σιγμοειδή συνάρτηση.

5. Όπως αποκαλύφθηκε από την ανάλυση του μοντέλου και των αποτελεσμάτων, η μεθοδολογία που ακολουθήθηκε για τη μεταφορά θερμότητας μεταξύ των ζωνών και των τοιχωμάτων του κυλίνδρου, παρότι ενισχύει το φυσικό υπόβαθρο του μοντέλου, παρουσιάζει ευαισθησία σε ανακριβή δεδομένα εισόδου και στον θόρυβο του σήματος της πίεσης του κυλίνδρου και έτσι μπορεί να εισαγάγει σημαντικό σφάλμα στα αποτελέσματα. Για το λόγο αυτό, μπορεί να χρησιμοποιηθεί στο μέλλον μια απλούστερη μεθοδολογία. Δηλαδή, θα μπορούσε να θεωρηθεί ότι ένα σταθερό ποσοστό της ενέργειας του καυσίμου της ζώνης χάνεται ως απώλεια θερμότητας. Εναλλακτικά θα μπορούσε να χρησιμοποιηθεί μια εμπειρική συσχέτιση για τον προσδιορισμό του ποσοστού αυτού.

Για τη μείωση του υπολογιστικού χρόνου του μοντέλου, προτείνονται τα ακόλουθα μέτρα:

1. Για να αποφευχθεί η χρήση των πολυωνύμων για τον υπολογισμό των ενθαλπιών (h) ειδικών θερμοχωρητικοτήτων (cp) και της ελεύθερης ενέργειας Gibbs (g^0), τα οποία αυξάνουν τον υπολογιστικό χρόνο, μπορούν εναλλακτικά να χρησιμοποιηθούν θερμοδυναμικοί πίνακες (JANAF) για κάθε χημικό στοιχείο που λαμβάνεται υπόψη. Ωστόσο, για να είναι γρήγορη η μέθοδος αυτή, απαιτείται αποδοτική διαχείριση μνήμης και βάσης δεδομένων.
2. Το προτεινόμενο μοντέλο προκειμένου να διατηρήσει ένα ισχυρό φυσικό υπόβαθρο δεν υιοθέτησε απλοποιητικές παραδοχές για τις θερμοδυναμικές διαδικασίες που χρησιμοποιούνται για τον υπολογισμό του όγκου, της θερμοκρασίας και εμμέσως της σύστασης της ζώνης, τα οποία επηρεάζουν τον σχηματισμό NO. Ωστόσο, οι υπολογισμοί αυτοί επιτυγχάνονται μέσω χρονοβόρων επαναληπτικών διαδικασιών. Έτσι, θα πρέπει να εξεταστεί η εισαγωγή παραδοχών όπως αδιαβατική, ισεντροπική/πολυτροπική, ισοβαρής διαδικασία/μεταβολή, με σκοπό τη μείωση του υπολογιστικού χρόνου.
3. Κατά τους υπολογισμούς του μοντέλου πραγματοποιείται ένας μεγάλος αριθμός πράξεων μεταξύ πινάκων/διανυσμάτων οι οποίες όμως εκτελούνται σειριακά. Ως εκ τούτου προτείνεται η παραλληλοποίηση του αλγορίθμου η οποία θα μειώσει σημαντικά το υπολογιστικό κόστος. Προφανώς, προκειμένου να αξιοποιηθεί η ικανότητα του παραλληλοποιημένου αλγορίθμου για μειωμένο χρόνο εκτέλεσης, πρέπει να τρέχει σε υπολογιστικό σύστημα με πολλαπλές κεντρικές μονάδες επεξεργασίας (*CPUs*) ή αντίστοιχα με μονάδες επεξεργασίας γραφικών (*GPU*), κ.λπ.
4. Προγραμματιστική βελτιστοποίηση του μοντέλου και αναβάθμιση της διαχείρισης μνήμης μπορούν να συνεισφέρουν στη μείωση του υπολογιστικού χρόνου.
5. Χρήση λιγότερο αυστηρών κριτηρίων σύγκλισης στις επαναληπτικές διαδικασίες που χρησιμοποιούνται.

6. Ο αλγόριθμος του μοντέλου χρησιμοποιεί διπλής ακρίβειας (*64 bit*) υπολογισμούς. Αν αντί αυτού χρησιμοποιούνταν απλή ακρίβεια (*32 bit*), ο υπολογιστικός χρόνος θα μειωνόταν σημαντικά, δεδομένου ότι οι απαιτήσεις επεξεργασίας και μνήμης θα είναι χαμηλότερες.
7. Μια από τις πιο χρονοβόρες διαδικασίες κατά τους υπολογισμούς του μοντέλου είναι η επίλυση του μη γραμμικού συστήματος για τον υπολογισμό της σύστασης ισορροπίας της ζώνης. Το σύστημα αυτό λύνεται, μετά από γραμμικοποίηση και απλοποίηση, με τη χρήση της μεθόδου απαλοιφής Gauss. Ωστόσο μπορούν να χρησιμοποιηθούν ταχύτερες τεχνικές, όπως π.χ. η διάσπαση LU για να μειωθεί ο υπολογιστικός χρόνος.
8. Το υπολογιστικό κόστος μπορεί να μειωθεί ουσιαστικά με τη χρήση προηγμένων υπολογιστικών συστημάτων, δηλαδή ταχύτερη μνήμη *RAM* και μνήμη μόνιμης αποθήκευσης (π.χ. solid state drives), πιο γρήγορους και σύγχρονους επεξεργαστές (*CPU*) με μεγάλο αριθμό αριθμητικών μονάδων, γρήγορο δίαυλο συστήματος, κ.λπ.
9. Μια άλλη προοπτική για μείωση του υπολογιστικού χρόνου, είναι να διασπαστεί ο αλγόριθμος σε τμήματα (δηλ. σε υπομοντέλα, ή ομάδες υπομοντέλων) τα οποία μπορούν να ενσωματωθούν σε ξεχωριστά εξειδικευμένα αυτόνομα υπολογιστικά συστήματα. Τα συστήματα αυτά θα είναι συζευγμένα υπό έναν διαχειριστή. Τέτοια υπολογιστικά συστήματα είναι τα συστήματα ολοκληρωμένων κυκλωμάτων για ειδικές εφαρμογές (*ASIC*) και οι προγραμματιζόμενες πύλες πεδίου (*FPGA*).

Δεδομένου ότι το προτεινόμενο μοντέλο συνιστάται για ολοκληρωμένες εφαρμογές στην έρευνα ή/και στο πρακτικό πεδίο, στο μέλλον θα μπορούσε να εμπλουτιστεί με επιπλέον υπομοντέλα/συστήματα, ώστε να είναι σε θέση να εφαρμοστεί αυτόνομα, να αυξήσει την ευελιξία και τη δυνατότητα εφαρμογής του και να μην επηρεάζεται από πιθανά εξωτερικά σφάλματα (π.χ. ανακριβή δεδομένα εισόδου). Τα προτεινόμενα νέα υπομοντέλα/συστήματα θα μπορούσαν να είναι τα εξής:

1. Σύστημα λήψης του δυναμοδεικτικού διαγράμματος.
2. Εξομάλυνση του αναλογικού σήματος πίεσης χρησιμοποιώντας συστήματα αναλογικών χαμηλοπερατών φίλτρων.
3. Θερμοδυναμικό μοντέλο ή ηλεκτρομηχανικό σύστημα για τον προσδιορισμό του *TDC* και συνεπώς αντιστοίχιση της πίεσης και της γωνίας στροφάλου (*CA*).
4. Απλοποιημένο μονοζωνικό μοντέλο προσομοίωσης για την πρόβλεψη του δυναμοδεικτικού διαγράμματος ώστε να χρησιμοποιηθεί έναντι του μετρούμενου, όταν αυτό δεν είναι διαθέσιμο. Ιδανικά, αυτό το μοντέλο θα πρέπει να έχει τη δυνατότητα να συλλαμβάνει τις μεταβολές στις ρυθμίσεις του κινητήρα, π.χ. *SOI*, ποσοστό *EGR*, πίεση υπερπλήρωσης/σάρωσης, κ.λπ.
5. Μοντέλο για την εκτίμηση της παροχής καυσίμου ή στην ιδανική περίπτωση, σύστημα για την άμεση μέτρησή της.
6. Μοντέλο σε συνδυασμό με αισθητήρες (π.χ. για τη μέτρηση της πίεσης και θερμοκρασίας στην πολλαπλή εισαγωγής, του O_2 στα καυσαέρια, κ.λπ.) για την εκτίμηση της ροής μάζας εισερχομένου αέρα.
7. Μοντέλο για την εκτίμηση των αρχικών συνθηκών στην πολλαπλής εισαγωγής (π.χ. προσομοίωση του ανοικτού κύκλου του κινητήρα) ή σύστημα μέτρησής τους ή συνδυασμός των δύο.

Παρόλα αυτά, υπάρχει η δυνατότητα, το προτεινόμενο μοντέλο να ενσωματωθεί σε υφιστάμενα, επικυρωμένα συστήματα λογισμικού και τεχνικού εξοπλισμού που χρησιμοποιούνται για την ανάλυση της απόδοσης του κινητήρα και των εκπομπών, στη διάγνωση και τον έλεγχο του κινητήρα.